Geometry, architecture and the erosive nature of mass-transport deposits in deep-marine environments: Ainsa Basin (Pyrenees) and Buzzard Field (North Sea)

Thesis submitted for examination for the award of Doctor of Philosophy (PhD)

University College London

Nicola Claire Dakin

MESci Cardiff University

2016

DECLARATION

I, Nicola Claire Dakin, confirm that the work presented in this thesis is my own. Where information has been derived from other sources, I confirm that this has been indicated in the thesis.

Nicola Claire Dakin.

April 2016

TABLE OF CONTENTS

TITLE PAGE

DECLARATION

ABSTRACT

ACKNOWLEDGMENTS

TABLE OF CONTENTS

LIST OF FIGURES

LIST OF TABLES

APPENDICES

LIST OF ACROYNMS

ABSTRACT

Muddy mass-transport deposits (MTDs) and complexes (MTCs) form a significant component of the stratigraphic record in modern and ancient deep-water basins worldwide. This study evaluates the sedimentary characteristics and architecture of such deposits from ancient deep-marine submarine fans and related deposits in the Middle-Eocene Ainsa Basin, Spanish Pyrenees and the Late Jurassic Buzzard Field, North Sea.

Outcrop measurements and descriptions have provided quantitative and semi-quantitative analyses to investigate the spatial and temporal distribution of these chaotic deposits across the Ainsa Basin, culminating in a new mass-transport classification scheme. Outcrops have provided important insights into mass-wasting processes, including the erosive nature at the base of cohesive flows, where associated erosive mechanisms are documented in the rock-record. Thin-section analyses of such erosive deposits show 'grading' of cohesive-flow deposits, interpreted as debris flows and concentrated density flows that entrained loosely consolidated sands on the seafloor. In some cases, deposits incorporate the compositional signature of the eroded sandy sediment gravity flow (SGF) deposit. Larger erosive features (megascours ~ 1 km width), formed from multiple mass-wasting events, are identified at outcrop to dramatically impact basin stratigraphy. MTDs appear to have been most erosive when they encountered changes in gradient, or when they accelerated and/or travelled at high velocity with high shear stresses, such as in a proximal submarine setting. The implications of erosive-flow processes are important for the degradation of sandstone reservoirs and the potential formation of mud-filled channels.

Core images and wireline data from the Buzzard Field formed the basis of a sedimentological interpretation of the hydrocarbon field, leading to an improved understanding of thickness variability across the field. Comparisons of the Buzzard and Ainsa basins suggest that regional and local tectonics played an important part in causing sediment instability on the basin slopes, and contributed to the abrupt termination of sand deposition in the basin.

Variable scales of mass-failure are considered as part of this study. Geometrical relationships of global deposits, and those documented in this research are compared. Results show outcrop measurements capture small-scale heterogeneities not observed in seismic datasets. Outcrop MTC dimensions (multiple stacked chaotic deposits) provide better parametres when scaling to seismic-scale analogues, such as for the Buzzard Field.

ACKNOWLEDGEMENTS

Firstly, I would like to thank my supervisor Professor Kevin Pickering for the opportunity to carry out this research study. The spectacular geology of Ainsa will forever contribute to my knowledge and understanding of deep-marine systems. Along my way, I have even learnt a little about wine. Kevin, your next bottle of *Ribero Del Duero* is on me.

This research was made possible from CNOOC-Nexen and partners. Dr. John Millington, thank you for your advice and also for the opportunity to undertake a 3-month internship at CNOOC-Nexen, which has progressed into my new career. To Cai Puigdefábregas, the short amount of time we spent together in the field was some of the most inspiring. Thank you for your time and sharing your geological wisdom, I hope that our paths will cross again. To Jim, thanks for your help with preparing thin-sections. To Maz, thank you for use of equipment in Birkbeck that was crucial for laboratory analysis.

Finishing this project has been a huge personal achievement and there are many people I am indebted to for countless words of encouragement. Mum, Dad, in those times I wasn't sure why I even decided to embark upon a PhD, I can fully assure you it was worth it in the end. I am forever grateful for your support throughout. A special thanks goes to Blanca. Your endless optimism and creative ideas for entertaining us on rainy days made field seasons in the mountains some of the most memorable. I still think a career in music video production is something you should consider. To Charo, Diego and family, thank you for your kind hospitality over the years and allowing us to take over both your flats with our field equipment. To Simon and Sarah-Jane, your patience of seemingly endless months of point-counting was quite impressive, thank you! To my fellow postgraduate friends Dr. Alexis, Dr. Mike, Dr. Marie, Dr. Verity, Dr. Jen and friends at UCL, we made it! To Emily, Kate, Matt, Sarah, Tess, Carys, Jude, Amy, Vicky, Miriam and friends outside UCL, you guys all made it possible through the challenging times. I hope to see you all soon. To my colleagues at Nexen, thank you for the encouragement and endless cakes over the past year, it really has helped.

Finally, my last acknowledgment is to Stuart Gibson. Of course I was joking when I said you weren't getting an acknowledgement, you even get your own paragraph. Your endless support and confidence in me to continue to the end has been unprecedented. Thank you for looking after me, especially towards the end of this project. Here's to a new chapter in our lives.

TABLE OF CONTENTS

CHAPTER 1 – INTRODUCTION **27**

1.1. INTRODUCTION **27**

1.1.1. Characterisation of MTDs and MTCs **30**

1.1.2. Deep-marine deposits in this study **34**

1.2. STUDY AREA: THE EOCENE AINSA BASIN, SPANISH PYRENEES **37**

1.2.1. Geographical setting **37**

1.2.2. The Pyrenean Orogeny **38**

1.3. GEOLOGICAL SETTING AND DEPOSITONAL ENVIRONMENTS **39**

1.3.1. South-central Pyrenees **39**

1.3.2. Deltaic to abyssal environments **45**

1.3.2.1. The Tremp-Graus Basin 45

1.3.2.2. The Ainsa Basin 46

1.3.2.2.1. Peri-Ainsa Basin carbonate platform 49

1.3.2.2.2. Resedimented carbonate deposits 50

1.3.2.3. The Jaca Basin 50

1.3.2.3.1. Outer-fan and basin-floor facies 50

1.3.3. Sedimentary systems of the Ainsa Basin **51**

1.3.4. The Lower Hecho Group **52**

1.3.4.1. Fosado (F-1, F-II) 52

1.3.4.2. Los Molinos (LM-1, LM-II) 52

1.3.4.3. Arro (Ar-I, Ar-II) 52

1.3.4.4. Gerbe (Ge-I, Ge-II) 52

1.3.5. The Upper Hecho Group **54**

1.3.5.1. Banastón (B-I, B-II, B-III, B-IV, B-V, B-VI) 54

1.3.5.2. Ainsa (A-I, A-II, A-III) 54

1.3.5.3. Morillo (M-I, M-II, M-III) 55

1.3.5.4. Guaso (Gu-I, Gu-II) 55

1.3.6. Model of submarine fan development **57**

1.3.6.1. Initial fan template 57

1.3.6.2. Early fan 58

1.3.6.3. Main fan accumulation 58

1.3.6.4. Fan abandonment 58

1.4. THE BUZZARD FIELD, NORTH SEA, UK **59**

1.5. RESEACH OBJECTIVES **60**

1.6. THESIS PLAN **62**

CHAPTER 2 – SEDIMENT GRAVITY FLOWS AND DEPOSIT CLASSIFICATION **64**

2.1 INTRODUCTION **64**

2.2 SEDIMENT GRAVITY FLOW PROCESSES **64**

2.2.1 Sediment-support mechanisms **64**

2.2.2 SGF processes **66**

2.2.2.1 Turbidity currents 67

2.2.2.2 Concentrated density flows 67

2.2.2.3 Inflated sandflows 68

2.2.2.4 Cohesive flows 68

2.2.2.4.1 Sediment slides 68

2.2.2.4.2 Sediment slumps 69

2.2.2.4.3 Debris flows 69

2.2.2.4.4 Cohesive deposits 73

2.2.3 Transformations between flow types **74**

2.2.3.1 Hybrid event beds 74

2.3 FACIES CLASSIFICATION AT OUTCROP **77**

2.3.1 MTD classification at outcrop **79**

2.4 EROSIVE DEBRIS FLOW PROCESSES IN SUBAERIAL AND SUBMARINE ENVIRONMENTS **82**

2.4.1 Erosive observations from subaerial debris flows 82

2.4.1.1 Field observations of erosive subaerial debris flows 83

2.4.2 Observations from submarine erosive debris flows 89

2.4.3 Strength-loss mechanisms and material entrainment 98

2.4.3.1 Liquefaction 98

2.4.3.2 Effective stress 99

2.4.3.3 Undrained and rapid loading 99

2.4.3.4 Basal shear 101

2.4.3.4.1 Monotonic shear 102

2.4.3.4.2 Cyclic shear 103

2.4.3.5 Ploughing 103

2.4.3.6 Erosional efficiency 104

2.4.3.7 Subaerial and submarine entrainment summary 105

2.5 SUMMARY 107

CHAPTER 3 – METHODOLOGY 108

3.1 INTRODUCTION 108

3.2 FIELDWORK METHODS 108

3.2.1 Study area and localities 108

3.2.2 Sedimentary logging 113

3.2.2.1 Construction of correlation panels 115

3.2.3 Estimating grain content 115

3.2.4 Photomontages 116

3.2.5 Measuring topography 116

3.2.6 Stratigraphic hierarchy 117

3.2.7 Geological mapping 118

3.3. SAMPLING AND LABORATORY METHODS 119

3.4. INDUSTRY INTERNSHIP 125

3.5 SUMMARY **128**

CHAPTER 4 – SEDIMENTARY CHARACTERISTICS OF MTDs AND MTCs, MIDDLE-EOCENE AINSA BASIN, SPANISH PYRENEES **130**

4.1. INTRODUCTION **130**

4.2. MTDs AT OUTCROP **130**

4.2.1 Type I MTDs **130**

4.2.1.1 Type Ia 131

4.2.1.2 Type Ib 131

4.2.1.3 Type Ic 131

4.2.2 Type II MTDs **132**

4.2.2.1 Type IIa 132

4.2.2.2 Type IIb 133

4.2.3 Type III MTDs **133**

4.2.3.1 Type IIIa 133

4.2.3.2 Type IIIb 134

4.2.4 Type IV MTDs 134

4.3. SEDIMENTARY CHARACTERISTICS OF MTDs AND MTCs **142**

4.3.1 MTD facies attributes and stacking patterns **143**

4.3.2 Topography, onlap and palaeocurrents **149**

4.3.2.1 Locality 16, Ainsa Quarry 149

4.3.2.2 Locality 40, Rio Sieste 154

4.3.2.3 Measured MTD topography 155

4.3.2.4 Palaeocurrents above MTD topography 156

4.3.3 Sandstone channels in MTDs **156**

4.3.4 Rafts and boulders **162**

4.3.4.1 Type Ic carbonate MTDs 164

4.3.5 Pebbles **168**

4.3.5.1 Clast orientation 172

4.4 INTERPRETATION 174

4.4.1 Flow classification and processes 174

4.4.1.1 Type I MTDs 174

4.4.1.1.1 Type Ia 174

4.4.1.1.2 Type Ib 174

4.4.1.1.3 Type Ic 176

4.4.1.2 Type II MTDs 179

4.4.1.2.1 Type IIa 179

4.4.1.2.2 Type IIb 181

4.4.1.3 Type IIIa and b MTDs 182

4.4.1.4 Type IV MTDs 183

4.4.2 Co-genetic deposits 185

4.4.3 Turbulent SGFs and flow deflection over cohesive MTDs 186

4.4.4 Sandstone channels in MTCs 188

4.4.5 Sedimentary characteristics of MTDs 188

4.4.5.1 Pebbles in Type II and III MTDs 188

4.5. SUMMARY 191

CHAPTER 5 – SEDIMENTARY ENVIRONMENTS AND QUANTITIATIVE ANALYSIS OF MTD NAD MTC DATA, MIDDLE-EOCENE AINSA BASIN, SPANISH PYRENEES 194

5.1. INTRODUCTION 194

5.2. SEDIMENTARY ENVIRONMENTS 194

5.2.1 Slope environments 202

5.2.1.1 Upper- mid- to lower slope environment 202

5.2.1.2 Low-gradient slope environment 203

5.2.1.3 Erosional lower-slope environment 204

5.2.1.4 Base-of-slope environments 209

5.2.2 MTDs and MTCs at the base of depositional systems **210**

5.2.2.1 MTDs and MTCs at the base of the distal Morillo System 211

5.2.3 Intraformational MTDs AND MTCs **213**

5.3 MTD AND MTC ANALYSIS **216**

5.3.1 MTCs **216**

5.3.2 MTDs **218**

5.3.2.1 Facies distribution 218

5.3.2.2 Spatial distribution 220

5.3.2.3 Stratigraphic distribution 222

5.3.3 Aspect ratios 225

5.4 GEOMETRY OF GLOBAL MTDs AND MTCs **225**

5.5 INTERPRETATION **229**

5.6 SUMMARY **234**

CHAPTER 6 – EROSIONAL FEATURES OF MTDs: APPLICATION TO ANCIENT SUBMARINE ENVIRONMENTS, MIDDLE-EOCENE AINSA BASIN, SPANISH PYRENEES **236**

6.1 INTRODUCTION **236**

6.2 MTDs SHOWING BASAL EROSION **237**

6.2.1 Fabric **237**

6.2.2. Characteristics of MTDs showing basal erosion **239**

6.2.2.1 Sandstone blocks incorporated into the base of MTDs 240

6.2.2.1.1. Locality 23 (Rio Ara, Morillo I Fan) 240

6.2.2.1.2 Locality 4 (Eña Quarry, Morillo II Fan) 241

6.2.2.2 Striated surfaces at the base of MTDs 245

6.2.2.3 Injected matrix 246

6.2.2.4 Ploughing of the palaeoseafloor 249

6.2.2.4.1 Locality 6 (Banastón V Fan, N-260 road section) 249

6.2.2.5 Scouring of the palaeoseafloor 250

6.2.2.5.1 Locality 62 (Rio Sieste, Morillo II Fan) 250

6.2.2.5.2 Locality 4 (Arro Fan, road to Los Molinos) 251

6.2.3 Basal geometry of scours **253**

6.2.3.1 Lateral terraced geometries 253

6.2.3.2. 'Flute-like' geometry 256

6.2.4. MTD thickness *versus* depth of erosion 257

6.3 MEGASCOURS **259**

6.3.1 Features of megascours **260**

6.3.2 Megascour outcrops **261**

6.3.2.1 Ainsa II Fan megascour, Ainsa town 261

6.3.2.2 Morillo I Fan megascour, Rio Ara 265

6.3.2.3 Guaso II Fan megascour, Guaso village 266

6.4. INTERPRETATION **267**

6.4.1 Occurrence of erosive MTDs **267**

6.4.2 Geometry of small-scale scours **267**

6.4.3 MTD thickness *versus* depth of erosion **269**

6.4.4 Strength loss mechanisms observed at outcrop **269**

6.4.4.1 Striations 270

6.4.4.2 Scouring 270

6.4.4.3 Ploughing 271

6.4.4.4 Injection 271

6.4.4.5 Plucking 272

6.4.4.5.1 Loss on momentum from plucking mechanism 278

6.4.5 Summary of erosive mechanisms documented at outcrop **279**

6.4.6 Megascours formed at or near the base-of-slope **281**

6.5 SUMMARY **283**

CHAPTER 7 - LABORATORY STUDY; MTD THIN-SECTION ANALYSIS FROM OUTCROP, MIDDLE-EOCENE AINSA BASIN, SPANISH PYRENEES 284

7.1 INTRODUCTION 284

7.2 PILOT STUDY RESULTS 285

7.2.1 Compositional data 285

7.2.2 Grading observed from compositional and grain-size data 288

7.3 ANALYTICAL STUDY RESULTS 289

7.3.1 Grading observed from compositional and grain-size data 289

7.3.1.1 Group 1: Type IIa MTDs showing basal erosion 290

7.3.1.2 Group 2: Type IIa MTDs that do not show basal erosion 293

7.3.1.3 Group 3: Anomalous data from Group 2 deposits 295

7.3.2 Thin-section images 296

7.3.3 Grain-size analysis based on grouped data 298

7.3.3.1 Group 1: Erosively-based IIa MTDs deposits 298

7.3.3.2 Group 2: Non-erosively-based IIa MTDs deposits 300

7.3.3.3 Group 3: Anomalous data from Group 2 deposits 301

7.3.3.4 Grain-size comparison between all Groups 302

7.3.4 Overall grading and compositional analysis 304

7.3.5 Compositional analysis normalised without matrix 306

7.4 DISCUSSION 310

7.4.1 Group 1 MTDs 311

7.4.2 Group 2 MTDs 311

7.4.3 Group 3 MTDs 312

7.4.4 Summary of MTDs observed in the Ainsa Basin 313

7.4.5 Shelf morphology 315

7.4.6 Flow processes 318

7.5 SUMMARY 319

CHAPTER 8 - THE JURASSIC BUZZARD FIELD, UK NORTH SEA **321**

8.1 INTRODUCTION **321**

8.1.1 Regional background **321**

8.1.2 Buzzard field structure and stratigraphy **325**

8.2 MTDS AND MTCS IN THE BUZZARD FIELD **332**

8.2.1 Core photographs **332**

8.2.2 MTD frequency analysis **338**

8.2.3 MTD distribution **339**

8.2.3.1 B2 MTC distribution 340

8.2.3.2 B2 sandstone distribution 340

8.2.3.3 LB4 and UB4 MTC distribution 341

8.2.3.4 B4 sandstone distribution 341

8.2.4 Channelised sandstone geometry in MTC **346**

8.2.5 Comparison of MTC thickness in proximal *versus* distal settings **348**

8.2.6 Basal erosion in core data **350**

8.2.7 Abrupt sandstone deposition **351**

8.3 INTERPRETATION **357**

8.3.1 Comparison of MTD and frequency analysis **358**

8.3.2 MTC distribution **359**

8.3.2.1 B2 359

8.3.2.2 LB4 359

8.3.2.3 UB4 360

8.3.3 Distal and proximal thickness variation **360**

8.3.4 Abrupt sandstone deposition **361**

8.3.5 Basal erosion **362**

8.4 SUMMARY **363**

CHAPTER 9 – SYNTHESIS **365**

9.1 INTRODUCTION **365**

9.2 DATA SYNTHESIS **365**

9.2.1 MTD classification scheme **365**

9.2.2 Sedimentary characteristics **366**

9.2.3 Sedimentary provenance **362**

9.2.4 MTDs *versus* MTCs and co-genetic deposits **369**

9.2.5 Depositional environments and MTD AND MTC thickness **369**

9.2.6 Scaling and geometry and scaling of MTDs AND MTCs **370**

9.2.7 Analogues and basin configuration **374**

9.3 EROSIVE SGFs **375**

9.3.1 Erosion from sandy SGFs (turbidity currents) **376**

9.3.2 Hybrid event beds **378**

9.3.3 Submarine debris-flow erosion **380**

9.3.3.1 Megascours 381

9.3.3.2 Identification of scours in seismic data 384

9.4 OBSERVATIONS AND ALTERNATIVE INTERPRETATIONS FROM GLOBAL OUTCROPS **385**

9.5 APPLICATION OF FINDINGS IN THIS STUDY **389**

9.6 CONCLUSIONS **391**

9.7 LIMITATIONS AND FUTURE RESEARCH RECOMMENDATIONS **396**

REFERENCES **399**

LIST OF FIGURES

Figure 1.1 – Topographic & velocity profile of the 1929 Newfoundland event 27

Figure 1.2 – Moscardelli and Wood (2008) MTD classification 29

Figure 1.3 – Identification of MTDs and MTC in core 31

Figure 1.4 – Submarine or seismic character of MTDs 32

Figure 1.5 – Frontally emergent and frontally confined MTDs 33

Figure 1.6 – MTDs and MTCs identified in seismic data 35

Figure 1.7 – MTDs and MTCs identified at outcrop 36

Figure 1.8 – Study area location map 37

Figure 1.9 – Structural sketch showing the main structural units of the central Pyrenees 39

Figure 1.10 –Chronostratigraphic diagram of study area 41

Figure 1.11 – Location map of the Ainsa Basin and surrounding main structural elements 43

Figure 1.12 – Cross-section across Buil syncline and Boltaña anticline 44

Figure 1.13 – Large-scale palaeogeographic reconstructions of the Ainsa Basin 48

Figure 1.14 –Transition from continental and shallow marine deposits, Ainsa Basin 49

Figure 1.15 –Basin-plain facies, Jaca Basin 51

Figure 1.16 – Geological map of the Ainsa Basin 56

Figure 1.17 – Evolution of deep-marine sandy systems in the Ainsa Basin 57

Figure 1.18 – Location map of the Buzzard Field and comparison of Ainsa Basin 61

Figure 2.1 – Particle support mechanisms in SGFs 66

Figure 2.2 – Summary of SGF flow characteristics 68

Figure 2.3 – Subaerial debris flows 71

Figure 2.4 – Experimental debris flows 72

Figure 2.5 – Cohesive deposits 73

Figure 2.6 – Schematic HEB profile 75

Figure 2.7 – HEB outcrops 76

Figure 2.8 – HEB flow processes 77

Figure 2.9 – Facies classification scheme 79

Figure 2.10 – Subaerial debris flow valley network in the Oregon Coast Range, USA 83

Figure 2.11 – Evidence for bedrock lowering from subaerial field outcrops 86

Figure 2.12 – Debris flow profile showing erosion (profiles are pre- and post-debris flow) 87

Figure 2.13 – Vertical erosion profile 88

Figure 2.14 – Cross-sectional channel profiles of debris flow gully pre- and post-debris flow 90

Figure 2.15 – Summary of debris flow characteristics 91

Figure 2.16 – Idealised cross-section of a debris flow 92

Figure 2.17 – Submarine megascour images identified in seismic data 94

Figure 2.18 – 'U'-shaped debris flow channels in submarine settings 95

Figure 2.19 – Erosive sandstones at the base of the Cerro Bola MTD 97

Figure 2.20 – Physical properties of samples taken at DSDP Site 384 100

Figure 2.21 – Flow-zones identified in debris flows 101

Figure 2.22 – Monotonic shear 102

Figure 2.23 – Experiments on subaerial debris flows 104

Figure 3.1 – Study area location map 109

Figure 3.2 – Legend for sedimentary logs and diagrams 114

Figure 3.3 – Comparison chart for estimating percentage composition 115

Figure 3.4 – Diagram showing topographic dimensions 116

Figure 3.5 – Hierarchical diagram of stratigraphy 117

Figure 3.6 – Outcrops sampled for pilot study 120

Figure 3.7 – Photomicrographs: compositional elements measured in thin-section study 122

Figure 3.8 – Map of Buzzard Field showing well locations 127

Figure 3.9 – I-point alignment 128

Figure 4.1 – Representative Type Ia deposits, Ainsa Basin 135

Figure 4.2 – Representative Type Ib deposits, Ainsa Basin 136

Figure 4.3 – Representative Type Ic deposits, Ainsa Basin 137

Figure 4.4 – Representative Type IIa deposits, Ainsa Basin 138

Figure 4.5 – Representative Type IIb deposits, Ainsa Basin 139

Figure 4.6 – Representative Type IIIa deposits, Ainsa Basin 140

Figure 4.7 – Representative Type IIIb deposits, Ainsa Basin 141

Figure 4.8 – Representative Type IV deposits, Ainsa Basin 142

Figure 4.9 – Images showing observations recognising MTDs within MTCs 144

Figure 4.10 – Logs showing MTDs within MTCs 145

Figure 4.11 – Facies Groups identified at outcrop 146

Figure 4.12 – Ainsa Quarry outcrop showing MTD mounded topography 150

Figure 4.13 – Sedimentary log of A5 core, Ainsa I Fan 152

Figure 4.14 – Intraformational MTD (Ainsa Quarry outcrop) 153

Figure 4.15 – MTDs showing no topographic relief 154

Figure 4.16 – Graph showing MTD thickness *versus* topography 155

Figure 4.17 – Palaeocurrent variation above MTD topography 157

Figure 4.18 – Erosive sandy channelised element within MTD (Rio Ara) 158

Figure 4.19 – Erosive sandy channelised element within MTD (Bruello) 160

Figure 4.20 – Erosive sandy channelised element within MTD (Guaso village) 161

Figure 4.21 – Rafts within MTDs 163

Figure 4.22 – Intrabasinal elements within MTDs 164

Figure 4.23 – Type Ic MTDs (Rio Sieste) 165

Figure 4.24 – Divisions of Type Ic MTDs 167

Figure 4.25 – Molluscan boring on pebbles 168

Figure 4.26 – Photomicrograph of pale-grey pebbles 169

Figure 4.27 – Photomicrograph of dark-grey pebbles 170

Figure 4.28 – Map of pebble composition analysis 171

Figure 4.29 – Clast orientation within Type IIb MTDs 173

Figure 4.30 – Large-scale Type Ib MTD (from Kane *et al.,* 2007) 175

Figure 4.31 – Processes and model of carbonate megaturbidites (from Ogata *et al.,* 2012) 177

Figure 4.32 – Model for origin of Type Ic MTDs in the Ainsa Basin 179

Figure 4.33 – Depositional model for Type IIb MTDs 182

Figure 4.34 – Depositional model for Tpye IIIa and b MTDs 184

Figure 4.35 – Ross Slide, County Clare, Ireland. Depositonal model for Type IV MTDs 185

Figure 4.36 – Hydraulic jump model 187

Figure 4.37 – Model for sedimentary inputs to Ainsa Basin 190

Figure 5.1 – Map showing approximate proximal and distal locations of MTDs, Ainsa Basin 195

Figure 5.2 – Sedimentary logs of representative depositional environments 198

Figure 5.3 – Images of slope MTDs and MTCs 203

Figure 5.4 – Guaso map and sedimentary logs (slope environments) 205

Figure 5.5 – View of proximal Banastón environment 206

Figure 5.6 – Cross-section through proximal Banastón environment 207

Figure 5.7 – MTDs identified in canyon environment (Usana) 208

Figure 5.8 – MTDs and MTC identified at base-of-slope environment (Forcaz Stream) 209

Figure 5.9 – Average thickness of MTDs and MTCs at the base of depositional systems 211

Figure 5.10 – Cross-section through distal Morillo environment 212

Figure 5.11 – Intraformational MTDs and MTCs, proximal Banastón environment 214

Figure 5.12 – Intraformational MTDs identified in the distal Morillo environments 215

Figure 5.13 – Average MTC *versus* MTD thickness 216

Figure 5.14 – Count of MTC thickness documented in different depositional environments 217

Figure 5.15 – Average MTD thickness (separated as facies) 218

Figure 5.16 – Geological map of MTDs documented in the Ainsa Basin 220

Figure 5.17 – Graph showing % of MTDs logged in distal *versus* proximal environments 221

Figure 5.18 – Temporal data of MTDs per system 222

Figure 5.19– Frequency of MTD thicknesses in the Ainsa, Morillo and Banastón systems 223

Figure 5.20 – Proximal-to-distal thicknesses, Ainsa Basin 224

Figure 5.21– Aspect ratios, Ainsa Basin 225

Figure 5.22 – Global geometry of MTD and MTC data 227

Figure 5.23 – Map showing MTD and MTC size in the Gulf of Mexico 228

Figure 5.24 – Depositional model for erosional, base-of-slope canyons 233

Figure 6.1 – Images showing variability of debrite fabric 238

Figure 6.2 – Graph showing grains in debrite matrix 239

Figure 6.3 – Sandstone blocks incorporated into base of MTDs (Rio Ara) 242

Figure 6.4 – Sandstone blocks incorporated into base of MTDs (Rio Eña Quarry) 243

Figure 6.5 – Sandstone blocks incorporated into base of MTDs (Rio Eña Quarry), close-up 244

Figure 6.6 – Striated surface at base of MTD (Debrite, Forcaz Stream) 245

Figure 6.7 – Striated surface at base of MTD (sediment slide/slump, Rio Sieste) 246

Figure 6.8 – Striated pavement from the Ainsa Quarry 247

Figure 6.9 – Injection of pebbles and debrite into underlying sandstone bed 248

Figure 6.10 – Model of pebbly sandstone 'jacking up' palaeoseafloor 250

Figure 6.11 – Erosively-based MTD showing 'U'-shaped scour, Morillo II System 251

Figure 6.12 – Erosively-based MTD showing 'U'-shaped scour, Arro System 252

Figure 6.13 – Architectural geometry of debrite showing vertical truncation 254

Figure 6.14 – Debrite eroding sandstone, Banastón V System, N260 255

Figure 6.15 – Debrite showing 'flute-like' geometry 256

Figure 6.16 – Spoon-shaped debrite scour along the Rio Eña 258

Figure 6.17 – Maximum thickness of MTD versus maximum erosion measured in the field 259

Figure 6.18 – Location map of megascours identified in the Ainsa Basin 260

Figure 6.19 – Mushroom-like diapiric sandstone structures located at the base of megascours 261

Figure 6.20 – Ainsa II System megascour 263

Figure 6.21 – Morillo I System megascour 265

Figure 6.22 – Guaso I System megascour 266

Figure 6.23 – Model displaying erosive debrite forming channel-like geometry 268

Figure 6.24 – Maximum thickness of debris flow measured against maximum erosion 269

Figure 6.25 – Wet-sediment deformation structures in coarse-grained sediments 272

Figure 6.26 – Instrumentation measuring pore-fluid pressure at base of debris flows 274

Figure 6.27 – Measurements of total basal normal stress and basal fluid pressure 275

Figure 6.28 – Grain-size compositions of flows showing negative and neutral pore-pressures 275

Figure 6.29 – Schematic diagram showing down-dip flow stress vectors 276

Figure 6.30 – Model for the 'plucking' mechanism at the base of debris flows 278

Figure 6.31 – Model for clastic injection into slide block 281

Figure 6.32 – Seismic section showing low-angle thrust faults on the lateral margin of MTD 282

Figure 7.1 – Ternary diagram showing compositional data debrites sampled in pilot study 286

Figure 7.2 – DF-1 photomicrographs (top-to-base) 282

Figure 7.3 – Data from point-count analysis from erosively- and non-erosively based MTDs 288

Figure 7.4 – Compositional analyses of Group 1 debrites 292

Figure 7.5 – Compositional analyses of Group 2 debrites 294

Figure 7.6 – Compositional analyses of Group 3 debrites 295

Figure 7.7 – Group 1, Group 2 and Group 3 debrites photomicrographs 297

Figure 7.8 – Grain-size data showing **'**normal' grading in Group 1 deposits 299

Figure 7.9 – Grain-size data from Group 2 deposits 300

Figure 7.10 – Grain-size data from Group 3 deposits 302

Figure 7.11 – All grain-size data 303

Figure 7.12 – Average compositional data for SGFs 304

Figure 7.13 – Ternary diagram showing compositional data without effect of matrix 305

Figure 7.14 – Enrichment of quartz and carbonate grains in debrites 306

Figure 7.15 – Group 1, 2 and 3 debrites bulk normalised without matrix 309

Figure 7.16 – Group 1 debrite bulk composition normalised without matrix 310

Figure 7.17 – 2-D model showing of erosive debrites preserved up and down-dip 313

Figure 7.18 – Surf zone to shelf fractional mill model 315

Figure 7.19 – 2-D model of the Ainsa Basin showing narrow shallow-marine shelf 316

Figure 7.20 –Model of sediment inputs to the Ainsa Basin 318

Figure 8.1 – Seismic data showing limit of resolution of Buzzard Field 322

Figure 8.2 – Palaeogeographic maps through the Upper Jurassic, UK North Sea 324

Figure 8.3 – The Buzzard Field structure map 326

Figure 8.4 – Cross-section through the Central Panel of the Buzzard Field 327

Figure 8.5 – Buzzard Field depositional model 328

Figure 8.6 – Stratigraphic model of Buzzard stratigraphy 331

Figure 8.7 – MTD facies observed in Buzzard core 333-336

Figure 8.8 – MTD facies (boulder) interpreted in core 337

Figure 8.9 – Graph showing percentage of MTD types identified from core data 338

Figure 8.10 – B2 MTD cross-section and distribution map 342

Figure 8.11 – B2 sandstone cross-section and distribution map 343

Figure 8.12 – LB4 and UB4 MTC cross-section and distribution maps 344

Figure 8.13 – UB4 sandstone cross-section and distribution map 345

Figure 8.14 – Channelised sandstone geometry in MTC (southern panel) 347

Figure 8.15 – Map of Buzzard Field, divided into proximal and distal settings 348

Figure 8.16 – Graph showing average thickness of MTCs in the Buzzard and Ainsa basins 349

Figure 8.17 – 'starry night' facies at base of MTC showing potential erosion into sandstone 351

Figure 8.18 – Top Buzzard MTC close-up in core 352

Figure 8.19 – B28-Y core photos and interpretation of MTC 353

Figure 8.20 – MTC above Buzzard Field cross-section and distribution map 355

Figure 8.21 – Photointerpretation of the Ainsa Quarry 356

Figure 8.22 – Striations at the top sandstone surface in the Ainsa Quarry 357

Figure 8.23 – Thinning of MTDs and MTCs in seismic profile 361

Figure 9.1 – MTC aspect ratios: width *versus* thickness (global dataset, Ainsa and Buzzard) 371

Figure 9.2 – MTC aspect ratios: width *versus* runout (global dataset and Buzzard) 373

Figure 9.3 – Channelised sandstone outcrop, Ainsa Basin 377

Figure 9.4 – Bed profile of tripartite event bed from thin-section 379

Figure 9.5 – Progressive entrainment model 381

Figure 9.6 – Megascour model 383

Figure 9.7 – Typical seismic resolution of megascours (from Bakke *et al.*, 2009) 384

Figure 9.8 – Megascours identified in seismic (from Posamentier and Martinsen, 2011) 385

Figure 9.9 – Debrite-filled scours at outcrop (from Cossey, 2011) 386

Figure 9.10 – Re-nterpreation of debrite-filled scour (from Cossey, 2011) 388

LIST OF TABLES

Table 2.1 – Facies classification scheme 78

Table 2.2 – MTD facies classification scheme 80

Table 2.3 – Characteristics of the 'head' and 'tail' of subaerial debris flows 84

Table 2.4 – Summary of erosive processes at the base of debris flows 106

Table 3.1 – Sedimentary log locations (Ainsa Basin) 112

Table 3.2 – Sample catalogue for thin-section analysis (Ainsa Basin) 124

Table 3.3 – Well data used for interpretation (Buzzard Field) 126

Table 4.1 – Summary of MTD facies attributes 147

Table 4.2 – Chi-test results from sedimentary logs 148

Table 5.1 – Depositional environments, Ainsa Basin 192

Table 5.2 – Maximum thickness of MTDs and MTCs at the base of sandy fan systems 210

Table 5.3 – Summary of MTC data 216

Table 5.4 – Summary of MTD data 219

Table 6.1 – Summary of erosion from MTD processes 280

Table 7.1 – Summary of Type IIa MTDs (Groups 1, 2 and 3) 314

Table 9.1 – Revised MTD classification scheme 368

APPENDICES

Appendix A: Published papers from work carried out during this research project.

(1) Scotchman, J. I., Pickering, K. T., Sutcliffe, C., **Dakin, N.,** Armstrong, E. (2015). Milankovitch cyclicity within the middle Eocene deep-marine Guaso System, Ainsa Basin, Spanish Pyrenees. Earth-Science Reviews, 144, 107-121.

(2) **Dakin, N**., Pickering, K., Mohrig, D., Bayliss, N. (2013). Channel-like features created by erosive submarine debris flows: Field evidence from the Middle Eocene Ainsa Basin, Spanish Pyrenees. Marine and Petroleum Geology. 41, 62-71.

Appendix B: Fieldwork diary
Appendix C: Sedimentary log data collected from fieldwork
Appendix D: Field base maps from the Guaso System
Appendix E: Global MTD and MTC geometry data
Appendix F: Point-count data collected from thin-section study

ACRONYMS

σ' = effective stress (N/m^2)

σ = total normal stress (N/m^2)

u_w = pore-water pressure (N/m^2)

ε_{vol} = volume strain

τ = shear stress

ρ_w = density of water (kg/m^3)

T=Tonne

MTD – mass transport deposit

MTC – mass transport complex

SGF – sediment gravity flow

CHAPTER 1

INTRODUCTION

1.1 INTRODUCTION

In 1929, the Grand Banks earthquake offshore Newfoundland recorded a magnitude of 7.2 on the Richter scale. This resulted in the down-slope movement of substantial volumes of sediment in high-energy flows, breaking submarine telegraph cables 724 km from the earthquake epicentre (Milne, 1897; Helen and Ewing, 1952; Hughes Clarke *et al.*, 1990). The fastest velocity (28 m/s; ~ 100 km/h) was recorded in the upper part of the continental rise, at ~ 4,000 m water depth. Mass failure along parts of the Newfoundland continental slope was the first conclusive evidence to show sediment gravity flows (SGFs) are capable of transporting substantial quantities of sediment over large distances (Helen and Ewing, 1952) (Figure 1.1.).

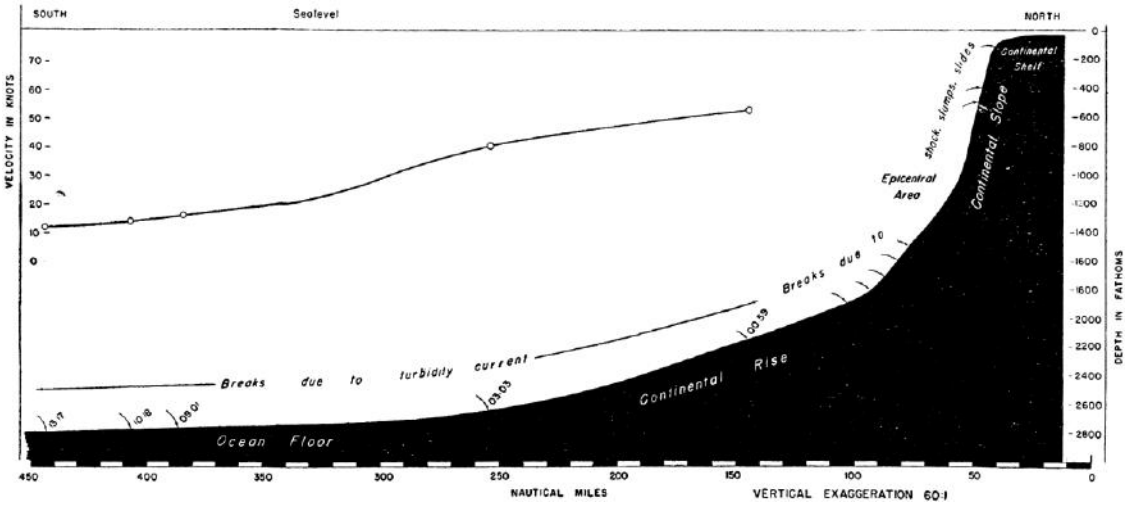

Figure 1.1. Topographic profile of Cabot Strait, Canada, with superimposed graph of the velocity of the turbidity current as determined by the successive cable breaks. Velocity profile shows waning flow down-dip. Figure from Helen and Ewing (1952).

It is now recognised that these flows are amongst the most energetic Earth surface processes and are a major control on the evolution of continental margins and other basin slopes, effectively moving sediment from shallow- to deep-water environments to construct depositional bodies such as submarine fans (Dott, 1963; Bouma, 1964; Nardin *et al.*, 1979; Garziglia *et al.*, 2008). A single mass-flow can

remobilise and deposit up to ten times the mass of sediment transported annually by all of the world's rivers (Talling *et al.*, 2007), involving up to several hundred thousand cubic kilometres of remobilised deposited sediments (Hampton *et al.*, 1996; De Blasio *et al*., 2004). Magnitude of sediment failure in a submarine setting can vary from local instability, such as the collapse of channel margins, to the catastrophic failure of substantial parts of continental margins. Such instability occurs when the downslope shear stress exceeds the resisting stress, causing gravitational movement (Hampton *et al.*, 1996; Callot *et al.*, 2009). Failure can occur as individual or multiple events. Retrogressive failure can cause the slope to re-equilibrate, resulting in the culmination of numerous adjacent failures that progress upslope (Anderson and Bjerrum, 1967; Coleman and Prior, 1988; Hampton *et al*., 1996).

Middleton and Hampton (1973) defined SGFs as the flow of sediment or sediment-fluid mixtures in both submarine and subaerial environments. Under the action of gravity, sediment in the flow is moved, and the sediment motion moves the interstitial fluid. Particles in dilute SGFs, such as non-cohesive turbidity currents, spend most of their time in suspension, rather than in contact with the seafloor and accumulate without a traction phase (Pickering and Hiscott, 2015). In more concentrated and cohesive muddy flows, particles are not free to move independently and sediment therefore accumulates *en masse*, referred to as mass-transport deposits (hereby abbreviated to MTDs). An MTD signifies (in so far as it is possible to ascertain) a single sediment transport and depositional event, whereas an MTC refers to multiple stacked events (Ricci Lucchi 1975; Posamentier and Martinsen, 2011). MTDs are typically muddy gravity-driven cohesive mass-flows that form chaotic deposits that have been reworked from originally *in situ* deposits prior to redeposition, with such deposits resulting from mass-wasting.

The term MTD encompasses several deformational processes including creep, slide, slump and debris flow processes (Figure 1.2), and are well established in scientific literature (Dott, 1963; Middleton and Hampton, 1973; Prior *et al.*, 1986; Nardin *et al.*, 1979; Laberg and Vorren, 1995; Maslin and Mikkelsen, 1997; McAdoo *et al.*, 2000; Carter, 2001; Krastel *et al*., 2001; Nygård *et al.*, 2002; Hafliadason *et al*., 2004; Lastras *et al.*, 2004; Hjelstuen *et al.*, 2007; Minisini *et al*., 2007; Gee *et al.*, 2001; Garziglia *et al.*, 2008; Henrich *et al*., 2008; Alves and Cartwright, 2009, 2010; Lawrence and Cartwright, 2009; Sawyer *et al.*, 2009; Alves, 2010; Gamberi *et al.*,

2011; Jackson, 2011, 2012; Posamentier and Martinsen, 2011; Richardson *et al*., 2011; Dondurur *et al*., 2013; He *et al*., 2013; Olafiranye *et al.*, 2013; Omosanya and Alves, 2013a, b). MTDs and MTCs form a significant component of the stratigraphic record in ancient and modern deep-marine basins worldwide, accounting for up to 40 % of subsurface strata, and are even locally documented up to 90 % in Pleistocene-Holocene sediments of the Nile submarine fan (Embley, 1980; Garziglia *et al*., 2008). Over time, the advancement of seismic imaging and ocean drilling has provided an opportunity to examine the morphology, acoustic signatures, sediment characteristics and depositional properties of modern and ancient landslides in deep-marine settings. However, even with such considerable technological improvement of remote sensing and side-scan sonar techniques, predicting the geometry and architecture of deep-marine sedimentary packages involves a high degree of uncertainty (Coleman and Prior, 1988).

GRAVITY INDUCED DEPOSITS			Genetic Classification Transport Mechanism	Descriptive Classification Sedimentary Structures	Seismically Recognizable Features (Moscardelli et al., 2006; this work)
Mass Transport Complex	Slide		Shear failure along discrete shear planes with little or no internal deformation or rotation	Essentially undeformed, continuous bedding	Continuous blocks without apparent internal deformation. High-amplitude, continuous reflections.
	Slump		Shear failure accompanied by rotation along discrete shear surfaces with various degrees of internal deformation	Plastic deformation particularly at the toe or base. Flow structures, folds, tension faults, joints, slickensides, grooves, rotational blocks	Compressional ridges, imbricate slides, irregular upper bedding contacts, duplex structures, contorted layers. Low- and high-amplitude reflections geometrically arranged as though deformed through compressive stresses.
	Debris Flow		Shear distributed throughout the sediment mass. Strength is principally from cohesion due to clay content. Additional matrix support may come from buoyancy. Plastic rheology and laminar state.	Matrix supported, random fabric, clast size variable, matrix variable. Rip ups, rafts, inverse grading and flow structures possible.	Mega rafted and/or detached blocks, irregular upper bedding contacts, lateral pinch-out geometries, oriented ridges and scours. Low-amplitude, semitransparent chaotic reflections.
Turbidity Current	Turbidite		Supported by fluid turbulence (newtonian rheology)	Normal size grading, sharp basal contacts, gradational upper contacts.	Lobate features Laterally continuous

Figure 1.2. Classification of gravity-induced deposits, including MTDs. From Moscardelli *et al.* (2006).

The continued global demand for hydrocarbons has led to increased exploration and production of oil and gas reserves into more challenging reservoirs (e.g., Stow and Mayall, 2000). Deep-marine clastic systems act as important hydrocarbon reservoirs across the world. Globally, over 1,200 - 1,300 deep-marine hydrocarbon fields are identified, forming ~ 15 % of the world's total hydrocarbon reserves (Richards *et al.*, 1998). Deep-marine reservoirs are deposited predominantly

from sandy sediment gravity-flows (e.g., turbidites) that deposit in confined (e.g., canyons and channels) to unconfined environments (e.g., lobes) and in a variety of slope and basin-floor fan settings (e.g., Richards *et al.,* 1998; Mayall *et al*., 2006). In hydrocarbon fields, muddy MTDs and MTCs generally form baffles and barriers between sandy reservoir intervals and can even form top seals (Alves *et al.*, 2014). Conversely, above certain porosities, some of these deposits may also comprise important hydrocarbon reservoirs, such as the Oligocene Frio Formation of south Texas (Ogiesoba and Hammes, 2012). Research in this thesis focusses on muddy MTDs and MTCs, likely to form baffles and barriers within reservoir intervals.

1.1.1 Characterisation of MTDs and MTCs

In an attempt to better understand MTD lithology and sedimentology, Tripsanas *et al*. (2008) investigated the sedimentological character and depositional textures of MTDs in piston cores from the offshore North American continental margin and the deep-water Gulf of Mexico. A variety of primary sedimentary structures were described from cores, including angular bedding contacts, shear zones, faults, partially and fully-mixed layers, highly distorted stratified sediments with convoluted folds and clasts of lithified or semi-lithified structures (Figure 1.3). Combined with field studies, this dataset has provided evidence of the complex nature of MTD facies, typically missed in seismic studies.

The vertical resolution of seismic data rapidly decreases with depth because velocity increases and frequency decreases, varying from 1/4 to 1/28 of signal frequency (Sheriff, 1992). Although sedimentological details are missed in seismic data, seismic profiles can show the gross geometry of shallow deposits from large-scale mass-failures, such as the Storegga Slide, offshore Norway (Bryn *et al.,* 2005). MTDs and MTCs form distinctive deposits in deep-water depositional systems, mainly due to their large size, distinctive morphology and chaotic internal character (Embley, 1980; Moscardelli *et al*., 2006, Moscardelli and Wood, 2008; Van der Merwe *et al*., 2009; Shipp *et al.,* 2011). The seismic character of MTDs and MTCs can be identified by a change in sedimentation patterns from non-chaotic, parallel reflectors to the lack internal reflectors. These can be identified as chaotic, low-amplitude or transparent amplitudes (Embley, 1980; Frey-Martinez *et al.,* 2006;

Garziglia *et al.*, 2008; Gamberi *et al.*, 2011; Moscardelli and Wood, 2008; Jackson, 2011, 2012; Olafiranye *et al.*, 2013; Alves and Lourenço, 2010).

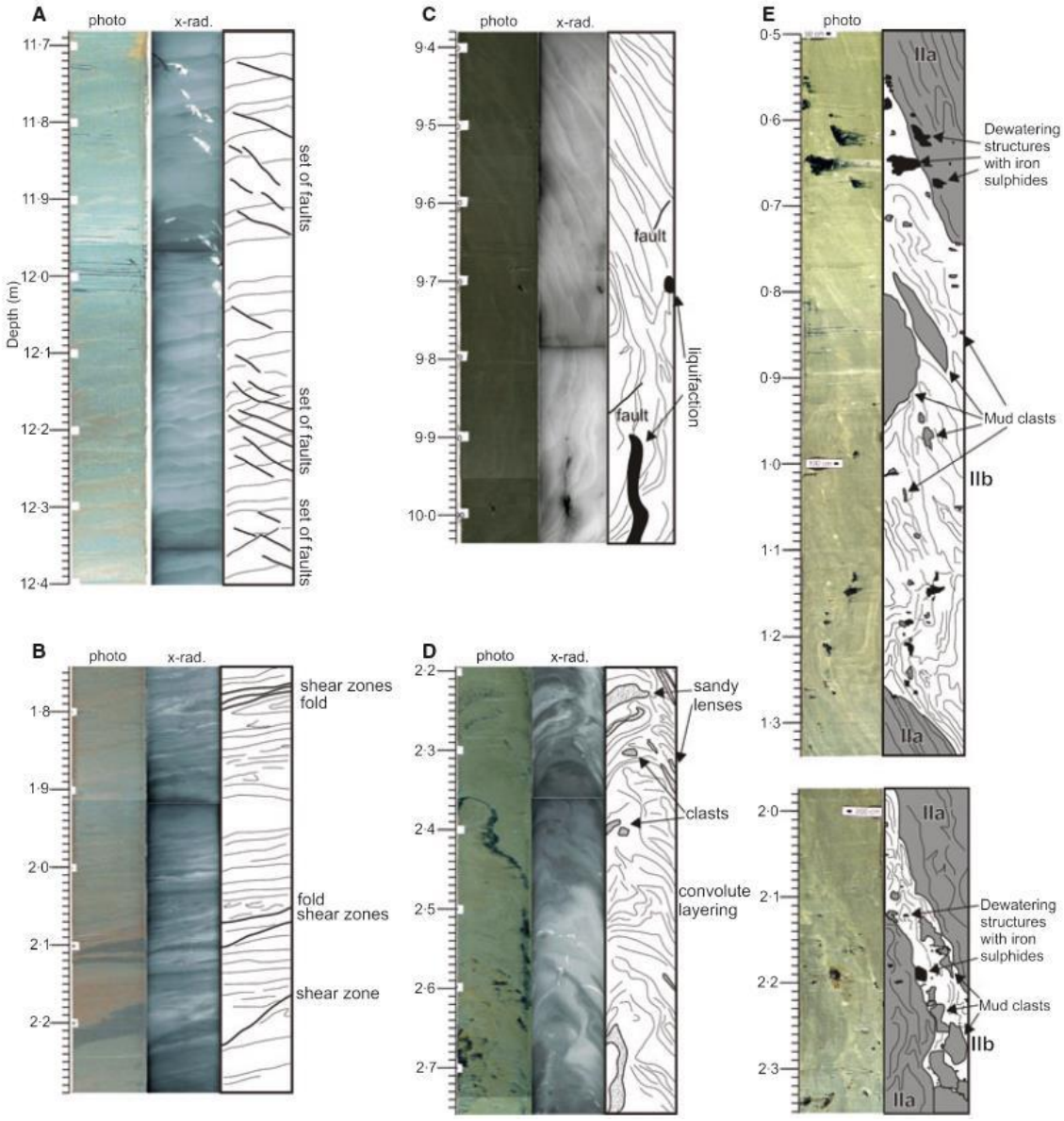

Figure 1.3. MTDs and MTCs identified in core. Photograph of x-radiographs and explanatory drawings of sediment facies from Bryant Canyon. Figure from Tripansas *et al.* (2008). See text for explanation.

Posamentier and Martinsen (2011) characterised MTD facies based on architectural and geometrical features from seismic datasets and swath bathymetry (Figure 1.4). Studying the gross geometry of MTDs and MTCs has proved useful for interpreting large-scale events, such as the collapse of a continental margin. For example, using 3-D seismic data from the Israeli offshore continental margin Frey-Martinez *et al*. (2006) identified frontally confined or frontally emergent profiles

interpreted as the downslope translation of unconsolidated fine-grained sediments (Figure 1.5). Other seismic-scale examples have identified MTDs and MTCs to have pronounced vertical relief (Figure 1.6-A), basal scours (Figure 1.6-B, D), chaotic internal reflectivity (Figure 1.6-C, D) and rapid thinning (Figure 1.6-C). For example, using seismic data acquired in the Rosetta province, northwest deep-marine Egyptian margin, Garziglia *et al.* (2008) identified seven MTDs on the upper-and mid-slope, down-dip from imbricated scars (300 km long and 200 m high) (Figure 1.6-D). The aerial extents of MTDs in the Garziglia *et al.* (2008) study are documented between 200 and 500 km^2 with volumes estimated between 3 to 500 km^3. Interpretation of the seismic line in Figure 1.6-D shows rafted blocks, 'staircase' geometries, headscarps, low-amplitude to transparent or chaotic reflectors, compressional structures and ridges, normal faults and tilted fault blocks. These large-scale, chaotic seismically resolvable events document MTDs and MTCs up to 300 ms in thickness, and show the gross geometry and potential scale of catastrophic mass-failure.

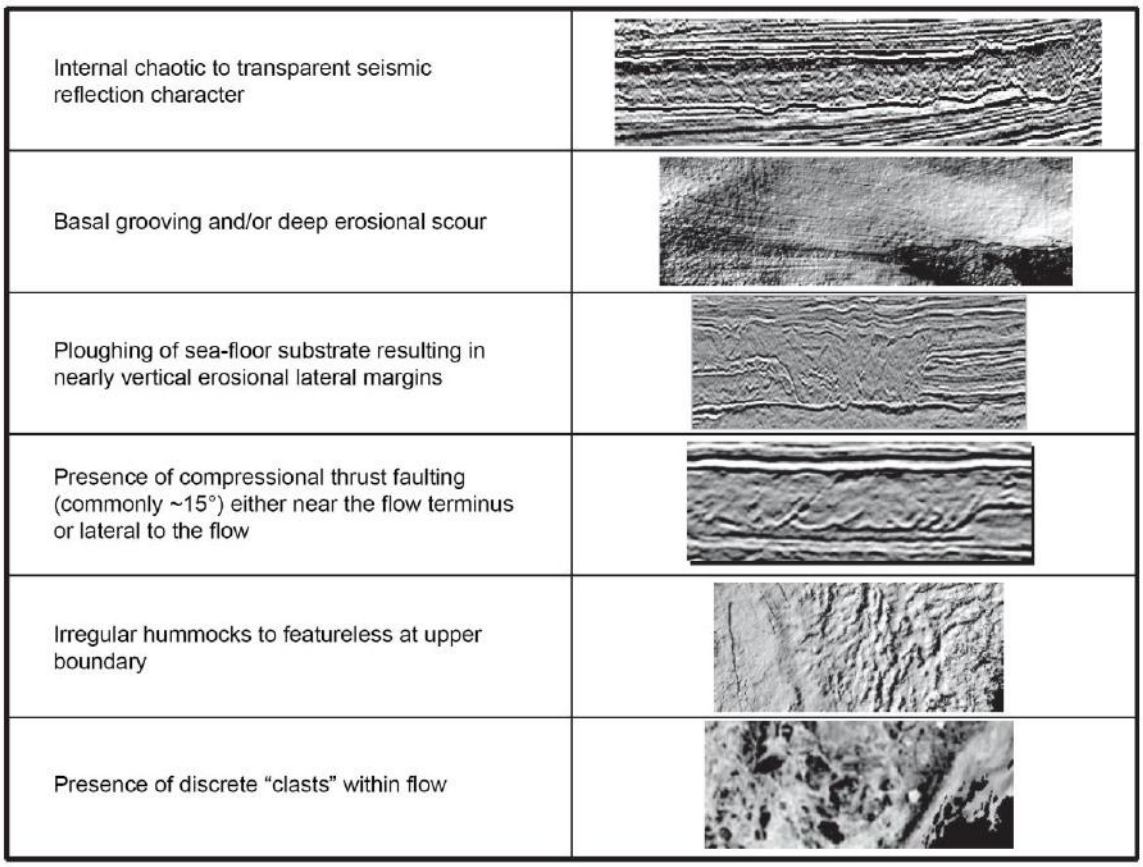

Figure 1.4. Submarine or seismic character of MTDs recognised in swath bathymetry or seismic data. Figure modified from Posamentier and Martinsen (2011).

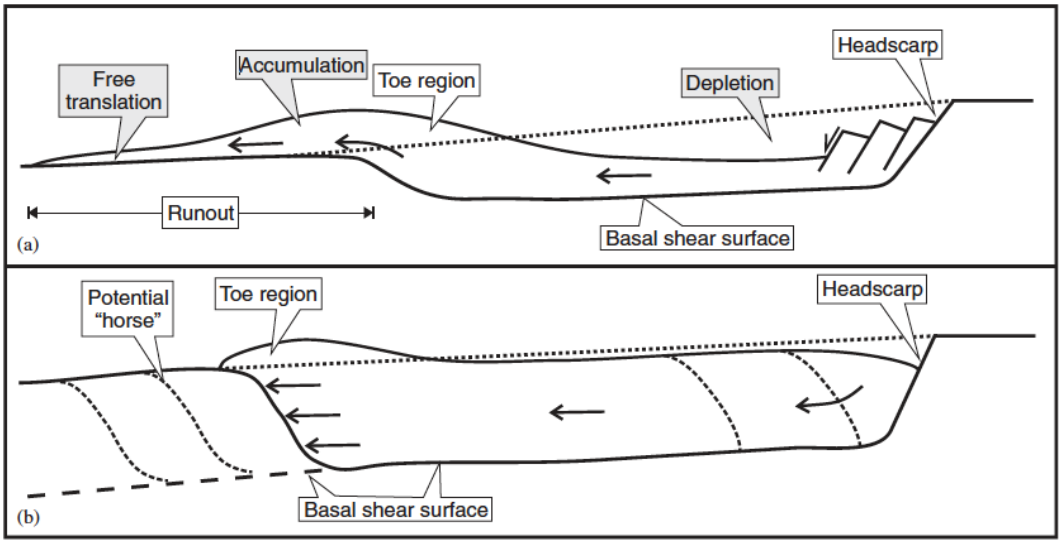

Figure 1.5. Schematic diagram showing the two main types of submarine landslide morphology, according to their frontal emplacement. (a) Frontally emergent and (b) frontally confined. Figure from Frey-Martinez *et al.* (2006).

In contrast to seismic data, outcrop studies identify the complex internal structure of deposits that are not typically seismically resolvable (Figure 1.7). Well-exposed ancient deep-marine depositional systems provide a critical understanding of the heterogeneity and geometry of sedimentary deposits that can be used to better predict sedimentary facies in these systems. Ancient examples include those documented from the: Permian Vischkuil Formation, Karoo Basin, South Africa (Van der Merwe *et al.*, 2009, 2011); Carboniferous Ross Formation, County Clare, Ireland (Posamentier and Martinsen, 2011); Cretaceous Akkeshi Formation, Hokkaido Island, Northern Japan (Naruse and Otsubo, 2011); Carboniferous Guandacól Formation, Argentina (Dykstra *et al.*, 2011), Middle-Eocene Ainsa Basin, south-central Pyrenees, Spain (Pickering and Corregidor, 2005; Dakin *et al.*, 2013); the Late Cretaceous-Palaeocene Rosario Formation, Baja California Peninsula (Dykstra and Kneller, 2009); the Lower-Upper Miocene Marnoso-arenacea Formation, Northern Apennines, Italy (Ricci-Lucchi, 1975; Amy and Talling, 2006; Magalhães and Tinterri, 2011; Malgesini *et al.*, 2015); and the Epiligurian Specchio unit, Early-Middle Rupelian interval of the Ranzano Formation, Northern Apennines, Italy (Ogata *et al.*, 2012). One example of such sedimentological detail identified at outcrop is the presence of post-depositional deformation and basal shear zones immediately beneath MTDs, which can be observed in continental slope and basin floor deposits (e.g., Ogata *et al.*, 2012; Alves and Lourenço, 2010, Alves 2015). Features such as basal shear zones are

generated in near-seafloor strata that deform in response to the gravitational collapse of megablocks and can provide a reliable estimate for the degree and slope of basal deformation during submarine slope failure (Alves and Lourenço, 2010).

1.1.2 Deep-marine deposits in this study

This research project is driven by the petroleum industry's need to understand how MTDs and stacked MTCs (essentially muddy, impermeable non-reservoir deposits) interact with and affect reservoir-grade sandstones. Submarine fans in proximal settings are complex and therefore, predicting changes in sedimentary features, such as bed thickness, sand content and overall heterogeneity away from wells is subject to considerable uncertainty. Reducing such uncertainty, with all of its economic implications, is the principal motivation for CNOOC-Nexen funding this PhD research project.

Regardless of the event magnitude, the internal structure of MTDs is generally seismically irresolvable and can be problematic to predict. Therefore, an outcome of this project is to bridge the gap between deposits that are sub-seismic in resolution. Outcrops from fieldwork provide essential data to constrain interpretations and predictions about reservoir heterogeneity. The Middle-Eocene Ainsa Basin, south-central Spanish Pyrenees can be used as an analogue for some hydrocarbon fields. The Buzzard Field, UK North Sea is similar in aerial extent to the Ainsa Basin and is therefore studied as an analogue as part of this research programme. Exceptional outcrop exposure of the relatively proximal Ainsa Basin provides a unique view of an ancient deep-marine environment. In this study, detailed outcrop descriptions and measurements document the geometry and architecture of MTDs and MTCs. Axial-to-lateral and proximal-to-distal variability, architectural elements, facies relationships (with fan systems, i.e., sandbodies and fine-grained stratigraphic intervals), and microstructures are documented in detail. These methods are adopted in order to gain a better understanding of processes that may occur within MTDs in less well-exposed environments, such as in most subsurface hydrocarbon fields.

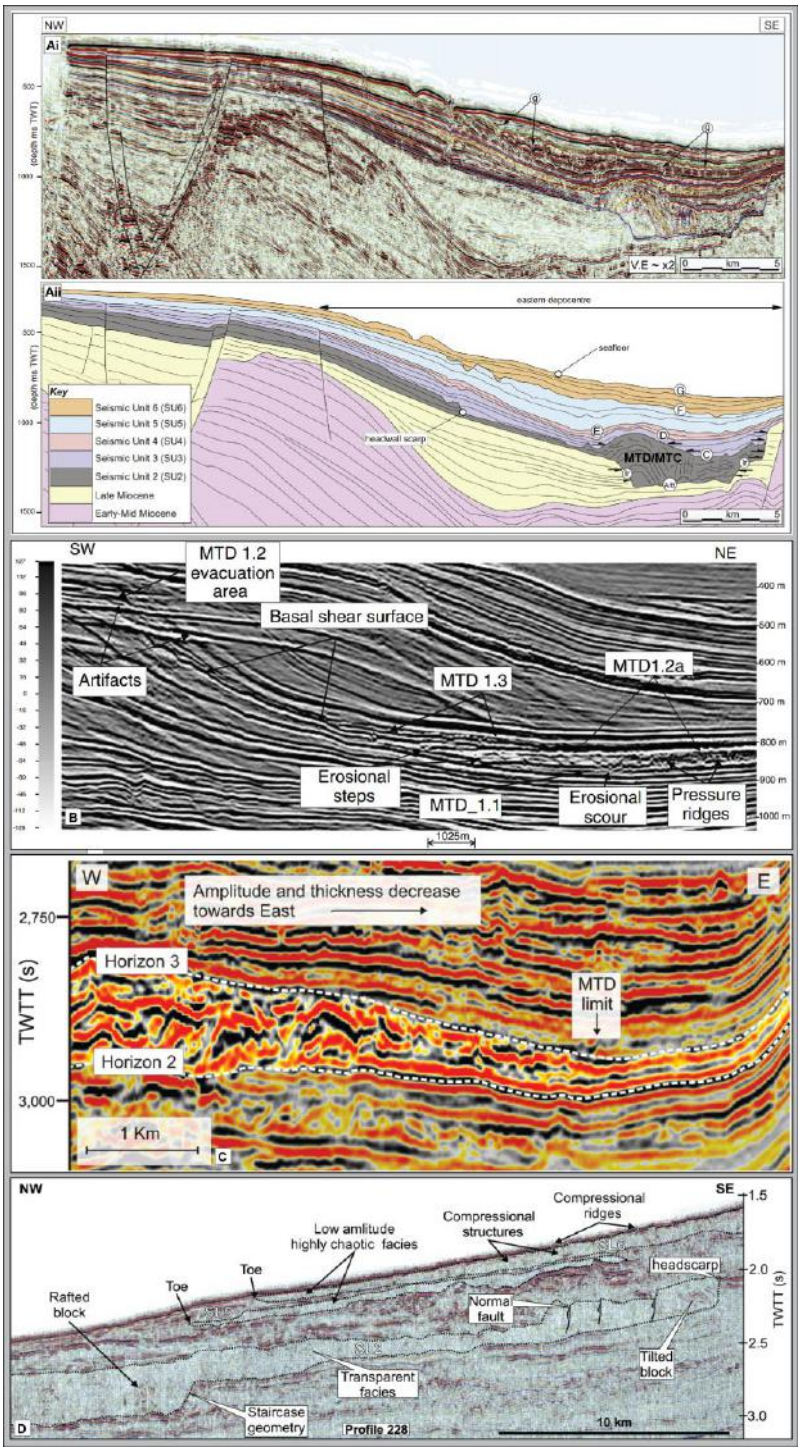

Figure 1.6. (A) Strike-orientated uninterpreted and geoseismic section showing SU2 unit (MTD) with pronounced vertical relief, offshore Angola. Figure from Olafiranye *et al.* (2013). (B) Internal architecture of MTD showing frontal ramps and scours, foredeep basin, Central Adriatic Sea. Figure from Della Valle *et al.* (2013). (C) Seismic section representative of MTD showing eastward thickness decrease, Espírito Santo Basin (SE Brazil) Figure from Gamboa *et al.* (2010). (D) Seismic line through the Rosetta province (NW Nile deep-sea turbidite system, Egyptian margin). Displays transparent facies with a 'staircase' geometry signifying a basin-wide MTC down-dip from the source area. Figure from Garziglia *et al.* (2008).

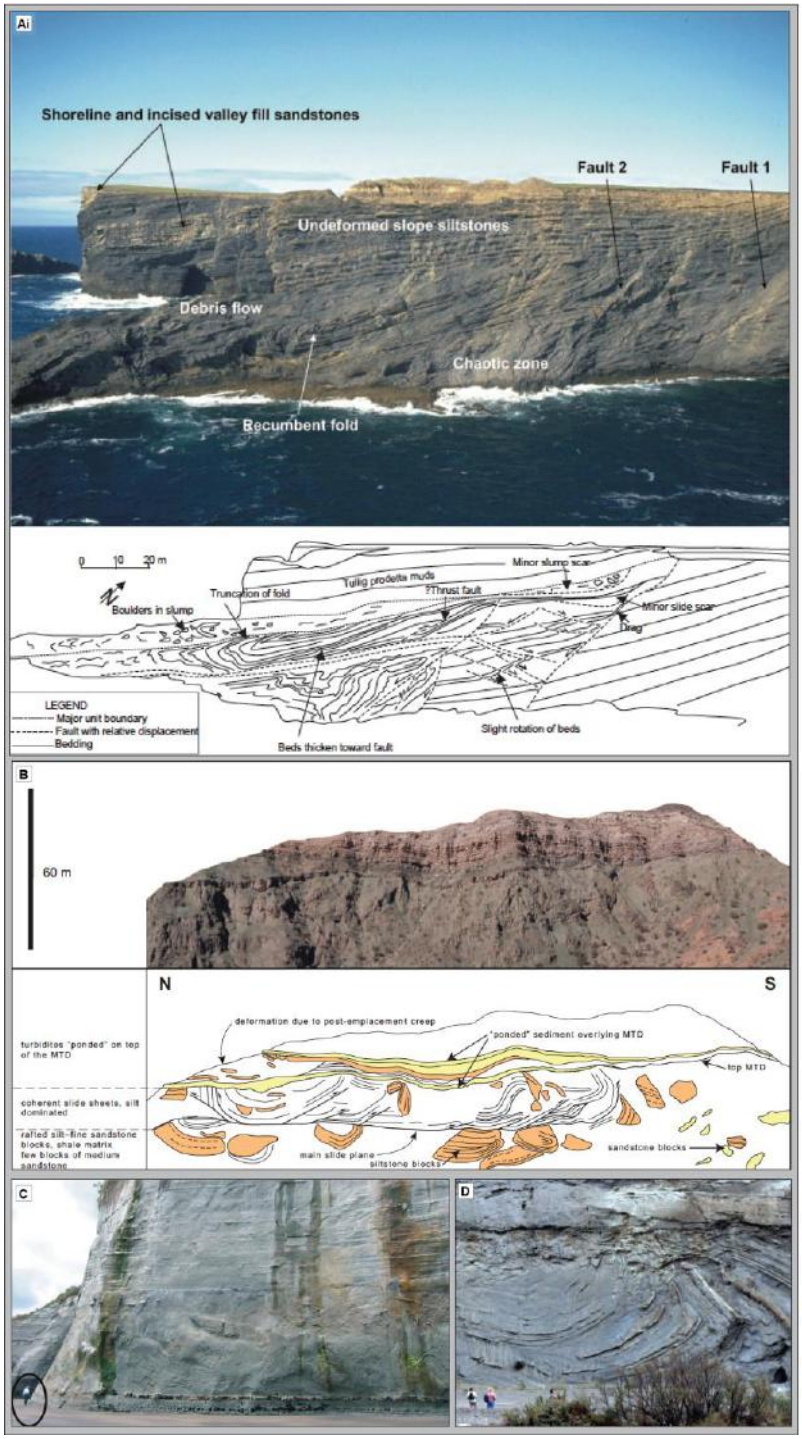

Figure 1.7. (A) Photo and interpretation of upper-slope MTDs, Upper Carboniferous Gull Island Formation, County Claire, Western Ireland. Figure from Posamentier and Martinsen (2011). (B) Photomosaic and line diagram of MTD showing series of imbricate thrust faults, Carboniferous Cerro Bola Formation, Argentina. Figure from Dykstra *et al.* (2011). (C) MTD showing sharp, planar upper and lower contacts comprising deformed sandstone blocks. Miocene Mount Messenger Formation, Taranaki Basin, New Zealand. Figure from King *et al.* (2011). (D) MTD showing Isoclinal recumbent folding in Middle Miocene Gordo Formation, Tabernas Basin, Spain. Figure modified from Posamentier and Martinsen (2011).

This study builds on previous work carried out by the UCL deep-water research group to provide new insights into MTDs and MTCs deposited during the complex geological history of the Ainsa Basin and surrounding areas. The ancient outcrops in the Ainsa Basin constitute the focus of this research. The following sections, therefore, consider the location, tectonic history and basin architecture.

1.2 STUDY AREA: THE EOCENE AINSA BASIN, SPANISH PYRENEES

1.2.1 Geographical setting

The present-day Pyrenees mountain belt separating France and Spain extends ~ 1,500 km from the Cantabrian platform in the west to the Mediterranean Sea in the east, and has an average width of ~ 200 km (Schellart, 2002). The field study area is located in the Middle-Eocene Ainsa Basin, situated in the south-central Spanish Pyrenees of the Huesca Province of Aragon, northeast Spain (Figure 1.8).

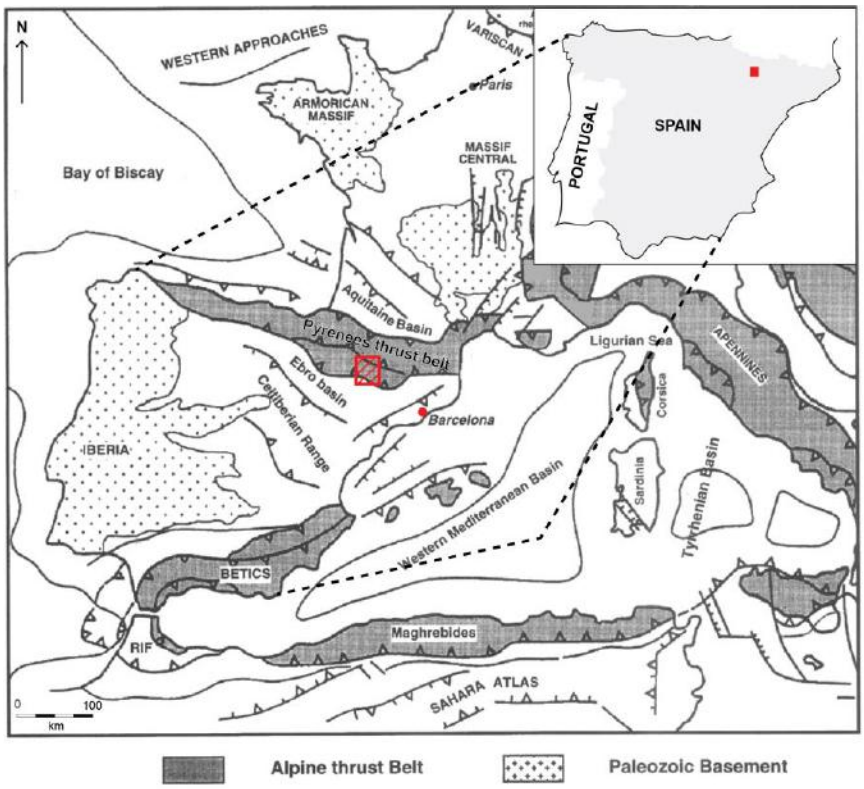

Figure 1.8. Location map of the study area (Ainsa Basin), located south-central Pyrenees, Northern Spain, hatched in the red box. Map modified from Mascle and Puigdefábregas (1998).

The Ainsa Basin is a deep-marine foreland and thrust-top (piggyback) sedimentary basin that formed during uplift of the Pyrenean mountain belt (Mutti and Ricci Lucchi, 1972, Mutti 1977, 1983; Muñoz *et al.*, 1994).

1.2.2 The Pyrenean Orogeny

The Pyrenees are defined as an E-W to ESE-WNW trending asymmetric, double-wedge continental belt that formed in response to cratonic convergence from the Late Cretaceous into the Early Miocene (Brunet, 1986; Choukroune *et al*., 1990; Muñoz *et al.*, 1994; Vergés *et al.*, 1995). Closure of the Tethys Ocean and seafloor spreading in the North Atlantic Ocean resulted in north-south convergence of the Iberian plate and putative subduction-underplating of the lower crust of the Eurasian plate, resulting in the Pyrenean orogeny (Muñoz *et al.*, 2013). Plate movements during the Paleocene to Miocene involved an essentially north-south convergence between the Iberian and European plates and continued into the Oligocene, resulting in the inversion of previous rift structures (Farrell, 1984; Puigdefábregas and Souquet, 1986; Gong *et al.*, 2008; Vissers and Meijer, 2012). Several phases of rifting occurred before the main phase of collision, associated with the opening of the North Atlantic. The opening of the Bay of Biscay caused Iberia to rotate ~ 35° counter-clockwise relative to Eurasia (Muñoz *et al.*, 2013).

The ECORS seismic transect runs 200 km perpendicular to the length of the Pyrenean orogenic belt extending from the Aquitaine (southern France) to the Ebro (Northern Spain) foreland basins (Figure 1.9). Crustal balancing of the ECORS seismic reflection profile estimated 120 – 165 km of shortening occurred along basal detachment between the Triassic Keuper evaporite Formation and undeformed Variscan basement rocks, resulting in the propagation of thin-skinned tectonic thrusts that penetrated Mesozoic stratigraphy (Desegaulx *et al.*, 1990; Puigdefàbregas *et al.*, 1992; Muñoz *et al.*, 1994; Vergés *et al.*, 1995).

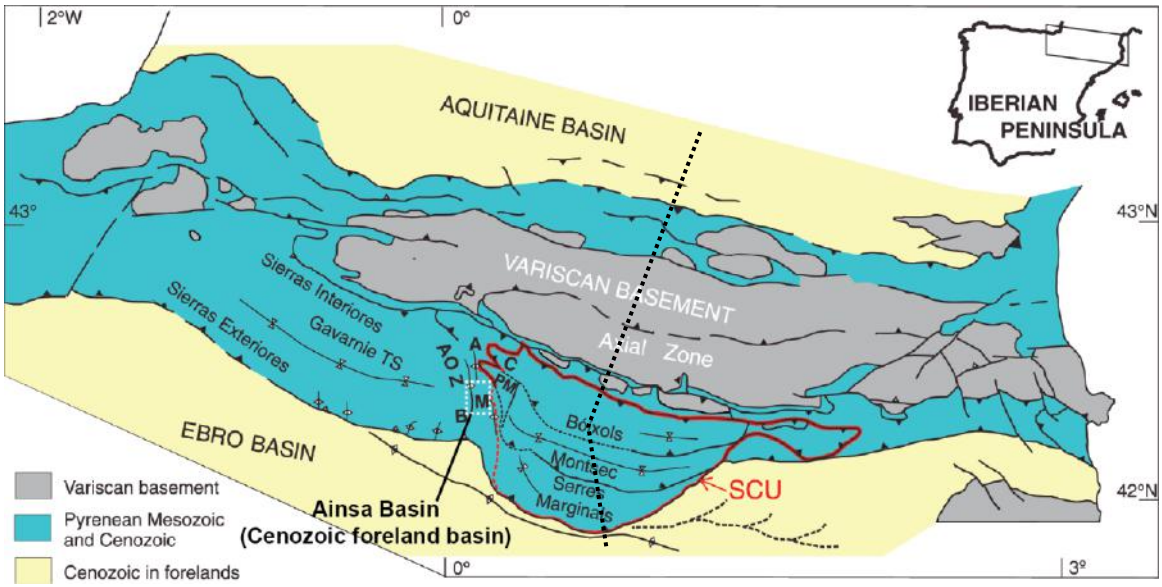

Figure 1.9. Structural sketch showing the main structural units of the central Pyrenees. A – Añisclo Anticline, AOZ – Ainsa Oblique Zone, B – Boltaña Anticline, M – Mediano Anticline, C – Cotiella, PM – Peña Montañesa, SCU – South Pyrenean Central Unit. The position of the ECORS cross-section shown by the dashed line. Modified from Muñoz *et al.* (2013).

Maximum rates of tectonic subsidence in the Ainsa Basin coincided with the maximum rate of shortening during the Late Lutetian, where up to 1.5 to 6 mm per year are calculated (Vergés *et al.*, 1995), broadly contemporaneous with the accumulation of deep-marine sediments of the Ainsa Basin. Rapid exhumation of the axial Pyrenees occurred during the Late Eocene to Early Oligocene and by the Miocene, erosion of the Pyrenees resulted in the deposition of conglomeratic valley fills and fans (Vincent, 2001; Michael *et al.*, 2014).

1.3 GEOLOGICAL SETTING AND DEPOSITIONAL ENVIRONMENTS

1.3.1 Structure and South-central Pyrenees

The Ebro Basin, located on the Iberian plate, evolved by plate flexure in response to south-directed thrust sheets of the Pyrenees (Figure 1.9). The pre-thrusting stratigraphic sequence of the south-central Pyrenean Unit (SCU) in the Ebro Basin is a result of extension in the Triassic, generating basin widening and the development of fluvial streams grading up to lagoonal deposits with varying clastic, carbonate and evaporite facies. The Triassic evaporites act as a basal detachment for thrusts in the region. Up to 1,500 m of Mesozoic to Paleocene shelf carbonates and siliciclastic

sediments overlie the Triassic shales and evaporites. These include Upper Cretaceous limestones, marls and calcarenites and Lower Eocene (Ypresian) Alveolina Limestone, found over most of the south-central Pyrenean basins (Figure 1.10). Deposition of the Alveolina limestones represents a widespread transgressive episode that proceeded the onset of thrusting in the Ainsa Basin (Mutti *et al.* 1983; Barnolas and Teixell, 1994; Bentham *et al*. 1996; Fernández *et al.*, 2004; Muñoz *et al.*, 2013). The Lower and Middle-Eocene platform carbonates are overlain by Middle- to Upper Eocene clastic sediments corresponding to distal parts of alluvial fans and deltas attached to the thrust fronts of the rising Pyrenees of the axial zone (Schellart, 2002).

The SCU is bound by the Cotiella-Bóixols, Montañesa-Montsec and External Sierras thrust sheets (north-to-south and youngest-to-oldest, respectively). A linked propagating thrust system along the Gavarnie thrust sheet underlies most of the Ainsa Basin (Puigdefàbregas *et al.,* 1992) (Figure 1.9). Within the SCU, a series of present-day north- to south-trending anticlines formed as a coherent and synchronous system from the Ypresian to the Early Priabonian, in association with westward thrust propagation with common detachment along Triassic evaporates (Figure 1.10). From east to west, these are named the Mediano, Olsón, Añisclo and Boltaña anticlines (Fernández *et al.*, 2012). One major syncline, the Buil syncline separates the Mediano and Boltaña anticlines and splays north around the Añisclo Anticline to form the Buerba and San Viciente synclines (Figures 1.11 and 1.16). To the east, the Mediano Anticline separates the mainly terrestrial, coastal and shallow-marine Tremp-Graus Basin and proximal deep-marine Ainsa Basin, and to the west, the Boltaña Anticline separates the Ainsa from the distal deep-marine Jaca and Pamplona Basins. A regional chronostratigraphic diagram for the Tremp-Graus, Ainsa to Jaca stratigraphy is shown in Figure 1.10.

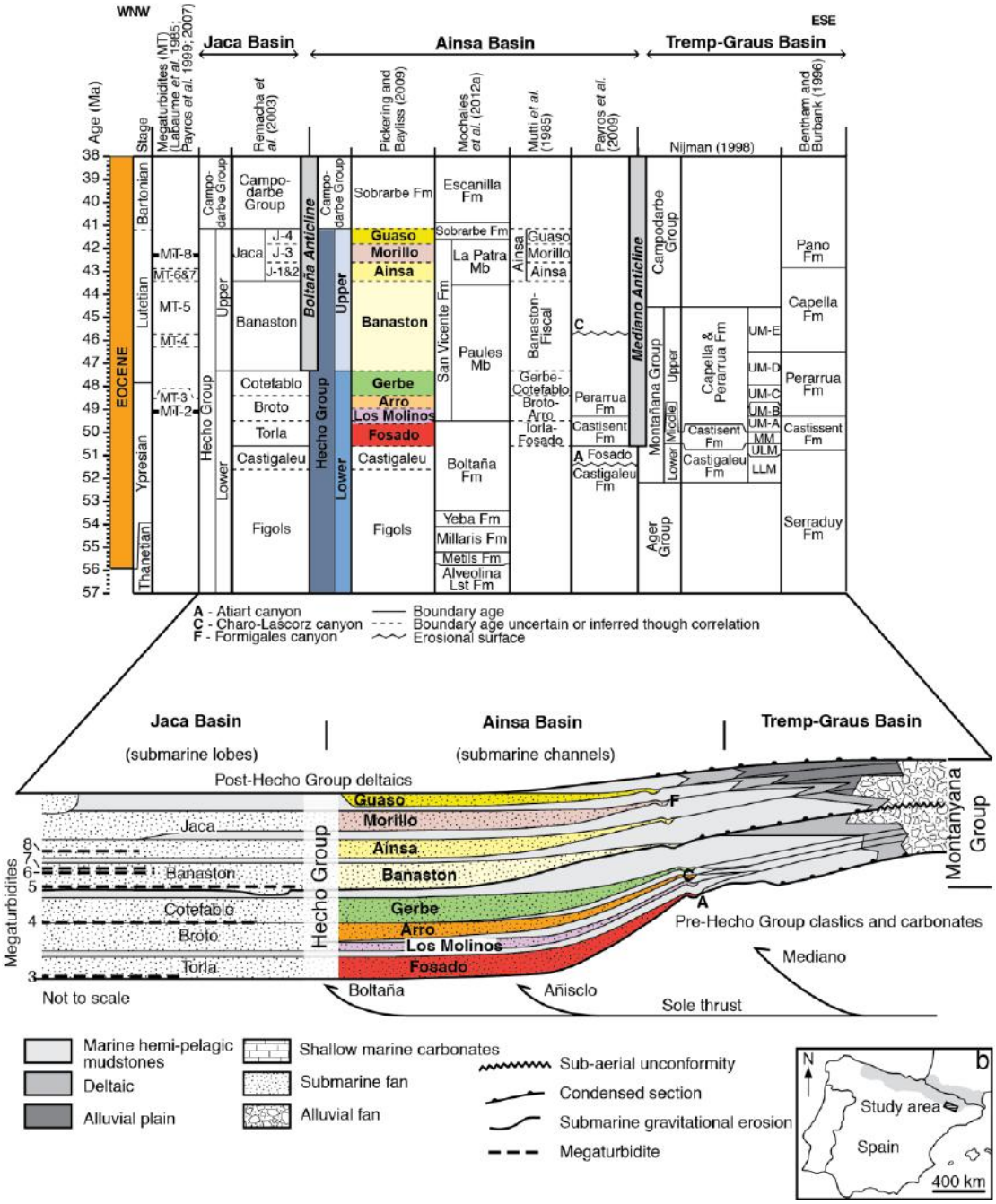

Figure 1.10. Chronostratigraphic representation of general stratigraphy of the Tramp-Graus, Ainsa and Jaca basins. Not to scale. Sedimentary systems documented in this study are highlighted in the Ainsa Basin. Figure modified from Scotchman *et al.* (2014).

The Mediano Anticline became a palaeo-high during the Ypresian and continued to grow as an anticline into the Lutetian (Muñoz *et al.*, 2013) (Figure 1.10). In the present-day, the Mediano Anticline is an upright detachment fold reaching up to 3,000 m of structural relief. The Mediano Anticline is ~ 20 km in length and plunges ~ 10 – 15° northward. Both the back and forelimbs dip up to 45° east and west. To the north, the plunge decreases and the Mediano fold opens out and dies out

towards the town of Ainsa, at a similar latitude to the southern termination of the Añisclo Anticline (Fernández *et al.*, 2012). The Boltaña and Añisclo anticlines formed as fault-propagation folds, both with over 2,000 m of structural relief at the present day (Muñoz *et al.*, 2013). The Boltaña Anticline is ~ 25 km in length and has a constant geometry along strike, with a horizontal fold axis and the back limb and forelimb that has constant dips, ~ 20 – 30° to the east for the backlimb and ~ 80 – 90° to the west for the forelimb (Fernández *et al.*, 2004; Mochales *et al.*, 2012) (Figure 1.11). The growth of the Boltaña Anticline began later during the Lutetian and produced a significant barrier to the west- and northwest-directed turbidity currents during this time (Farrell *et al.*, 1987).

The geometry of the Añisclo Anticline can be divided into three segments with varying trends and geometries (Fernández *et al.*, 2012). The Olsón Anticline, ~ 10 km south of the southern tip of the Añisclo Antlicline, is a symmetrical detachment fold, with both limbs dipping 20 – 25°, and has ~ 1,000 m of structural relief (Fernández *et al*., 2012). The Olsón Anticline has no surface expression in the present day Ainsa Basin configuration. The present-day axial configuration of the fold axes of the Mediano, Olsón, Añisclo and Boltaña anticlines trend north-south. However, recent studies document clockwise vertical-axis rotation varying from 70° at the Mediano Anticline in the east Mediano Anticline to 55° at the Boltaña Anticline in the west (Muñoz *et al.*, 2013). Axial rotation of the anticlines is attributed to a difference of ~ 50 km of displacement on the Gavarnie thrust sheet. Following early thrusting, it is believed that the sole Gavarnie thrust broke the surface in several places. The growth of the Boltaña Anticline to the west of the Ainsa Basin suggests that the basin had become detached as a thrust-sheet-top basin during the Lutetian (Farrell *et al*., 1987; Dreyer *et al.*, 1999; Fernández *et al.*, 2004).

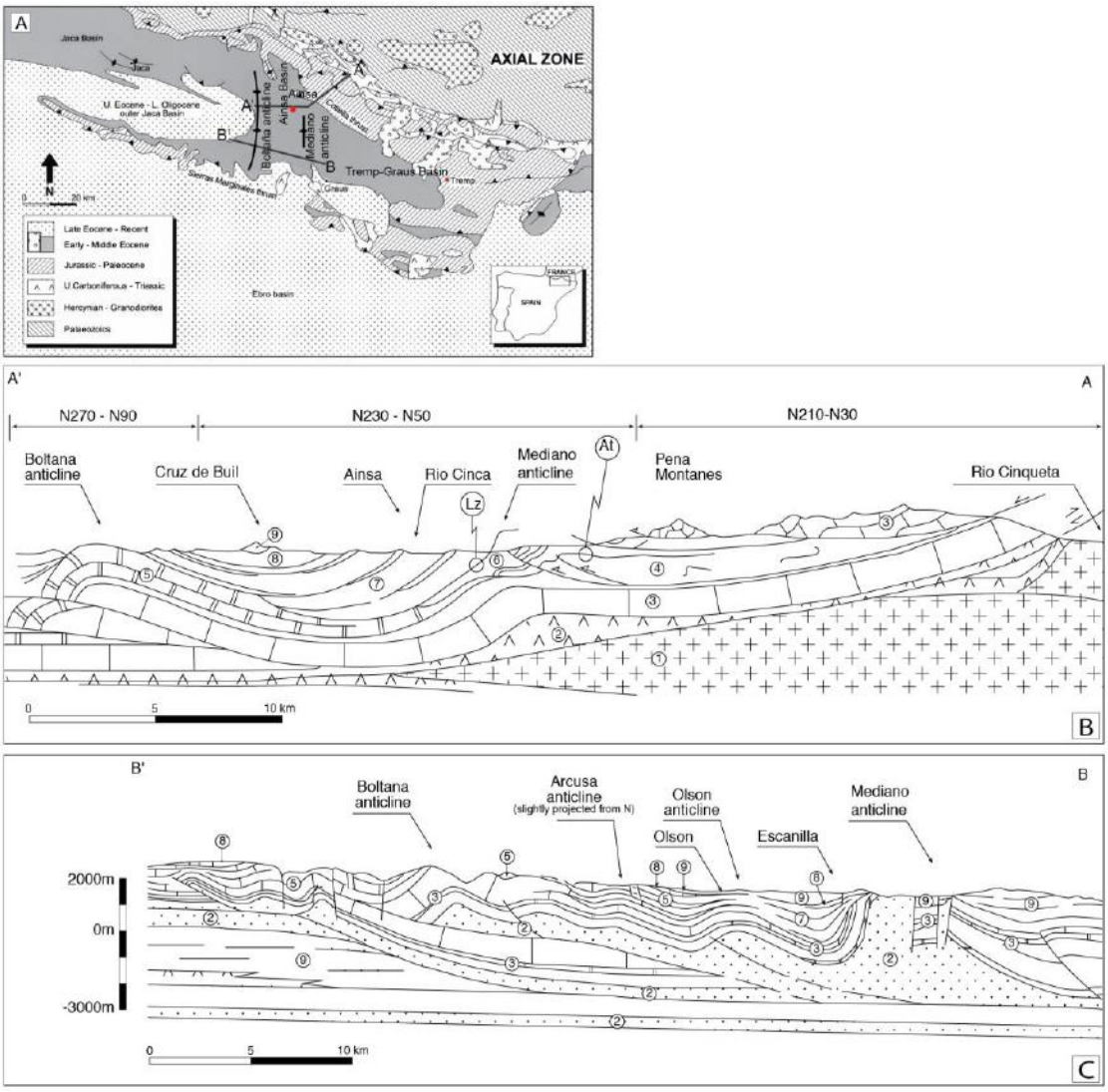

Figure 1.11. (A) Location map of the Ainsa Basin and surrounding main structural elements. The A'-A and B'-B lines correspond to the structural cross-sections shown in (B) and (C) - Structural sections across the northern and southern parts of the Ainsa Basin study area. Thrust-related structures, including the intra-basinal Arcusa and Olson growth anticlines are shown. The stratigraphic units are numbered as follows: 1/ Palaeozoic basement; 2/ Triassic (including salt deposits); 3/ Upper Cretaceous, Paleocene and lowermost Eocene (mostly limestones); 4/ Lower Eocene marls; 5/ Lower Eocene shallow-marine limestones and sandstones (Guara Formation); 6/ Lower Eocene Arro SGF deposits; 7/ Middle Eocene Ainsa SGF deposits; 8/ Middle to Upper Eocene deltaic complex of the Sobrarbe Formation; 9/ Middle to Upper Eocene fluvial deposits of the Escanilla Formation. Modified from Dreyer *et al.* (1999).

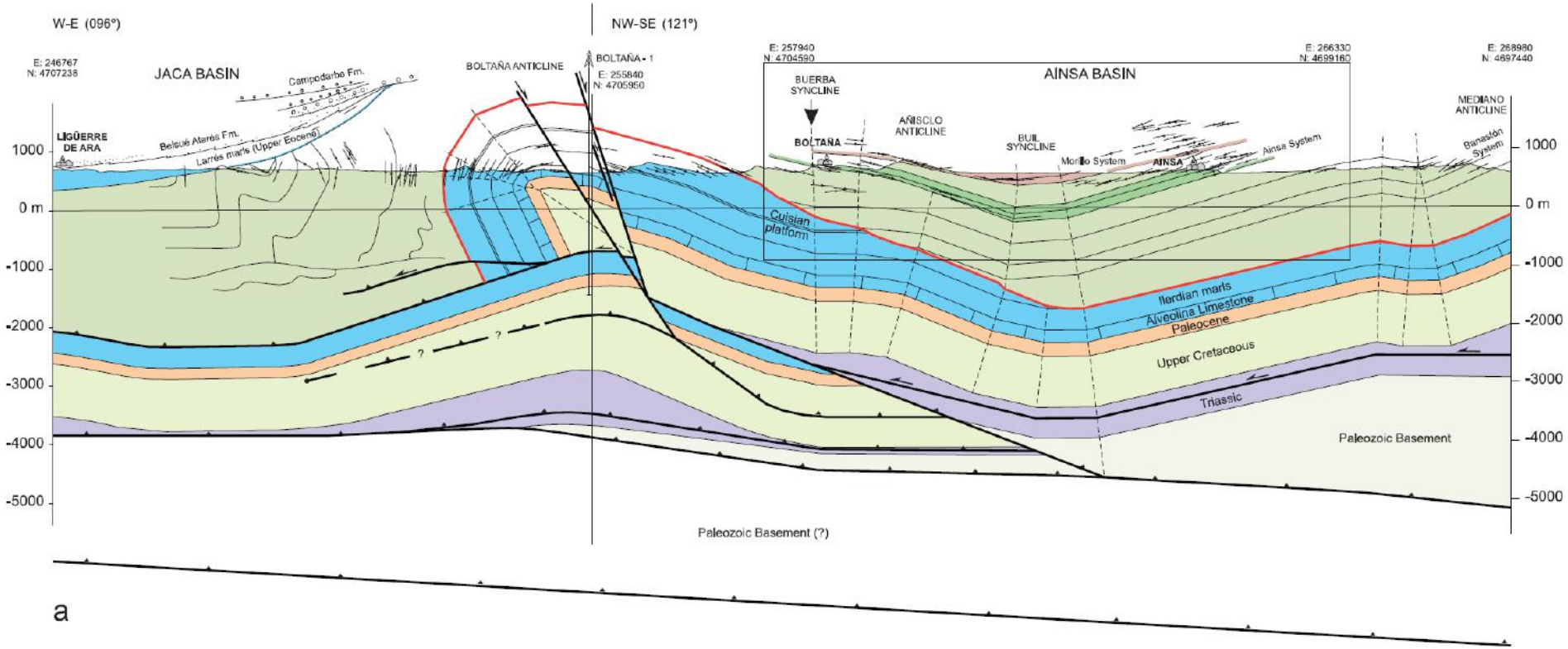

Figure 1.12. Cross-section across the northern sector of the Buil syncline and Boltaña Anticline. Vertical scale is indicated in metres and horizontal scale is indicated by UTM zone 31 coordinates. From Fernandez *et al.* (2004)

1.3.2 Deltaic to abyssal environments

The SCU evolved with mainly non- to marginal-marine environments in the eastern sectors, whilst farther west in the Ainsa Basin there was an overall change from fluvio-deltaic to deep-marine environments (Boer *et al.*, 1991; Verges *et al.*, 1995), (Figure 1.10). Palynofloral and microfaunal data suggest a tropical to subtropical climate with moderately high rainfall. The hinterland was dominated by coniferous vegetation on upland and well-drained lowlands with swamps and mangrove belts that developed on poorly-drained areas (Pickering and Corregidor, 2005). Source areas were located in the rising axial zone of the Pyrenees, with transport routes of these sediments differing in length and gradient and controlled by embryonic structures related to thrust propagation (Figures 1.11 and 1.12).

The Hecho Group, first defined by Mutti and Ricci Lucchi (1972) and Mutti (1977, 1983), was interpreted as an elongate lobate series of stacked submarine-fan systems ~ 175 – 250 km in length and up to 40 – 50 km in width. The submarine fans cumulatively reach up to 3,500 m in thickness with a total estimated sedimentary volume of 21,000 – 26,000 km^3 (Mutti and Ricci Lucchi, 1972, Mutti 1977, 1983; Ogata *et al.*, 2012). Sediments of the Hecho Group include the fluvio-deltaic complex of the Montañana Group in the Tremp-Graus Basin to the east of the Ainsa Basin, which appears to have fed the channelised proximal deep-marine Ainsa Basin into the distal non-channelised deep-marine Jaca Basin (Mutti and Ricci Lucchi, 1972). Based on micropalaeontological evidence, the submarine fans deposited in the Ainsa Basin are interpreted as deposited in water depths between 400 – 800 m (Pickering and Corregidor, 2005). The sedimentary succession of the regional Hecho Group is subdivided into eight depositional sandy systems, interpreted as genetically-linked deep-marine sandy fans, vertically separated by up to several tens of metres of muddy fine-grained sediments, predominantly marlstone (Figures 1.10 and 1.16).

1.3.2.1 Tremp-Graus Basin

The Tremp-Graus Basin is confined between the Bóixols and Montec thrusts and is dominated by alluvial, deltaic, nearshore and shallow-marine deposits (Nijman and Nio, 1975). The Montañana Group of the Tremp-Graus Basin is a prograding fluvio-

deltaic succession, upper Ypresian to upper Lutetian in age. It comprises a minimum of six megasequences, separated by major onlaps and unconformities in the basin flanks (Marzo *et al.,* 1988). The Castisent Formation of the Montañana Group represents a phase of strong fluvial progradation, enhanced by late Ypresian sea-level fall (Marzo *et al.,* 1988). The Castisent fluvial sandstones typically comprise calcite cemented calc-lithic arenites with 20 – 32 % quartz, 5 – 8 % feldspars, 23 – 42 % non-carbonate rock fragments, and 10 – 30 %, (locally up to 64 %) of carbonate lithoclasts. The carbonate clasts are mainly derived from the Mesozoic of the Cotiella-Montsec Nappe exposed in the basin flanks, and to a lesser degree from Palaeozoic carbonates and intra-basinal calcrete nodules. Other rock fragments include Hercynian metamorphic and igneous material from the basement of the Pyrenees (Marzo *et al.,* 1988).

Vincent (1999) documents the sedimentary supply of two interfingering Late Lutetian fluvial systems preserved at the northern margin of the Tremp-Graus Basin that formed in response to uplift of the Pyrenees. One system is a mountain-belt-derived, high-gradient, bedload-dominated alluvial fan gravelly system, originating from the axial zone of the rising Pyrenean mountain belt, known as the Sis valley. The Sis conglomerate is a major facies type comprised of cobble- and pebble-grade diamicton composed of subordinate sandstone to mudstone, lacustrine limestone and coal, with a minor percentage (< 5%) of pebbles sourced from a granitic source (Vincent, 1999, 2001). The palaeovalley interfingers with a more easterly, basin-axis-derived, lower gradient and poorly drained alluvial system, distributing sediments to the deep-marine Ainsa Basin. During the Late Lutetian, the palaeoshoreline migrated to the western margin of the Tremp-Graus Basin (Nijman, 1998).

1.3.2.2 The Ainsa Basin

Due to the advancing southwestward-directed thrust sheets from the deformation front of the SCU, syndepositional tectonics in the Ainsa Basin are prevalent throughout its depositional history (Pickering and Bayliss, 2009). The Hecho Group in the Ainsa Basin is conventionally subdivided as two tectono-stratigraphic stratigraphic units: the Upper and Lower Hecho Groups. These two tectono-stratigraphic successions represent unconformity-bound depositional units of the deep-marine stratigraphy

related to the transition between a foreland basin to thrust-top (piggyback) basin (Figure 1.10). This transition involved a major phase of thrust propagation that shifted the depocentres towards the west and increased basin gradients. In the stratigraphy, this is represented by a basal angular unconformity that is inferred to extend from the delta plain to the basin floor (Pickering and Bayliss, 2009). The Upper Hecho Group (Banastón, Ainsa, Morillo and Gerbe systems) were deposited during the growth of the Mediano, Olsón, Añisclo and Boltaña anticlines (Fernández *et al.*, 2012), with the Boltaña Anticline not fully developing until the early Lutetian. Systems of the Lower Hecho Group (Fosado, Los Molinos, Arro and Gerbe systems), deposited in the Ypresian, were not confined by the embryonic Boltaña Anticline and, therefore, the oldest systems are not preserved in the west of the basin as they likely bypassed the Ainsa Basin, depositing basinwards towards Jaca. The oldest fan system, the Banastón System, in the Upper Hecho Group onlaps to the Boltaña Anticline, for example as seen in the road outcrop leading to Sabiñanigo, showing that the anticline formed a sufficient topographic high at the time of deposition of the Upper Hecho Group (Figures 1.10 and 1.12).

The Ainsa Basin is a structurally-confined slope, base-of-slope and proximal basin-floor (typically channelised) deep-marine basin-fill. Sediment inputs were fed from fluivo-deltatic environments to the east, from the Tremp-Graus Basin (Figures 1.13 and 1.14), with the more energetic SGFs bypassing westwards into more distal marine settings in the Jaca and Pamplona basins. The sedimentary infill of the Ainsa Basin includes up to ~ 4 km of deep-marine synorogenic sediments deposited over ~ 10 Ma (Pickering and Corregidor, 2005). The channelised portion of the submarine fans in the Ainsa Basin appear to have been mainly confined to the synsedimentary topographic depression created by the growing Mediano Anticline in the east, i.e., west of the prograding delta slope (Mutti, 1977): this growth anticline probably helped to 'pin' the shelf-slope break throughout the entire basin history. The north-south trending Boltaña Anticline was an important structural feature, as it was active during deposition and not only controlled the deposition of sediments, but defined the boundary between the proximal Ainsa Basin and distal Jaca Basin, where proximal turbidite channels in the east grade laterally into distal turbidite lobes to the west (Mutti, 1983; Farrell *et al.*, 1987). During the accumulation of the Lower Hecho Group, the Ainsa Basin had a more east-west orientation but prior to deposition of the

Upper Hecho Group underwent ~ 30^{o} of clockwise rotation on the Gavarnie thrust sheet (Muñoz *et al*., 2013).

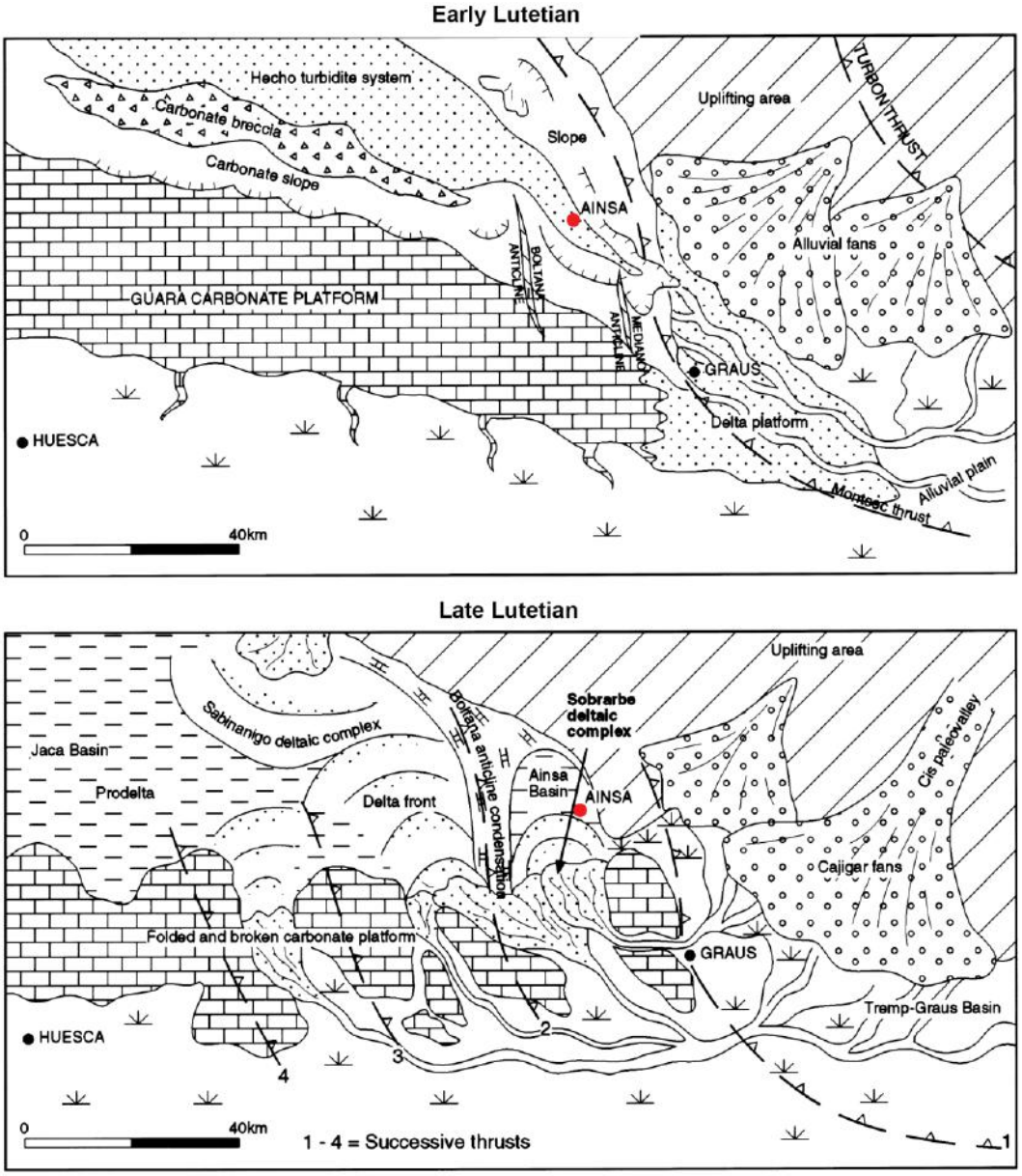

Figure 1.13. Large-scale palaeogeographic reconstructions of the Ainsa Basin and surrounding areas during deposition of the Sobrarbe deltaic complex. Early Lutetian – Early stage progradation, corresponding to deep-marine deposition in the Ainsa Basin depositing SGF sandstones in the study area and a major carbonate platform existed in the southwestern portion of the South Pyrenean Foreland Basin. The Mediano Anticline is present as an intra-slope lineament, and the Boltaña Anticline was likely to represent a subtle submarine high. The main source area was located in the uplifted terrains at the northern margin of the Tremp-Graus Basin. Late Lutetian – Late stage deltaic progradation. Shallow-marine to fluvial conditions existed in the Buil Syncline in the Ainsa Basin. Shallow-marine conditions, from carbonates to muddy coastal plain environments existed at basin margins. From Dreyer *et al*. (1999).

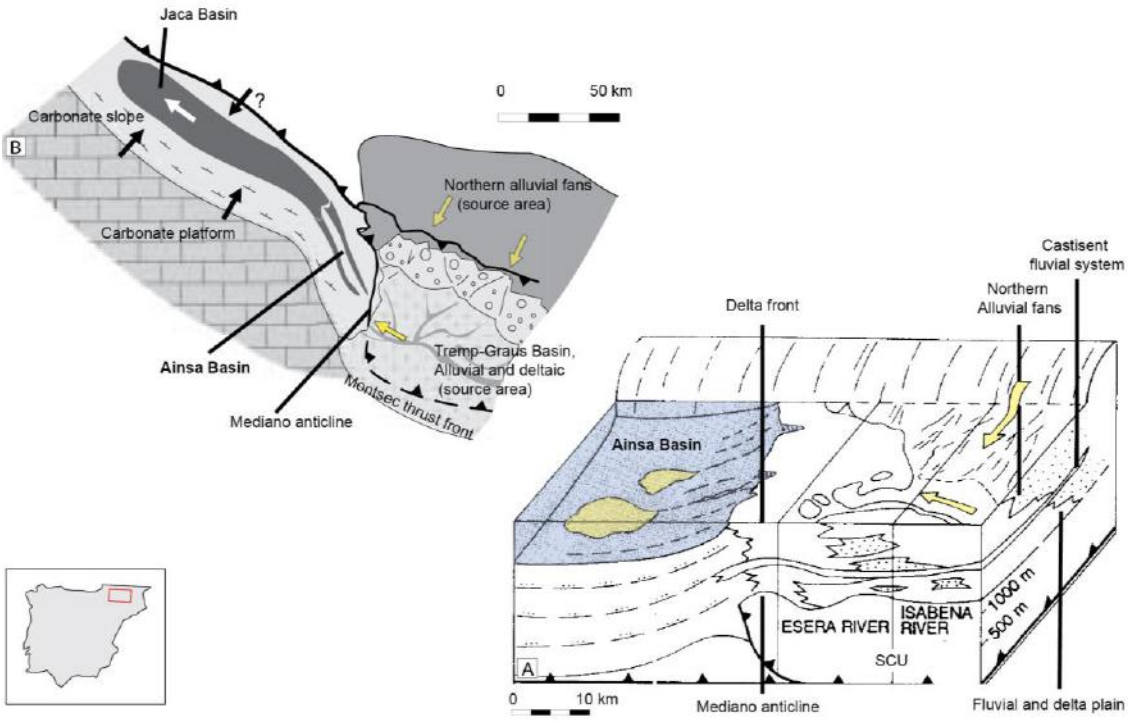

Figure 1.14. (A) Proximal schematic block diagram showing the transition from continental and shallow marine deposits (Tramp and Ager basins), to deep-marine sediments (Ainsa Basin) separated by the Mediano Anticline during the Eocene. Modified from Puigdefábregas *et al.* (1992). (B) Overview of sediment dispersal from the Tremp-Graus Basin, through the proximal Ainsa Basin, into the distal Jaca Basin. Arrows denote main direction of sediment transport. Modified from Fernández *et al.* (2004).

1.3.2.1.1 Peri-Ainsa Basin carbonate platform

During the latest Cretaceous and Early Tertiary, the Pyrenean part of the Iberian continent was located at ~ 37°N latitude. Shallow-marine carbonate platforms and ramps fringed both the northern and southern margins of the Ainsa Basin (Payros *et al.*, 2006). To the south, the Sierra Guara carbonate platform (Guara Formation) extended to the Sierras Exteriores in the Southern Pyrenees (Figure 1.13). The Guara Formation was deposited in a shallow-marine environment (< 120 m) during the Ypresian and Lutetian and comprises massive-bedded limestones from 50 m in the west to over 100 m in thickness in the east (Nichols, 1987; Huyghe *et al.*, 2012).

1.3.2.2.2 Resedimented carbonate deposits

Parts of the fringing carbonate platforms and ramps surrounding the deeper-water Ainsa and Jaca basins were subject to resedimentation processes, probably associated with seismic activity below the tectonically active margins. In the Jaca Basin, the presence of such redeposited carbonates as both olistoliths and finer-grained 'megaturbidites' are documented (Labaume *et al.*, 1983a, b, 1985, 1987; Ogata *et al.*, 2012), as identified in the stratigraphic column (Figure 1.10). Several carbonate deposits are as thick as 250 m, and as voluminous as 50 km^3, and extend for a considerable distance to provide stratigraphic markers across basin-floor and depositional lobe facies (Mutti, 1983; Remacha and Fernández, 2003).

1.3.2.3 Jaca Basin

The Jaca Basin is located to the west of the Boltaña Anticline extending up to 250 km from the Ainsa Basin to the general region of Pamplona in the west (Mutti, 1983) (Figures 1.10 and 1.14). The Jaca Basin mainly contains Eocene non-channelised deep-marine successions. Between Jaca and Pamploma, these sediments consist of a thick succession of basin-floor deposits with rare large resedimented carbonate megabreccia deposits (Puigdefábregas and Souquet, 1986; Farrell *et al.*, 1987; Puigdefàbregas *et al.,* 1992; Payros *et al.,* 2009).

1.3.2.3.1 Outer-fan and basin-floor facies

Outer-fan SGF deposits of the Hecho Group are well exposed in the area of Broto, where they comprise alternating non-channelised sandbodies and associated thin-bedded sediments and also show thickening-upward trends, interpreted as lobe-fringe and lobe deposits (Mutti, 1977). These facies are identified from thin-bedded deposits that include cyclic vertical variations depicted by changes in sand-to-shale ratios (Figure 1.15). The average thickness of turbidite sandstone packages vary between 3.22 and 3.98 cm. Hemipelagic beds are measured between 4.09 and 4.77 cm (Mutti, 1977).

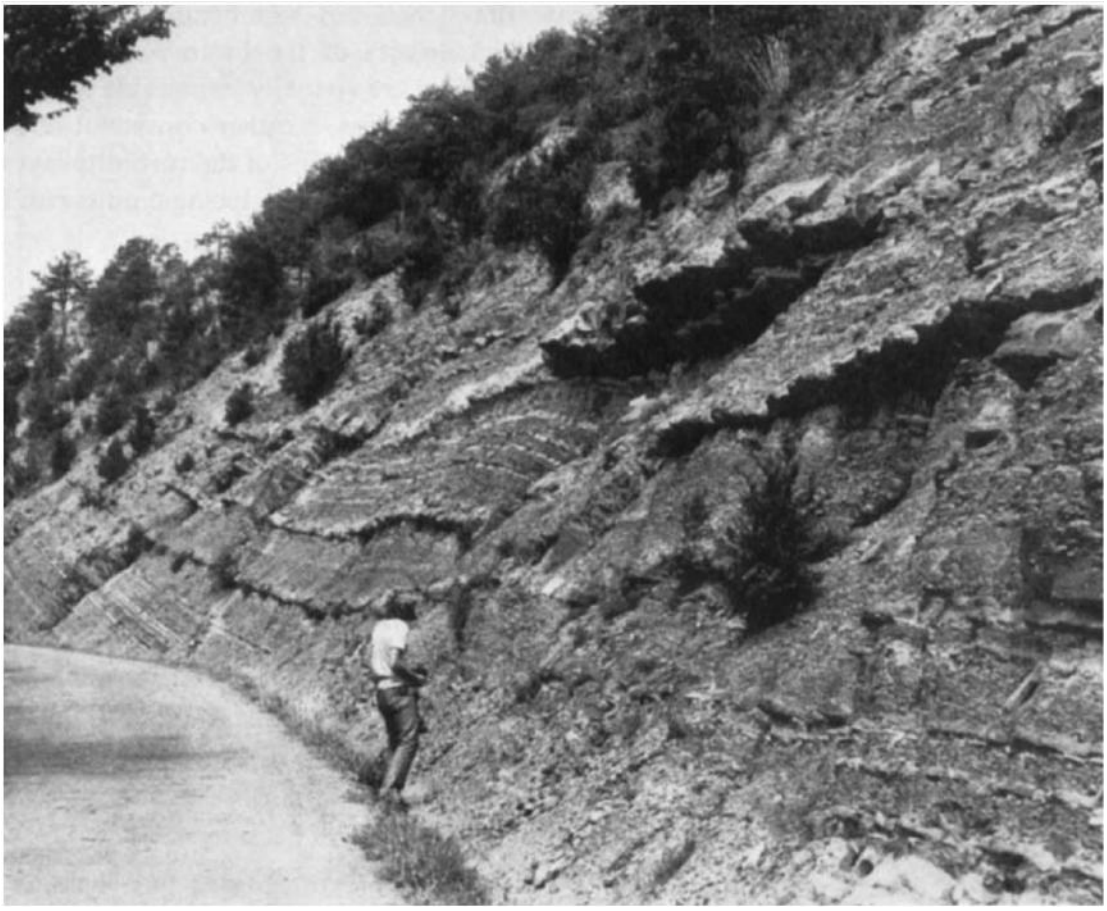

Figure 1.15. Basin plain facies. Turbidite beds are laterally continuous across the outcrop and have a low sand: shale ratio. From Mutti (1977).

Basin-plain sediments of the Hecho Group are found in the distal Jaca Basin and are identified by alternating thin beds of sandstone, siltstone, mudstone and hemipelagic marls, with average sandstone beds measured at 1.04 cm and average hemipelagic sediments at 5.01 cm (Mutti, 1977). Sedimentary features of the thin-bedded Hecho Group basin plain deposits result from the transport and deposition of turbidity currents that gradually lost their suspended load with distance.

1.3.3 Sedimentary systems of the Ainsa Basin

The UCL deep-water research group mapped the systems of the Ainsa Basin, published in Pickering and Bayliss (2009) (Figure 1.16). Geological mapping shows that the coarse clastic supply was confined to the submarine fans deposited in the Ainsa Basin, whereas inter-fan sediments are represented by finer-grained laminated to homogenised hemipelagic mudrocks with common sandy fine-grained laminated

very thin-bedded SGF deposits (Pickering and Bayliss, 2009). The thin-bedded SGF deposits in intrafan sediments are interpreted as accumulating mainly from a combination of direct river-derived sediment input (e.g., as hyperpycnal flows), redeposition during storms and small-volume slope instability processes. The background pelagic and hemipelagic marlstones and very thin nummulite-rich packstones are interpreted as being sourced from the flanking carbonate shelves, river mouths and by the advection of sediment over the shelf edge during storms (Pickering and Corregidor, 2000, 2005).

The focus of this research is on the Upper Hecho Group of the Ainsa Basin. The field area is ~ 8 by 10 km, from the oldest lower slope erosional channel complex of the Banastón System in the east, around the village of Usana, to the lateral equivalent of the basin floor deposits of the Banastón System to the northwest, around the town of Boltaña, outlined in Chapters 4 and 5. Field locations visited during fieldwork and discussed in this project are shown on the geological map (Figure 1.16), with co-ordinates presented in Chapter 3 (Figure 3.1and Table 3.1).

The eastern area of the Ainsa Basin is structurally complex, dominated by thrusts and comprises the oldest sandstone systems (Fosado, Los Molinos, Arro and Gerbe, younging respectively, as part of the Lower Hecho Group). Each system comprises 1 to 6 individual sandbodies interpreted as discrete submarine fans recording the evolution of the Ainsa Basin throughout its ~ 10 Ma depositional history, from basin initiation to shallowing-up trend. In this study, nomenclature from Mutti (1972) is used, whereby the 8 sandy systems are named according to the town upon which they are best exposed. The Lower Hecho Group comprises: Fosado (2 systems); (2) Los Molinos (1 system); (3) Arro (3 systems); (4) Gerbe (2 systems); and the Upper Hecho Group comprises: (5) Banastón (6 systems); (6) Ainsa (3 systems); (7) Morillo (3 systems), and (8) Guaso, (2 systems), which are in comparison less deformed than the Lower Hecho Group. These systems are described below.

1.3.4 Lower Hecho Group

1.3.4.1 Fosado (F-I, F-II)

The Fosado System of the Lower Hecho Group represents the onset of deep-marine sedimentation and comprises two remnants of channelised sandbodies, interpreted as lower-slope erosional channels and are up to 30 m in thickness (Pickering and Bayliss, 2009).

1.3.4.2 Los Molinos (LM-I, LM-II)

The Los Molinos System comprises two channelised sandbodies, interpreted as being confined erosional base-of-slope channels up to 90 m in thickness (Pickering and Bayliss, 2009).

1.3.4.3 Arro (Ar-I, Ar-II)

The Arro System is interpreted to have three discrete sandbodies fed by the Charo Canyon, which incised 200 m – deep and 1,000 m into the Castisent formation of the Montañana sequence. The Charo Canyon acted as a sediment conduit for deep-marine flows. The Charo canyon-fill comprises chaotic mudstone facies and lenses of coarse sandstone and conglomerates (Mutti, 1983). It is interpreted that the Fosado and Arro channel-levee systems were a result of sudden phases of relative lowering of sea level, documented by the deep incision into the underlying shelf deposits (Mutti, 1983). The Arro sandbodies contain abundant organic detritus, including wood fragments, suggesting fluvio-deltaic systems fed these deep-marine channels (Pickering and Bayliss, 2009). The sandy fans are characterised by a base-of-slope facies. Key factors influencing the architecture of the Arro System is related to an increase in sediment supply, related to the early stages of an intrabasinal local thrust of the Castisent formation (Millington and Clark, 1995a, b).

1.3.4.4 Gerbe (Ge-I, Ge-II)

The Gerbe System comprises two sandbodies interpreted as erosive lower-slope erosional channels. The sandy part of the channel varies from up to 60 m in Ge-I, to 210 m in Ge-II (Pickering and Bayliss, 2009). These sandbodies are characterised by

conglomerates and pebbly sandstones at the base of the sandy fans. The Gerbe System is deformed by the Los Molinos thrust (Figure 1.16), but appears less deformed than the older Arro System, suggesting progressive thrust-related strain prior to, and after, deposition of this system (Pickering and Bayliss, 2009).

1.3.5 Upper Hecho Group

1.3.5.1 Banastón (B-I, B-II, B-III, B-IV, B-V, B-VI)

The Banastón System is divided as two distinct erosional-depositional environments; lower-slope erosional channels or canyons around the villages of Usana-Banastón and Las Cambras and less-confined depositional fans around the village of San Viciente and town of Boltaña, respectively (detailed in Chapter 4). The Banastón System comprises six principle sandbodies showing varying degrees of lateral confinement, designated I-VI in ascending order. The sandbodies are laterally offset and are interpreted as low-sinuosity and confined channels (Bayliss and Pickering, 2015a).

The lower-slope erosional channels of Banastón V and VI are composed of chaotic deposits interpreted as sediment slumps, slides and debrites (Bayliss and Pickering, 2015a). Deposits of Banastón V and VI Fans reflect the increase of pebbly-mudstones and conglomerate horizons mapped in the lower-slope erosional channels in Usana-Banastón. During deposition of the Banastón System, the basin configuration was narrow and confined, showing strong structural control (Remacha and Fernández, 2003). The relatively distal Banastón Systems shows much less lateral confinement compared to the proximal Banastón-Usana area, with a more gradual shaling out on both margins of the channelised sandbodies (Bayliss and Pickering, 2015a).

1.3.5.2 Ainsa (A-I, A-II, A-III)

The Ainsa System comprises three structurally confined, basin-floor axial deep-marine fans. Each submarine fan comprises individual channels 5 to 30 m deep and hundreds of metres in width (Pickering and Corregidor, 2005, Pickering *et al.*, 2015). The Ainsa I Fan comprises up to ~ 55 m of coarse clastic sandstones. Typical

channel-axis deposits comprise amalgamated pebble to medium-grained sandstones with minor thinner bedded facies. Levee-overbank and intra-channel off-axis deposits are characteristically thin- to very thin-bedded sandy SGF deposits (Pickering *et al.* 2015).

1.3.5.3 Morillo (M-I, M-II, M-III)

The Morillo System comprises three confined and channelised deep-marine fans. The base of the Morillo System is defined with a thick (~ 20 m) debris-flow deposit. MTDs of the Morillo System are comprised of abundant pebbles, found in both pebbly sandstones and pebbly mudstones. Pebbly bar forms are well-exposed in the Rio Sieste, interpreted as large amounts of bypass, suggest high seafloor gradients at the time of deposition (Bayliss and Pickering, 2015b).

1.3.5.4 Guaso (Gu-I, Gu-II)

The Guaso System comprises two main depositional deep-marine fans punctuated by isolated medium- to thick sand packages within the inter-fan fine-grained sediments. The geological map in Pickering and Bayliss (2009) suggest that the deep-marine sediments of the Ainsa Basin are fed from a structurally confined point source to the east, although two sediment sources are postulated by Scotchman *et al*. (2015). Palaeocurrents are found to be consistently between ~ 270 – 300°. The Guaso and Morillo systems are documented as being fed by a more southerly source, related to movement of the Mediano Anticline (Pickering and Corregidor, 2005). Shallow dipping bedding planes (~ 10 – 12°), gently undulating topography and dense vegetation necessitates careful geological mapping within the Guaso System, particularly around Guaso village. To understand the geometry of MTDs in a pro-delta setting (Sutcliffe and Pickering, 2009), parts of the Guaso System were re-mapped resulting in different observations from the published map in Pickering and Bayliss (2009), presented in Chapter 5.

Simplified Geological Map, Eocene Ainsa basin

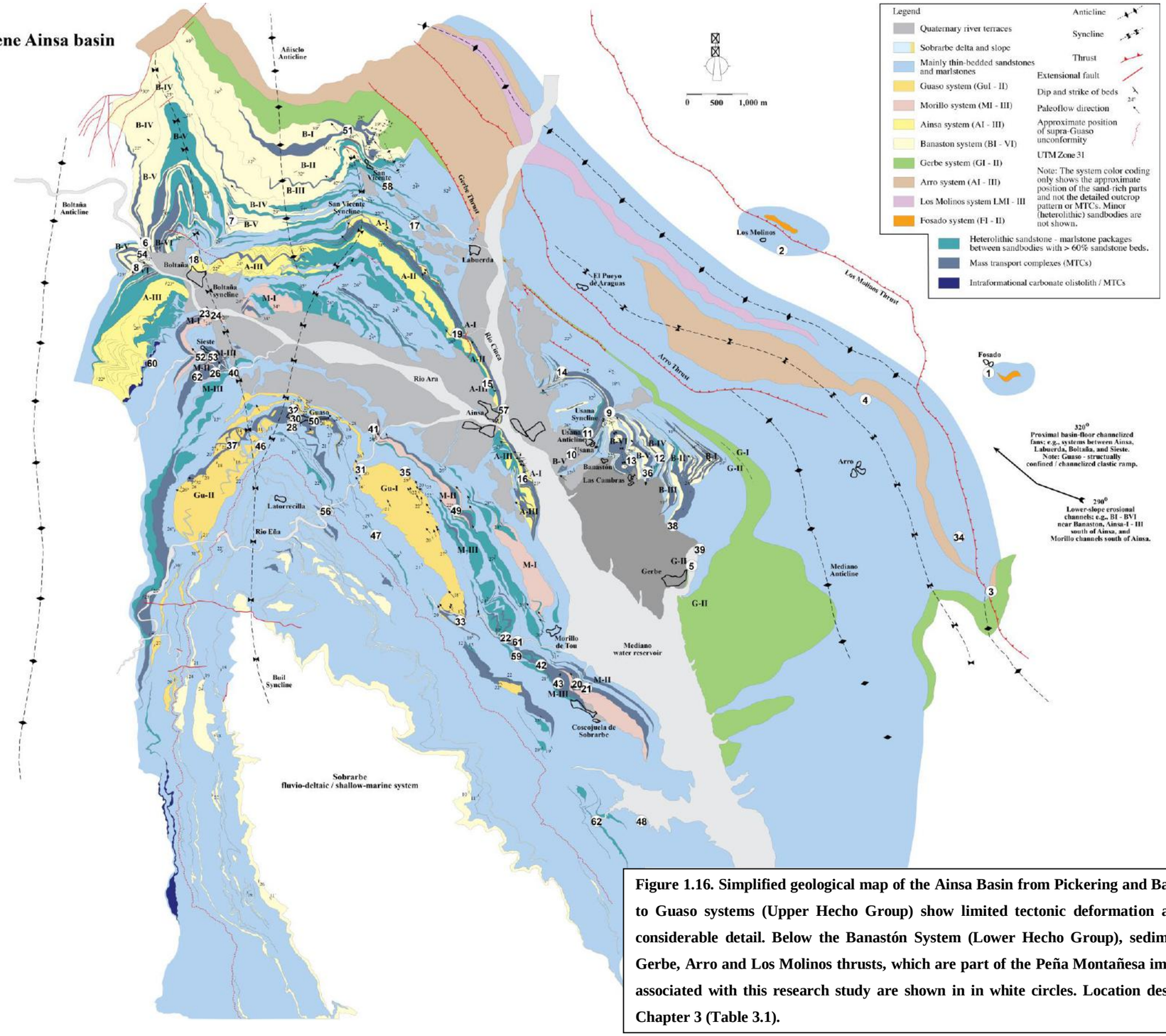

Figure 1.16. Simplified geological map of the Ainsa Basin from Pickering and Bayliss (2009). The Banastón to Guaso systems (Upper Hecho Group) show limited tectonic deformation and have been mapped in considerable detail. Below the Banastón System (Lower Hecho Group), sediments are deformed by the Gerbe, Arro and Los Molinos thrusts, which are part of the Peña Montañesa imbricate fan. Field locations associated with this research study are shown in in white circles. Location descriptions are presented in Chapter 3 (Table 3.1).

1.3.6 Model of submarine fan development

Pickering and Corregidor (2005), modified by Pickering and Bayliss (2009) and Pickering *et al.* (2015), developed a predictive depositional model for submarine-fan growth and abandonment, based on outcrops in the deep-marine Ainsa Basin (Figure 1.17).

1.3.6.1 Initial fan template – Phase 1

The initial phase of submarine fan development is dominated by the deposition of Type Ia MTDs (mud-rich sediment slumps/slides), typically found immediately below of clastic sequences. Deposits immediately beneath sandy-fan sequences are largely absent of extrabasinal materials, such as pebbles, and can form a topographic template for fan accumulation (Pickering and Corregidor, 2005). This predictive sequence is interpreted as a result from a fall in the relative base sea-level causing large-scale collapse of fine-grained (muddy) basin slope sediments, or could related to tectonic oversteepening.

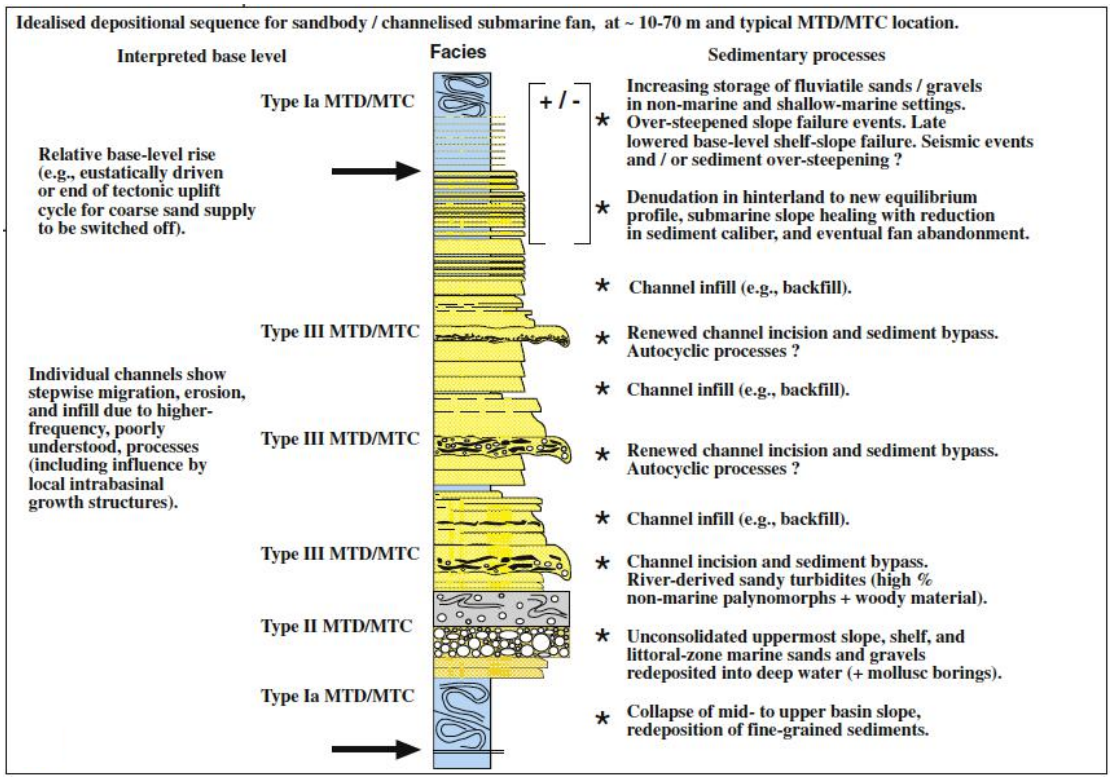

Figure 1.17. Idealised clastic sequence of a single sandbody (depositional fan) based on the Ainsa Basin. From Pickering and Corregidor (2005).

1.3.6.2 Early fan – Phase 2

The overlying early stages of fan development are generally characterised by infilling of complex sea floor topography created by mounded cohesive sediment slides and debris-flow deposits. The first sands deposited in submarine fan systems are relatively unconfined, with thin- to medium bed thickness (i.e., 3 to 30 cm thick according to the Campbell, 1967 bed-scale classification) and can be very coarse-grained, sourced from the upper slope, or shelf environments. The development of amalgamated channel systems at the base-of-slope, or basin floor deposited coarse clastics (sandy SGF deposits) within which, conglomerates, pebbly mudstones and sandstones are typically located (Type III MTDs). The pebbles are well-rounded and can have abundant molluscan borings, showing they resided in the littoral zone for some time and were probably sourced from fluvial rivers and deltas (Pickering and Corregidor, 2005).

1.3.6.3 Main fan accumulation – Phase 3

The main sandbody (up to many tens of metres in thickness) show several cycles of development and infill of erosional channels suggesting significant channel bypass, which would have sourced the sandy lobes in the Jaca Basin (discussed earlier). Pickering and Corregidor (2005) also suggest that larger, well-established deep-marine channels are typically associated with fine-grained levee-overbank sedimentation what interfinger with thin-bedded and fine-grained basin slope deposits.

1.3.6.4 Fan abandonment

Submarine fans in the Ainsa Basin typically show gradual abandonment, depositing up to tens of metres of fine-grained, very thin-bedded SGF deposits and laminated mudrocks that appear tabular over hundreds of metres down flow and gently lens over tens of metres across flow. This thinning- and fining-up sequence can be up to a few metres in thickness, which immediately precedes mudrock deposition where limited sand is transported to the deep-marine environment. Channel abandonment is

interpreted as a change in sediment supply caused by a significant reduction of the coarse-grained clastic supply to the basin, potentially related to a rise in relative sea level (Pickering and Corregidor, 2000).

1.4 THE BUZZARD FIELD, NORTH SEA, UK

An overview of the Buzzard Field, UK North Sea is presented here, but with further detailed analysis in Chapter 8. The Buzzard Field (operated by CNOOC-Nexen), although a relatively small sedimentary basin (~ 8 km by 10 km in area), is one of the biggest producers of hydrocarbons in the North Sea at the present day (Figure 1.18-A, B). For any analogue it is important to address the subject of scaling to ensure that basins of comparable size are chosen to allow realistic comparisons of deposit thicknesses, geometry and architecture between basins. The Ainsa Basin is 8 x 10 km, approximately the same size as the Buzzard Field (Figure 1.18-C). Figure 1.18-C shows these basins in comparison to much larger systems, such as the passive/active continental margin of the Mississippi Delta, Gulf of Mexico.The Buzzard Field has been extensively drilled, with boreholes showing thin-to-thick, generally structureless sandstones across the basin, and interpreted as deposited in a proximal submarine-fan system (Doré and Robbins, 2005; Ray *et al.*, 2010). Cored wells have identified a variety of MTDs and MTCs. These remobilised deposits represent periodic failure from the shelf, slope and growing faults throughout basin evolution over time (Doré and Robbins, 2005).

Acoustic diffraction in the Buzzard Field, attributed to the presence of a thick Cretaceous chalk boundary layer capping the sandstone reservoir, has led to the absence of high-resolution seismic profiles in the area. There is a high degree of uncertainty regarding sandstone (reservoir) correlations across the Buzzard Field. Boreholes provide a limited ‘snapshot’ of the subsurface geology and sedimentary logs have provided a general understanding of the spatial positions of reservoir sands. An added complication to acquire an accurate understanding of the subsurface reservoir results from the presence of MTDs and MTCs, which comprise a significant proportion of the Buzzard stratigraphy. Understanding the relationship between sand-rich SGF deposits (i.e., reservoir intervals) and mud-rich SGF deposits (i.e., MTDs that form baffles and barriers) is critical to reduce uncertainties for reservoir

modelling and therefore optimise hydrocarbon production. Some critical features, which are not resolvable from available Buzzard Field data includes onlapping relationships, erosion and run-out at the sub-seismic scale, i.e., below several tens of metres vertical stratigraphy, and over many tens of metres laterally (i.e., along bedding). Based on a three-month internship undertaken at CNOOC-Nexen, an evaluation of the MTDs and MTCs was undertaken as part of this research study.

1.5 RESEARCH OBJECTIVES

The aims of this research project can be summarised as:

- Identify and classify MTDs and MTCs found in the Ainsa Basin and to deduce a robust sedimentological criteria for their classification;
- Develop criteria for differentiating between individual MTDs within MTCs through detailed outcrop descriptions and logging these deposits throughout the stratigraphy to establish variation, thickness and abundance of MTDs and MTCs in the Ainsa Basin;
- Interpret the depositional processes that occurred in the lower-slope, base-of-slope and proximal basin-floor settings;
- Document the architectural relationships MTDs and MTCs have with underlying and immediately overlying sandy SGF deposits;
- Map in detail areas not currently mapped in the Ainsa Basin, in order to gain a better understanding of MTDs and MTCs in different environments in the Ainsa Basin, and;
- Provide a better understanding of erosive flow processes not previously documented at outcrop and the implications that erosive debris flows have in submarine environments, and how this research relates to petroleum exploration.

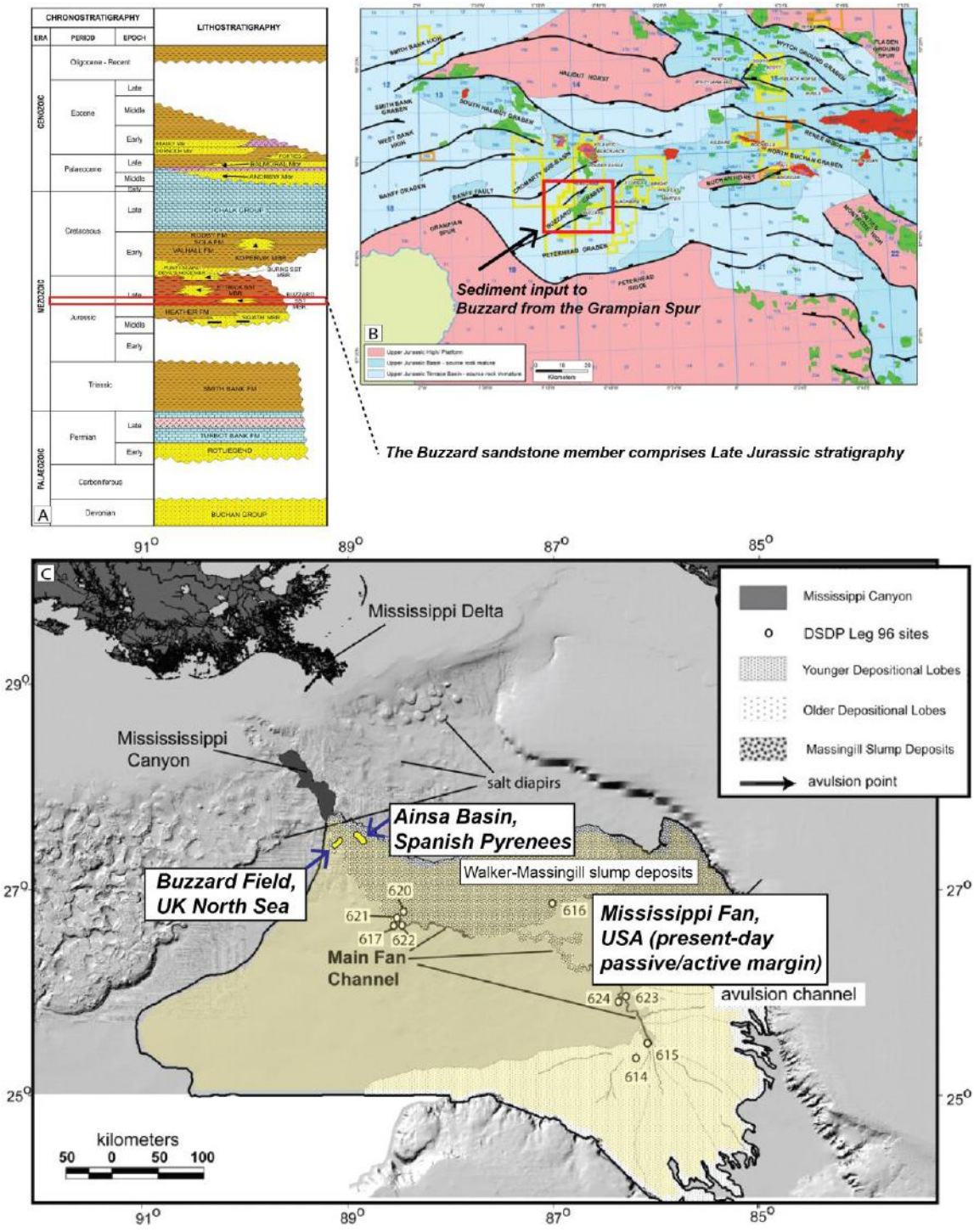

Figure 1.18. (A) Stratigraphic column of the Northern North Sea highlighting Late Jurassic stratigraphy of the Buzzard sandstone member. Image from in-house CNOOC-Nexen report (B) Location of Buzzard Field offshore Scotland, UK. ED 1950, UTM 30N. Image from in-house CNOOC-Nexen report (C) Map to show similarities in scale between the Ainsa and Buzzard Basins, compared to the Mississippi Fan, Gulf of Mexico. Image modified from Talling *et al.* (2010).

1.6 THESIS PLAN

This thesis is separated into 9 chapters with core research chapters (4-7) presented as original research documented from the Ainsa Basin. Chapter 8 presents original research documented from in-house data from CNOOC-Nexen.

- Chapter 1 (this chapter) introduces the study areas and outlines the thesis aims and rationale, introducing the geological setting and stratigraphy of the Ainsa Basin, the focus of this study.

- Chapter 2 provides a review SGF flow processes, a literature review of erosive processes in subaerial and submarine environments and MTD classifications at outcrop.

- Chapter 3 details the datasets and methodologies used for the analysis for fieldwork in the Ainsa Basin, laboratory work and industry methods undertaken at CNOOC-Nexen.

- Chapter 4 describes MTDs and MTDs identified at outcrop, documents their sedimentary characteristics and discusses depositional models for deposits identified.

- Chapter 5 describes how depositional environments control the types of MTDs and MTCs deposited in a proximal deep-marine sedimentary succession. An updated geological map of the Guaso System is published in: Scotchman, *J. I., Pickering, K. T., Sutcliffe, C., Dakin, N., Armstrong, E. 2015. Milankovitch cyclicity within the middle Eocene deep-marine Guaso System, Ainsa Basin, Spanish Pyrenees. Earth-Science Reviews, 144, 107-121.* A copy is provided in the digital appendix (Appendix A). A quantitative approach is used to document the geometry of MTDs and MTCs in the Ainsa Basin and how these deposits vary spatially (proximal-to-distal) and stratigraphically (per system). The geometry of global deposits is also presented here.

- Chapter 6 documents MTDs that show basal erosion at outcrop. The main elements of this chapter are published in Marine and Petroleum Geology: *Dakin, N., Pickering, K., Mohrig, D., Bayliss, N. (2013). Channel-like features created by erosive submarine debris flows: Field evidence from the Middle*

Eocene Ainsa Basin, Spanish Pyrenees. Marine and Petroleum Geology. 41, 62-71. A copy is provided in the digital appendix (Appendix A). Since publication, results from further field observations are presented in Chapter 7.

- Chapter 7 presents a new laboratory analysis of erosively-based MTDs at outcrop.

- Chapter 8 is based on data collected during a 3-month internship at CNOOC-Nexen. MTDs and MTCs documented from the Buzzard Field are documented with comparisons made with the Ainsa Basin.

- Chapter 9 synthesises the principal results of this research in context with the Buzzard Field and brings together different aspects of MTDs and MTCs documented in this study.

CHAPTER 2

SEDIMENT GRAVITY FLOWS AND DEPOSIT CLASSIFICATION

2.1 INTRODUCTION

Sediment-transport processes are typically complex, involving multi-phase granular flow, and thus form a wide variety of organised to disorganised deposits (Pickering and Hiscott, 2015). This complexity has meant that over the past 60 years, the nomenclature for SGF processes and their deposits in deep-water settings has been widely discussed (Dott, 1963; Walker, 1970, 1975a, 1975b; Mutti and Ricci Lucchi, 1972; Hendry, 1972; Middleton and Hampton 1973; Carter, 1975; Nardin, 1979; Lowe, 1982; Pickering *et al*., 1986; Postma, 1986; Ghibaudo, 1992; Mulder and Alexander 2001; Dasgupta, 2003; Talling *et al.*, 2012; Pickering and Hiscott, 2015). Firstly, this chapter explores the terminology and classification schemes of SGFs, and their deposits in deep-marine settings. These classifications are subsequently applied to outcrops observed in the Ainsa Basin (this study). Secondly, this chapter documents literature studies presenting erosive processes of cohesive flows documented in subaerial environments, with studies showing erosively-based MTDs in submarine environments also presented. The aim is to apply the mechanical principals of these erosive studies to outcrops documented in the Ainsa Basin (Chapters 6 and 7).

2.2 SEDIMENT GRAVITY FLOWS

2.2.1. Sediment support mechanisms

In sediment gravity flows, only a few support mechanisms are believed as responsible for maintaining sediment in suspension: (1) turbulence; (2) buoyancy; (3) grain collisions; (4) excess pore pressure, and; (5) matrix strength (Pickering and Hiscott, 2015). The relative importance of the various support mechanisms are summarised in Figure 2.1.

(1) ***Turbulence*** characterises low-viscosity fluids, where inertial forces dominate viscous forces. Turbulence is the superimposition of swirling eddies and seemingly random

velocity fluctuations. Turbulent flows lose their sediment load by settling, and therefore become increasingly less concentrated during the depositional phase (Pickering and Hiscott, 2015).

(2) ***Buoyancy*** is the support provided to an object by a dense surrounding fluid. If the surrounding fluid has the same density as the object, then it will appear to 'float' within the fluid. If the fluid is denser than the object, the object will be positively buoyant. If the fluid is less dense, downward gravitational forces will dominate. Buoyancy permits relatively dense sediment-water mixtures (i.e., debris flows) to carry large clasts at low velocities.

(3) ***Grain collisions*** occur only in flows with high grain concentrations. Collisions transfer some of the downstream momentum of moving particles to an upwardly-oriented dispersive pressure (Bagnold, 1956), as faster moving grains ricochet off more slowly moving grains. This results in an expansion of the flowing mass by reducing the vertical spacing between the particles.

(4) ***Excess pore pressure*** results when a dispersion of grains settles too quickly to allow the interstitial pore fluid to escape upward. Low permeability impedes upward flow of water, causing fluid pressures in the pore spaces to exceed hydrostatic pressure, and thus keeps the grains separated. Therefore, friction is reduced and grains can move relative to one another.

(5) ***Matrix strength*** is a property of concentrated mixtures of clay-rich sediments due to molecular and surface forces (Dott, 1963). Forces resisting movement results from shear strength and includes frictional resistance and cohesion among the particles. MTDs result from mass-wasting (such as the slope). In these types of flows, shear stress must overcome yield strength for the sediment-fluid mixtures to flow, discussed in Section 2.2.2.4.

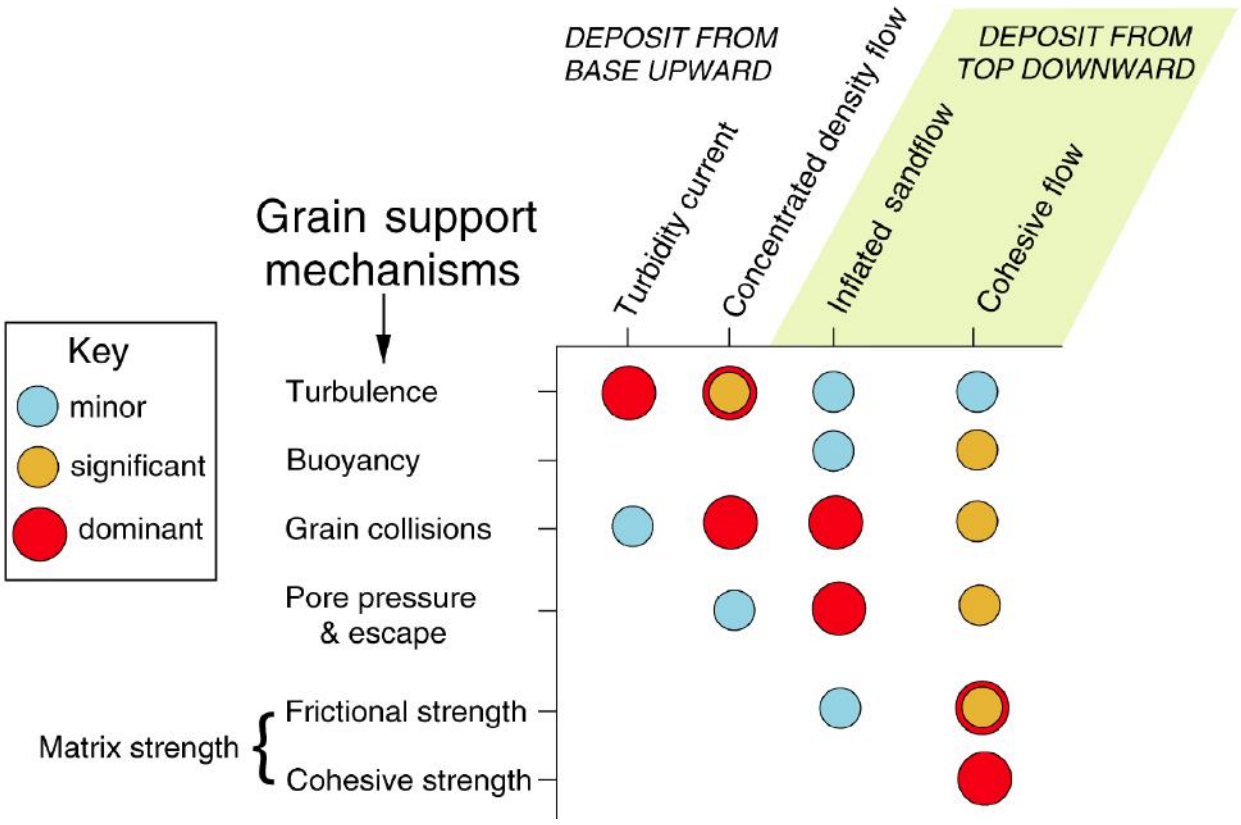

Figure 2.1. Relative importance of particle-support mechanisms for the four varieties of SGF recognised. Where red and orange symbols are superimposed, the support varies from significant to dominant. Figure from Pickering and Hiscott (2015).

2.2.2 SGF processes

Pickering and Hiscott (2015) modified the SGF original classification scheme of Mulder and Alexander (2001), with the former adopted for use in this study. SGFs are subdivided according to their rheological behaviour; predominantly cohesive or frictional flows and are identified as: (1) turbidity currents; (2); concentrated density flows; (3) inflated sandflows, and; (4) cohesive flows (Pickering and Hiscott, 2015) (Figure 2.2). Sediment gravity flow processes (including the mass-transport processes, as introduced in Chapter 1) are presented below.

2.2.2.1 Turbidity currents

Turbidity currents are frictional, non-cohesive flows held in suspension and transported by the upward component of fluid turbulence (Middleton and Hampton, 1973). Ideally, turbidity currents are fully turbulent and dilute flows, with ~ 9 % sediment concentration by volume (Bagnold, 1962). Higher sediment volumes (> 9 %), result in more frequent grain collisions (Sumner *et al.* 2009), which are likely to suppress flow turbulence in sediment flows, with turbulent flows becoming laminar when grain concentration reaches 20 to 30 % (Bagnold, 1954). Therefore, 'ideal turbidity currents', where sediment is supported by the upward flow of fluid escaping between the grains, are not able to exist at high concentrations (*cf.* Shanmugam, 2002).

2.2.2.2 Concentrated density flows

Concentrated density flows (~ 15 – 40 % grains by volume) are frictional flows analogous to high-concentration turbidity currents (e.g., Lowe, 1982) that deposit their load from suspension and are likely to have at least some phase of laminar flow with suppressed turbulence. Gradual aggradation of concentrated density flows is also proposed to occur in sustained steady or quasi-steady currents, with particles slowed by hindered settling effects (Middleton, 1984; Kneller and Branney, 1995). Deposits from these flows can show a strong *a*-axis fabric, related to shear near the aggrading bed that strongly aligned the particles.

2.2.2.3 Inflated sand flows

Inflated sandflows (~ 40 – 70 % grains by volume) are frictional flows that lack significant cohesive strength, but do possess frictional strength because of grain-to-grain interlocking when concentrations become very high (also referred to as hyperconcentrated density flows *cf.* Mulder and Alexander, 2001). As a result, deposition from inflated sandflows takes place by frictional 'freezing'. Although cohesion is not a significant contributor to particle support (Figure 2.1), a small amount of interstitial mud is required to permit these sandflows to operate on low-angle slopes.

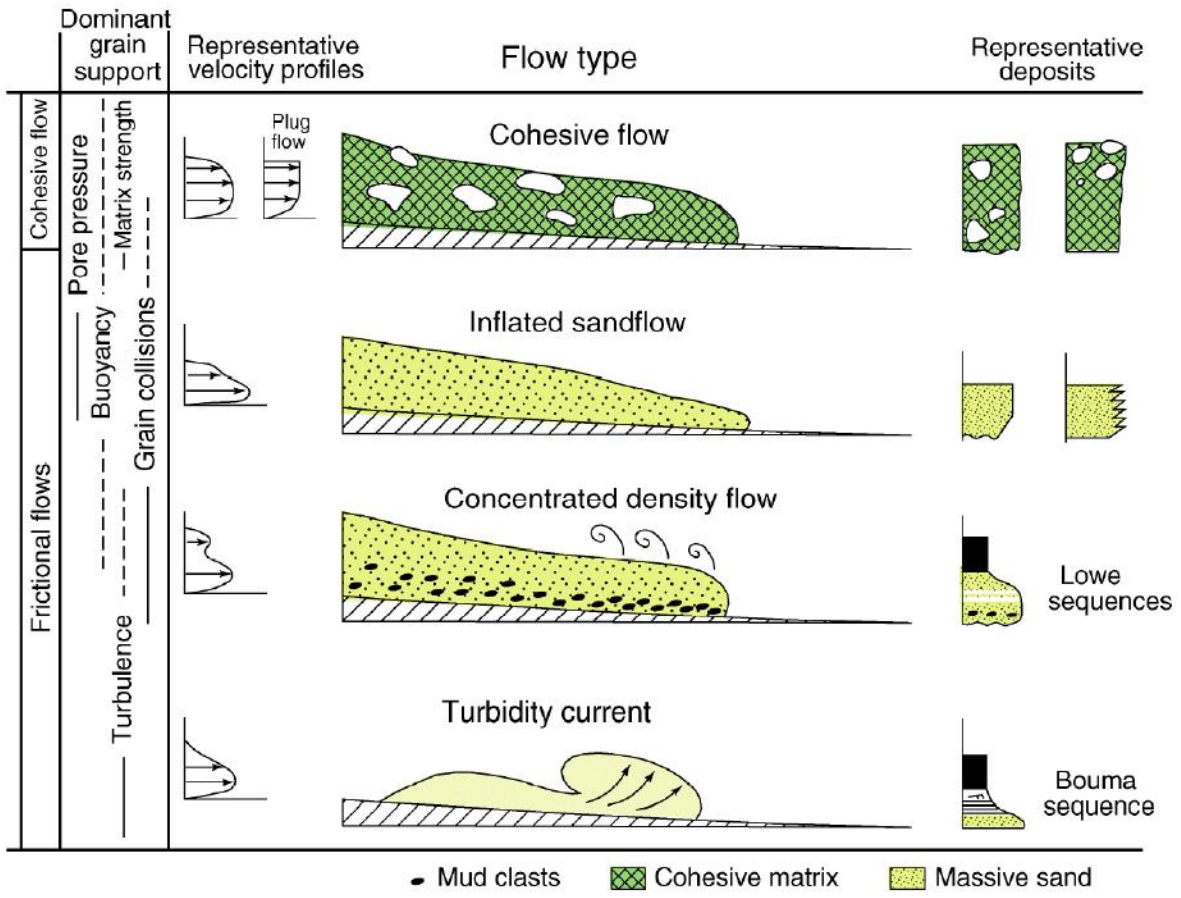

Figure 2.2. Summary of flow characteristics, typical deposits and grain-support mechanisms for cohesive and frictional (non-cohesive SGFs). Figure from Pickering and Hiscott (2015) *cf.* Mulder and Alexander (2001).

2.2.2.4 Cohesive flows

2.2.2.4.1 Sediment slides

A slide is a coherent mass of sediment, translated down-slope with no or little internal deformation (Leeder, 1999; Shanmugam, 2002). Slides possess two key features: a rupture surface and a displaced mass of rock and/or sediment (Hampton *et al.*, 1996). The area of translation occurs above discrete basal shear zones or décollement horizons. Slides are variable in terms of morphology as the displaced mass may remain intact or become highly deformed and break up into distinct blocks (Hampton *et al.*, 1996). Submarine slides can travel up to hundreds of kilometres, e.g., Storegga slide, Mid-Norway Margin (Bryn *et al.*,

2005). Slides can be grouped according to their basal geometry shear surface which include: translational, rotational and multiple retrogressive (Coleman and Prior, 1988): (1) translational slides have an inclined parallel or roughly planar basal shear zone that allows the movement of sediment down slope, and; (2) rotational slides are common in homogenous muds, which are prone to rotational failure and generally give rise to rupture surfaces that are concave up (listric) in shape. In this study, the term 'slide' is used for both a process and a deposit.

2.2.2.4.2 Sediment slumps

A slump is a coherent mass of sediment that moves on a concave-up glide plane. The sediment undergoes rotational movement and causes internal deformation (Shanmugam, 2006). Slumps can form on slopes as low as 0.1° or less and can range in thickness from 0.5 m to several hundreds of metres on continental margin slopes (Posamentier and Martinsen, 2011). Slumping is a common process where there is a significant involvement of clay-size sediments. Depth of the basal shear surface is determined by the pressure gradient within the sediment. Where pore pressure approaches or balances the normal stress of the overburden, slippage occurs along a basal shear surface (Posamentier and Martinsen, 2011). In this study, the term 'slump' is used for both a process and a deposit.

2.2.2.4.3 Debris flows

Debris flows (or mudflows) are agitated mixtures of solids with a diverse grain-size with the primarily support mechanism related the cohesive strength of the matrix (arising from electrostatic attraction between fine particles in the mud fraction), grain-to-grain interactions and excess pore pressure. Yield stress is one of the main characteristics of cohesive flows, associated with the presence of clay particles throughout the sediment mass (Coussot *et al.*, 1996). Once movement is triggered, the flowing mass remains in an undrained state, with flow surges able to travel at many metres per second (Hungr *et al.*, 2005). The cohesive forces of clay minerals dramatically affect the flow behaviour of SGFs by: (1) increasing the

viscosity, and; (2) providing matrix support forming internal resistance and laminar flow (Middleton and Hampton, 1973; Pickering and Hiscott, 2015). For this reason, excess pore pressures are likely to occur in cohesive debris flows due to a slower dissipation of pore pressure (Talling *et al.,* 2012). Mud, comprising the matrix of debris flows provides strength to support the capacity transporting silt to very-coarse grains to boulder-sized clasts and rafts up to tens of metres in length (Leeder, 1999). Rheological models of debris flows are based on non-Newtonian fluids, where motion and flow strength is related to flow viscosity of the sediment-water mixture, i.e., Bingham viscosity in a Bingham model.

There are distinct differences in debris flow behaviour in natural environments between flows with bulk densities of less than ~ 1.5 tonnes/m^3 and those greater than ~ 1.8 tonnes/m^3; the former behave similarly to a mud slurry, where coarse grains are moved around like normal bedload at the base of the flow and are in contact with the bed. The latter show an intermittent pulsing flow, where the head of the flow appears laminar with coarse grains present homogenously throughout and the flow between pulses is similar to that of a mud-slurry (Davies, 1990). Using naturally occurring debris flow events, Takahashi (2007) classified subaerial debris flows between stony, turbulent-muddy and viscous debris flows. Stoney debris flows are observed to accumulate large stones and boulders at the flow front with mudflows typically flowing directly behind the stony 'head' of the flow. This type of flow contains little water, but still acts as a flow under gravity. From head to tail, turbulent-muddy debris flows are able to support large boulders, witnessed from vigorous ash ejection from active volcanoes, and viscous debris flows show turbulent flow at the head of the debris flow, followed by hyperconcentrated laminar flow at the end of the flow (Figure 2.3).

Granular flows in laboratory experiments are defined as gravity-driven masses of discrete particles (grains and boulders) supported by an interstitial fluid (Hü *et al*., 2008), i.e., debris flows in a natural environment. In laboratory experiments, varying the velocity and internal dynamics of fluid saturated clay, silt, sand and rafted debris make these flows characteristically difficult to model and predict (Marr *et al.,* 2001). Coherency of a flow describes the extent to which the head of a flow erodes, breaks apart or entrains ambient water for a given dynamic pressure and shear stress (Parsons *et al.,* 2007). Figure 2.4 shows

'strongly', 'moderately' and 'weakly' coherent SGFs from laboratory experiments of Marr *et al.* (2001), showing how both turbulent and laminar dynamics exist within one flow.

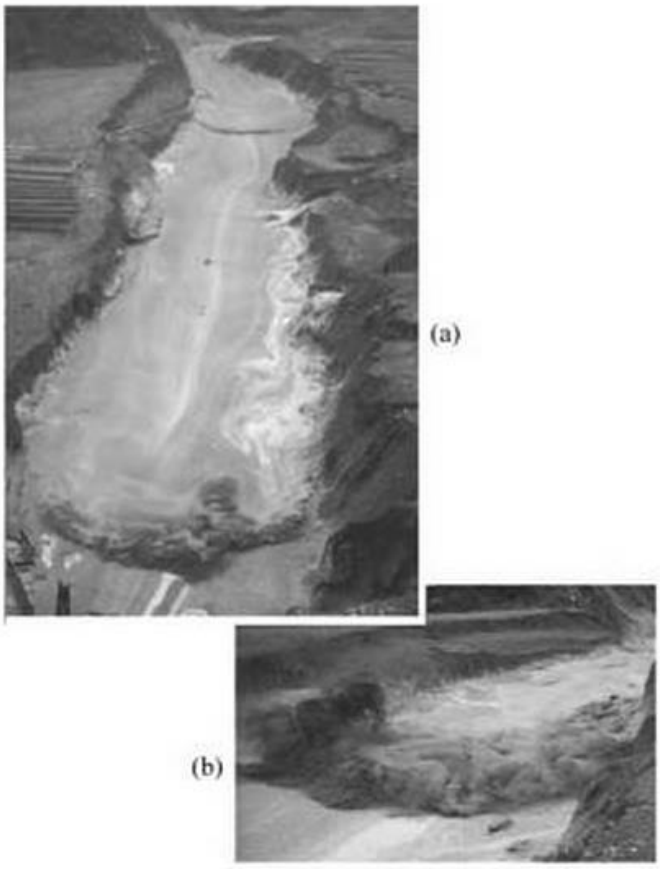

Figure 2.3. Debris flow from the Jiangjia Gully, Yunnan, China. These images display the turbulent head of the debris flow and a laminar tail. From Takahashi (2007).

Strongly coherent flows with high yield strength (Figure 2.4-A) have a thick laminar debris flow 'head' and a thinner 'body' (or 'tail' *sensu stricto* Davies, 1990), with a weak subsidiary turbulent turbidity current peeling off the head. Moderately coherent flows (Figure 2.4-B) show laminar debris-flow processes definable almost to the head, but also show sediment entrainment into turbulent flow. The head of weakly coherent flows (Figure 2.4-C) are fully turbulent and can therefore be characterised as a low-concentration turbidity current (i.e., < 30 % grain concentration), which is followed by a definable, non-turbulent flow behind the head, as seen in viscous debris flows described by Takahashi (2007) (Figure 2.3). Weakly coherent (or low yield strength) debris flows may resemble fluid mud layers and are able to transform locally from (and to) turbulent flow. The transformation of moderately to

weakly coherent debris flows primarily occurs via entrainment of ambient fluid into the slurry, resulting in wholesale dilution of the flow. The conversion of a high yield-strength coherent debris flow to a turbidity current is relatively inefficient, as most of the sediment remains in the slurry phase (Parsons *et al.*, 2007; Talling *et al.*, 2012). The transformation of moderately to high yield-strength coherent cohesive flows primarily occurs via grain-by-grain erosion of sediment from the fronts of flows.

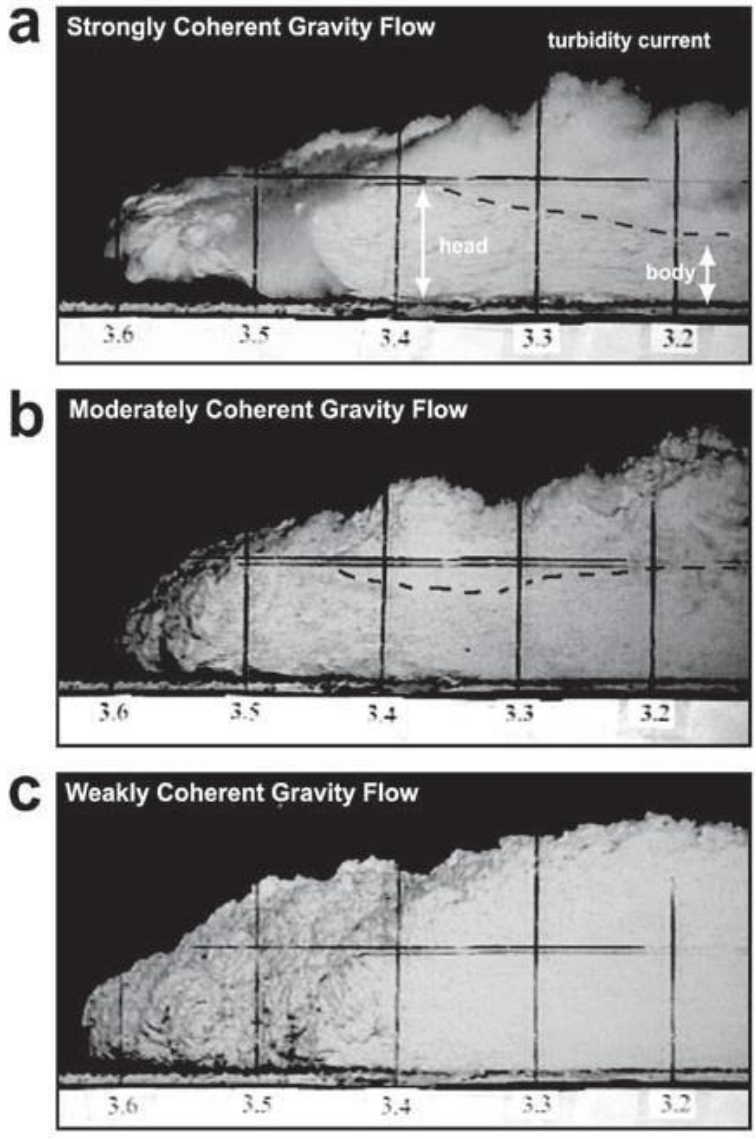

Figure 2.4. (A) Head of a high yield-strength coherent gravity flow: 35 % kaolinite, 40 % water, 20 % 110 µm sand and 5 % 500 µm sand. (B) Head of a moderately coherent sandy gravity flow: 25 % kaolinite, 40 % water, 30 % 110 µm sand and 5 % µm sand. (C) Head of a weakly coherent sandy gravity flow: 15 % kaolinite, 40 % water, 40 % 110 µm sand and 5 % 500 µm sand. Figure from Parsons *et al.* (2007).

2.2.2.4.4 Cohesive deposits

Cohesive flows deposit sediment *en masse* by freezing, such that the majority of larger and smaller grains (and mud clasts, if present) do not segregate by differential settling during deposition (Enos *et al.*, 1977; Iverson *et al.*, 1997; Talling *et al.*, 2012; Pickering and Hiscott, 2015). The material at the sides or front of the flow consolidates first with the centre of the flow remaining fluid for longer. When a debris flow comes to a rapid halt, the deposit can continue to consolidate *in situ*. Shultz (1984) classified debrites from outcrops in a proximal alluvial-fan deposit, Cutler Formation, Colorado, USA. Figure 2.5-A shows the debrite classification scheme from Shultz (1984) with lithofacies associations shown in Figure 2.5-B.

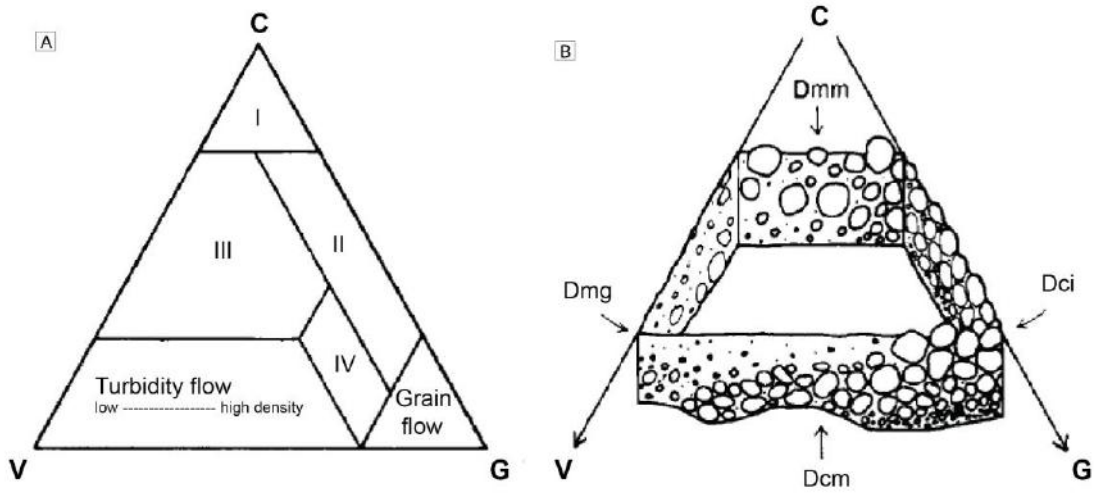

Figure 2.5. Poles represent cohesive-plastic (C), viscous-fluid (V), and granular-collisional (G) behaviour. (A) Conceptual ternary classification of sediment flows (debris flow Types I [high-strength laminar flow, viscous interaction], II [clast-rich laminar flow, collisions], III [low-strength, laminar or turbulent flow, viscous interaction], and IV [low-strength, laminar or turbulent flow, collisions]), (B) Schematic diagram of relationships among debrite subfacies (Dmm, Dmg, Dci and Dcm), refer to text. Modified from Shultz (1984).

Flow regimes and lithofacies models of Shultz (1984) are intended as a basis for identifying transport modes and a single flow may pass through more than one flow regime. Flows are interpreted as approaching viscous-fluid behaviour (V) with increasing water content, cohesive-plastic behaviour (C) with increasing clay content and granular-collisional behaviour (G) with increasing clast content and shear rate. Diamictite lithofacies (D) are

subdivided into four subfacies based on fabric and bed geometry: Dmm – Massive matrix-supported diamictite; Dmg – Graded matrix-supported diamictite; Dci – Inversely graded, clast-supported diamictite; Dcm – Massive clast-supported diamictite. Dmm and Dmg facies in general represent deposits of flows of greater and lesser yield strength, respectively. In this study, the term 'debris flow' is used for the flow process and 'debrite' or debris-flow deposit is used for consequential deposits.

2.2.3 Transformations between flow types

In some cases, mass disaggregation of slides can transform into debris flows, and even turbidity currents (Hampton *et al.,* 1996; Shanmugam, 1996). Depending on sediment composition, magnitude of failure, slope angle, water content, resisting stress and shear stress, the sedimentological behaviour of submarine landslides can behave a number of different ways: (1) landslides can translate downslope with no evidence of internal movement, such as a sediment slump or slide (e.g., Prior *et al.* 1984); (2) landslides can undergo transformation from a solid mass (slump or slide) to a solid-fluid slurry (debris flow) by disaggregation of blocks and incorporating water into the flow as it moves downslope (e.g., Fleming *et al.* 2003), or (3) if there is sufficient energy in the flow (e.g., liquefaction resulting from seismic shock waves), failure may be ignited and instantaneously travel down-dip as a debris flow (e.g., De Blasio *et al.,* 2004).

2.2.3.1 Hybrid event beds

Hybrid event beds (HEBs) are a type of SGF-deposit that show characteristics intermediate between classic turbulent turbidity currents and cohesive debris flows, interpreted to record deposition of material *en masse,* and 'linked' as part of the same event bed (Haughton *et al.,* 2003; Talling *et al.,* 2004; Amy *et al.,* 2005; Haughton *et al.,* 2009; Jackson *et al.,* 2009; Fonnesu *et al.,* 2015). Classic turbidites (i.e., deposits showing complete or partial Bouma divisions) fractionate clays during flow and settle from suspension to generate a discrete muddy cap. Conversely, HEBs are interpreted to have a cleaner, sandier, lower portion and an

upper division appearing as a poorly sorted and/or chaotically structured muddy-sand or sandy-mud. HEBs typically comprise up to five divisions (H1 – H5) (Figure 2.6).

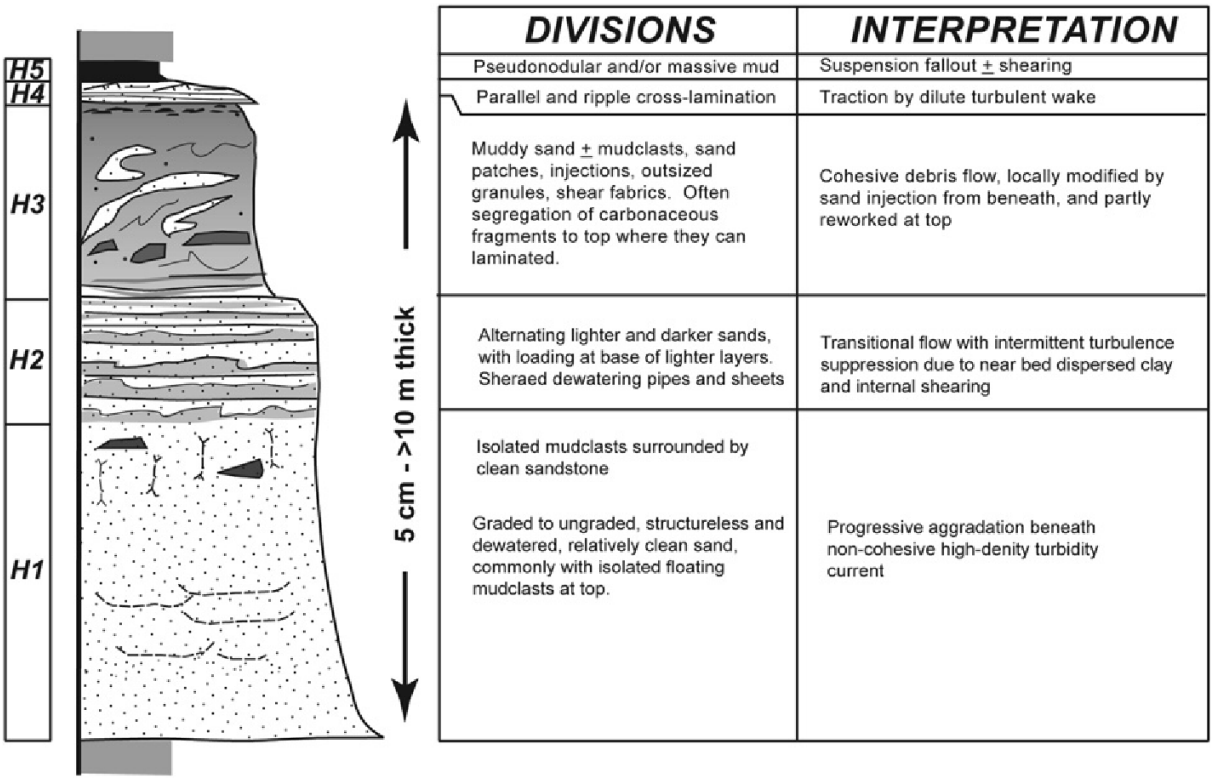

Figure 2.6. Schematic log showing 'ideal' organisation of a typical five-part (H1-H5) hybrid event bed. Figure from Haughton *et al.* (2009).

The lower divisions (H1 and H2) are emplaced by the frontal part of the flow depositing coarser (sand) grains, interpreted as the deposits from high-density turbidity currents. The H3 division captures segregation of the muddier part of the flow and comprises finer-grain sizes that form part of the 'linked' debrite. H3 units are typically 0.05 – 1.5 m thick and contain poorly-sorted, fine-grained brecciated sandstones and significantly more mud than in the H1 and H2 units. The H4 division is not always documented at outcrop, but where present (dominantly found down-dip), it is sandy, fine-grained, laminated and caps the H3 division, interpreted as the final very fine-grained 'tail' of the flow. The H5 division can show unstructured muds related to suspension fallout. Jackson *et al.*, (2009) show examples of muddy linked debrites at outcrop from northwest Borneo (Figure 2.7). Facies 4, identified in Figure 2.7 (H3 of the Haughton *et al.*, 2003 scheme), are documented as mud-rich sandstones with matrix-supported clasts. The upper debrite displays an irregular lower contact

with the underlying sandy-SGF deposit and appears to either erode, or gradationally overlie sandy SGF deposits, interpreted as high-density turbidites (Facies 1, Figure 2.7).

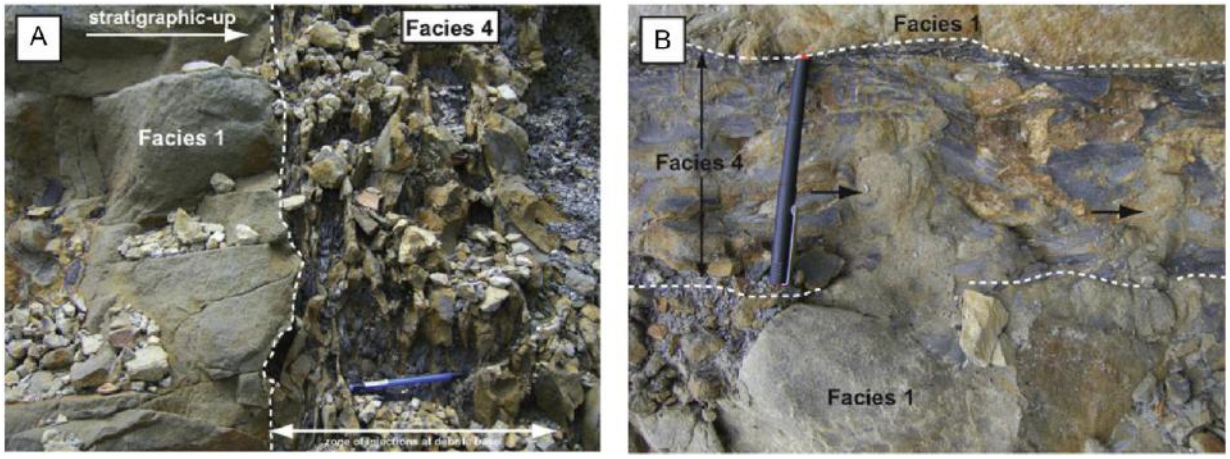

Figure 2.7. Oligo-Miocene West Crocker Formation, northwest Borneo. (A) Muddy linked debrite overlying turbidite sandstone (Facies 1). Brecciated sandstone within overlying debrite (B) The upper debrite (Facies 4) displays an irregular lower contact with the underlying sandy SGF deposit (Facies 1). The upwards injection of sandstone into the overlying debrites and the irregular margins to the injections. Figure is modified from Jackson *et al.* (2009).

The discussion of HEBs is relevant to this research because minor basal erosion is observed at the base of the 'linked debrite' within HEBs (Figure 2.8). In the Ainsa Basin, debrites are also observed to have an erosive base, typically eroding into sandy substrates, however are not interpreted as co-genetic in origin (Chapters 6 and 7). Depositional models of co-genetic flows that comprise discrete flow processes, resulting in the deposition of HEBs are shown in Figure 2.8.

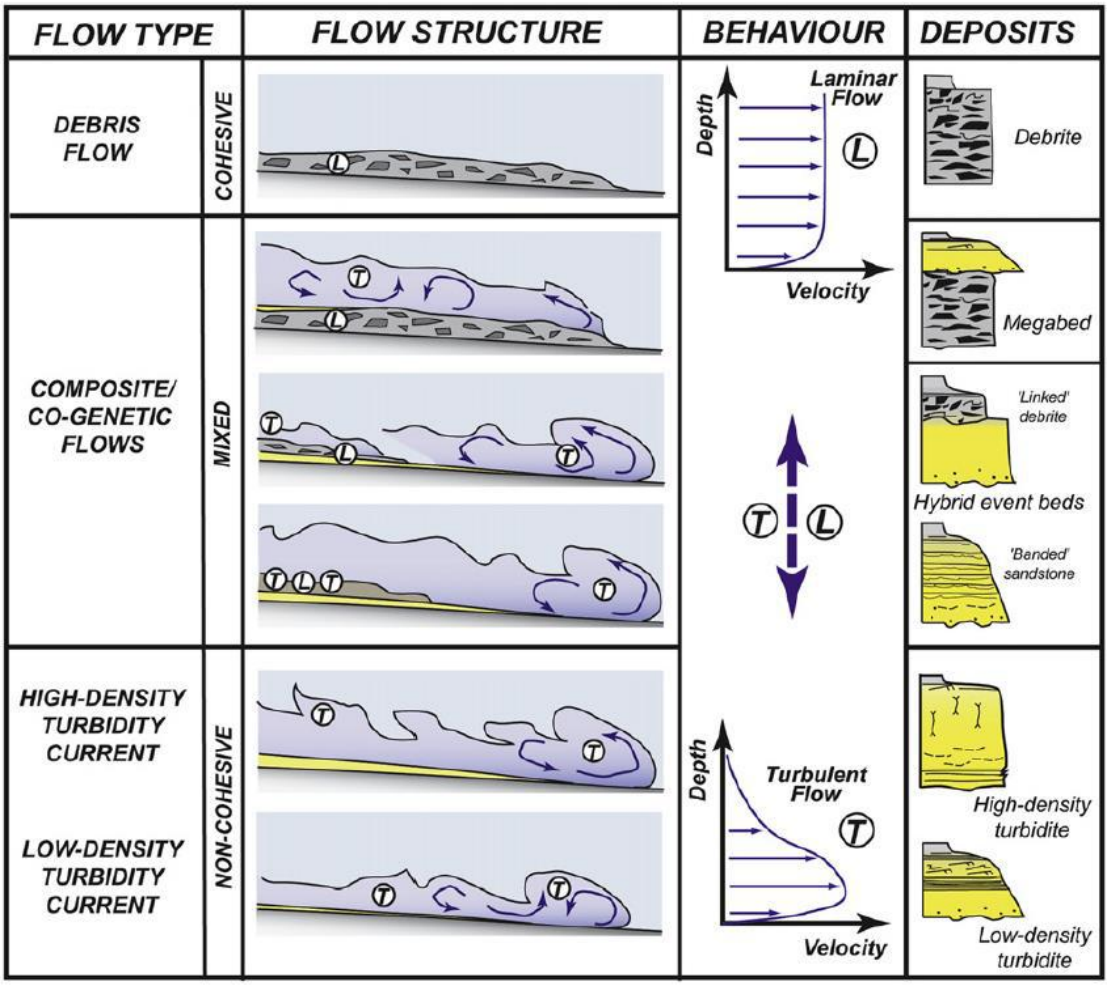

Figure 2.8. Classification scheme for event beds emplaces by subaqueous SGFs. Figure from Haughton *et al.* (2009).

2.3 FACIES CLASSIFICATION AT OUTCROP

Facies refers to sediments, or bodies of sedimentary rock with specific characteristics that are physically, biologically or chemically similar in nature (Pickering *et al.*, 1986, 1989; Van Wagoner, 1990). To determine a suitable scheme for outcrops identified in the Ainsa Basin, the classification schemes of Pickering *et al.* (1986, 1989) and their subsequent deposits are explored here. This scheme describes sedimentary deposits based upon facies at outcrop (Table 2.1 and Figure 2.9). In this classification, MTDs are referred to as 'chaotic deposits' (Facies F), which constitute a mixture of sediments with no apparent internal organisation, typically sourced from large-scale downslope mass movements.

Class	Group1: Disorganised	Group 2: Organised
Facies A: Gravels, muddy gravels, gravelly muds, pebbly sands, 25 % gravel grade	**A1.1** Disorganised gravel **A1.2** Disorganised muddy gravel **A1.3** Disorganised gravelly mud **A1.4** Disorganised pebbly sand	**A2.1** Stratified gravel **A2.2** Inversely graded gravel **A2.3** Normally graded gravel **A2.4** Graded stratified gravel **A2.5** Stratified pebbly sand **A2.6** Inversely-graded pebbly sand **A2.7** Normally graded pebbly sand **A2.8** Graded stratified pebbly sand
Facies B: >80 % sand grade, <5 % pebble grade	**B1.1** Thick to medium-bedded, disorganised sands **B1.2** Thin-bedded, coarse-grained sands	**B2.1** Parallel stratified sands **B2.2** Cross stratified sands
Facies C: Sandstone-mudstone couplets and muddy sands, 20-80 % sand-grade, < 80 % mud-grade	**C1.1** Poorly sorted muddy sands **C1.2** Mottled muddy sands	**C2.1** Very-thick to thick bedded sandstone-mudstone couplets **C2.2** Thick bedded sandstone-mudstone couplets **C2.3** Medium bedded sandstone-mudstone couplets **C2.4** Thin bedded sandstone-mudstone couplets **C2.5** Very-thin bedded sandstone-mudstone couplets **C2.6** Laminae sandstone-mudstone couplets
Facies D: Silts, silty-muds and silt-mud couplets > 80 % mud, <40 % silt, 0-20 % sand	**D1.1** Structureless silt **D1.2** Muddy silt **D1.3** Mottled silt and mud	**D2.1** Graded stratified silt **D2.2** Thin regular silt and mud laminae
Facies E: < 95 % mud grade, < 40 % silt grade, < 5 % sand and coarser grade, < 25 % biogenic material	**E1.1** Structureless muds **E1.2** Mottled muds	**E.2.1** Graded muds **E2.2** Laminated muds and clays
Facies F: Chaotic deposits	**F1.1** Rubble **F2.1** Coherent folded and contorted strata **F1.3** Brecciated and balled strata	N/A

Table 2.1. Brief description of Pickering *et al.* (1986, 1989) SGF classification facies scheme. The reader is referred to this original classification scheme for detailed descriptions and comprehensive reference list.

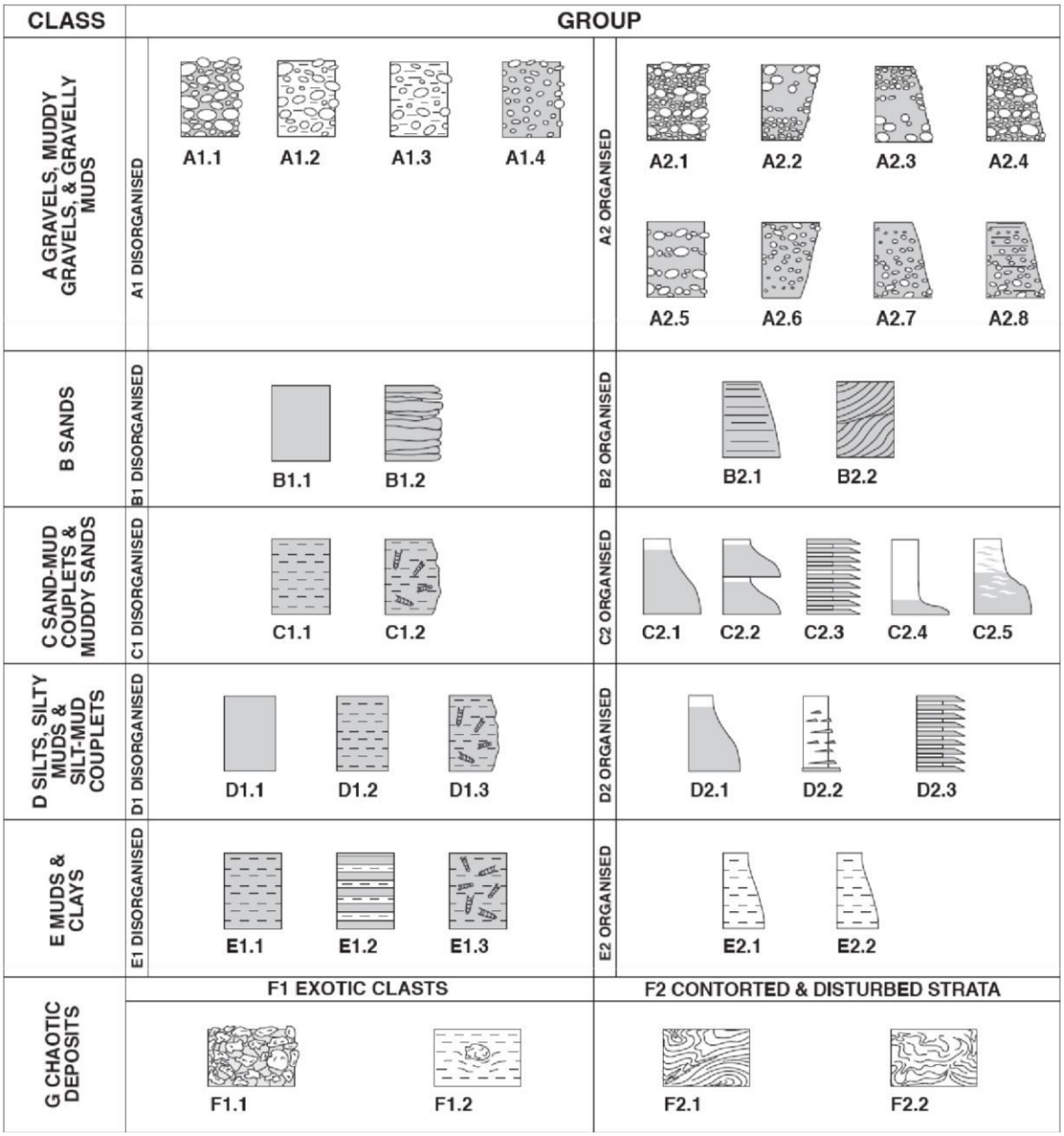

Figure 2.9. Summary of Pickering *et al.* (1986, 1989) SGF classification facies scheme.

2.3.1 MTD facies classification at outcrop

MTDs and MTCs were introduced as the focus of this study in Chapter 1, with examples showing how these cohesive flows typically form distinctive deposits, recognised in the subsurface from core, seismic data and outcrop analogues (Figures 1.2, 1.5 and 1.6,

respectively). Pickering and Corregidor (2005) proposed a descriptive classification scheme based on outcrops of MTDs observed in the Ainsa Basin (Table 2.2). Deposits in this study are described as single events (i.e., MTDs), a modification of the original classification scheme which were described as MTCs.

MTD Type		**Outcrop characteristics**	**Interpreted transport process**
Type I	**Ia**	Typically tens of metres thick. Comprised of intra-formational muddy and heterolithic sediments. Generally occur between sandbodies. Visco-plastic deformation, varying degrees of disaggregation	Sediment slide (mid/upper slope) basin slope.
	Ib	Thin (decimetre- to metre-scale) intra-formational deformed horizons of clearly local origin, with folded, attenuated, and partially disaggregated sands in a sandy to muddy matrix. Typical of off-axis environments.	Sediment slide (local, e.g., channel margin failure)
	Ic	Marl-matrix carbonate platform material. Various degrees of viscoplastic deformation.	Sediment slide (carbonate platform collapse)
Type II		Typically range m to tens of m thick. cumulative erosion at the base of tens of m. Contains extra-formational material, e.g., very well-rounded pebbles, shallow-marine shells and abundant reworked nummulites	Multiphase granular flow (shelf and fluvio- deltaic input)
Type III		Thinnest type, typically dm-m thick. Typically contain extra-formational clasts of very well-rounded pebbles, and angular to rounded intra-formational silt-mud clasts. Tend to contain greatest proportion of sand-grade sediment. Documented to occur within sandbodies	Flow transformation (erosive concentrated density current bulking up and freezing)

Table 2.2. Classification of MTDs identified in the Ainsa basin, and interpreted sediment transport processes. Modified from Pickering and Corregidor (2005).

Mass-transport processes in deep-marine settings should include only processes where the majority of grains in a flow do not move freely with respect to others, and the main grain-support mechanism is not fluid turbulence (Posamentier and Martinsen, 2011). The deposits classified by Pickering and Corregidor (2005) represents a range of flow processes, including sediment slumps, slides, concentrated density flows and debris flows that deposit conglomerates, pebbly mudstones, mud-flake breccias and pebbly sandstones. Type Ia, Ib and Ic deposits represent sediment slides. Under ideal circumstances, sediment slides and slumps can be differentiated, with slides and slumps showing varying degrees of internal deformation. A sediment slide includes all down-slope *en masse* translations of gravitationally-driven slope instability of material, whereas a sediment slump is a rotational slide, i.e., a particular type of sediment slide. Thus, all slumps are slides but not all slides are slumps. However, separating these MTDs at outcrop is subjective as it is not always possible to distinguish, without reasonable doubt, which process was responsible for the resultant deposit at outcrop. For the purpose of this study, slumps and slides are classified together. Type II deposits represent multiphase granular flows and Type III deposits represent flow transformations comprising the most amount of sand grains and generally contain pebbles (Table 2.2).

To accurately document, measure and log MTDs in the field, the distinction between sandy SGF deposits (i.e., deposited from high and low-concentrated density flows) and cohesive deposits (i.e., debrites) was critical. Identifying and interpreting specific long-distance transport mechanisms and flow characteristics is difficult to achieve when explaining the origin of various deep-marine deposits at outcrop, as deposits rarely reflect the original flow structure. This is due to many of the depositional processes not being unique to a particular transport mechanism and a variety of late-stage depositional processes can leave their imprint on a deposit (Mulder and Alexander, 2001; Sumner *et al.*, 2009). However, chaotic to well-mixed mudstones are able to support clasts and rafts in a poorly-sorted matrix typically classified as mud-rich cohesive deposits (i.e., debrites). For this study, the Pickering and Corregidor (2005) scheme was used to classify MTDs at outcrop, however where appropriate, modifications were made to this classification, presented in Chapter 4.

2.4 EROSIVE DEBRIS FLOW PROCESSES IN SUBAERIAL AND SUBMARINE ENVIRONMENTS

An important aspect of this research project has been to evaluate the ability of cohesive flow to erode an underlying substrate, informally referred to as "erosivity" of debris flows in proximal submarine settings (i.e., near to the base-of-slope where hydraulic jumps might be expected). The following section evaluates erosive debris flows in subaerial and submarine environments.

2.4.1 Erosive observations from subaerial debris flows

Subaerial debris flows are important geomorphological processes that occur in steepland valleys and mountainous regions worldwide (Stock and Dietrich, 2003). They are extremely powerful events and pose a serious natural hazard. They can claim hundreds of lives every year and cause millions of dollars worth of property damage (Takahashi, 1981; Costa, 1984; Davies, 1986; Matthews *et al.*, 1999; Breien *et al.*, 2008; VanDine and Bovis, 2002; Mangeney *et al.*, 2010; Jakob *et al.*, 2013; Gartner *et al.*, 2015). Japan, Canada, North America, Indonesia, Tasmania, Costa Rica, India, New Zealand and Norway are some of the countries subject to the frequent devastating affects from debris flows, and therefore understanding initiation conditions, event-frequency and run-out is important to evaluate potential human impact (Costa, 1984).

Subaerial debris flows tend to occur in areas of steep drainage and are typically caused by short periods of intense rain falling (flash floods, for example linked to the El Niño-La Niña climatic oscillations) onto already saturated soils during severe storms, leading to soil instability (Davies, 1986; Breien *et al.*, 2008). They can also form from collapsed glacial lakes and natural dams (VanDine and Bovis, 2002; Breien *et al.*, 2008). Figure 2.10 shows a typical debris-flow-prone subaerial steepland valley environment producing a network of debris flows as they flow and accumulate downslope.

Figure 2.10. Subaerial debris flow valley network in the Oregon Coast Range, USA. Debris flows were initiated from a severe storm in 1996, which initiated at the valley heads and scoured sediment to expose the Tyee sandstone bedrock (white areas). Road at top right indicates scale. From Stock and Dietrich (2003).

2.4.1.1 Field observations of erosive subaerial debris flows

Takahashi (1981) first documented large erosive scarps, resulting in the evacuation of sediments that formed debris flows. However, damage from these flows was not observed in the underlying road paving downstream of the flow, therefore Takhashi (1981) suggested that fully freighted/loaded debris flows appeared to have little erosive effect away from the source area. Zicheng (1987) also described how maximum erosion occurred near debris flow formation in the upper reaches of the valley, but also noted when enough water was present in the flow large quantities of unconsolidated loose sediment present in the channel valleys was entrained into the flow body.

Other studies have highlighted a gap in our understanding of subaerial debris flow processes. They illustrate how these dynamic events can cause huge amounts of erosion not

only up-dip but also down-dip in subaerial settings (Davies, 1986, 1990). Davies (1986) described the behaviour of debris flows observed in the field reporting an unsteady, 'pulsing' nature between periods of relatively low flow rate or zero-flow, an observation true of many other eye-witness accounts. Flow properties between the head (pulse) and tail (between pulses) of each debris flow surge were markedly different, where the head of the debris flow was observed to have the highest density, viscosity and velocity and was seen to scour the channel bed (Table 2.3).

Characteristic	Pulse (head of flow)	Between pulse (tail of flow)
Flow density	High > 2.1 T/m^3	Low < 1.6 T/m^3
Sizes present above bed	Bimodal; fines and gravel	Unimodel; fines dominant
Location of coarse load	Throughout flow depth	Bedload only
Appearance	Laminar	Turbulent
Viscosity	High	Lower
Velocity	High; ~ 3 – 10 m/s	Low; ~ 1 – 2 m/s
Effect	Strongly erosive	Depositional

Table 2.3. Characteristics of the 'head' and 'tail' of subaerial debris flows. From Davies (1986).

Debris flows are now known as one of the primary processes that sculpt and erode subaerial steepland valleys as they catastrophically flow down-slope (Mangeney *et al*., 2010). Debris flow magnitude is calculated as the total volume of material moved to the depositional area during an event (Hungr *et al*., 2005). Hungr e*t al*. (1984) described a measure of erosion defined as the yield rate; the volume eroded per metre of channel length. Entrainment of sediment can potentially accelerate or decelerate a flow depending on the nature of underlying erodible material, topography, and dynamics of the flow, which is typically limited to a weak erodible layer (Mangeney *et al*., 2010). In subaerial environments, the weak erodible layer is typically defined by the presence of loose material in a channel that has been remobilised by previous events. Stock and Dietrich (2006) studied episodic debris flows in

the subaerial steepland valley of Joe's Canyon, Wasatch Range, Utah, USA. The valley bedrock comprises Palaeozoic-age quartzite, known as the Oquirrh Formation. This study shows abundant abrasion marks and decimetre-sized blocks missing from jointed bedrock along the length of the valley channel (Figure 2.11). At the site of deposition, boulder-fronts were found at the terminal margins and leveés of the debris-flow deposits, which were interpreted to originate from plucked sandstones from the valley channel. Other examples of 'block-plucking' have also been observed in the Mesozoic granite and diorite valley floor, San Gabriel Mountains, Southern California and in the Santa Cruz Mountains, Western California. These present-day examples that show active bedrock erosive processes occurring during debris flow passage (Stock and Dietrich, 2003).

Until recently, relatively few physical parameters of debris flows were documented. Although many field observations and video recordings of debris flows existed (e.g., Davies, 1986, 1990), these data sets did not quantify the amount of sediment erosion and entrainment through debris-flow processes. However, with increased technology, such as the use of automated sensor networks, erosion bolts and force plates drilled in the bedrock of steepland valleys, recent studies have quantified the distribution of basal forces and the complex erosional-depositional processes of debris flows. These studies have helped to understand the physical processes that occur in subaerial environments (Stock and Dietrich, 2003, 2006; Huggel *et al*., 2004; Hungr *et al*., 2005; Jakob *et al*., 2005; Breien *et al*., 2008; Santi *et al*., 2008; Mangeney *et al*., 2010; Berger *et al*., 2011; Schürch *et al*., 2011; McCoy *et al*., 2013).

Breien *et al*. (2008) provide a detailed quantitative case study from glacial lake outburst floods, Fjærland, Western Norway. Digital terrain models were generated pre- and post debris-flow events to quantify the differences in elevation change along the passage of the channel path. Figure 2.12-A shows the debris flow track divided into 6 sections, termed the 'upper-flat', 'cliff', 'upper-steep (6a)', 'mid (6b)', 'lower-1 (6c)' and 'lower-2' sections, which are located progressively down-dip from the source area. Cross-sectional profiles are shown from sections 6a, 6b and 6c (Figures 2.12-B, C and D, respectively) to show changes in the width and depth of the channel after erosive debris-flow events.

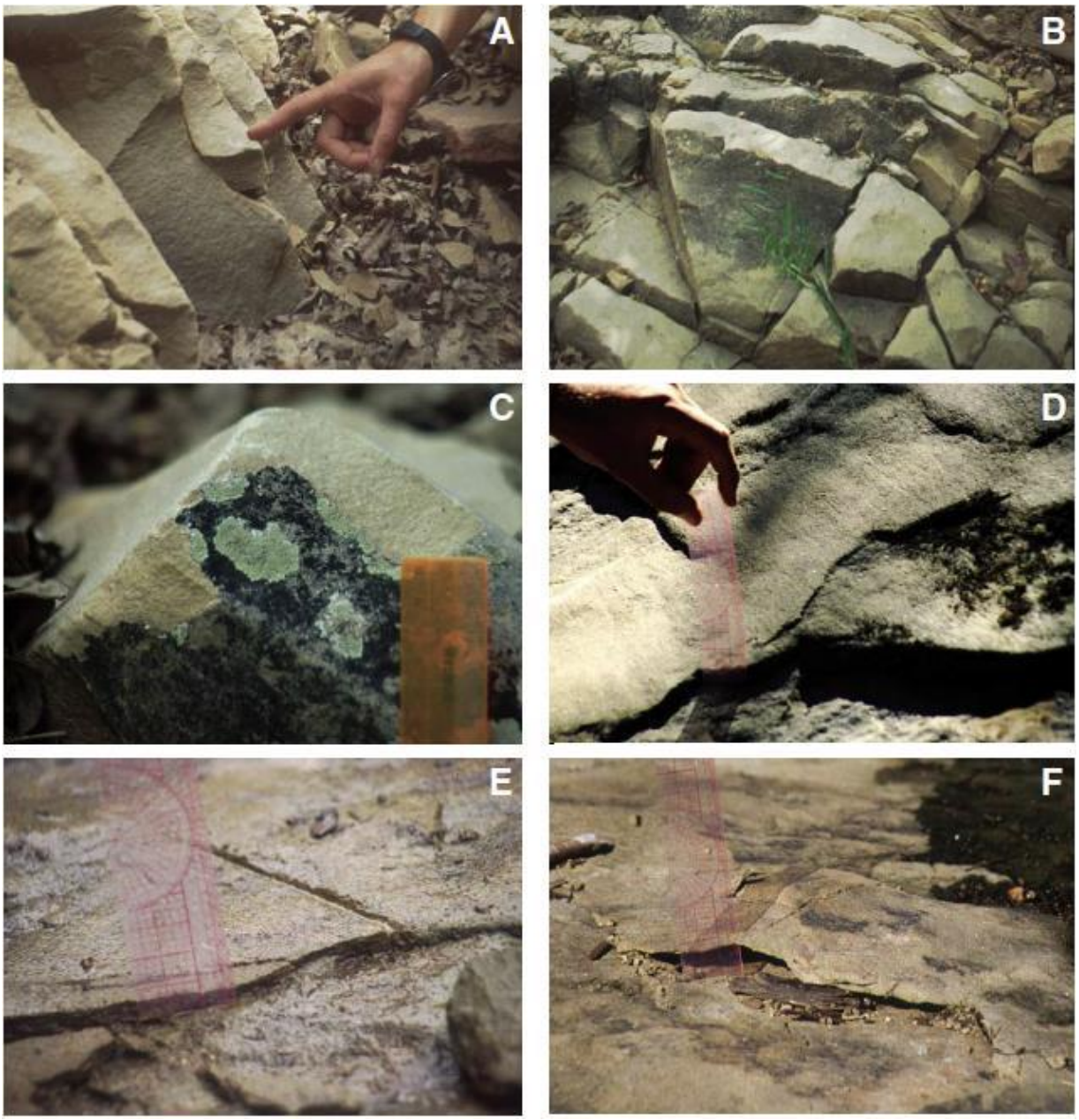

Figure 2.11. Evidence for bedrock lowering from Stock and Dietrich (2006). (A) Impact lowering resulting in removal of decimetre-sized blocks of quartzite. (B) Plucking and abrasion (C) Tensile failure of quartzite (D) Removal of sandstone grains (~ 0.5 – 1 mm in diametre). (E) 1-3 mm deep groove indicating sustained sliding contact of particle for at least 190 mm along the bed. (F) Post-weathering 'tent' feature after debris-flow passage.

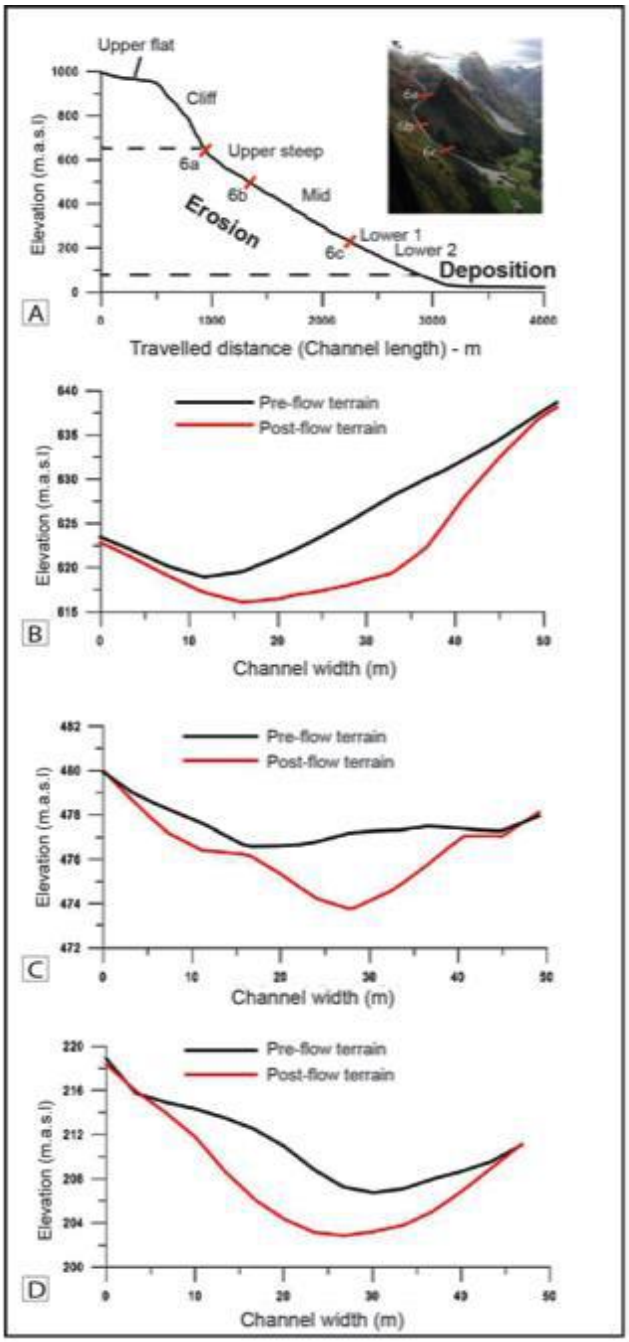

Figure 2.12. (A) Profile of debris flow track. Gradient varying from 4° at the top of the valley to 60° at the steep rock-cliff, to ~ 12° at the base of the valley. Dashed lines indicate areas of erosion and deposition. (B, C, D) Cross-sectional channel profiles progressing downslope (from B to D, respectively) of the debris flow gully pre- and post-debris flow. Modified from Breien *et al.* (2008).

The initial 60° slope at the 'cliff' section allowed the flow to gain momentum and velocity. Incipient erosion developed at the base of the steep cliff face (location 6a shown in

Figure 2.12-A). As the debris flow continued to propagate downslope, it eroded the channel bed. The amount of vertical erosion is not evenly distributed throughout the channelised flow length. The lowest yield rates are located in the mid-section of the flow path (80 m^3/m) and the highest yield rates (212 m^3/m) are recorded in the lower-section of the flow path, occurring just before deposition (Figure 2.13).

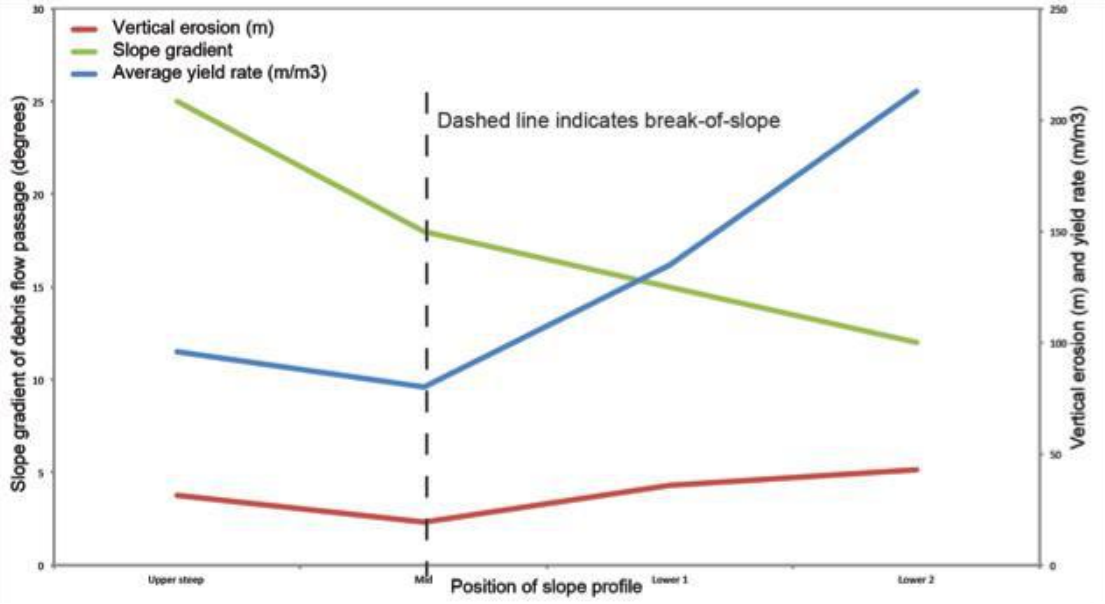

Figure 2.13. Graph showing increase in vertical erosion and yield rate at the break-of-slope in a subaerial environment. Data re-plotted from Breien *et al.* (2008).

The slope gradient (green line, Figure 2.13) decreases at the mid-point position along the slope profile. At this break-of-slope, both the average yield rate (m^3/m) and the amount of vertical erosion (m) increase from 96 to 213 m^3/m and 1.3 to 5.12 m, respectively. From initiation to the point of deposition, the debris flow volume increased from 25,000 – 240,000 m^3 recording a significant increase of sediment entrained into the flow (215,000 m^3). This study recorded that incision increased at the change of gradient, suggesting that a change in angle of slope may affect the way that debris flows erode the bedrock. The highest yield rate occurred near deposition, at the end of the flow. Breien *et al.* (2008) suggest that high vertical and longitudinal shear forces are translated to the underlying bed to produce a positive feedback effect; therefore, debris flows with a higher sediment volume are able to cause more erosion due to higher basal-drag and frictional forces.

Berger *et al*. (2011) provided a similar detailed quantitative case study from field data on erosive debris flows in the Illgraben catchment, western Switzerland. Using scour sensors, the magnitude of channel-bed erosion was measured downslope from debris-flow initiation. Erosion was measured up to 0.5 m towards the end of the Illgraben debris-flow fan that deposited at the base-of-slope. Figure 2.14 shows channel-width cross-sectional profiles from topographic surveys before and after a debris-flow event. These results are similar to those presented in Breien *et al*. (2008). Measurements of pressure fluctuations against the scour sensors in the Breien *et al*. (2008) and Berger *et al*. (2011) case studies suggest that inter-particle collisions impact, fracture and loosen the bedrock enabling efficient erosion where shear rates were higher. These studies also found that the rate of erosion depended on sediment volume, meaning erosion increased as the unit discharge increased.

2.4.2 Observations from submarine erosive debris flows

Middleton and Hampton (1973) described debris flows in submarine environments as the "*sluggish downslope movement of mixtures of granular solids, clay minerals, and water in response to the pull of gravity…resembling the flow of wet concrete*". Since this time, debris flows have been identified as catastrophic, high-density, variable and complex flows, which typically possess a stark rheological contrast to the 'sluggish' movement of sediment previously described.

Laboratory experiments by Mohrig *et al*. (1998, 1999) have shown how, under some circumstances, hydroplaning of debris flows can be responsible for long-distance run-out of subaqueous debris flows, lubricated by a thin layer of overpressured seawater that significantly reduced the drag and magnitude of the shear stresses imparted by the overriding flows into the substratum. In cases where this reduction was large and the strength of the substratum was high, the result would be minimal to no erosion of the bed. Such research has improved our understanding of debris-flow processes. Although we have a greater understanding of the long run-out distances that some debris flows can travel, how submarine debris flows interact and erode into underlying substrate is less widely documented.

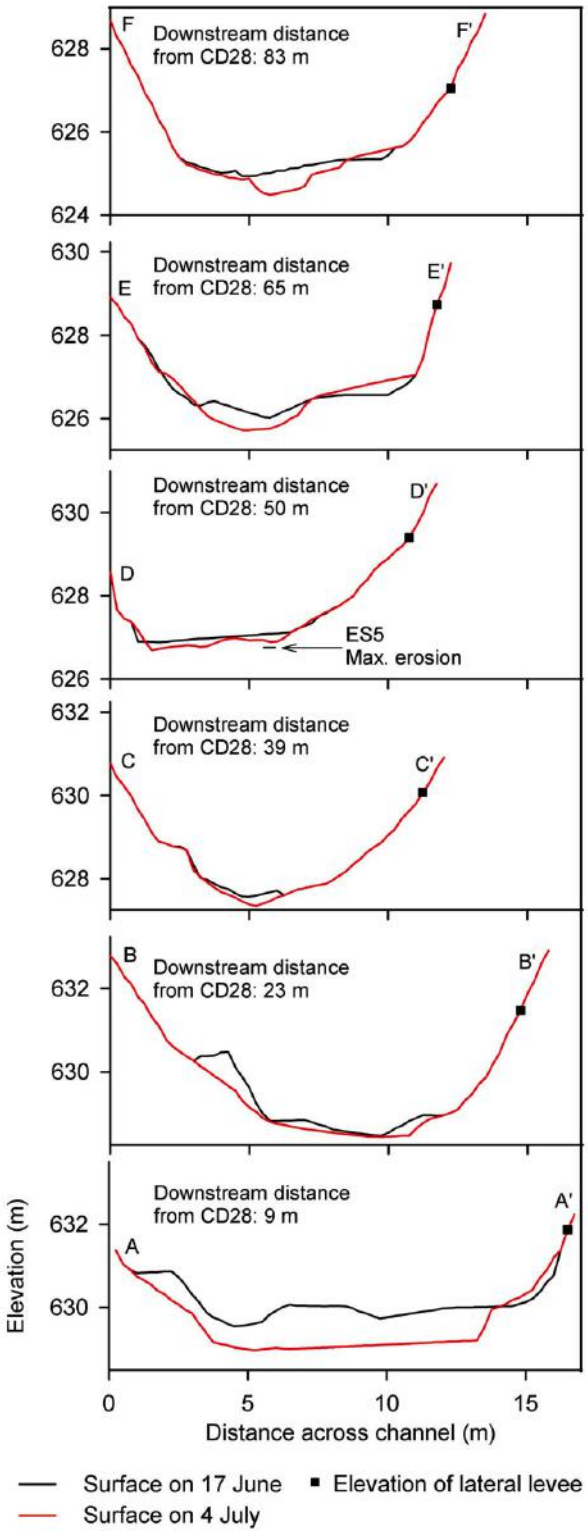

Figure 2.14. Cross-sectional channel profiles progressing downslope (from A to F, respectively) of the debris flow gully pre- and post-debris flow. Modified from Berger *et al.* (2011).

Early schematic diagrams of seafloor profiles show debris flows and other MTDs to scour the seafloor, as illustrated by Prior (1984), showing the dashed line of 'former seafloor' (Figure 2.15). However, only relatively recently have basal contacts of MTDs, and specifically debris flows, in the submarine realm been described as potentially erosive (Lastras *et al*., 2004; Masson *et al*., 1993; Nygård *et al*., 2002; Carter, 2001; Sawyer *et al*., 2012; Toniolo *et al*., 2003; Mohrig and Marr, 2003; Davies, 1986; Gee *et al*., 1999, Gee *et al*., 2005, Gee *et al*., 2001; Phillips, 2006; Alves and Cartwright, 2009, 2010, Alves, 2010, Alves *et al.*, 2013, Omosanya and Alves, 2013a,b, Alves *et al.*, 2014, Alves, 2015).

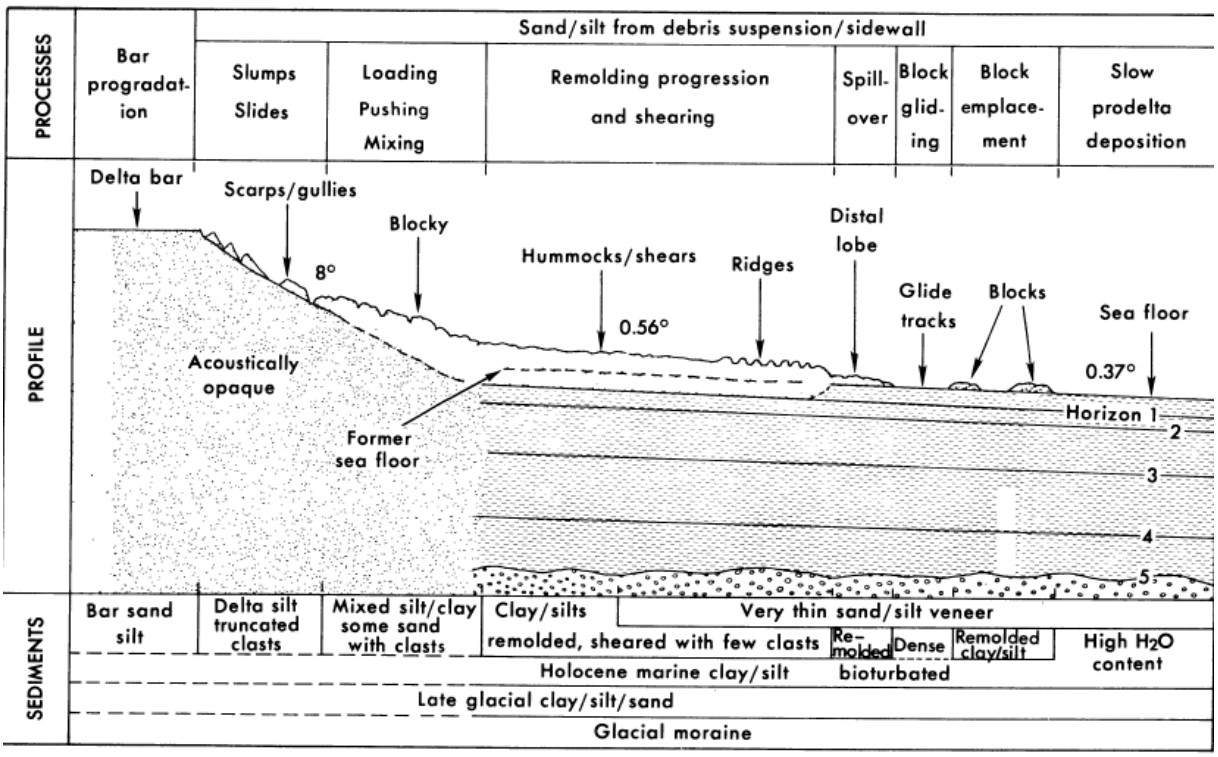

Figure 2.15. Summary of debris flow characteristics relating to process mechanisms and deposits of a longitudinal profiles from a delta front to the distal margin of the debris flow. From Prior (1984). Note the former seafloor interpretation implies removal/erosion.

Gee *et al*. (1999, 2001) were the first researchers to consider the erosive impact that debris flows have in deep-marine systems. Gee *et al*. (1999, 2001) interpreted a two-phase erosive debris-flow event on the northwest African Margin. The flow, termed the Saharan debris flow, had a run-out of 400 km travelling on low-gradient slopes (as little as 0.05°), and composed of a lower, thin (~ 5 m), homogenised sandy-volcaniclastic debris-flow phase (L-

DFP) and an upper, thick (~ 25 m), heterogeneous muddy-pelagic phase (U-DFP). Analysis of coccolith assemblages and marl-clasts within the L-DFP show the same signature as the substrate immediately beneath suggesting erosion and mixing of the underlying substrate. Results suggested that the seafloor had been subject to ~ 3 m of erosion.

Nygård *et al.* (2002) documented the geometry and genesis of glaciogenic debris flows (GDFs) on the North-Sea Fan, Storegga Slide, Norwegian North Sea. Results from seismic profiles suggested the cross-sectional profile of GDF deposits produced 'chute-like' structures with a potentially erosional base in the centre of the chute, as seen in Figure 2.16. This central area identified the most transparent seismic reflectors, suggesting debris flows were the cause of erosion, however core-data would be required to identify the lithofacies in the seismic data.

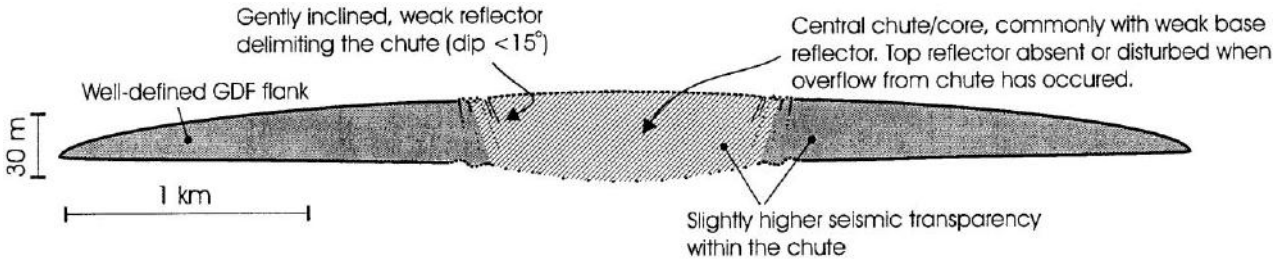

Figure 2.16. Idealised cross-section of a GDF. The 'core' of the chute structure, identified by the transparent seismic facies locates the debris flow where erosion is identified on seismic. From Nygård *et al*. (2002).

Erosively-based MTDs, including debrites, are typically interpreted from seismic-reflection datasets interpreted as the result of sufficient shear stresses from slides or debris flows that contain tools at the base of the flow that scour the substrate forming linear erosional grooves or surfaces (Alves and Cartwright, 2009; Posamentier and Martinsen, 2011, De Blasio and Elverhøi, 2011). Posamentier and Kolla (2003) first described the presence of long linear grooves at the base of debris-flow sheets, lobes and channel deposits from 3-D seismic data on the basin-floor of Indonesia, Nigeria and the Gulf of Mexico. These erosional scours were measured up to 40 m deep, 700 m wide and up to 20 km long. McGilvery and Cook (2003) described the seismic facies of MTDs along the continental slope, offshore Brunei to be comprising dim, chaotic amplitude horizons, punctuated by high-amplitude and local packages continuous reflections, interpreted as rafted slump blocks within a muddy

debris-flow matrix. The basal surfaces of these MTDs exhibited grooves, similar to those recorded by Posamentier and Kolla (2003). McGilvery and Cook (2003) and Posamentier and Kolla (2003) attributed these grooves from the presence of large cohesive blocks of sediment lodged at the base of debris flows, which ploughed into the substrate, and remained there for long distances (up to 20 km) before either being lifted off the base of the flow, or being disaggregated, observations also documented by Omosanya and Alves (2013).

Moscardelli *et al*. (2006) used high-resolution seismic datasets to research submarine large-scale scour features (tens to hundreds km) in offshore Venezuela and Trinidad. As observed in the Nygård *et al.* (2002) study, basal incision of MTDs are characterised by a deep, wide, erosional scour located in the centre of partially confined flows. Erosive basal surfaces of MTDs form a variety of scour dimensions that range from megascours that form up-dip in proximal areas measured ~ 3 km width, 133 m deep and up to 60 km in length to 'cat-claw' scours (up to ~ 10 m deep) which form down-dip, distally from the source area (Figure 2.17). To form these large erosional features, sustained energy is required to plough the substrate for long distances, and so confinement was believed to be an important aspect. The geometry of 'cat-claw' scours comprise a series of shallow, radiating scours with the apex closing down-dip from the direction of travel. The transition of megascours to cat-claw scours is attributed to an abrupt change in deposit-flow conditions and is used as evidence between the transition of confined to unconfined flows. The sharp terminations of scours are documented to occur with the transition from non-hydroplaning to hydroplaning flow (Moscardelli *et al*. 2006). The authors state that MTDs are able to transition from laminar to turbulent flow when passing from confined to unconfined settings, enabling interaction with the substrate. Although this data is interpreted to show erosion by MTDs, due to the gross-resolution of seismic data, limits the detail of MTD architectural elements and without physically coring these features, it is not possible to determine exactly what MTDs are responsible for the scouring action, although transparent facies suggest debris-flow deposits. Other seismic studies identify similar shallow- (a few metres incision into the seafloor), to deep (tens of metres into the seafloor) erosional glide planes at the base of slides and slide blocks within chaotic amplitudes, interpreted as debrites (e.g., Alves and Cartwright, 2009, 2010, Omosanya and Alves, 2013a, b). In these datasets, sediment slides/slumps and debris-

flow deposits are identified using coherence seismic volumes, RMS amplitude maps and time-dip maps.

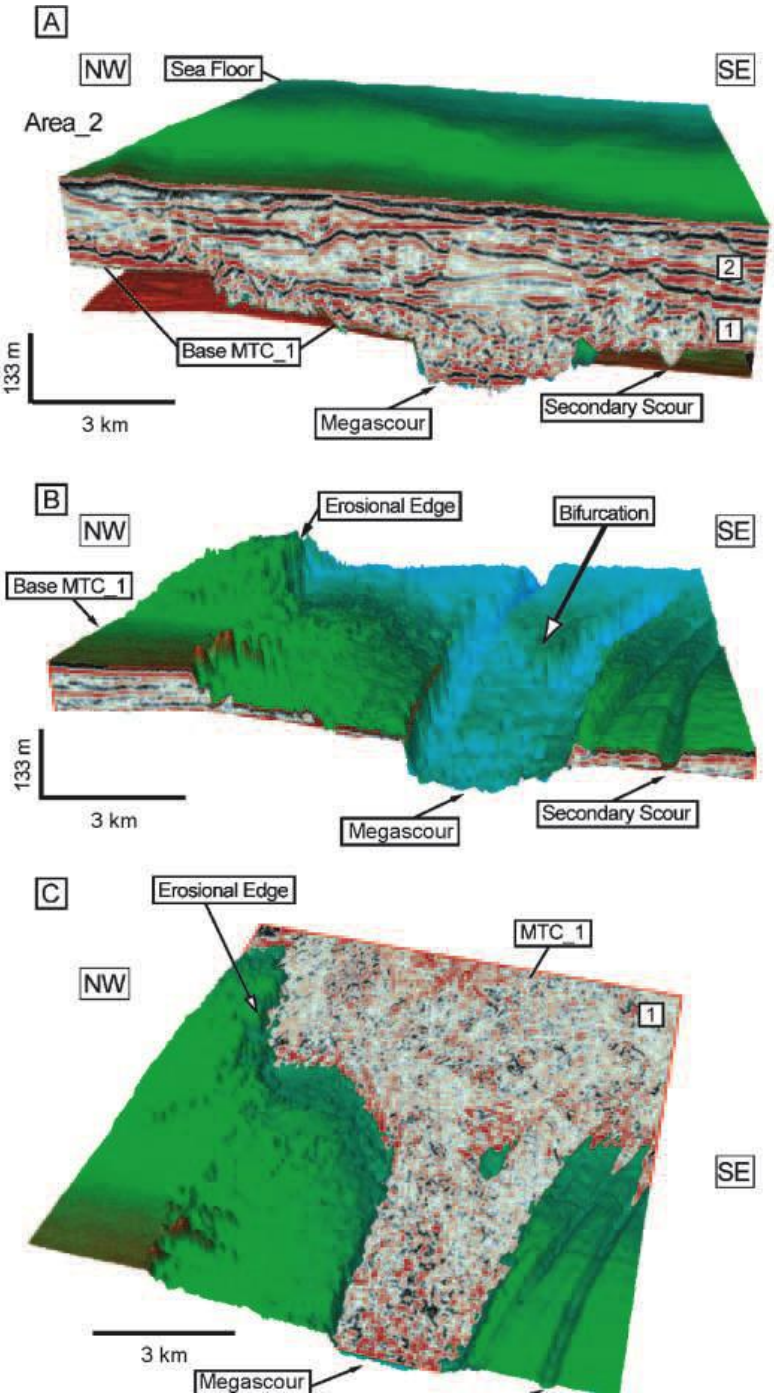

Figure 2.17. Megascour images from MTCs. (A) Erosional edge of MTC reaches maximum incision in the centre of the erosional scour. (B) Backstripped image shows basal erosion edge from MTC. (C) MTC time-slice through megascour showing geometry of scour shape. Modified from Moscardelli *et al*. (2006).

Figure 2.18 summarises outcrop observations from subaerial debris-flow events in Mt Thomas, Canterbury, New Zealand (Pierson, 1980). Although not described in the text, the diagram shows a bedded debris-flow deposit (6.6 m in thickness) comprising smaller individual events (MTDs), each ~ 1 – 1.5 m in thickness. At the base of the deposit is a 'U-shaped' channel cut into the underlying soil. This understated observation is significant, as it implies that the erosive mechanism of submarine, e.g., 'chute-like' observations of Nygård (2002) and Moscardelli *et al*. (2006), and subaerial processes e.g., Pierson (1980), could be analogous.

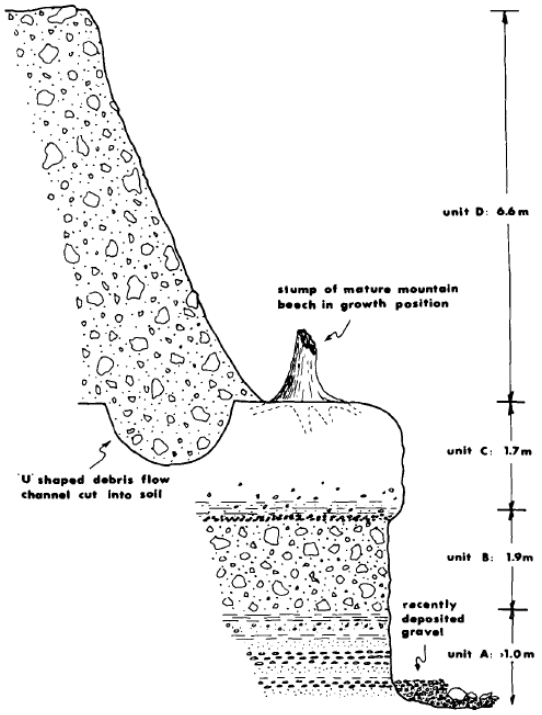

Figure 2.18. 'U'-shaped debris flow channel (Unit D) identified to cut in to underlying soil. Debris-flow deposit comprising clay boulders with indistinct parallel layers 1.0 to 1.5 m thick (individual flows). Analogous to the 'channel-like' geometries identified in submarine settings. From Pierson (1980).

A study by Ducassou *et al*. (2012) analysed sediment cores from four depth horizons of the Nile deep-sea submarine fan system: (1) within the Rosetta submarine channel axis at 1700 m water depth; (2) within a small salt-tectonic basin in the eastern fan at 1300 m water depth; (3) within a non-channelised open slope at 2,600 m water depth, and; (4) in the distal fan fringe at 3,050 m water depth. From the 42 sediment cores collected, 41 debrites were identified in 18 cores. Microfossil assemblages in debrites were analysed to determine their

origin by relating benthic marker species to the following depth distributions: neritic (0 – 200 m); epibathyal (200 – 400 m); mesobathyal (400 – 1,500 m); lower bathyal (1,500 – 3,000 m); and, abyssal (> 3,000 m). Results conclude that many thin debris flows (20 – 150 cm) found in the Rosetta submarine channel, the salt-tectonic basin and the distal fan fringe had travelled over 200 km to distal parts of the Nile submarine fan and showed negligible signs of erosion containing only neritic forams and resulted from gradual failure of the continental slope. However, micropalaeontological analyses from debrites derived from an open slope, found up to 8 m in thickness and travelling up to 150 km, contained neritic to lower bathyal sediments. This suggests sediment erosion and entrainment along the length of the slope profile, from the upper to lower slope (0 to 2,600 m water depth). These debrites show prominent stratigraphic layering, interpreted to have resulted from retrogressive failure and erosion by bulldozing of the seafloor. The lithology and texture of erosive and non-erosive debrites analysed in the sediment cores are predominantly ungraded and comprise mud-clasts in a muddy-sand matrix. In the study from Ducassou *et al.* (2010), non-erosive debrites are found in channelised environments and erosive debrites are found in non-channelised slopes. It was concluded that in a channelised environment, high pore-pressures are sustained due to the lateral restriction by the presence of levees, which allows hydroplaning to occur at the base of debris flows, as observed in the experimental work of Mohrig *et al*. (1998).

Erosion through debris flow processes at outcrop is rarely alluded to, however, an outcrop study presented by Dykstra *et al*. (2011) is unique, showing the presence large-scale sands plucked and incorporated into the base of an ancient ~ 120 m-thick debrite from the Carboniferous Cerro Bola outcrop, northwestern Argentina. This outcrop observation potentially suggests a process, other than basal scour at the base of MTDs, previously discussed for modern submarine fans (Figure 2.19). The outcrop presented in Dykstra *et al.* (2011) presents a succession of shallow marine and fluvio-deltaic sandstones, interpreted as glacio-eustatic lowstand deposits, related to the growth of the Gondwanan ice sheet. During deglaciation, these lowstand deposits were flooded and sediment was resedimented into deeper water, resulting in deposition of the 120 m debrite. The surface between the MTD and the underlying deltaic- to shallow marine deposits is irregular. Blocks of sandstone, varying from a few metres to tens of metres wide and a few metres to ~ 10 m thick are common near the base of the deposit. The blocks are interpreted as ‘plucked’ from the underlying

fluviodeltaic sediments during movement of the MTD and incorporated into the resedimented mass. Individual blocks exhibit disaggregation by attenuation and boudinage in the inferred transport direction. However, the study does not postulate on the significance of the plucked sandstones, which is a major contributor to erosive debris flow processes documented in this study within the Ainsa Basin.

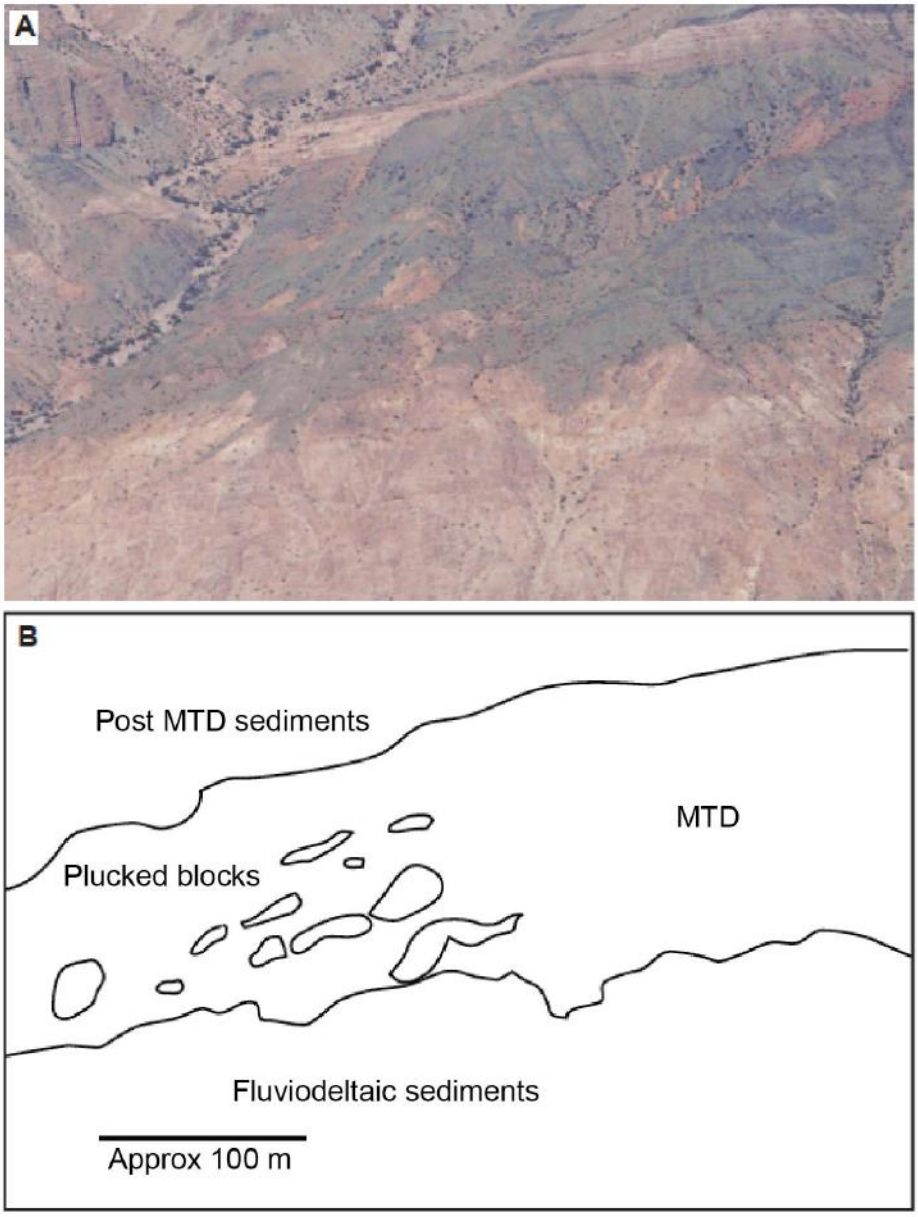

Figure 2.19. (A) Topography at the base of the Cerro Bola MTD, showing sandstone blocks that have been plucked from the underlying fluvio-deltaic sandstones and incorporated into the resedimented mass. B) Line drawing of Part A, showing boundary and blocks in mass-transport deposit. From Dykstra *et al.* (2011).

Basal surfaces of MTDs can vary in the strike-orientated appearance and tend to be concave-up (and therefore easily mistaken as a channel), or conformable if non-erosional. De Blasio and Elverhøi (2011) remark *"...how can this evidence (i.e., erosional scours from debrites) be reconciled with the hydroplaning hypothesis*", referring to the pioneering work of Mohrig *et al*. (1998, 1999). Computer simulations indicate that hydroplaning affects mainly the head of debrites, while the rest of the body lags behind, however the lift forces at the front of the flow are believed to diminish the higher the volume of the slide. Another hypothesis from De Blasio and Elverhøi (2011) discusses erosion occurring at the tail of a submarine slide as hydroplaning reduces shear stress at the base, but does not completely eliminate it.

2.4.3 Strength-loss mechanisms and material entrainment

Mechanisms that cause strength loss or material entrainment in landslides and debris flows within subaerial and submarine settings, as discussed in Section 2.4, are presented.

2.4.3.1 Liquefaction

The term liquefaction can be used for complete liquefaction (i.e., the complete loss of effective stress) and also for partial liquefaction, i.e., the generation of excess pore pressures (De Groot *et al*., 2006). Pore-fluid pressure plays a critical role in debris flows because it counteracts normal stresses at grain contacts and thereby reduces normal intergranular friction, and appears to be most prominent in soils with relatively weak grains (George and Iverson, 2011). Liquefaction of granular sediment refers to a temporary collapse of a loose soil skeleton, or a sudden loss of pore-fluid pressure due to excessive strain causing a loss of the effective stress, followed by an increase in pore-pressure and loss of strength under undrained conditions (Lowe, 1975). Liquefaction can occur in sands, including coarse fractions, and can occur following large displacement (e.g., Lowe, 1975, 1976).

2.4.3.2 Effective stress

As SGFs travel in a submarine environment, it is assumed that the rocks at the seafloor surface are physically comparable to saturated to semi-saturated soils in subaerial environments, depending on the amount of cementation or lithification that may have occurred in the short term. The stress state of saturated soils is called the effective stress, calculated as:

$$\sigma' = \sigma - u_w$$

where:

σ' = effective stress

σ = total normal stress

u_w = pore-water pressure

Excess pore-water pressure is defined as the difference between the actual pore pressure and the hydrostatic pore pressure. Excess pore pressure can cause a significant decrease in shear resistance and therefore a decrease in the effective stress (Fredlund and Rahardjo, 1993). The change in volume and shear strength of a saturated soil is controlled by a change in the effective stress, which alters the equilibrium state. Effective stress is proven to be the only stress state variable controlling the behaviour of a saturated soil.

2.4.3.3 Undrained and rapid loading

Rapid undrained loading was documented by Hutchinson and Bhandari (1971), who observed an increase in pore pressure from a piezometer embedded near the basal surface of an earthflow, which was subjected to rapid deposition of material from upslope. Flowing debris causes intense shearing within a thin shear band leading to a textural change within the underlying material (grain crushing). The modified sediment contains a greater proportion of fines and is capable of denser packing. De Groot *et al*. (2006) characterise undrained loading in soils by two important limiting cases: (1) the soil is completely saturated with water, i.e.,

no gas is present in the pore fluid, and; (2) no drainage occurs. The full bulk weight of the debris flow is transferred to the pore-water by undrained loading. This may cause high pore pressure and a corresponding loss of strength causing liquefaction of the channel bed (Hungr *et al.* 2005; Sassa and Wang, 2005).

If soil is contractive, pore pressure is expected to increase during undrained shear, which may yield partial or complete liquefaction. Soils at the seafloor surface are likely to be undrained, as shown in DSDP data, where samples collected at > 50 m below the seafloor have ~ 50 % water content, suggesting that at the seafloor, water content will be much higher (Figure 2.20). Saturated soils typically have a unit weight of 20 kN/m^2. Undrained loading appears to be the principal mechanism able to mobilise material on gentle slopes, as documented by Hungr *et al*. (2005) and Mangeney *et al*. (2010), showing that debris flows are able to derive most of their volume by entraining loose saturated material from their path.

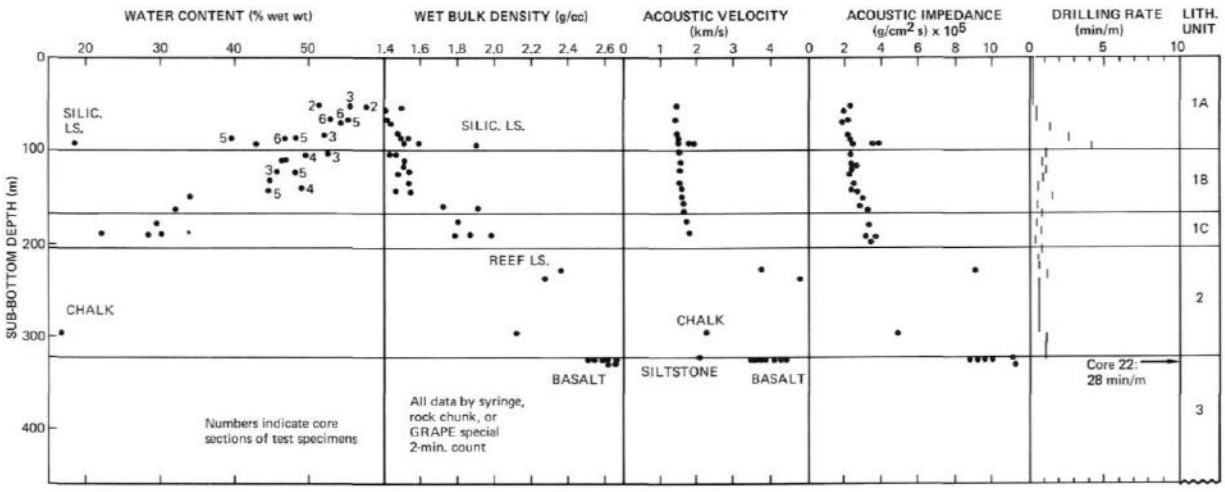

Figure 2.20. Physical properties of samples taken at DSDP Site 384.

Greater erosive forces result from debris flows overriding a saturated substrate, as the bed material can be hugely mobilised and entrained into the flow (Hungr *et al.*, 2005). Iverson *et al.* (2010) advanced our understanding in the dynamics of debris flows in subaerial environments. A series of experiments at the USGS debris-flow flume facility in Vancouver, reveal how debris flows are able to entrain static sediment and how this can subsequently result in flow-momentum and growth. Results of this experimental study show that rapid loading of debris flows generates high pore-pressure in the basal surface sediments, which

facilitates entrainment into the overriding debris flow. Flows that encountered the wettest-bed sediments behaved almost explosively enabling highly efficient entrainment. These flows were able to entrain more material and exhibited longer run-outs, as identified in the Mangeney *et al.* (2010) and Farin *et al.* (2013) experiments. Flows that lost speed during entrainment were still observed to have a longer run-out than those of bare-bed controls. These saturated bed observations from Hungr *et al.* (2005) and Iverson *et al.* (2010) are particularly valuable to understand erosive processes in submarine environments, due to the wet-bed-nature of antecedent deposits in submarine channels and fan deposits.

2.4.3.4 Basal shear

Laboratory experiments from Davies (1990) used a moving-bed flume to document the behaviour and characteristics of high-concentration sediment waves that behaved similarly to surges or pulses reported in natural debris flows. Results from this laboratory experiment showed that each experimental debris-flow pulse comprised three major 'flow-zones', including rapid and slow shear at the head of the flow and fluidal-motion at the tail, Figure 2.21.

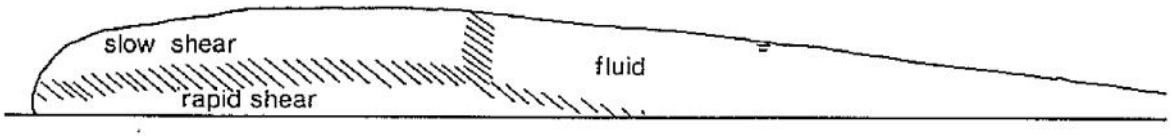

Figure 2.21. Three 'flow-zones' identified: (1) rapid shear (2) slow shear, and (3) fluidal. From Davies (1990). Flow direction is to the left.

Shear-properties of each flow-zone are described as: (1) a high basal shear zone at the head of the flow. Grain velocity was noted to increase with height from the base; (2) a slow shear zone in the upper region at the head of the flow. Grain velocity was observed to be close to the average velocity and grains sheared past each other slowly giving the appearance of a solid, non-shearing 'plug' of sediment, and; (3) fluid-like motion shearing rapidly in the 'tail' of the flow. The transition between zones 2 and 3 occurred within a few grain diameters (~ 8 mm). This study suggested that if large volumes of material are carried by dispersive

stress (based on high-concentration pulsing flows that transport large boulders in a dense, highly viscous slurry), debris flows are capable of scouring the channel-bed through viscous basal shear by increasing the drag force, resulting in further enhancement of entrainment intensity. Observations and quantitative data collected from field studies propose the same erosive mechanism, whereby a fluid-poor snout of a debris flow exerts the greatest collisional stress on the underlying bed enabling erosion at the head of the flow and deposition occurring at a later stage, towards the tail of the flow (Stock and Dietrich, 2006).

2.4.3.4.1 Monotonic shear

As a debris flow travels over a static position on the seafloor, it can impose monotonic shearing of the substrate, resulting in shearing increasing in the same direction. This effect, which firstly yields contraction, i.e., volume decrease by shearing, then secondly yields dilation, i.e., volume increase by shearing (Figure 2.22) (De Groot *et al.*, 2006).

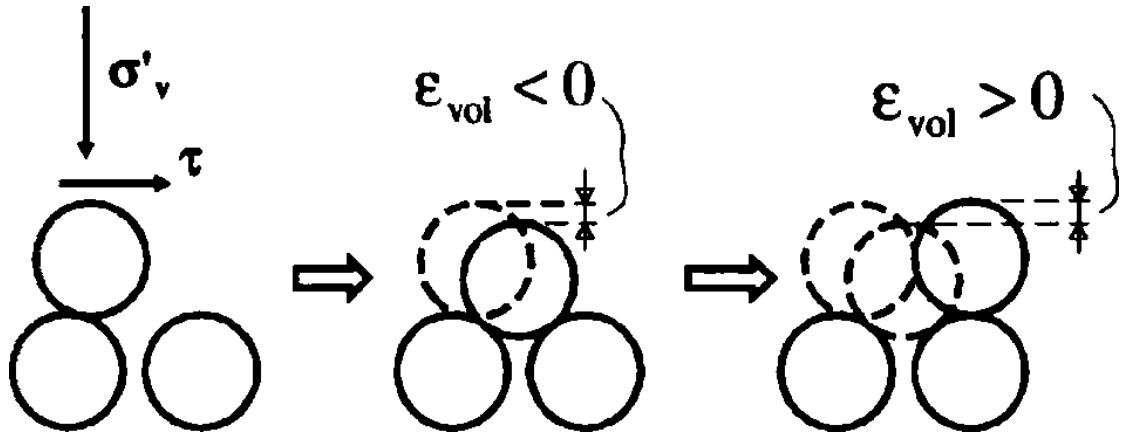

Figure 2.22. Contraction and dilation by rearrangement of grains through monotonic shear. From De Groot *et al*. (2006).

An undrained response to monotonic shear (where the total vertical stress is kept constant and shear stress gradually increases), shows that the effective vertical stress (σ'_v) is firstly reduced by the contraction induced excess pore pressure, and then increased by the dilation induced "suction" i.e., forming negative pore pressure. This process is revisited because field evidence shows large semi-consolidated sandstone blocks incorporated into the base of MTDs (Chapter 6).

2.4.3.4.2 Cyclic shear

Cyclic shear is defined by a series of cyclic stresses on the sediment, generally induced by earthquakes. Densification of a sandy soil is nearly always a result of cyclic shearing. Dilation does not play a role in most cases of cyclic shearing, but severe vibration can induce loosening, i.e., liquefaction (De Groot *et al*., 2006). The repetitive motion of debris flows in quick succession may also result in cyclic shear of the substrate.

2.4.3.5 Ploughing

Other experimental studies have documented debris flow erosivity on unconsolidated sediments. Major (1997) examined the depositional process and characteristics of subaerial large-scale experimental debris flows using a 95 m-long, 2 m-wide debris flow flume sloping at 31° at the USGS flume facility, Vancouver. Multiple deposits were released on consecutive days and were allowed to accumulate. Sediment accumulated abruptly on a 3° run-out slope at the mouth of the flume and deposited in a complex manner through a combination of shoving forward and shouldering aside previously deposited debris and through progressive vertical accretion (Figure 2.23). It was found that the depositional process of each experiment was strongly influenced by the water content of the source material and deposit platforms were influenced by both water and by substrate topography. These studies showed the deposition of similar, yet separate debris flows, are able to produce homogenous, structureless, poorly sorted matrix-supported deposits having little stratigraphic distinction and suggests ploughing mechanisms of unconsolidated sediments.

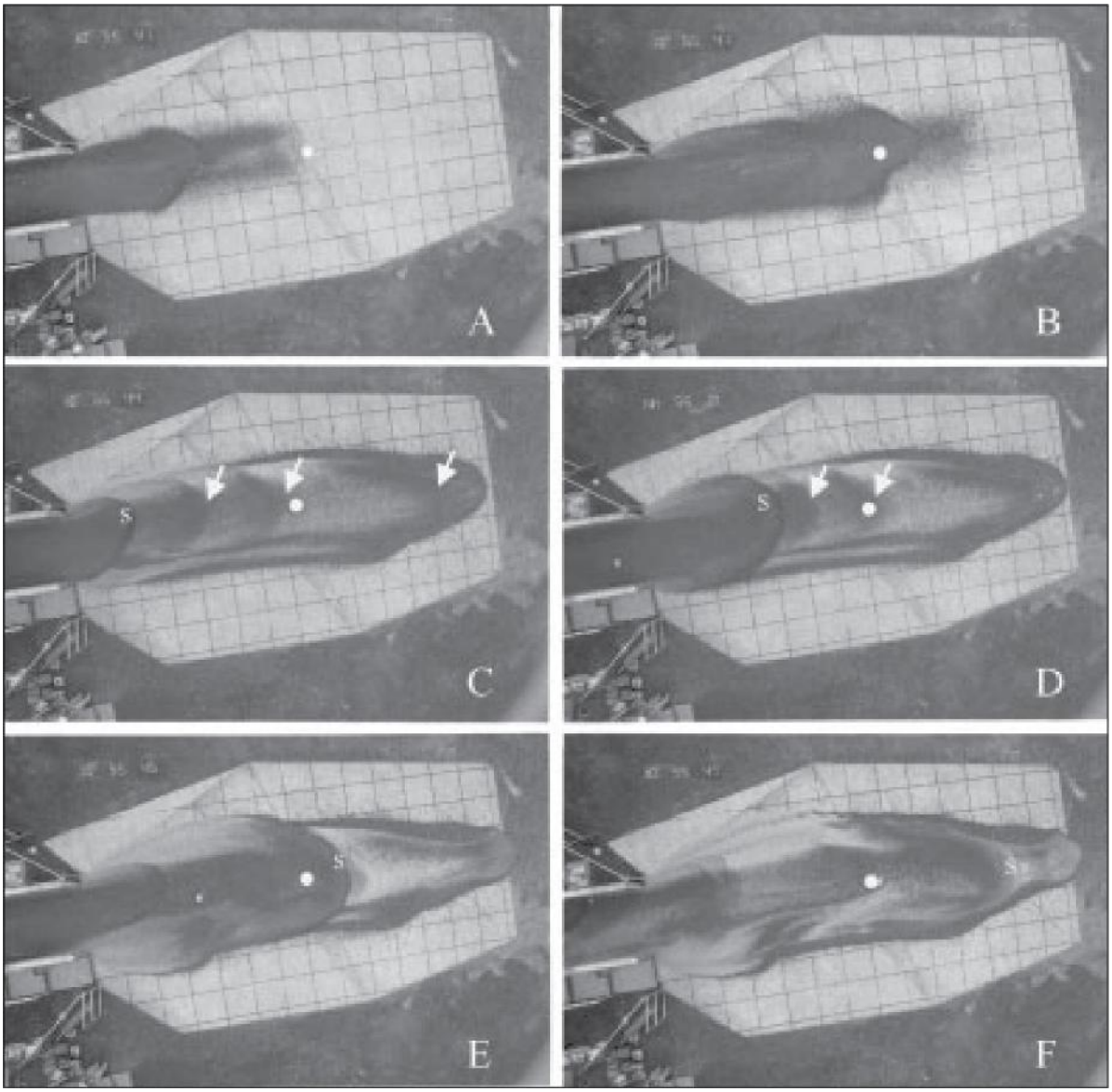

Figure 2.23. Sequence of aerial photographs illustrating deposition of an experimental debris flow on the run-out surface. Coarse debris at the front of surges was enveloped into the sediment deposited in lateral margins, as wave decelerated and debris was shouldered aside. From Major (1997).

2.4.3.6 Erosional efficiency

Laboratory experiments of Mangeney *et al*. (2010) used dry granular material (comprising subspherical, cohesionless and rigid glass beads) flowing over an inclined plane covered by an erodible bed to mimic natural flows travelling over deposits built up from earlier events.

Upon release of the flow, the avalanche is seen to excavate static material at the flow front (equivalent to the erodible underlying substrate in a natural channel environment), associated with the energy exchange between the flowing and static masses. Whilst the kinetic energy of the flowing mass is consumed, the potential energy of the static grains is converted into kinetic energy. This study showed that a higher efficiency of erosion occurred on higher angles because an initially static substrate is more easily destabilised by a small perturbation. Erosion processes were also observed to increase the flow mobility over slopes and can develop surging fronts that travel at almost constant velocities. Farin *et al*. (2013) identified several conditions required for continued flow momentum in the flow propagation phase of granular flows by adding energy to the system to overcome friction. This was achieved by: (1) increasing the slope angle; (2) increasing the volume at a constant ratio; (3) increasing the kinetic energy by bulking up from entraining the erodible bed; (4) enlarging the channel width, thus reducing friction against the channel margin, and; (5) increasing the angle at the release zone (e.g., in natural environments) or the gate inclination (e.g., in experiments) which gives a higher initial driving force due to the pressure gradient.

In moving debris flows, grains are redistributed throughout the sediment flow transferring and localising the load in filamentary structures, called force chains (McCoy *et al*., 2013). Using field measurements, McCoy *et al.* (2013) measured the basal forces related to these force chains from debris flows initiated in the steepland valley of Chalk Cliffs, Colorado, USA. The basal normal force had a large magnitude, high frequency and a fluctuating component (21 kN, ~ 50 times larger than the average mean force). The fluctuating components of debris flows in this study were interpreted as flow particles and force chains impacting the bed. Natural debris flows have a wide distribution of grain-sizes resulting in a broader distribution of basal forces on the substrate, and therefore are more likely to have an increased number of impacts with the substrate.

2.4.3.7 Subaerial and submarine entrainment summary

A summary of material entrainment is provided as a reference table for erosive processes (Table 2.4), which are identified in field outcrops in the Ainsa Basin (Chapters 6 and 7).

Setting	Observation	Impact on the substrate	Process	Reference
Subaerial	Emergence of boulder fronts	Shearing and grain-collisional forces in granular material causing erosion	Longitudinal sorting	Iverson (1997), Stock and Dietrich (2006)
Subaerial	Turbulent front	Erosion. Loss of strength and destabilisation of the bedrock (or substrate)	Massive drag and shear forces at the base of the head of the flow	Davies (1986)
Subaerial	Positive feedback mechanism	Erosion	Debris flows with a higher sediment volume are likely to cause more erosion due to higher basal-drag and frictional forces	Breien *et al.* (2008); Berger *et al.* (2011)
Subaerial	Saturation of sediment at depth and at the seafloor surface	Erosion	Explosive interaction with the underlying sediment at a change in gradient	Iverson *et al.* (2010)
Subaerial	Flow momentum and growth	Erosion	Pore pressure differences between flow and substrate. Undrained and cyclic loading	Iverson *et al.* (2010)
Subaerial	Liquefaction	Loss of strength and destabilisation of the bedrock (or substrate) due to loss of effective stress	Temporary collapse of a loose soil skeleton, or a sudden loss of pore-fluid pressure due to excessive strain causing a loss of the effective stress. Cyclic and monotonic shear.	De Groot *et al*. (2006)
Subaerial	Rapid deposition of material on substrate	Undrained loading	If soil is contractive, pore pressure increases and may yield partial or complete liquefaction - Loss of strength and destabilisation of the bedrock (or substrate)	Hutchinson and Bhandari (1971); De Groot *et al.* (2006)
Submarine	Coccolith assemblages suggest mixing of substrates	Erosion	Not specified	Gee *et al*. (1999, 2001)
Submarine	Chute-like structures with erosional base in centre	Erosion	Not specified	Nygård (2002)
Submarine	Linear erosional scours and grooves	Erosion	Ploughing and dragging objects at the base of flow	McGilvery and Cook (2003); Posamentier and Kolla (2003), Posamentier and Martinsen, (2011); De Blasio and Elverhøi (2011); Moscardelli *et al*. (2006); Alves and Cartwright (2009); Omosanya and Alves (2013a, b)
Submarine	Mixed neritic to abyssal microfossil assemblages in deposits on abyssal plain	Erosion	Bulldozing of the seafloor	Ducassou *et al*. (2012)
Submarine	Plucked sandstone blocks into MTD	Erosion	Not specified	Dykstra *et al*. (2011)

Table 2.4. Physical properties of subaerial and submarine debris flows resulting in basal erosion of the underlying substrate

2.5 SUMMARY

Firstly, this chapter reviewed concepts of SGF (including MTD) processes. The term MTD encompasses several deformational processes including creep, slide, slumps and debris flows (Moscardelli and Wood, 2008; Posamentier and Martinsen, 2011; Talling *et al.*, 2012). Results from this study are predominantly based on fieldwork; therefore, adopting a suitable MTD classification scheme was an integral component for this research. The MTD classification scheme of Pickering and Corregidor (2005) makes a comparison of sedimentological characteristics following the hierarchical and descriptive facies of Pickering *et al.* (1986, 1989), relevant for understanding the transport processes resulting in different deposits. The nature of this classification scheme provides a sound basis to identify and discuss different mass-wasting processes in the Ainsa Basin, therefore this scheme was adopted and based on observations in this study, and modified where appropriate (Chapter 4).

Secondly, this chapter reviewed and identified key studies that documented erosive debris flow processes in subaerial and submarine environments. Concepts of erosive debris flows in subaerial environments are becoming widely acknowledged. Debris flow characteristics constantly change in response to sediment entrainment and changes in water content suggesting viscosity, cohesion, friction and collision varied with time, distance and depth of the flow (Breien *et al*., 2008). Debris flows are able to gain mass by entraining material as they descend steep slopes and channels through destabilisation, shear and mobilising loose or static bed material from deposits in channels from previous events (Hungr *et al.*, 2005; Jakob *et al*., 2013; McCoy *et al*., 2013). There is emerging evidence from literature that the basal surfaces of some MTDs in submarine settings are also erosive (e.g., Alves and Lourenço, 2010). Some authors suggest bulldozing mechanisms, others suggest dragging objects scour the seafloor, and others elude to 'plucking' of underlying strata, however all of these processes are yet to be applied in submarine environments and sufficiently documented and supported from outcrop studies. The mechanics of entrainment by debris flows remains a fundamental question to be fully satisfied. One aim of this study is to document MTDs showing basal erosion at outcrop and address the subsequent erosive mechanism (Chapters 6 and 7).

CHAPTER 3

METHODOLOGY

3.1 INTRODUCTION

Research in this study is focused on the descriptions and measurements of MTD and MTC outcrops in the Ainsa Basin, Spanish Pyrenees. Several field-based techniques were employed during this investigation. From these data, evaluations on the various mass-transport architecture and facies are identified. Laboratory and industry-based methods are also outlined during an internship undertaken at CNOOC-Nexen.

3.2 FIELDWORK METHODS

A total of six field seasons were undertaken in the Ainsa Basin study area, totalling ~ 9 months of fieldwork. A fieldwork diary is presented in Appendix B. Initial fieldwork involved a reconnaissance study to locate suitable outcrops for further study and to obtain preliminary information such as MTD facies type and stratigraphic position within the basin. Data collection comprised detailed outcrop descriptions and sedimentary logging, resulting in ~ 3.2 km of sedimentary logs. Data from fieldwork is presented as a series of photomontages, sedimentary logs, cross-sections and histograms in Chapters 4, 5, 6 and 7.

3.2.1 Study area and localities

The study area encompasses ~ 20 km^2 around the town of Ainsa (Figure 3.1). The elevation of the region varies from 500 to 1,300 m above sea level. Pickering and Bayliss (2009) and Pickering and Cantalejo (2015) published a detailed geological map of the Upper Hecho Group, which included a less-detailed facies map of the Lower Hecho Group in the Ainsa Basin (Figure 1.16, Chapter 1). Fieldwork in this study was also focused on the Upper Hecho Group as it is less tectonically complicated by syn- and post-depositional thrusting.

The reconnaissance study involved using the detailed geological map of the Upper Hecho Group (Pickering and Bayliss, 2009) and locating outcrops exposing MTDs and MTCs. From here, outcrops suitable for further study were defined as type and/or representative localities (Figure 3.1 and Table 3.1).

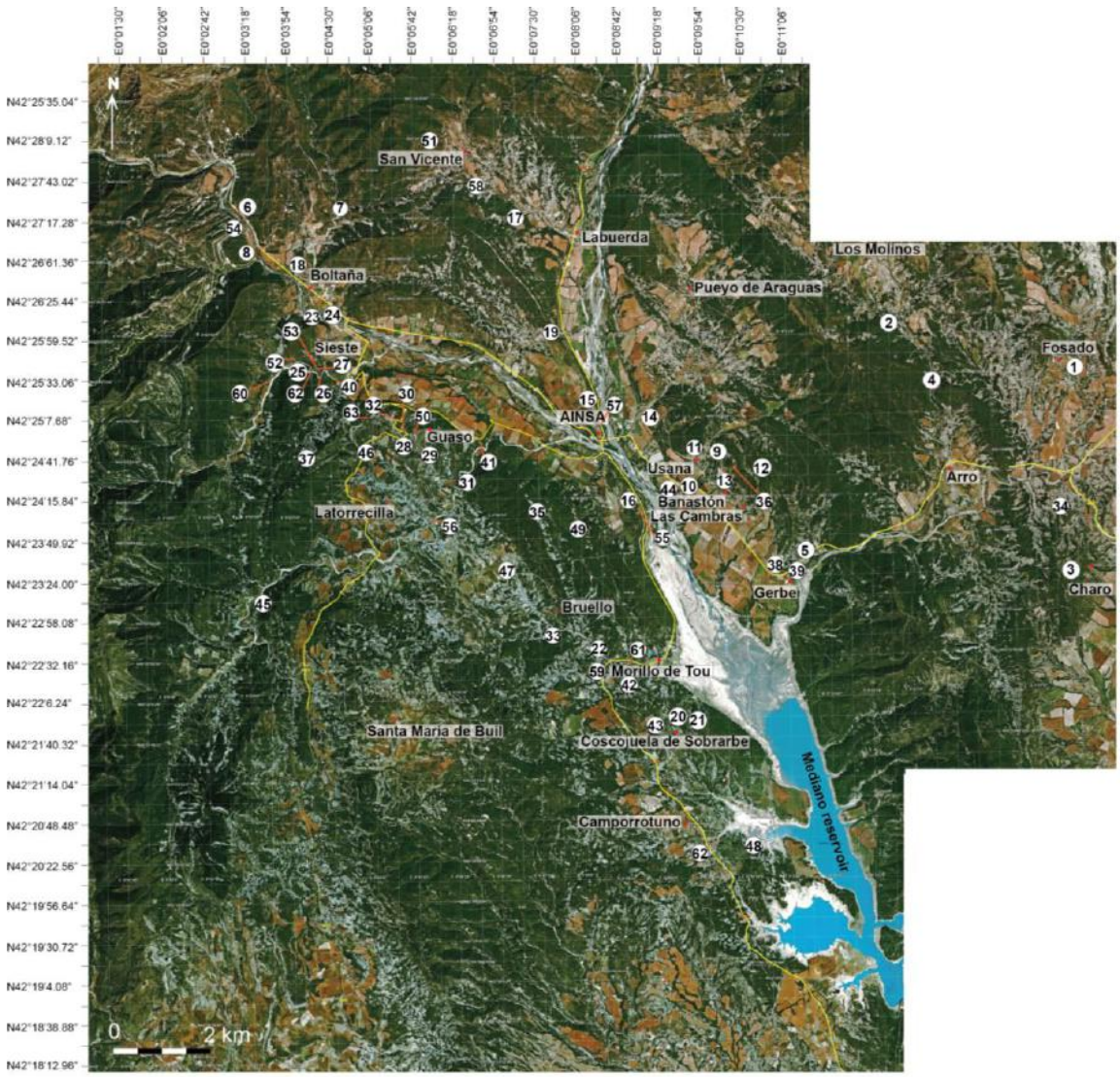

Figure 3.1. Satellite map of the study area, showing the localities of measured sections. For a summary of the main characteristics of each section, see Table 3.1. Map compiled from Google Earth. Map data ©2015 Google.

Locality	Sedimentary log or Locality name	GPS location	System/Fan	Depositional environment (from Pickering and Bayliss (2009); Bayliss and Pickering (2015a); Bayliss and Pickering (2015b); Pickering *et al.* (2015)
1	Fosado stream	42°25'25.41"N 0°15'22.44"E	Fosado	Proximal channel complex
2	Los Molinos stream	42°25'49.18"N 0°13'04.77"N	Los Molinos	Off axis from channel complex
3	Arro Canyon	42°23'26.53"N 0°15'14.22"E	Arro	Upper slope canyon
4	Road to Los Molinos	42°25'22.81"N 0°13'17.04"E	Arro	Proximal channel complex
5	Conglomerate	42°23'41.12"N 0°11'57.15"E	Gerbe II	Proximal channel complex
6	Boltaña N-260	42°27'10.70"N 0°03'22.60"E	Banastón IV, V, VI	Distal system complex
7	Boltaña River	42°27'23.62"N 0°04'37.61"E	Banastón V	Distal channel complex
8	Road to Sabiñanigo	42°26'54.07"N 0°03'23.55"E	Banastón V, VI	Distal channel complex
9	Banastón Quarry	42°24'55.83"N 0°10'16.75"E	Banastón V	Proximal channel complex
10	Usana N-260	42°24'26.91"N 0°09'24.87"E	Banastón VI	Base of slope
11	Usana Canyon	42°24'41.69"N 0°09'44.94"E	Banastón V, VI	Erosional lower-slope canyon
12	Las Cambras Path	42°24'08.17"N 0°10'38.76"E	Banastón I, II, III, IV, V, VI	Proximal system complex
13	Banastón Road	42°24'13.59"N 0°10'16.50"E	Banastón) V	Base of proximal channel complex
14	Road to Pueyo Araguas	42°25'18.46"N 0°09'18.58"E	Banastón VI	Erosional lower-slope canyon
15	Ainsa megascour	42°25'10.80"N 0°08'20.09"E	Ainsa II	Base of slope mega scour
16	Ainsa Quarry	42°24'14.55"N 0°08'53.21"E	Ainsa I	Proximal channel complex
17	Ainsa - path from Labuerda	42°26'54.16"N 0°07'04.15"E	Ainsa I	Proximal channel complex
18	Boltaña path	42°26'45.10"N 0°03'56.26"E	Ainsa III	Distal channel complex
19	Forcaz stream	42°26'02.02"N 0°07'38.34"E	Ainsa II	Base of slope proximal channel complex
20	Coscojuela valley western path	42°21'49.72"N 0°09'25.19"E	Morillo II	Proximal channel complex

21	Coscojuela valley eastern path	42°21’52.03”N 0°09’39.23”E	Morillo II	Proximal channel complex
22	Road to Bruello	42°22’55.43”N 0°07’45.91”E	Morillo III	Marginal to proximal channel complex
23	Rio Ara (log)	42°26’12.67”N 0°04’12.18”E	Morillo I	Distal channel complex
24	Rio Ara - Sandstone channel eroding into MTD (Locality)	42°26’12.08”N 0°04’15.99”E	Morillo I	Distal channel complex
25	Rio Sieste (log)	42°25’37.44”N 0°04’15.25”E	Morillo I, II, III	Distal system complex
26	Sieste meander bend (Locality)	42°25’25.27”N 0°04’20.14”E	Morillo II	Distal channel complex
27	Carbonate viewpoint (Locality)	42°25’38.91”N 0°04’19.75”E	Morillo II	Carbonate MTD
28	Guaso scour	42°25’06.53”N 0°05’21.24”E	Guaso II	Distal channel complex
29	Guaso village	42°24’57.84”N 0°05’37.47”E	Guaso II	Distal channel complex
30	Guaso road - sandstone channel eroding in to MTD (Locality)	42°24’59.91”N 0°05’33.46”E	Guaso II	Distal channel complex
31	Eña stream	42°24’43.41”N 0°06’33.27”E	Guaso I	Distal channel complex
32	Road to Guaso	42°24’59.17”N 0°05’29.84”E	Guaso II	Distal channel complex
33	Bruello stream	42°22’54.07”N 0°07’43.99”E	Guaso I	Slope
34	Charo stream	42°23’55.45”N 0°15’31.77”E	Arro I	Slope
35	Base Guaso I	42°23’45.31”N 0°07’34.65”E	Guaso I	Base of system
36	Base BV (proximal)	42°24’13.75”N 0°10’16.66”E	Banastón	Base of system
37	Base Guaso II	42°24’41.61”N 0°04’26.84”E	Guaso II	Base of System
38	Base Banastón II (proximal)	42°23’35.98”N 0°11’03.32”E	Banastón II	Base of System
39	Gerbe channel margin failure	42°23’20.85”N 0°11’10.98”E	Gerbe I	Proximal channel complex
40	Top of Sieste log	42°25’34.04”N 0°04’32.26”E	Morillo III	Distal channel complex
41	Eña Quarry	42°24’47.44”N 0°06’32.95”E	Morillo II	Distal channel complex
42	Morillo de Tou stream	42°22’20.46”N 0°08’40.96”E	Morillo II, III	Marginal to proximal channel complex
43	Coscojeula de Sobrarbe	42°21’41.76”N 0°09’18.01”E	Morillo II	Marginal to proximal channel complex
44	Dunes	42°24’17.88”N 0°09’26.28”E	Banastón VI	Proximal base of slope

45	Gabardilla	42°22’59.27”N 0°03’20.37”E	Guaso I	Distal slope
46	Road to Latorrecilla	42°24’34.92”N 0°04’52.27”E	Guaso II	MTD
47	Pro-delta MTDs and MTDs	42°23’34.35”N 0°06’58.04”E	Post Guaso II	Slope
48	New MTDs identified	42°20’35.82”N 0°10’26.77”E	Guaso I	Slope/proximal environment
49	Dead bird path	42°23’57.39”N 0°08’05.30”E	Morillo II, III	Channel complex
50	Type IIb MTD, Guaso village	42°24’58.96”N 0°05’44.49”E	Guaso I	Channel complex
51	Banastón path, San Vicente	42°28’14.69”N 0°06’10.74”E	Banastón III	Distal channel complex
52	Sieste road (upper)	42°25’47.29”N 0°03’58.11”E	Morillo I	Distal channel complex
53	Sieste road (lower)	42°25’43.86”N 0°04’17.75”E	Morillo I	Distal channel complex
54	Base of BV, distal	42°27’21.61”N 0°03’13.85”E	Banastón V	Base of system
55	Erosive MTD, Ainsa Quarry	42°24’00.45”N 0°08’54.94”E	Ainsa I	Channel complex
56	Eña stream scour	42°24’02.18”N 0°06’00.97”E	Morillo II	Intraformational MTD
57	Type 1a MTD beneath megascour (Locality)	42°25’09.11”N 0°08’22.93”E	Ainsa I	Base of slope
58	Type Ia MTD in Barranco (Locality)	42°27’17.03”N 0°07’04.85”E	Ainsa III	Slope
59	Type Ia MTD	42°22’31.10”N 0°08’20.58”E	Morillo III	Slope
60	San Martin Type Ic MTD	42°25’30.55”N 0°03’34.12”E	Ainsa III	Base of slope
61	Morillo de Tou Type 1c MTD	42°22’28.43”N 0°08’45.59”E	Morillo II	Slope
62	New MTDs identified (Camporrotuno)	42°20’32.47”N 0°09’55.88”E	Guaso I	Slope
63	Gusao ‘round the back’	42°25’09.55”N 0°05’06.68”E	Guaso II	Distal channel complex

Table 3.1. Sedimentary log locations of MTD and MTCs discussed in text. System terminology after Pickering and Bayliss (2009). Environmental interpretations after Pickering and Bayliss (2009) and Pickering *et al.* (2015), with additional interpretations in this study.

3.2.2 Sedimentary logging

Detailed bed-by-bed sedimentary logging formed an integral component of data collection in the field and was used to define the character of sedimentary successions, characterise lithology of MTDs in deep-marine siliciclastic systems, document facies associations and to measure stratigraphic thickness. Logs were also used to correlate between geographically separated regions. To acquire detailed observations and sedimentary logs, most stratigraphic sections were measured along river valleys, road cuttings, and hiking tracks, which have excellent exposure and accessibility. Logs were completed using a 5 m metric tape, with every bed ≥ 10 mm recorded. A Bosch laser rangefinder (with an inbuilt inclinometer function) was used to measure outcrop sections that were inaccessible, largely due to steep or dangerous cliff faces. Sedimentary logs were compiled in the field using sedimentary logging sheets that were subsequently digitally drafted using Adobe Illustrator (CS5). At each locality, the sedimentary succession was denoted a particular deep-marine environment. MTD-type, lithology, bed thickness, grain size and sedimentary structures were recorded in a field notebook or on logging sheets. Grain sizes for sandy SGF deposits were estimated using the Wentworth classification scheme (Wentworth, 1922), with pebbles > 4 cm in diameter (*a*-axis). For sandy SGF deposits (i.e., sandstones, mudstones and siltstones), bed thicknesses were measure according to the Ingram (1954) classification. This classification is not used to characterise MTDs, as the thinnest MTD measured in the Ainsa Basin is 0.15 m, already a 'medium bed' under the standard siliciclastic classification system (Wentworth, 1922). Therefore, the following bed thickness classification is used to classify the thickness of MTDs at outcrop:

Very thin: < 1 m;

Thin: 1 – 2 m;

Medium: 2 – 5 m;

Thick: 5 – 10 m, and;

Very thick: > 10 m.

Symbols used in outcrop interpretations and sedimentary logs presented in this thesis are shown in Figure 3.2.

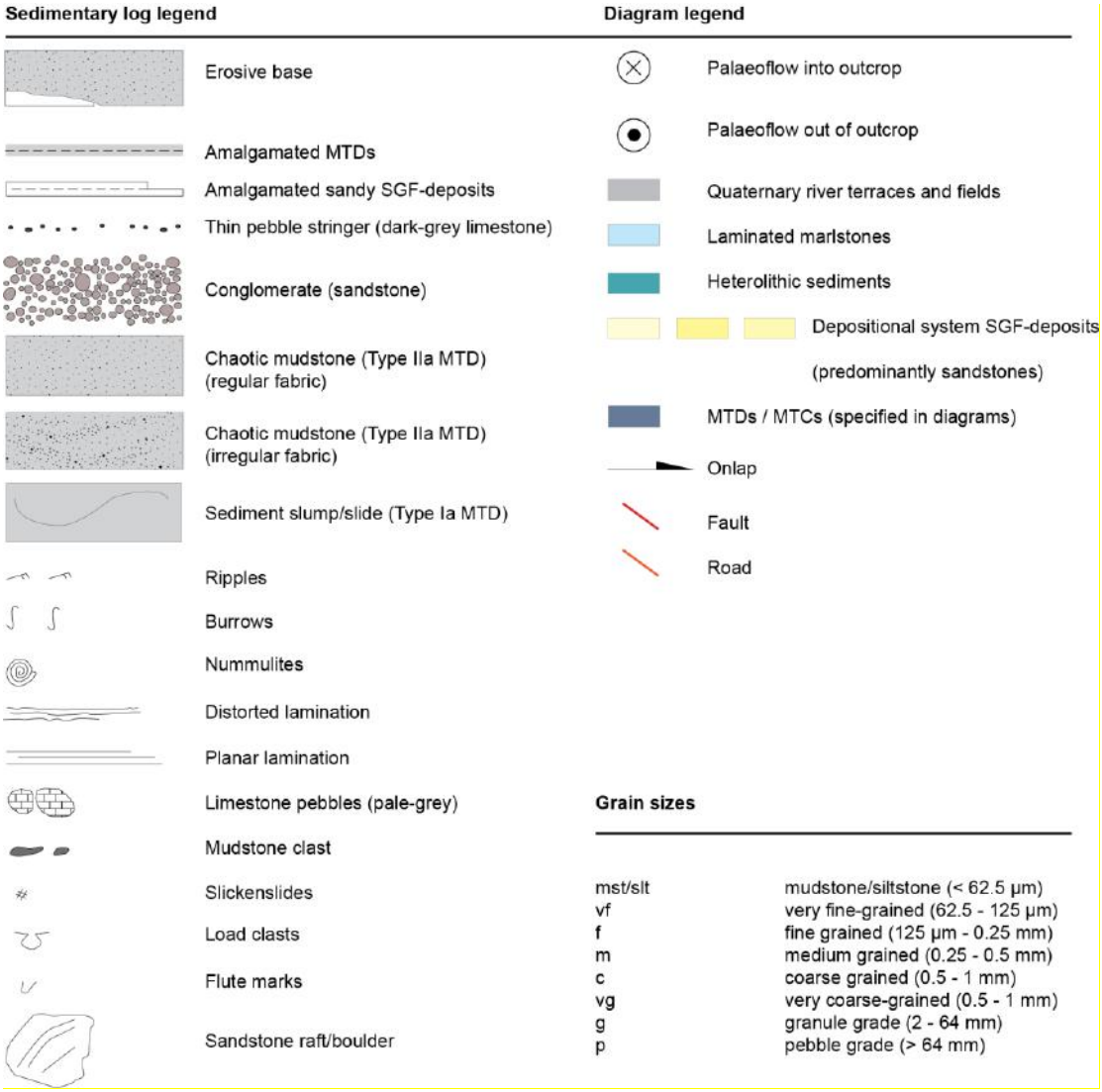

Figure 3.2. Legend for sedimentary logs and diagrams.

In this study, the MTD facies scheme of Pickering and Corregidor (2005) for the Ainsa Basin was adopted (Table 2.3, Chapter 2). As discussed in Chapter 1, the term 'MTD' is used to define a single depositional event (e.g., debrite) and 'MTC' is used to define two or more stacked MTDs. This difference is important, as outcrops in this study were logged both to separate and group these events as necessary. In this study, a 'sandy SGF-deposit' is used to include individual sandstone beds, or an association of predominately sandy deposits at outcrop where it is difficult to determine with a reasonable degree of confidence if they represent deposition from a turbidity current. The term 'debris flow' is used for the flow process and 'debrite' or debris-flow deposit is used for consequential deposits. When analysing MTDs from sedimentary logs in this study, the following terms are defined:

- '*Facies Pairs*' are defined as two discrete vertically stacked MTDs separated by MTD facies associations, and;
- *'Stacking patterns'* are defined as the stratigraphic order of each Facies Pair, which is denoted with a corresponding '*Facies Number'*.

MTD and MTC data were collected from descriptions and sedimentary logs at outcrop and input into a database, permitting the evaluation of the MTD type, facies associations, thickness variations and the distribution of different deposits around the Ainsa Basin to be analysed. The raw data is provided in Appendix C.

3.2.2.1 Construction of correlation panels

Sedimentary logging permitted correlation between localities, so that detailed correlation panels could be used as an aid to environmental interpretations in the Banastón and Morillo systems. Such correlation panels are essential to understand the lateral and vertical facies distributions, lateral thickness variations and any potential stratigraphic patterns. The integration of detailed sedimentological descriptions (documented in field notebooks and sedimentary logs), and interpretations (illustrated in correlation panels) provided an improved understanding of architectural styles and hierarchical stacking of depositional elements in the history of a basin fill.

3.2.3 Estimating grain content

To determine a consistent methodology to evaluate the percentage of grains within a chaotic mudstone (i.e., Type II MTD), the following chart was used to compare percentage grain composition (Figure 3.3).

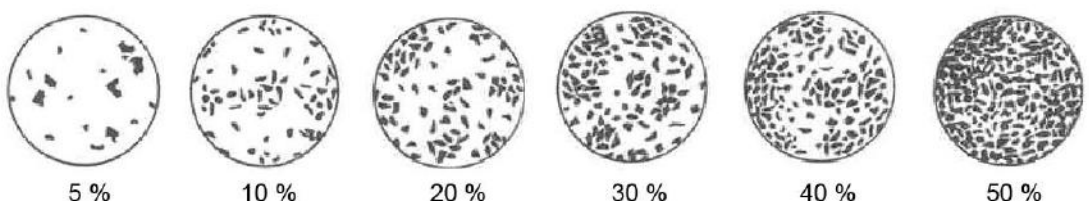

Figure 3.3. Comparison chart for estimating percentage composition. Redrawn from Terry and Chillingar (1989).

This is a semi-quantitative method to determine the amount of grains observed in Type II MTDs, as weathered surfaces of muddy deposits can typically be highly variable. A modified version of the original chart is used here to reduce the uncertainty between 1, 2, 3, 7, 15, 25 and 40 % grain content.

3.2.4 Photomontages

Photographs were taken using a Canon Powershot with a 12.2-megapixel display. For photo panels, photographs were stitched together using the *automerge* function in Adobe Photoshop. Photos were imported and interpreted in Adobe Illustrator (CS5).

3.2.5 Measuring topography

Where present, topographic dimensions were measured to constrain if any relationship exists between MTD thickness and topography preserved at outcrop. MTDs were grouped as Type I and Type II deposits (sediment slides/slumps and debrites, respectively). Taking into account limitations of exposure, outcrops were individually assessed to ensure that topography, not erosion from overlying SGF deposits, was measured. Maximum topographic dimensions were measured as the greatest vertical distance above the average thickness of a laterally continuous deposit (shown in Figure 3.4).

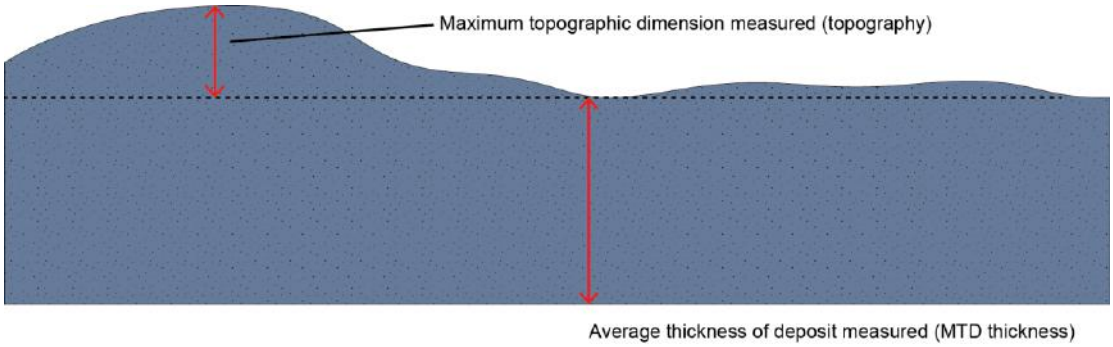

Figure 3.4. Schematic diagram showing topography dimensions measured at outcrop. Measurements of amplitude above the average mean were taken.

3.2.6 Stratigraphic hierarchy

Depositional systems of the Ainsa Basin are described using the architectural elemental analysis scheme of Campbell (1976), as outlined in Pickering and Cantalejo (2015) (Figure 3.5).

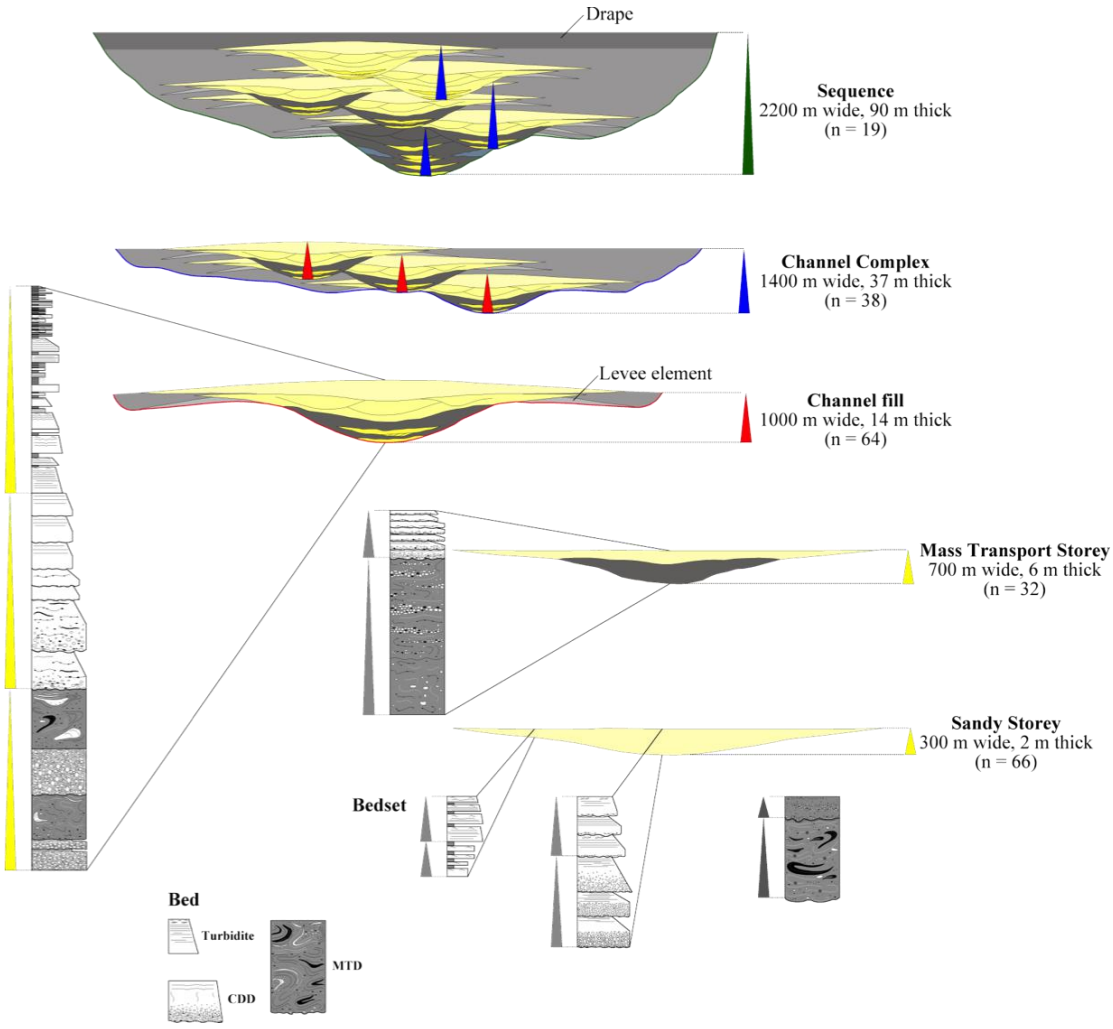

Figure 3.5. Hierarchical diagram with logs. From Pickering and Cantalejo (2015).

Lamina and ***laminasets*** are 1st order hierarchical divisions representing the smallest identifiable packages of sediment (Campbell, 1967). Beds are a 2nd order stratigraphic division bound by bedding surfaces. ***Beds*** form over short durations and therefore can be considered a stratigraphic time unit allowing interbasinal correlation (Campbell, 1967). Sediment gravity-flows, including MTDs and sandy SGF deposits (such as turbidites) represent beds. ***Storeys*** are composed of one or more bedsets and represent the 3rd order stratigraphic division. ***Complexes*** are 4th order depositional bodies, represented by MTCs and channel complexes. ***Sequences*** are 5th order

divisions, with the base defined by an MTC and characterised by a regional drape or abandonment facies. ***Systems*** are 6th order depositional bodies and represent two or more sequences, typically separated from other systems by fine-grained mudstones. The basin-fill succession of the Ainsa Basin consist of several stacked deep-marine systems, which are termed sandy/depositional systems in this study and form the Upper and Lower Hecho Groups, discussed in Chapter 1. Within each system (i.e., the Morillo System), discrete fans comprised of genetically time-bound surfaces create sequences (i.e., Morillo I Fan). Second and fourth-order stratigraphy (beds and complexes, respectively) represent the focus of this study.

3.2.7 Geological mapping

The most comprehensive and detailed geological map yet published of the Ainsa Basin is that of Pickering and Bayliss (2009), with modifications by Pickering and Cantalejo (2015). During the research project, the Guaso System was remapped to include pro-deltatic slumps identified above the Guaso System around Guaso village. Field base maps were acquired from satellite images from Google Maps© and were flattened to remove any topographic effects and distortion associated with elevation. Acetate overlays were used to record additional information over the base maps. Satellite images were used for the lack of topographic detail in the area around Guaso village. The satellite images were effective base maps to trace resistant bedding surfaces due to shadows cast on the satellite image that are difficult to visualise at ground level. Therefore, a combination of field-based outcrop observations and satellite aerial images were used to for mapping lithological units and boundaries. Base maps were imported into Adobe Illustrator (CS5) and stitched together using lines of latitude and longitude to ensure an accurate match (Figure 3.1). Various techniques were employed during the course of field mapping, which included traversing streams, rivers, walking paths and roads. Where permissible, shallow-dipping sandstone bedding planes were walked out to determine the plan view geometry of the sandbodies. A handheld GPS was used to mark waypoints at each locality and to follow tracks to precisely locate geographic positions. At each locality, a sedimentary log and outcrop description was recorded in a field notebook. Using Adobe Illustrator (CS5), the same simplified facies scheme was used from Pickering

and Bayliss (2009), which was revised to include a more detailed classification scheme for MTDs described in Chapter 5. Field base maps are provided in Appendix D.

3.3 SAMPLING AND LABORATORY METHODS

As part of the evaluation of erosively-based MTDs, thin-sections were made from Type II (chaotic mudstone) rock samples collected in the field and analysed under a light-transmitting microscope. Representative whole-rock samples of SGF deposits were carefully collected from consolidated outcrops using a geological hammer and a chisel. It was ensured that samples were collected from individual deposits (MTDs), not from amalgamated deposits (MTCs).

A pilot study was initially undertaken to determine an effective method for sampling mud-rich and typically well-weathered deposits. Whole-rock samples from Type II MTDs were collected at outcrop and were documented as either 'erosive' (where visual or evident erosion is frozen *in situ* at outcrop, such as blocks of sandstone incorporated into the base of debris-flow deposits, or where an irregular base is observed to incise into the underlying substrate), or 'non-erosive' (where erosion is not observed at outcrop, such as the base of the showing tabular basal surfaces with no interaction of the underlying substrate). In the pilot study, single rock samples were taken from 29 chaotic mudstones. Of this sample population, 22 MTDs showed basal erosion at outcrop and 9 appeared as non-erosive. From these, four outcrops were selected to undertake a more rigorous sampling technique, collecting samples at equal increments from base-to-top of each deposit. Multiple rock samples were taken from 4 chaotic mudstones, which were sampled systematically from the base-to-top in equal vertical increments (DF-1, DF-2, DF-3 and DF-4) (Figure 3.6)

Figure 3.6. (A) DF-2 White dashed line indicates base of Type IIa MTD eroding into muddy substrate and potentially eroding into sandstones. White line is ~ 50 m in length (Locality 24) (B) DF-3 White dashed line indicates base of Type IIa MTD showing non-erosive planar base. Compass for scale (10 cm) (Locality 4) (C) DF-4 -Type IIa MTD showing irregular base. White dashed line indicates reference point to depth that MTD erodes to. Type IIa MTD does not show the 'plucking' process at this outcrop. Pencil is for scale (15 cm) (Locality 6).

Locality 23 shows sandstone blocks 'plucked' into the base of Type IIa MTDs (Chapter 6, Figure 6.3), sampled as 'DF-1'. Sample 'DF-2' (Figure 3.6-A) was taken near Locality 24, observed to erode into mudstone. Through mapping, it also appeared to erode into sandstone, however this is not observed directly at outcrop. Sample DF-3 was taken at Locality 4 (Figure 3.6-B), and appeared as non-erosive at outcrop. Sample DF-4 was taken at Locality 6 (Figure 3.6-C), where although blocks of sandstone were not incorporated into the base, the Type IIa MTD shows an irregular base, and therefore was interpreted as likely to be erosive.

Sandy SGF deposits (i.e., turbidites) were also sampled and used as a reference for sand-rich deposits to be able to differentiate between the composition debris-flow deposits that might have been eroded and incorporated into debris flows. Sandy SGF deposits of different grain-sizes were selected at outcrop to account for grain-size differences.

In the laboratory, sieve analyses of the rock samples could not be undertaken, as the digestion process required for ancient lithified sediments would eliminate the calcite cement, calcite grains, calcareous muds and carbonate grains. The crushing process required for sieve analysis would also grind the rock producing smaller grain-sizes, resulting in erroneous data. Therefore, samples were prepared for thin-section at the Open University. All debrite samples required resin impregnation due to the muddy nature of the samples. Thin sections were analysed under a transmitted-light microscope using standard point-counting methods to determine the variation between erosively-based and non erosively-based deposits, and also to compare any differences in composition between debrites and sandy SGF deposits. Standard point-count techniques were undertaken using methods from Middleton *et al.* (1985), with every grain that fell under a grid-point measured. Thin-sections were also photographed and described. Between 500 and 1,000 counted points were taken for each sample to ensure statistically valid results.

Point-count analysis was undertaken to identify the bulk composition of grains and the relative abundance of grains *versus* matrix found in debrites. Polycrystalline and monocrystalline quartz, carbonate grains, lithic fragments (sedimentary and metamorphic), feldspar (P and K), nummulites, coral fragments, opaque minerals, mica and calcite were identified and their abundance calculated. Polycrystalline quartz grains are likely to be metamorphic fragments, but in this study, they are grouped with monocrystalline quartz ('total quartz'), as they are the same mineral composition. Matrix was identified as silt- and mud-grade elements, below 0.06 mm (Figure 3.7).

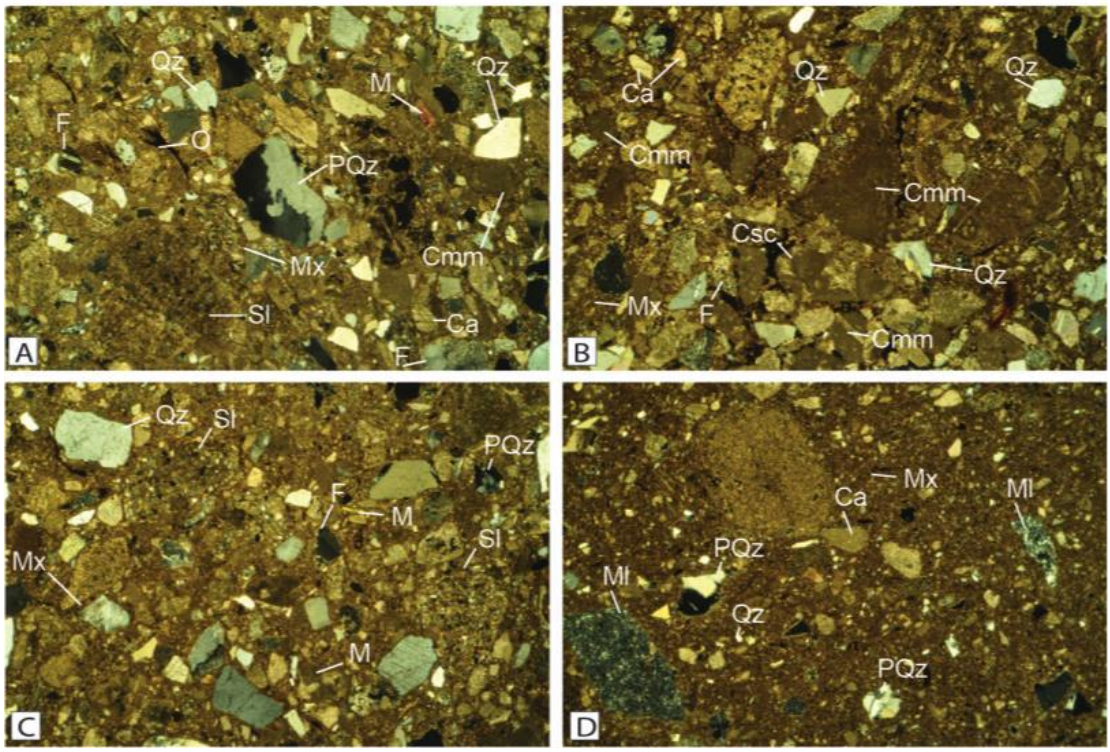

Figure 3.7. (A) Photomicrograph of E-A1 (B) Photomicrograph of E-D1 (C) Photomicrograph of E-F1 (D) Photomicrograph of E-I1. (Csc) Carbonate grain (sparry cement); (Cmm) Carbonate grain (micritic matrix); (PQz) Polycrystalline quartz; (Qz) Quartz; (F) Feldspar; (Ca) Calcite; (M) Mica; (Sl) Sedimentary lithic fragment; (Ml) Metamorphic lithic fragment; (Mx) Matrix; (O) Opaque minerals. Images are 4.4 mm wide.

Grain-size analyses were undertaken to determine variation in grain-sizes throughout all deposits sampled. To minimise misidentification between silt and clay grains, 0.06 mm was the lowest sand fraction recorded. Grain-sizes were recorded as:

- Fine pebble gravel (4 - 6 mm) – maximum grain size;
- Very-coarse sand (1 - 2 mm);
- Coarse sand (0.5 - 1 mm);
- Medium sand (0.25 - 0.5 mm);
- Fine sand (0.125 - 0.25 mm), and;
- Very fine sand (0.06 - 0.125 mm), minimum grain size.

The sampling technique undertaken for the four MTDs sampled from top-to-base provided a meaningful dataset. This included sampling greater than three samples per deposit and ensuring samples were taken systematically from top-to-base at equal increments. Based on this evaluation, a further 129 debrite samples were collected and prepared as thin sections from 18 other debris-flow deposits in the Ainsa Basin, culminating a sample population of 22 deposits (including the 4 MTDs that formed part of the pilot study). A full sample catalogue is provided in Table 3.2.

	Pilot study	Sample name	Distance from base (m)	Samples taken	Thickness (m)	System	Erosive base?	Analysis	Co-ordinates or locality
1	Y	E2	N/A	1	N/A	Banaston V	Y	Erosive debris-flow deposit	6
2	Y	E3	N/A	1	N/A	Banaston V	Y	Erosive debris-flow deposit	7
3	Y	E4	N/A	1	N/A	Banaston V	Y	Erosive debris-flow deposit	6
4	Y	E5	N/A	1	N/A	Banaston V	Y	Erosive debris-flow deposit	6
5	Y	E6	N/A	1	N/A	Banaston IV	Y	Erosive debris-flow deposit	6
6	Y	E9	N/A	1	N/A	Morillo II	Y	Erosive debris-flow deposit	41
7	Y	E10	N/A	1	N/A	Morillo I	Y	Erosive debris-flow deposit	53
8	Y	E14	N/A	1	N/A	Morillo II	Y	Erosive debris-flow deposit	26
9	Y	E16	N/A	1	N/A	Morillo I	Y	Erosive debris-flow deposit	21
10	Y	E17	N/A	1	N/A	Guaso II	Y	Erosive debris-flow deposit	56
11	Y	E18	N/A	1	N/A	Ainsa I	Y	Erosive debris-flow deposit	16
12	Y	E19	N/A	1	N/A	Arro	Y	Erosive debris-flow deposit	4
13	Y	E20	N/A	1	N/A	Arro	Y	Erosive debris-flow deposit	4
14	Y	E21	N/A	1	N/A	Banaston V	Y	Erosive debris-flow deposit	6
15	Y	E22	N/A	1	N/A	Banaston V	Y	Erosive debris-flow deposit	6
16	Y	E23	N/A	1	N/A	Morillo I	Y	Erosive debris-flow deposit	24
17	Y	E24	N/A	1	N/A	Morillo I	Y	Erosive debris-flow deposit	24
18	Y	E25	N/A	1	N/A	Morillo I	Y	Erosive debris-flow deposit	52
19	Y	E26	N/A	1	N/A	Morillo II	Y	Erosive debris-flow deposit	41
20	Y	E27	N/A	1	N/A	Guaso II	Y	Erosive debris-flow deposit	32
21	Y	NE1	N/A	1	N/A	Morillo III	N	Non-erosive debris-flow deposit	45
22	Y	NE3	N/A	1	N/A	Guaso II	N	Non-erosive debris-flow deposit	37
23	Y	NE4	N/A	1	N/A	Guaso II	N	Non-erosive debris-flow deposit	29
24	Y	NE5	N/A	1	N/A	Morillo III	N	Non-erosive debris-flow deposit	43
25	Y	NE7	N/A	1	N/A	Morillo III	N	Non-erosive debris-flow deposit	48
26	Y	NE8	N/A	1	N/A	Guaso II	N	Non-erosive debris-flow deposit	28
27	Y	NE9	N/A	1	N/A	Morillo III	N	Non-erosive debris-flow deposit	53
28	Y	NE11	N/A	1	N/A	Fosado	N	Non-erosive debris-flow deposit	1
29	Y	NE12	N/A	1	N/A	Guaso II	N	Non-erosive debris-flow deposit	31
30	Y	FL1	N/A	1	N/A	Morillo I	N/A	Sandy SGF deposit	
31	Y	FL2	N/A	1	N/A	Morillo I	N/A	Sandy SGF deposit	
32	Y	FL3	N/A	1	N/A	Ainsa II	N/A	Sandy SGF deposit	
33	Y	FL4	N/A	1	N/A	Banaston V	N/A	Sandy SGF deposit	
34	Y	TR1	N/A	1	N/A	Morillo II	N/A	Sandy SGF deposit (mud-rich sandstone)	
35	Y	TR2	N/A	1	N/A	Ainsa III	N/A	Sandy SGF deposit (mud-rich sandstone)	
36	Y	TU1	N/A	1	N/A	Banaston V	N/A	Sandy SGF deposit (coarse-grained)	
37	Y	TU2	N/A	1	N/A	Morillo II	N/A	Sandy SGF deposit (Fine-grained)	
38	Y	TU3	N/A	1	N/A	Morillo II	N/A	Sandy SGF deposit (coarse-grained)	
39	Y	DF 1.1	0.00	7	9.00	Morillo I	Y	Composition and grain size analysis	23
40	Y	DF 1.2	1.50						
41	Y	DF 1.3	3.00						
42	Y	DF 1.4	4.50						
43	Y	DF 1.5	6.00						
44	Y	DF 1.6	7.50						
45	Y	DF 1.7	9.00						
46	Y	DF 2.1	0.00	5	6.00	Morillo I	?	Composition and grain size analysis	23
47	Y	DF 2.2	1.50						
48	Y	DF 2.3	3.00						
49	Y	DF 2.4	4.50						
50	Y	DF 2.5	6.00						
51	Y	DF 3.1	0.20	3	6.00	Arro	?	Composition and grain size analysis	4
52	Y	DF 3.2	3.00						
53	Y	DF 3.3	6.00						
54	Y	DF 4.1	0.00	3	5.00	Banaston V	Y	Composition and grain size analysis	6
55	Y	DF 4.2	2.50						
56	Y	DF 4.3	5.00						
57	N	E-A1	0.00	6	2.70	Banaston V	Y	Composition and grain size analysis	42°27'05.31"N, 0°03'25.65"E
58	N	E-A2	0.54						
59	N	E-A3	1.08						
60	N	E-A4	1.62						
61	N	E-A5	2.18						
62	N	E-A6	2.70						
63	N	E-B1	0.00	4	1.80	Banaston V	Y	Composition and grain size analysis	42°27.04.10"N, 0°03'26.02"E
64	N	E-B2	0.50						
65	N	E-B3	1.00						
66	N	E-B4	1.80						

67	N	E-C1	0.20						
68	N	E-C2	0.70						
69	N	E-C3	1.20	5	2.05	Banaston III	Y	Composition and grain size analysis	42°28'14.01"N, 0°06'10.88"E
70	N	E-C4	1.70						
71	N	E-C5	2.05						
72	N	E-D1	0.00						
73	N	E-D2	0.42						
74	N	E-D3	0.84	5	1.70	Morillo II	Y	Composition and grain size analysis	42°25'34.76"N, 0°04'20.34"E
75	N	E-D4	1.28						
76	N	E-D5	1.70						
77	N	E-E1	0.00						
78	N	E-E2	0.40	4	1.25	Morillo II	Y	Composition and grain size analysis	42°25'34.76"N, 0°04'20.34"E
79	N	E-E3	0.80						
80	N	E-E4	1.25						
81	N	E-F1	0.00						
82	N	E-F2	0.52						
83	N	E-F3	1.04	5	2.08	Morillo III	Y	Composition and grain size analysis	42°25'35.61"N, 0°04'28.04"E
84	N	E-F4	1.56						
85	N	E-F5	2.08						
86	N	E-G1	0.00						
87	N	E-G2	0.42						
88	N	E-G3	0.84	5	1.70	Morillo I	Y	Composition and grain size analysis	42°25'43.98"N, 0°04'04.79"E
89	N	E-G4	1.28						
90	N	E-G5	1.70						
91	N	E-H1	0.00						
92	N	E-H2	0.50	4	1.20	Morillo	Y	Composition and grain size analysis	42°24'53.39"N, 0°06'43.93"E
93	N	E-H3	0.80						
94	N	E-H4	1.20						
95	N	E-I1	0.00						
96	N	E-I2	1.50	4	4.50	Morillo I	Y	Composition and grain size analysis	42°26'11.26"N, 0°04'11.57"E
97	N	E-I3	3.00						
98	N	E-I4	4.50						
99	N	NE-B1	0.00						
100	N	NE-B2	1.30						
101	N	NE-B3	2.80	5	4.30	Banaston	N	Composition and grain size analysis	42°27'02.19"N, 0°03'25.88"E
102	N	NE-B4	4.30						
103	N	NE-B5	5.50						
104	N	NE-C1	0.00						
105	N	NE-C2	1.05						
106	N	NE-C3	1.89	5	3.57	Morillo II	N	Composition and grain size analysis	42°22'23.13"N, 0°08'41.47"E
107	N	NE-C4	2.73						
108	N	NE-C5	3.57						
109	N	NE-D1	0.00						
110	N	NE-D2	0.55	4	1.64	Morillo II	N	Composition and grain size analysis	42°22'19.51"N, 0°08'40.08"E
111	N	NE-D3	1.10						
112	N	NE-D4	1.64						
113	N	NE-E1	0.00						
114	N	NE-E2	2.00	4	6.00	Morillo II	N	Composition and grain size analysis	42°22'17.87"N, 0°08'38.48"E
115	N	NE-E3	4.00						
116	N	NE-E4	6.00						
117	N	NE-F1	0.00						
118	N	NE-F2	0.25						
119	N	NE-F3	0.50	5	1.00	Ainsa I	N	Composition and grain size analysis	42°24'13.38"N, 0°08'50.24"E
120	N	NE-F4	0.75						
121	N	NE-F5	1.00						
122	N	NE-G1	0.00						
123	N	NE-G2	0.35	4	1.00	Guaso I	N	Composition and grain size analysis	42°23'39.77"N, 0°07'36.34"E
124	N	NE-G3	0.70						
125	N	NE-G4	1.00						
126	N	NE-H1	0.00						
127	N	NE-H2	1.20	4	3.60	Guaso I	N	Composition and grain size analysis	42°25'03.35"N, 0°05'23.90"E
128	N	NE-H3	2.40						
129	N	NE-H4	3.60						
130	N	NE-I1	0.00						
131	N	NE-I2	0.15	4	0.50	Banaston	N	Composition and grain size analysis	42°24'26.41"N, 0°09'26.28"E
132	N	NE-I3	0.25						
133	N	NE-I4	0.50						
134	N	NE-J1	0.00						
135	N	NE-J2	0.25						
136	N	NE-J3	0.50	5	1.00	Morillo II	N	Composition and grain size analysis	42°24'53.39"N, 0°06'43.93"E
137	N	NE-J4	0.75						
138	N	NE-J5	1.00						

Table 3.2. Sample catalogue of samples taken from Type II MTDs (samples from the pilot study are included).

Composition and grain-size analyses were carried out using standard point counting, with methods described previously, to determine vertical grading and compositional differences between each deposit. Eighteen sandy SGF deposits were sampled at outcrop to compare the composition between mud-rich debrites, however, the vertical sampling technique was not undertaken for the sandy SGF deposits. Of

the sandy SGF deposits samples taken, two appeared as muddy sands at outcrop, with the aim to observe compositional similarities or differences between muddy-sands (sandy SGF deposits) and sandy-muds (debrites). Results from these analyses (the pilot study and full analytical study) are presented in Chapter 7.

3.4 INDUSTRY INTERNSHIP

A three-month internship was undertaken at CNOOC-Nexen in the Buzzard Field developments team, based in Uxbridge. In-house data was provided during the project, which included conventional well data from 69 wells and high-resolution photographs from 17-cored wells. The name, location and deviation data available for each well used in this project is summarised in Table 3.3, with a map of well locations in Figure 3.8.

Well Name	Type	Location	Deviation (°)	Core	Wireline Log Suite	Dipmeter	Biostratigraphic data
19/10_1	Appraisal	SP	SV				
19/10_1z	Appraisal	SP	30-35				
20/1_3	Appraisal	NP	30-35				
20/1_4	Appraisal	CP	SV				
20/1_5	Exploration	NT	5-10				
20/1_5z	Exploration	NP	40-45				
20/6_1	Exploration	SP	unknown				
20/6_2	Exploration	CP	SV				
20/6_3	Appraisal	Sp	SV				
20/6_3z	Appraisal	SP	45-50				
20/6_4	Appraisal	CP	SV				
20/6_4z	Appraisal	CP	25-30				
20/6_5	Appraisal	CP	SV				
20/6_6	Appraisal	ST	5-10				
20/06a_B1A	Production	CP	5-10				
20/06a_B2	Production	SP	40-45				
20/06a_B3	Production	SP	30-35				
20/06a_B4	Production	CP	50-55				
20/06a_B5	Production	CP	20-25				
20/06a_B6	Production	CP	20-25				
20/06a_B7	Production	SP	45-50				
20/06a_B8	Production	SP	20-25				
20/06a_B9	Production	CP	20-25				
20/06a_B10	Production	SP	25-30				
20/06a_B11	Production	CP	55-60				
20/06a_B12	Production	SP	55-60				
20/06a_B13	Production	ST	55-60				
20/06a_B14	Production	CP	60-65				
20/06a_B14z	Production	CP	55-60				
20/06a_B15	Production	CP	55-60				
20/06a_B16	Production	SP	65-70				
20/06a_B16z	Production	SP	80-85				
20/06a_B17	Production	SP	60-65				
20/06a_B18	Production	CP	70-75				
20/06a_B18z	Production	CP	65-70				
20/06a_B19	Production	CP	35-40				
20/06a_B20	Production	CP	50-55				
20/06a_B21	Production	NP	60-65				
20/06a_C1	Injector	CP	15-20				
20/06a_C2	Injector	CP	5-10				
20/06a_C3	Injector	CP	25-30				
20/06a_C4z	Injector	CP	20-25				
20/06a_C5	Injector	CP	SV				
20/06a_C6	Injector	CP	15-20				
20/06a_C6z	Injector	NP	20-25				
20/06a_C7z	Injector	CP	10-15				
20/06a_S1	Injector	SP	20-25				
20/06a_S2	Injector	SP	10-15				
20/06a_S3	Injector	SP	15-20				
20/06a_S4	Injector	SP	15-20				
20/06a_S5	Injector	SP	SV				

Table 3.3. Green highlighted boxes show data shows summary of well data used in this study. NT – Northern Terrace, NP – Northern Panel, CP – Central Panel, SP – Southern Panel, ST – Southern Terrace. SV- sub-vertical wells (0 - 5°).

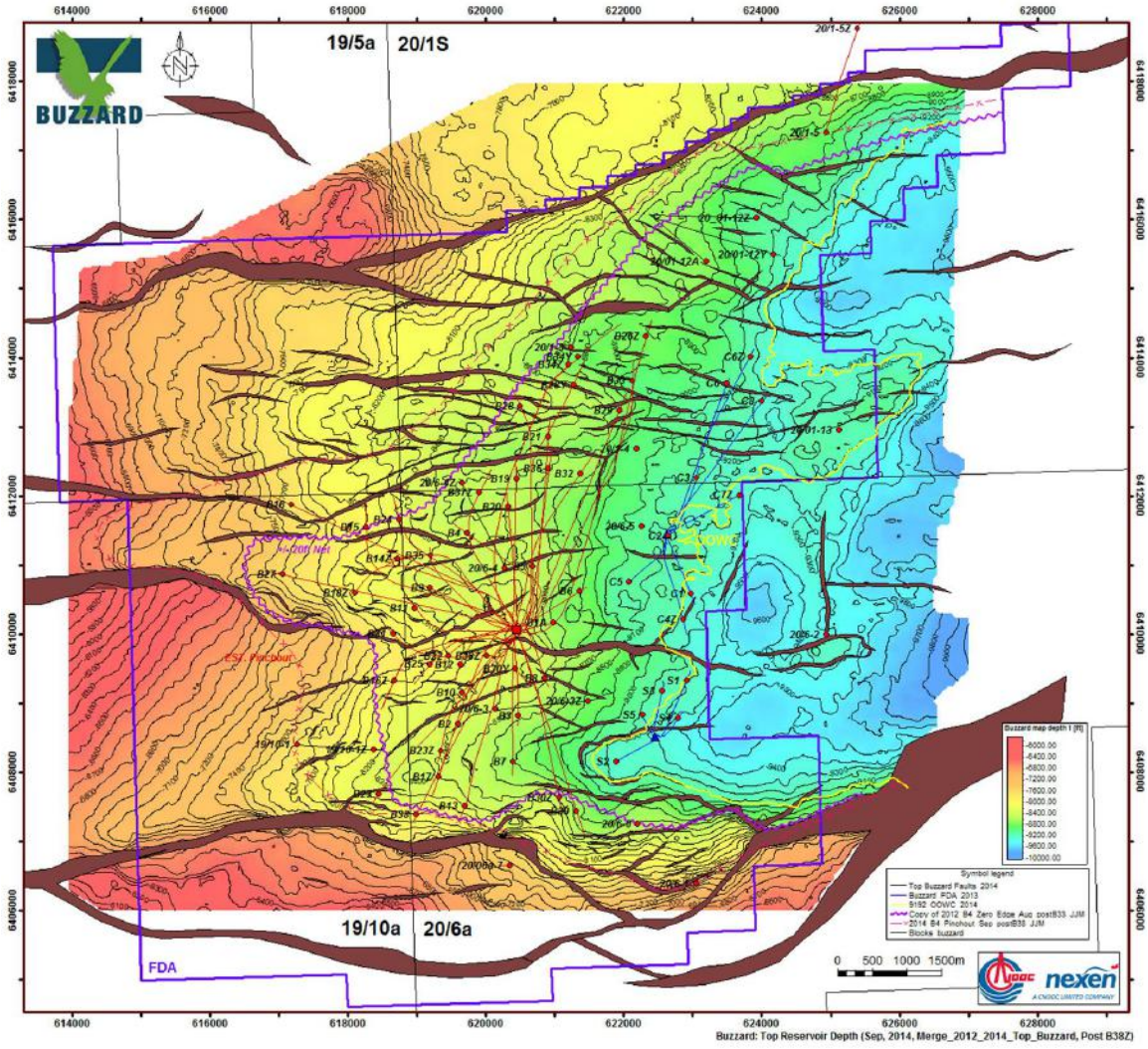

Figure 3.8. Map of the Buzzard Field showing well locations. In-house data from CNOOC-Nexen.

Photographs were used to identify MTD facies types across the basin. Petrel (2013.3) was used as a platform to integrate well data (gamma, sonic, log and density logs) and Seisworks was used to acquire images of seismic data (Chapter 8). Applying the Duxbury (2009) scheme, biostratigraphic data was used to ensure accurate well correlations between wells across the field. High-resolution photo panels of cored wells were a key focus to describe and classify types of MTDs present in the subsurface. I-Point software was used to calibrate core to log shifts and to determine the true vertical thickness of MTD and MTC units (Figure 3.9).

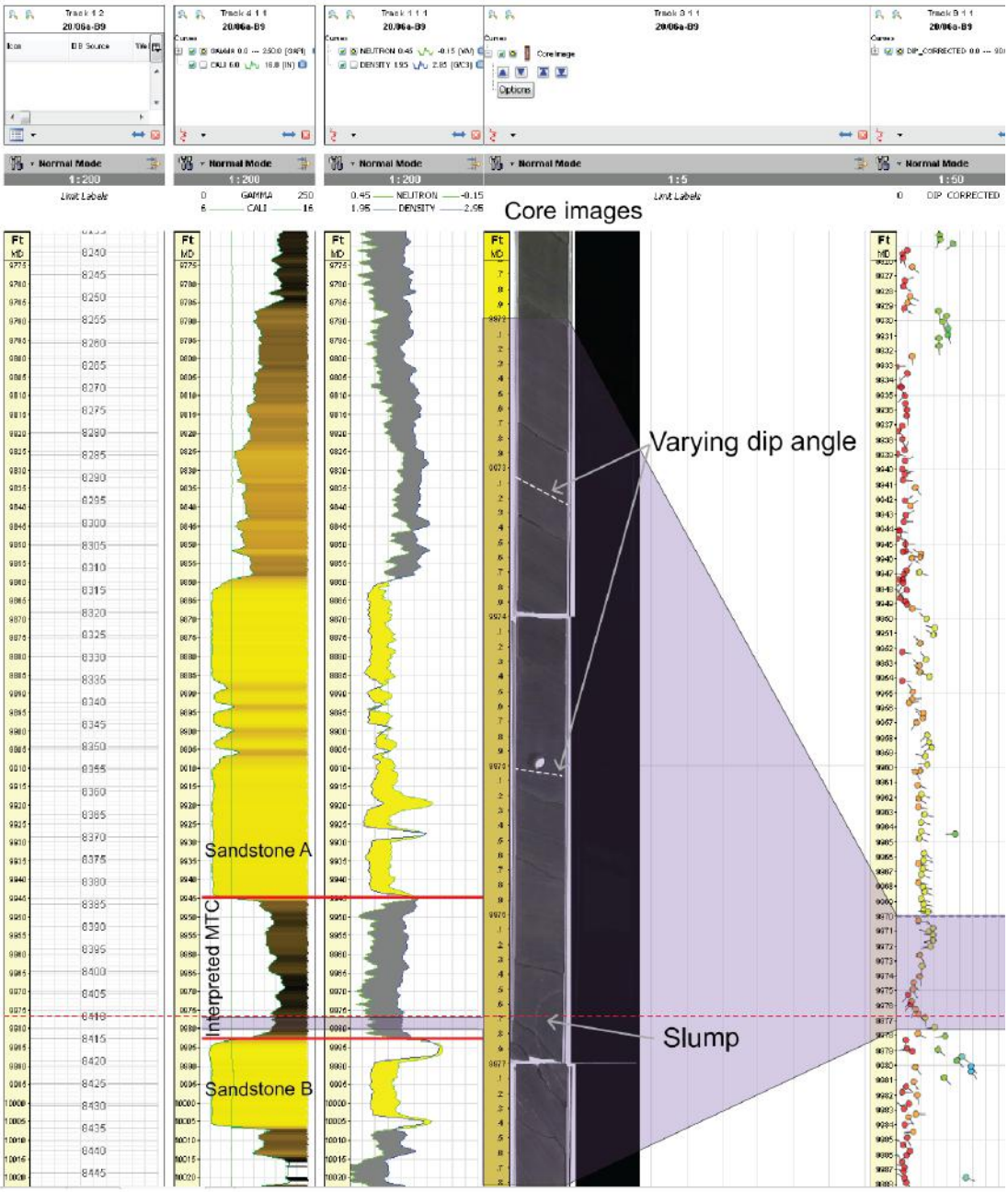

Figure 3.9. Aligned well and core photographs using I-point. Transparent purple area shows common depth point of core, gamma, neutron-density and dip data display. Red upper and lower boundaries show interpreted MTC between sandstones A and B.

The presence of major MTD or MTC intervals and sandstone reservoirs immediately above these chaotic intervals were interpreted by creating a set of basin-wide well-top correlations. The 'made/edit surface' function in Petrel gridded this data to create distribution maps of sandstones immediately above MTD and MTCs within Buzzard stratigraphy. For gridding these data, a convergent interpolation gridding algorithm was used, with no trends applied to data or algorithms.

3.5 SUMMARY

Fieldwork methodology, including sample collection, is outlined above. Sedimentary logging was a key data source for collecting stratigraphic data of MTDs and MTCs. Photographs provided core evidence of MTD and MTC characteristics and facies associations (Chapters 4, 5 and 6). Geological mapping aided understanding of the lateral extent of new deposits shown in this study (Chapter 5). The pilot study for sampling Type II MTDs (chaotic mudstones) was undertaken to evaluate the compositional and grain-size variation in MTDs that showed basal erosion and to how best evaluate how to sample deposits. It was found that a more rigorous sampling technique was required to provide a meaningful dataset of individual deposits (Chapter 7). Industry methods used Petrel, I-Point software and core photographs to determine the character of MTDs in the Buzzard Field, UK North Sea (Chapter 8).

CHAPTER 4

SEDIMENTARY CHARACTERISTCS OF MTDs AND MTCs, MIDDLE-EOCENE AINSA BASIN, SPANISH PYRENEES

4.1 INTRODUCTION

Field observations and data in this chapter document the sedimentary characteristics, internal structure and architecture of MTDs and MTCs in a slope and proximal basin-floor environment of the Ainsa Basin, Spanish Pyrenees. Field data is presented in the following sections:

(1) *MTDs at outcrop:* MTDs are firstly presented and described from outcrops. Where deposits documented in this study differ from the original classification of Pickering and Corregidor (2005), modifications are presented.

(2) *Sedimentary characteristics of MTDs and MTCs*: This section explores the characteristics of MTDs and MTCs including: topography, fabric, architecture and the presence of rafts, pebbles and boulders.

4.2. MTDs AT OUTCROP

Sedimentary log names and location numbers of localities used throughout this thesis are summarised in Chapters 1 and 3 (Figure 1.16, Table 3.1 and Figure 3.1).

4.2.1. Type I MTDs

In keeping with the original classification of Pickering and Corregidor (2005), for the purpose of simplification and for practical use in the field, failed masses of mudstones/marlstones that show subtle dip-changes to more coherent folds are grouped as Type I MTDs.

4.2.1.1 Type Ia MTDs

Type Ia MTDs are composed of mudstones and marlstones that show semi-coherent folded and contorted bedding. These MTDs occur within thick mudstone packages, interpreted as interfan deposits, or typically (but not exclusively) at the base of the sandy submarine fans. Thicknesses vary from tens of centimetres to tens of metres. Top and basal surfaces can be planar to highly irregular and internal surfaces and may show slide or shear fabric, such as slickenlines or crystal-fibre slickenslides. The bases of these deposits are predominantly observed as non-erosive. However, local erosion is observed in some cases (Figure 4.1-E). In core, microfaults are a common pervasive feature in many Type Ia MTDs, with normal faults predominating over reverse faults (Pickering and Corregidor, 2005, Pickering *et al.,* 2015). Representative examples of Type Ia MTDs in the field are shown in Figure 4.1.

4.2.1.2 Type 1b MTDs

Type Ib MTDs comprise intrafan heterolithic mudstones, marlstones and thin- to medium-bedded sandy SGF deposits that show semi-coherent folded and contorted bedding. These MTDs occur between thick sandbodies, within submarine fan sediments. Thicknesses vary from tens of centimetres to a few metres. The maximum thickness of channel margin failure deposits is 1.8 m. The bases of Type IIa MTDs are observed to have eroded sandy substrates within sandy-fan deposits. The basal surface typically shows a lateral stepped geometry, approximately perpendicular to palaeoflow. Locally coherent horizontal bedding may pass abruptly into sub-vertical strata. Slickenslides are present at the base, suggesting basal detachment and movement along a plane of weakness. These deposits typically occur in off-axis channel sites and represent localised redeposition events (Pickering and Corregidor, 2005) (Figure 4.2).

4.2.1.3 Type Ic MTDs

Type Ic MTDs typically comprise discontinuous bedded carbonates and where preserved at outcrop, occur within chaotic mudstones. Thicknesses vary up to several

metres. Top surfaces tend to be parallel to bedding and basal surfaces can be highly irregular. The carbonates are highly resistant, however individual carbonate beds can weather to a well-rounded, 'smoothed' and blocky character. In some cases, individual beds are composed almost entirely of nummulites (Figure 4.3). These MTDs can have a similar textural composition with the Roncal megabed and other megaturbidites documented in the Jaca Basin (Labaume *et al.*, 1983a, b, 1985, 1987; Payros *et al.*, 1999; Ogata *et al.*, 2012). Type Ic MTDs are derived from the collapse of the carbonate platform fringing the Ainsa Basin (Pickering and Corregidor, 2005), discussed later in this chapter (Section 4.3.4.1).

4.2.2 Type II MTDs

The appearance of Type II MTDs show considerable sedimentological variability at outcrop, however are identified as matrix- to clast supported chaotic mudstones. To further classify these MTDs in the field, these deposits were separated into Type IIa and Type IIb MTDs, a modification of the Pickering and Corregidor (2005) classification.

4.2.2.1 Type IIa MTDs

Type IIa MTDs occur at the base- or within intrafan sediments and typically range from tens of centimetres to tens of metres in thickness. The matrix is predominantly structureless, with grain content varying between < 5 – 50 % (i.e., grains sized between 0.2 – 2 mm in diameter). The fabric of these deposits is observed to vary between well to poorly mixed (i.e., homogenous to heterogeneous). Many deposits contain pebbles and are referred to as matrix-supported pebbly mudstones. Pebbles (> 4 mm) are composed of extra-formational material including well to very well-rounded pebbles composed of pale and dark-grey limestone, sandstone, chert, metamorphic and occasionally igneous rock. Abundant nummulites and deformed bedded sandstone rafts (up to 10 m in width) are typically found floating in the matrix of these deposits and often align parallel to bedding (Figure 4.4). The top surfaces of Type IIa MTDs are observed to occasionally form topography over lengths of tens of

centimetres to metres, and the bases are typically observed to erode into sandy substrates (Dakin *et al.,* 2013), as presented in Chapter 6.

4.2.2.2 Type IIb MTDs

Type IIb MTDs occur within intrafan sediments and typically range from tens of centimetres to tens of metres in thickness. These deposits are often found infilling the base of channel-like scours, however are they are also identified as more tabular beds (Figure 4.5). Type IIb MTDs are clast-supported and have a muddy to muddy-sand matrix, containing up to 50 % grains (also referred to as conglomerates). Pebbles (> 2 mm) are composed of extra-formational material including well to very well-rounded pebbles composed of pale and dark-grey limestone, sandstone, chert, metamorphic and occasionally igneous rock. These deposits often contain abundant nummulites. Clast-supported mudstones show rare pebble imbrication and typically only the largest clasts in any bed have an imbricate texture (e.g., Figure 4.29).

4.2.3 Type III MTDs

Type III MTDs comprise the highest proportion of sand-grade sediments of all MTDs. Pebbles in these MTDs are composed of extra-formational material including well to very well-rounded pebbles composed of pale-grey limestone, sandstone, chert, metamorphic and occasionally igneous rock. To further classify these MTDs in the field, deposits were separated into Type IIIa and Type IIIb MTDs, a modification of the Pickering and Corregidor (2005) classification.

4.2.3.1 Type IIIa MTDs

These MTDs typically occur within intrafan sandstones with thicknesses varying from tens of centimetres up to several metres. These deposits can be matrix- or clast-supported. The bases of these deposits are commonly erosive, forming either channelised or tabular deposits. The top surfaces of these deposits are not observed to form topography (Figure 4.6).

4.2.3.2 Type IIIb MTDs

Type IIIb deposits occur within intrafan sediments, with thicknesses typically varying from tens of centimetres up to 2 metres. Type IIIb deposits show clast-supported conglomerates infilling the base of channel-filled scours. The main differentiation criterion between IIIb deposits is that the basal surface of the scour is draped by a thin sandstone or pebbly sandstone prior to deposition of the clast-supported conglomerate (Figure 4.7).

The clast-supported pebble-filled channels shown in Figure 4.7 are each preceded by a fine- coarse-grained sandstone. The pebbly sandstones show erosive bases, scouring the underlying bedded sandstone/mudstone stratigraphy.

4.2.4 Type IV MTDs

Type IV MTDs are an addition to the Pickering and Corregidor (2005) classification based on observations in this study. These deposits are rarely observed in the Ainsa Basin stratigraphy, and where observed are typically poorly exposed and weathered. Thicknesses are measured varying from tens of centimetres up to a few metres. Discrete beds at outcrop show variable MTD facies characteristics between chaotic, homogensised fabric to more coherent deformed mudstone/marlstones (i.e., Type Ia and IIa MTDs). One facies can be more dominant than the other, or occur in broadly equal abundance within one deposit at outcrop (Figure 4.8). When Type IV deposits are found immediately beneath a Type Ic MTD, these deposits typically contain brecciated bioclastic and carbonate clasts within the matrix (Figures 4.8-B and 4.24-C).

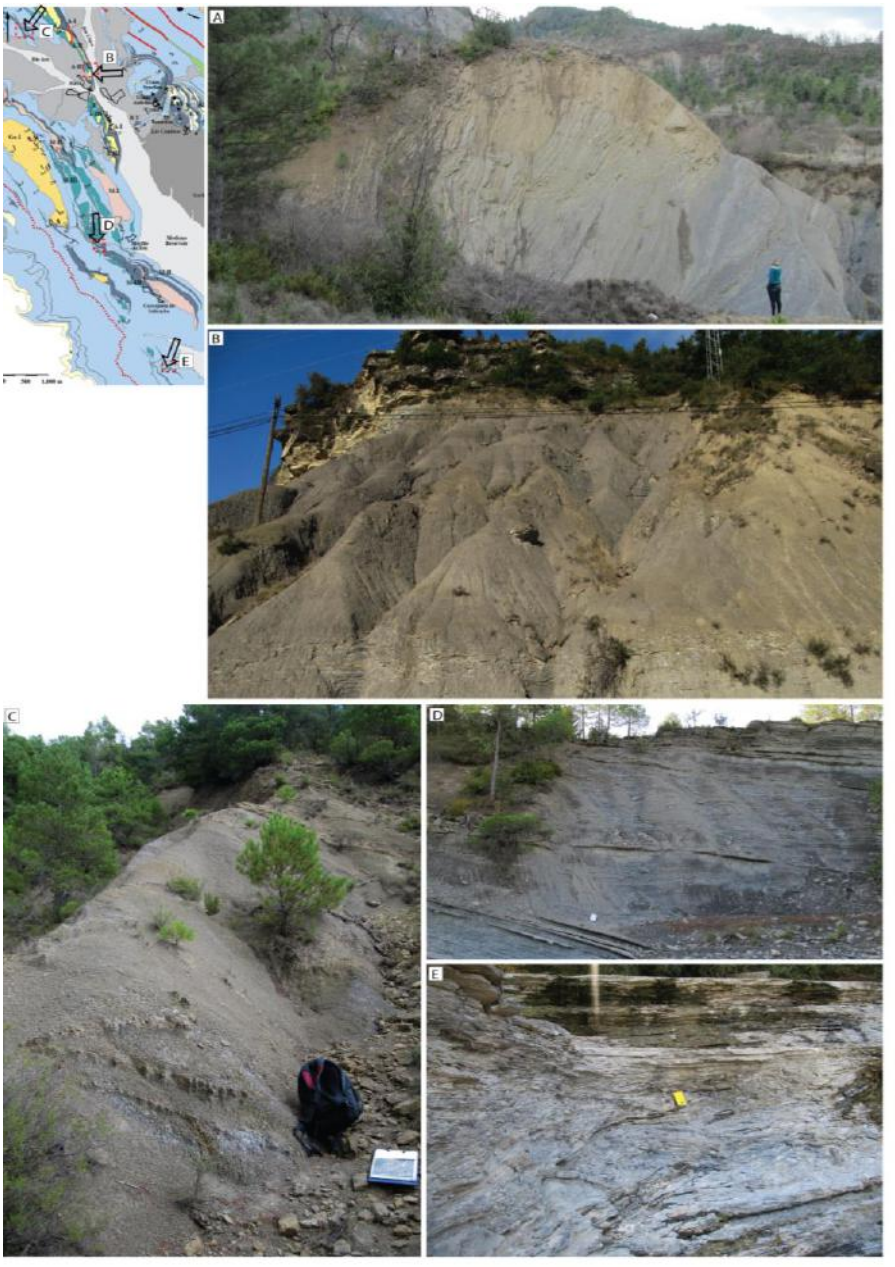

Figure 4.1. Representative Type Ia MTDs identified in the Ainsa Basin. Type Ia MTDs comprise contorted mudstone elements and are predominantly found within mudstone packages interpreted as interfan or at the base of sandy submarine fans. Locations are identified on map inlay with arrow showing direction of view. (A) 20-25 m mudstone package showing angular dip change, Los Molinos (Locality 34). Person for scale (B) Folded mudstone stratigraphy beneath Ainsa II Fan (Locality 57). Pylon for scale (6 m). (C) Folded mudstone stratigraphy within undeformed mudstone stratigraphy, Ainsa III (Locality 58) Rucksack for scale (50 cm) (D) 6 m package of mudstones showing subtle dip change within undeformed mudstones. Above Morillo III Fan, Morillo De Tou (Locality 59). Clipboard for scale (35 cm). (E) Contorted mudstone showing folds, Guaso System off-axis environment, near Camporrotuno, Locality 48. Yellow notebook for scale (20 cm).

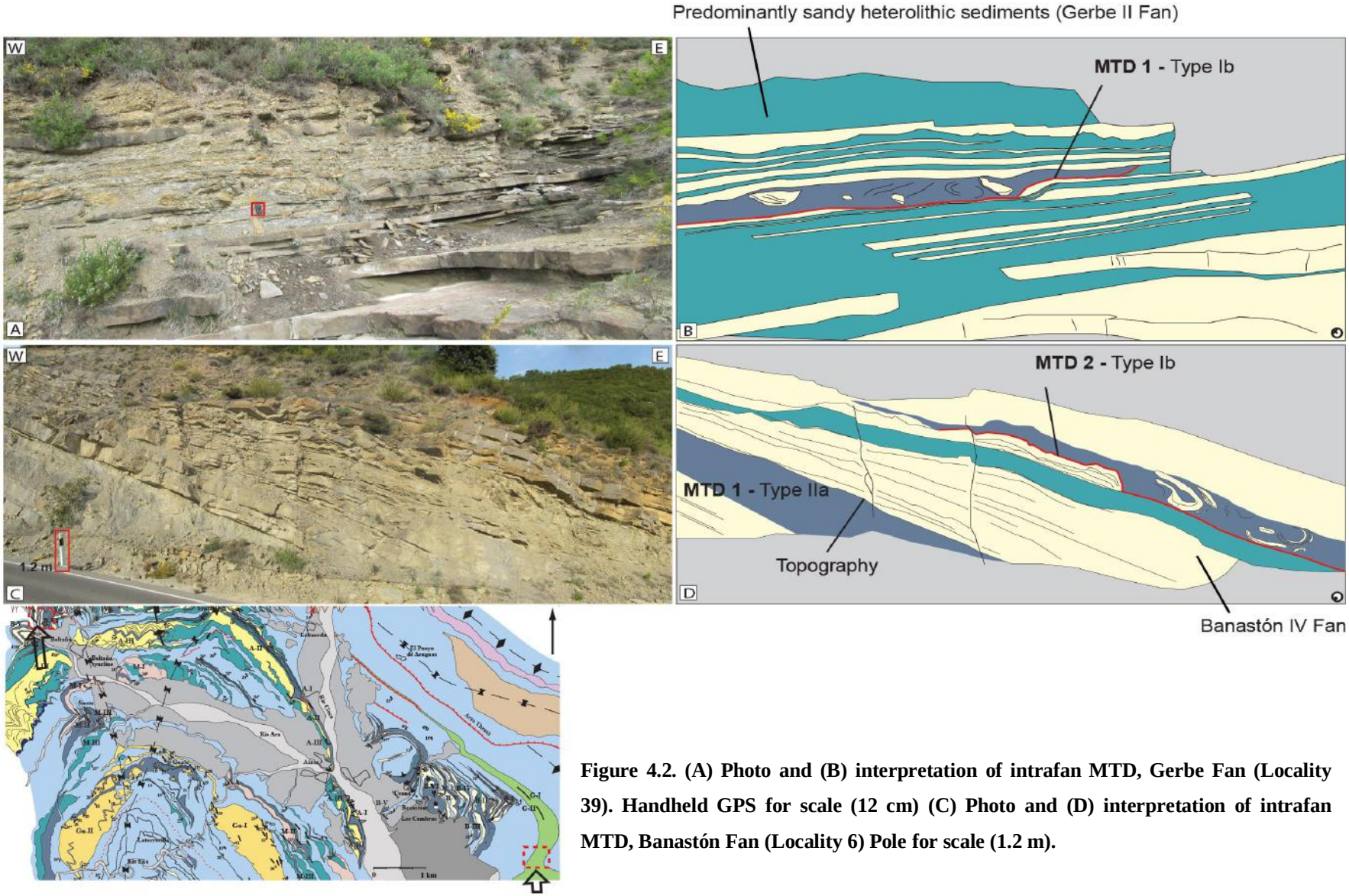

Figure 4.2. (A) Photo and (B) interpretation of intrafan MTD, Gerbe Fan (Locality 39). Handheld GPS for scale (12 cm) (C) Photo and (D) interpretation of intrafan MTD, Banastón Fan (Locality 6) Pole for scale (1.2 m).

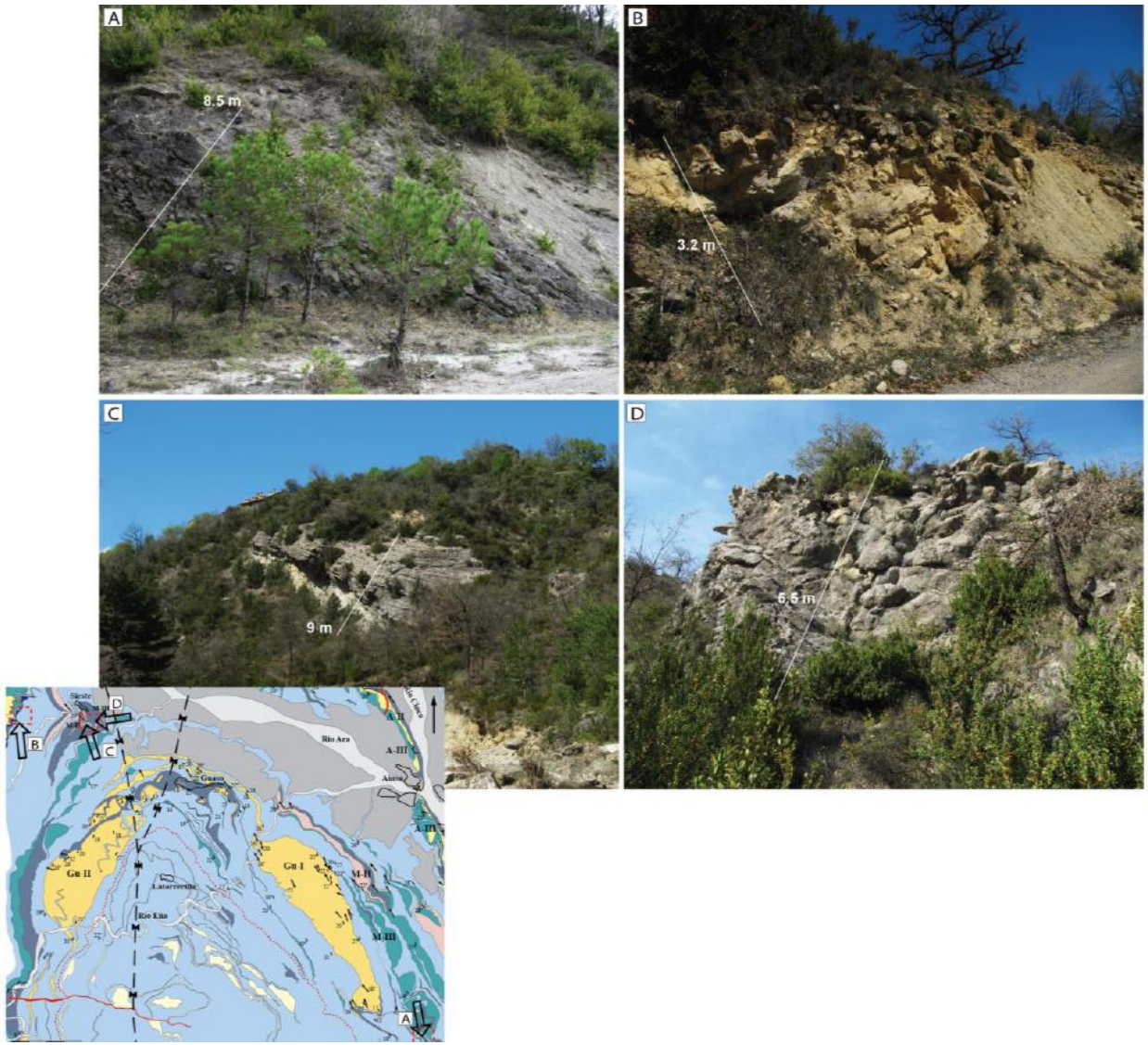

Figure 4.3. Type Ic MTDs located around the Ainsa Basin. (A) Morillo De Tou. East is to the left of the image. Limestone package is ~ 8.5 m thick (Locality 61) (B) San Martin (as documented in Pickering and Corregidor, 2005). East is to the right of the image. Limestone package is 3.2 m thick (Locality 60) (C) Rio Sieste. West-southwest is to the left of the image. Limestone package is ~ 9 m (D) Rio Sieste. South is to the left of the image. Limestone package is 5.5 m thick (Locality 26). Inlay map shows locations, with arrows pointing towards the direction of view.

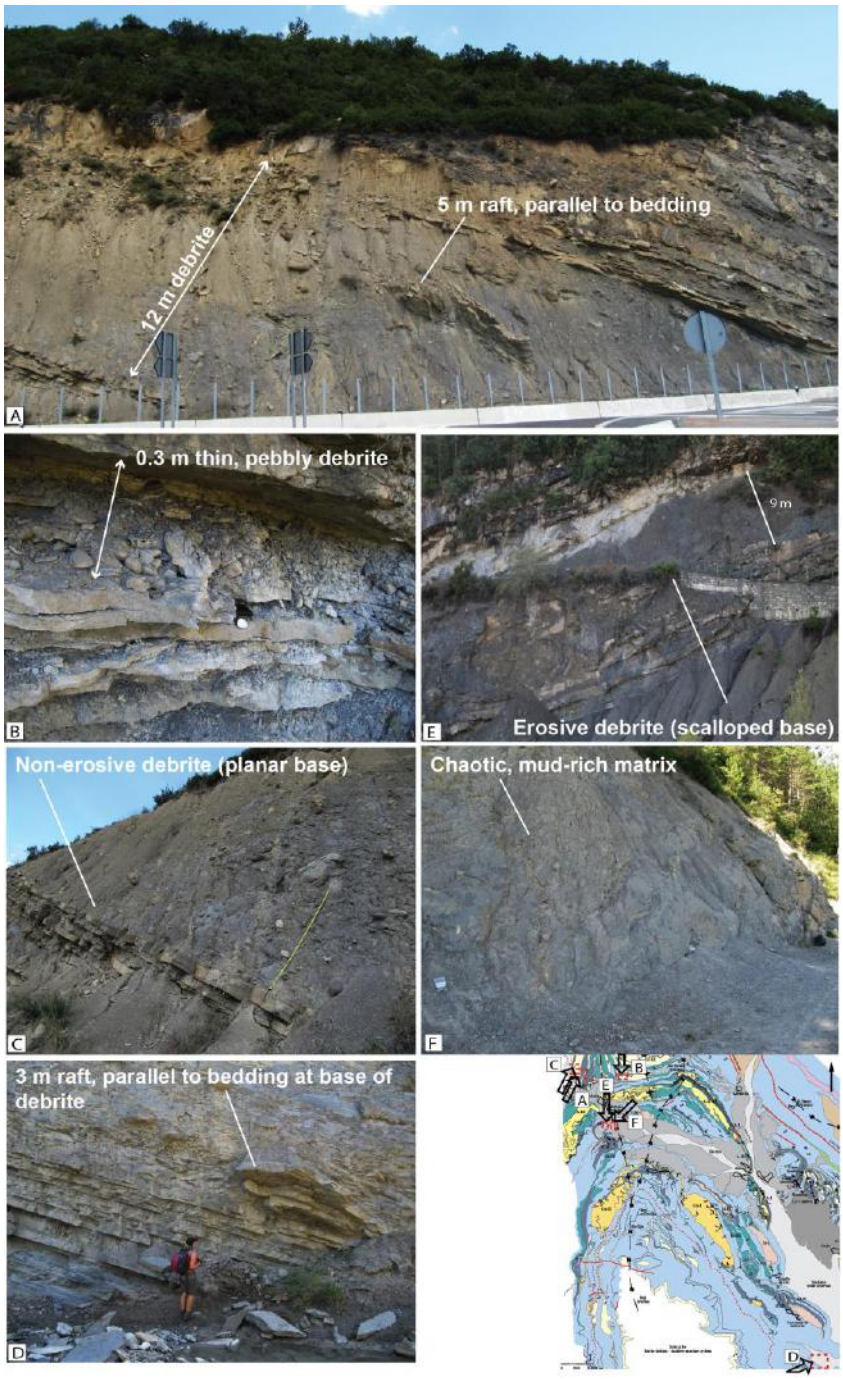

Figure 4.4. Type IIa MTDs documented around the Ainsa Basin (A) Boltaña Road (Locality 6) MTD is 12 m thick. Matrix is able to support large deformed raft near the top of the deposit, parallel to bedding (B) Thin pebbly mudstone, Banastón River (Locality 7) MTD is 0.32 m thick, compass-clinometer for scale (10 cm) (C) Thick MTD showing erosion at base. Matrix-supported and contains pebbles, Boltaña Road (Locality 6) Tape measure for scale (1 m) (D) 5.5 m-thick deposit with 3 m raft at base. No erosion is observed at this locality, near Camporotuno (Locality 62) Person for scale. (E) 9 m-thick pebbly mudstone showing erosion in to base of lower sandstone, Rio Ara (Locality 23) MTD is 9 m thick (F) Pebbly mudstone containing deformed rafts (base not exposed), Rio Ara (Locality 24) MTD is 6 m thick, rucksack for scale (50 cm).

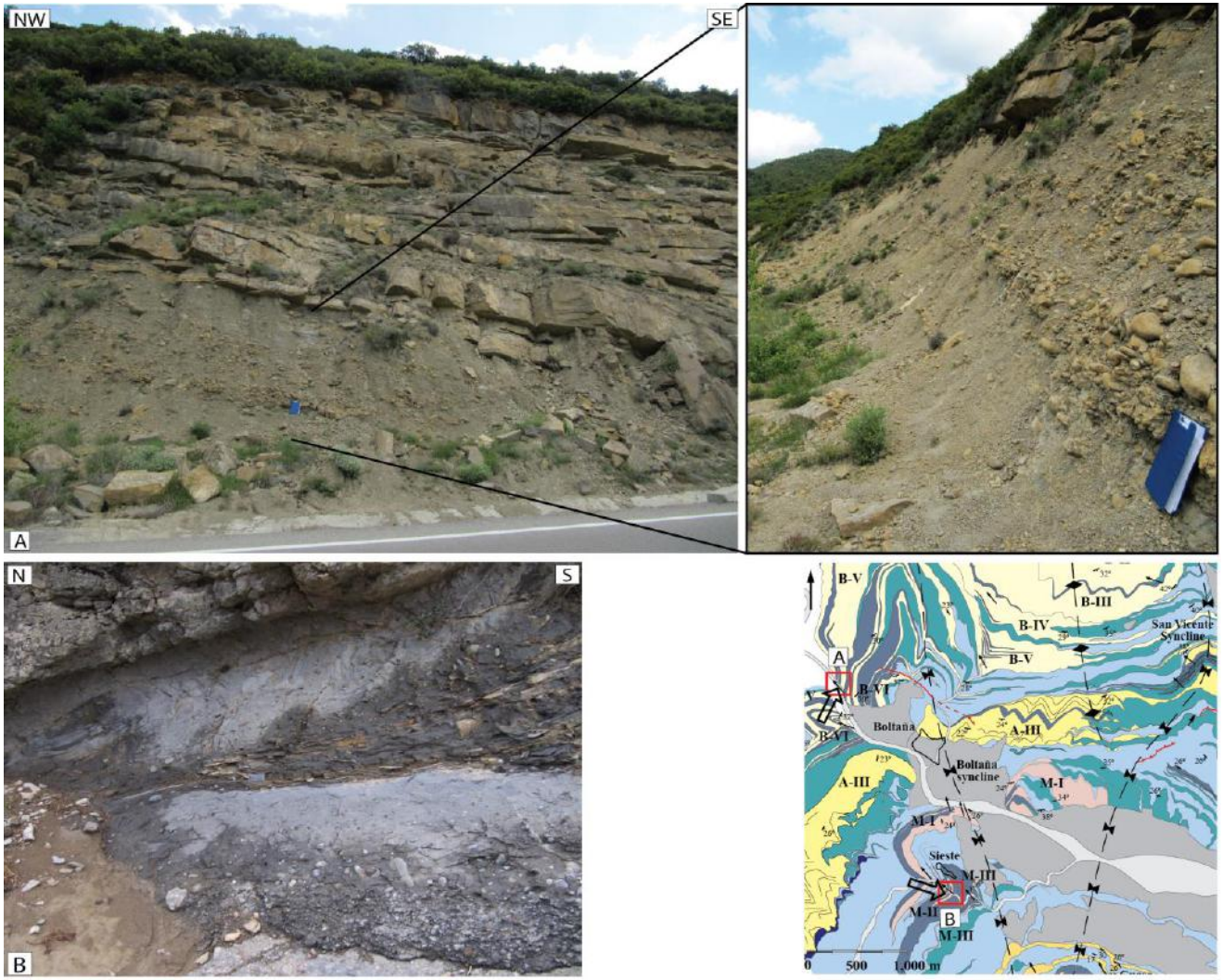

Figure 4.5. (A) Succession of clast-supported Type IIb and Type IIa MTDs (Locality 6). Clipboard for scale (35 cm). (B) Stacked Type IIa MTDs. Lower deposit exhibits 'graded' pebbles concentrated near base of deposit Rio Eña (Locality 62) Compass-clinometer for scale (10 cm).

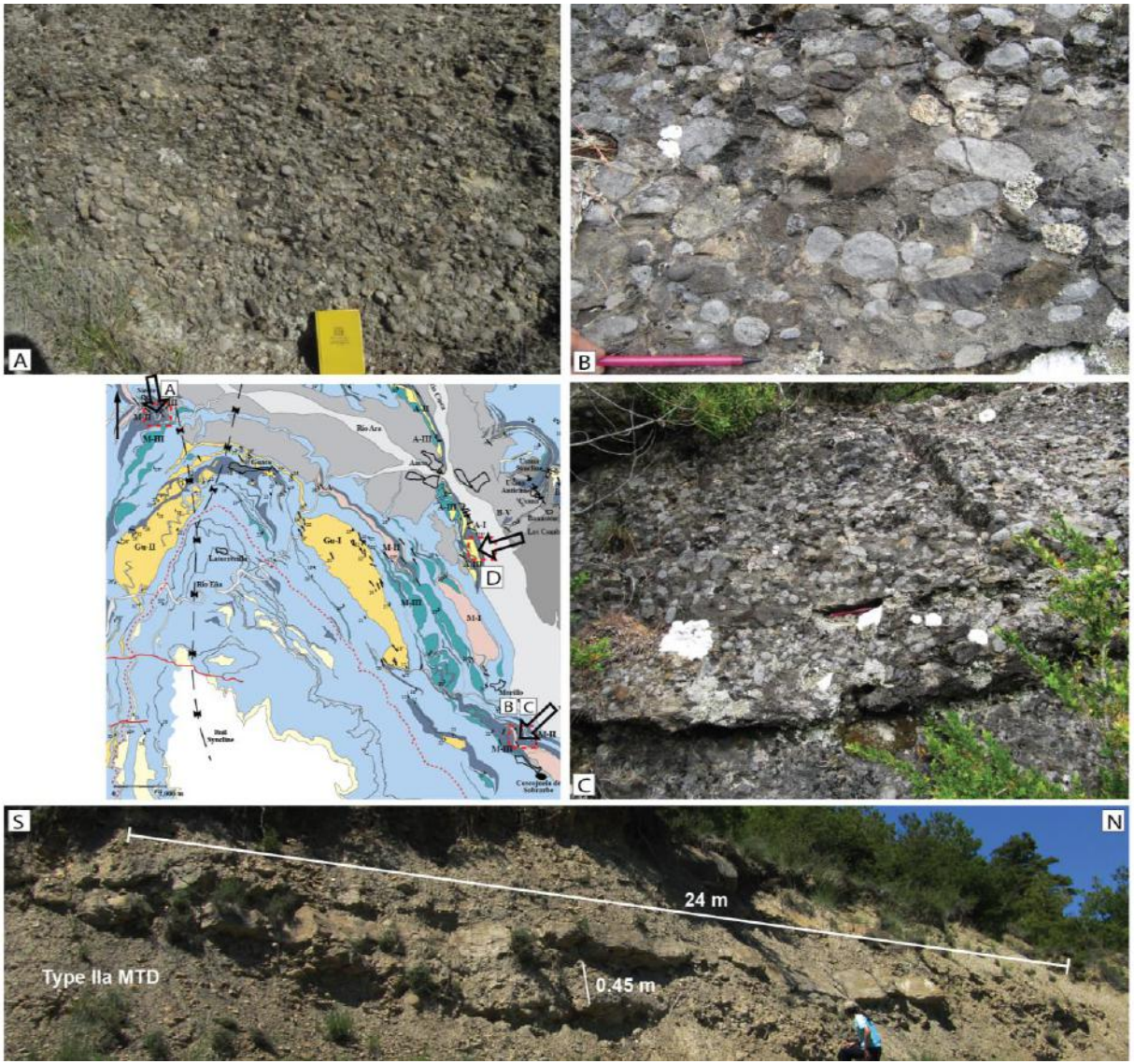

Figure 4.6. Examples of Type III MTDs - clast-supported pebbly-sandstone around the Ainsa Basin. (A) Morillo II Fan, Rio Sieste (Locality 27). Notebook for scale (20 cm). (B and C) Morillo II Fan, Coscojuela de Sobrabre (Locality 43). Pencil for scale (15 cm). (D) channelised pebbly sandstone element showing erosive base into underlying Type IIa MTD. Inlay map shows locations, with arrows pointing towards the direction of view.

Figure 4.7. (A) Type IIIb MTD showing channelised basal geometry. Pebbles have poor to moderate imbrication (Figure 4.29). Sandstone bed drapes the base of the scour (Locality 11). (B) Type IIIb MTD showing channelised basal geometry with sandstone draping the base of the 1.2 m scour. Notebook for scale (20 cm) (Locality 50). (C) Type IIIb MTD showing a more 'tabular' geometry. Pebbly sandstone shows erosive base into underlying thin sandstone beds (Locality 7). Inlay map shows locations and orientation of view.

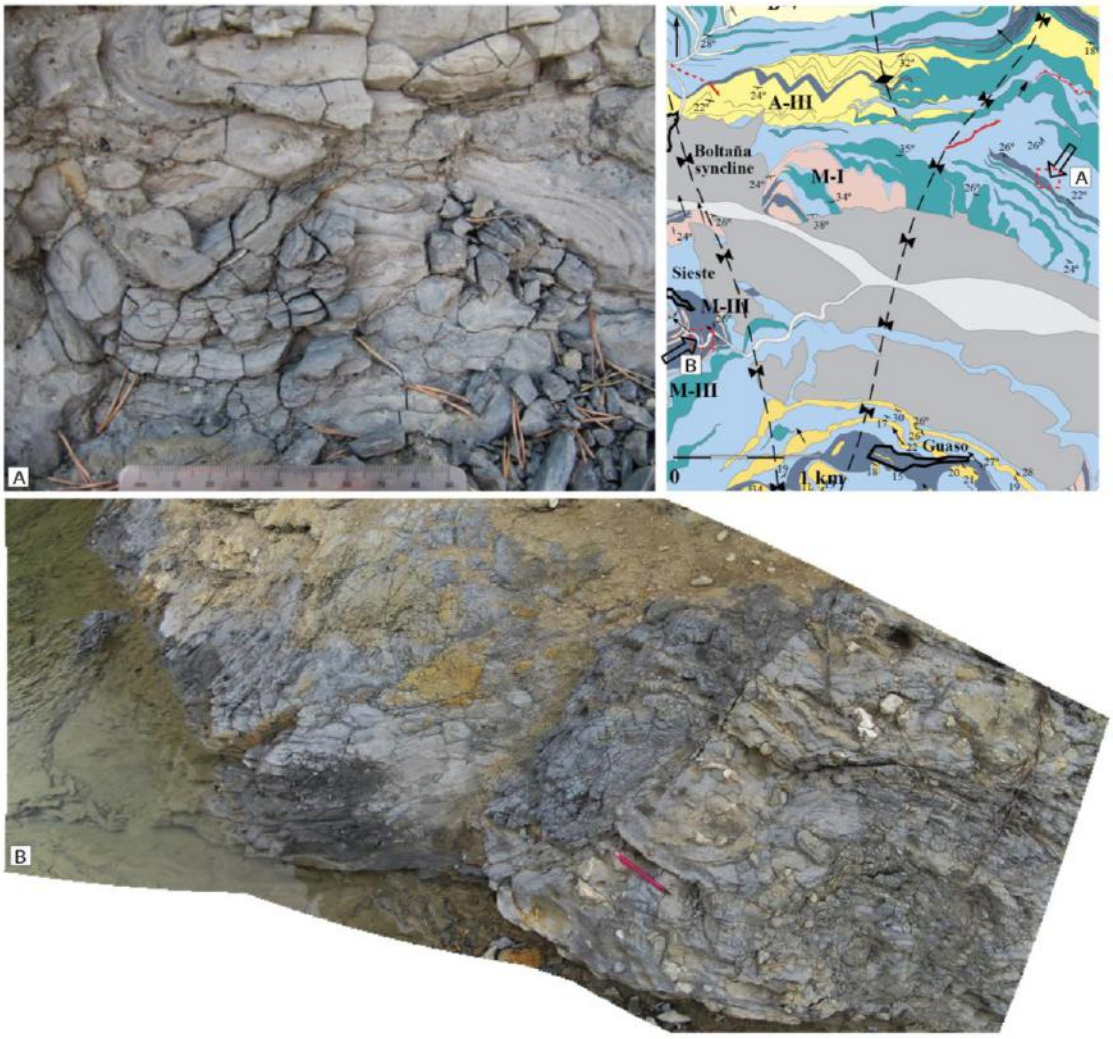

Figure 4.8. (A) MTD showing mixed Type Ia/IIa facies (Locality 58). Grain-size chart for scale (10 cm) (B) Mixed Type Ia/IIa MTD facies located beneath Type Ic MTD (Locality 26, Rio Sieste). Pencil for scale (15 cm).

4.3 SEDIMENTARY CHARACTERISTICS OF MTDs AND MTCs

Architectural elements relate to the bounding surfaces, sedimentary facies, facies associations and hierarchy of depositional geometries that collectively form the building blocks of sedimentary architecture (Pickering *et al.*, 1995). In this section, sedimentary characteristics of MTDs and MTCs are explored.

4.3.1 MTD facies attributes and stacking patterns

Distinguishing between discrete MTDs within MTCs at outcrop can be difficult as it is not always obvious whether compositional or fabric changes are present due to varying internal dynamics of individual flows, or whether individual MTDs have unique sedimentary properties (*cf*. figure 10 of Major [1997]. In the Major (1997) study, amalgamation surfaces of successive debrites proved difficult or impossible to observe without an intervening yellow sand layer). In the field, if thin, graded- to non-graded laterally continuous sandstone beds were not observed between deposits, then MTD facies attributes were used as key indicators to suggest vertically stacked deposits were likely deposited from discrete events. The following MTD facies attributes were identified:

(1) vertical burrows at the top of a deposit (to suggest a break in time between deposition of MTDs);

(2) truncated basal surfaces (inferred as indicating at least some consolidation of the lower deposit suggesting a break in time between deposition of MTDs);

(3) 'channelised' deposits' (e.g., MTDs showing channel-like basal geometry, as documented in Chapter 6);

(4) topography of lower MTDs within an MTC;

(5) different fabric properties (including graded fabric within Type IIa, b and III MTDs, varying sand concentrations within the fabric of Type IIa MTDs and also colour variations), and;

(6) different pebble concentrations in Type IIa and III MTDs.

Examples of discrete MTDs documented within MTCs at outcrop are shown in Figure 4.9.

Figure 4.9. Field observations that allow the recognition of multiple MTDs within an MTC. White dashed lines indicate discrete MTDs (Locality 63) (A) Channelised sandstone element, separating MTDs within MTC (Locality 63) Tape measure for scale (30 cm) (B) Stacked Type IIa MTDs showing sharp break between deposits, differentiated by distinct colour difference, (Locality 29) compass-clinometre for scale (10 cm) (C) Type IIa MTD showing erosion surface above Type Ia MTD (Locality 40). Yellow notebook for scale (20 cm).

When producing sedimentary logs in the field, where possible, MTCs were broken down into discrete depositional events (e.g., Figure 4.10, Localities 31 and 44). Using the sedimentary logs recorded in the field, the potential genetic relationships between successive events within an MTC were evaluated (i.e., genetically related beds *sensu stricto* hybrid event beds, Haughton *et al.* [2003, 2009]). Only MTCs comprised of two discrete deposits (MTDs) were used to define facies pairs and the stacking patterns of MTDs (Figure 4.11).

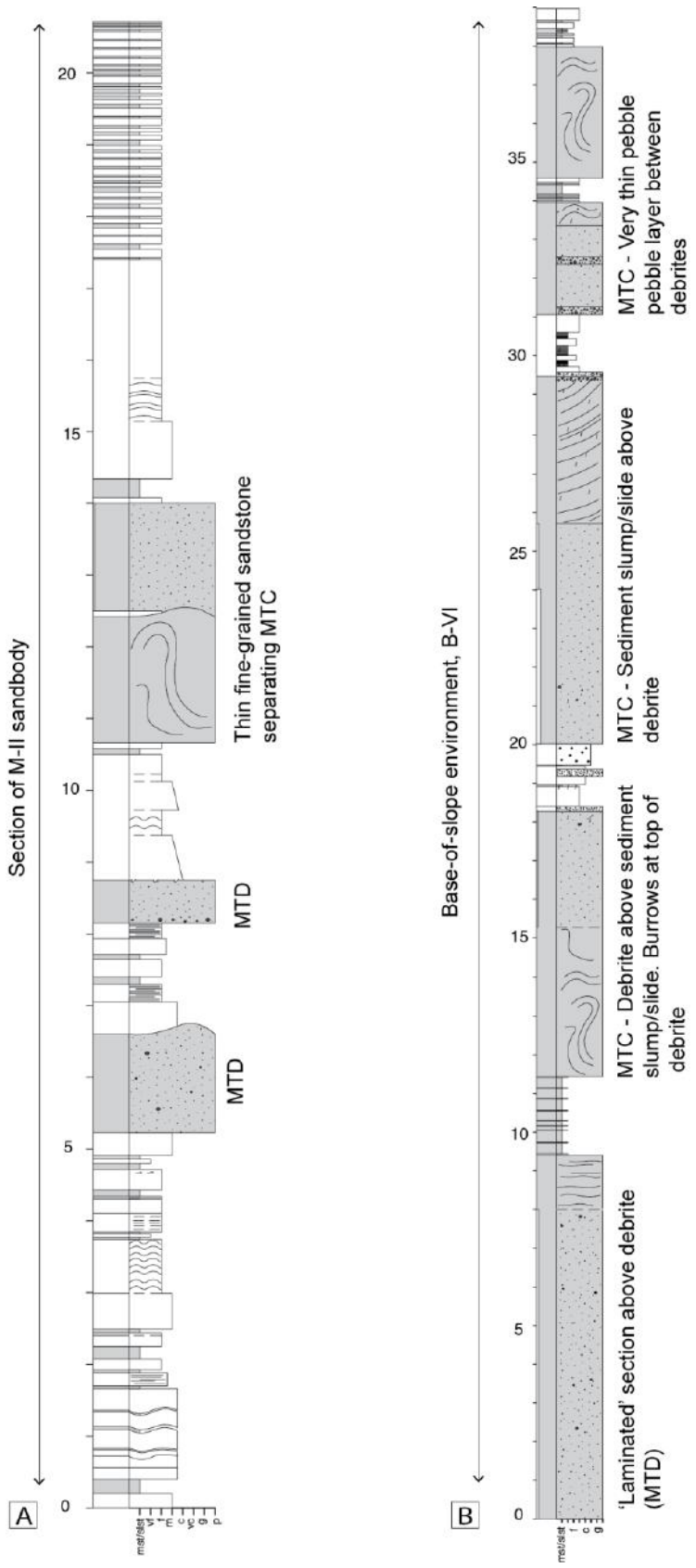

Figure 4.10. (A) At 11 m, MTC comprising lower Type Ia deposited below Type IIa MTD. M-II Fan (Locality 31) (B) MTCs comprising Type IIa and Type Ia MTDs, with pebble layers. B-VI Fan (Locality 44). Scales of sedimentary logs are in metres.

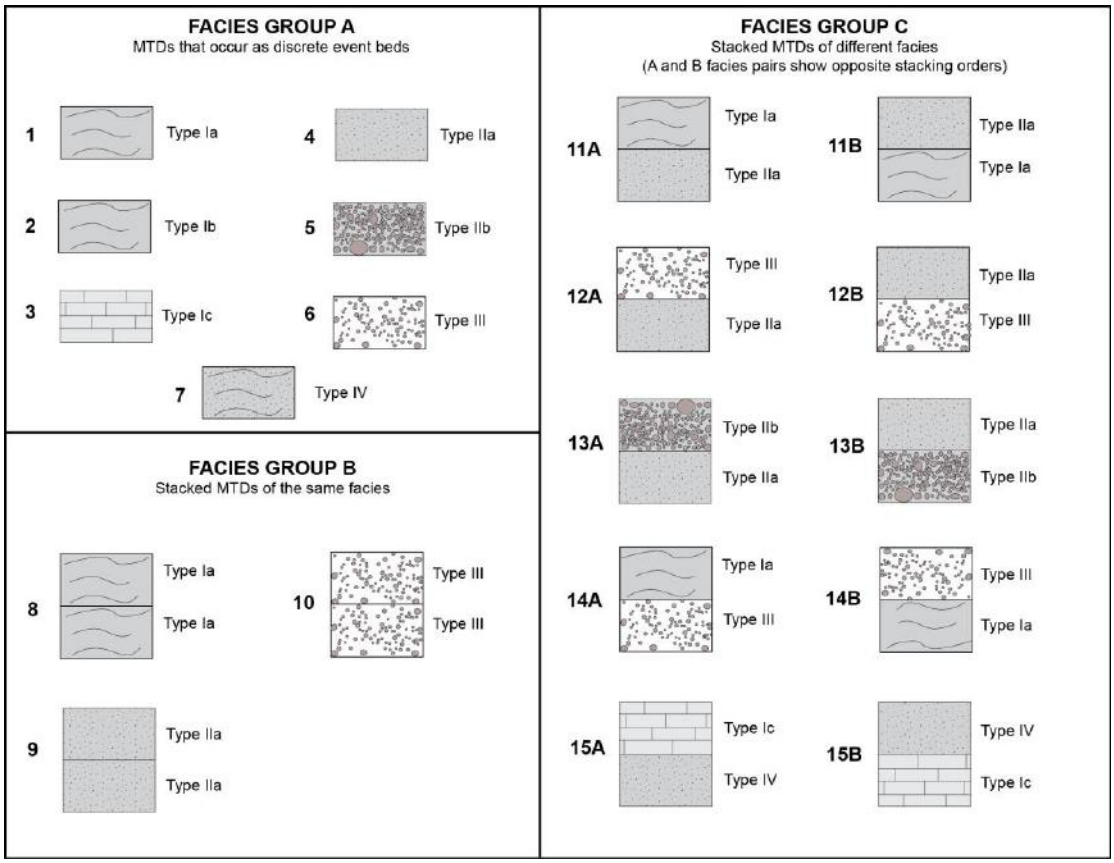

Figure 4.11. Stacking patterns of vertically stacked Facies Pairs logged in the Ainsa Basin that forms 3 Facies Groups (A, B and C). Facies Numbers 1 to 15B denotes number relating to stacking pattern.

Facies Group A represent MTDs documented as discrete event beds, such as they appear as isolated chaotic deposits within non-deformed sandstones and/or mudstones packages (Numbers 1 to 7). Facies Groups B and C represent MTCs (stacked MTDs), where thirteen stacking patterns are identified (Numbers 8 to 15B). Facies Group B shows Facies Pairs comprised of the same MTDs (i.e., vertically stacked Type IIa deposits). Facies Group C shows Facies Pairs comprised of different MTDs. For example, Facies Pair '11A' represents a Type Ia MTD deposited above a Type IIa MTD, and '11B' shows the reverse stacking pattern.

A summary of the MTD facies attributes, with total number of occurrences are identified between each facies pair (Table 4.1).

Facies Group	Facies pairs	Facies number	Number of occurances found in sedimentary log	Facies associations
FACIES PAIR A - Discrete MTDs	Type Ia MTD	1	91	Occur as discrete chaotic deposits within non-deformed sandstones/mudstones
	Type Ib MTD	2	3	
	Type Ic MTD	3	4	
	Type IIa MTD	4	68	
	Type IIb MTD	5	6	
	Type III MTD	6	39	
	Type IV MTD	7	7	
FACIES PAIR B - stacked MTDs of the same facies	Stacked Type Ia MTDs (MTC)	8	38	In some cases, slickenslides found between sediment slump/slides Sediment slumps/slides do not contain nummulites Different sediment slump/slides show different dip angles In some cases, burrows at top lower sediment slump/slide
	Stacked Type IIa MTDs (MTC)	9	17	In some cases, vertical grading of sand (higher sand concentration at the base) In some cases, debrites can show laminated top In some cases, concentration of pebbles at base of debrite In some cases, colour variation between debrites In some cases, upper debrite shows erosion into lower debrite In some cases, differing concentration and sizes of pebbles between debrites In some cases, different fabric properties (i.e. well-mixed or patchy) between debrite In some cases, burrows at top of lower debrite In some cases, different sand concentrations between debrites
	Stacked Type III MTDs (MTC)	10	4	In some cases, pebbly sandstones show normal grading In some cases, pebbly sandstones show clast-supported base/matrix-supported top Stacked pebbly sandstones typically show different sized pebbles
FACIES PAIR C - stacked MTDs of different facies (A and B facies pairs show opposite stacking order)	Type Ia and Iia MTDs (MTC)	11A	20	Multiphase slump/debrites (commonly found in Guaso System MTCs) In some cases, burrows at top of lower debrite In some cases, lower debrite shows topography
		11B	11	Multiphase slump/debrites (commonly found in Guaso System MTCs) In somes cases, upper debrite truncates lower sediment slump/slide In some cases, burrows at top of lower sediment slump/slide In some cases, lower sediment slump/slump shows topography
	Type IIa and III MTDs (MTC)	12A	4	In some cases, upper pebbly sandstone shows erosive base or infills topography
		12B	6	In some cases, upper debrite erodes into lower sandstone In some cases, underlying pebbly sandstone can produces topography
	Type IIa and Iib MTDs (MTC)	13A	3	Upper conglomerate is typically channelised
		13B	19	Upper debrite can be erosive incorporating underlying pebbles
	Type Ia and III MTDs (MTC)	14A	5	In some cases, underlying pebbly sandstone produces topography
	Type Ic and IV MTDs (MTC)	15A	4	Base of upper carbonate is typically brecciated Lower debrite shows angular bioclastic clasts beneath carbonate rafts

Table 4.1. Summary of MTD facies attributes found between vertically stacked discrete MTDs. Facies attributes documented between MTDs are noted '*in some cases*' as not all outcrops show all the described characteristics.

To consider the genetic relationship between stacking patterns of MTCs comprised of different deposits (Facies Group C), a probability value (p-value) was calculated using a chi-test to compare observed data with the expected distribution. Facies Group A occur as isolated deposits and Facies Group B comprises MTDs of the same facies, therefore it is not possible to undertake a similar chi-test analysis. To achieve this for Facies Group C, the following hypotheses were considered:

Null Hypothesis: There is no relationship between the stacking patterns of Facies Pairs.

Alternative Hypothesis: There is a relationship between the stacking patterns of Facies Pairs.

In these hypotheses, facies 'relationships' relate to the random or predictable pattern of stacked MTD facies. If the chi-test determined a P-value of < 0.5, the Null Hypothesis is rejected. Results are shown in Table 4.2.

	Facies	Facies Pair	Actual range (observed number)	Expected range (Total/number of subjects)	Chi-test (result from Excel)	Result
Facies Group C	Type Ia and IIa	11A	20	15.5	0.10	< 50% ***reject*** null hypothesis
		11B	11			
		TOTAL	**31**			
	Type IIa and III	12A	4	5	0.53	> 50 % ***keep*** null hypothesis
		12B	6			
		TOTAL	**10**			
	Type IIb and IIa	13A	3	11	0.0006	< 50% ***reject*** null hypothesis
		13B	19			
		TOTAL	**22**			
	Type Ia and Type III	14A	5	2.5	0.03	< 50% ***reject*** null hypothesis
		14B	0			
		TOTAL	**5**			
	Type Ic and IV	15A	4	2	0.05	< 50% ***reject*** null hypothesis
		15B	0			
		TOTAL	**4**			

Table 4.2. Results of chi-test facies analysis for Facies Pairs that show different MTDs in stacked succession.

The p-value for stacking patterns of Facies Pair 12 (A and B) was > 0.5, therefore the Null Hypothesis is accepted, i.e., there is no significant relationship between the stacking patterns between Type II and Type III MTDs. The p-value of stacking patterns of Facies Pairs 11, 13, 14 and 15 is < 0.5, therefore the Null Hypothesis is rejected, consequently suggesting a potential relationship between the stacking patterns of the following Facies Pairs:

(1) *Facies Pairs 11a, b:* Type Ia deposits immediately above Type IIa deposits (Facies 11A) are documented as more abundant.

(2) *Facies Pairs 13a, b:* Type IIa deposits immediately above Type IIb deposits (Facies 13B) are documented as more abundant.

(3) *Facies Pairs 14a, b:* Type Ia deposits immediately above Type III deposits (Facies 14A) are documented as more abundant.

(4) *Facies Pairs 15a, b:* Type Ic deposits immediately above Type IV deposits (Facies 15B) are documented as more abundant.

A possible explanation for these results is that these events were deposited from co-genetically related events (e.g., Sohn *et al*., 1999, 2002 and *sensu-stricto* Haughton *et al*., 2003, 2009), or potentially from similar source areas.

4.3.2 Topography, onlap and palaeocurrents

This section explores topographic relationships between muddy MTDs and sandy SGFs. Following mass-failure, as a cohesive flow freezes, MTDs can form a rugose upper surface that create depocentres to pond or compartmentalise succeeding deposits (Dykstra *et al*., 2006, 2011). The Ainsa Basin contains examples of Type Ia and IIa MTDs that created topography, denoted by an irregular upper surface, and also outcrops that do not show topography, denoted by a 'flat' upper surface, as presented in the following case studies.

4.3.2.1 Locality 16, Ainsa Quarry

The Ainsa Quarry, ~ 1.5 km south of Ainsa town, (Locality 16, Figure 4.12) exposes stratigraphy deposited as part of a proximal basin-floor fan succession (Pickering and Corregidor 2000, 2005, Pickering *et al*., 2015). The Ainsa Quarry outcrop comprises several channel complexes, vertically separated by fine-grained deposits that represent episodic channel abandonment, showing three phases of channel incision and backfill (fig. 15 p. 776 Pickering and Corregidor, 2005; Arbués *et al.,* 2007; Pickering *et al*., 2015) (Figure 4.12).

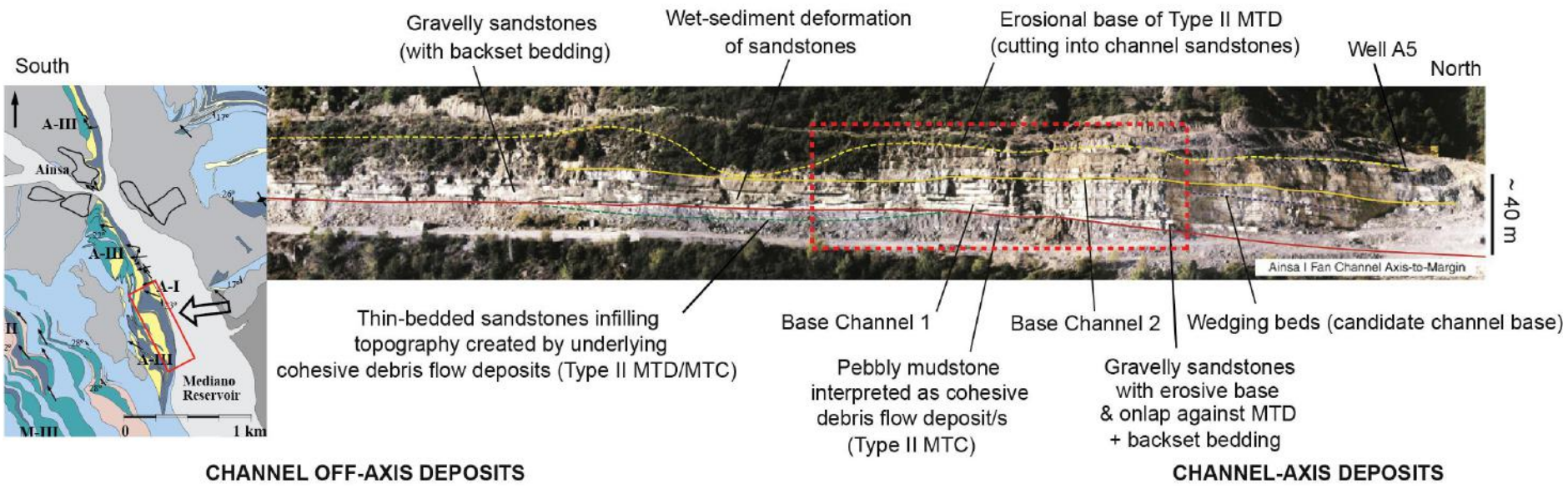

Figure 4.12. Ainsa I channelised sandstone in Quarry ~ 1.5 km south of Ainsa. Section shows at least 2 defined channels and mounded topography above a Type IIa MTC. Red dashed box on photo shows location of photomontage in Figure 4.14. Map inlay shows stratigraphic location with angle of view shown by arrow pointing west. Modified from Pickering *et al.* (2015).

At the base of the quarry outcrop, a Type IIa MTD (pebbly mudstone) is exposed at present-day ground level, slightly off-axis to the main channel deposits to the north (Figure 4.12). The Type IIa MTD is ~ 115 m wide and up to ~ 3.8 m thick (near the centre of the outcrop), and the margins are < 30 cm thick, thus forming a domed geometry in a 2-D cross-section. Pickering *et al*. (2015) describe the Well A5 core (~ 60 m long) through the Ainsa I Fan. The A5 was logged independently for the purpose of this study (*cf*. fig. 4 in Pickering *et al*., 2015). The A5 core shows the base of the Ainsa I Fan is ~ 11 m below present-day ground level, providing evidence that the Type IIa MTD exposed at the base of the quarry was deposited during construction of the Ainsa I Fan (Figure 4.13). During early deposition of the sandy channel deposits, the slope is envisaged to have been unstable potentially due to the load imposed by the sandy SGFs.

At outcrop, the matrix of the Type IIa MTD is chaotic and is mud-dominated, with < 5 % sand-grade material. The MTD is dominantly matrix-supported but can appear clast-supported in places. Pebbles are poorly sorted and are composed of very well-rounded, dark-grey limestones ranging from granules up to 45 cm (in *a*-axis). Poor pebble imbrication was measured at this locality (Figure 4.29). Beds of different sedimentological character onlap the northern and southern margins of the Type IIa topographic high (Figure 4.14). Four medium-bedded, coarse- to very coarse-grained sandy SGFs deposit onlap the northern margin, whereas heterolithic sediments comprising sandstones and mudstones that are thin-bedded, fine-to medium-grained, onlap the southern margin. Flute marks are observed at the base of the upper sandy SGF deposit immediately above the MTD, showing that the flow that deposited the sandstone bed was turbulent, at least in its earliest phase.

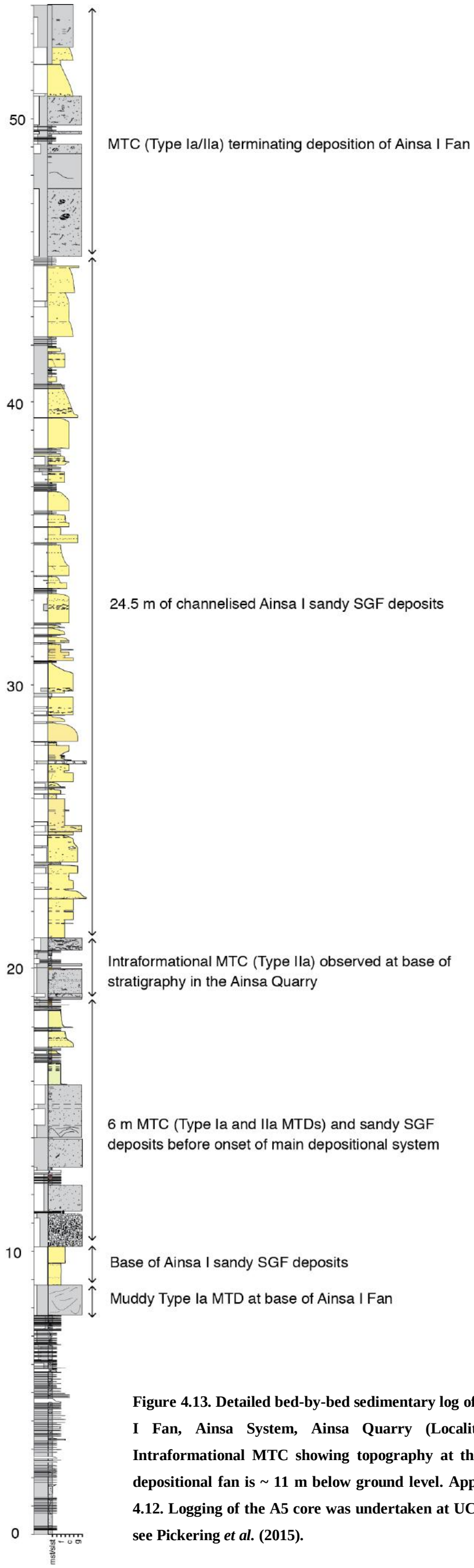

Figure 4.13. Detailed bed-by-bed sedimentary log of the A5 core, logged for this study (Ainsa I Fan, Ainsa System, Ainsa Quarry (Locality 16). Vertical scale is in metres. Intraformational MTC showing topography at the base of the quarry is shown. Base of depositional fan is ~ 11 m below ground level. Approximate log position marked on Figure 4.12. Logging of the A5 core was undertaken at UCL. For a summary of the drilling results, see Pickering *et al.* (2015).

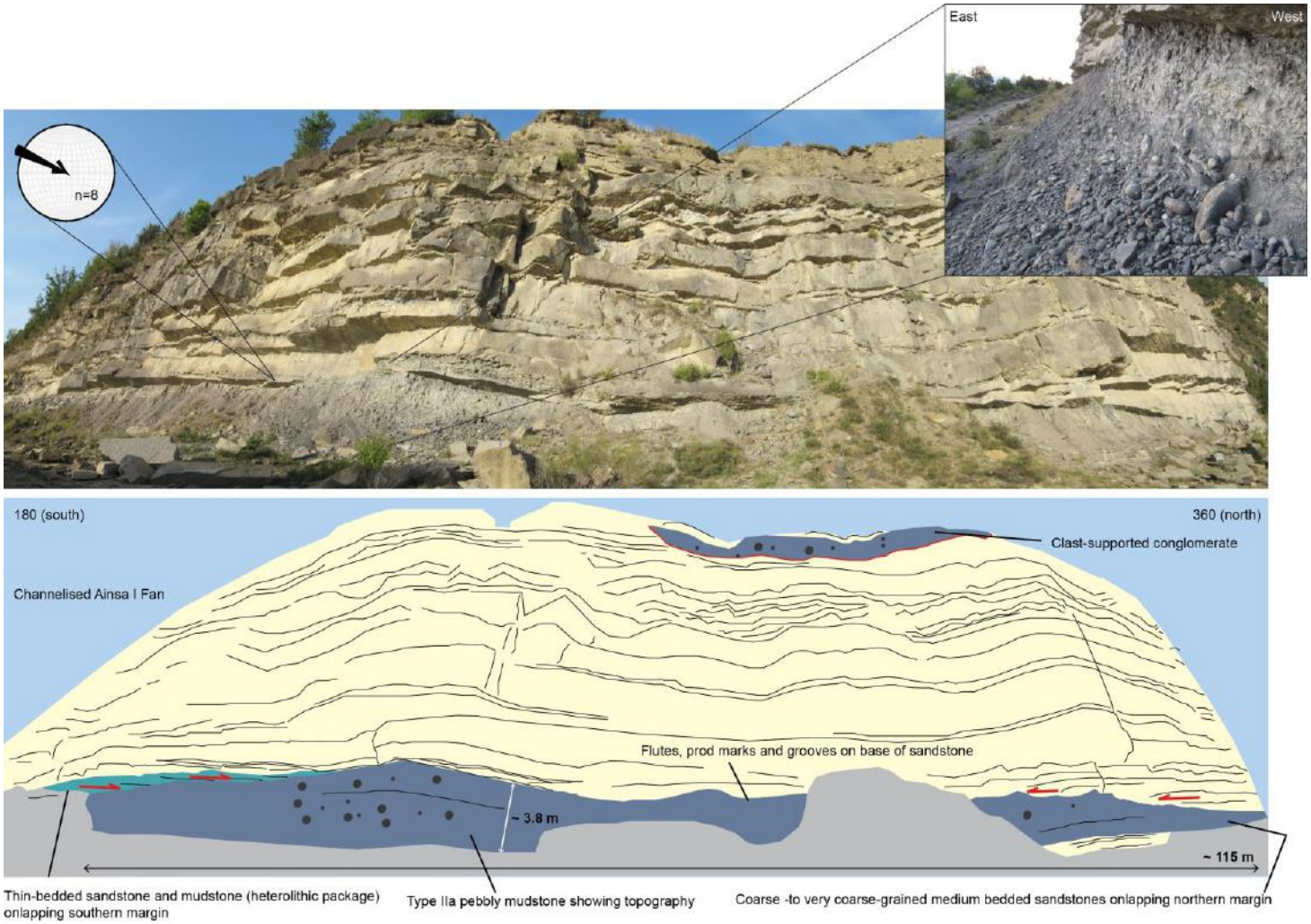

Figure 4.14. Photomontage showing topography of Type IIa MTD (pebbly mudstone), Ainsa I Fan, Ainsa Quarry (Locality 16). Photograph is taken at the base of the Quarry outcrop. The more distal and proximal geometry of this MTD are unknown. Palaeoflow is oblique to the outcrop and towards ~ 320°.

4.3.2.2 Locality 40, Rio Sieste

The Morillo System is up to ~ 260 m thick and is the penultimate deep-marine sand-prone system in the Ainsa Basin, with the Morillo III fan interpreted as a lower-slope submarine fan (Bayliss and Pickering, 2015b). At Locality 40, Type Ia and IIa MTDs are measured up to 2.2 m, deposited between medium-grained amalgamated tabular sandstones. Flutes are observed at the base of some sandy SGF deposits to suggest a turbulent flow deposited these sandstones. Unlike the Ainsa Quarry outcrop, these MTDs do not show any evidence of rugose topography (Figure 4.15).

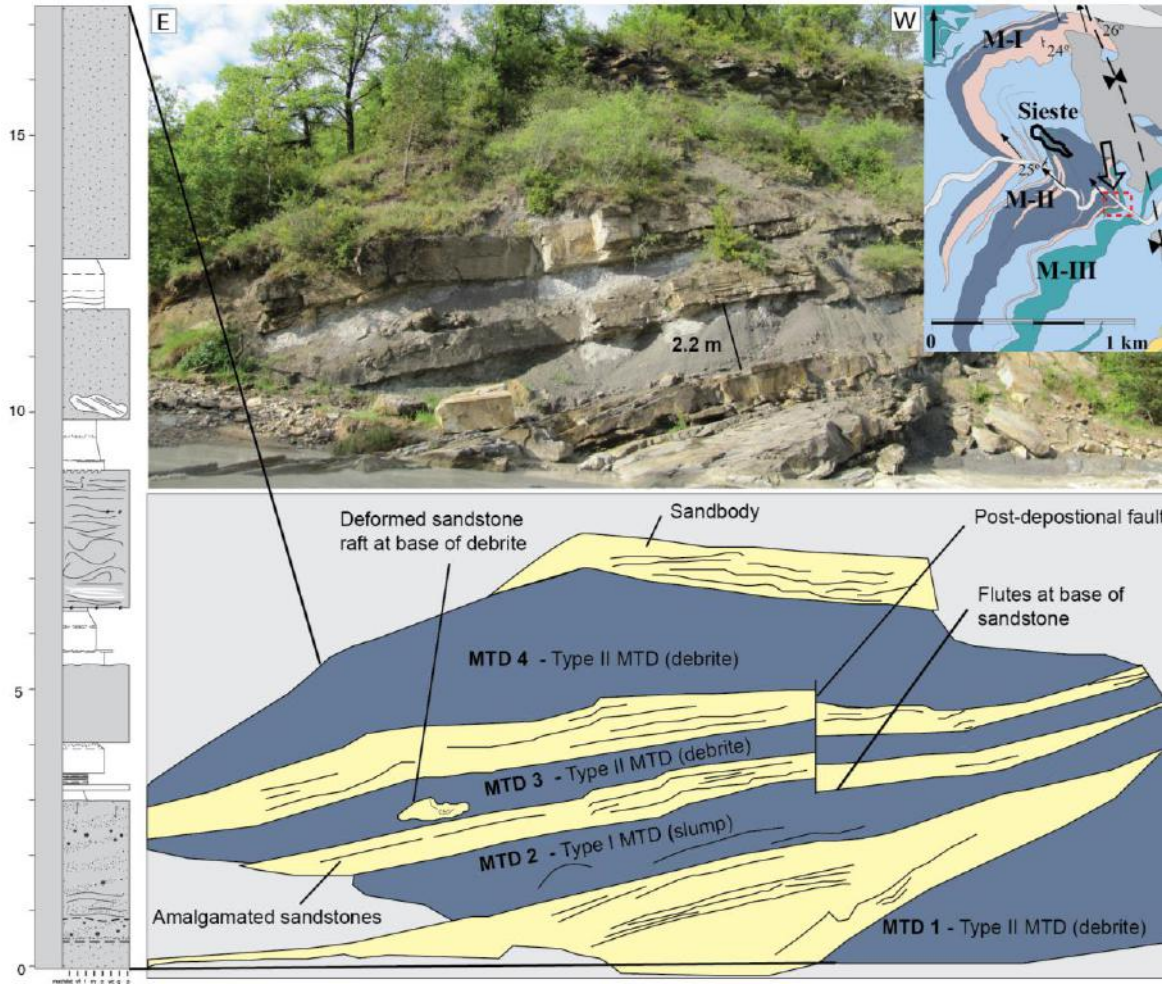

Figure 4.15. Type I and II MTDs do not show topographic relief at outcrop, Morillo III section, Rio Sieste. Sedimentary log displayed to the left of Figure. Apparent splaying of sandstone beds to the left of figure is a function of perspective. Red dashed box in map inlay shows locality (Locality 40), with arrow orienting view of photo. Palaeoflow oblique to the outcrop and towards ~ 320°.

4.3.2.3 Measured MTD topography

Wherever rugose topography was observed, topographic dimensions were measured to document the relationship between Type Ia and Type IIa MTD thickness and topography. Taking into account the limitations of exposure, outcrops were individually assessed to try and ensure that topography formed from cohesive flows was measured and not erosion from overlying SGF deposits. Figure 4.16 below shows results of topography *versus* thickness.

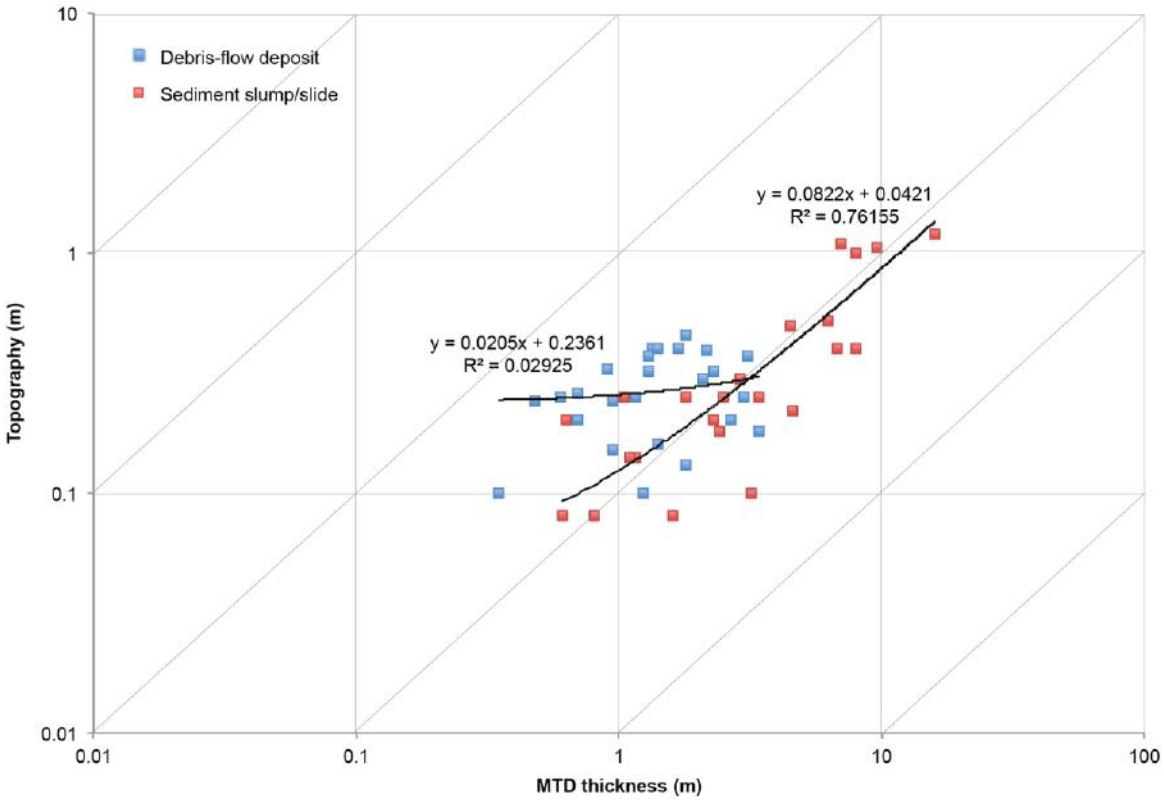

Figure 4.16. Type Ia and Type IIa MTD thickness *versus* topography. Type Ia MTDs show a positive relationship with thickness *versus* topography. Log-log scale.

Topographic relationships can be very subtle, and range from centimetres up to a few metres. Type Ia MTDs are thicker than Type IIa MTDs, measured up to 16 m, and with topography measured up to 3.4 m. There is a fairly positive correlation between Type Ia MTDs and topography compared to a very poor relationship between Type IIa MTD thickness and topography.

4.3.2.4 Palaeocurrents above MTD topography

This section considers how topography above MTDs may have influenced overlying palaeocurrent patterns. When deposited above MTDs, the bases of sandy SGF deposits can be exposed, as recessive weathering erodes the immediately underlying muddy MTD relative to the consolidated sandstones. Palaeocurrent indicators such as flutes, grooves and prod marks were measured to document the dispersion of palaeocurrents to document how pre-existing topography can affect the passage of subsequent sandy SGFs. The next case study presents evidence of potential flow deflection over an MTD showing topography (Locality 62). A muddy Type IIa MTD has weathered > 1 m underneath a sandbody, exposing the basal surface of the lower sandy SGF deposit (Figure 4.17).

The upper surface of the Type IIa MTD is irregular, forming a single mound ~ 0.33 by 1.2 m. The base of the sandy SGF deposit is highly variable, showing flute marks infilled with gravel-lags (grains measuring ~ 0.5 to 8 mm in diameter). Palaeocurrents across the topographic mound show moderate dispersion from 300^{o} and 346^{o}, possibly due to flow deflection around the MTD.

4.3.3 Sandstone channels in MTDs

This section documents how sandy SGFs erode and deposit sandstones into underlying MTDs on the palaeoseafloor. The first case study is from the Morillo I Fan (Locality 24), where a coarse-grained structureless sandy SGF element is observed to erode 4.5 – 6 m into a Type IIa MTD forming a channelised geometry (Figure 4.18).

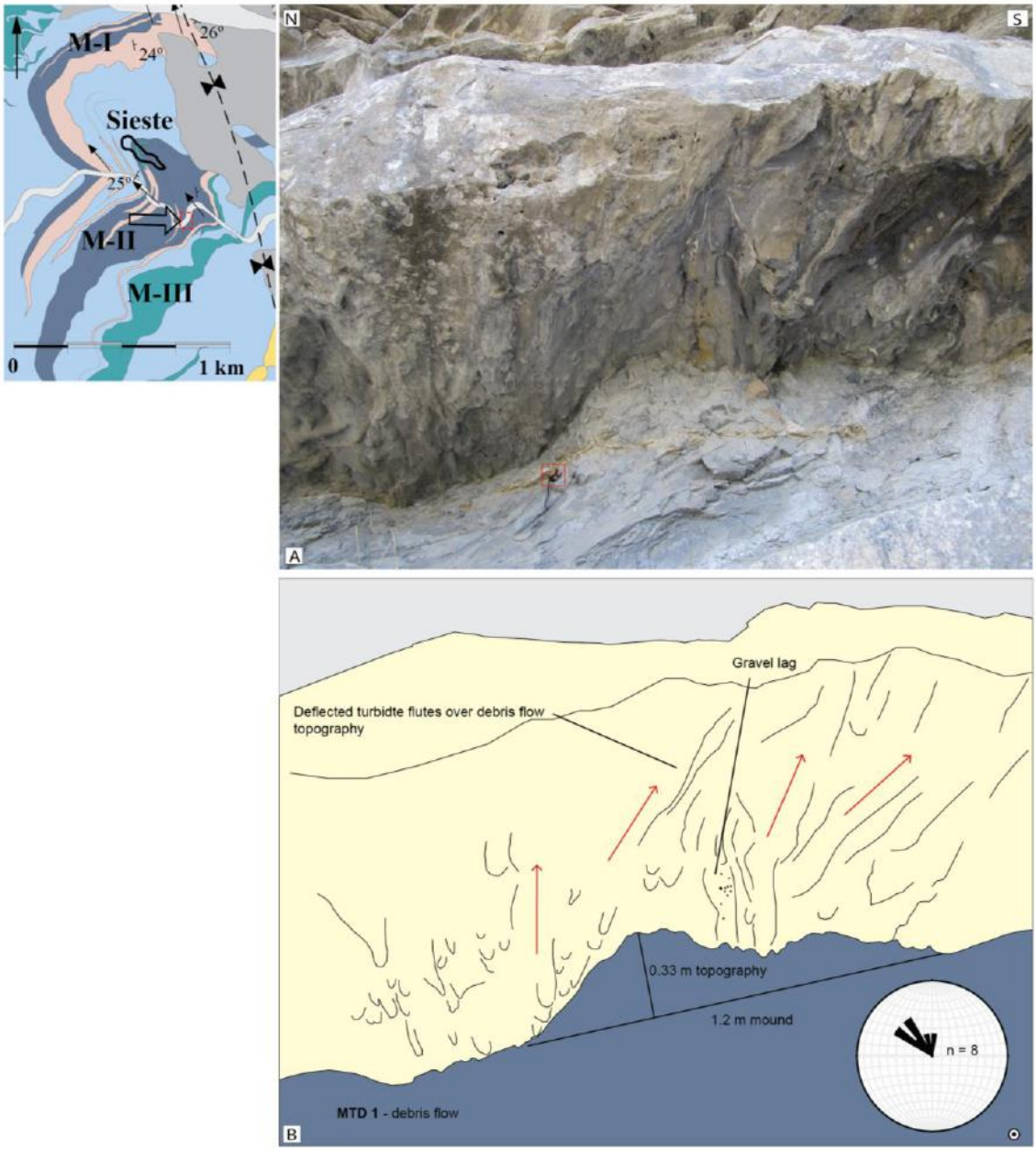

Figure 4.17. Evidence of flow deflection over a cohesive MTD. View looking up at base of sandy SGF-deposit. Red dashed box in map inlay shows locality (Locality 62), with arrow orienting view of the outcrop in this figure.

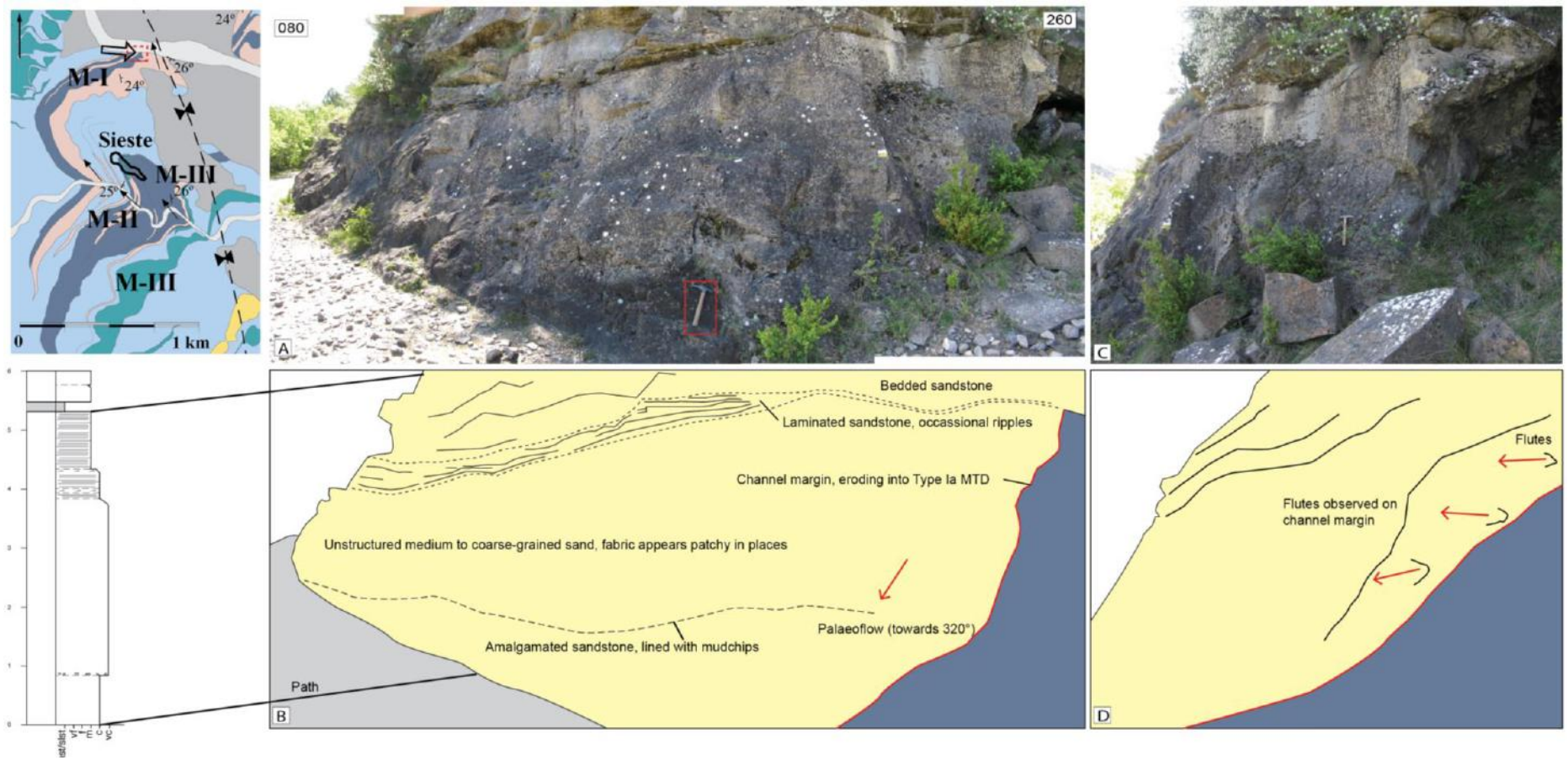

Figure 4.18. Thick channelised sandy SGF deposit eroding into a Type IIa MTD. Flute marks observed on western channel margin (eastern channel margin in not exposed). Red arrows indicate palaeoflow (towards ~ 320°). Hammer for scale (35 cm). Red dashed box in map inlay shows locality (Locality 24), with arrow orienting view of outcrop in this figure.

The sandstone eroding into the underlying MTD is ~ 5.3 m thick and ~ 35 m wide, although the base of the sandy SGF deposit is not exposed and therefore the exact thickness is unknown. An irregular surface lined with mudclasts is documented near the bottom of the outcrop to suggest the 5.3 m sandstone package comprises amalgamated sandy deposits. The sandstone is coarse-grained and is dominantly structureless, however the fabric appears potentially fluidised in places. The lateral western margin (towards 260^{o}, Figure 4.18) is relatively steep, at ~ 60^{o}, with the base of the margin exposed adjacent to the recessively weathered Type IIa MTD. Bilaterally symmetrical and elongate flutes marks, measured to up 20 cm long and 8 cm wide are observed at the base of the channel margin, measured towards ~ 320^{o}. Above the thick sandstone bed, tabular, non-erosive, thin-bedded fine- to medium-grained sandy SGF deposits are observed to 'passively' deposit over the lower channelised sandstone and adjacent MTD stratigraphy, suggesting that the palaeoseafloor was relatively flat after the channel incision.

The second case study is from the margin of the Guaso I Fan (Locality 33, near the village of Bruello). Within a 40 m cliff section, an isolated sandstone channel, ~ 4 - 5 m thick, is documented to erode into a Type IIa MTD composed of fine-grained mudstones/marlstones (Figure 4.19). The channel base contains many flute casts, indicative that a highly turbulent flow incised this channel (Figure 4.19). Due to the sandstone thickness (~ 8 m), the channel axis is likely to comprise amalgamated sandstones, deposited from multiple flows. The axial region passes into laterally extensive sheet-like sandstones, similar to 'wings' as described by Elliott (2000). In this model, these event beds are deposited from large out-sized flows.

Figure 4.19. Sandstone SGF deposit eroding into Type Ia MTD, showing fluted basal surface of sandy SGF. Image taken by Author and modified from Sutcliffe and Pickering (2009). Basal sandstone surface shows corkscrew flutes eroding into MTD. Red dashed box in map inlay shows locality (Locality 33), with arrow orienting view of outcrop in this figure. The cliff section is ~ 40 m high and inaccessible for any detailed observations and measurements.

The final case study is from the Guaso I Fan (Locality 30), near Guaso village. The roadside outcrop exposes a cross section down-dip of an erosional-depositional channelised element, comprising sandy SGF deposits within an MTD. A detailed cross-section was undertaken along the Guaso roadside outcrop (Locality 30) by logging 22 sedimentary logs over ~140 m to show the cross-sectional variation of architectural elements in an MTC. The roadside outcrop shows a complex architecture of mass-transport deposition between thin stringers of sandy SGF deposits, channel-like sand-filled geometries and gravel lenses. Contacts between MTDs are not always horizontal and thin sandstones deposited between MTDs are observed to deposit within depositional lows and generally thicken and thin over a few metres (Figure 4.20).

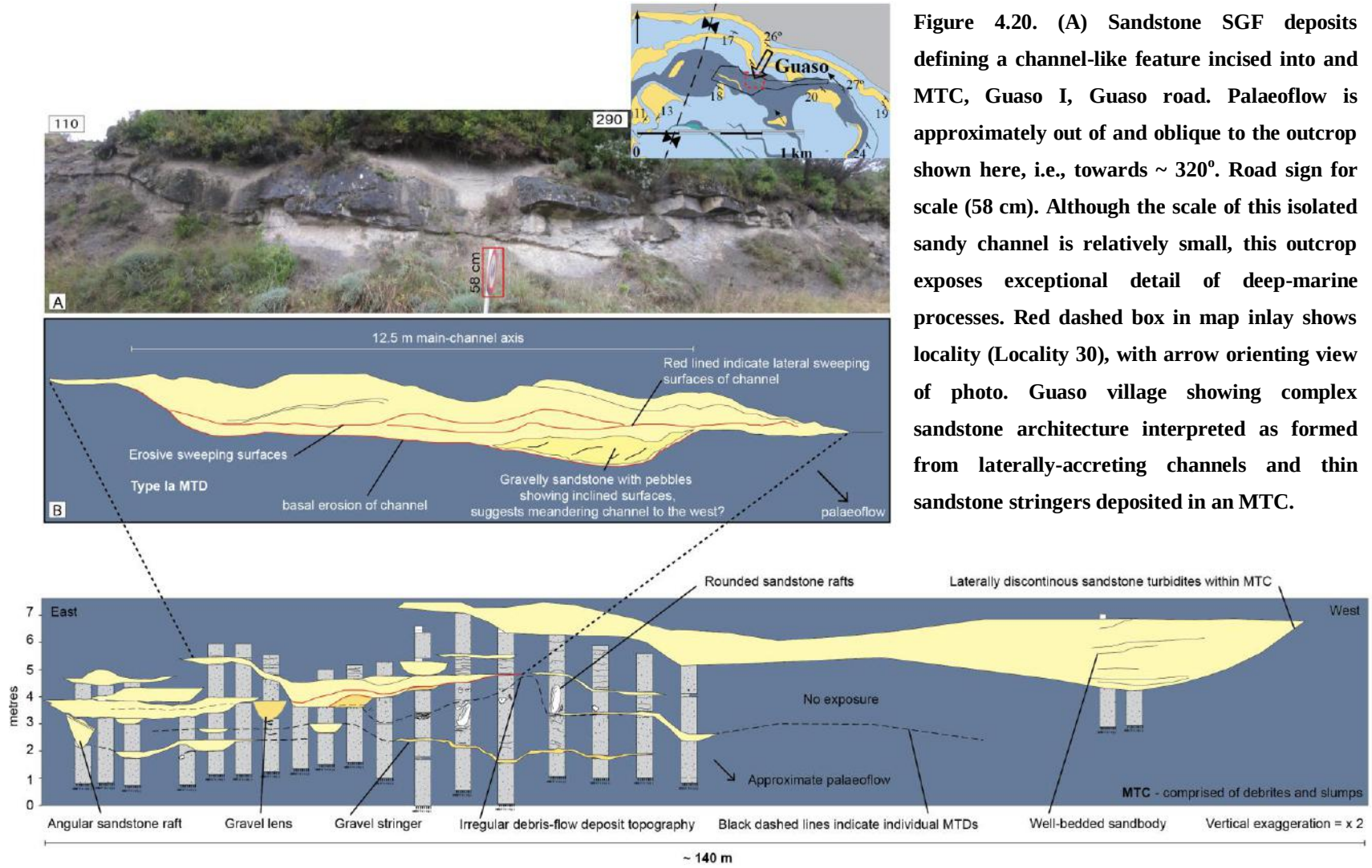

Figure 4.20. (A) Sandstone SGF deposits defining a channel-like feature incised into and MTC, Guaso I, Guaso road. Palaeoflow is approximately out of and oblique to the outcrop shown here, i.e., towards ~ 320º. Road sign for scale (58 cm). Although the scale of this isolated sandy channel is relatively small, this outcrop exposes exceptional detail of deep-marine processes. Red dashed box in map inlay shows locality (Locality 30), with arrow orienting view of photo. Guaso village showing complex sandstone architecture interpreted as formed from laterally-accreting channels and thin sandstone stringers deposited in an MTC.

The outcrop at Locality 30 shows a 12.5 m-thick channel with ~ 0.8 m of axial incision into the lower MTC (comprising a sequence of Type Ia and Type IIa MTDs). Unlike Locality 24, flute marks are not observed at the base or at the margins of the sandstone sequence. The basal sandy SGF deposit is a gravelly-sandstone situated in the western corner of the channel (towards 290^{o}, Figure 4.20), showing inclined surfaces that thin and pinch-out eastwards, towards the centre of maximum incision. Above the gravelly sandstone bed is a series shallow inclined surfaces of graded fine- to medium-grained erosional sandstones that sweep down and dip towards the southeast (towards ~ 110). The architectural elements of the isolated sandbody within the MTC suggest meandering, with lateral accretion surfaces and a gravelly point-bar deposit on the margin (e.g., Peakall *et al.*, 2007; Bayliss and Pickering, 2015b). The channel is capped by a Type IIa MTD to suggest a relatively short-lived preferential flow pathway of erosive flows that resulted in the deposition of channelised sandy SGF deposits (i.e., turbidites).

4.3.4 Rafts and boulders

In this study, rafts refer to angular and 'bedded' sandstones and boulders refer to structureless and rounded clasts such as sandstones, which are either located at the base or appear to 'float' in the middle or at the top of deposits, suggesting matrix strength of arrested flows. This section describes various sandstone boulders and rafts (> 30 cm diameter) documented within MTDs.

Rafts have variable sedimentary and morphological characteristics showing varying degrees of deformation (Figure 4.21). Rafts incorporated in a discrete MTD can be graded or ungraded (structureless) comprising fine- to coarse-grained sandstone. If sandstone boulders are coarse-grained, they are typically nummulite-rich (Figures 4.21-A and B). Some rafts show sandstones that are thin- to medium bedded (Figures 4.21-C and D). Rafts are observed to have different degrees of deformation and can be moderately- to well-rounded or can be highly folded and thin-bedded sandstones and siltstones that appear in the process of degradation, showing angular and highly attenuated margins (Figure 4.21-C). Sandstone rafts that show deformation and disaggregation appear to have been deformed during passage of the flow. Figures 4.21-E and F show a large ~ 5 m bedded sandstone raft with a deformed frontal snout.

A sheared and deformed thin sandstone bed appears to infill topography, separating MTDs. Rafts up to 18 m in the Guaso System are observed embedded and weathered from outcrop. In these examples, rafts are bedded and discontinuous and could be easily mistaken as an *in situ* sandy SGF deposit. Extrabasinal features observed in rounded boulders within MTDs around the village of Usana, (Locality 44) are shown in Figure 4.22.

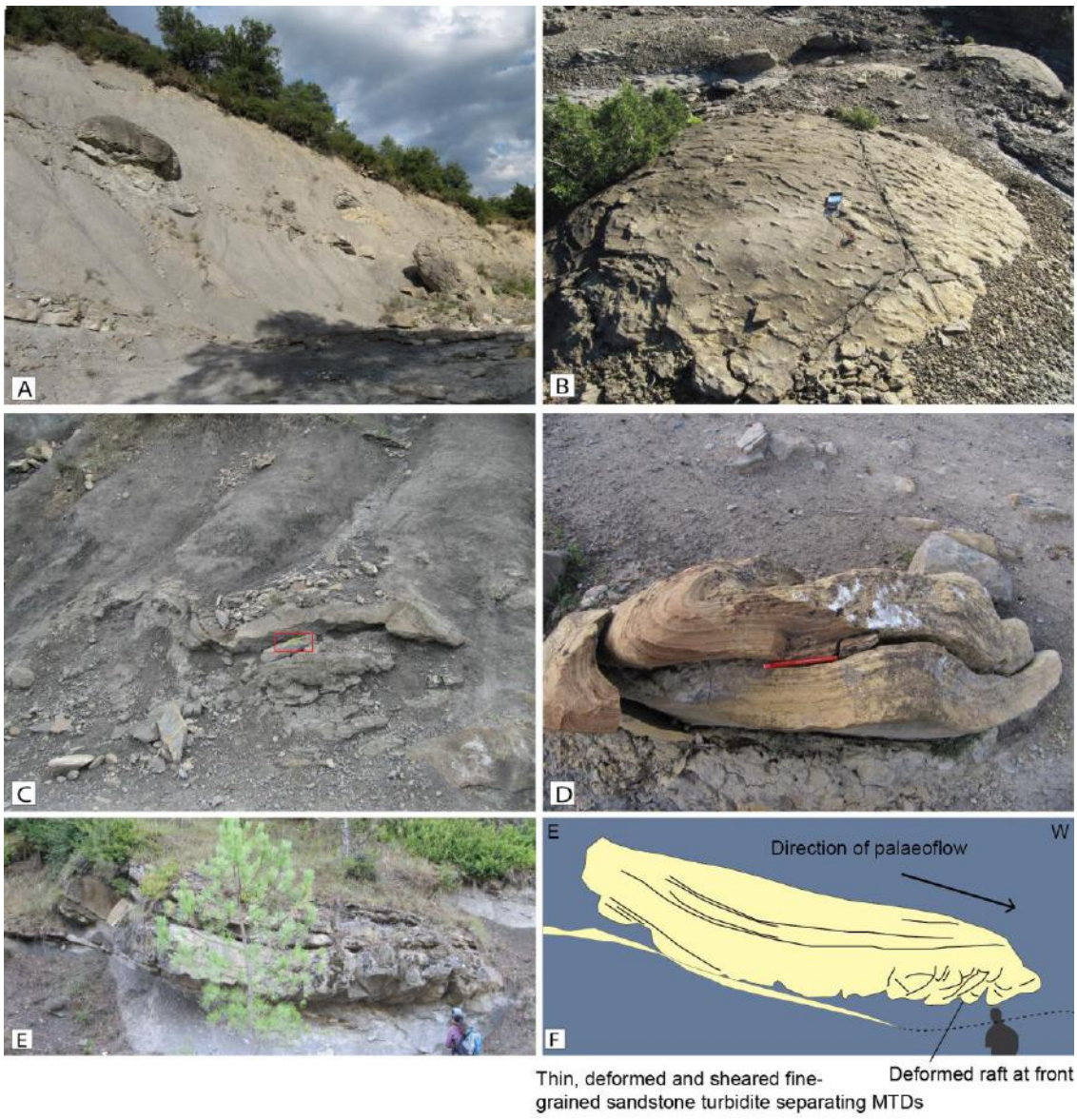

Figure 4.21. (A) ~ 2 m rounded very coarse-grained, nummulite-rich sandstone rafts, Morillo III Fan, Rio Sieste (Locality 40) (B) ~ 1.8 m rounded medium-grained nummulite-rich sandstone raft, Guaso II, Road to Latorrecilla (Locality 46) (C) ~ 4.10 m bedded medium-grained sandstone raft in process of degradation, Morillo I Fan, Rio Ara. Pencil for scale (15 cm) (Locality 23) (D) ~ 0.45 m bedded fine-grained contorted sandstone raft, Guaso I Fan, Gabardilla (Locality 45). (E) Photo and (F) interpretation of 'crumpled' snout of sandstone raft (Locality 14).

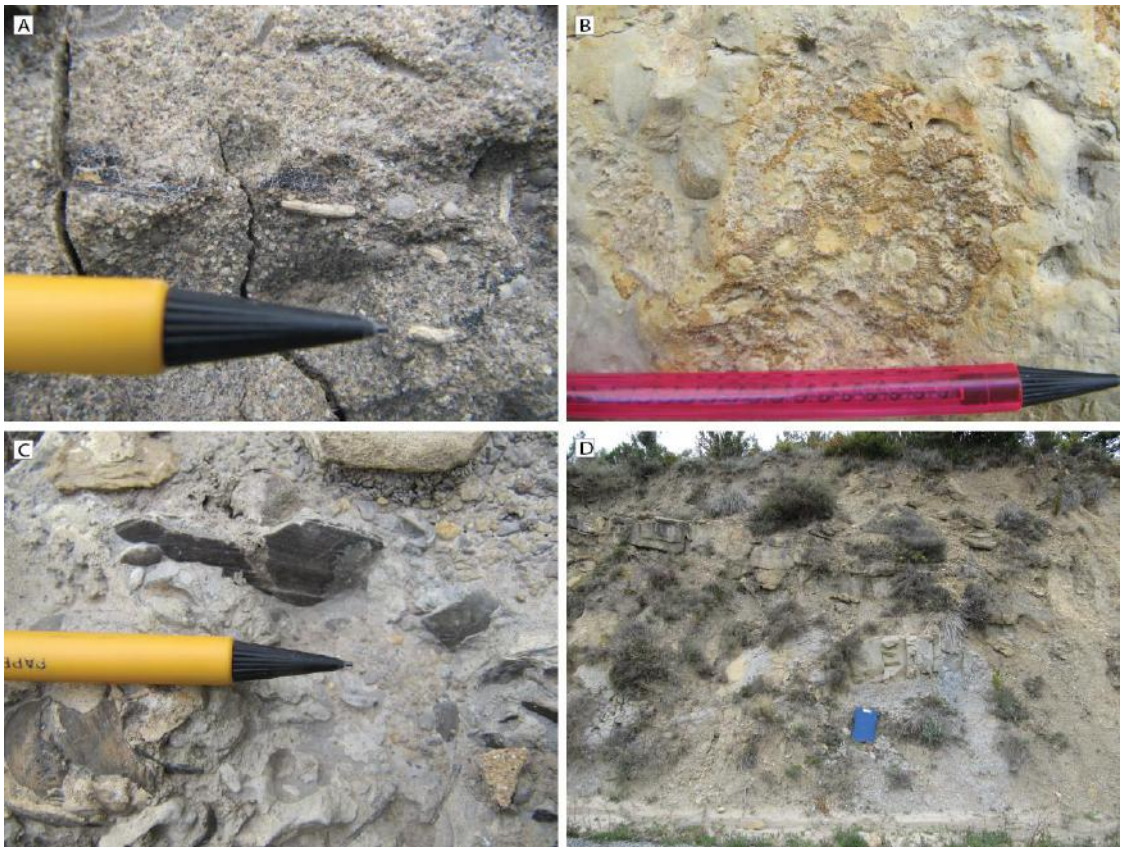

Figure 4.22. (A) Woody fragments and broken echinoid spines (e.g., right of pencil tip) in coarse- to very coarse-grained sandstone boulder (B) Solitary coral in fine-grained muddy boulder (C) Broken shelly fragments (bivalves) in fine-grained muddy boulder (D) ~ 2 m rounded boulder/raft comprising only mud, no fossils observed. Clipboard for scale (35 cm) (Locality 44).

Nummulites, echinoid spines, woody material and solitary corals are generally identified in sandstone boulders, whereas as calcareous muds are generally devoid of any fossil debris. The finer-grained fossil-rich boulders would have been incorporated from shallow water, potentially on the shelf, where enough light would favour the conditions of living organisms.

4.3.4.1 Type Ic carbonate MTDs

Type Ic MTDs are located at the base of the Morillo III Fan, in Locality 27 (Rio Sieste) (Figure 4.23).

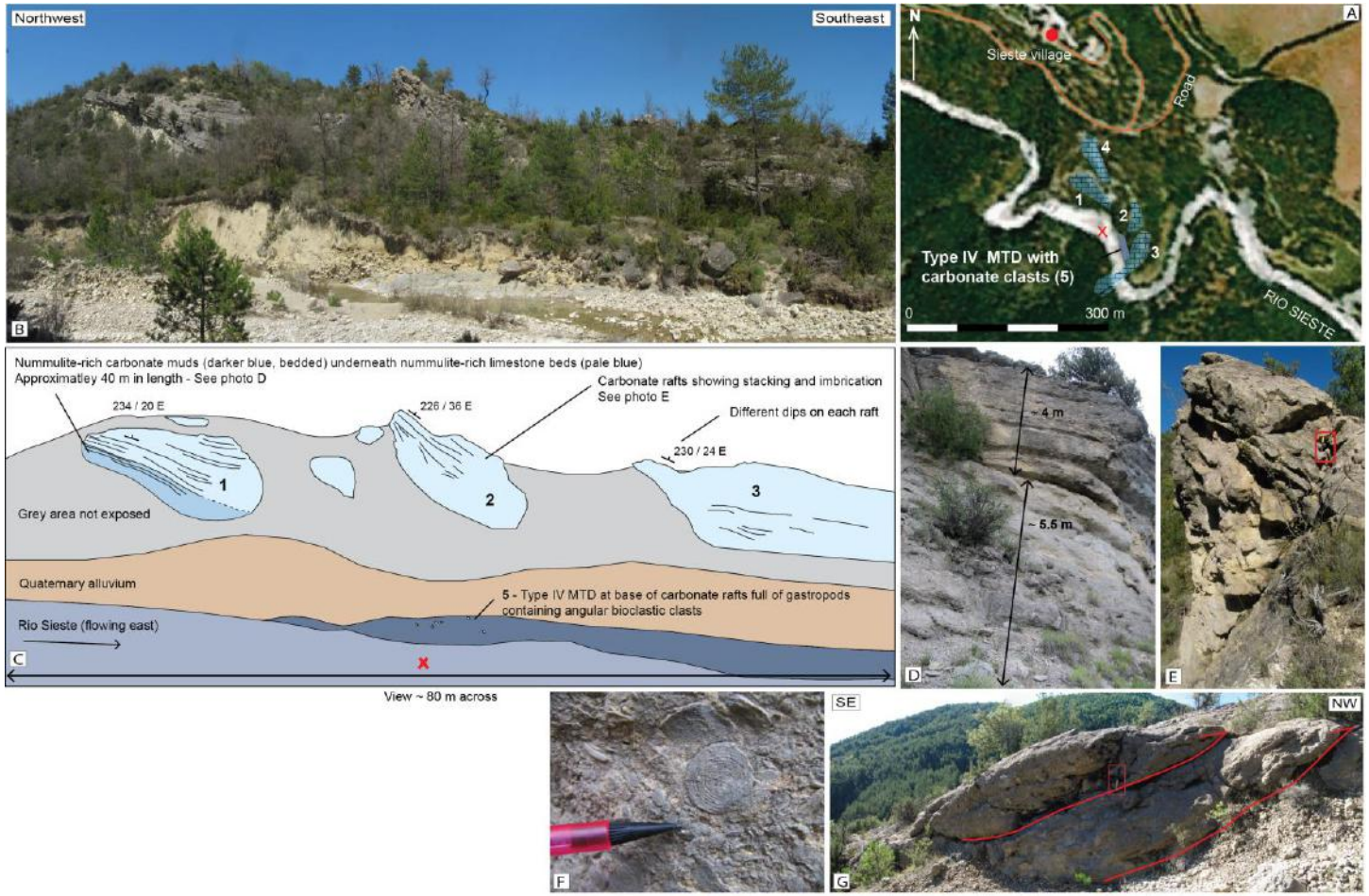

Figure 4.23. (A) Map of Rio Sieste showing approximate locations of carbonate rafts. Red 'x' marks location and numbers 1, 2 and 3 correspond with numbered rafts in images B and C. Map image from Google Earth (B) Photo, and (C) Interpretation of Type Ic carbonate rafts in the Rio Sieste looking approximately north (Locality 27). Three rafts (1, 2 and 3) identified to show imbrication from the southeast. The recessively weathered intervals between each carbonate raft are interpreted as mudstones. Image is ~ 80 m across. (D) Well-bedded structure of raft 1. ~ 4 m scale drawn (E) 4.9 m of blocky (brecciated) and poorly-bedded carbonates at the base of raft 2, with 1.5 m well-bedded limestone at top of raft. Limestone is 6.4 m thickness. Hammer for scale (35 cm) (F) Nummulite-rich carbonates (G) Raft 4 showing imbrication towards the northwest. Hammer for scale (35 cm).

These Type 1c MTDs form discrete packages of carbonate beds, which can be composed almost entirely of nummulites (Figure 4.23-F). The bedding plane of each carbonate package was measured at 20^{o}, 36^{o} and 24^{o} from horizontal in 1, 2 and 3, respectively (Figure 4.23). When rotated to remove the structural bedding dip (20^{o}), this gives primary dips for the three carbonate packages of 0^{o}, 4^{o} and 16^{o} (Figure 4.23). Imbrication measured at this locality also suggests palaeoflow towards 318^{o} (present co-ordinates), akin to the dominant palaeocurrent directions in the Ainsa Basin. These units are interpreted as discrete rafts that show imbrication, determined from the variable dips and lithological characteristics documented at outcrop. Raft 1 (Figure 4.23) shows two distinct lithologies; the basal 5 m is very fine-grained (almost muddy) and relatively soft, containing abundant nummulites; and the top 4 m of thin- to thick- bedded very hard resistant limestones are observed above the calcareous mudstone, which also contains abundant nummulites, separated by a sharp bedding surface (Figure 4.23-D). The nummulite-rich carbonate muds underneath the resistant limestones in Raft 2 are not observed at outcrop. Raft 2 is moderately bedded, ranging from thick- to massive, unstructured beds (from 1.5 to 4.9 m thick). The lower bed (4.9 m) appears brecciated and the upper bed (1.5 m) is well-bedded and structureless, both show abundant nummulites. Raft 3 is observed down to the riverbed of the Rio Sieste. The lower beds also appear brecciated and contain abundant nummulites. Figure 4.23-G is located on the north side of the Rio Sieste (Raft 4), where the carbonates are accessed along a path from the road adjacent to Sieste village (Locality 27). Imbrication is observed towards the northwest.

Carbonate rafts are typically characterised by a distinct sequence of divisions, shown in Figure 4.24. This field example is from Raft 3 (Figure 4.23) located at the riverside of the Rio Sieste. To discuss key features identified in the field, these MTDs are divided into 3 Divisions. Division I is located at the base of the succession, comprising a Type IV MTD (labeled 5 in Figure 4.23), ~ 6 m in thickness. It is not possible to attribute one facies over within this MTD, showing a poorly mixed to homogenised chaotic fabric to more coherent folded mudstone deposits. Nummulites, intact to disarticulate gastropods and echinoid spines are found in the MTD matrix. White- to pale grey angular bioclastic and carbonate clasts are also scattered throughout and appear to be breaking up from the basal surface of the overlying brecciated carbonate block. Division II is characterised by brecciated bedded

carbonates, which is overlain by Division III, showing bedded carbonates that appear undisturbed. Individual carbonate beds appear structureless.

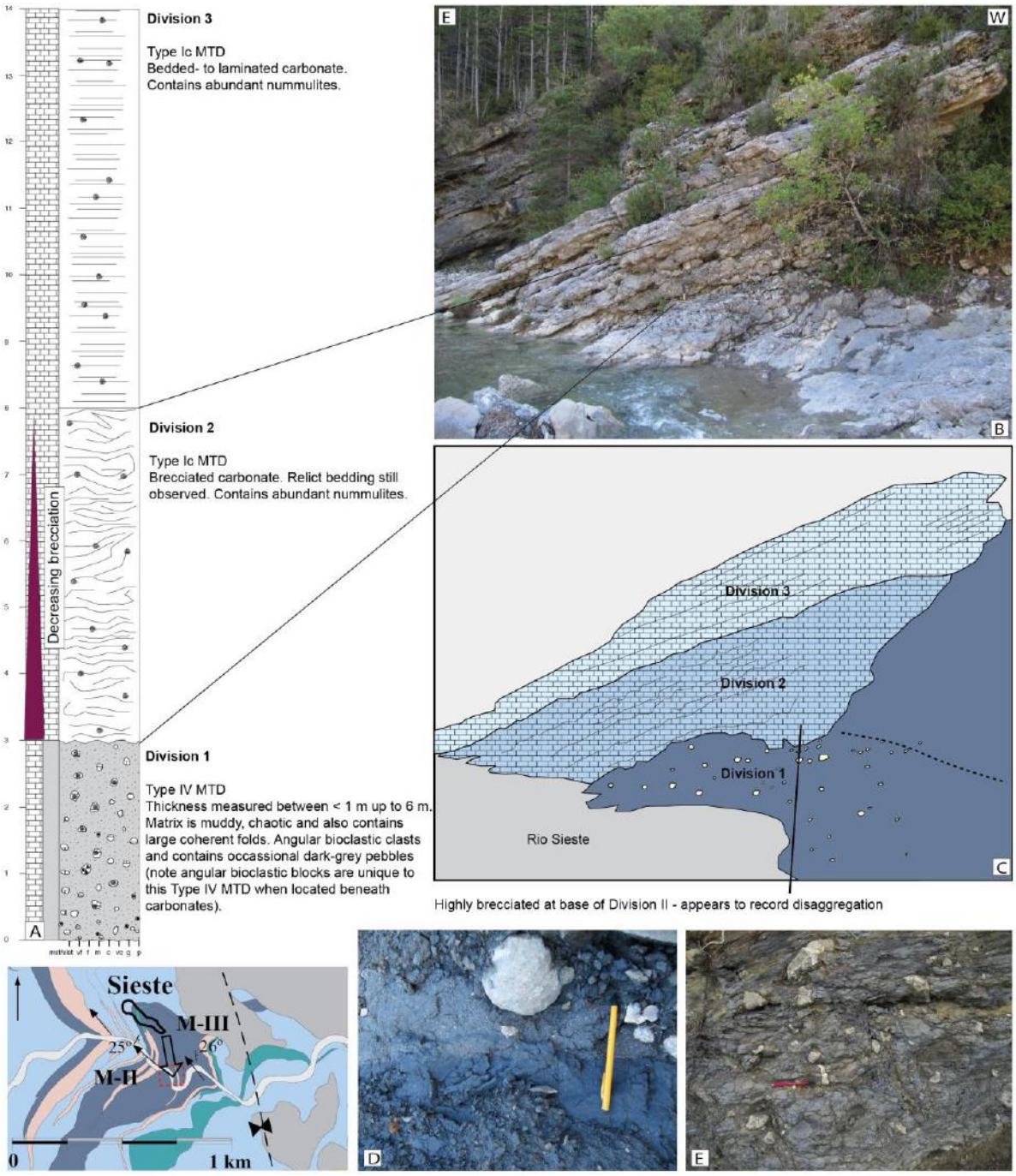

Figure 4.24. (A) Interpreted divisions and sedimentary log through Type Ic MTD (Locality 27). (B) Photo of Locality 27 (B) photo interpretation of Type Ic MTD, split into 3 Divisions (I, II and III). (D and E) Type IV MTD directly beneath carbonates showing angular bioclastic clasts. Pencil for scale in both images (15 cm).

4.3.5 Pebbles

Most pebbles observed in MTDs are rounded to very well-rounded and commonly show molluscan borings in the well- and very well-rounded limestones and sandstones, showing they resided in the littoral zone for some time (Pickering and Corregidor, 2005) (Figure 4.25).

Figure 4.25. Molluscan borings on very well-rounded sandstone pebble showing at least some residence time in littoral zone, Banastón V, Boltaña River (Locality 7).

Pebbles are composed of very dark-grey limestones, very pale-grey limestones, chert, sandstones, quartzite, rarely igneous rocks (such as granite) and metamorphic rocks (such as schist). To document the compositional variability of limestone pebbles in different MTD facies, limestone pebbles were noted as 'pale' or 'dark-grey' as they show unique sedimentary characteristics in the field. At outcrop, pale-grey limestones are moderately- to well-rounded and have a rough surface, whereas dark-grey limestones are well- to very well rounded and have a very smooth surface. To gain further insight to the compositional differences between these limestones, samples were taken for thin-section analysis (Figures 4.26 and 4.27).

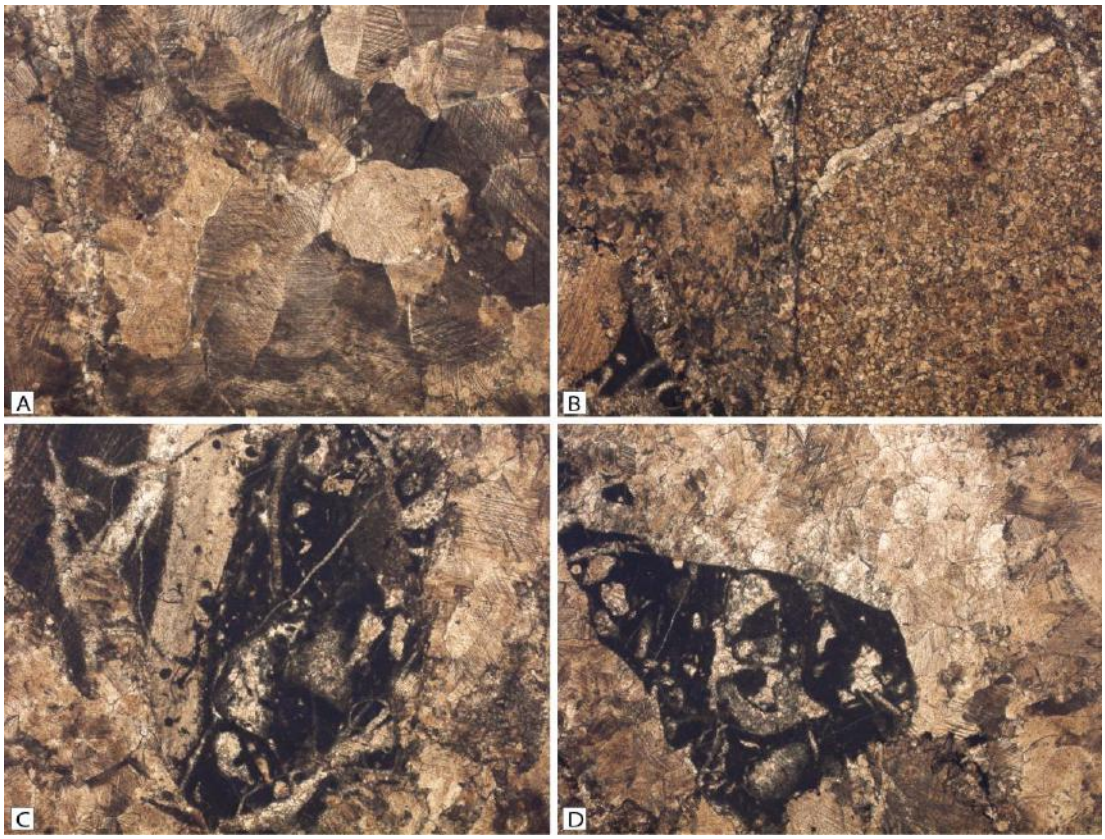

Figure 4.26. Photomicrographs of pale-grey limestone pebbles. All photos in PPL and width of view is 2.2 mm across (A) recrystallised matrix (B) dolomite grain showing vein (C, D) muddy, fine-grained subangular carbonate clasts showing evidence of shelly fragments. Pebble samples from Locality 42.

Thin-sections of pale-grey limestone pebbles show pervasive alteration to sparry calcite cement, with the original structures not preserved in the matrix (Figure 4.26-A). Fossils and shelly fragments are not observed in the matrix, however this could be related to the pervasive recrystallisation. Extraformational clasts are observed within the thin sections (e.g., Figures 4.26-B, C and D). In Figure 4.26-B a rounded clast has been altered to calcite, showing a neomorphic structure. It is not possible to determine the original composition of this clast due to pervasive alteration. In Figures 4.26 C and D, subrounded to subangular clasts, up to 2 mm in length are observed showing shelly fragments replaced with sparry calcite. The dark matrix suggests micrite is prevalent throughout these clasts and has not gone through obvious diagenetic changes.

Thin-sections of the dark-grey limestone pebbles show different sedimentological characteristics to the pale-grey limestone pebbles. Thin sections

show the pebbles are dark in colour suggesting a micritic matrix, which has not been altered to sparry cement. There are high abundances of forams, bryozans, peloids, gastropods and intact shelly fragments. The internal structures of the fossils show replacement to sparry cement (Figure 4.27).

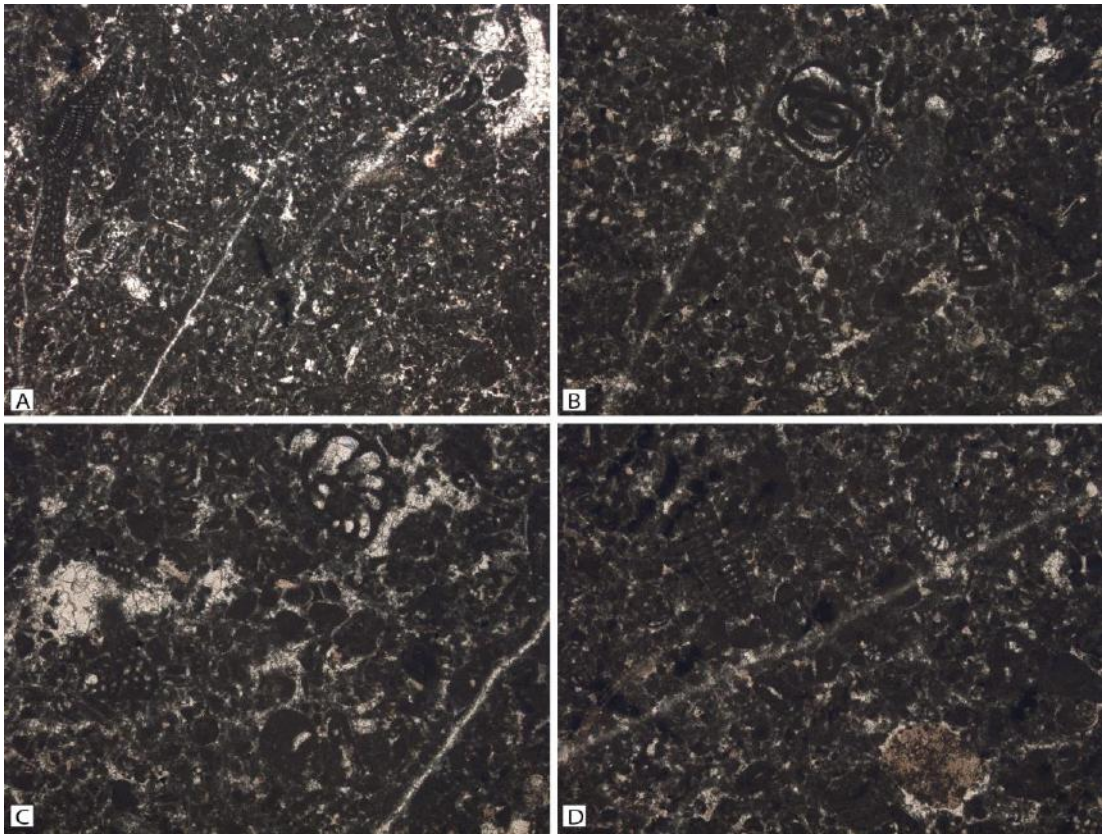

Figure 4.27. Photomicrographs of dark-grey limestone pebbles found in debris-flow deposits. All photos in PPL. Width of view is 4.4 mm across in A and 2.2 mm across in B, C, D. Pebble samples from Locality 16.

The difference in composition between the pebbles suggests that they were originally deposited in different depositional environments, although there is insufficient evidence to provide absolute ages or environments of the limestones in this study. The pale-grey limestone pebbles containing rounded to angular fragments of other limestones, suggest the input of other clasts into the original depositional system.

A pebble composition frequency analysis was carried out in 56 MTDs (22 Type IIa MTDs, 23 Type III MTDs and 11 Type IIb MTDs) around the Ainsa Basin. Using chalk, pebbles were marked and systematically counted in a 1 m^2 transect, if the bed was big enough. If the bed or MTD was < 1 m, two 30 cm^2 grid were used.

Pebble compositions were marked as: (1) pale-grey limestones; (2) dark-grey limestones, (3) sandstone; (4) angular bioclastic clasts; (5) quartzite and metamorphic or igneous fragments, and; (6) chert. Figure 4.28 shows the distribution of MTDs around the Ainsa Basin with principal clast analysis shown as pie charts.

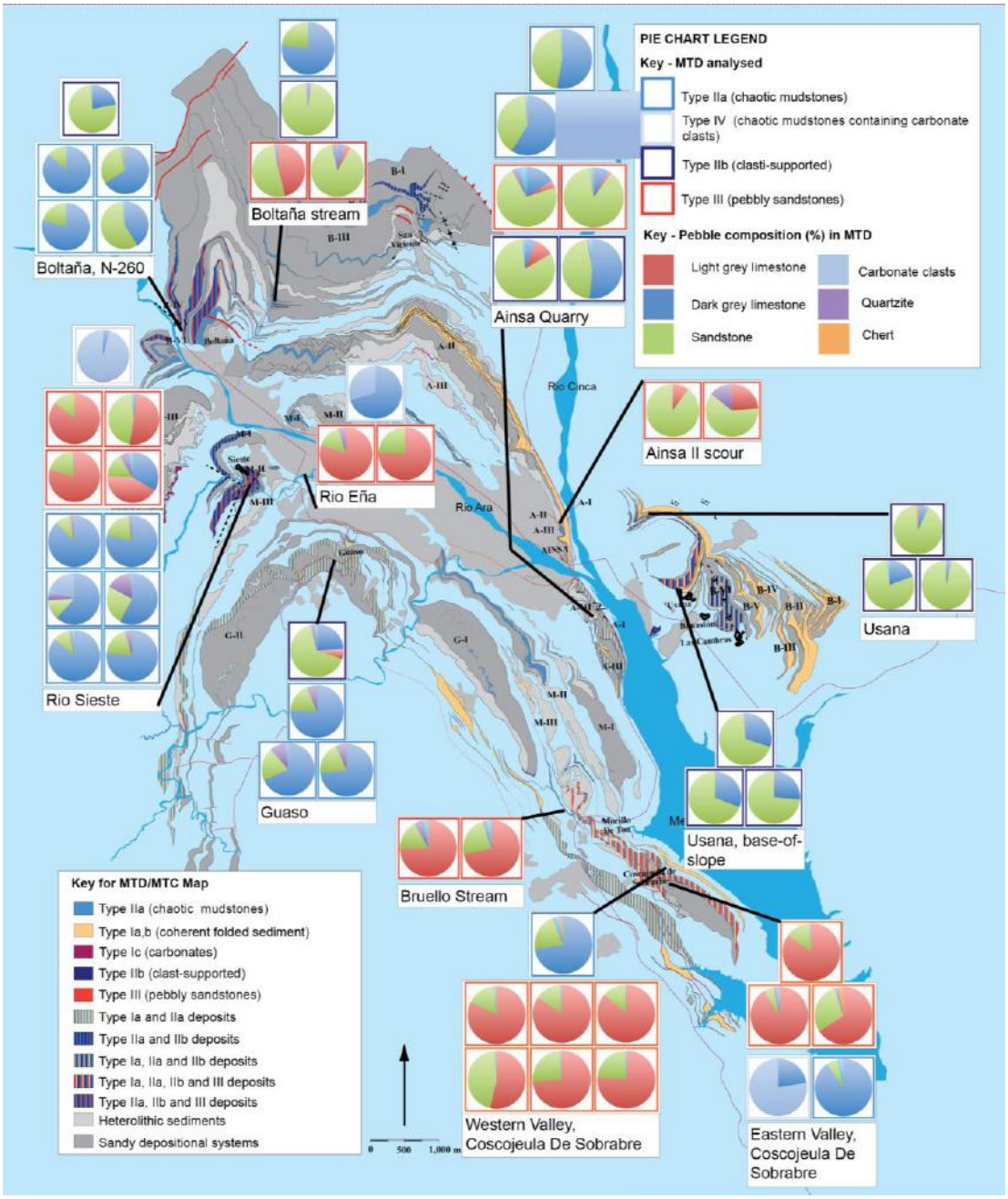

Figure 4.28. MTD pebble composition analysis. The key for pie charts show the type of MTD and the percentage pebble composition in each MTD. The MTDs are grouped by MTD facies type (i.e., Type IIa, Type Ia, Type IIb and Type III) per sedimentary log.

Results show that Type III MTDs show an abundance of pale-grey limestone pebbles (Figure 4.28). Type IIa deposits appear not to contain any pale-grey

limestones and are dominated by the presence of dark-grey limestone pebbles. Only in some cases do Type IIb MTDs exhibit pale-grey pebbles and are typically dominated by the presence of dark-grey pebbles and some sandstones.

4.3.5.1 Clast orientation

Clast orientations were also considered as part of pebble analysis. Outcrops suitable for the measurement of pebble analysis are scarce, and are mainly found in clast-supported conglomerate facies (i.e., Type IIb MTDs). Equant pebbles are not used in the analysis, therefore data was only taken for clasts with apparent axial ratios of 1.5:1 or greater (e.g., Shultz, 1984). For this reason, only a few outcrops permit this analysis type. Apparent imbrication was documented by measuring the angle between each clast's apparent long (*a*-) axis and the trace of the bedding plane in each outcrop. Results are shown and compared to flute marks at the base of sandy SGF deposits in Figure 4.29.

Imbricated pebbles do not show such a clear palaeoflow direction compared to flute marks at the base of SGF deposits, however there does appear to be poor to moderate imbrication of pebbles in clast-supported Type IIb MTDs in Localities 11 and 6 (Banastón System). Pebble imbrication from the Ainsa Quarry (Locality 16) is fairly poor.

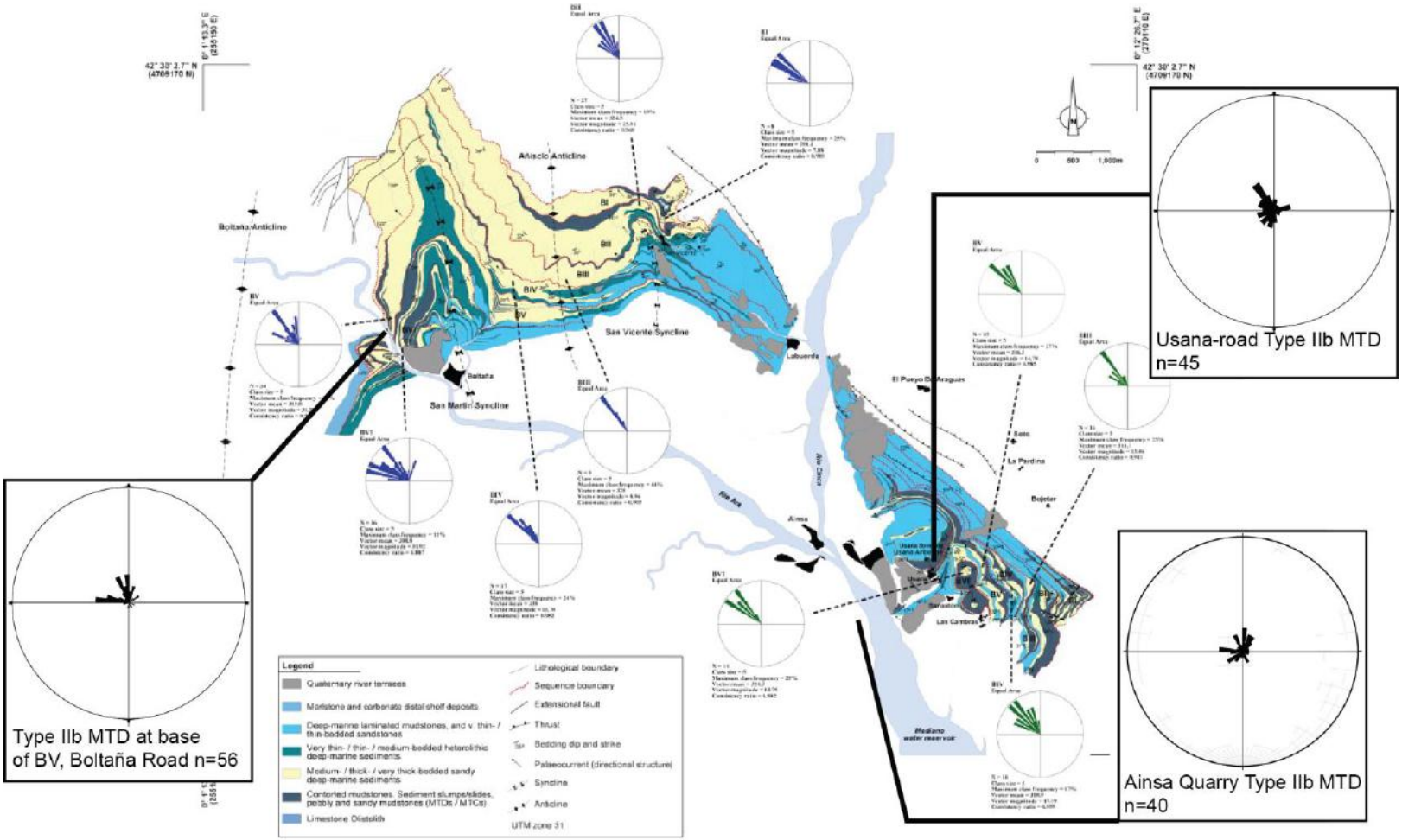

Figure 4.29. Comparison of pebble imbrication analysis in conglomerates and flute marks at the base of sandstone SGF deposits. Localities 11, 16 and 6 were used for this study. Map from Bayliss and Pickering (2015a).

4.4 INTERPRETATION

Data in this chapter presents a series of approaches that document the variability of MTDs from the bed-scale to larger, stacked complexes in the Ainsa Basin. In this section, transport process and models are applied to deposits observed in the field. Sedimentary characteristics, including sediment provenance are also interpreted.

4.4.1 Flow classification and processes

It is commonly inferred that SGF flows comprise two end-members; between fully laminar (cohesive) and fully turbulent flows (non-cohesive) (e.g., Sumner *et al.,* 2009). Mass-transport deposits identified in this study represent a range of processes, including slides, slumps, turbidity currents, debris- and multiphase flows.

4.4.1.1 Type I MTDs

4.4.1.1.1 Type Ia MTDs

Type Ia MTDs are often documented as MTCs, comprised of multiple, discrete deposits. These MTDs show various degrees of sediment deformation; from subtle dip-changes, to more contorted and folded stratigraphy and are ultimately defined in the field by the preservation of primary lamination. Folded sediments are interpreted as slumps and sediment packages that show subtle dip changes are interpreted as slides. At outcrop, it is not possible to separate different processes that result in these types of mass failure and the governing transport mechanisms are similar for both deposits, with basal shear stresses occurring along a single, or multiple planes that permit gravitational movement of the sediment downslope in a submarine setting (e.g., Dott, 1963; Nardin *et al.,* 1979). Type Ia MTDs (i.e., sediment slumps/slides) are transported downslope as rigid to semi-ductile coherent masses of sediment and are therefore more likely to preserve higher topographic relief because of greater cohesion, e.g., Figure 4.16. This data compliments experimental data from Major (1997), who found that deposits from saturated flows (i.e., Type IIa MTDs) typically had a low-relief surface morphology. Type Ia MTDs are interpreted as the deposits of cohesive mass flows that failed from the slope (either upper- mid and/or lower),

developed irregular seafloor topography and were able to create accommodation space for subsequent sandy SGFs to infill.

4.4.1.1.2 Type Ib MTDs

Type Ib MTDs are predominantly composed of contorted sandstones within a chaotic mudstone matrix, documented in this study between 0.45 cm and 1.8 m thick and appear as a single failure event (Figure 4.2). The source for these MTDs is within sandy depositional fans, interpreted as mass-wasting processes such as sediment slumps or slides sourced from localised submarine channel margins or levees (Pickering and Corregidor, 20005). Only small-scale Type Ib MTDs (measured up to 2 m) are documented in this study, however analogous large-scale examples are documented from other ancient basins, e.g., the Rosario Formation, Baja California, Mexico, presented in Kane *et al.* (2007), Figure 4.30.

Figure 4.30. Large slump in channel-proximal locality, interpreted as the inner-levee of a channel complex. Upper Cretaceous Rosario Formation, Baja California, Mexico. The outcrop faces the channel axis i.e., viewer is looking in an approximately channel-distal direction. From Kane *et al.* (2007).

In this large-scale Type Ib MTD, a zone of deformation occurs within the channel-proximal levee and trends parallel to the channel belt. Deformation includes some localised folding, but is dominated by slide blocks and sheet up to 100 m (maximum thickness). For failure to occur in these sediments, basal shear stress occurs along a single, or multiple

planes of weakness that permit gravitational movement of the sediment downslope in a submarine setting (e.g., Alves and Lourenço, 2010, Alves, 2015).

4.4.1.1.3 Type Ic MTDs

Exceptional exposure of Type Ic MTDs are located in the Morillo System (Figures 4.23 and 4.24). This study focusses attention on this depositional system, however Pickering and Corregidor (2000, 2005) also mapped Type Ic MTDs along Rio San Martin, associated with the Ainsa System (Figure 1.16). Pohl and McCann (2014) and Bayliss and Pickering (2015b) also documented Type Ic MTDs in the Morillo System, however there are differences in interpretation between the sediment source and transport processes related with these MTDs. During the Eocene, shallow-marine carbonate platforms surrounded the southern margin of the Ainsa Basin (Pickering and Corregidor, 2005). Pohl and McCann (2014) suggested that the Type Ic MTDs documented at Locality 26 (Rio Sieste) represent large-scale failure of these marginal basin carbonates, likely to be derived from the Guara carbonate platform, southwest of the Ainsa Basin. Bayliss and Pickering (2015b) proposed the same Type Ic MTDs are derived from carbonate-rich SGFs (i.e., turbidity currents).

Evidence for major carbonate-platform failure is documented in the Jaca Basin, with the deposition of so-called 'megaturbidites'. The term 'megaturbidite' is a descriptive label, modified from previous process interpretations and refers to the unusual size of the deposit, implicitly to an exceptionally large catastrophic event (Labaume *et al.,* 1987; Payros *et al.,* 1999). Megaturbidites are interpreted as a single event, consisting primarily of re-sedimented marginal carbonates that can be traced for up to ~ 75 km down-dip, with deposit thicknesses up to 200 m (e.g., the Roncal megabed and other megaturbidites, as described by Johns *et al*., 1981; Labaume *et al.,* 1983a, b, 1985, 1987; Payros *et al.,* 1999; Ogata *et al.,* 2012). Megaturbidites are interpreted to show an overall vertical decrease in grain size, forming a megabreccia with large slabs of carbonate platform debris at the base and calcareous mudstone at the top (Payros *et al.,* 1999; Ogata *et al.,* 2012).

Ogata *et al.* (2012) separate and describe 'Megaturbidite 5' documented in the Hecho Group, south-central Pyrenees into five divisions. From the base: (1) carbonate matrix-supported megabreccia with huge slabs of fossiliferous platform carbonates up to 100 m across and several tens of metres thick; (2) carbonate matrix-supported megabreccia

with large rip-up clasts of calcareous mudstone and basin-plain turbidites; (3) graded matrix-supported carbonate microbreccia with cm-sized (but rarely larger) mudstone clasts; (4) coarse- to fine-grained normally-graded biocalcarenite with a sub-ordinate terrigenous fraction, poorly preserved horizontal and ripple lamination commonly occurring in alternating sets, and; (5) homogeneous calcareous mudstone (Figure 4.31).

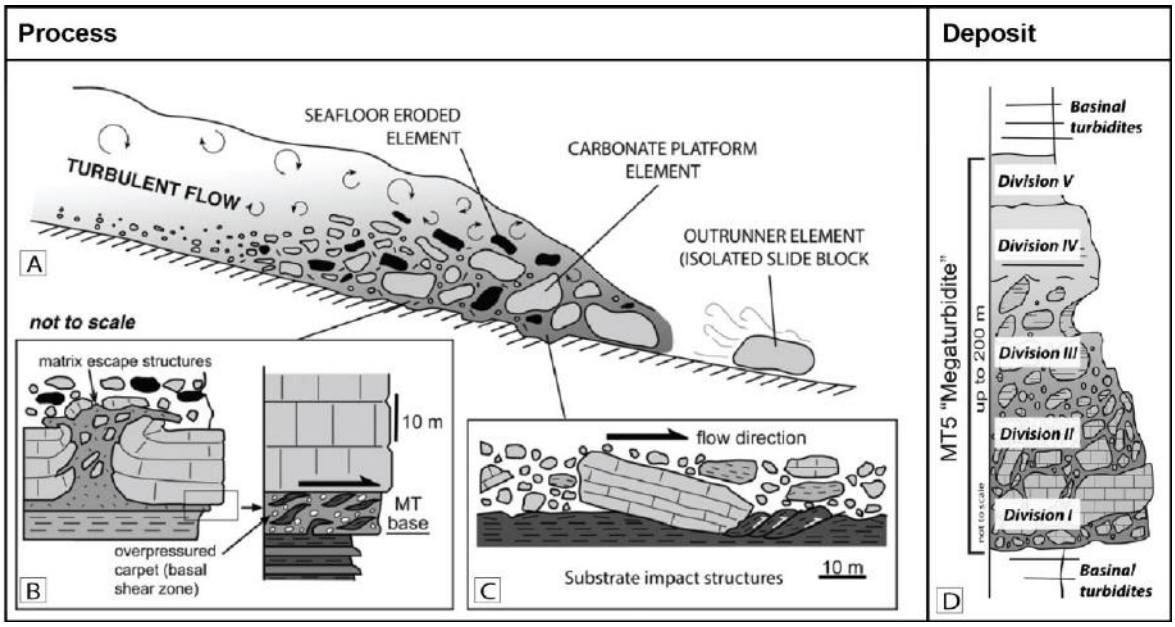

Figure 4.31. (A) Conceptual cartoon showing inferred sliding processes of megaturbidite (B) Cartoon representing the development of overpressure basal carpet and "mushroom"- like fluid escape structures (C) Cartoon showing basal erosion caused by slide blocks impacting the seafloor (D) Conceptual stratigraphic log of megaturbidite showing internal subdivisions. Figure modified from Ogata *et al.* (2012).

Following tectonic activation, the suggested mode of transport and emplacement of megaturbidites is attributed to fast moving, inertia driven avalanche/blocky flows under excess pore pressure (Ogata *et al.*, 2012). Strain at the base of megaturbidites is interpreted to likely occur during late stages of slide evolution (i.e., after the hydroplaning phase and during deceleration and emplacement), when excess pore pressure dissipates leading to the arrest of the mass through frictional freezing and its mass is transferred to the underlying seafloor. In this model, Division I (Figure 4.31-D) is characterised by brittle deformation (brecciation) at the base of massive carbonate slide blocks. Erosion at the front of the flow incorporates large blocks of slope mudstones and basin-plain turbidites, which float on the top of Division II. A slower moving granular flow, composed of loose skeletal material from the shelf (Division III) closely follows the frontal blocky part of the flow, giving way

to a classical bipartite turbidity current (Divisions IV and V). Ogata *et al.* (2012) indicate various soft sediment deformation structures documented beneath the main mass transported blocky part of the flow (Division I).

Results from this study suggest that Type Ic MTDs identified at the base of the Morillo III Fan, Locality 27 (Rio Sieste), appear as discrete imbricated MTDs interpreted as slide blocks, or rafts (*sensu stricto* Labaume *et al.,* 1989; Payros *et al.,* 1999; Ogata *et al.,* 2012), and supports the interpretation that they accumulated at or near a base-of-slope setting (*cf*. Nardin *et al.,* 1979). It is suggested that the Type Ic MTDs are blocks of carbonates that failed from the local margin (e.g., Pohl and McCann, 2015; Bayliss and Pickering, 2015b). Imbrication of the carbonate rafts in the Rio Sieste stack towards the northwest (towards 320^{o}) and suggest a source area for these deposits from the southeast, not oblique from the carbonate platforms to the south and southwest as suggested in Pohl and McCann (2014). It is therefore, more reasonable that the limestone MTDs in the Rio Sieste probably were sourced from slope failure from an intrabasinal carbonate margin in a shallow-marine environment around the Mediano Anticline, as observed at the viewpoint from the path leading east from the village of Samtier, which is directly along strike from the Rio Sieste. Given the palaeogeographic setting in a tectonically active basin, it is likely that sediment failure was seismically triggered, likely from the continued syndepositional uplift of the Mediano Anticline that would have created instability of the constituent limestone stratigraphy (Figure 4.32). Oversteepening of the slope may have also contributed to the failure of the margin (e.g., Alves and Lourenço, 2010, Alves, 2015).

The carbonate blocks identified in the Morillo System do not show the same five divisions as observed in 'megaturbidite 5' (as documented in Ogata *et al.,* 2012), however the base of Raft 3 in this study (Figure 4.24) exposes a significantly brecciated carbonate (*sensu stricto* Division I of Ogata *et al.,* 2012). Type Ic MTDs in the Rio Sieste are also much smaller, up to 40 m in width and 11 m height, compared to the megaturbidites documented in the Jaca Basin (up to 200 m in height). Exposure may be an issue, however there is insufficient evidence to confirm whether these blocks were part of a much bigger flow (i.e., a megaturbidite, as Localities 27 and 61 also do not have associated calcareous mudstones at the top of the rafts.), or whether they occur as discrete elements (*sensu stricto* isolated slide blocks in the model of Ogata *et al.,* 2012). The angular brecciated carbonate clasts incorporated into the poorly-mixed matrix of the Type IV MTD beneath the Carbonate MTD (Division I, Figure 4.37) could provide evidence of basal shear at the base

of the slide blocks (e.g., Figure 4.31 *cf.* Ogata *et al.* 2012; Alves and Lourenço, 2010, Alves, 2015).

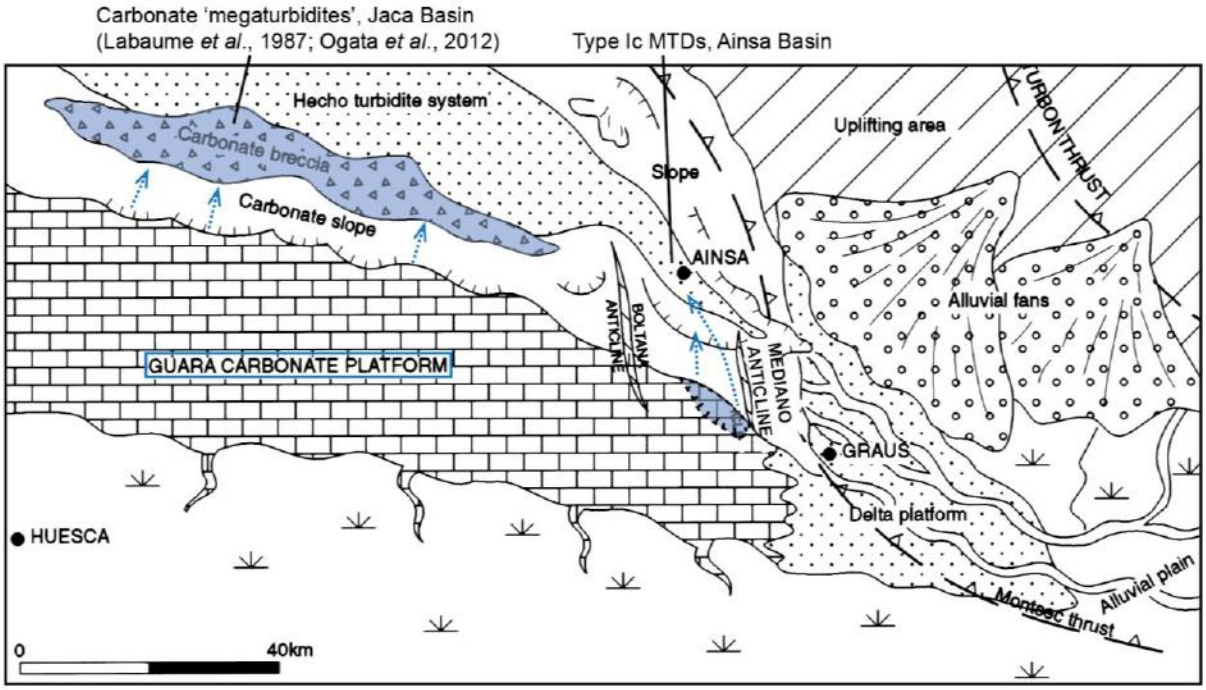

Figure 4.32. Model for shallow-marine source of Type Ic MTDs identified in deep-marine Ainsa stratigraphy . Map is modified from Dreyer *et al.* (1999).

4.4.1.2 Type II MTDs

4.4.1.2.1 Type IIa MTDs

Type IIa MTDs are the most variable deposits identified at outcrop. Individual Type IIa deposits have bed thicknesses of < 1 m (very-thin) up to 12.5 m thick (very-thick) and generally show cumulative thicknesses up to tens-of-metres (i.e., MTCs). These deposits are classified as chaotic mudstones to matrix-supported pebbly mudstones set within in a chaotic matrix. The grain content in the matrix is observed as highly variable, between < 5 to 50 % and the fabric is observed to vary between 'patchy' (heterogeneous) and well-mixed (homogenised). The constituent pebble compositions comprise igneous, metamorphic and lithified biogenic material, but are more commonly composed of carbonates (dark-grey limestones) and sandstones (Figure 4.26). Some partially clast-supported pebbly mudstones are observed to show 'grading' (Figure 4.5-B) and other matrix-supported pebbly mudstones show a random distribution of pebbles (Figure 4.4-B).

Outsized clasts (pebbles and/or sandstone rafts) can settle at the top or base of the deposit due to being either positively or negatively buoyant (e.g., Figure 4.4-A) or are typically distributed chaotically through the ungraded mud-rich matrix, largely supported by buoyancy and cohesiveness of matrix (Pierson, 1980). Some deposits show basal erosion and others show topography. A pebbly mudstone is observed to erode into the underlying sandy SGF deposit suggesting basal shear (Figure 4.4-E). Other deposits interpreted as eroding into sandy substrates are further discussed in Chapters 6 and 7 (Dakin *et al.,* 2013). Type IIa MTDs are interpreted as cohesive, forming irregular sea floor topography to create accommodation space for subsequent sandy SGFs to infill (e.g., Ainsa Quarry outcrop, Figure 4.12), although they are shown to form less topography than Type Ia MTDs (Figure 4.16). Type IIa deposits that do not show any evidence of topography at outcrop may have deposited from flows that were sufficiently dilute to allow unhindered gravitational settling, resulting in a 'smooth' upper surface. However, limited 2-D exposures may simply mean that any topography cannot be observed at the scale and orientation of the outcrop.

The chaotic nature of these deposits with floating outsize clasts suggests emplacement from submarine debris flows. Many debris flows probably involved multiphase fluid flow (i.e., components with cohesive muds and other parts of the flow characterised by non-cohesive grain interaction) involving both solid and fluid forces (Sohn *et al.,* 1999). The observed variability of Type IIa deposits suggests that multiple models could be applied to the observed spectrum of these chaotic facies, reflecting the unique properties of these flows. Debris flows exhibit a wide range of rheological properties and, therefore, a wide spectrum of debris flow processes exist, of which mud-rich and clast-rich end-members can be modelled as a viscoplastic fluid (Johnson, 1970; Nardin, 1979) or an inertial grain flow (Takahashi, 1978). Both models assume deposition occurs *en masse*, as the driving shear stress drops below the plastic yield strength (viscoplastic model), or as the grains lock because of a decrease is the dispersive pressure (inertial grain-flow model) (Sohn *et al.,* 1999). Deposits from Type IIa facies have the diagnostic criteria of true cohesive debris flows, where silt to boulder-sized elements are set in a mud- to grain rich matrix.

Type IIa MTDs are able to carry large volumes of debris, including very large rafts and boulders for kilometres on relatively low slopes (*cf*. Fisher, 1983). Rafts are observed as angular to well-rounded, and some are identified in the process of disaggregation (e.g., Figure 4.21-C). Large outsized rafts are typically observed to have strong alignment,

orientated roughly parallel to bedding (Figure 4.4-A/D), indicative of laminar flow (Fisher, 1983). Sandstone rafts that show a significant amount of disaggregation appearing *in situ*, suggests break-up occurs during debris flow sediment transport (Figure 4.21-C). The bedded nature of some rafts, interbedded between mud and varying-graded sandstones suggests that they have come from eroded slope deposits, potentially channels. However, some rafts contain abundant nummulites and shelly fossils, so it is likely that these rafts were eroded from shallow-marine environments and have been caught up within the flow. The crumpled snout of the large sandstone raft (Figure 4.21-E) suggests a high degree of basal shear at the base of the raft as it travelled downslope at the base of the Type IIa MTD (i.e., debrite). Figure 4.21-E also shows deformation of the raft to suggest the sand was semi-lithified at the time and the base of the raft interacts with the underlying sandstone bed, observed as sheared in the direction of palaeoflow. This evidence suggests the raft was either dragged along either at the base of the MTD, or it travelled downslope as an isolated block. A study by Jackson (2011) used 2-D seismic sections to interpret the geometry and deformation of megaclasts within large-volume cohesive flows, interpreted as debrites, (up to 350 m thick by 5 km in length) in the Santos Basin, offshore Brazil, which are at a different scale of MTDs/MTCs documented in the Ainsa Basin. This study concluded that the megaclasts were deformed as the cohesive debris flow was in motion due to differential shear stresses and a weakly turbulent nature associated with the flow (e.g., Mulder and Alexander, 2001). Although this study presents a scale several orders of magnitude larger than the Ainsa Basin, the amount of deformation sandstone rafts show in the field suggest that debris flows are subject to a great amount of shear enabling the rounding, disaggregation and crumpling of sandstone rafts as they travel downslope within a cohesive body (e.g., Alves and Lourenço, 2010, Alves, 2015).

4.4.1.2.2 Type IIb MTDs

Type IIb deposits are classified as clast-supported pebbly mudstones and are generally measured as the thinnest MTDs. The sand-to-mud ratio of the matrix in this facies-type is variable, however is mainly dominated by mudstone. The constituent pebble composition comprises sandstones and carbonates (dark-grey limestones) (Figure 4.27). These MTDs are observed as poorly sorted- to graded deposits that can show evidence of some imbrication (Figure 4.29). In deposits that show concentrated pebbles near the base (Figure

4.5-B), the internal succession of structures in Type IIb deposits are consistent with temporal changes in flow type associated with the passage of multiphase granular flow, i.e., a flow with varying spatial and temporal rheological properties both vertically and laterally within the flow. It is concluded that in some cases, these MTD can form a lower division of a two-layer, or bipartite deposit, supporting the conclusion of Pickering and Corregidor (2005), Figure 4.33.

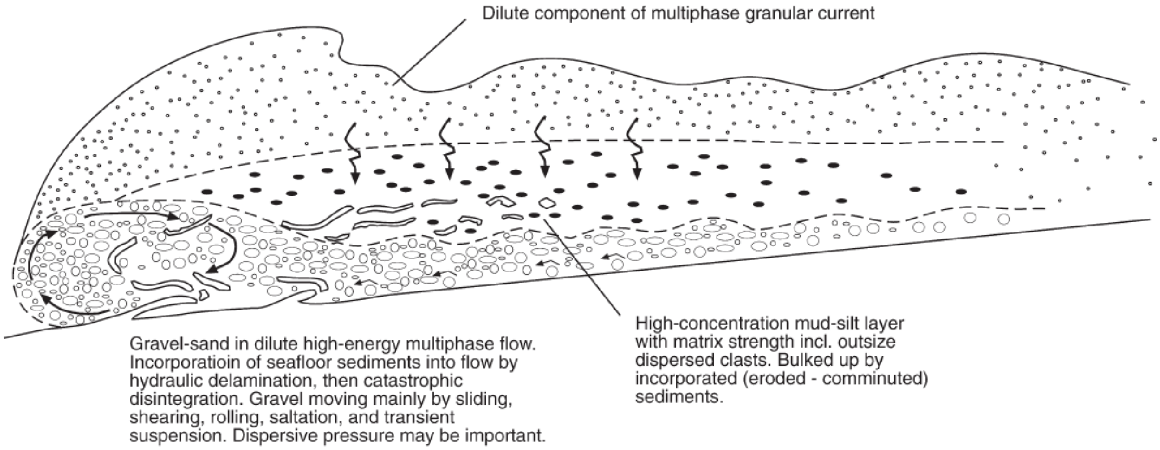

Figure 4.33. (A) Multiphase granular flow process to explain Type IIb with pebble concentrations at the base. From Pickering and Corregidor (2005).

The lower deposit comprising poorly sorted pebbles in a muddy matrix suggests emplacement by debris flow processes, typically defined by an erosional base. The muddy matrix likely enhanced the mobility of the flow by lubricating frictional clast interactions to maintain high pore fluid pressure. The upper deposit (Type IIa) is disorganised and comprised of a hyperconcentrated flow, as described by Sohn (1999, 2002). In comparable deposits, the majority of multiphase deposits show clast-supported pebbles and cobbles in the lower part of the flow and matrix-supported pebbles in the upper part. Grading of pebbles near to base of Type IIa MTDs may be possibly associated with kinetic sieving, where smaller grains percolate into spaces that open up between larger grains and are likely to create zones of intense basal shear (Legros, 2002; Talling *et al.*, 2012).

4.4.1.3 Type III a and b MTDs

Type III MTDs are composed of the highest proportion of sand-grade sediments typically comprised of a coarse sandy matrix. Type III MTDs are documented as both matrix and

clast-supported. In clast-supported deposits, poorly developed reverse or inverse grading is likely to reflect high dispersive pressure between large clasts (Lowe, 1976, 1982). Due to resistive weathering of this facies type, clasts were not measured for imbrication analysis. These deposits are interpreted to reflect deposition from a range of processes, including deposition from concentrated sandy, high-density flows, rapid deposition by cohesionless processes, i.e., frictional freezing at the base of a high-concentration turbidity current (Lowe 1976, 1982). These flows may have been locally erosive along its flow path from reworking upper parts of underlying stratigraphy (Lowe, 1982). These deposits are maintained in a dispersed state against the force of gravity by an intergranular dispersive pressure arising from grain interactions within the shearing sediment. In this model, grain dispersive pressure can be maintained by: (1) the interstitial fluid being denser than the ambient fluid; (2) the interstitial fluid becoming turbulent, or; (3) escaping pore fluids partially liquefying or fluidising the dispersed particles. Deposition of sediment occurs as the applied shear stress drops below the yield strength of the moving material and deposit *en masse* by frictional grain resistance (frictional freezing). Should these flows become turbulent, high-density turbidity currents may show normal grading.

There are a few examples of Type IIIb deposits showing channel-like clast-supported MTDs (with a mixed sandy to muddy matrix) immediately overlying a pebbly sandstone showing an erosive base (Figures 4.7-A/B). A possible transport mechanism to explain these deposits are that they are the products of multiphase granular flows, as described by Sohn (1999), where sediments may have undergone flow transformations, or multiphase density flows (between debris flow, concentrated density flow and turbidity currents). In this model, debris flows (i.e., the clast-supported conglomerate) are interpreted to have travelled on and behind a water-rich, gravelly sandy bed (i.e., high-concentration turbidity current) carrying well-rounded pebbles as a basal concentrated layer on a traction carpet, forming a multiphase flow (Figure 4.34).

4.4.1.4 Type IV MTDs

Type IV deposits comprise mixed facies types of Ia and IIa deposits. A possible explanation for the deposition of this facies showing ‘transitional’ elements between debris flow (identified at outcrop by a chaotic matrix) and sediment slump/slides (identified as folded mudstone stratigraphy) is a deposit recording partial flow transformation, where the

deposit records the evolution from Type Ia to Type IIa cohesive flows, near to the source of failure. In this instance, cohesive forces, such as the shear stress, may have overcome ignition processes for mass movement to occur. An example of an equivalent Type IV MTD is presented from the Ross Formation, County Clare, Ireland, interpreted by Posamentier and Martinsen (2011) (Figure 4.35).

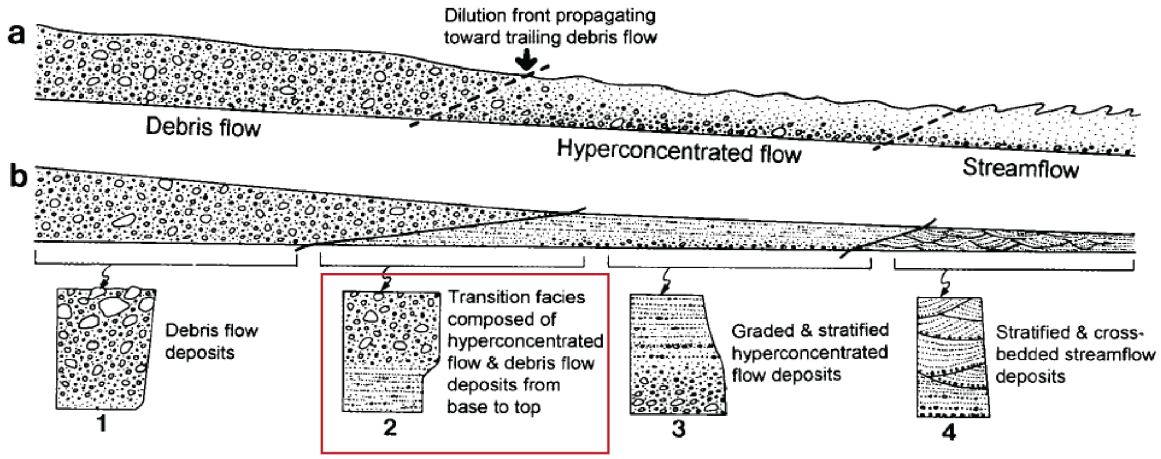

Figure 4.34. (A) Hyperconcentrated flow generated by dilation at the leading edge of debris flow (B) Resultant deposits from this sediment flow showing representative facies in proximal and distal parts. Modified from Sohn *et al.* (1999).

The Ross Slide (Figure 4.35) outcrop reveals that the deformational style from near to far (lower left or lower right) appears as a debrite showing extensive internal deformation, with a slide in the background showing little internal deformation. Mutti *et al.* (2006) and Ogata *et al.* (2010) described such deposits as 'blocky debris flow-deposits' from the Specchio Unit, Northern Appenines and proposed a conceptual model of a mass-transport facies evolutionary scheme. The rapid change of deformational style in MTDs shows that they are part of a continuum of deposits formed by changing processes, depending on internal strain and local factors (Mutti *et al.*, 2006; Ogata *et al.*, 2010; Posamentier and Martinsen, 2011), an observation also documented in seismic data by Omosanya and Alves (2013) in the Espírito Basin, offshore Brazil. In the Ainsa Basin, a mud-rich slope may suggest why a higher percentage of transitional facies are found in proximal areas.

Type IV ‘mixed facies’ deposits are also identified under Type Ic MTDs (Figure 4.24). The study by Ogata *et al*. (2012) shows a zone of basal shear under slide blocks up to 100 metres across and several tens of metres thick (Figure 4.31-B). They interpret a 1 – 2 m zone of basal shear, comprising mud-clast and carbonate breccia, separating the slide block from underlying underformed bedded sediments. The facies identified in the Ainsa Basin show similarity to observations from Ogata *et al.* (2012).

Figure 4.35. Ross Slide, Upper Carboniferous County Clare, Ireland. From Posamentier and Martinsen (2011). Person for scale.

4.4.2 Co-genetic deposits

Facies attributes documented in this study identified discrete MTDs within MTCs at outcrop. To determine whether stacked MTDs were deposited as separate events triggered at different times and juxtaposed together, or whether they were co-genetic in origin, chi-tests were undertaken to determine a probability value that would accept or reject the null hypothesis “*there is no relationship between facies patterns”.* The p-value from the chi-test supports the relationship between Facies Pairs 11A, 13B, 14A and 15B, suggesting a predictive sequence of events formed by co-genetically linked MTDs, with failure triggered

at the same time but evolving separate flow processes (*sensu stricto* Haughton *et al.*, 2003, 2009). Using outcrops from the Karoo Basin, South Africa, Van der Merwe *et al.* (2009, 2011) also explored the possibility co-genetic mass-transport events. They discussed the process relationship between sandstone slides and debrites, suggesting one example from outcrop could have originated from a single co-genetic event. Fine- to medium grained highly deformed sandstone clasts are suspended in a debritic siltstone matrix. The foundered sandstone slide is comprised of coarser sand compared to the sandstone clasts in the debrite. It was therefore concluded that the slide and debrite were events triggered at different times from a different place. The chi-test results presented in this study require the addition of more data to gather statistically valid results, which would require more field data from another ancient basin.

4.4.3 Turbulent SGFs and flow deflection over cohesive MTDs

Identifying relict topography (i.e., an undulose upper surface resulting from the deposition of cohesive MTDs/MTCs) at outcrop can be difficult, as topography may be "apparent" because it formed from later SGFs that sculpted the top of underlying flat-surfaced cohesive deposits (MTDs). This section considers flow variables documented from the scientific literature that affects the flow regime of SGFs in submarine settings, and relating them to process interpretations observed in the Ainsa Basin.

Uniform and non-uniform flow describes spatial changes in flow velocity, which typically occur in SGFs that exhibit turbulent behaviour, such as turbidity currents (Middleton, 1967; Lowe, 1976; Kneller, 1995). Uniform flow is defined as a succession of fluid particles having identical velocity vectors at a point fixed in space so that a flow remains unchanged with time. In a non-uniform flow, velocity is not the same at every point. For example "waxing" or "waning" flow conditions provide a temporal change in flow velocity at a given point. Waning, or depletive flow describes fluid particles that have successively lower velocities, so that the flow passing a fixed point becomes slower. Waxing, or accumulative flow describes fluid particles that have successively higher velocities at a fixed point, thereby representing acceleration in a flow (Kneller, 1995). Depending on flow thickness and the height of an obstacle in a flow (such as a mounded cohesive MTD), as an SGF overrides an irregular topographic profile, variable basal flow

conditions may affect the vector of the flow and may locally increase or decrease flow velocity.

Waxing and waning flows are commonly associated with hydraulic jumps, which occur at transitions between supercritical and subcritical flow (this is not a one-way process but can also occur as cyclic steps). Hydraulic jumps cause abrupt changes resulting in a rapid increase in thickness and decrease in downstream velocity (Sumner *et al.*, 2009), (Figure 4.36). In a supercritical flow regime, inertial forces dominate the gravitational force; therefore the flow travels faster resulting in a flow that is relatively thin and fast. In a subcritical flow regime, gravitational forces exceed inertial forces, therefore, the flow travels slower, resulting in a flow that is relatively thick and slow (Sumner *et al.*, 2013). Fluid turbulence is commonly seen at the transition between super- to subcritical flow. In a subaerial open-channel fluvial setting, hydraulic jumps occur due to the presence of weirs. Sumner *et al.* (2013) use direct measurements in active submarine density currents in the Bosphorus Strait, Black Sea to discuss the importance of hydraulic jumps in marine systems.

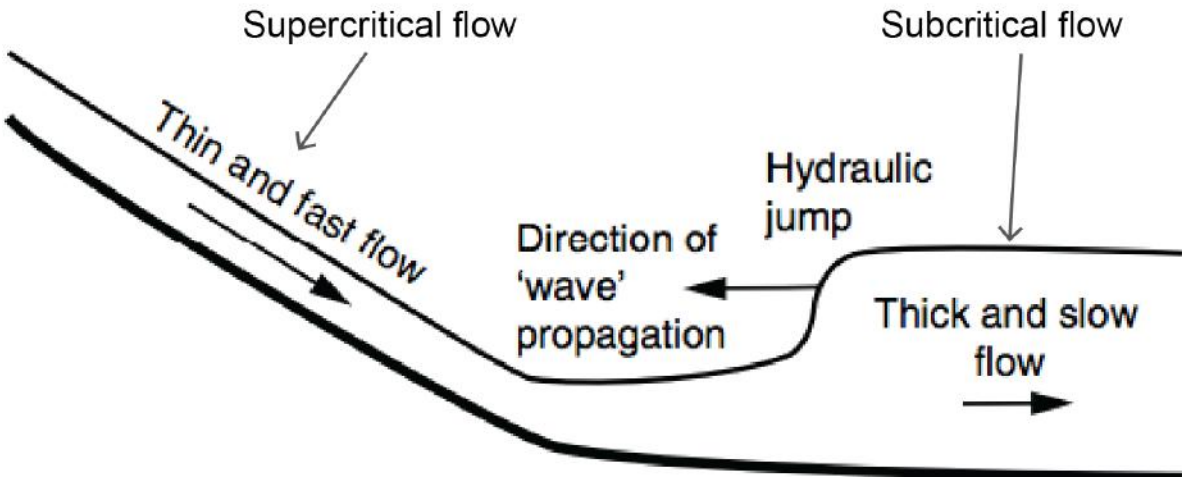

Figure 4.36. Schematic diagram showing key features of a hydraulic jump. From Sumner *et al.* (2009) Abrupt changes in flow velocity and density is commonly found at hydraulic jumps, where flow rapidly decreases and flow thickness abruptly increases. These phenomena are thought to be a key control governing sediment distribution in deep water systems.

Based on outcrop data observed in the Ainsa Basin, hydraulic jumps (as those identified in subaerial settings and those documented in submarine settings in Sumner *et al.* 2013) could form from the presence of pre-existing topographic mounds on the seafloor from cohesive MTDs, such as in the example of the Ainsa Quarry (Figure 4.12). It is

interpreted that the cohesive MTD created an irregular topographic surface on the seafloor. Depending on the flow thickness relative to the topographic profile, sandy SGFs (now preserved as sandstones onlapping the margins, Figure 4.13) are likely to have been diverted around the obstacle. If turbidity currents were flowing at a supercritical flow rate, coupled with an uneven topographic surface acting as a barrier to flow, they may have enhanced the amount of erosion on the seafloor. By changing the gradient and flow conditions, a localised hydraulic jump may have formed; increasing turbulence related to a change from super- to subcritical flow. Measurements of palaeoflow vary between 292° and 330°, therefore, a change in flow conditions may have diverted the vector of a turbidity current, and also could have formed a hydraulic jump causing local pockets of turbulence and therefore may enhance erosion. Evidence of flow deflection is also observed at Locality 24, where topography from cohesive deposits may have deflected the vector of the overlying flows. It is therefore suggested that the topographic signature of the underlying substrate can affect the transport direction of turbidity currents (Figure 4.17).

4.4.4 Sandstone channels in MTCs

Contrary to turbidity-current flow deflection and/or enhanced erosion of a topographic template formed by cohesive deposits, evidence from outcrops in the Ainsa Basin also show how sandy SGFs may have eroded and infilled small-scale discrete sandstone channels within MTDs (Figures 4.18 and 4.19). Flute marks preserved at the base of a very-thick structureless sandy channel margin at Locality 24 and 33 (Figures 4.18 and 4.19) suggests erosion, forming an isolated large scoured channel, and deposition from a large sandy flow. One model to suggest this type of erosion could be from large turbulent events and result from the late expansion phase of the channel that formed ‘wings’ following initial aggradational filling of the channel axis (Elliott, 2000). On the contrary, thin- to medium sandstone beds show laterally accreting amalgamated channelised sandstones at Locality 30 (Figure 4.20). This may suggest erosion from multiple events that routed their way along existing channel pathways. The gravelly sandstone (Figure 4.20) may suggest sedimentation by traction-dominated processes and the accumulation of a point-bar in the inner bend of a sinuous channel element (e.g., Peakall *et al.*, 2007; Elliott, 2000).

4.4.5 Sedimentary characteristics of MTDs and MTCs

4.4.5.1 Pebbles in Type II and III MTDs

Pebbles that are found in deep-marine sediments would have been stored in subaerial environments for considerable time periods to form the well- to very-well rounded clasts, with evidence for an up-dip source including the presence of molluscan borings. Pebbles within MTD facies of the Ainsa Basin were mainly delivered into the deep-marine environment from mass-transport processes relocating them from fluvial, near-shore and deltaic systems (Pickering and Corregidor, 2005).

The variation of pebble compositions between Type IIa and Type III MTDs (i.e., the dominance of fossiliferous dark-grey pebbles documented in pebbly mudstones compared to the dominance of calcite-cemented pale-grey pebbles in pebbly sandstones, Figure 4.28), imply different sediment source areas to the Ainsa Basin. A study by Gupta and Pickering (2008) carried out point-count analysis on sandstone samples and from this data also postulated different carbonate sources. These authors suggest the main source area for sediment input into the deep-marine succession was from the rising Pyrenean Orogen, that funneled Cretaceous-aged extrabasinal sediment through the Tremp-Graus Basin (Mutti, 1977; Marzo *et al*., 1988; Vincent, 1999), however intrabasinal carbonate grains were derived from the coeval marginal shelf, where carbonate factories were active during deposition of the Ainsa Basin. A similar provenance study of siliciclastic SGF deposits of the Hecho Group was undertaken throughout the Ainsa and Jaca basins (Caja *et al.*, 2010), which showed analogous results; that carbonate grains within sandy SGF deposits of the Hecho Group are found to be mainly derived from Cretaceous and Paleocene limestones, and intrabasinal grains were sourced from coeval shelf carbonate factories.

Three main fan-delta systems were active during the deposition of the Hecho Group: (1) the Campanúe fan-delta, comprises conglomerates and sandstones derived from Mesozoic and Paleozoic source rocks; (2) the Sis conglomerate (also referred to as the San Esteban Fan), and; (3) the Claramunt Fan. The Sis fluvial system showed evidence of the first significant exhumation event in the Pyrenean Orogen, dated around 54 Ma (Early Ypresian) (Vincent, 1999, 2001; Caja *et al.*, 2010) (Figure 4.37).

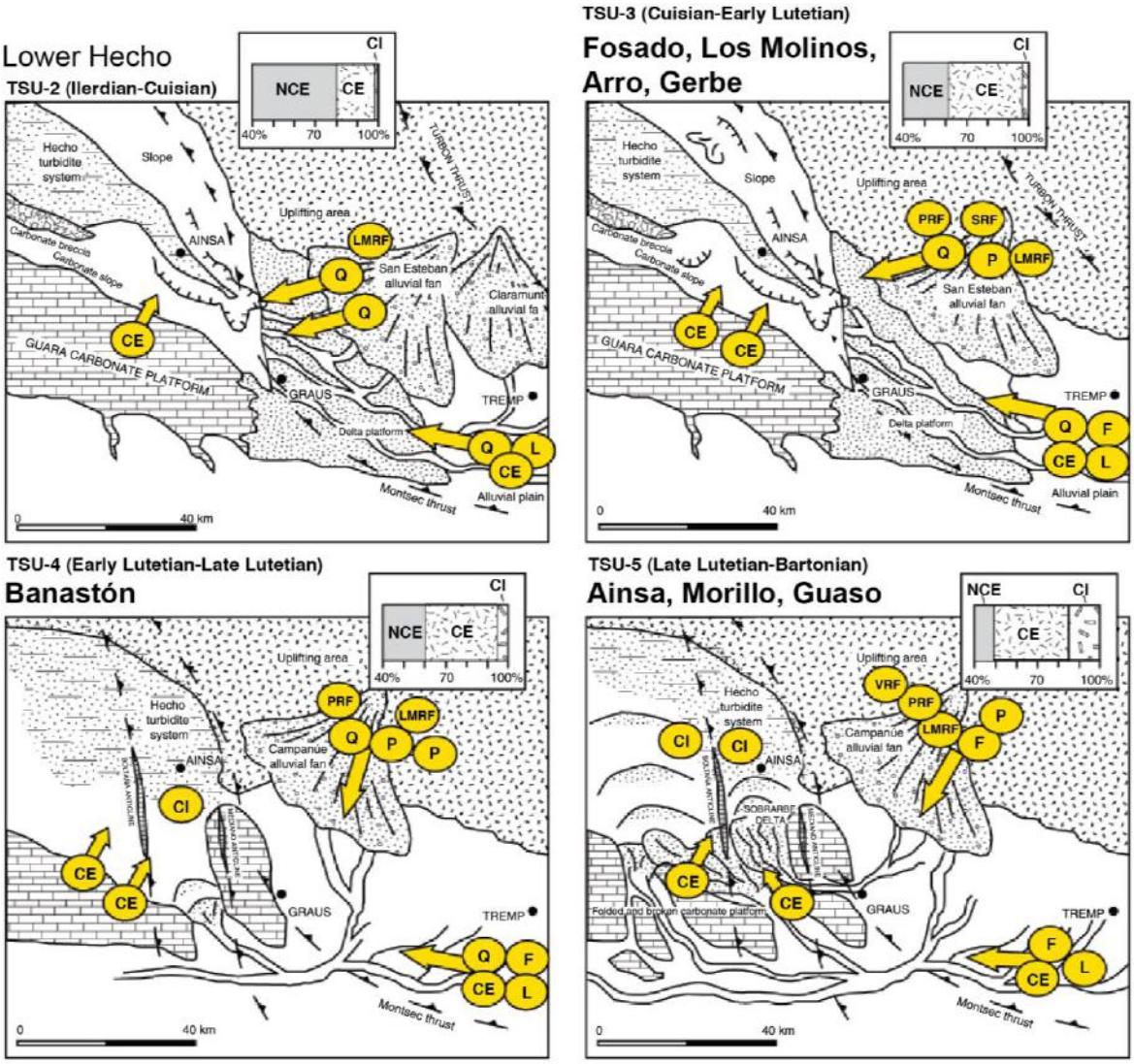

Figure 4.37. Palaeogeographic reconstruction of the Ainsa Basin and surrounding areas during the Eocene. TSU – Teconostratigraphic unit, CE – extrabasinal carbonates. CI – Intrabasinal carbonates. F – Feldspar, L – Lithics, Q – Quartz, SRF – sedimentary rock fragments. Modified from Caja *et al.*, (2010).

This study examined the occurrence of different compositions of pebbles within different MTD facies. Although the rising Pyrenees and onset of exhumation may explain the presence of pebbles in the basin, pebbly sandstones and pebbly mudstones appear to show different sources. The abundance of extrabasinal carbonate pebbles are attributed to the exhumation of the rising Pyrenees, such as the Sis Valley which could have sourced pebbles during deposition of the Gerbe System (further discussed in Chapter 5), although this is difficult to constrain. The Sis palaeovalley is a stacked conglomerate body ~ 20 km long, 6 to 7.5 km wide and 1,400 m thick (Puigdefábregas *et al.*, 1985; Vincent, 1999, 2001). This system established and drained the deforming Pyrenean Orogen, which

initiated in the Late Paleocene (59.5 Ma). The palaeovalley was active for 38 Ma into the Early Lutetian (Vincent, 2001). Although the pebble compositional analysis carried out in this study is not sufficient to be used as provenance data, it does compliment the idea of at least two sediment sources input into the basin. Pebbly sandstones are deposited contemporaneously within depositional systems and may represent storage areas being tapped further up the shelf, where the 'pale-grey' limestones are being sourced. Mud-rich debrites are likely to be sourced from the lateral margins of the Ainsa Basin, which could suggest a late-stage sedimentary input to the system.

4.5 SUMMARY

From the identification of MTD facies associations and architectural elements, the complexity of MTD facies has been explored in the Middle Eocene Ainsa Basin. The principal characteristics of these deposits are summarised as follows:

- The abundance of woody material and disarticulated bioclastic material, articulated echinoid spines, solitary corals and gastropods in some debrites, suggest redeposition from a shallow-marine and terrestrial sediment source area.

- The classification scheme of Pickering and Corregidor (2005) purposefully uses more general terms to avoid the controversy of high-concentration *versus* low-concentration, or concentrated turbidity currents, sandy debris flow, debris flow, etc. The complexity of these deposits is discussed with flows that may have transitional properties between turbidity currents and debris flows (Lowe *et al.*, 2003), linked flow processes (e.g., Haughton *et al.*, 2003, 2009) and multiphase flows (e.g., Sohn *et al.*, 1999, 2002). The fundamental sedimentological difference between mass flows (i.e., Type I, II and III MTDs documented in this study) and fluidal flows (i.e., turbulent flows such as turbidites) is depositional: mass flow deposits are emplaced by immobilisation of the flowing medium, whereas fluidal flow deposits form by grain-by-grain accretion of sediment on the bed (Shultz, 1984).

- In the absence of thin sandstone beds between MTDs (*sensu stricto* Major, 1997), facies attributes can help to identify individual MTDs within MTCs at outcrop. These include burrowing at the top of deposits, fabric contrasts (including grading), erosive basal surfaces and colour variations. In some cases, chi-tests of vertical

stacking patterns suggest a potential co-genetic origin to the deposition of sequential MTDs (Facies Pairs 11A, 13B, 14A and 15B), such as Type Ia deposits overlying Type IIa MTDs, however more data is required to gather statistically valid results.

- Imbricated and stacked carbonate rafts (Type Ic deposits) in the Rio Sieste suggest large-scale failure of a carbonate margin. Palaeodirection suggests imbrication towards 320° to imply failure from the southeast (around the Mediano Anticline).
- Type IIb MTDs appear to be deposited from bipartite flows and can either form the lower unit of a Type IIa deposit, or the form the upper unit of a Type III deposit. Some Type IIb deposits show poor- to moderate clast imbrication in clast-supported deposits to suggest low-strength flows with viscous interaction (i.e., where grains can affect each other's motion by close passage in a flow).
- Type IV facies may record the triggering process of the downslope evolution of mud-rich sediment slumps/slides to debris-flows, near to the source of failure and may also document basal shear from the bypassing of Type Ic MTDs.
- Topography is more apparent in Type Ia MTDs, with the greatest vertical relief documented in the thickest deposits measured, and therefore topography appears to be linked to cohesion of the failed material. Cohesive debris flows can produce rugose topography, whereas more dilute debris flows (where for example, dispersive pressure was more important as a grain-support mechanism), will tend to show lower relief. Topography observed at outcrop may be vertically exaggerated from overriding erosive sandy SGFs. This could be attributed to a topographic template creating a subtle change in gradient, resulting in the flow to transform from super- to subcritical and creating a hydraulic jump in the overriding flow. This transition of the flow regime could result in erosion and thus enhance the topographic relationship exposed at the present day.
- Sandy SGFs interpreted as the product of turbulent forces are capable of significant erosion into a muddy substrate, able to create backfilled channelised sandstones, and also lateral accretion surfaces suggest preferential pathways through MTDs at the surface of the palaeoseafloor.
- Sandstone rafts show varying degrees of disaggregation within debrites to suggest shear at the base and within the debris flows as they travel down-dip, likely to result from differential shear stresses and a weakly turbulent flow.

- Petrographic and compositional observations from pebble analysis in Type II and Type III MTDs has provided insight into sedimentary sources. Alluvial fans (such as the Sis palaeovalley, Vincent 1999) from the rising hinterland were likely to input pebbles into the marine Ainsa Basin and was possibly met by a late-stage river input into the system, or failure from the margins of the basin.

CHAPTER 5

SEDIMENTARY ENVIRONMENTS AND QUANTITATIVE ANALYSIS OF MTD AND MTC DATA, MIDDLE-EOCENE AINSA BASIN, SPANISH PYRENEES

5.1 INTRODUCTION

This chapter provides a quantitative approach to document the geometry of MTDs and MTCs in the proximal basin setting of the Ainsa Basin. Based on literature studies (e.g., Mutti and Ricci Lucchi, 1972; Puigdefábregas and Souquet, 1986; Millington and Clark, 1995a, b; Pickering and Bayliss 2009, Sutcliffe and Pickering, 2009, Bayliss and Pickering, 2015a, 2015b, Pickering *et al.*, 2015), the sedimentary succession of the Ainsa Basin is broadly categorised into depositional environments. Firstly, these depositional environments are introduced, and correlative MTD facies are described. Parts of the Guaso System were also re-mapped in order to refine the published geological map of the Ainsa Basin as published by Sutcliffe and Pickering (2008), Pickering and Bayliss (2009) and Pickering and Cantalejo (2015). This map is published in Scotchman, J.I., Pickering, K.T., Sutcliffe, C., ***Dakin, N***., Armstrong, E. (2015). Secondly, to determine spatial characteristics, such as proximal- to distal environments, palaegeographical settings, geometrical and stratigraphic analyses are presented from measurements obtained in the field. In this analysis, MTCs comprise multiple stacked deposits of either the same or different chaotic facies. These are grouped and evaluated as one unit to determine average and maximum MTC thickness. MTDs (discrete individual deposits) are also identified and evaluated according to facies and stratigraphic distribution. The geometries of MTDs and MTCs documented globally are also considered as part of this analysis. The raw data used to evaluate these deposits is provided in Appendix C.

5.2 SEDIMENTARY ENVIRONMENTS

To determine the type and spatial distribution of MTDs and MTCs, the Ainsa Basin can be broadly divided into ‘proximal’ and ‘distal’ depositional areas (*sensu stricto*

Alves and Cartwright, 2009). Proximal environments range from upper- to lower-slope settings in the east (around Charo and Banastón, respectively), to mainly base-of-slope environments, coinciding with the present-day Mediano Reservoir. Basin-floor and more distal environments are located in the west around Guaso, Sieste and Boltaña (Figure 5.1).

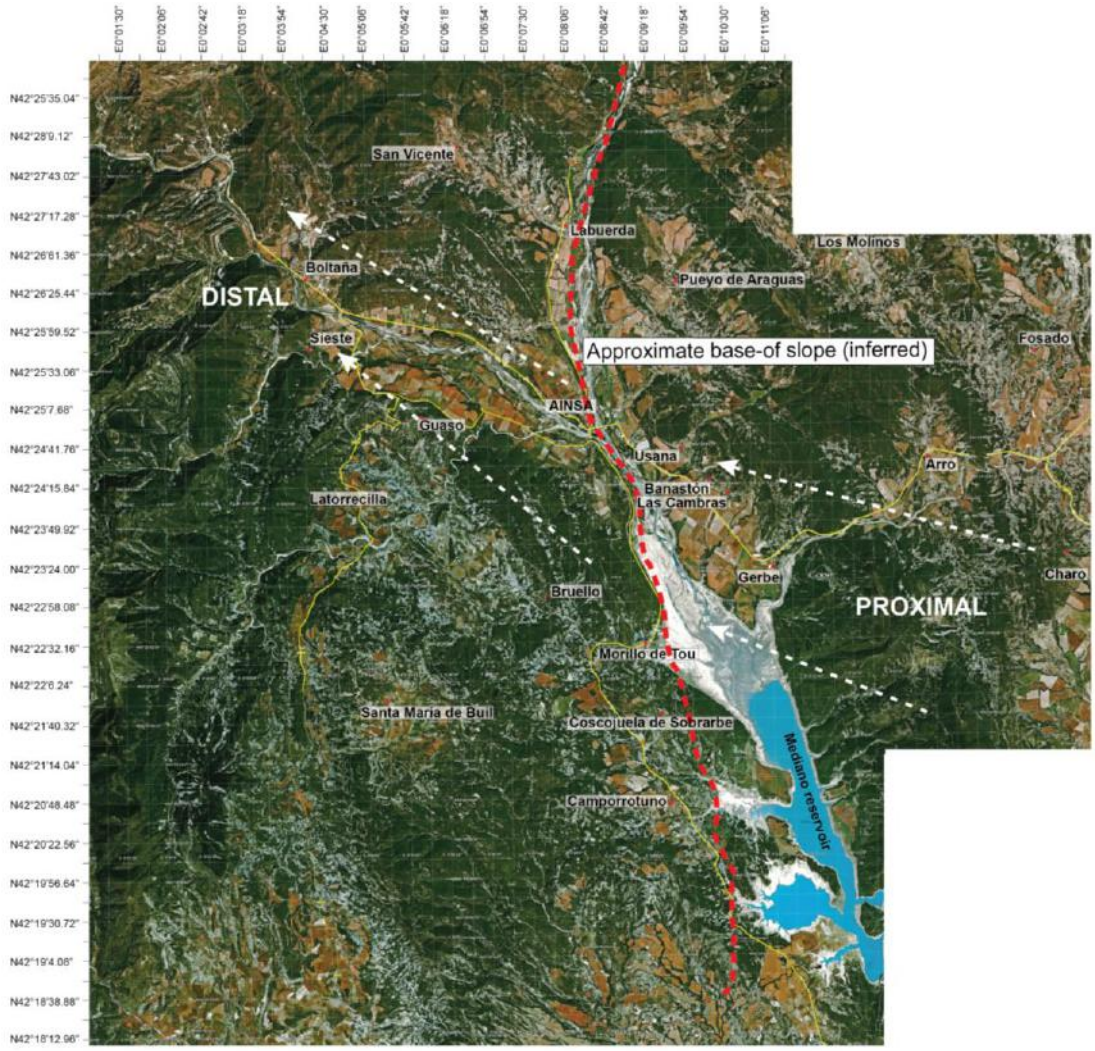

Figure 5.1. Map showing approximate proximal and distal locations of MTDs relative to the base-of-slope within the Ainsa Basin. The base of slope was not likely to have been stationary through deposition of the 8 depositional systems within the Upper and Lower Hecho Groups and therefore this boundary is inferred. Approximate palaeoflow orientation is projected by white dashed arrows.

Exposure within the Banastón, Morillo and Guaso systems can be separated into distinct sub-systems to permit proximal and distally equivalent parts to be studied and compared (Figure 5.1). Proximal facies of the Banastón System occur around the

villages of Usana, Banastón and Las Cambras, with equivalent distal facies located around Boltaña and San Viciente. The proximal Morillo System is located around Coscojuela de Sobrarbre and Morillo de Tou and distal Morillo is located around the village of Sieste. The proximal Guaso System is located around Coscojuela de Sobrarbre, Morillo de Tou and Bruello and the distal Guaso System is located around Guaso village.

Following this proximal and distal classification, stratigraphy is further divided into temporal stratigraphic locations to show where MTDs and MTCs are found in relation to sandbodies (i.e., marginal or immediately beneath depositional fans). These interpretations are primarily based on the geological map of Pickering and Bayliss (2009). The following environments identified and used in this study are summarised in Table 5.1, and type localities with the associated sedimentary logs are shown in Figure 5.2 (A to D). A very-thick MTC, measured up to ~ 60 m, is located at the base of the Ainsa II Fan deposited within a base-of-slope setting (Figure 5.2-A). The MTC comprises at least 18 individual muddy Type Ia deposits, separated by laterally continuous individual sandstone beds (< 15 cm thickness) and a 1.5 m package of non-deformed interbedded heterolithic sediments, interpreted as *in situ* deposits. Type Ia and IIa intraformational MTDs (deposited within sandy SGF-deposits of the Ainsa II Fan) are measured up to 0.5 m thickness (Figure 5.2-A). Type Ia and IIa, b intraformational MTDs and MTCs are also identified within the Arro Fan, deposited in a proximal marine setting (Figure 5.2-B). These chaotic deposits account for 61 % of the 128 m log measured in the field. A very-thick MTC, measured up to 60 m is located to the lateral margin of the Morillo II Fan (Figure 5.2-C). The MTC comprises at least 16 interbedded Type Ia and IIa MTDs, punctuated by very-thin to medium bedded graded sandstones. MTDs and MTCs in an erosional base-of-slope setting are identified with common erosional features, in the vicinity of the village of Usana (Figure 5.2-D). Representative MTDs and MTCs in the youngest sediments associated with the Ainsa Basin, within fine-grained muddy and laminated sediments, post deposition of the Guaso II Fan are presented in Figure 5.4, Log B. These deposits are interpreted as accumulated in a proximal slope setting.

Environment	Location	Type of MTDs documented
Slope (upper, mid, lower)	Located between the shelf slope break to the base of slope. The exact position of slope environments cannot be determined at outcrop (i.e., upper, mid, lower-slope environments), however erosional lower-slope canyons can be identified in the field from mapping and logging.	Upper, mid and lower-slope environments dominated by Type Ia MTDs, Type IIa and Type IV facies are also documented. Lower-slope environments can form erosional canyons (e.g., Pickering and Bayliss, 2009, Bayliss and Pickering, 2015a). Type Ia, b, Type IIa, b, Type IIIa, b and Type IV facies are documented.
Base of slope	Base of slope to basin floor transition resulting from a change in gradient. Can be identified in the field by the onset of depositional systems and/or imbrication.	Type Ia, b, c, Type IIa, b, c, Type IIIa, b and Type IV facies.
Base of submarine fan	MTDs located directly beneath and deposited immediately before the onset of a depositional system. Location is identifiable in the field.	Type Ia, b and Type IIa, b facies
Marginal to submarine fan	MTDs found laterally adjacent to the main sandy depositional system. Location is determined from geological mapping.	Type Ia, b, Type IIa, b, c, Type IIIa, b and Type IV facies.
Intraformational	MTDs found within sandy fan sequences, deposited contemporaneously to a depositional system.	Type Ia, b, Type IIa, b, c, Type IIIa, b and Type IV facies.

Table 5.1. Depositional environments and the presence of MTDs identified at outcrops in the Ainsa Basin.

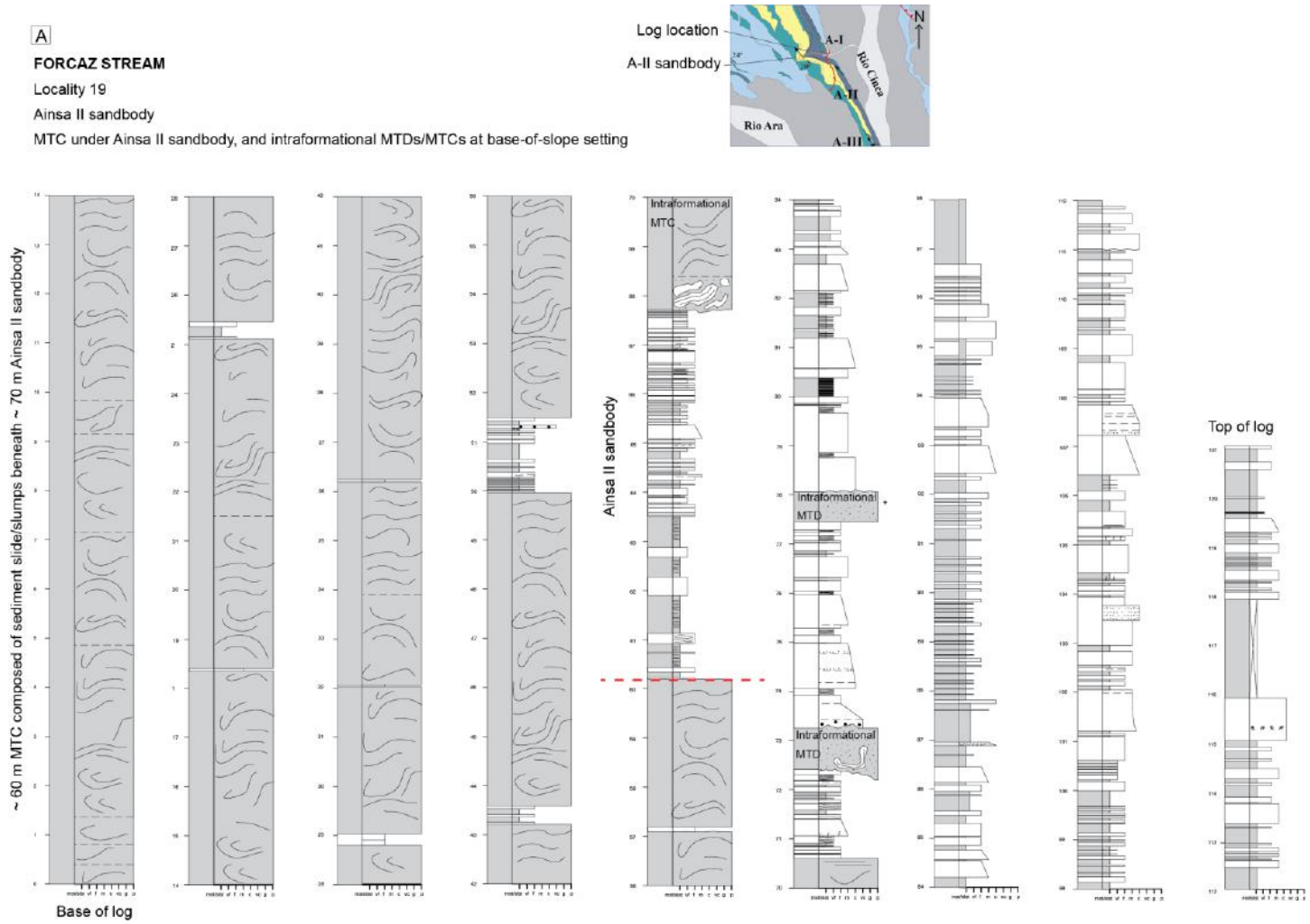

Figure 5.2-A. Forcaz Stream. Sedimentary log of an MTC at the base of a proximal depositional system (Locality 19). Vertical scale is shown in metres.

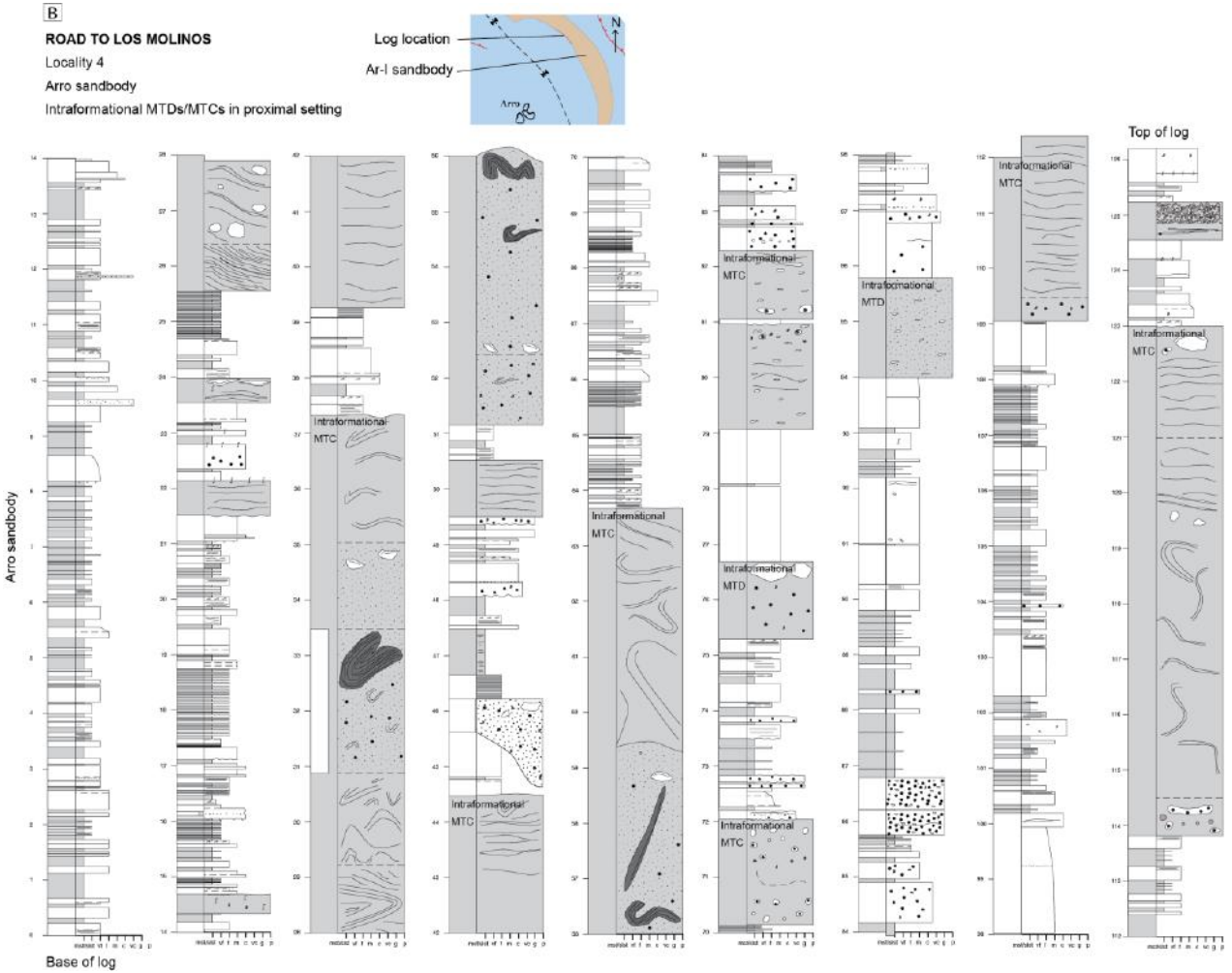

Figure 5.2-B. Intraformational MTDs logged within the Arro System (C) MTDs logged above the Guaso II Fan (Locality 4). Vertical scale is shown in metres.

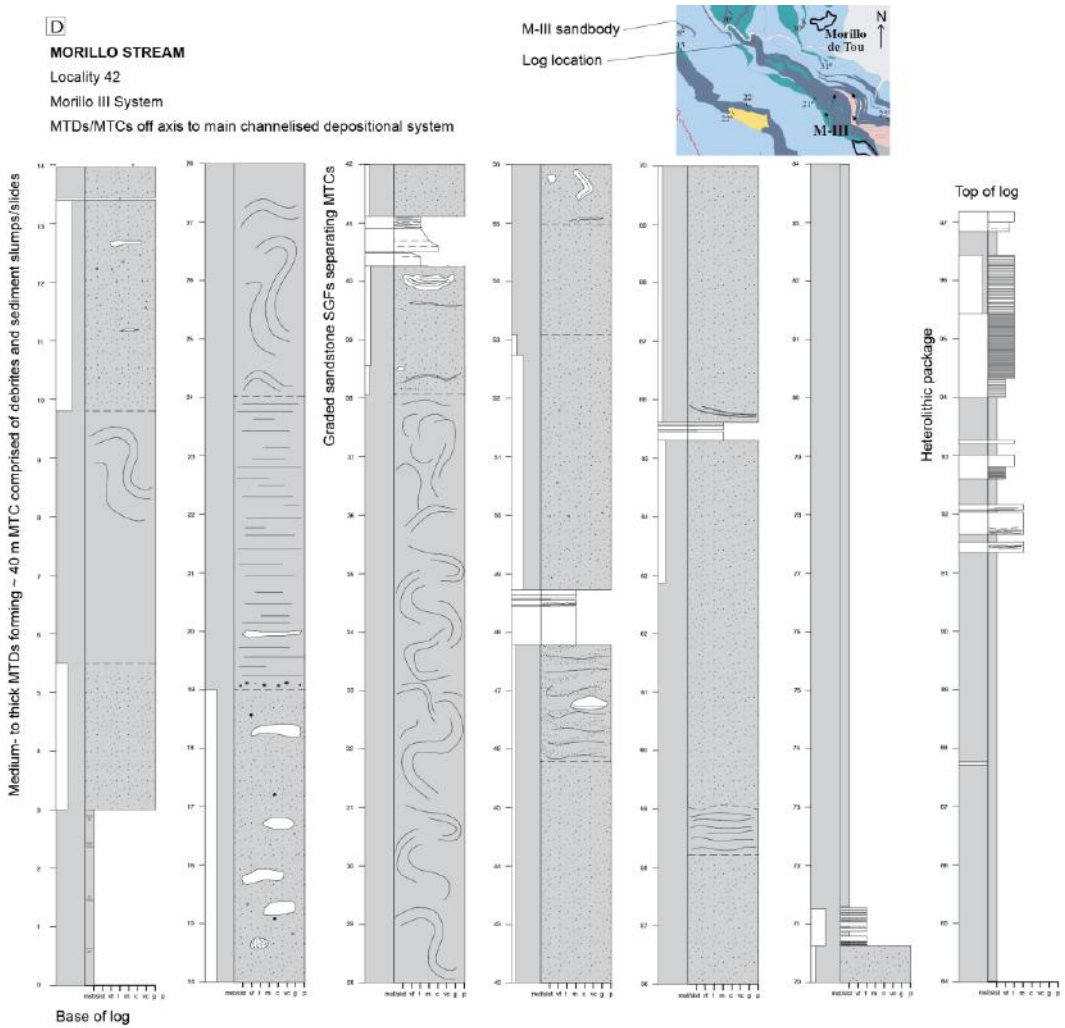

Figure 5.2-C. MTDs and MTCs deposited off-axis to the main depositional systems (Locality 34). Vertical scale is shown in metres.

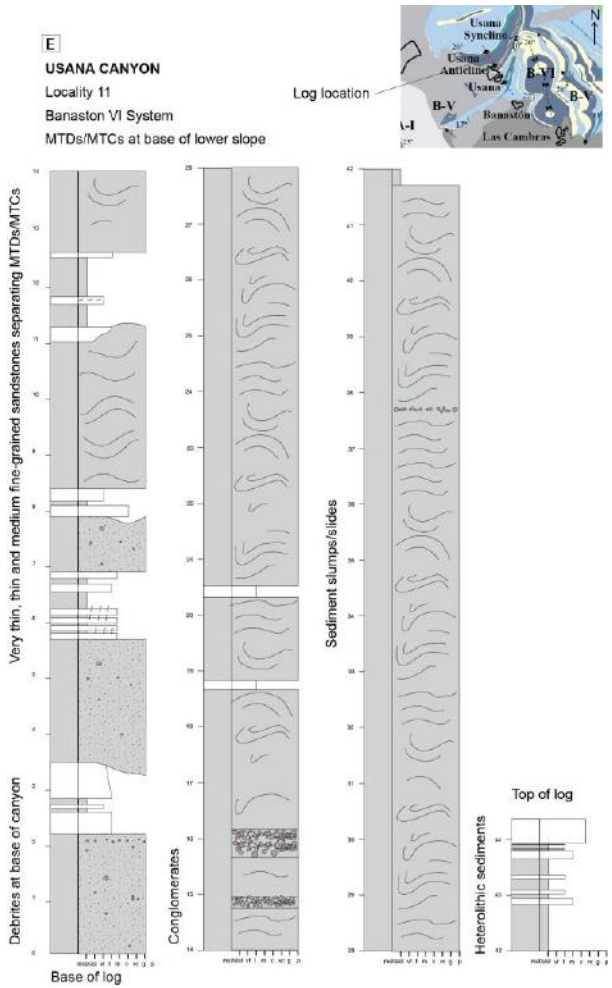

Figure 5.2-D. MTDs and MTCs deposited at the base of an erosional lower-slope environment (as interpreted by Bayliss and Pickering, 2015a) (Locality 11). Vertical scale is shown in metres.

A further breakdown of depositional environments, with typical MTDs documented in each depositional setting is explored in the following sections.

5.2.1 Slope environments

MTD and MTC types identified on upper, mid, lower and base of slope environments in the Ainsa Basin are considered below. From the shelf-slope break into deep-water, slope gradients can vary considerably from steeper upper slopes, to the base-of-slope and basin floor (which can still have relatively high gradients), and ultimately abyssal plains, which have gradients of less than one in a thousand (Middleton, 1993). The Lower Hecho Group is structurally complex, therefore unfortunately it has not proved possible to calculate or confidently estimate seafloor gradients during this research. In this study a 'steep' gradient is used qualitatively.

5.2.1.1 Upper-, mid- to lower-slope environment

Generally, it is not possible to identify the precise position on the palaeoslope based on outcrops in the Ainsa Basin and the 'up-slope' Tremp-Graus Basin. However, these environments are recognised in literature from the area of Charo in the east, to the palaeobase-of-slope near Usana and Banastón in the west (e.g., Puigdefábregas and Souquet, 1986; Millington and Clark; 1995a, b). MTDs identified on the upper-, mid- and lower-slope generally comprise isolated Type Ia MTDs, ranging from a few metres to decimetres in thickness (Figure 5.3). Type IIa and Type IV MTDs are also documented in this environment, although coarse-grained MTDs (i.e., those containing pebbles and sand-rich Type IIa MTDs) are not generally recognised, unless within a lower-slope canyon environment (discussed in Section 5.2.1.3).

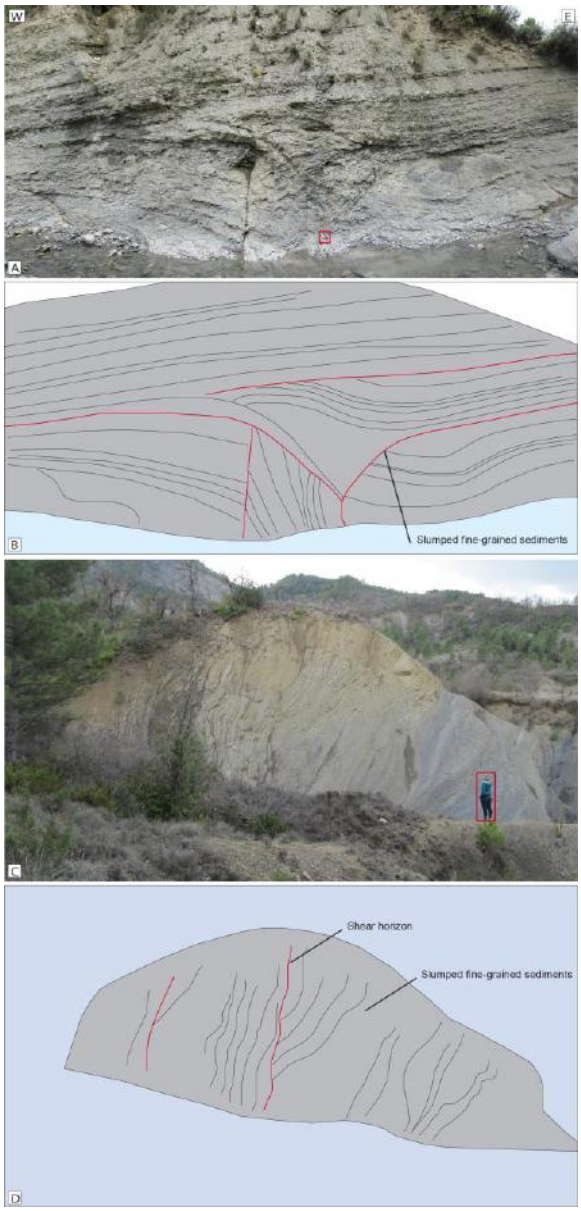

Figure 5.3. (A, B) ~ 3.5 m-thick Type Ia MTD in fine-grained mudstones in slope environment, post Guaso II (Locality 33). Compass-clinometre for scale (10 cm) (C, D) ~ 15 m-thick Type Ia MTC in fine-grained mudstones in upper to mid-slope environment, Los Molinos (Locality 34). Person for scale.

5.2.1.2 Low-gradient slope environment

The Guaso System is the youngest clastic submarine fan in the deep-marine part of the Ainsa Basin, which in turn is overlain by ~ 150 to 200 m of fine-grained slope, pro-delta and deltaic sediments of the Sobrarbe Delta (Sutcliffe and Pickering, 2009; Scotchman *et al.*, 2015). MTDs were re-mapped from Pickering and Bayliss (2009),

particularly in the area around Camporrotuno, Coscojuela de Sobrarbe and above the Guaso II sandbody to capture MTDs and MTCs not previously mapped (Figure 5.4). Thick (up to 7 m) Type Ia and muddy Type IIa (containing a few nummulites, but no pebbles) were documented in this pro-deltaic slope setting, (Figure 5.4 Log B, Locality 47). To show thickness variability and where other MTDs and MTCs occur in the Guaso System, three sedimentary logs (A, C and D) are also presented (Figure 5.4).

Thin (< 2 m) intraformational Type Ia and IIa deposits are identified within the Guaso I Fan (Log A). Type Ia MTDs between 4 and 8 m (medium- to thick beds) are identified in the pro-deltaic slope laminated mudstone sequence (Log B). Thin- to medium beds (1.8 to 2.5 m) Type Ia, IIa MTDs are identified at the base of the Guaso II Fan (Log C). Medium to very-thick beds (up to 12 m) of Type Ia, IIa MTDs are identified to the margin of the Guaso II Fan (Log D).

5.2.1.3 Erosional lower-slope environment

Six sandy depositional systems have been identified and described from the Banastón System (B-I to B-VI Fans, younging respectively), separated by MTDs and MTCs, interpreted as lower-slope erosional channels (Pickering and Bayliss 2009, Bayliss and Pickering, 2015a). The present-day geometry of the individual systems are 'V-shaped', pointing up-dip towards the direction of palaeoflow (from the east) (Figure 5.5). Locality 12 (Las Cambras path) provides moderately continuous exposure from B-I to B-V and the southern limb of the B-VI ridge (Locality 11, Usana Canyon) provides continuous exposure of B-V to B-VI. Together, a relatively detailed sedimentary record is provided throughout the entire proximal Banastón System (B-I to B-VI), exposing MTDs and MTCs deposited at or near the base of slope during main sedimentary input into the basin.

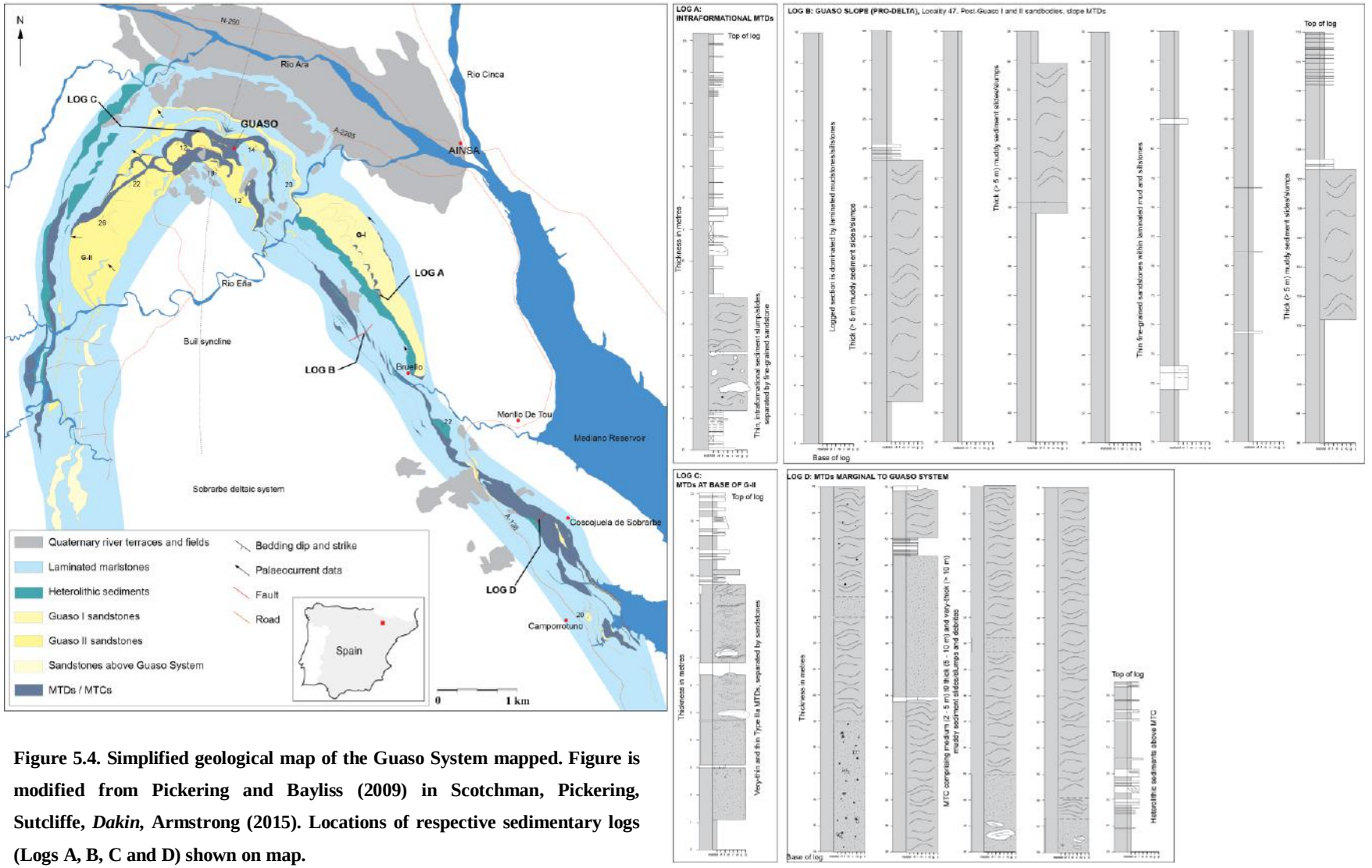

Figure 5.4. Simplified geological map of the Guaso System mapped. Figure is modified from Pickering and Bayliss (2009) in Scotchman, Pickering, Sutcliffe, *Dakin*, Armstrong (2015). Locations of respective sedimentary logs (Logs A, B, C and D) shown on map.

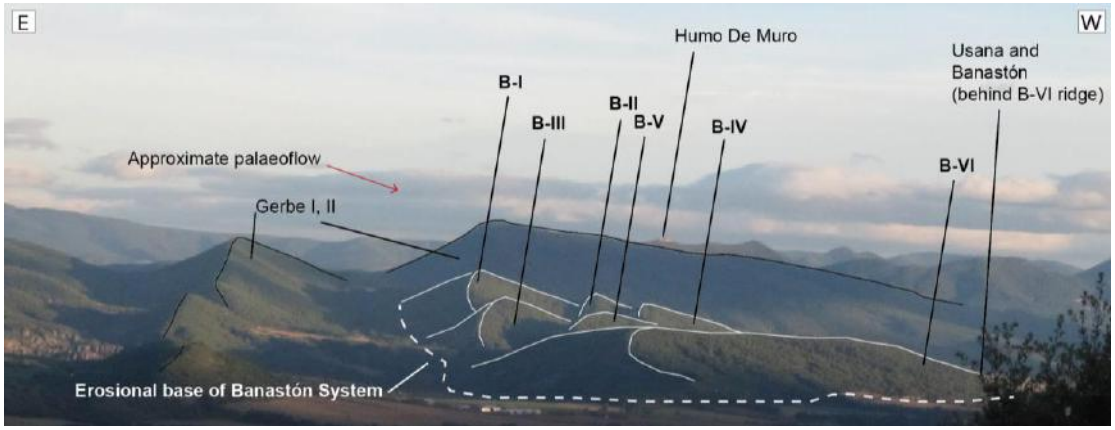

Figure 5.5. Line interpretation above photograph looking south from Morillo de San Pietro to show the position of the proximal Banastón Systems (I to VI), Usana-Banastón. Horizontal distance is ~ 2 km.

Up to five confined erosional canyons are mapped around the villages of Las Cambras, Usana and Banastón, showing an overall shift in depositional axis, towards the northwest. The canyons are dominated by slump-facies (denoted green, Figure 5.6), with sandy SGF-deposits deposited at the top of each canyon. A well-exposed asymmetrical ~ 1km canyon (shown between logs 2 and 4) in the village of Usana has been named 'Usana Canyon' for the purpose of this study. The base of the Usana canyon is erosional, incising ~ 80 m. A Type IIa MTD (0.65 m thickness) is observed to erode into fine-grained sandstone bed. The majority of the MTDs identified in Middle Eocene Usana Canyon are composed of Type Ia and Ib MTDs. However, pebbly Type IIb MTDs are documented throughout this environment (Figure 5.7).

Pebbles are found near the base of the canyon and generally decrease vertically through the stratigraphy. Thin (10 – 20 cm) pebble conglomerate stringers (Figure 5.7-B) and conglomerate-filled channels (Figure 5.7-C) suggest high-energy flows bypassed the system. Conglomerates (at this location and other locations around the Ainsa Basin, e.g., Figure 4.7, Chapter 4) are typically observed to have a channel-like shape, showing erosion into the underlying deposit with maximum incision at the centre and thinner margins. Using sedimentary logs recorded in the field, a cross-section of the erosional lower-slope environment at Usana has been constructed (Figure 5.6).

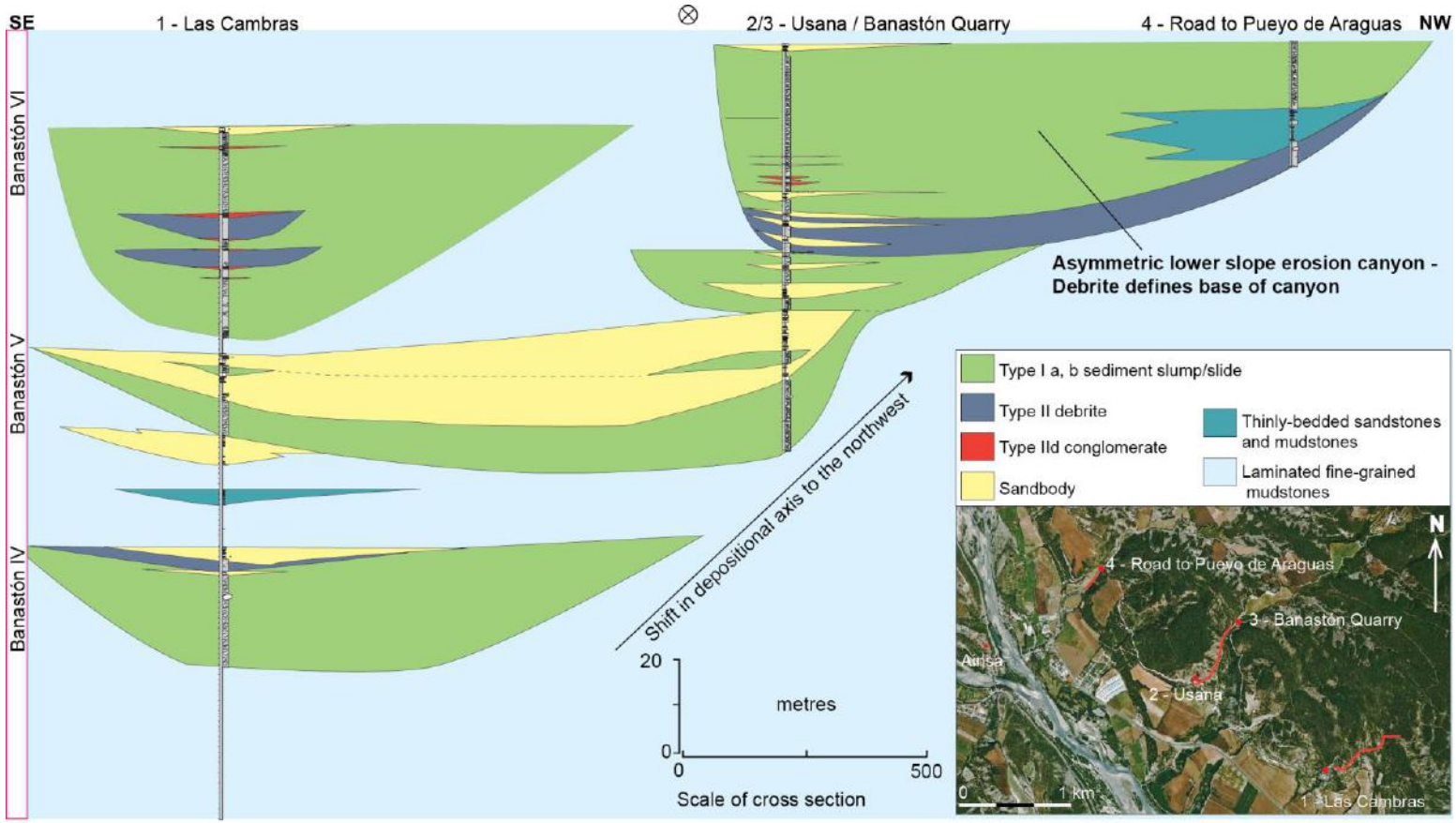

Figure 5.6. Correlation panel of Las Cambras, Usana Canyon, Banastón Quarry and Road to Pueyo de Araguas logs showing geometry of proximal lower slope erosional canyon. Palaeoflow is towards the northwest, out of figure. The sedimentary succession of sandbodies interbedded between Type Ia MTDs continues for 42 m from the base of the log, when Type IIa and d MTDs (debris flows and conglomerates) are first observed. Thin sandy SGF deposits are deposited stratigraphically above the canyon, terminating the sedimentary sequence at this locality.

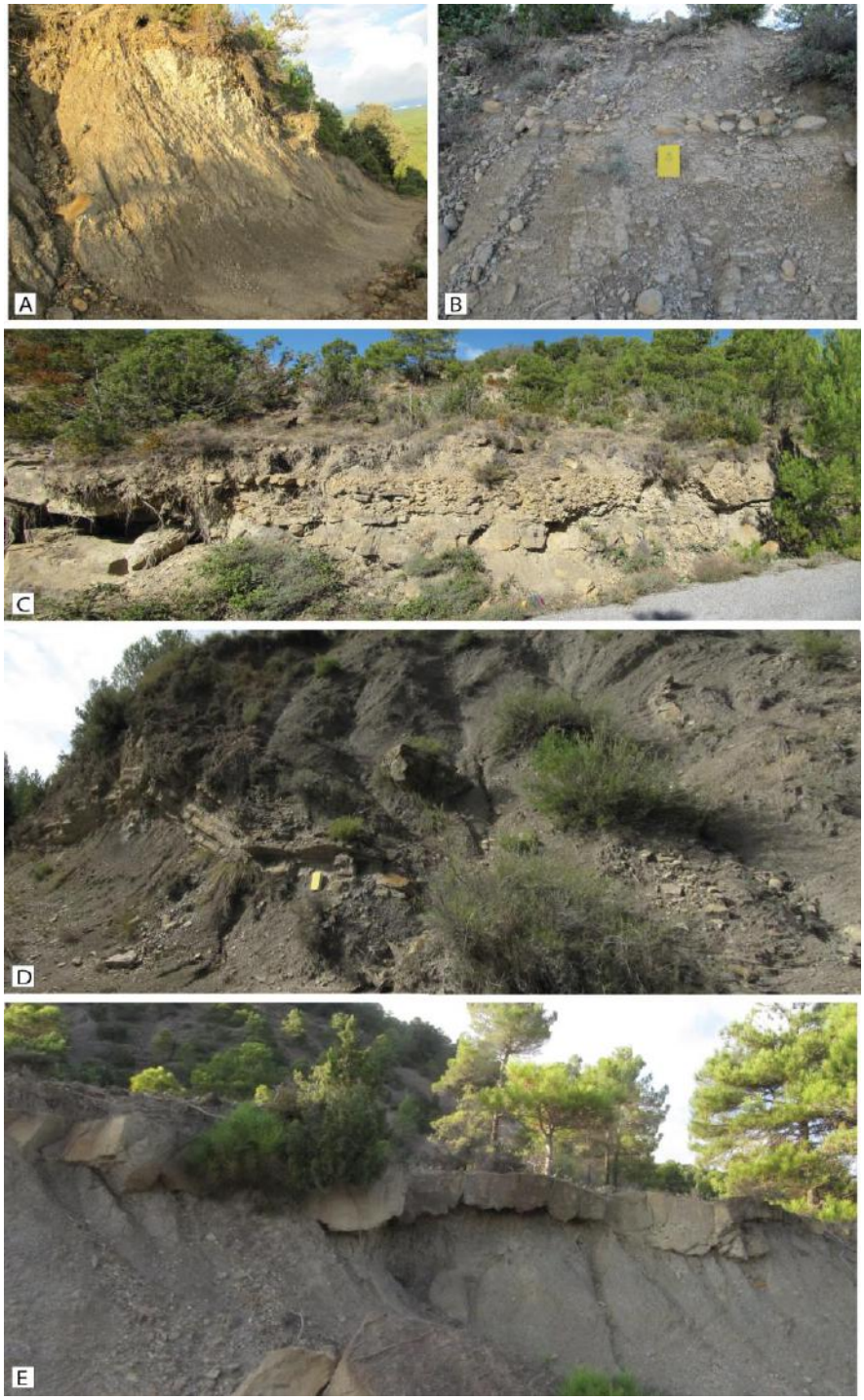

Figure 5.7. MTD facies deposited within in a lower slope erosional canyon setting, Usana (Locality 11, see Figure 5.6) (A) Muddy Type Ia MTD, can show obvious signs of transport (i.e., large folds) or show very subtle dip changes (slides). Outcrop is 4.8 m thick from path (B) Thin, Type IId conglomerate lag showing imbrication within Type Ia facies. Notepad for scale (20 cm) (C) Medium-bedded conglomerate-filled channel showing imbrication. Rucksack for scale (50 cm) (D) Large bedded sandstone raft up to 10 m in length within muddy Type Ia facies. Notepad for scale (20 cm) (E) Thin- to medium bedded sandstones infilling irregular Type Ia topography. Sandstone is 32 cm maximum thickness.

5.2.1.4 Base-of-slope environment

The Ainsa I, II and III fans form laterally continuous sandy channelised deposits located along the present-day Mediano Reservoir, interpreted as the palaeo- base-of-slope for this system (Pickering and Corregidor, 2005, Pickering *et al.*, 2015). The base of the Ainsa II Fan (Forcaz Stream, Locality 19) is underlain by a ~ 60 m MTC, comprising up to 18 Type Ia MTDs, composed of laminated mudstone (Figure 5.8). The orientation of fold axes from this deposit suggests a downslope translation from the east (Pickering and Corregidor, 2005) (for sedimentary log from this location, see Figure 5.2-A).

Figure 5.8. Tight, approximately vertical fold axis (when rotated to palaeo-horizontal) in distorted mudstones, base of Ainsa II Fan, Forcaz Stream (Locality 19). Total thickness of MTD is ~ 15 m and is part of a ~ 60 m MTC.

The presence of very-thick Type Ia MTDs at the base of the Ainsa II Fan suggests a proximal location to the slope.

5.2.2 MTDs and MTCs at the base of depositional systems

Table 5.2 summarises the type and maximum thickness of MTDs and MTCs logged immediately beneath depositional systems in the Ainsa Basin.

Locality	Fan	MTD or MTC found at base of depositional system	Max thickness (m)
4	Arro II (proximal)	Type Ia MTD	11.53
38	Banastón II (proximal)	Type Ia/Type IIa MTC	28.00
36	Banastón V (proximal)	Type Ia MTD	7.70
37	Base of Banastón V (distal)	Type IIa and IIb MTC	10.84
6	Base of Banastón VI (distal)	Type IIa MTD	13.10
17	Ainsa I (proximal)	Type Ia MTD	23.30
19	Ainsa II (proximal)	Type Ia MTC	45.03
25	Morillo I (distal)	Type Ia/IIa/IIb	22.63
31	Morillo II (distal)	Type IIa MTD	8.88
21	Morillo II (proximal)	Type Ia/Type III MTC	49.72
27	Morillo III (distal)	Type Ic/Type IV MTC	26.00
35	Guaso I (distal)	Type Ia/Type IIa MTC	3.10
37	Guaso II (distal)	Type Ia/Type IIa MTC	26.96

Table 5.2. Summary table showing type and maximum thickness of MTDs and MTCs deposited at the base of sandbodies interpreted as fans. Data is ordered according to order in stratigraphy.

Typically, Type Ia, Type IIa, IIb and Type III MTDs mark the base of depositional systems both proximally and distally within the Ainsa Basin. The thickest MTC (stacked deposits) is documented at the base of the proximal Morillo II Fan (~ 50 m), Locality 21. Figure 5.9 shows the average thickness of MTDs and MTCs documented at the base of fans, grouped by Type.

MTDs and MTCs that comprise Type Ia deposits (i.e., A and B on graph) are double the average thickness of MTDs and MTCs that comprise Type IIa deposits (26 *versus* 10.5 m, respectively), complimenting average thickness data in Table 5.4.

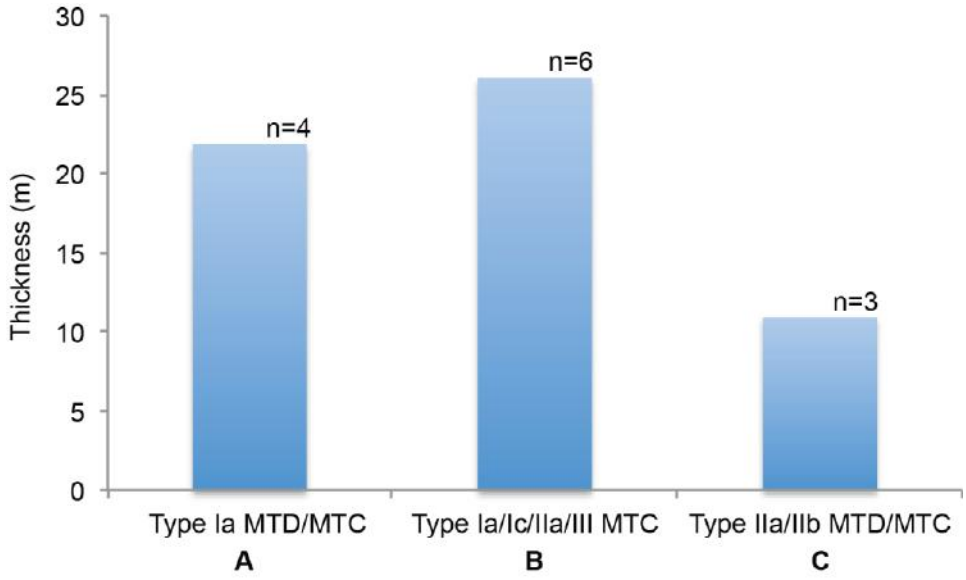

Figure 5.9. Average MTD and MTC thickness at the base of depositional fans. MTCs are grouped by Type. This shows MTCs containing Type Ia deposits are much thicker.

5.2.2.1 MTD and MTCs at base of the distal Morillo System

The Morillo System is the penultimate deep-marine sand-prone stratigraphic unit and comprises three structurally-confined, coarse-grained and channelised mid-slope to lower slope submarine fans (Bayliss and Pickering, 2015b). The distal Morillo System has exceptional exposure around Barcelo Monasterio de Boltaña, the Rio Ara and Rio Sieste (Localities 23, 52, 25). For this reason, ~ 500 m of sedimentary logs were measured to document the relatively distal stratigraphy of Morillo Systems I, II and III to show types of MTDs and MTCs at the base of this depositional system in a distal setting, shown in Figure 5.10. The width of major sandbodies and MTDs or MTCs located in areas that were not accessible to log were measured from the geological map to produce a scaled model of the geometry of the distal part of the Morillo System.

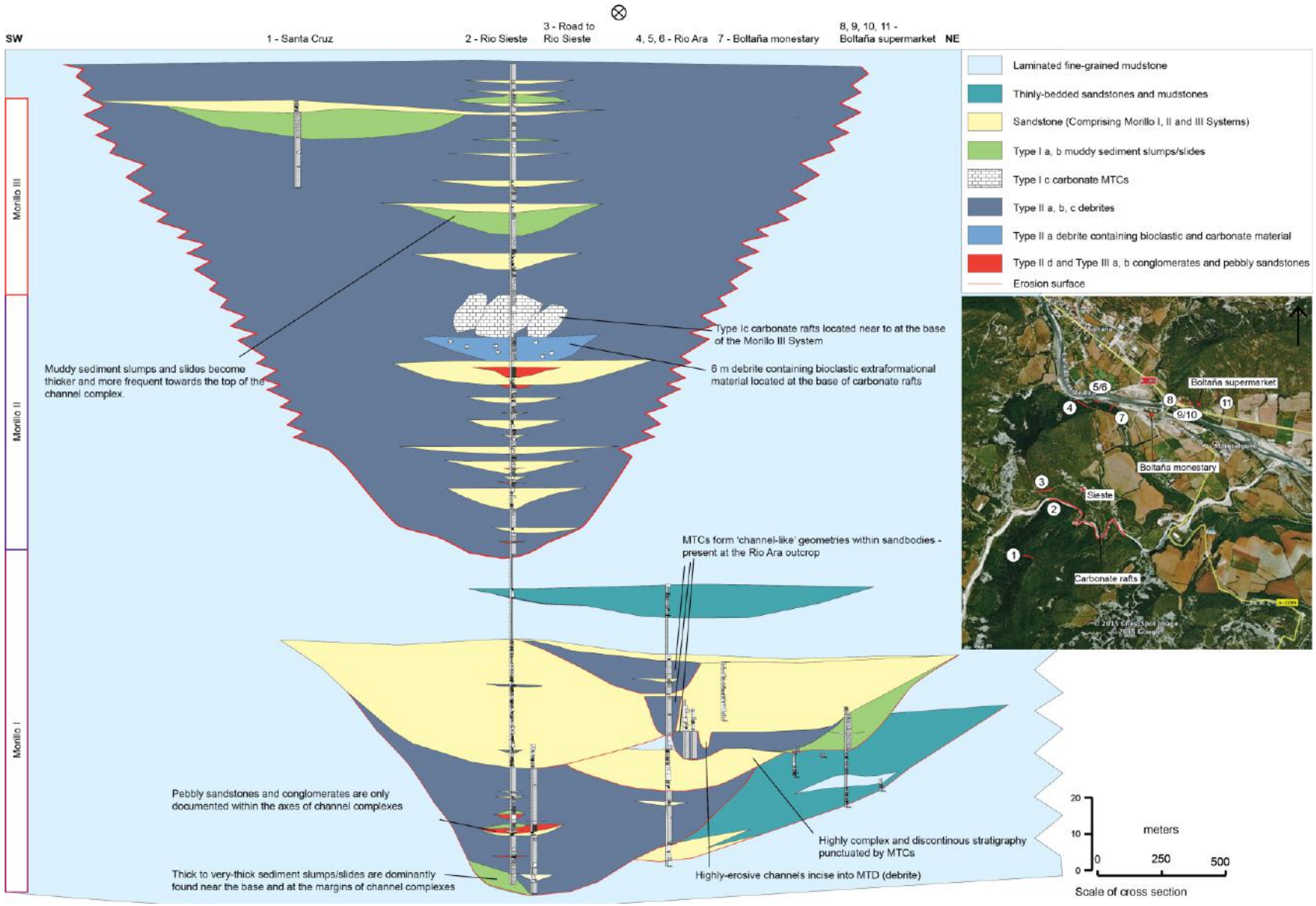

Figure 5.10. Correlation panel showing MTD and MTC types and geometry for M-I, M-II and M-III depositional fans. Panel is updated and modified from Bayliss and Pickering (2015b).

Multiple stacked Type IIa MTDs form 'channel-like features' at the base of the distal Morillo I Fan, with Type Ia MTDs mainly documented at the margins of the channel-like erosional scour. The Morillo I Fan above the 10 m-thick basal Type IIa/b MTDs is ~ 34.5 m thick, comprising abundant amalgamated fine- to coarse-grained sandy SGF deposits.

Compared to M-I, Morillo Fans M-II and M-III show a very different architectural style, with thin to medium-bedded sandbodies up to 6 m thickness, separated by MTCs. Type IIa MTDs also dominate the stratigraphy at this location, however higher in the stratigraphy within M-III, MTDs become dominated by Type Ia deposits. Type IIb and III deposits (pebbly sandstones and conglomerates) are only observed in the axial-parts of erosional systems, a feature also identified in Figure 5.6 in the erosional lower-slope canyon in Usana. MTDs and MTCs identified at the base of Banastón sandbodies in the proximal environment dominantly comprise Type Ia MTDs, compared to the dominance of Type IIa MTDs at the Rio Ara and Rio Sieste location.

5.2.3 Intraformational MTDs and MTCs

Intraformational MTDs and MTCs are mud-rich chaotic facies within sandy fan deposits (i.e., during deposition of a submarine fan). Figure 5.11 shows Type IIa MTDs between sandstone beds documented in the proximal Banastón Quarry outcrop (Locality 9). Thin- to medium-bedded sandstones of the BV sandbody in the Banastón Quarry are deposited between thin- to medium-bedded Type Ia MTDs up to 4.5 m in thickness (Figure 5.11). Contorted sandstone beds observed in MTD-2 are likely to have been incorporated from the basal sandstones under this MTD. Sandstones deposited above MTD 2 are discontinuous and show progressive onlap up-dip in the system, towards the east (060^{o} in Figure 5.11). Other intraformational facies, which includes channel margin failure (Type Ia, b, Type IIa, b and Type III MTDs) are shown in Figure 5.12.

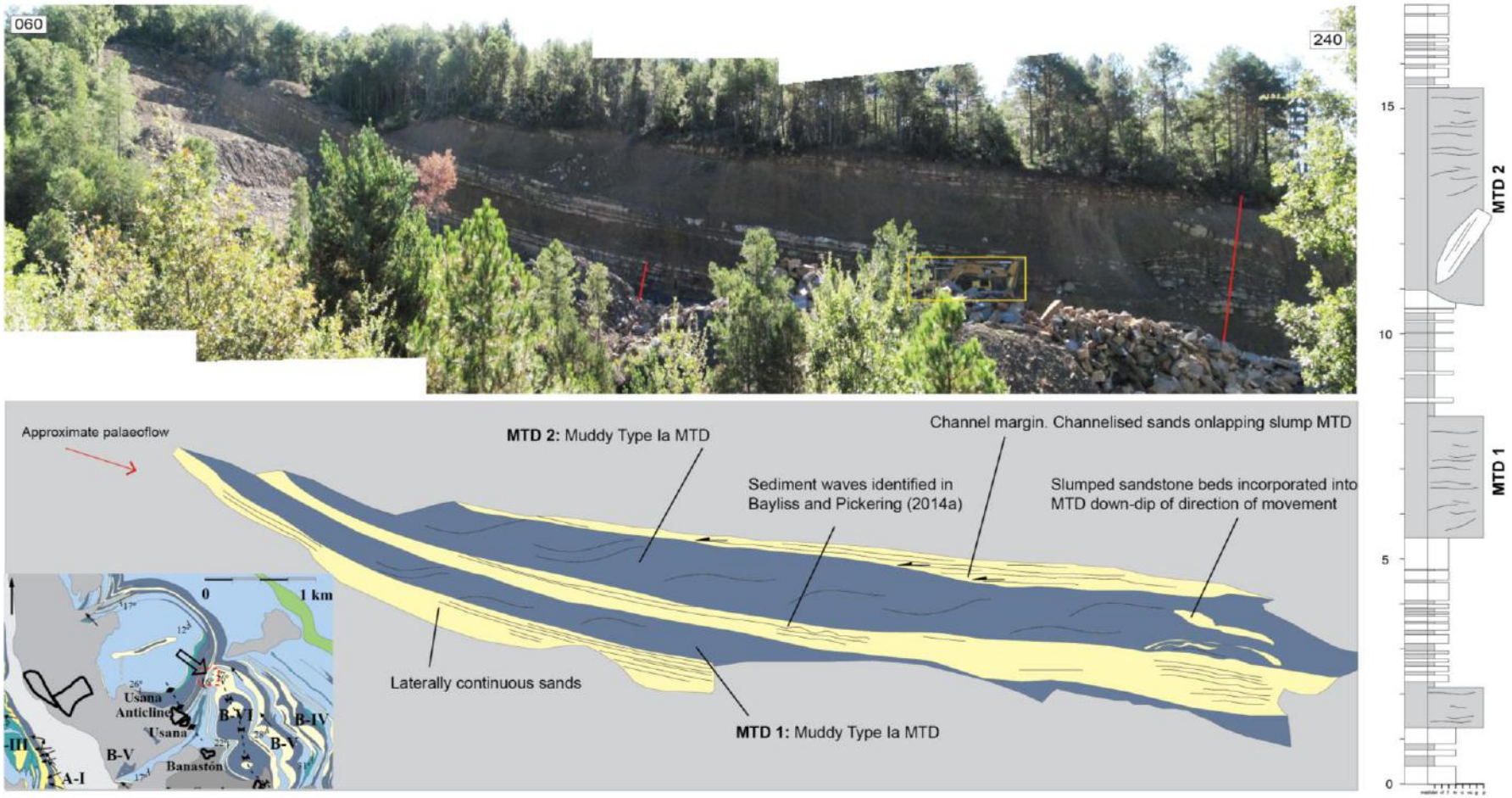

Figure 5.11. Photomontage of the Banastón Quarry (Locality 9). Corresponding sedimentary log to the right of figure. Approximate log locations marked on photograph. Digger for scale (highlighted in yellow box). 4.5 m cohesive Type 1a MTD.

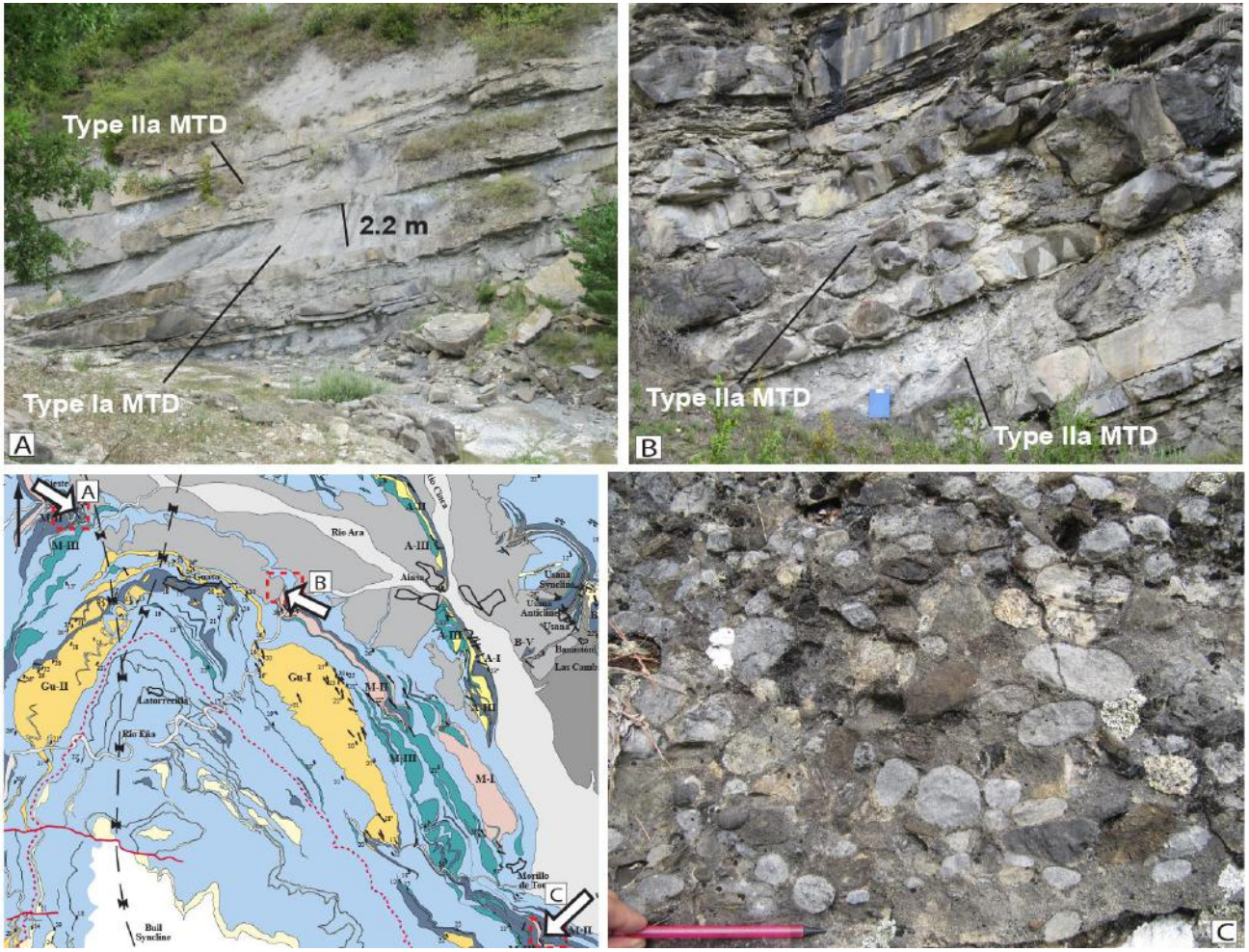

Figure 5.12. (A) Non-erosive Type Ia and Type IIa MTDs (2.2 m thick) deposited within Morillo III Fan (Locality 40). (B) Type IIa and b MTDs, showing erosion and down-dip of erosion, respectively (confirmed from thin section analysis in Chapter 6). Deposited during deposition of Morillo II Fan. Clipboard for scale (35 cm) (Locality 41). (C) Type III MTD (clast-supported), deposited during deposition of Morillo II Fan. Pencil for scale (15 cm) (Locality 20).

5.3 MTD AND MTC ANALYSIS

In this section, MTD and MTC measurements are evaluated according to spatial and stratigraphic locations, as identified in Section 5.2.

5.3.1 MTCs

A total of 121 MTCs (i.e., multiple deposits comprising greater than 1 event) were measured throughout the Ainsa Basin. Key statistics of these deposits are summarised in Table 5.3 and Figure 5.13. This dataset is relatively limited, as MTC and MTD-type is highly dependent on which intervals were logged at each location around the Ainsa Basin. However, the significant time for data collection in the field permitted almost all accessible outcrop sections to be logged, to reduce bias in analysis of this dataset.

	No. MTCs measured	Average thickness (m)	Standard deviation	Max/Min (m)
MTCs	121	12.47	13.3	80/0.81

Table 5.3. Summary of total MTC data from Fosado, Los Molinos, Arro, Gerbe, Banastón, Ainsa, Morillo and Guaso systems.

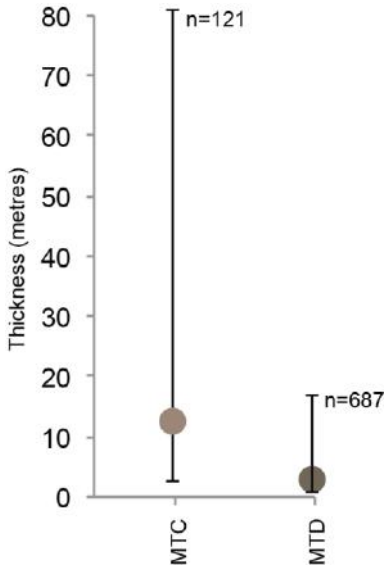

Figure 5.13. Average, maximum and minimum thickness of MTCs compared to MTDs.

Average MTC thickness is measured as ~ 12.5 m, compared to ~ 2.5 m for the average thickness of individual events (MTDs, Table 5.3). To deduce spatial information from these data, MTC thickness is grouped according to depositional environment (e.g., Table 5.1) (Figure 5.14).

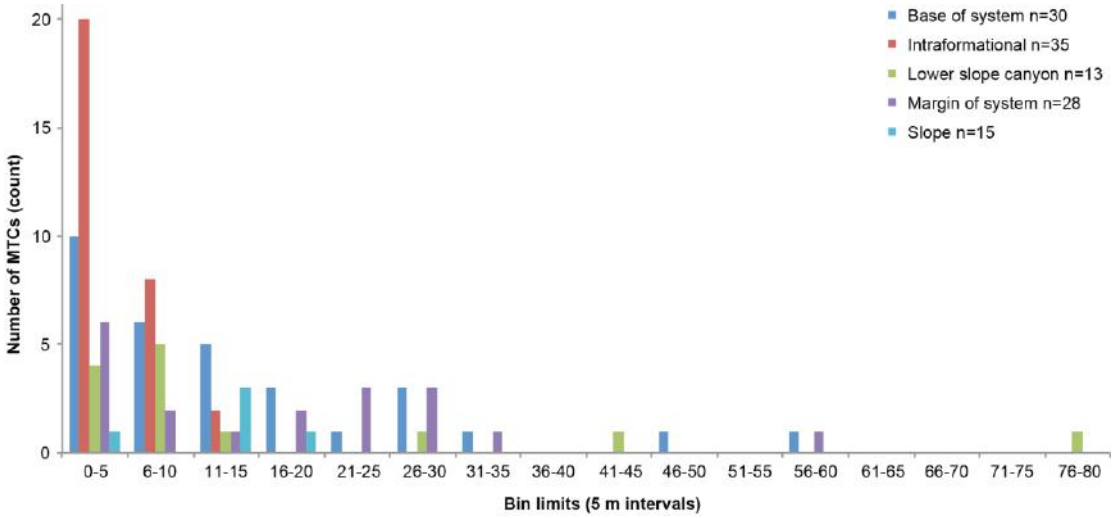

Figure 5.14. Count of MTC thicknesses documented in different environments. This data includes MTCs measured under all systems in the Ainsa Basin.

The data distribution of intraformational MTCs (measured as very-thin up to thick [12 m, measured in Arro II, Locality 4]), show a high abundance (n = 30) over a narrow data range. Other depositional environments show a wider distribution of MTC thicknesses, (measured as very-thin to very-thick) from < 5 m up to 80 m, recorded in Usana (Figure 5.6, Locality 11), interpreted as incision of the lower- to base-of-slope (discussed in section 4.5.1.2). Thick- to very-thick MTCs (> 5 m) are also documented beyond the base-of-slope at the base of depositional systems, with the maximum MTC measured as 45 m (Figures 5.2-A and 5.8, Locality 19). Overall, MTC thickness is dominated by deposits measured < 30 m.

These data show the gross thicknesses of MTCs in a proximal deep-marine environment, however to determine facies relationships, MTCs are subdivided into discrete events (MTDs).

5.3.2 MTDs

5.3.2.1 Facies distribution

A total of 686 MTDs (individual deposits) were logged and measured throughout the Ainsa Basin. Key statistics of these deposits are summarised in Table 5.4 and shown in Figure 5.15. Due to the absence of data collected in the Fosado System, this data was not included within any statistical analysis. Uncertain MTD values (i.e., where it is not clear what are individual events [MTDs] or what are part of an MTC) are also omitted from MTD analysis.

Type Ia and IIa facies dominate MTD stratigraphy accumulating ~ 46 % and 45.5 % of all MTDs, respectively. Type Ic, IIb, Type III and IV MTDs accumulate ~ 10 % of the stratigraphy (note these values exclude the presence of sandstone and laminated mudstone facies). Individual event thicknesses range between 0.15 m (minimum) to 18.3 m (maximum) (Figure 5.15).

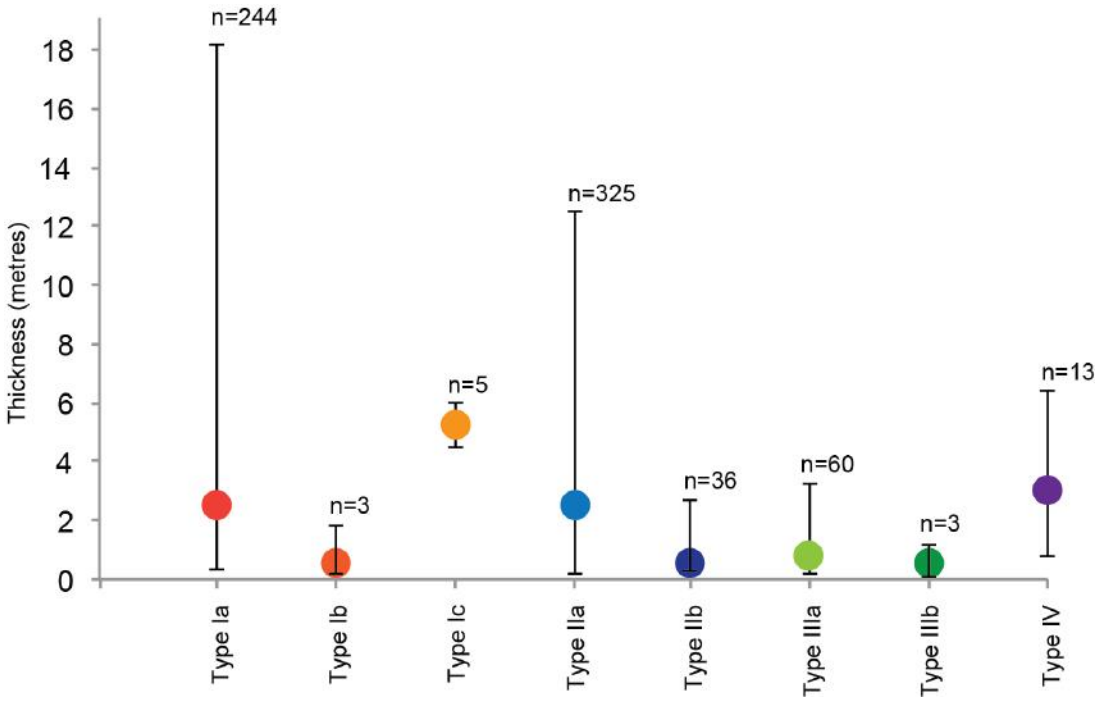

Figure 5.15. Average, maximum and minimum thickness of MTDs (MTCs are omitted from analysis).

Type Ic MTDs are the thickest (mean = 5.16 m), followed by Type Ia (3.35 m), Type IV (mean = 2.89 m), Type IIa (mean = 2.61 m), Type III (1.1 m), Type IIb and IIIb are the thinnest MTDs measured (mean = 0.65 m).

MTD type	No. MTDs measured	Average thickness (m)	Standard deviation	Max/Min (m)	Sum / cumulative thickness of MTD thickness (m)	% of all MTDs
Type Ia	244	3.35	2.60	18.3/0.4	814.65	**46**
Type Ib	3	0.5		1.3/0.35	3.6	**0.2**
Type Ic	5	5.16	0.76	6/4.2	25.7	**1.5**
Type IIa	319	2.5	2.36	12.5/0.15	797.8	**45.3**
Type IIb	35	0.65	0.52	1.6/0.2	22.13	**1.3**
Type IIIa	63	0.76	0.65	3.2/0.12	48.3	**2.7**
Type IIIb	4	0.5	0.97	2.5/0.	5.98	**0.3**
Type IV	14	3.02	1.97	6.4/0.87	39.37	**2.24**
Grand Total	**686**	**-**	**-**	**-**	**1757.53**	**100**

Table 5.4. Summary of total MTD data from Los Molinos, Arro, Gerbe, Banastón, Ainsa, Morillo and Guaso systems.

5.3.2.2 Spatial distribution

The geological map published by Pickering and Bayliss (2009) uses a simplified facies scheme with all MTDs and MTCs represented in a blue-grey colour (Figure 1.16). This study, however, presents a more detailed colour scheme to distinguish between MTD facies types, thereby permitting the location of MTDs to be spatially identified in the Upper Hecho Group (Figure 5.16).

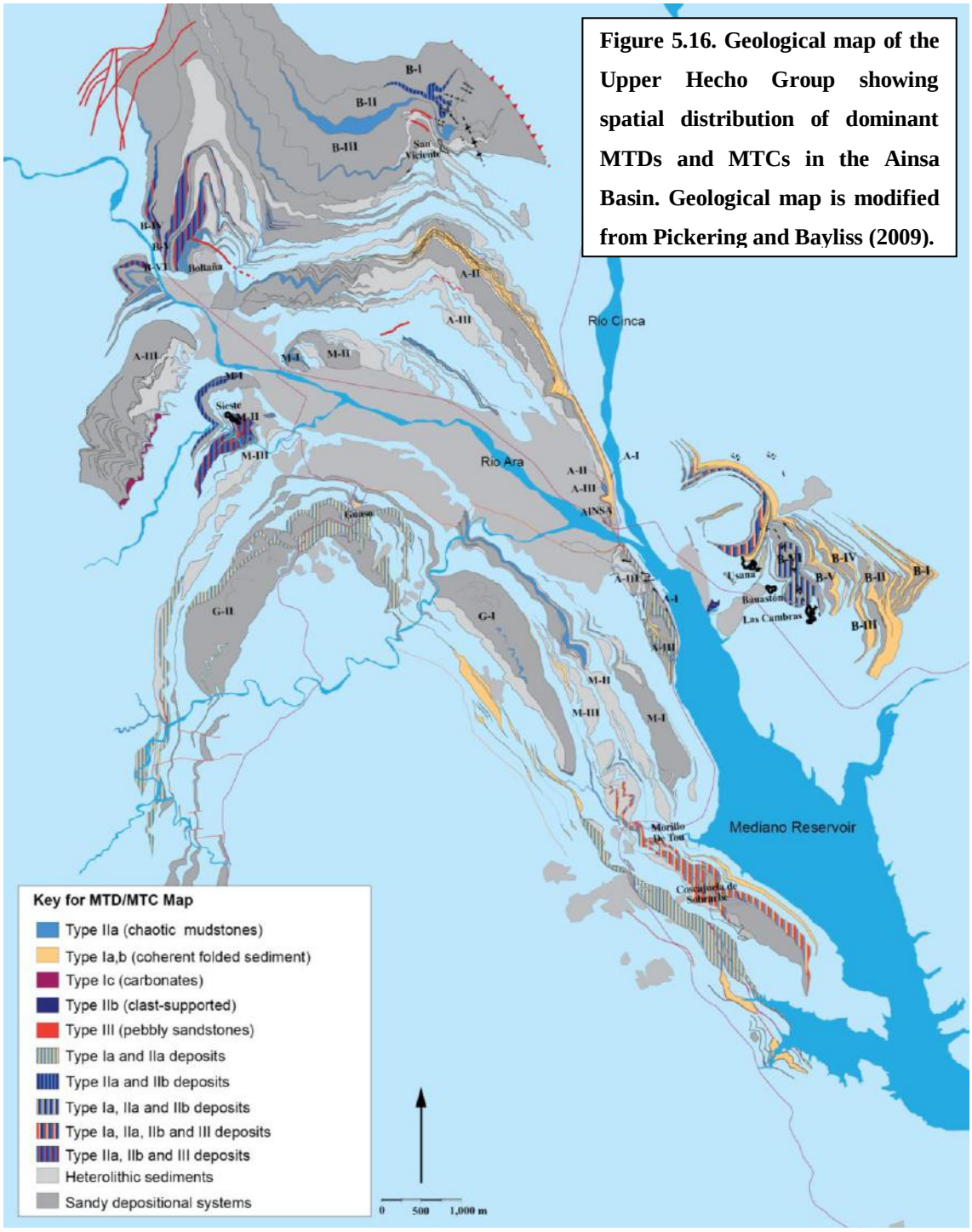

Figure 5.16. Geological map of the Upper Hecho Group showing spatial distribution of dominant MTDs and MTCs in the Ainsa Basin. Geological map is modified from Pickering and Bayliss (2009).

The geological map shows that the majority of Type Ia, Ib MTDs (pale orange) are typically documented around the villages of Banastón, Usana, Morillo de Tou, Ainsa and south of San Viciente, and are not found as abundant around the villages of Boltaña and Sieste (more distal settings). Type IIa (mid-blue), Type IIb (indigo) and Type III (coral) MTDs are documented in this more distal setting. To deduce spatial information on MTD facies type between proximal (e.g., Usana, Ainsa and Banastón) and distal locations (e.g., Boltaña and Sieste, based on Figure 5.1), discrete chaotic events were counted from sedimentary logs that were recorded in the field (Figure 5.17).

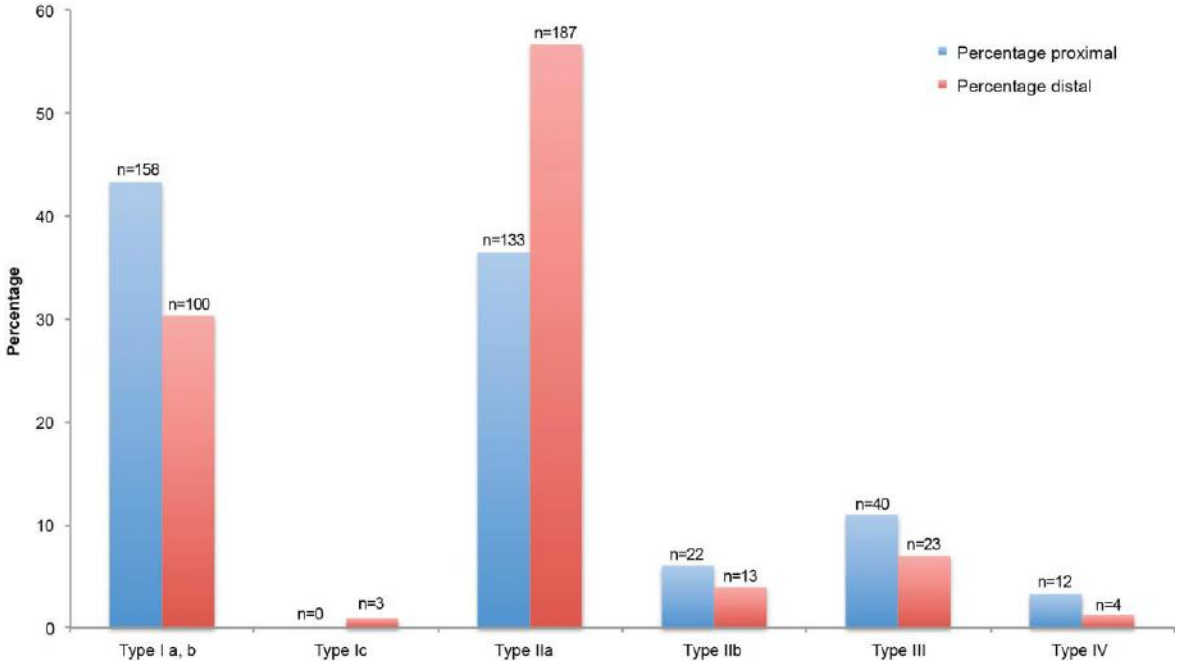

Figure 5.17. Graph showing percentages of MTDs logged in distal *versus* proximal environments. Count values of MTDs logged are defined by n=x above bars in chart.

These proximal settings show a greater abundance of Type Ia, b (43 *vs.* 30 %), Type IIb (8 *vs.* 5 %), Type III (12 *vs.* 8 %), and Type IV (5 *vs.* 1.5 %) facies compared to those in more distal environments. In distal settings (away from sediment input from the shelf), Type Ic (2 % *vs.* not present) and IIa facies (58 *vs.* 38 %) are documented as greater in abundance compared to their proximal counterparts.

5.3.2.3 Stratigraphic distribution

To deduce how MTD facies vary stratigraphically (i.e., through time), the abundance of MTDs were ordered according to system they were documented (Figure 5.18).

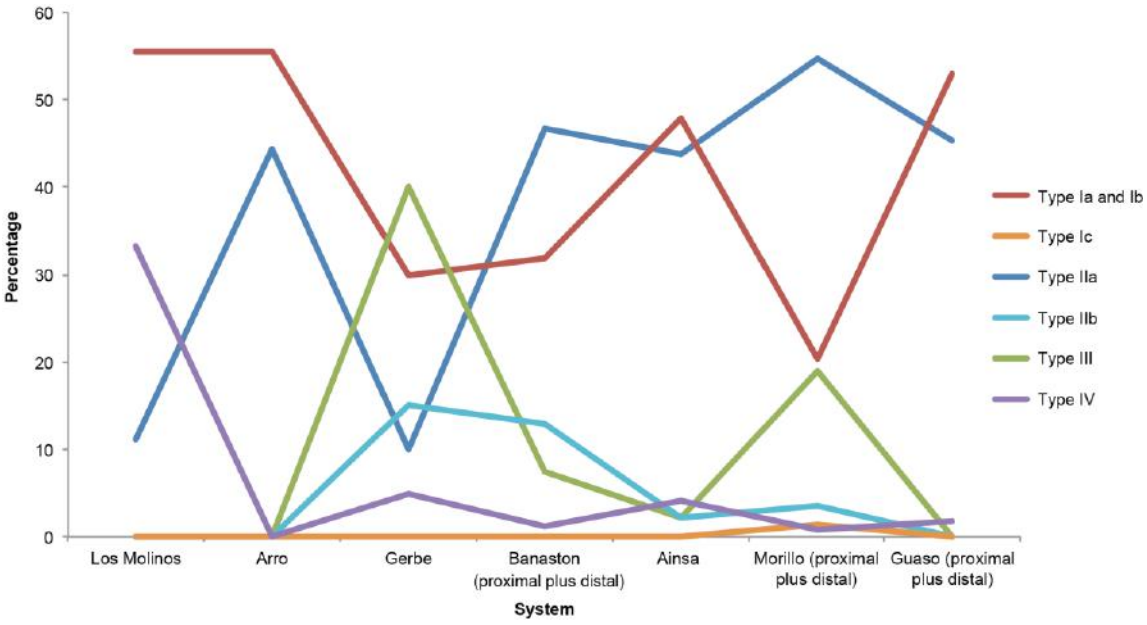

Figure 5.18. Count of Type I, II, III and IV MTDs logged per system (younging to the right).

Type I (a, b) deposits are most abundant in the Los Molinos, Arro, Gerbe, Ainsa and Guaso systems, comprising 20 to 55 % of MTDs. Type IIa MTDs comprise between 11 to 54 % of deposits and are most abundant in the Banastón and Morillo systems. Type Ic MTDs are documented in the Morillo System. Type IIb and III (a, b) MTDs (clast-supported pebbly conglomerates and pebbly sandstones) are absent until deposition of the Gerbe System, where they comprise 15 % and 40 % of MTDs, respectively. The Banastón, Ainsa and Morillo systems have similar abundances of Type IIb deposits until deposition of the Guaso System, where Type IIb and Type III MTDs are largely absent. Type IV MTDs vary from 33 to 0.9 % of MTDs in all systems, apart from in the Arro System, where this facies type is absent.

Due to accessibility and the greatest amount of exposure, MTDs were mainly logged in the Banastón, Morillo and Guaso systems (Fosado = 1; Arro = 48; Los Molinos = 9; Gerbe = 20; Banastón, = 174; Ainsa = 52; Morillo = 225, and Guaso = 179), permitting an MTD thickness frequency analysis of these systems (Figure 5.19).

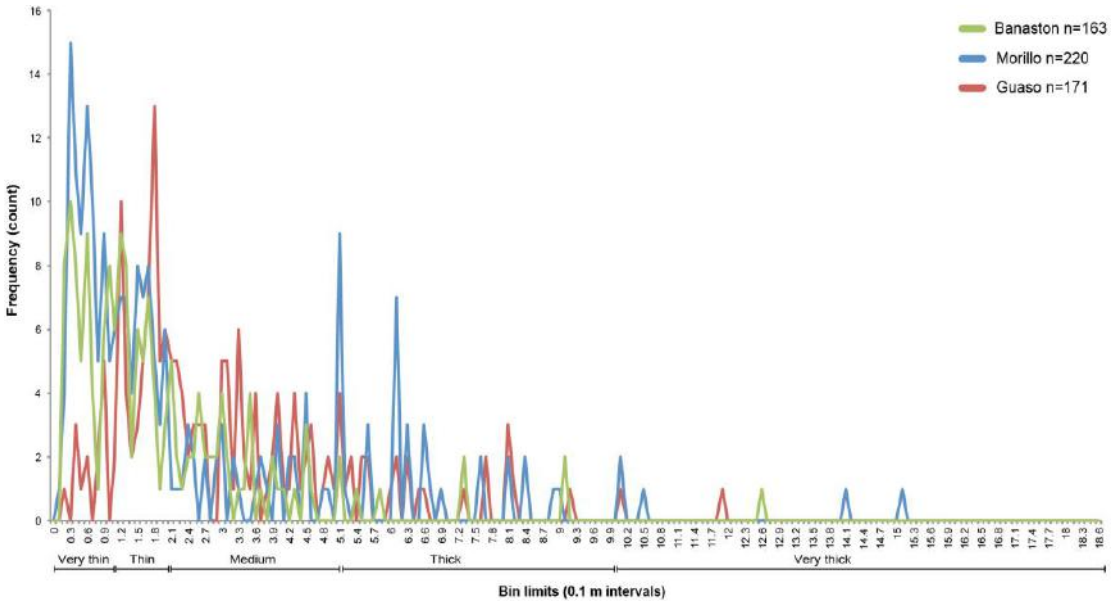

Figure 5.19. Frequency of all MTDs logged in the Banastón, Morillo and Guaso systems. Frequency of MTD thicknesses are calculated within 0.1 m intervals.

Data distribution of the Banastón and Morillo systems are similar, showing a greater abundance of very-thin MTDs (< 1 m thickness). However, in the Guaso System, thin- to medium-bedded MTDs (1 to 2 m thickness) are dominant. The Banastón and Morillo systems show the thickest MTDs, recorded up to ~ 15 m in thickness.

To determine the spatial variation of these depositional systems, the data were divided into 'proximal' and 'distal' locations, based on whether they were deposited slopewards at the base-of-slope, or 'distally' i.e., basinwards, away from the base-of-slope (Figure 5.1). Figure 5.20 shows the variation in MTD thickness in these systems based on these assumptions. The average thickness of Type Ia, Type IIa and Type III MTDs decrease distally in the Banastón, Morillo and Guaso systems. The average thickness of Type IIb deposits increases distally in Banastón and Morillo (from ~ 0.5 to ~ 0.8 m in both systems). The average thickness of transitional facies increases in the Morillo System (from not present to 1.2 m proximal to distal, respectively), and decreases in the Banastón and Guaso systems (from ~ 1 m to not present proximal to distal, respectively in Banastón, and from 4.2. m to 2.5 m proximal to distal, respectively in Guaso). Carbonate MTDs are not present in the proximal parts of the Banastón or Guaso systems.

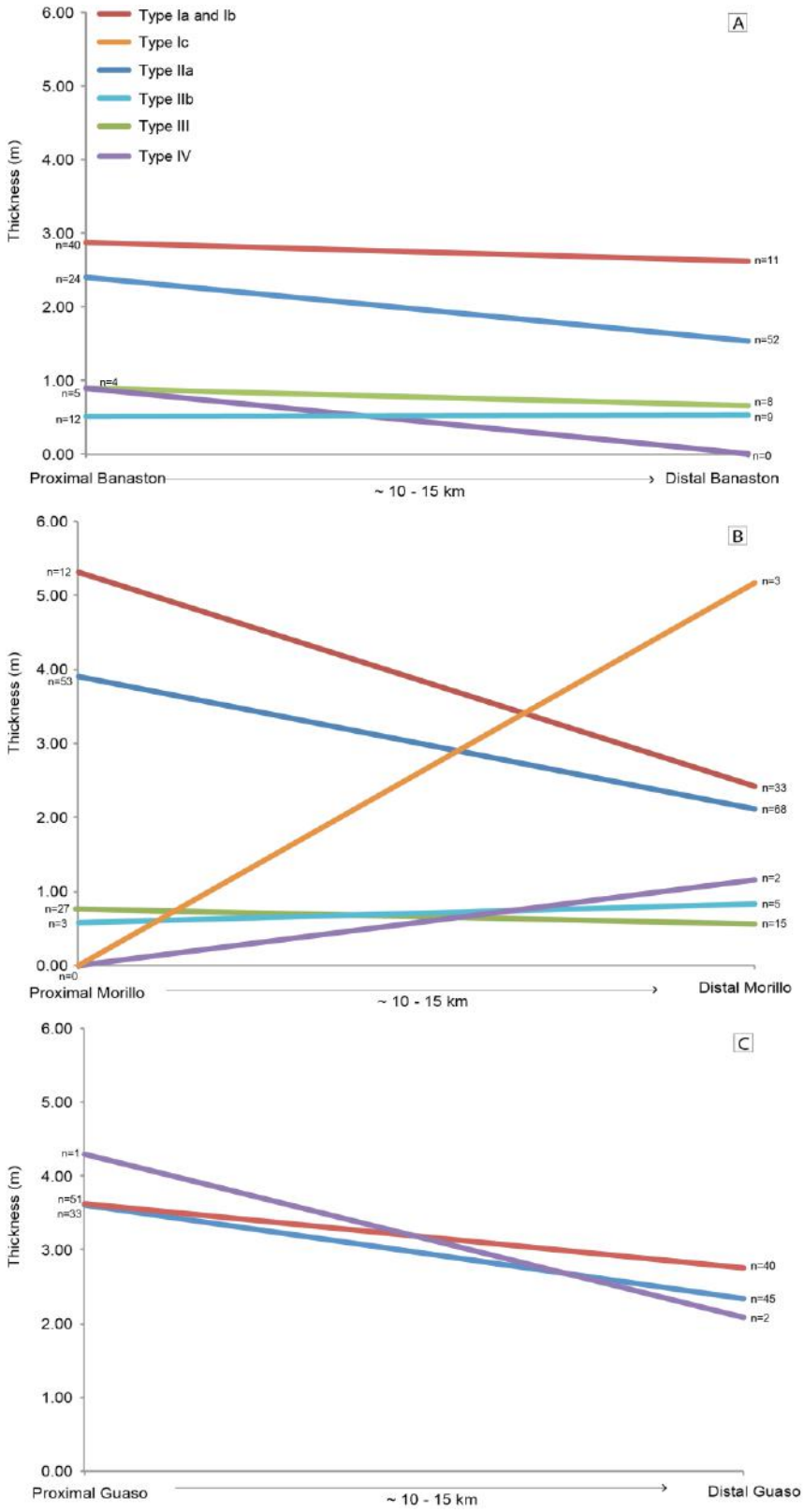

Figure 5.20. Average thickness change of MTDs (proximal to distal). (A) Banastón (carbonate MTDs are not present) (B) Morillo (all MTD facies present) (C) Guaso (conglomerates, pebbly sandstones and carbonates are not present). Count value of averaged data (both proximally and distally) are denoted by n=x adjacent to each facies type on graphs.

5.3.3 Aspect ratios

Using logged sections and outcrop measurements gathered in this study and from the geological map of Pickering and Bayliss (2009), width-to-thickness ratios were determined for both MTDs and MTCs in the Ainsa Basin (Figure 5.21). Deposits with only partial exposure were omitted from this dataset.

Intraformational MTDs and MTCs, i.e., chaotic deposits within sandy fan sequences, are observed to have a lower aspect ratio (lower thickness to width ratios) compared to those found on the slope, at the base of-, and marginal to- depositional systems.

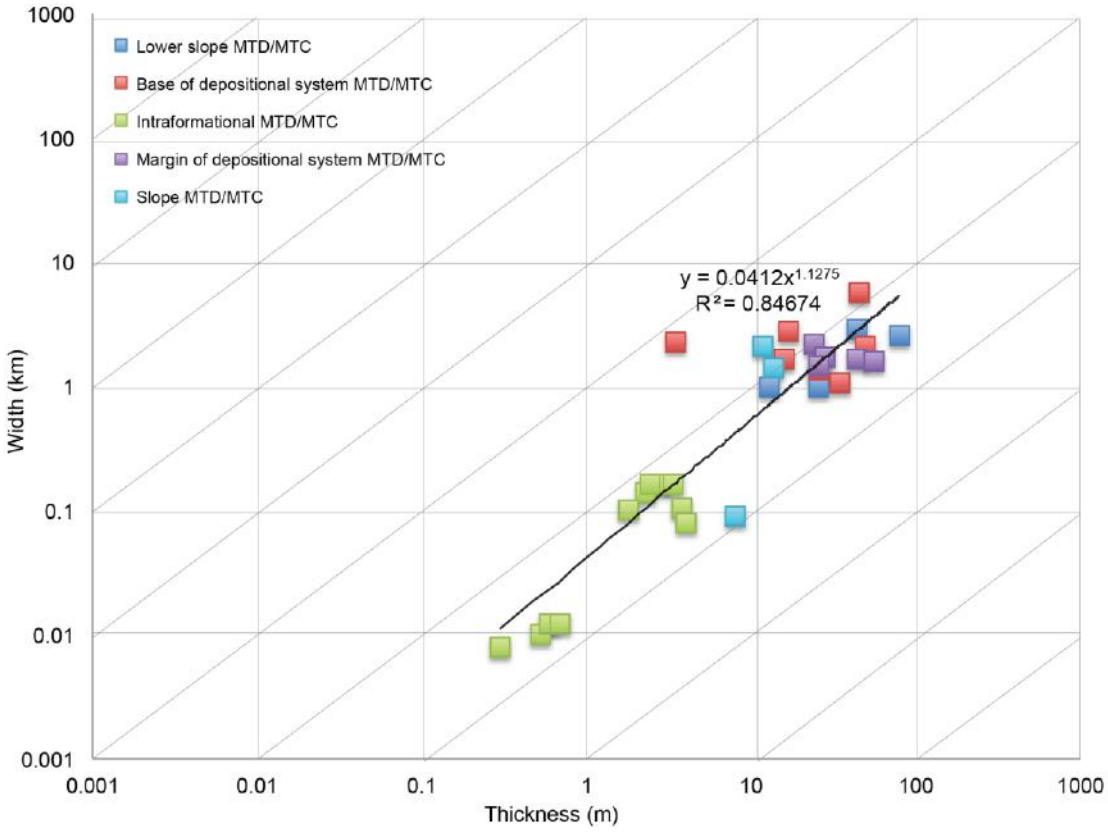

Figure 5.21. Width to thickness plot of MTDs and MTCs. Only accurate width measurements are used (either at outcrop or measurements from the geological map). Log-log scale.

5.4 GEOMETRY OF GLOBAL MTDs AND MTCs

Data from 238 published submarine MTDs and MTCs were compiled independently for this study to document the geometry of MTDs and MTCs found globally (*cf.* study

by Singh, 2010). Information was compiled from the scientific literature, which used seismic datasets and swath bathymetry to obtain data on both ancient and recent MTDs and MTCs. Geometrical parameters that have been recorded include volume, aerial extent, run-out, thickness and width. Summary results are shown in Figure 5.22. The raw data collected in this study is shown in Appendix E.

The R-squared value presented in each graph shows the square of the correlation coefficient, providing a measure of the reliability of the linear relationship between the *x* and *y* values. Values close to 1 indicate excellent linear reliability. Log-log plots show broadly linear relationships between predicting volume, run-out, area and widths of MTDs and MTCs. Volume is documented between 0.001 km^3 (Gulf of Alaska [Schwab and Lee, 1993]) and 76,000,000 km^3 (Atlantic passive margin, Grand Banks [Prior and Coleman, 1979]). Width is documented between 1.5 km (South Caspian Sea Basin [Richardson *et al.,* 2011) and 500 km (Mauritania slide complex, northwest African passive margin [Henrich *et al.,* 2008]). Area is documented between 6 km^2 (Western Mediterranean Sea [Lastras *et al.,* 2004; Berndt *et al.,* 2012]) and 120,000 km^2 (Barents Sea passive margin [Hjelstuen *et al.,* 2007]). Thickness is documented between 45 m (North Sea [Nygard *et al.,* 2002]) and 1000 m (Norwegian Margin [Bryn *et al.,* 2005; Haflidason *et al.,* 2005]). Finally, run-out is documented between 1.9 km (Ursa Basin, Gulf of Mexico [Sawyer *et al.,* 2009]) to 800 km (Norwegian Margin [Bryn *et al.,* 2005; Haflidason *et al.,* 2005]). It is recognised this dataset is not conclusive of all submarine failure events documented in literature; however the data evaluated provides a range of deposits to reflect the variation of scale and magnitude of mass-failure events.

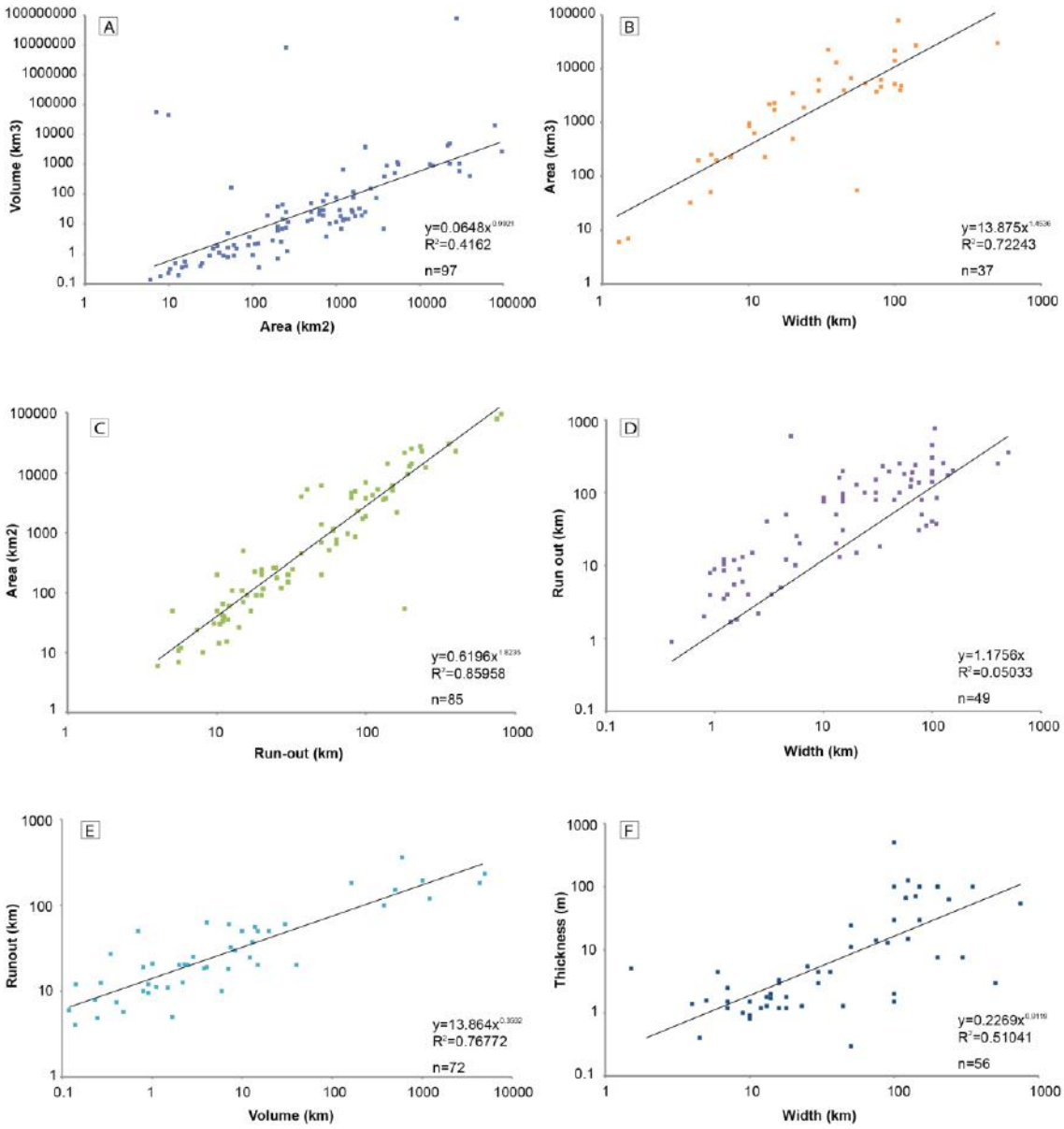

Figure 5.22. Global MTD and MTC geometry data from literature. (A) Area *vs.* volume (B) Width *vs.* area (C) Run-out *vs.* area (D) Width *vs.* run-out (E) Volume *vs.* run-out (F) Width *vs.* thickness. All graphs show log-log plots. See Appendix D for tabulated data used to construct these graphs.

Assigning a thickness to a particular event in seismic data is challenging, as it is not known whether these seismic-scale events are comprised of a single, or multiple stacked deposits. Average deposits (MTDs) in the Ainsa Basin are typically ~ 2 m in thickness, recorded up to 18 m. Average stacked deposits (MTCs) are measured as 12.5 m, recorded up to 80 m (Figure 5.13), showing that average deposit thicknesses are both sub-seismic resolution (~ 20 – 25 m [Chopra *et al.*, 2006]). Global MTD dimensions at the scale of seismic resolution, may either reflect multiple failure, or

mass basin-margin failure, and are likely to be events much larger than those documented in the Ainsa Basin. For example; the Mississippi Fan, Gulf of Mexico, contains MTD and MTCs that have formed sheets or lobes covering extensive portions of submarine fans, identified in Chapter 1 (Figure 1.19 and shown in 5.23) (Walker and Massingill, 1970; Hans Nelson *et al*., 2011). In this depositional system, the western MTD and MTC sheet extends 100 km wide and has a 300 km run-out distance, with a maximum thickness of 550 ms (Figure 5.23).

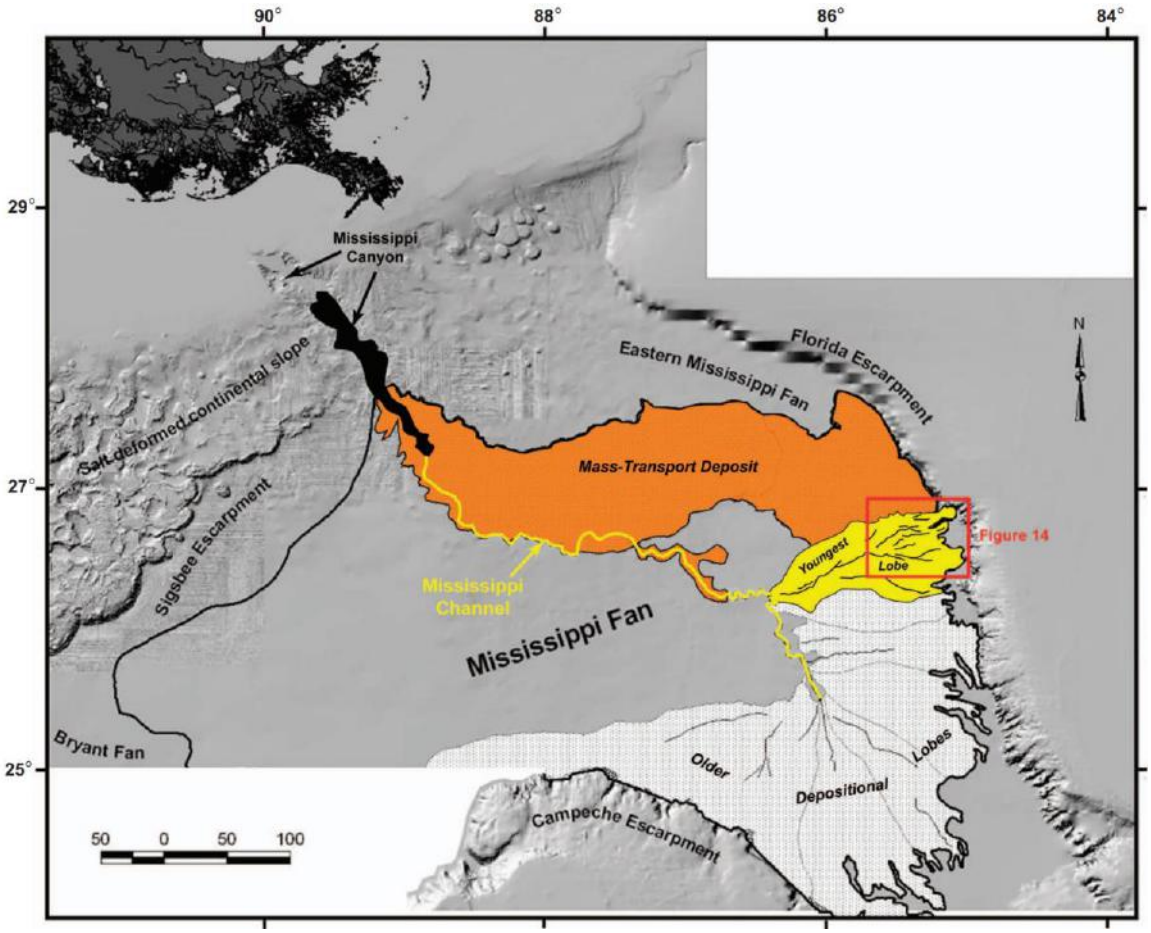

Figure 5.23. Map of the eastern Gulf of Mexico showing the extent of the Mississippi Fan and surrounding geomorphic features. Image from Hans Nelson *et al.* (2011).

To compare MTD and MTC dimensions documented in Ainsa and Buzzard, results are synthesised with the global dataset in Chapter 9 (Synthesis).

5.5 INTERPRETATION

Outcrop exposure and a well-defined palaeogeography of the Ainsa Basin has enabled the characteristics of MTDs and MTCs to be described according to temporal stratigraphic position and interpreted palaeoenvironments (e.g., Mutti, 1977; Puigdefábregas and Souquet, 1986; Millington and Clark, 1995a; Pickering and Bayliss, 2009, Bayliss and Pickering, 2015a, 2015b, Pickering *et al.*, 2015). These are identified as: (i) slope (upper and mid); (ii) erosional lower-slope canyons; (iii) base-of-slope; (iv) base of- and marginal to the inferred axis of depositional systems, and (v) intraformational environments. These stratigraphic inferences have led to an appreciation of depositional differences linked to the various sedimentary environments. MTD and MTC thicknesses and MTD facies were taken from sedimentary logs to evaluate the spatial distribution of MTDs and MTCs in different depositional environments within the Ainsa Basin.

Overall, Type Ia and IIa MTDs each account for ~ 46 and 45.5 % of MTD facies in the Ainsa Basin, respectively. These MTDs occur in all environments identified in the Ainsa Basin, thus are the most commonly occurring MTD facies types. All other MTDs account for ~ 10 % of deposits. Type III MTDs are the next frequently occurring, forming ~ 2.7 % of MTD stratigraphy. Type IV deposits comprise ~ 2.5 % of MTD stratigraphy and Type Ib, Ic, IIb account for < 1 % of deposits and (Table 5.4).

Due to outcrop exposure, it is not typically possible to quantitatively assess ponding or palaeotopography in the Ainsa Basin, which may have influenced thickness variations in accumulated deposits. Therefore, the effect of topographic confinement has not been taken into consideration when analysing thickness data. The average thickness of Type Ia MTDs is thicker compared to Type IIa deposits (3.35 m *versus* 2.61 m, respectively) (Table 5.4). MTDs and MTCs comprised of Type Ia deposits at the base of fans are found to be double the thickness compared to MTDs comprised only of Type IIa deposits (22 to 26 m average value, Figure 5.9). The thickest MTD (single event) is an 18.3 m event at the base of Ainsa II Fan, which culminates the thickest MTC (multiple events), comprised entirely of Type Ia deposits ~ 45 m (Locality 19, Figure 5.2-A). Type Ia deposits are also found interbedded with

Type IIa, b and Type III MTDs, and can also form discrete MTDs within MTCs as part of intraformational deposits (Figure 5.4, Log C).

Spatial analysis (determined from the proximal-to-distal evaluation) shows that folded mudstones (Type Ia MTDs) dominate MTD stratigraphy in proximal slope environments (43 *vs.* 30 %, Figure 5.17). Type IV MTDs (facies showing 'mixed' chaotic to folded mudstones) are also found in greater abundance in proximal and slope settings (5 *vs.*1.5 %, Figure 5.17). A possible explanation for the presence of such deposits in these environments may be related to both external parameters, such as magnitude of failure or length of the Ainsa Basin, and internal parameters, such as flow conditions of cohesive MTDs (including momentum, fluidity and volume). From ignition to deposition, the distance the flow travelled may not permit long run-out distances. Therefore, in some cases, disaggregation of Type Ia to more chaotic Type IIa deposits could be inhibited.

Type IIa MTDs dominate MTD stratigraphy down-dip in the system, beyond the base-of-slope (58 % *vs.* 38 %, Figure 5.17). Talling *et al.* (2012) discuss flow behaviour of high-, moderate- and low-strength cohesive flows. High-strength cohesive muddy flows form relatively thick deposits near to slope environments, however can form outsized mega-beds in submarine fan sequences (e.g., Figure 5.19). Moderate-strength cohesive muddy flows form relatively thin deposits that often occur in low-gradient fan fringe and basin plain settings. Low-strength cohesive debrites tend to be absent in more proximal systems, suggesting these flows can bypass proximal areas without depositing, or that they formed via flow transformation from an initial turbidity current. Based on the abundance of Type IIa MTDs identified in the proximal Ainsa Basin, these deposits likely deposited from moderate- to high-strength debris flows.

MTD spatial analysis shows that average thickness is greater in proximal locations (i.e., at or near to the base-of-slope) and decreases basinwards over ~ 8 to 10 km (Figure 5.20). Although average MTD thickness pinches out down-dip, large out-sized events (thick- to very thick deposits, > 5 m) are present at base of depositional systems beyond the base-of-slope (e.g., ~ 9 m debrite, Locality 23), or at distal fan environments (e.g., Figure 4.1-A, Locality 6, Boltaña Road). These out-sized events could be related to large-volume flows from significant failure of the slope, or local

confinement, such as scour infill that result in a very thick deposit. The distal expression of these thicker, more extreme events are likely to occur in the proximal Jaca Basin, further down-dip of the Ainsa Basin. Erosion may also be a factor in the 'bulking up' of MTDs, creating thicker deposits down-dip (e.g., debris flows in subaerial environments Breien *et al.*, 2008; Berger *et al*., 2011), discussed in Chapter 2.

Stratigraphic analysis shows that Type II (a, b) MTDs are only more abundant than Type Ia MTDs in the Banastón and Morillo systems. All other systems (Arro, Gerbe, Ainsa and Guaso) show Type Ia deposits as the dominant MTDs. The Guaso System contains thicker MTDs (thin to medium-bedded, 2 – 5 m deposits) compared to the Banastón and Morillo systems (dominated by very thin MTDs, < 1 m 52 *versus* 45 %, respectively, Figure 5.19), and contains more Type Ia MTDs. This data supports the conclusions of Bayliss and Pickering (2015a, 2015b), who suggested high gradients during the accumulation of these depositional systems as the Ainsa thrust-top (piggyback) basin was uplifted related to tightening of the Mediano, Añisclo and Boltaña anticlines. Steeper gradients during deposition of the Banastón and Morillo systems could be responsible for ignition processes that destabilised sediment on the seafloor, as discussed in Chapter 2 (Farin *et al.*, 2013). The prograding Sobrarbe deltaic system meant that during Guaso deposition, the main subaerial and shallow-marine sediment supply was relatively more proximal to the deep-marine systems in the Ainsa Basin. As observed in the MTD distribution data (Figure 5.17), proximal basin locations show a greater abundance of sediment slides/slumps. Shallowing of the Guaso System may also have meant lower gradients, resulting in more slope stability and, therefore, less gravitational momentum to submarine failure events and shorter run-out to form debrites.

The occurrence of pebbly MTDs (Type II and III deposits) differs between depositional systems (e.g., Caja, 2010 and personal communication with Puigdefábregas). In this study, they are first documented to appear in the Gerbe System, and remain as an integral component of MTDs during deposition of the Banastón, Ainsa systems, with abundances peaking during deposition of Morillo System, and then are significantly less documented during deposition of the Guaso System (Figure 5.18). The 'switching on and off' of pebbles deposited in deep-marine

systems could be related to a mixture of mature rivers and alluvial fans from the rising Pyrenees in the hinterland, both inputting sediment into the basin.

The type of MTDs and MTCs deposited in a slope environment appears to be dependent on the location of the main sedimentary routing system. When located off-axis to the main sedimentary input, or within laminated mudstones separating two depositional systems (e.g., new sediment slumps/slides mapped in the pro-delta Guaso System, Figure 5.4), MTDs are dominated by Type Ia facies, interpreted as instability of a fine-grained slope resulting in mass-failure (e.g., Pickering and Corregidor, 2005; Posamentier and Martinsen, 2011). MTDs containing pebbles are typically found within intrafan settings, however on a slope, coarser-grained MTD facies are generally only present within axial environments of the main sedimentary routing system that feeds sediment to deep-marine fans, such as in the axis of the Usana Canyon (Figure 5.6) and the axis of the M-II and M-III Fans (Figure 5.10).

The thickest MTC is ~ 80 m, located in the Usana Canyon in an erosional lower-slope environment and comprises multiple MTD facies types. Type IIa MTDs are observed to incise the base of the Usana Canyon and may mark the onset of deposition of a sandy submarine fan (Figure 5.10). The canyon is likely to have acted as a conduit for high-energy sediment gravity-flows, formed by the incision of multiple bypassing flows, depositing sediment further down-dip in the system. The deposition of isolated SGF deposits (Figure 5.7-E), along with the presence of thin pebble beds (Figure 5.7-B, C), and conglomerate-filled channels suggests a relatively long-lived canyon system. The uppermost 40 m of stratigraphy in the canyon is dominated by sediment slumps and slides, shown in the sedimentary log (Figure 5.6). This may suggest that after the main phase of bypass and erosion, the canyon walls (consisting of fine-grained muds), were likely to become unstable and infill any vacated space, depositing sediment slumps/slides from the surrounding slope. A depositional model is shown in Figure 5.24.

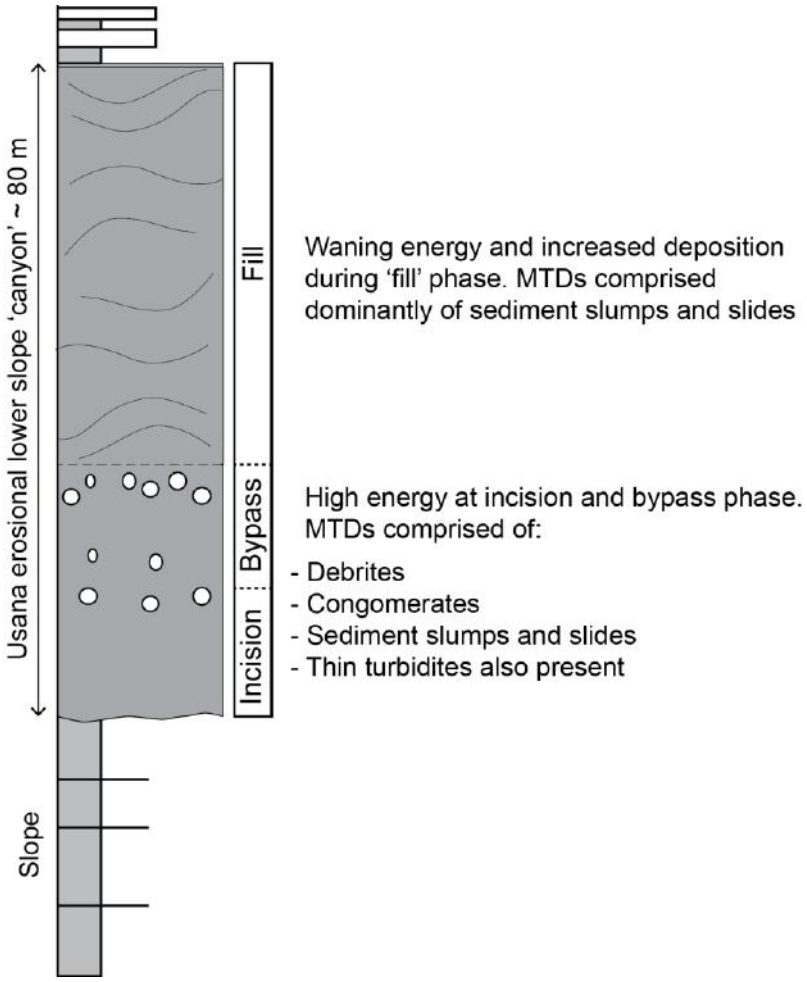

Figure 5.24. Stratigraphic depositional model of lower-slope erosional canyon environment, Usana. High energy flows coming through the system at the 'incision' and 'bypass' phase. Waning energy and increased deposition of sediment slides/slumps during the 'fill' phase.

Fitting with the model presented by Pickering and Corregidor (2005) (Figure 1.18, Chapter 1), this study identifies both individual and multiple failure events at the base of submarine fans, measured between ~ 3 to ~ 60 m, with deposits predominantly comprised of Type Ia and IIa MTDs (Table 5.2, Figure 5.9). Chaotic events may be precursor events to deposition of submarine fans for several reasons, including: (1) prograding deltaic and marginal marine sequences that impose additional litho- and hydrostatic stress to the slope, resulting in destabilisation of the upper slope, or; (2) sea-level fall, resulting in exposure of the upper slope and thus causing destabilisation of the upper slope (e.g., Maslin and Mikkelsen, 1997). Allogenic processes may result in major depositional changes that occur in the basin, causing failure an order of magnitude greater than intraformational MTCs deposited contemporaneously within depositional systems. Intraformational MTDs and MTCs

(i.e., chaotic sediments deposited within sandy fan sequences) are the thinnest deposits measured in stratigraphy of the Ainsa Basin, measured between 0.68 m to a maximum of 12 m. These deposits tend to have lower aspect ratios (Figure 5.21), potentially related to lower event magnitudes and may be thinner, resulting from autogenic processes, such as channel avulsion or channel margin/levée failure.

Seismically resolvable MTDs and MTCs, such as those identified in Figure 1.6 (Chapter 1) and 5.23 (this chapter), are larger-scaled events compared to those identified in the Ainsa Basin (Figures 5.13 and 5.15). Hans Nelson *et al.* (2011) comment that the abundance and magnitude of failure in passive margins (e.g., along the Atlantic margin) is greater than in active tectonic margins (e.g., the Ainsa Basin), supported by data collected in this study. Frequent shaking by earthquakes results in sediments becoming denser with time and thus does not mobilise as well into debris flows, compared to less consolidated sediment of passive margins (Lee *et al.*, 2004). Maximum run-out distances appear to be less restricted in passive margins (also active volcanic edifices e.g., Prior and Coleman, 1979), which are typically associated with large river sources that rapidly deposit unconsolidated sediment. Consequently, large-scale massive failures of the continental margin can deposit long MTD sheets that cover large portions of the Mississippi Fan (Figure 5.23).

5.6 SUMMARY

Categorising MTDs and MTCs in relation to the various deep-marine fan and related environments (proximal, distal, upper-, mid- and lower-slope, base-of-slope, base- and marginal- to depositional systems and intraformational environments) has enabled an overall understanding of spatial and temporal stratigraphic thickness trends and are a key parameter in understanding the complexity of these deposits in a tectonically active proximal deep-marine system.

- 121 MTCs (i.e., comprising multiple stacked events) were documented in this study. The average MTC thickness (12.5 m) in the Ainsa Basin is typically less than seismic resolution (~ 20 – 25 m, Chopra *et al.*, 2006). Maximum MTC thickness is measured up to 80 m.

- 686 MTDs (individual events) were documented in this study. Average MTD thickness is ~ 2.5 m, with maximum MTD thickness measured up to 18 m.
- Type Ia and IIa MTDs are the most frequently occurring chaotic deposits, to suggest frequent failure of the slope.
- Type Ia MTDs are measured as the thickest deposits, likely to reflect their highly cohesive nature.
- The type and abundance of MTDs and MTCs documented in a proximal deep-marine environment are variable. Average MTD thickness pinches out distally to suggest the dominant cohesive nature of these deposits result in a thinning down-dip. However, some of the thickest discrete events (> 10 m) are documented in distal settings to show outliers related to mass failure of the near shore environment. These large-scale events were likely to have also deposited in the Jaca Basin, down-dip of Ainsa.
- The lower-slope erosional Usana Canyon acted as a funnel where high-velocity SGFs were focussed down-slope and locally bypassed through a single conduit. These environments exhibit the coarsest grain-sizes in MTDs, which include conglomerates, pebbly mudstones and pebbly sandstones. Off-axis to the main sedimentary routing system in slope environments (i.e., away from canyons), sediment slump/slides predominate.
- Mapping the Guaso System has identified thick sediment slumps and slides in the fine-grained sediments, comprising the pro-deltaic slope of the prograding Sobrarbe Delta.
- As the Ainsa Basin evolved, tectonic controls meant it was likely that gradients of the slope changed through time. This is reflected in MTDs documented between different systems. At times of higher gradients, systems show abundant coarser grain-sizes in MTDs (i.e., conglomerates and pebbly sandstones), also debrites. At times of lower gradients (e.g., in Guaso), MTDs are dominated by Type Ia MTDs.
- The Ainsa Basin was tectonically active. Frequent shaking by earthquakes results in sediments becoming denser with time and thus does not mobilise as well into debris flows, compared to less consolidated sediment of passive margins (Lee *et al.,* 2004).

CHAPTER 6

EROSIONAL FEATURES OF MTDs: APPLICATION TO ANCIENT SUBMARINE ENVIRONMENTS, MIDDLE-EOCENE AINSA BASIN, SPANISH PYRENEES

6.1 INTRODUCTION

Erosive sediment transport processes and resultant MTDs are well documented from subaerial environments (e.g., Stock and Dietrich, 2003; Iverson *et al*., 2011; Mangeney *et al*., 2010; De Blasio and Elverhøi, 2011a, b; Schürch *et al*., 2011; Farin *et al*., 2013; McCoy *et al*., 2013). As outlined in Chapter 2, erosive processes are known to occur in submarine settings (Lastras *et al*., 2004; Masson *et al*., 1993; Nygård *et al*., 2002; Carter, 2001; Sawyer *et al*., 2012; Toniolo *et al*., 2003; Mohrig and Marr, 2003; Davies, 1986; Gee *et al*., 1999, 2001, 2005; Phillips, 2006; Alves and Cartwright, 2009, Alves, 2010, Alves *et al*., 2013, Omosanya and Alves, 2013a, b). Such erosive processes remain less well understood, particularly from ancient outcrops in deep-water deposits. Outcrops of the Ainsa Basin expose MTDs, some of which show basal erosion frozen *in situ* (Dakin *et al*., 2013 and references therein), enabling new observations of erosive debris-flow mechanisms preserved in an ancient submarine environment. This study documents some cases where the erosive mechanism is preserved at outcrop. These outcrops have enabled insights into local-scale erosion, including larger-scale 'channel-like' features or megascours up to ~ 1 km in width, interpreted as having been created from erosive sediment-gravity flows (probably MTDs). This chapter is based upon research published by Dakin *et al*. (2013) in the international peer-reviewed journal *Marine and Petroleum Geology* (see Appendix A). This chapter is outlined in the following sections:

(1) *MTDs showing basal erosion at outcrop*. Outcrops and architectural elements of MTDs showing basal erosion are identified in the Middle-Eocene Ainsa Basin, south-central Spanish Pyrenees. Facies associations, the internal structure and basal geometry of these deposits are explored in this section.

(2) *Megascours*. The formation of larger-scale features, termed megascours (*sensu stricto* Moscardelli *et al*., 2006) are presented. Transport and erosive debris-flow processes are discussed at the end of this chapter. Combined experimental results from the scientific literature and detailed outcrop observations in the Ainsa Basin, a model for erosion by MTDs, is proposed.

6.2 MTDs SHOWING BASAL EROSION

6.2.1 Fabric

Fabric refers to the spatial arrangement of particles in a sedimentary body, including packing and grain orientation (Schultz, 1984). Type IIa deposits are typically comprised of a chaotic mudstone matrix containing disarticulated and articulated shells, grains (< 2 mm), granules, pebbles (< 4 cm), cobbles and boulder-sized fractions dispersed throughout the matrix (Figure 6.1).

Basal surfaces of MTDs can show flat, non-erosive bases. However, in many cases, MTDs (predominantly chaotic mudstones) typically show an irregular basal surface, appearing to interact with the underlying substrate, resulting in erosion into sandy SGF deposits. Sedimentary logs were compiled to document the variability of fabric in chaotic mudstones (Type IIa MTDs) that show both irregular and planar bases. A comparison chart for estimating the percentage composition of grains *versus* matrix (presented in Chapter 3) was used to investigate an approximate percentage grain count (< 2 mm in *a*-axis) of these deposits at outcrop. Results are shown in Figure 6.2. Grain count in chaotic mudstones is observed as highly variable, with deposits showing almost no grains present, i.e., < 5 %, up to 50 % grains. MTDs that showed basal erosion into underlying sandy SGF deposits at outcrop generally have a greater grain content (40 and 50 % grains) compared to MTDs that do not show basal erosion (5 to 20 % grains, Figure 6.2-A). The fabric of Type IIa MTDs eroding into a sandy substrate are typically well-mixed or homogenised, and the grain-component (up to 50 % grains) is typically observed to decrease vertically through the deposit to suggest 'grading'. Data is also grouped into the number of MTDs that showed basal erosion by system (Figure 6.2-B). The Banastón and Morillo systems show a higher number of MTDs observed as having basal erosion.

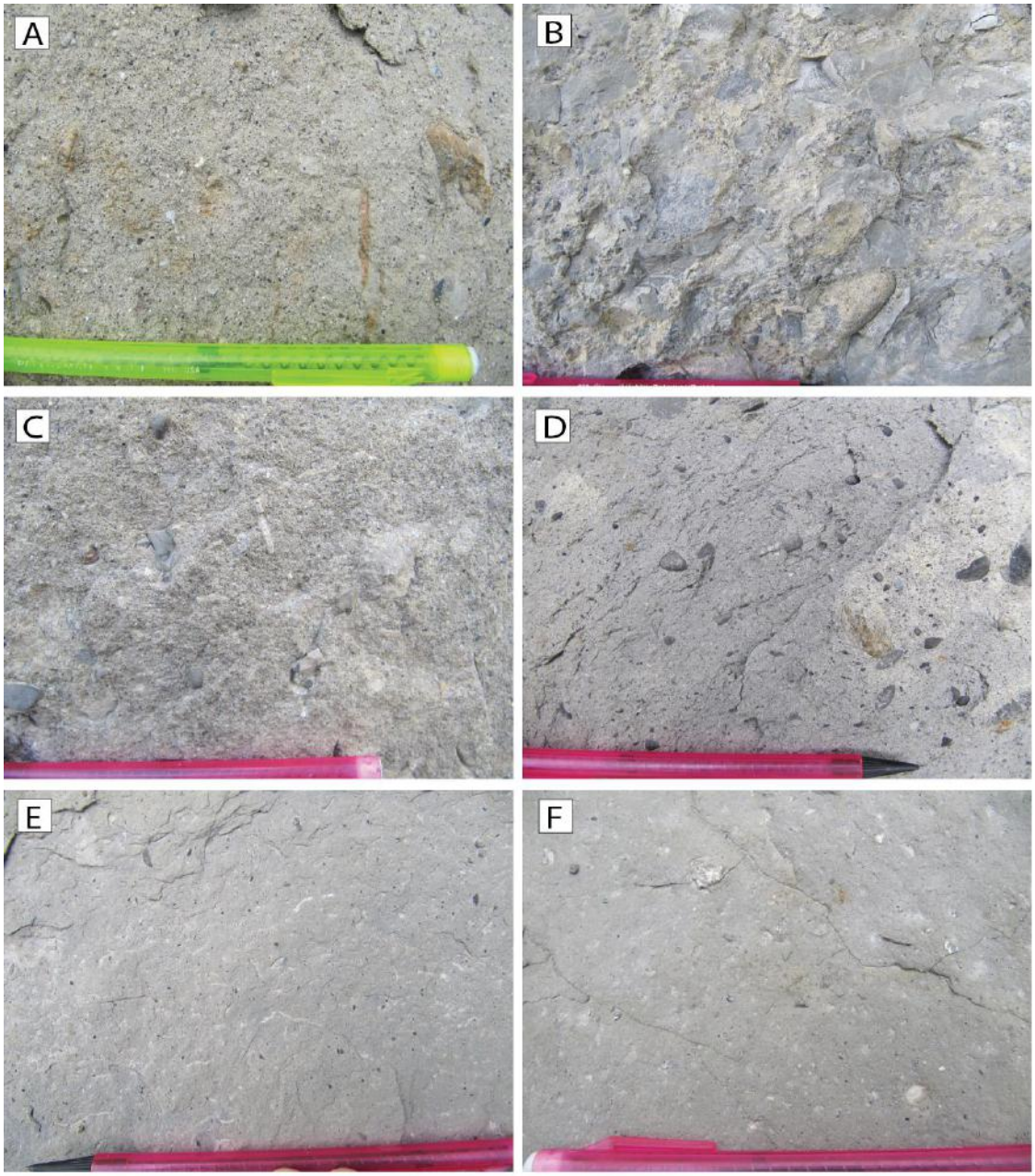

Figure 6.1. Variable fabrics in Type IIa MTDs at a macroscopic scale (A) Type IIa MTD showing basal erosion on road leading to Rio Sieste, Morillo I Fan (Locality 53) (B) Type IIa MTD showing basal erosion (MTD 2, Figure 6.15), Rio Ara, Morillo I Fan (Locality 23). (C) Type IIa MTD showing basal erosion, Rio Sieste, meander bend, Morillo II Fan (Locality 26). (D) Type IIa MTD showing basal erosion (MTD 1 Figure 6.14), Rio Ara, Morillo I Fan (Locality 23). (E) Type IIa MTD showing non-erosive base, Guaso I Fan (Locality 50) (F) Type IIa MTD showing non-erosive base, Morillo de Tou stream, Morillo III Fan (Locality 43). Pencil for scale in each photograph (15 cm).

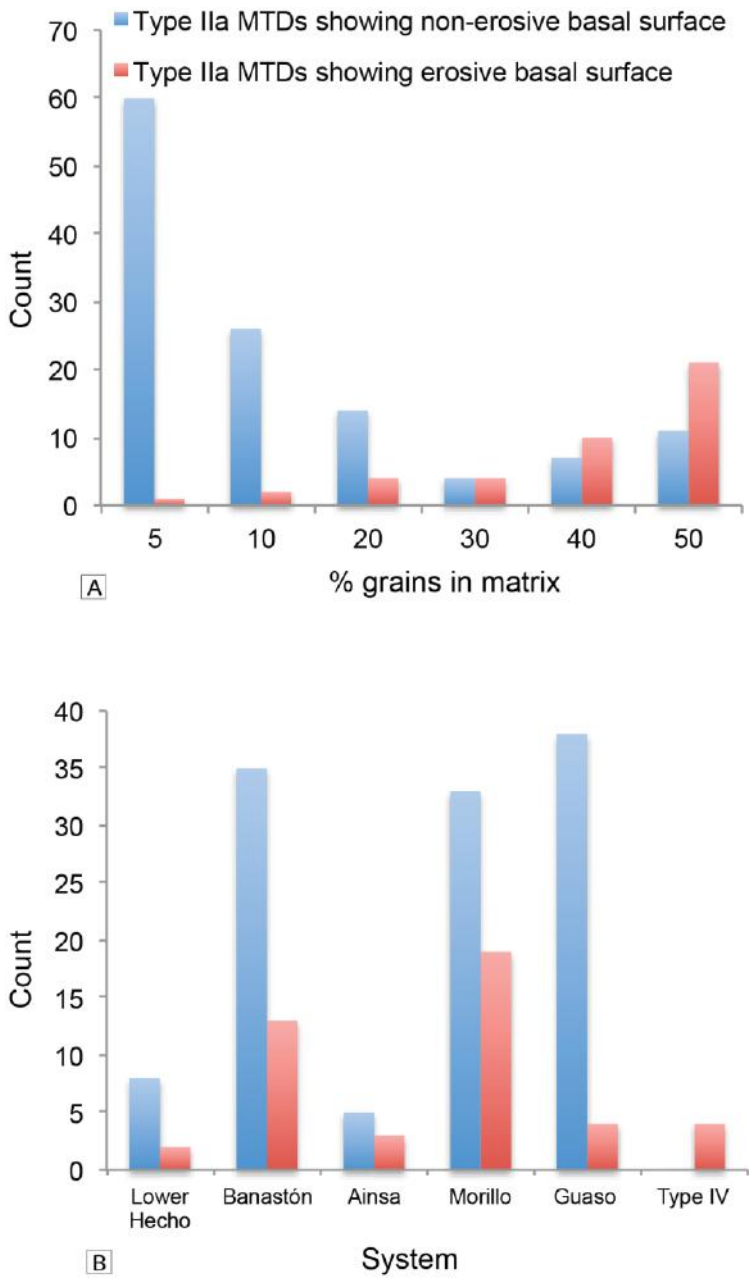

Figure 6.2. (A) Count of number of MTDs compared to percentage of grains in chaotic mudstone matrix. (B) Count of number of MTDs that show basal erosion into underlying sandy substrates per system (younging of systems is to the right).

6.2.2 Characteristics of MTDs showing basal erosion

This section explores examples of MTDs that show different styles of erosion and interaction with the substrate. Due to the rheological contrasts between sand and mud,

erosion of an underlying sandy substrate, e.g., a sandy SGF deposit, is more visible than preserved erosion features into underlying muddy substrates.

6.2.2.1 Sandstone blocks incorporated into the base of Type IIa MTDs

6.2.2.1.1 Locality 23 (Rio Ara, Morillo I Fan)

Locality 23 (along a hiking trail adjacent to the Rio Ara, west of Barcelo Monasterio de Boltaña) is an important outcrop showing angular, semi-lithified sandstone blocks incorporated into the base of the MTD (Figure 6.3).

The base of the Morillo I Fan exposes ~ 4.5 m of coarse- to very coarse-grained, medium- to thick- bedded nummulite-rich sandstones, interpreted as six amalgamated sandy SGF deposits, which show sharp grain-size breaks and grading. These sedimentary features are observed in the sedimentary log, to the left in Figure 6.3. Stratigraphically above these coarse-grained sandstones, a ~ 9 m Type IIa deposit is observed (MTD 1), showing a highly irregular base. The MTD is muddy, but has a high coarse- to very coarse grain content (up to 50 % grains). The fabric is homogenous, however grains appear to vertically decrease towards the top of the deposit to < 5 %. The deposit is pebble-rich, poorly sorted and contains abundant broken shelly fragments, corals and nummulites. Pebble sizes vary from 0.5 cm to 50 cm, are well rounded, composed of dark-grey limestones, sandstones, chert, and rarely granite. From the top-right in Figure 6.3-B, the basal surface of the MTD is observed to incise into the lower bedded coarse-grained amalgamated sandy SGF deposits. Overall, the erosional scour is approximately 20 m in length and incises up to 2.8 m towards the centre of the erosional scour, forming a broad 'U-shaped' geometry. Above the erosion surface, angular contorted sandstone rafts (up to 3.2 m) are incorporated into the base of the deposit.

The lateral margin of the scour formed by MTD 1 is accessed from the path and records in considerable detail the nature of the marginal incision surface. To the right of Figure 6.3-C, the MTD shows a planar basal surface with the underlying sandstones, however, as the basal surface is traced towards the path (towards the centre of the scour), it is observed to gradually incise 60 cm into the underlying sandstone. Above the incision surface, angular to subangular semi-lithified sandstone blocks from 0.03 m to 2.3 m (maximum dimension) have been incorporated, or

'plucked', into the base of the deposit (up to a maximum of 0.8 m from the base). In some cases, the sandstone blocks were not fully detached from the sandstone substrate and are observed as only partially incorporated into the base. The lateral margins of the 'U-shaped' scour show a greater number of sandstone blocks compared to the centre of maximum incision.

Stratigraphically above MTD 1 (Figure 6.3), there is a very coarse-grained, nummulite-rich sandstone bed (~ 1.2 m maximum thickness), interpreted as a sandy SGF deposit infilling residual topography from MTD 1. The sandy SGF deposit exposes aligned relict mudclasts that show amalgamated sandstone surfaces (Figures 6.3-D and E). The aligned mudstone clasts define horizontal stratification of the bed and provide a reference frame for the overlying erosion surface. Stratigraphically above this sandstone is an MTD (MTD 2) showing an irregular basal surface. Although this deposit does not show the 'plucking' mechanism as described at the base of MTD 1, from top-right to bottom-left, the sandstone bed pinches out completely, forming a triangular-geometry suggesting wholesale erosion of the sandstone. The MTD contains rounded pebbles, composed of sandstones, limestones and semi-lithified subangular sandstone blocks floating in a muddy matrix. Fine- to granule-grain sizes are present in the matrix. The presence of floating clasts show inverse grading and suggests that the matrix had strength at the time of deposition.

6.2.2.1.2 Locality 4 (Eña Quarry, Morillo II Fan)

The Eña Quarry (Locality 41) is accessed from a track leading to the Rio Eña, south of the A-2205. This outcrop exposes two Type IIa MTDs, with one deposit showing *in situ* basal erosion (MTD 2) (Figure 6.4). The sedimentary succession exposes ~ 4.75 m of sandy SGF deposits that are fine- to medium-grained and very thin- to medium-bedded (Pickering and Bayliss, 2009). MTD 1 is relatively tabular in geometry as the basal surface is planar and does not appear to interact with the underlying sandy substrate. However, the fabric of MTD 1 is analogous to MTDs showing erosion at outcrop, where up to 50 % medium- to coarse-grained grains are present in a well-homogenised matrix (i.e., MTD 1 in the Rio Ara outcrop). This MTD was sampled, with results presented in Chapter 7.

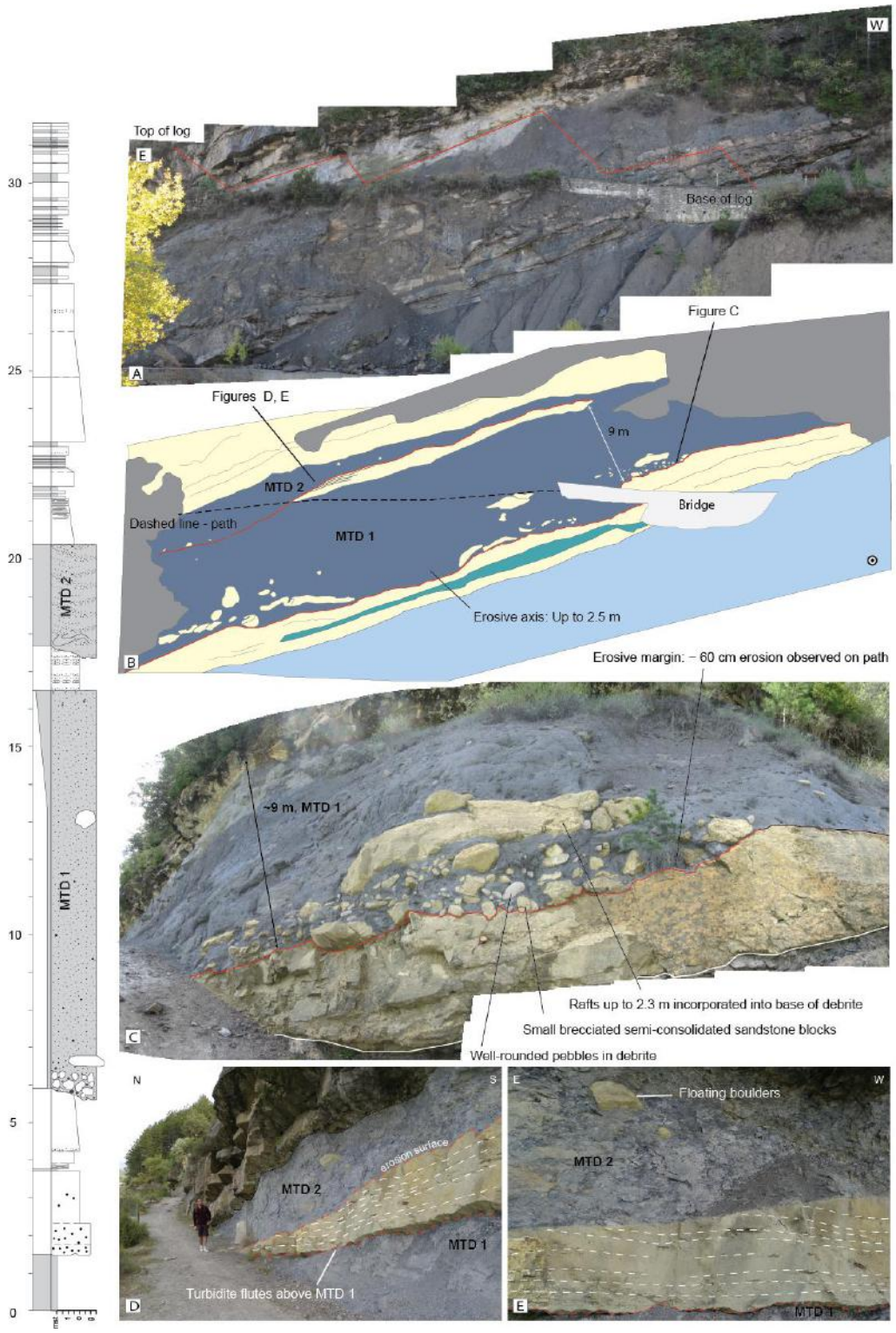

Figure 6.3. (A) Outcrop of erosive Type IIa MTDs in Morillo I Fan, looking south across the Rio Ara (Locality 23). Younging towards left (east). Log position shown as red line. Corresponding sedimentary log left of diagram, with vertical scale shown in metres (B) Photo interpretation. Palaeoflow is approximately out of the diagram, showing a down-dip cross-sectional view (C) Close up showing erosive base of MTD 1 along path, as indicated in Figure 6.3-B (D, E) Close-up showing the erosive base of MTD 2. Figures 6.3-C, D and E modified from Dakin *et al.* (2013).

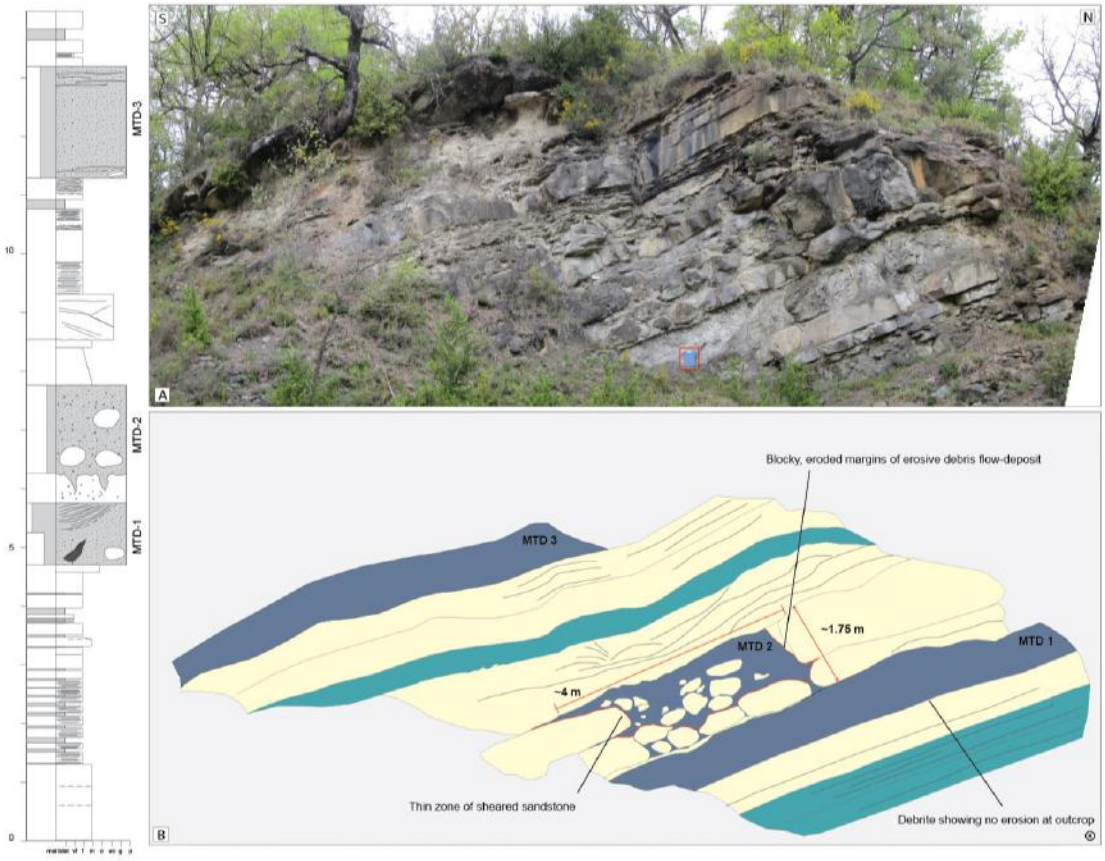

Figure 6.4. (A) Morillo II Fan, Eña Quarry (Locality 41). Clipboard for scale (35 cm). Sedimentary log is displayed on the left. Younging is to the left of figure, towards the south. (B) MTD in centre of outcrop (MTD-2) truncates sandstone beds. Palaeoflow is approximately into outcrop (i.e., towards ~ 320 ^{O}).

The fabric of MTD 2 of the Eña Quarry outcrop shows ~ 50 % medium to coarse grains, in a homogenised matrix with a few small granule-grade pebbles are observed in the matrix (Figure 6.4). MTD 2 is ~ 4 m in width and has a unique basal geometry as it does not form a tabular or 'U-shaped' cross-section, but shows almost vertical truncation of the adjacent sands, shown close-up in Figure 6.5. Unlike laterally continuous beds usually observed in sandy SGF deposits, 'Sand 1' and 'Sand 2' are truncated sandstone beds, where a ~ 4 m sandstone incision zone is observed (Figure 6.5-A). The stratigraphically upper bed (Sand 2) is truncated and replaced by a mud-rich chaotic facies containing semi-lithified angular to semi-angular sandstone blocks that appear as either plucked and *in situ*, or removed from outcrop. A close up of the southern margin highlights the erosive contact zone, where a 5.5 cm 'shear zone' is identified by a colour variation at the terminal margin of the sandstone bed

(shaded area, Figures 6.5-B and C). The stratigraphically lower bed (Sand 1) is also truncated, however the sandstone blocks appear only partially disaggregated, and in some cases are still attached to the bed. Many of the angular sandstone blocks from Sand 1 are observed and interpreted to remain relatively *in situ*. The matrix appears to be 'injected' into Sand 1, until the sandstone bed beneath is encountered.

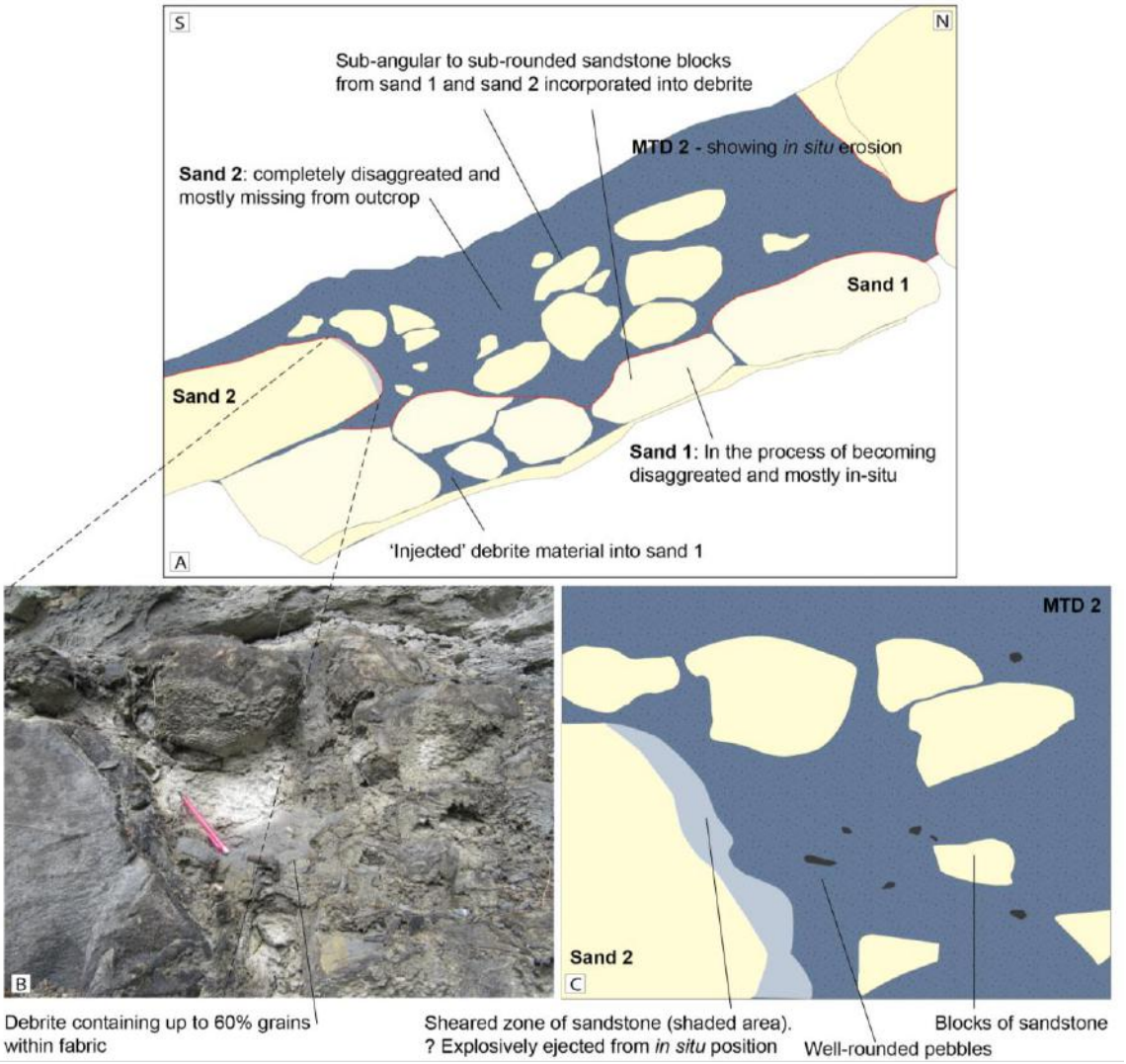

Figure 6.5. (A) Architectural geometry of MTD showing vertical truncation of lower sandstone beds (close-up of Figure 6.4). Palaeoflow is approximately into outcrop. (B) Photo, and (C) interpretation of sheared margin of 'Sand 2' (Locality 41). Pencil for scale (15 cm).

6.2.2.2 Striated surfaces at the base of MTDs

Striated surfaces at the base of MTDs are exposed where recessive weathering of muddy deposits expose the top surface of resistant underlying sandy SGF deposits. In some cases, the top surface of sandstone beds are observed as striated, crumpled or pitted with pebble marks. A fine-grained sandstone rock sample, located beneath an MTD with basal erosion is shown in Figure 6.6 (Locality 19, Forcaz Stream, Ainsa II Fan). The line drawings identify ripple-like features and scours that form gravel-filled striations parallel to palaeoflow.

Figure 6.6. (A) Plan view of rock-sample (9 cm) showing preserved soft-sediment striated surfaces on basal sand from Ainsa II Fan, Forcaz Stream (Locality 19). Arrow denotes palaeoflow direction (to the left of all diagrams). (B) Line interpretation (C) Oblique view of soft-sediment deformation. (D) Line interpretation. Crest fronts are perpendicular to palaeoflow and grooves are parallel to palaeoflow.

Soft-sediment deformation is observed at the top surface of a sandstone bed, located immediately below a coherent 23 m Type Ia MTD (coherent mudstones exhibiting folded fabric), Figure 6.7. Basal shear of the Type Ia MTD appears to have only affected the top ~ 5 cm of the underlying sandstone.

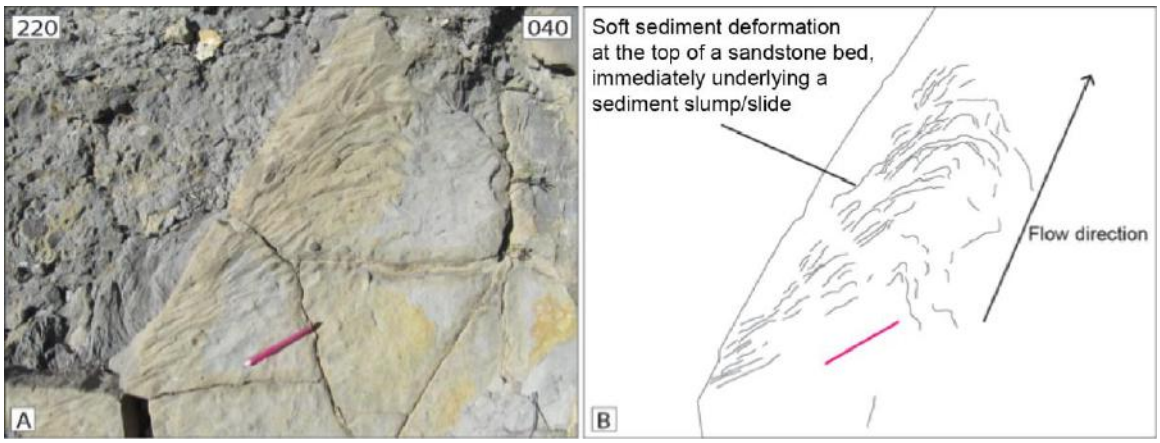

Figure 6.7. (A) Morillo II Fan, Rio Sieste (Locality 40). Pencil for scale (15 cm). (B) Line-interpretation of top sandstone surface beneath weathered Type Ia MTD.

Linear grooves, pebble marks, embedded pebbles and striated nummulites are observed on the tops of sandstones, Figure 6.8 (Locality 16, Ainsa Quarry, Ainsa I Fan). The long axes of pebbles are measured approximately parallel to palaeoflow, showing the palaeo-direction of the bypassing flow (towards ~ 320^{o}).

6.2.2.3 Injected matrix

In some cases, the matrix of Type IIa MTDs are locally observed as 'injected' into underlying sandstone beds (e.g., Figure 6.9). The distal Banastón fans III-VI are well exposed parallel to the N-260, west of Boltaña, Locality 6. Figure 6.9-A shows a 2.23 m medium- to coarse-grained sandy SGF deposit underlying a thin Type IIa MTD (0.9 m maximum thickness). The sandstone shows an irregular, potentially fluidised fabric. The basal surface of the MTD immediately above the sandstone bed is irregular and contains well-rounded dark-grey pebbles. The pebbles are observed to penetrate ~ 1.2 m into the underlying sandy SGF deposit forming an irregular 'whale-tail' structure. Blocks of partially disaggregated sandstone (up to 1.5 m in width) at

the top of the sandstone bed are also observed as partially dislodged from their original *in situ* position.

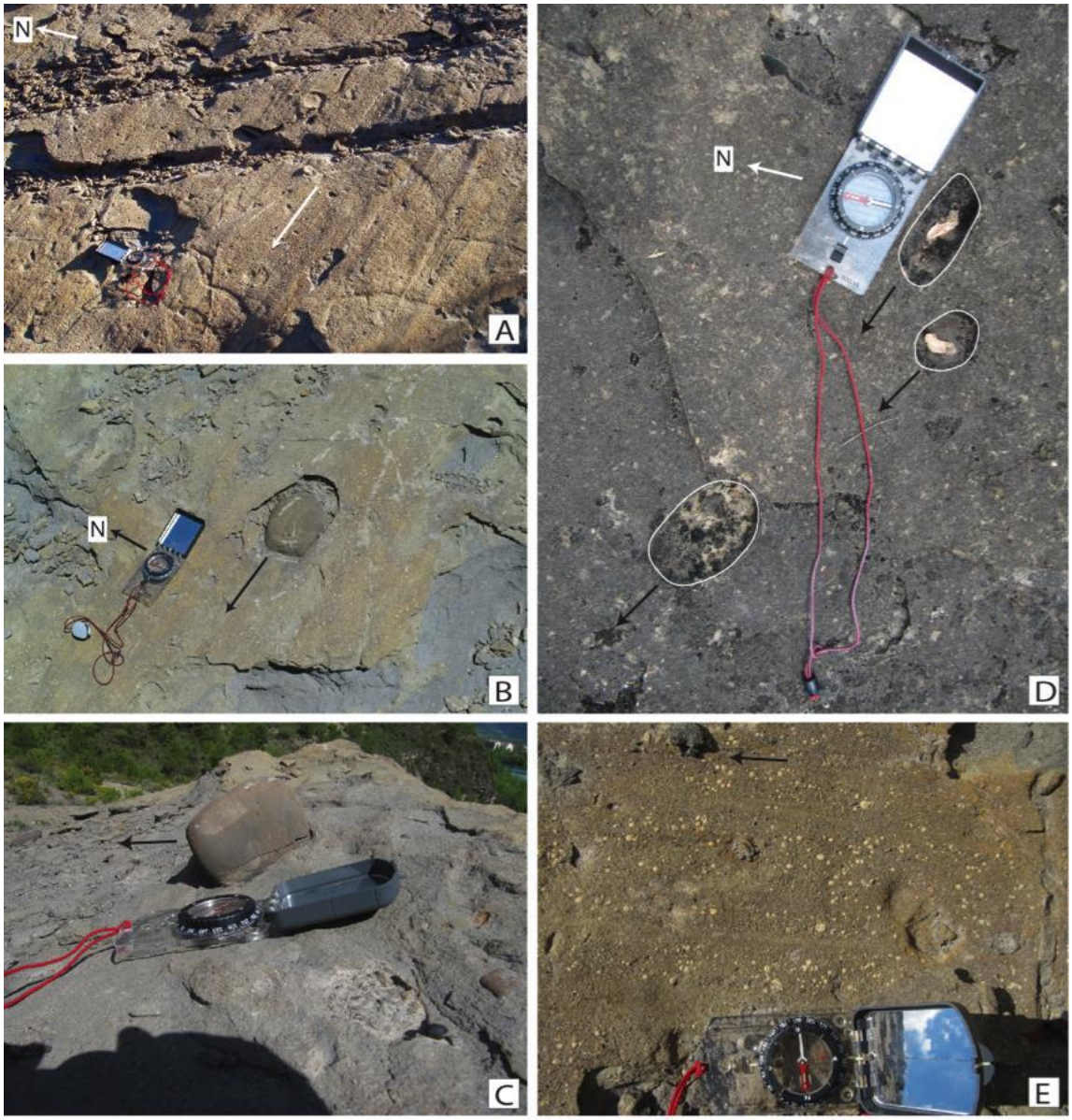

Figure 6.8. (A) Preserved striated pavement from the Ainsa Quarry, Ainsa I Fan. (Locality 7) (B, C) Pebbles embedded in to sandstone pavement. B-axis parallel to direction palaeoflow. (D) Hollowed-out pebble-pockmarks; *b*-axis parallel to palaeoflow. (C) Lineation of nummulites scoured in to sandstone pavement. Arrows denote palaeoflow direction, however, measurements are shown in Figure 6.20, Ainsa megascour. Diagram modified from Dakin *et al.* (2013). Compass for scale in each image (10 cm)

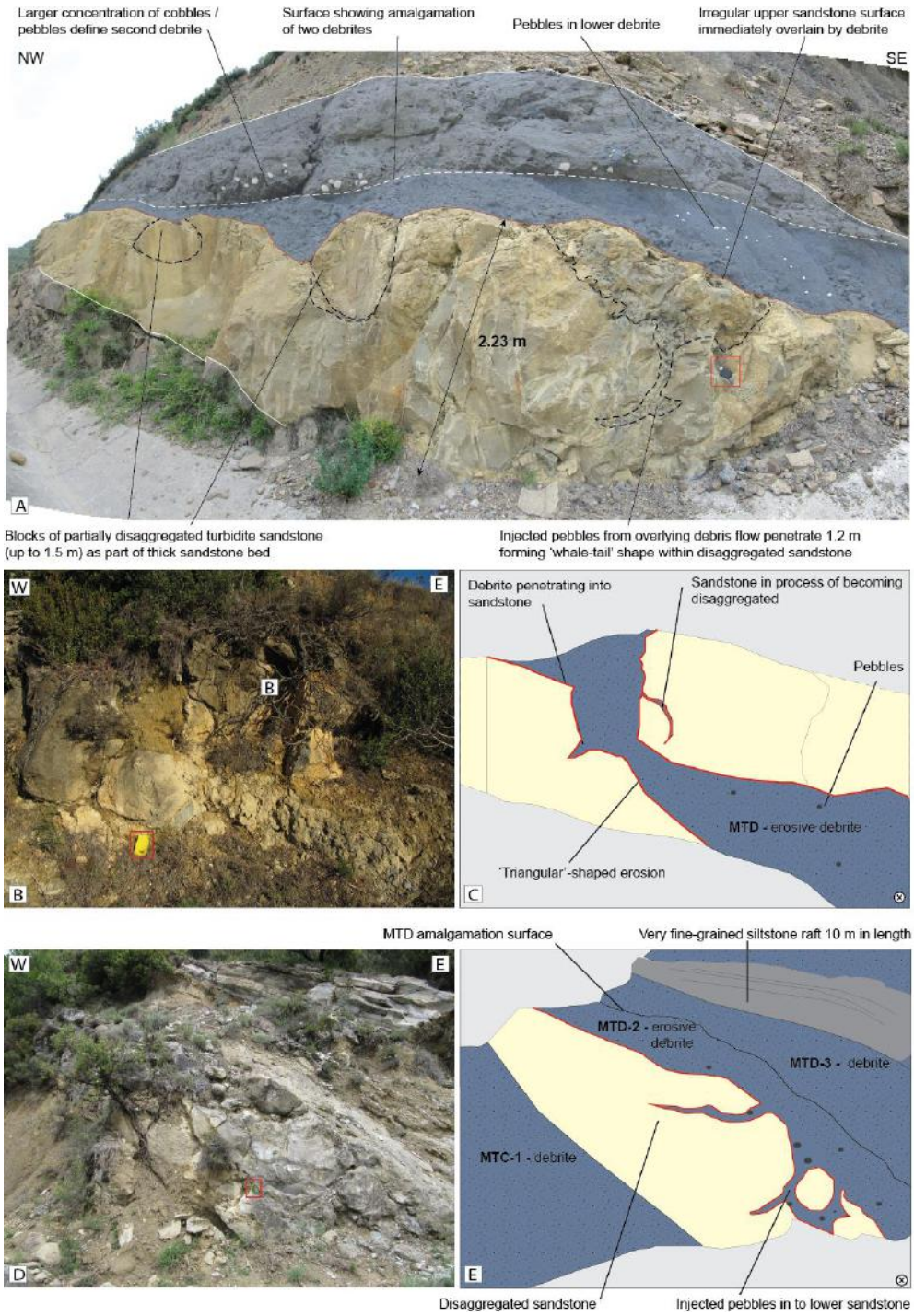

Figure 6.9. (A) Injection of pebbles and matrix of Type IIa MTD into underlying sandstone bed, Banastón V Fan. Compass for scale (10 cm) (Locality 6). Figure from Dakin *et al.* (2013). (B) Photo of Type IIa MTD on corner of road to Sieste village. Yellow notebook for scale (20 cm) (Locality 52), with (C) photo interpretation of Type IIa MTD showing basal erosion into underlying sandstone (D) Photo of Type IIa MTD on road to San Martin (road to Sieste village), and (E) photo interpretation of MTD-2 eroding into underlying sandstone. Pencil for scale (15 cm). Apparent splaying of sandstone beds is due to perspective of the photograph.

Other examples of injection processes are observed in Figures 6.9-B to E. The matrix of a Type IIa MTD is observed as 'injecting' or loading into the underlying sandstone bed, at the corner of the road leading to Sieste village (Locality 52) (Figure 6.9-B). The MTD is 'sandwiched' between a sandstone bed that is ungraded, medium-grained and ~ 2 m-thick. The upper and lower 'injected' top and base of the MTD is highly irregular, appearing to also penetrate the sandstone margins, separating blocks of sandstone from the surrounding bed. The fabric is homogenised and contains medium- to coarse grains (~ 50 %) and some well-rounded pebbles (sandstones and dark-grey limestones) up to 7 cm. Figures 6.9-D and E show another example of 'injected' Type IIa MTD on the road south of Sieste village (Locality 53). The basal surface of MTD 2 is irregular and is observed to penetrate the underlying ungraded medium-grained thick-bedded sandstone. The matrix shows the same homogenised fabric, containing up to 50 % medium- to coarse grains and some well-rounded pebbles (sandstones and dark-grey limestones). Pebbles in the matrix of the MTD are also observed 'injected' into the sandstone, as observed in Figure 6.9-A.

6.2.2.4 Ploughing of the palaeoseafloor

6.2.2.4.1 Locality 6 (Banastón V Fan, N-260 road section)

A unique stratigraphic relationship is recorded at Locality 6. A discontinuous pebbly sandstone (Type III MTD) is observed to plough into and beneath a thin package of *in situ* interbedded sandstones and mudstones (Figure 6.10). Ploughing processes such as this appear to utilise and take advantage of rheological contrasts, which may only occur on local scales. Pickering and Corregidor (2005) interpret this geometric relationship as 'hydraulic jacking' of the seafloor. This relationship is also observed in lateral terracing of MTDs that exhibit basal erosion, presented in section 6.2.3.1.

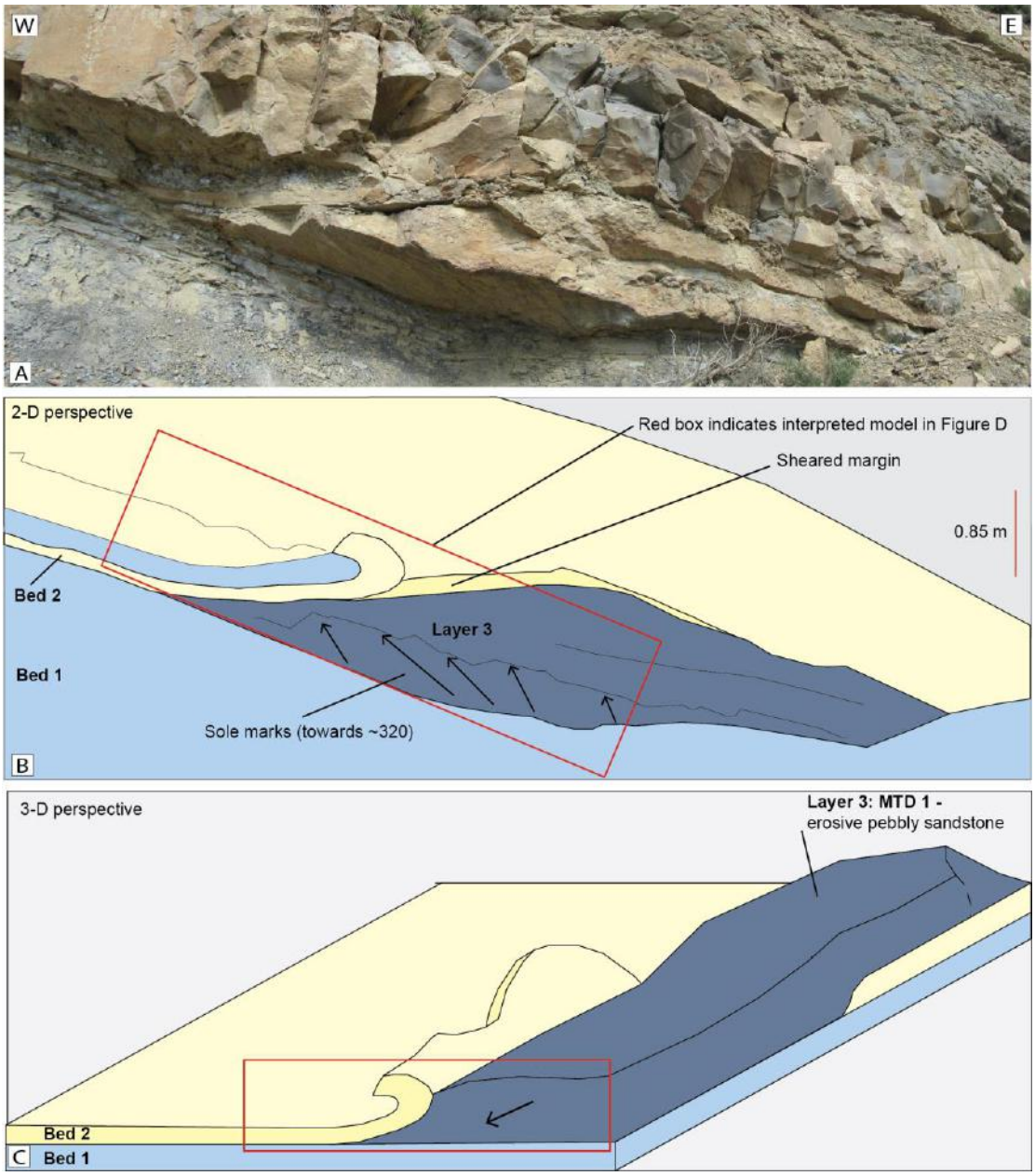

Figure 6.10. (A) Model of pebbly sandstone 'jacking up' palaeoseafloor (Locality 6.) Scouring of flow utilises rheological contrasts. Palaeoflow is oblique and out of outcrop (towards 320°).

6.2.2.5 Scouring of the palaeoseafloor

6.2.2.5.1 Locality 62 (Rio Sieste, Morillo II Fan)

Locality 62 is at a prominent meander in the Rio Sieste. The basal surface of the pebbly mudstone is observed scour into and truncate the underlying sandy SGF deposits to form a channel-like geometry (Figure 6.11).

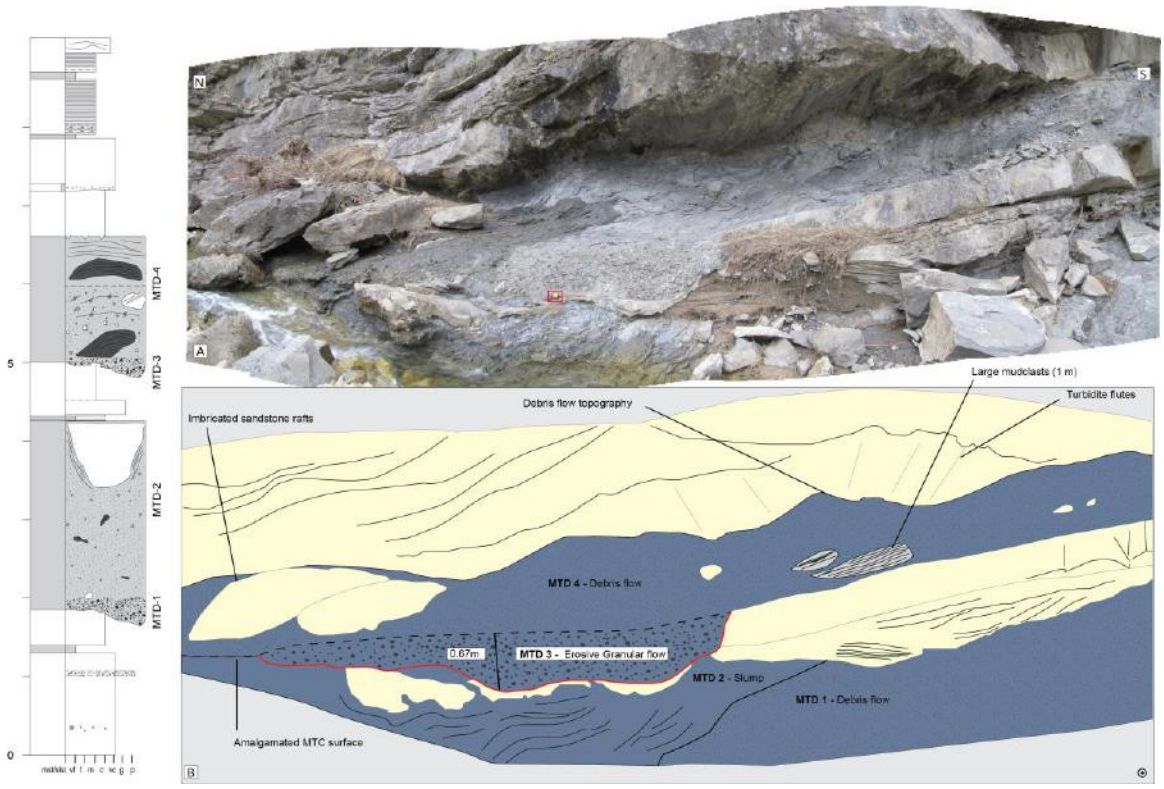

Figure 6.11. (A) Morillo II Fan, Rio Sieste (Locality 62). Measuring tape for scale (8 cm). Palaeoflow is approximately out of outcrop. Sedimentary log (displayed on left) was logged left of this image. Younging is to the left of figure. (B) Photointerpretation. MTD-3 erodes and scours basal sandstone.

The base of the sedimentary succession exposes an MTC comprising a lower Type IIa deposit (MTD 1), and an upper Type Ia (MTD 2). A 60 cm sandstone bed is then deposited and truncated by MTD 3, comprising a lower granular clast- to matrix-supported pebbly mudstone (MTD 3). The basal surface forms a 'U-shaped' scour, observed to fully erode the 60 cm sandstone.

6.2.2.5.2 Locality 4 (Arro Fan, road to Los Molinos)

Locality 4 is along the road north to Los Molinos from Arro (Hf-0106-Aa). Here, the Arro System is exposed adjacent to Barranco de la Nata de Arro. The sedimentary succession at this location exposes a series of sandbodies interbedded between MTDs. Figure 6.12 shows a Type IIa MTD with an erosive base showing channel-like erosion.

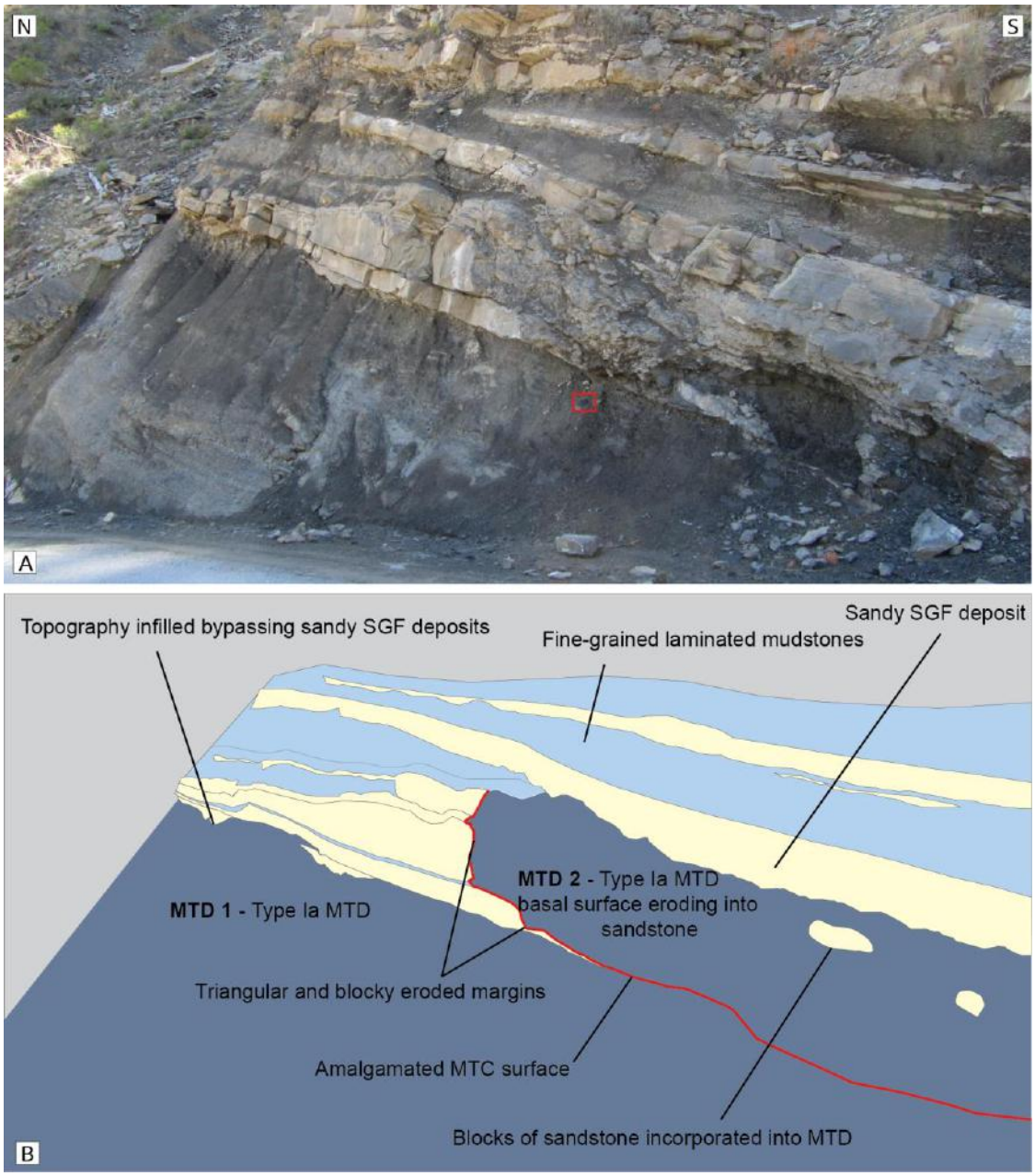

Figure 6.12. (A) Photo, and (B) interpretation of Type IIa MTD showing basal erosion into the underlying sandstones. Compass-clinometre used as scale (10 cm). Arro System, Road to Los Molinos, (Locality 4).

At Locality 4, 0.52 m of medium-grained bedded sandy SGF deposits are truncated below a 2.5 m – thick Type IIa MTD (maximum thickness). The base of the MTD is irregular and shows angular sandstone blocks incorporated into the deposit, although these are found nearer the top of the deposit. The chaotic mudstone matrix at this locality is muddier than those observed at other erosive MTD sites, containing a homogenous mud with ~ 10 % grains.

6.2.3. Basal geometry of scours

Due to the synclinal structure of the Ainsa Basin (Mutti and Ricci Lucchi, 1972, Mutti, 1983; Fernández *et al.*, 2004), stratigraphy generally dips parallel to palaeoflow, therefore, critical proximal and their correlative distal outcrops are rarely visible, which means that the detailed geometry of MTDs are not easily traced down-system. However, where such exposures are accessible (e.g., in road cuttings or along streambeds and rivers), valuable evidence can be gathered of the geometry of erosive scours up- and down- palaeoflow. Type IIa MTDs are typically located immediately above erosive scours that are 'channel-like' in geometry, perpendicular to palaeoflow.

6.2.3.1 Lateral terraced geometries

The lateral basal surfaces of MTDs, which show erosion into the underlying substrate, are observed as terraced, showing 'triangular' or 'blocky' geometries (Figures 6.13 and 6.14). In all studied outcrops, the lateral 'triangular' geometry of the eroded bed dips towards the direction of incision. If the underlying erodible substrate is bedded (i.e., sandy SGF deposits separated by a thin mud-cap), then erosion is typically observed to occur preferentially along the muddy substrate and incise through underlying sandstone beds at the narrowest point.

The outcrop adjacent to the N-260 west of Boltaña exposes the Banastón V Fan, Locality 6. Here, a ~ 19 m succession of sandy SGF deposits comprising thin to thick-beds of fine- to very coarse-grained sandstones are exposed, Figure 6.14 (Pickering and Bayliss, 2009). Above these sandy SGF deposits, a ~ 14.5 m MTC comprises ~ 17 MTDs, separated by thin, non-contorted fine-grained mudstones to suggest deposition from multiple events. Sandstones on the western margin are truncated laterally showing 'blocky'- to 'triangular' margins and immediately above the irregular basal surface is a ~ 2 m MTD (maximum thickness). The basal surface of the MTC is irregular and shows a 1.2 m Type IIa MTD incising into the underlying sandy SGF deposits. Immediately above the basal surface, blocks of angular to subrounded sandstones up to 30 cm in length are incorporated into the base of the deposit. The grain fabric is well-homogenised containing coarse- to very-coarse

grains (up to 50 % grains). The MTD contains very well-rounded sandstone and dark-grey limestone pebbles.

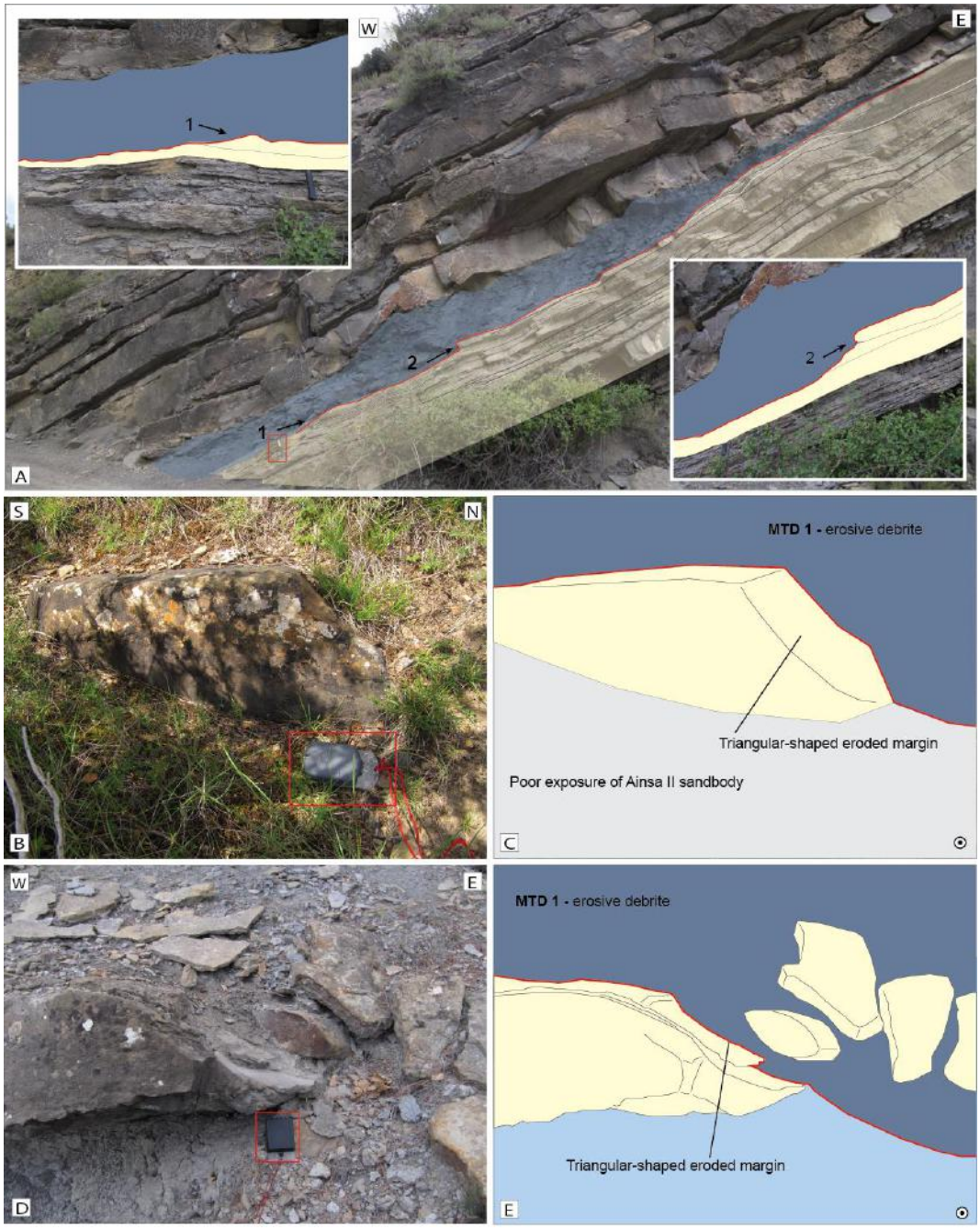

Figure 6.13. (A) Photo-interpretation of Type IIa MTD showing basal erosion. Forcaz Stream, Ainsa II Fan (Locality 19). Arrows (1) and (2) indicate gradual erosional step-down. Arrow 1 is rotated to show triangular geometry Maximum incision is towards the path, interpreted as the centre of the scour. Palaeoflow is approximately into outcrop. Hammer for scale (34 cm). (B and C) Lateral triangular step-down, Ainsa megascour (Locality 15.) Compass for scale (10 cm) (D and E) Guaso MTD displaying lateral triangular step-down (Locality 50). Compass for scale (10 cm).

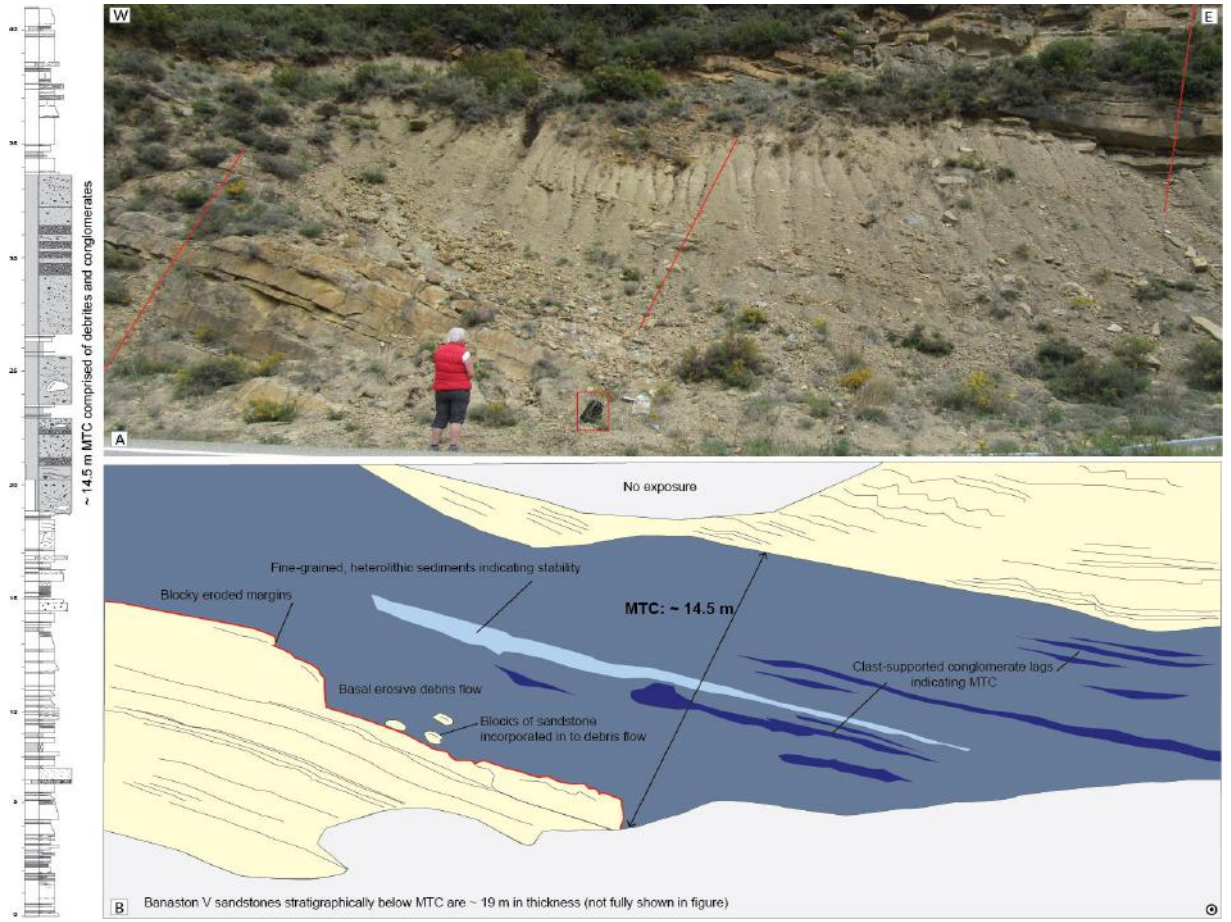

Figure 6.14. (A) Banastón V Fan, N260, west of Boltaña (Locality 54). Rucksack for scale (50 cm). Red lines show approximate positions of sedimentary log (displayed on the left). Younging is to the right of figure. (B) The basal MTD in the ~ 14.5 m MTC is erosive, eroding ~ 2 m of bedded sandstones. Palaeoflow is approximately out of outcrop.

6.2.3.2 ‘Flute-like’ geometry

At Locality 13 (Banastón System near to Banastón village), Type IIa and b deposits are found immediately above an unstructured coarse-grained sandy SGF deposit (~ 58 cm in thickness). MTD 1Ia is a chaotic mudstone, which is observed to erode into the underlying sandstone, forming a localised asymmetrical scour, ~ 1.4 m in length. The scour is ‘flute-like’ in shape, showing a shallow gradient towards the direction of palaeoflow (Figure 6.15).

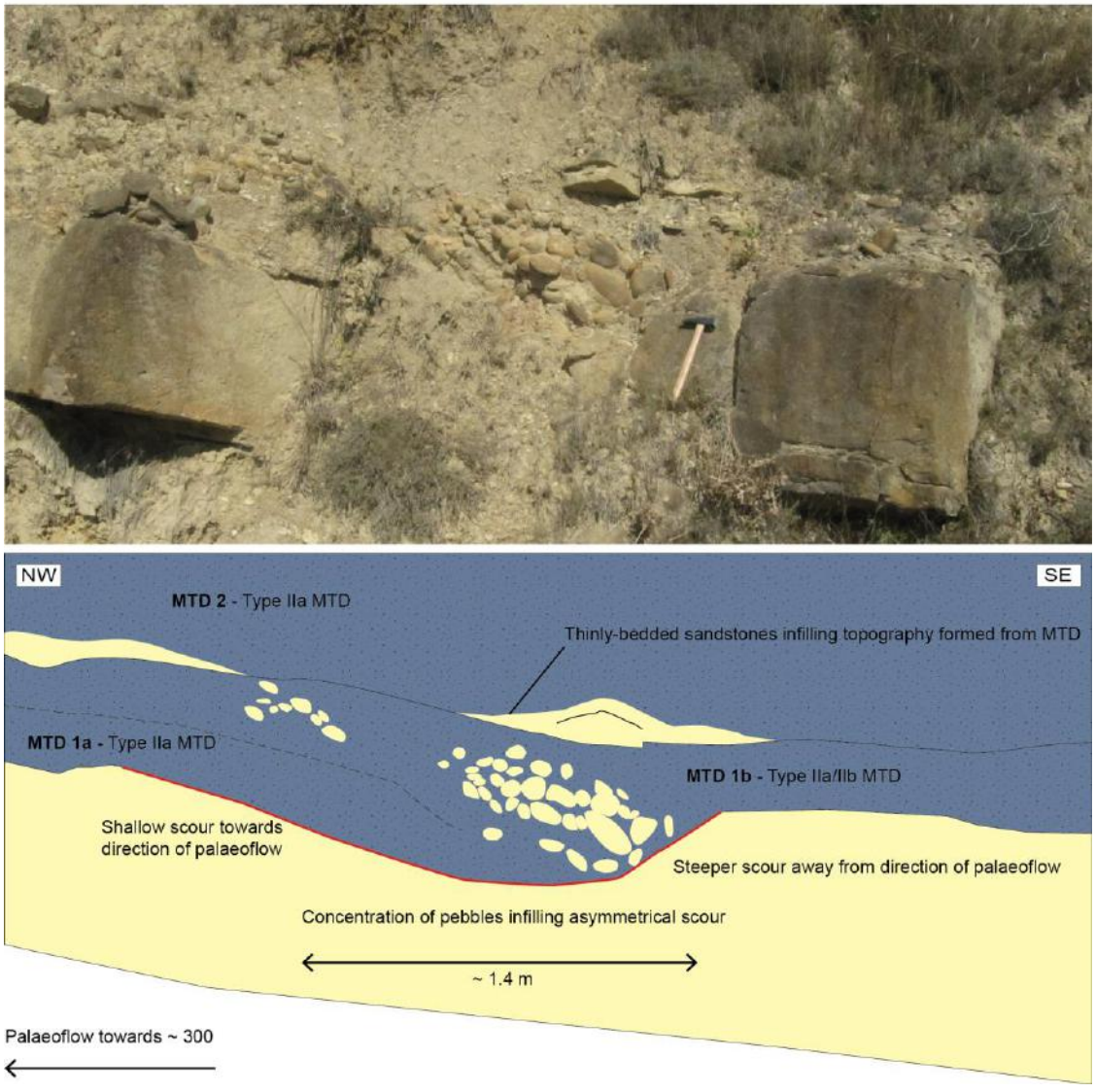

Figure 6.15. (A) Photo, and (B) interpretation of Type IIa/IIb MTD showing ‘flute-like’ geometry with shallow margins towards direction of palaeoflow. Hammer for scale (35 cm) (Locality 13).

MTD 1b (deposited above MTD 1a) shows a clast-supported pebble accumulation, showing imbrication to suggest a high velocity associated with the flow. The sandstones above the MTC are thin-bedded and infill any residual topography produced by the MTC. The localised down-dip flute-like geometry of this scour may be related to processes such as hydraulic jumps. However, currently there is no experimental data on hydraulic jumps that occur in cohesive deposits to substantiate this interpretation.

The outcrop in Guaso II, Rio Eña (Figure 6.16) shows an overall flute-like geometry, documented at Locality 56. The basal geometry of the scour broadens in the direction of palaeoflow, analogous to flutes created by turbulent flow. Immediately above the scour surface is a Type IIa MTD, which records *in situ* erosion (Figure 6.16). To the south-east (towards 160^{o}), the margins of the scour are well preserved (Figures 6.16-C, D, E and F). Here, angular sandstone blocks are partially incorporated into the base of the deposit, as seen in Figure 6.5. Sandstone blocks are 'missing' from the centre of the scour, suggesting they could be deposited further down-dip (not exposed in this cross-section), a similar relationship is observed at the Rio Ara outcrop (Figure 6.3). Sandstones above the MTD infill any residual topography and compensational stacking is observed on a decimetre to centimetre scale.

6.2.4 MTD thickness *versus* depth of erosion

The depth of maximum observed erosion into underlying substrates was measured, together with the maximum thickness of each MTD (Figure 6.17). Figure 6.17 shows a wide scatter of data reflecting a high amount of uncertainty of measuring outcrop dimensions in the field. However, there appears to be a weak but positive, broadly linear relationship between maximum MTD thickness and maximum erosion of the substrate. From this dataset, it appears that predicting MTD thickness versus erosion is difficult to determine with full confidence.

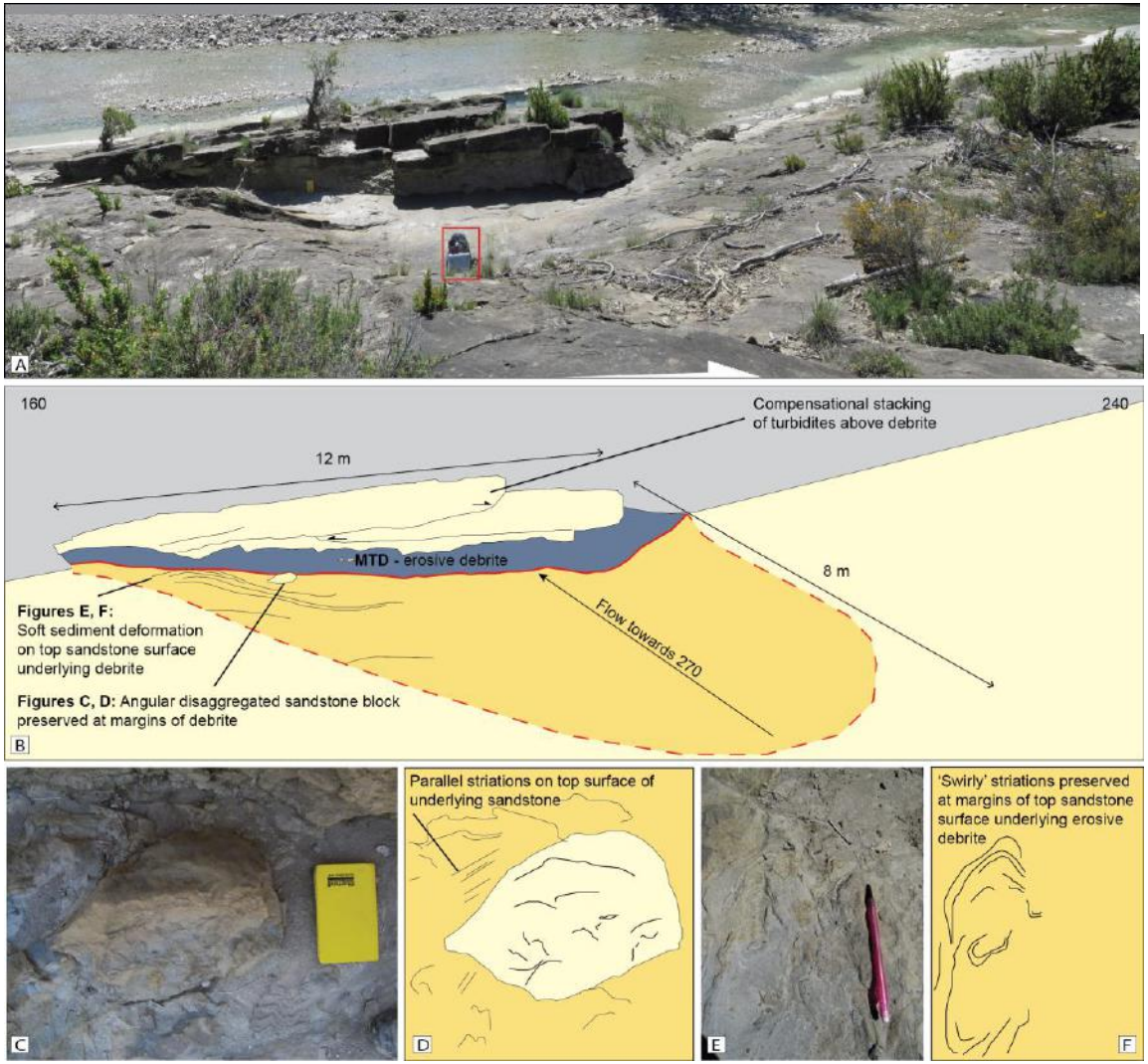

Figure 6.16. (A, B) Photo and photointerpretation of an elongate spoon-shaped scour, Rio Eña, Guaso II Fan (Locality 16). Rucksack for scale (50 cm). Arrows denoted flow direction. (C, D) Photo and photointerpretation of sandstone blocks to left of Figure B (E, F) Photo and photointerpretation of striations preserved at the left of Figure B.

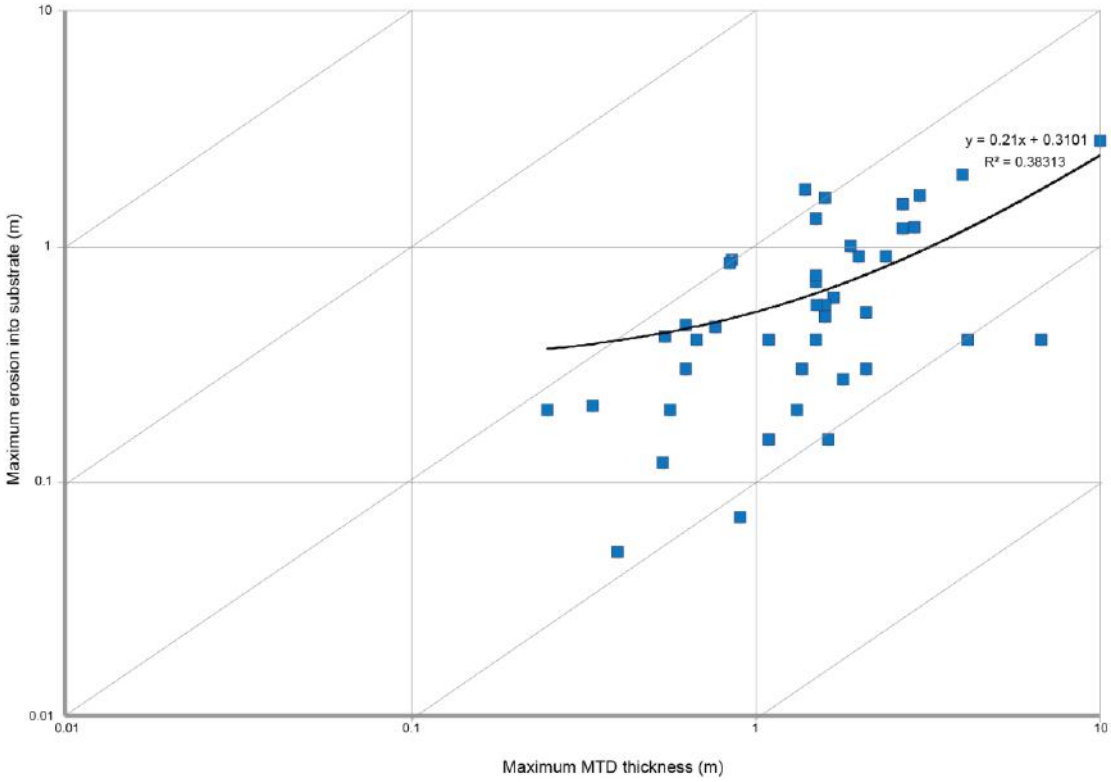

Figure 6.17. Log-log graph showing maximum thickness of MTD *versus* maximum erosion measured in the field. N = 42.

6.3 MEGASCOURS

Megascours, as identified in the field by Dakin *et al*. (2013), are believed to have formed from multiple events, i.e., retrogressive failure, creating channel-like geometries, similar to the basal-scour geometry of individual events (Figures 6.11, 6.12). This study identifies three 'megascours', however it is likely more are present in the Ainsa Basin (*cf*. Bayliss and Pickering, 2015b, figure 7), Figure 6.18. The 3-D geometry of megascours located in the Ainsa Basin is difficult to model accurately due to a lack of up or down-dip exposure. However, fieldwork provides excellent 2-D cross-sectional profiles to measure maximum dimensions, thickness and sedimentological detail, not obtainable through seismic studies. Although submarine seismic studies investigate scales much larger than the megascours found in the Ainsa Basin, a major advantage of combining seismic studies (e.g., Prior *et al.*, 1984; Maslin and Mikkelsen, 1997; McGilvery and Cook, 2003; Postamentier and Kolla, 2003;

Moscardelli *et al.*, 2006; Minisini *et al.*, 2007; Minisini and Trincardi (2009); Posamentier and Martinsen, 2011) and fieldwork (this project) allows comparable processes to be understood at different scales to determine both geometry and sedimentology.

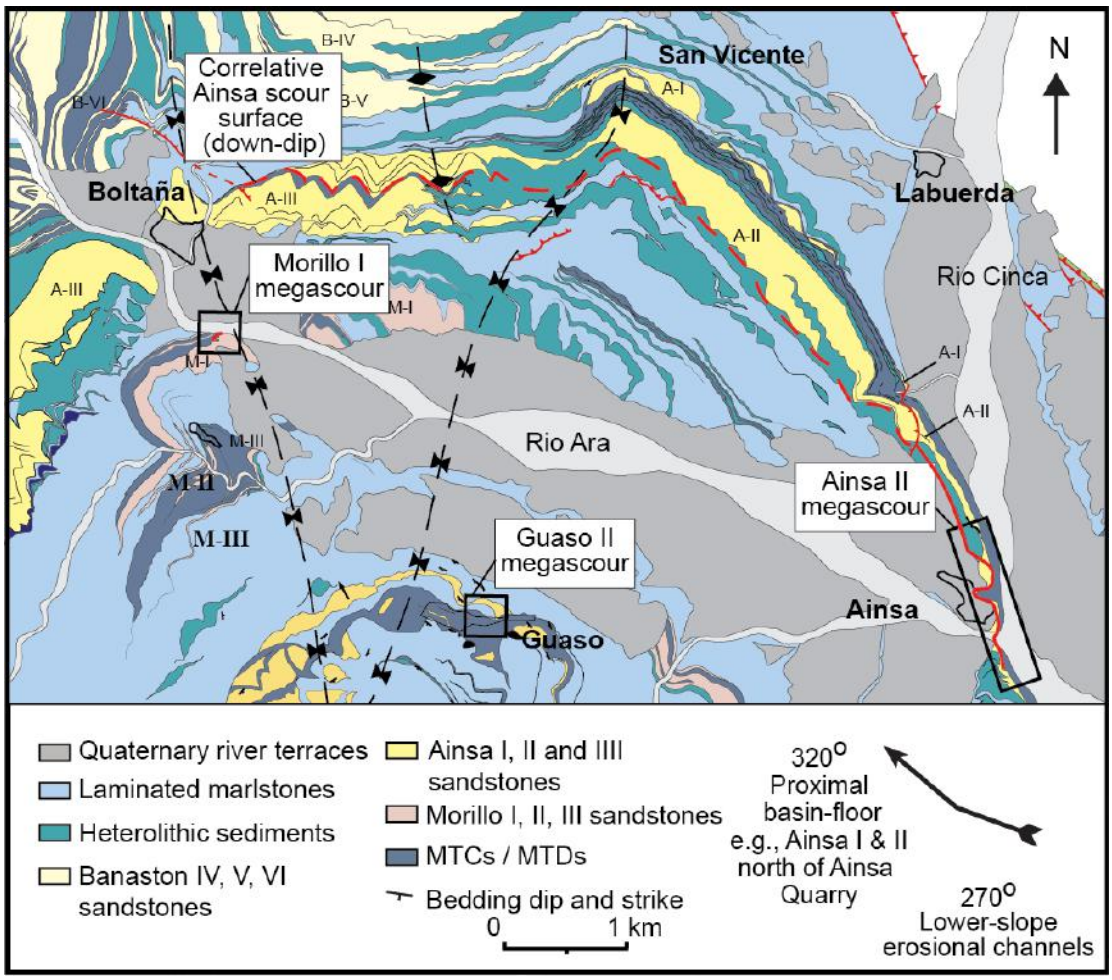

Figure 6.18. Location map of Ainsa II, Morillo I and Guaso II megascours documented in this study. Figure Modified from Dakin *et al.* (2013). Ainsa, Guaso and Morillo megascours shown in black boxes. Red dashed line shows correlative surface (MTD) from up-dip Ainsa II megascour.

6.3.1 Features of megascours

Large contorted sandstone blocks (up to 3 m) are found emplaced at the base of the Ainsa, Morillo and Guaso megascours, Figure 6.19.

Figure 6.19. Mushroom-like diapiric sandstone structures located at the base of megascours (A) Base of Guaso megascour (Locality 28). Hammer for scale (35 cm) (B) Base of Ainsa II megascour (Locality 15). Grain-size card for scale (10 cm) (C) Base of Morillo I megascour, (Locality 24). Pencil for scale (15 cm).

The bedded sandstones appear as isolated rafted blocks that show diapiric convex-up like structures, observed only at or near the base of megascours.

6.3.2 Megascour outcrops

6.3.2.1 Ainsa II Fan megascour, Ainsa town

The Ainsa II Fan is interpreted as a laterally offset-staked channelised submarine-fan bounded by erosional surfaces (Bakke *et al.*, 2008; Pickering and Corregidor, 2005). At its thickest, the Ainsa II sandstones are ~ 70 – 75 m thick, and are well exposed along strike approximately parallel to the Rio Cinca. By correlating two key outcrops across the Rio Ara, a ~ 1-km-wide 'spoon-shaped' megascour is identified, comparable to small-scale seismic examples of Minisini and Trincardi (2009). Figure 6.20-A shows a cross-sectional profile between the northern and southern outcrops in an oblique view to palaeoflow (essentially westward into the outcrop). The maximum amount of incision appears to have occurred towards the centre of the megascour and therefore, is no longer preserved in the stratigraphy due to erosion from the present-day Rio Ara.

The northern locality (Figure 6.20-B), with good cliff exposure shows channel fills containing mainly amalgamated sandy SGF deposits, eroded by a sharp margin (~ 75°) that has removed up to ~ 35 m of previously deposited Ainsa II channelised sandstones leaving only ~ 4 m of sandstones preserved beneath the basal scour. Towards the centre of the megascour, the base flattens and has an irregular scalloped geometry. Slickensides are absent along the margins of the scour, which together with no observable fault surface, suggests that it is a primary erosional sedimentary contact and not due to faulting (*cf.* Fleming and Johnson, 1989).

Closer to the town of Ainsa, but still within the northern outcrop, the base of the megascour contains isolated very well-rounded pebbles, some of which are embedded into the upper surface of the underlying Ainsa II Fan sandstones. Most pebble imprints are preserved as elongate depressions (Figure 6.20), probably due to significant bypass as the pebbles impacted the seafloor, were dragged a short distance, and then re-entrained into the essentially bypassing flow. Using the drag marks left by such pebbles, the spindle-shaped sole marks are oriented from 060° - 240° NE to SW and 120° - 300° ESE to WNW (N = 16) with a dominant east to west imbrication of the ab planes, i.e., suggesting that a predominantly westward-directed debris flow excavated the scour (Figure 6.20-D, Figure 6.20-A). The megascour was subsequently filled mainly by heterolithic material, including thin pebbly mudstones, thin sandstone packages and finer-grained silty marlstones, that onlap the northern margin.

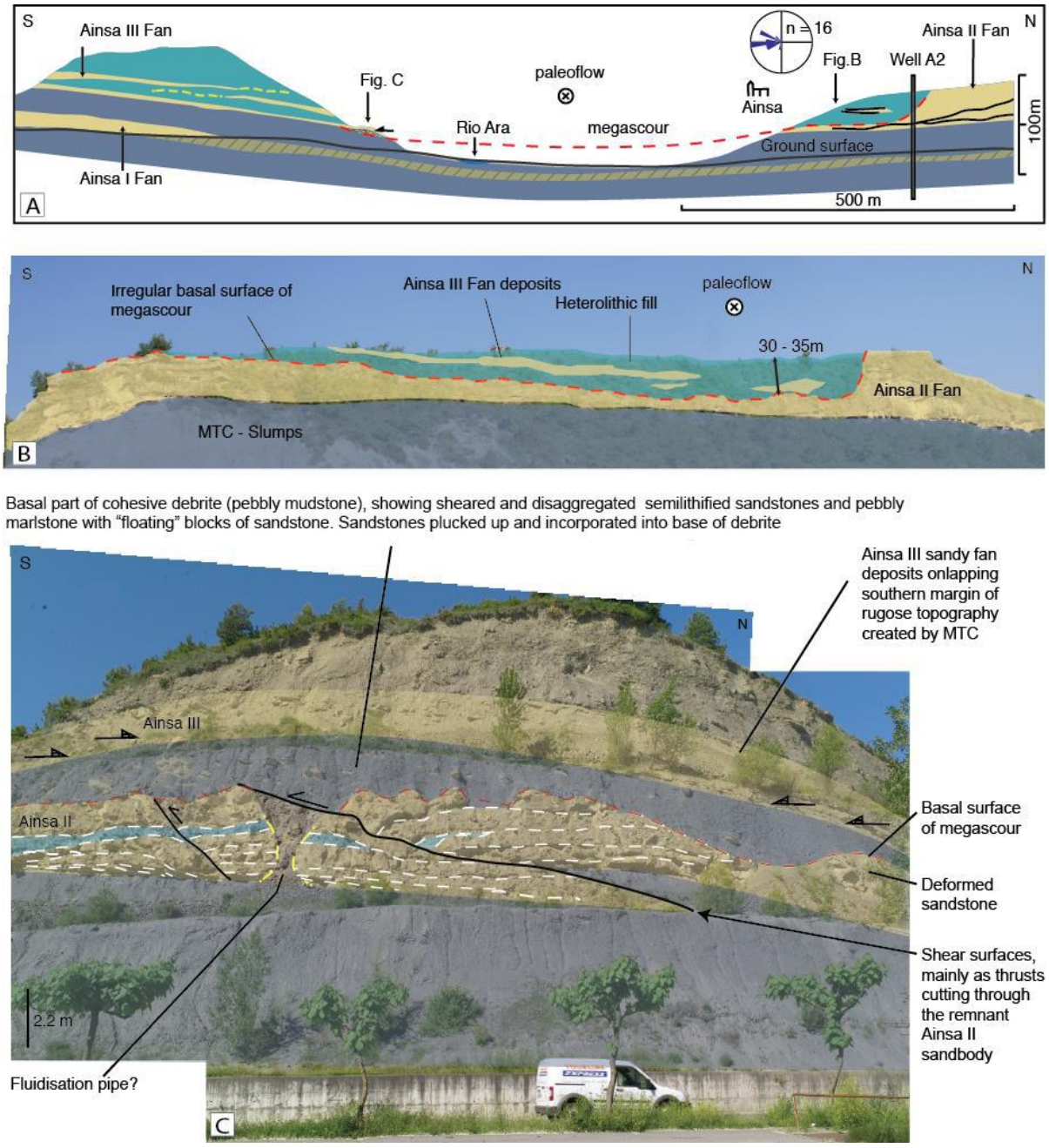

Figure 6.20. (A) Schematic diagram showing overall geometry of Ainsa megascour. (B) Northern lateral margin of scour showing ~ 35 m infill of heterolithic sediments, (C) Southern lateral margin of scour showing thrusts through the deformed sandstones. Van for scale (~ 3 m). Figure from Dakin *et al*. (2013).

On the southern outskirts of Ainsa, across the Rio Ara, an outcrop ~ 15 m high (Figure 6.20-C) shows the megascour immediately overlain by deformed and thrusted Ainsa II Fan sandstones. Between the northern and southern outcrops and across palaeostrike of the basin slope, the megascour changes stratigraphic position to the base of the Ainsa II Fan sandstones, from an initial relief of ~ 35 m. The irregularity

of the megascour surface may be due to lateral ramps and variations that allow the basal scour to traverse through the stratigraphy. This southern outcrop, here identified for the first time as the same megascour surface, contains sheared and thrusted sandstones immediately underlying a ~ 3 m thick pebbly mudstone. The MTD contains subangular sandstone blocks, up to 80 cm in width that have been 'plucked' from the underlying, semi-lithified *in situ* sandstone beds. The structural relationship shown in Figure 6.20-C can be explained by an upward-cutting ramp, related to the development of thrust faults (*cf.* Bull *et al.*, 2009), which may explain features of the thrusts seen in the southern outcrop. The pervasively sheared and thrusted sandstones are preserved in the process of disaggregating bedded sandy SGF deposits. It is likely that these residual, semi-lithified, sandstones were deformed by substantial shear stresses acting on the seafloor. The mixing of sandstone blocks into the chaotic, matrix-supported, pebbly mudstone found immediately above these deformed sandstone beds, indicates that this pebble-rich chaotic mudstone is connected to the flow that eroded the sandstones, producing the megascour. A cone-shaped fluidisation pipe, containing subangular sandstone blocks, vertically cuts through the sheared sandstones. This feature suggests the production of elevated pore-fluid pressures within the substrate associated with its deformation during emplacement of the overriding debris flow.

Mapping shows that the ~ 35 m erosional surface observed near Ainsa, which effectively marks the termination of Ainsa II Fan deposition in this area, is likely correlated with a ~ 4 m-thick pebbly mudstone interval separating the Ainsa II and III fans immediately north of Boltaña (Figure 6.18). In the outcrops immediately north of Boltaña that are oriented across palaeoflow, there is little evidence to suggest the down-fan continuation of a deep erosional channel cutting into the Ainsa II Fan sandstones. This observation supports the interpretation of a debris flow(s) that were erosive, deeply scouring into the base-of-slope setting (near Ainsa). The same flows were likely to be hydroplaning, laminar flows several kilometres farther out into the basin.

6.3.2.2 Morillo I Fan megascour, Rio Ara

The Morillo I Fan is interpreted as being deposited during narrowing and confinement of the Ainsa Basin with the abundance of pebbly sandstones related to increased seafloor gradients (Pickering and Bayliss, 2009, Bayliss and Pickering, 2015b). At the Rio Ara, Locality 23, a cross-sectional profile down-dip of palaeoflow (approximately out-of-outcrop) shows a 'U-shaped' scour, ~ 20 m in width and 17 m at the maximum point of incision, towards the centre of the scour (Figure 6.21).

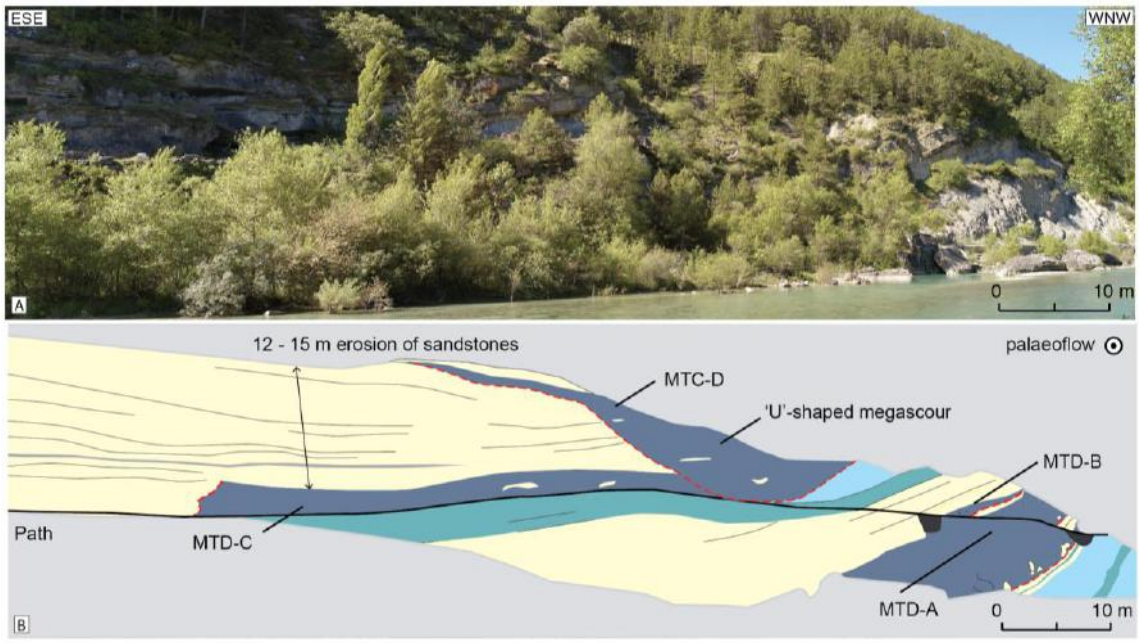

Figure 6.21. (A) Photo of Morillo I Fan, (B) Photo-interpretation of outcrop showing megascour geometry. ~ 12 – 15 m of sandstones are truncated. Photo location is taken east of Figure 6.3-A, interpreting MTD A and B as Type IIa MTDs showing erosion preserved *in situ*. Younging is to the left (Locality 23). Modified from Bayliss and Pickering (2015b).

Sandy SGF deposits on the western margin are not present at this locality due to exposure. However, the eastern margin of the scour is observed to truncate 12 – 15 m of multiple bedded sandstones, showing an overall 'triangular' geometry (Figure 6.21-B). Laterally continuous sandstone beds are not identified at the base of the scour, therefore it is inferred that the base of MTC-D erodes and amalgamates into MTC-C, although this surface is not obvious at outcrop. A large contoured sandstone block is observed at this discrete surface at outcrop (Figure 6.19-C). Although highly weathered, the sedimentary succession (MTC D) that infills the megascour contains some thin-bedded sandy SGF deposits between MTDs, comprising multiple chaotic events, and is easily accessible up a track. Lateral ramps and thrusting are not

observed at this outcrop, as documented in the Ainsa II megascour. Mapping shows the scour is not continuous down-dip suggesting local erosive processes formed this feature, such as those identified forming ‘flute-like’ erosion (Figure 6.15 and 6.16).

6.3.2.3 Guaso II Fan megascour, Guaso village

The Guaso II Fan is interpreted as the end-signature of deep-marine deposition in the Ainsa Basin, deposited during differential tectonic uplift of the underlying Boltaña thrust allowing sedimentation in a ramp-like setting (Sutcliffe and Pickering, 2009). The Guaso I Fan, west of Guaso village exposes two thin sandbodies that form resistant ridges. Between the sandstone topographic highs, a ‘saddle’ structure has formed eroding the less-resistant muddy sediments. At the maximum dip of the saddle structure, an asymmetrical scour ~ 500 m in width and 80 m at the maximum point of incision is observed (Figure 6.22).

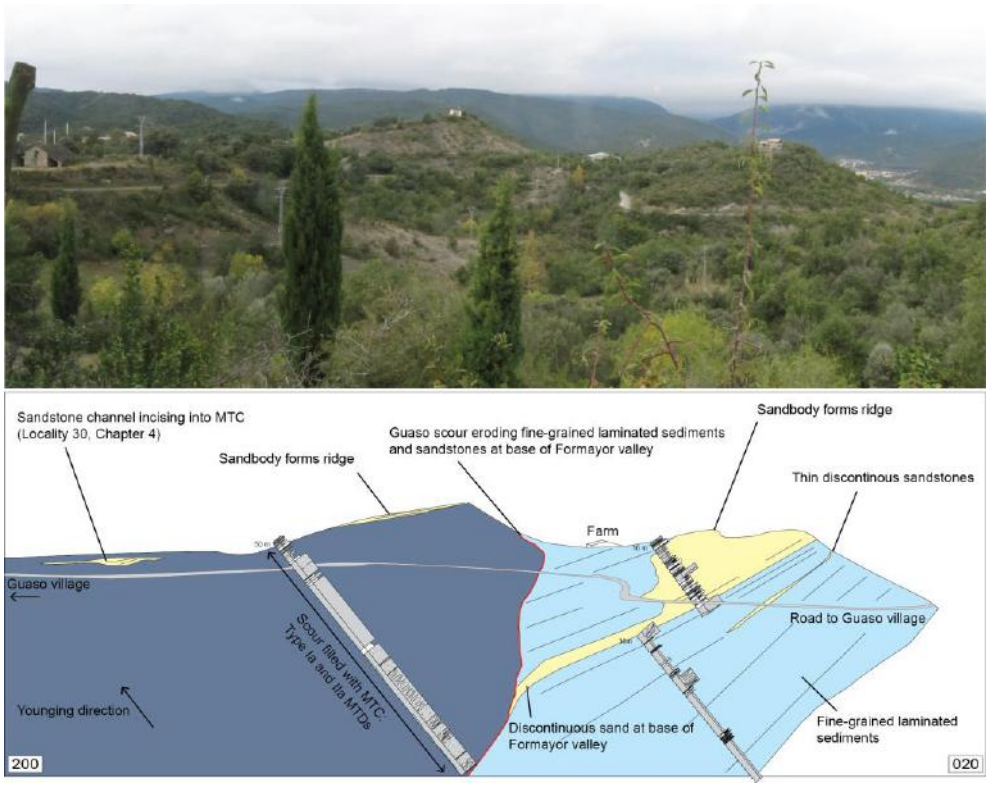

Figure 6.22. (A) Photo of Guaso I Fan and megascour of Guaso II, (B) Photointerpretation of outcrop showing the margin of a megascour eroding up to 80 m of fine-grained sediments. Younging is to the left. Thickening of sandstones is purely perspective and exposure due to a valley.

From the base-to-top of Formayor valley (accessible from a track leading off the main road A-2205), a ~ 50 m MTC comprises multiple bedded Type Ia and IIa deposits. MTDs at the base of the MTC are observed to erode into underlying fine-grained mudstones and sandstones of the Guaso I System.

6.4 INTERPRETATION

Based on outcrop evidence presented in this study, this section discusses facies associations and the geometry of erosively-based MTDs at outcrop, and applies data from experiments to observations collected in the field.

6.4.1 Occurrence of erosive MTDs

The Banastón and Morillo systems are observed to have a higher number of MTDs that show basal erosion compared to other systems in the Ainsa Basin (Figure 6.2-B). Data presented in Figure 5.18 (Chapter 5), showed that the Banastón and Morillo systems comprised a higher abundance of Type IIa MTDs, concluded to support the idea that the Ainsa Basin was likely to have higher gradients during time of deposition (e.g., Bayliss and Pickering 2015a, 2015b). This may suggest that slope gradient is a primary control on the erosive ability of any debris flow in a submarine setting, an observation in subaerial settings from Breien *et al.* (2008) and Berger *et al.* (2011), where a change in gradient increased the amount of entrainment in a debris flow (e.g., Chapter 2, Figure 2.12).

6.4.2 Geometry of small-scale scours

In most cases, outcrops are exposed perpendicular to palaeoflow. The lateral basal margins are observed to have ‘scalloped’, ‘triangular’ or ‘blocky’ geometries that truncate underlying sandstones, above which Type IIa MTDs are typically immediately present. From the margin of the basal scour, erosion surfaces commonly step laterally, with maximum incision either towards the centre of the deposit, utilising rheological contrasts between the underlying sandstones and mudstones of a

bedded substrate. The resulting ‘channel-like’ geometry is analogous to sandstone channels that form by eroding, bypassing and depositing turbidity currents. Erosion at the base of MTDs are likely to result from an area of maximum shear stress that the flow exerts on the substrate, such as the snout of a debris flow (Davies, 1990; Stock and Dietrich, 2006) (Figure 6.23).

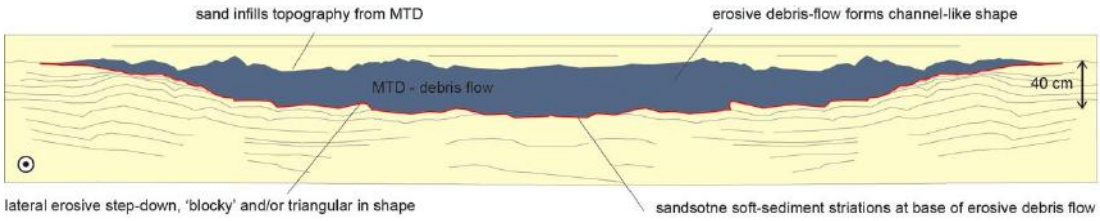

Figure 6.23. Model showing channel-like geometry of Type IIa MTD showing basal erosion. Model is based on Forcaz Stream (Locality 11). Maximum incision is 40 cm in this example.

From outcrop data alone, it is unknown if the base of a debris flow has a uniform area of high basal shear stress enabling the formation of ‘channel-like’ scours. From larger-scaled outcrops (i.e., Cerro Bola Formation, Argentina, Dykstra *et al.*, 2011), erosion is observed over hundreds of metres down-dip from an MTD ~ 120 m in thickness, suggesting if flow conditions and sediment properties are favourable, the base of debris flows are able to uniformly affect the substrate. From seismic data in the Espírito Basin, Alves and Cartwright (2009) recognise the existence of a principal axial zone of sediment translation differing from the marginal parts of MTDs. These larger-scaled analogues enable the formation of ‘channel-like’ features to form at the base of both slides, and debris flows. Where exposure permits in the Ainsa Basin, the proximal and distal geometry of erosive MTDs can be evaluated, and suggests that at least small-scale features can form ‘flute-like’ geometries (Figures 6.15 and 6.16). This may suggest that in some cases, the basal surface geometry has a discontinuous expression on the seafloor. This is further discussed in Section 9.3.3 1, Chapter 9.

The basal geometry of MTD-2 in the Eña Quarry outcrop (Figure 6.4) is unusual due to near-vertical steep-sided margins not observed at other outcrops. The absence of sandstone blocks in upper Sand 2 compared to lower Sand 1 suggests the outcrop records dynamic processes occurring at the time of both erosion and deposition. As the debris flow impacted the palaeoseafloor, shear stress was sufficient

to erode, partially incorporate and transport the sandstone blocks from the upper sand (Sand 2) down-dip of flow direction compared to the stratigraphically deeper Sand 1. If overpressure were responsible for erosion of Sand 1 and 2, concave-up structures would be expected, as fluids escape vertically through stratigraphy. Vertical fluid escape processes alone does not explain the relative roundness of the sandstone boulders at this location.

6.4.3 MTD thickness *versus* depth of erosion

Subaerial field observations and measurements from Breien *et al*. (2008) show a positive relationship between the volume of material and its ability to erode the substrate (yield rate) (Figure 6.24-B). This relationship could be analogous to findings in this study from a submarine environment, where thicker deposits appear to erode deeper into the underlying substrate.

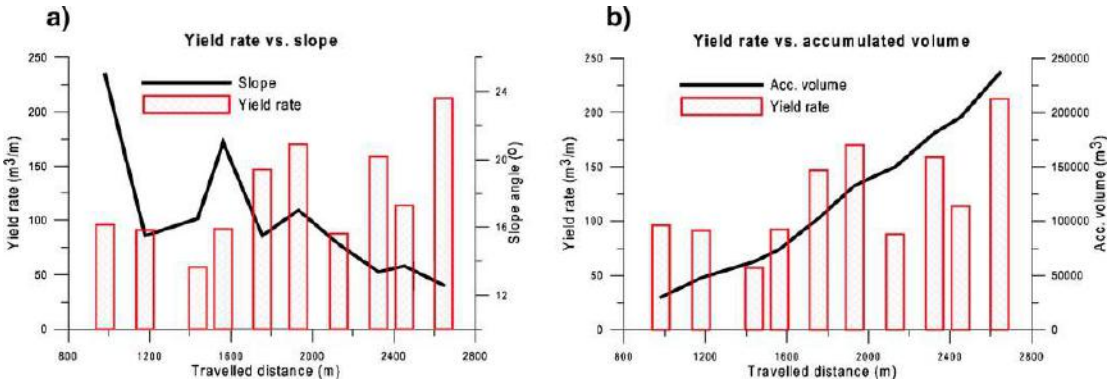

Figure 6.24. Maximum thickness of debris flow measured against maximum erosion (values in metres). N = 35. Figure from Breien *et al*. (2008).

6.4.4 Strength loss and erosive mechanisms observed at outcrop

Ancient submarine MTDs in the Ainsa Basin show a variety of basal erosive behaviours that occur from small-scale interaction with the substrate (Figure 6.6 and 6.7) to larger-scale physical interaction (Figure 6.21, 6.21 and 6.22). Features documented in this study include striations at the base of MTDs (Figure 6.6, 6.7), ploughing into underlying deposits (Figure 6.10), whole-scale scouring of underlying deposits (Figure 6.11, 6.12), plucking of semi-lithified sandstones into the base of

MTDs (Figure 6.3, 6.5) and 'injecting', or loading and entrainment of MTDs into underlying sandy SGF deposits (Figure 6.9). These features are discussed here.

6.4.4.1 Striations

Soft-sediment striated surfaces provide a unique insight of the interactive processes that occur between the substrate and the base of submarine erosive debris flows. This feature is only exposed where recent erosion has exposed the top surface of sand.

Flow-parallel grooves and embedded-pebble striations are found at the base of the Ainsa II megascour (Figure 6.8). Pebbles entrained within the passing debris flow have a long residence time at the base and are consequently able to scour the substrate as they move downslope by being bounced and dragged along the seafloor, then embedding on and into the underlying sand surface. In the Ainsa Basin, grooves are measured to be no more than 1 m in length. However, these short linear grooves could be associated with outcrop exposure. At locality 40, (Figure 6.8, Rio Sieste), the top surface of a sandstone bed immediately beneath a slump is contorted. Based on the evidence presented in this study, it is suggested that flow-parallel grooves and basal drag are likely to be related to the interactive frictional zone at the base of the MTDs (*sensu stricto* Davies, 1990; Breien *et al.*, 2008; Alves and Cartwright, 2009; Berger *et al.*, 2011). At the time of deposition, the underlying sediments are suggested to have been semi-or partially lithified, suggesting a hiatus between deposits.

6.4.4.2 Scouring to form channel- or gutter-like geometries

Scouring and bulldozing is suggested to be a major contributor to erosive processes in submarine settings (e.g., Alves and Cartwright, 2009; Posamentier and Martinsen, 2011; Ducassou *et al.*, 2012). Although documented as scales of magnitude smaller than seismic data, small-scale channel-like scours at outcrop are analogous to seismic-scale scours at the base of MTDs (e.g., Gee *et al.*, 2005). In seismic data, grooves are documented up to 750 m wide and 50 m deep and extend for several kilometres (Moscardelli *et al.*, 2006). In these seismic examples, the linearity of these grooves is

associated with linear, rather than turbulent flow at the base of MTDs (e.g., Gee *et al.* 2005).

6.4.4.3 Ploughing

The ploughing mechanism observed in the Ainsa Basin is only observed at one locality (Figure 6.10, Locality 6). This is where a Type III MTD has undercut bedded mudstones and sandstones. Baas *et al.* (2013) show how sandy SGFs are able to enter cohesive soft muddy substrates without losing their shape, driven by bed shear stress exceeding the bed cohesive strength. These flows produce unique turbidites with internal mud layers, mixed cohesive to non-cohesive sediment layers and flame and load structures. It is envisaged that this mechanism forms only local disturbances in the stratigraphy.

6.4.4.4 Downward injection, or erosion and entrainment

Soft-sediment deformation structures form pene-contemporaneously in gravitationally unstable profiles with a denser layer (e.g., sandy turbidite) overlying a less-dense hydroplastic layer (e.g., muddy layer) and typically form ball-and-pillow structure, load casts, flame structures and pseudonodules (Middleton and Hampton, 1973; Neuwerth *et al*., 2006). Deformation mechanisms include dewatering, liquefaction and brittle deformation and are generally related to seismicity, density contrasts or gravitational instability (Neuwerth *et al*., 2006). Figure 6.25 summarises common wet-sediment (also called soft-sediment) deformation structures observed in fine- to gravel- grade granular beds.

A pebbly mudstone is observed to ‘inject’ into underlying sandstones (Figure 6.9), suggesting soft-sediment deformation of the underlying bed. The pebbles form a pointed ‘whale-tail’ structure depositing pebbles 1.2 m into the underlying substrate, unlike rounded load casts that form ball-and-pillow structures. Injected fabrics also show the opposite vertical profile to those presented in load cast formation, where a chaotic mudstone overlies a sandy SGF deposit. The geometrical difference between ball-and-pillow structures and injected mudstones therefore suggests different

processes are involved. Chaotic mudstones that appear as injected into underlying sandstones, could be related to a temporary loss of the soil structure of the substrate (e.g., Hungr, 2005, 2007). In some cases, overriding debris flows may be denser compared to the saturated underlying sandy-substrate, providing an inverse density profile of load-cast structures presented previously. From outcrops presented in this study, it is suggested that as the 'head' of the debris flow travels over undrained sandy soils at a stationary point on the seafloor, it rapidly loads, impacts, compresses and contracts the underlying granular sediment (e.g., De Groot *et al.*, 2006; Mangeney *et al.*, 2010). Excess pore pressure is induced, thus removing the effective stress and potentially results in full or partial liquefaction of the substrate. At this point, the overriding flow may be able to 'fill' the inherently unstable bed.

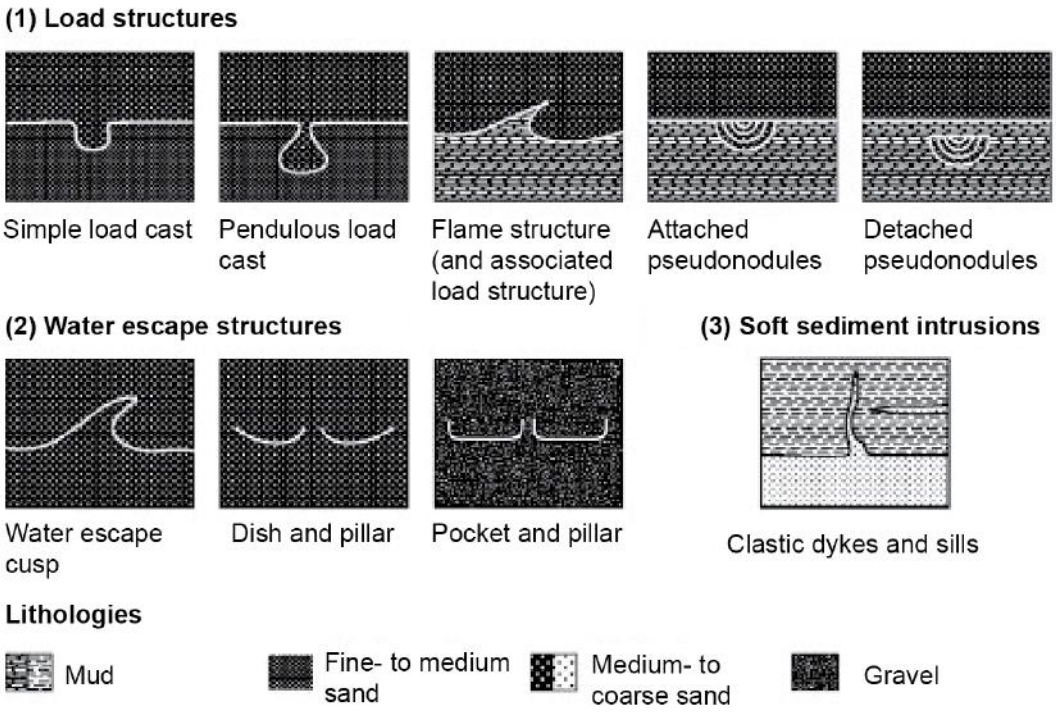

Figure 6.25. Wet-sediment deformation structures in coarse-grained sediments. Modified from Neuwerth *et al*. (2006).

6.4.4.5 Plucking of sandstone blocks into the base Type IIa MTDs

Type IIa MTDs that show large angular semi-consolidated sandstone blocks 'plucked' and incorporated into the base of deposits is a unique erosive mechanism only eluded

to in Dykstra *et al.* (2011). Exceptional exposures show the process of fragmenting and 'plucking' of underlying semi-lithified sandstones into or near the base of the debris-flow deposits (e.g., Rio Ara, Morillo I Fan, Figure 6.3), suggesting in these examples, that at least the lower part of the flow froze *in situ* during basal erosion. The angularity of the sandstone blocks incorporated into the base of the deposit suggests that the sands were semi-lithified at the time of erosion and/or they were eroded relatively locally. A higher abundance of semi-lithified sandstone blocks are commonly preserved at the basal margins of the erosive sour. This may result from higher stress regimes at the centre of erosion, or may be related to the relatively 'fluidal' central part of the flow compared to the 'sticky', or more viscous margins (e.g., Nygård *et al*., 2002; Stock and Dietrich, 2003). A model for the plucking mechanism is presented below.

Large-scale debris flow experiments from Major and Iverson (1999) at the USGS flume facility measured pore-fluid pressure at the base of several ~ 10 m^3 experimental debris flows. An instrumentation port was located along the runout area, and measured pore-fluid pressure and bed-normal stress at the base of the overriding flow (Figure 6.26). Results from the debris flow experiments, are shown in Figure 6.27. Samples A to G show varying compositions of mud, sand and gravel-grade sediment. The graphs in Figure 6.27 show time elapsing to the right. Results show that the pore-fluid pressure at the base of debris flows is close to zero near the flow front and increases only after the flow front has passed. An observation of these experiments is that negative pore-fluid pressure can be produced directly behind the head of the flow, highlighted by the green dashed line in Figure 6.27. Although shown in the diagrams of Major and Iverson (1999), this observation is not mentioned in their results. Samples B, E and G, record up to minus 1.8 kPa, highlighted and is immediately followed by an increase to 2 kPa, beneath the green dashed line. The negative pore-fluid pressure measured is ~ 50 % of the maximum pore-fluid pressure and occurs over less than one 10^{th} of a second.

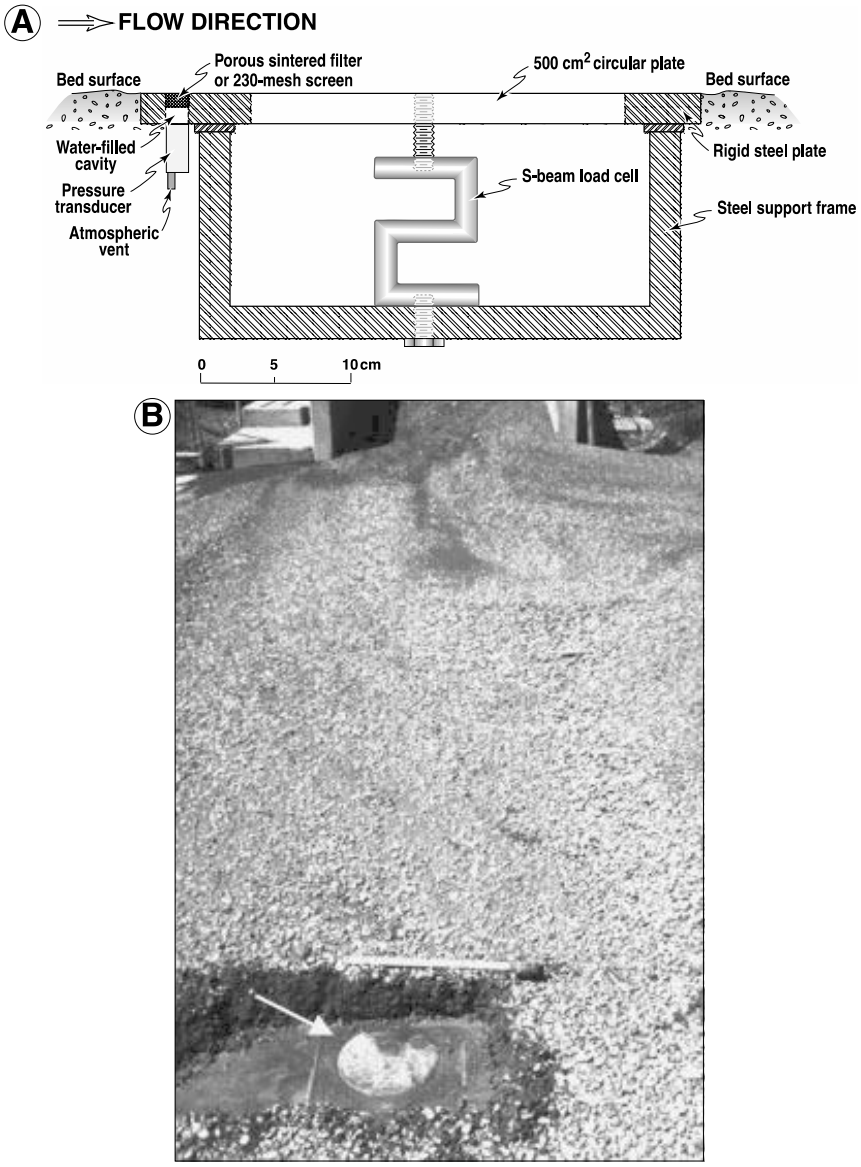

Figure 6.26. (A) Instrumentation configuration for measuring pore-fluid pressure at the base of experimental debris flows. (B) Instrumentation plate excavated from beneath deposit (12.5 cm thick). Arrow marks position of the fluid-pressure sensor. From Major and Iverson (1999).

Negative basal pore-pressure is documented in both 'loamy and sandy to gravelly' debris-flow deposits with an average grain size of 3.2 mm (51.8 to 66.2 wt% gravel, 31 to 46.6 wt% sand and 9.8 to 1.5 wt% mud [clay and silt]). Neutral basal pore-pressure is documented in relatively muddy debris-flow deposits with an average grain-size of 0.75 mm (13.5 wt% gravel, 84.4 wt% sand and 2.1 wt% mud [clay and silt]) (Figure 6.28). This data suggests that sandy coarser-grained flows are more likely to have negative pore-pressure at the base of the flow compared to finer-grained flows.

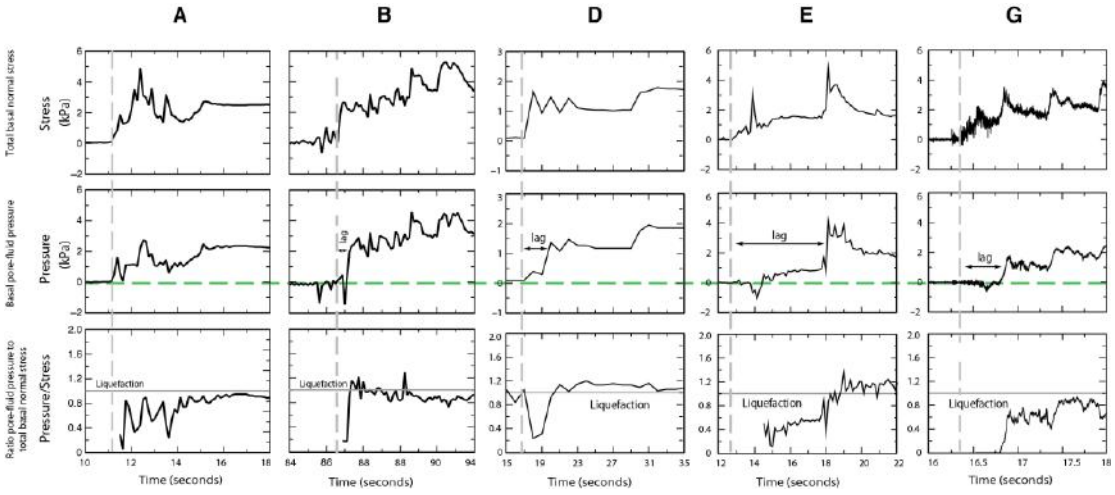

Figure 6.27. Representative measurements of total basal normal stress and basal fluid pressure. For A and B, the experimental debris composed of sandy gravel containing ~ 1% mud (silt and clay). For D, E and G, experimental debris flows composed of sandy gravel containing between 2 and 10 % mud (silt and clay). Green dashed line highlights zero pore-pressure. The front (or head) of the flow is denoted by the pale grey vertical dashed lines. Figure modified from Major and Iverson (1999).

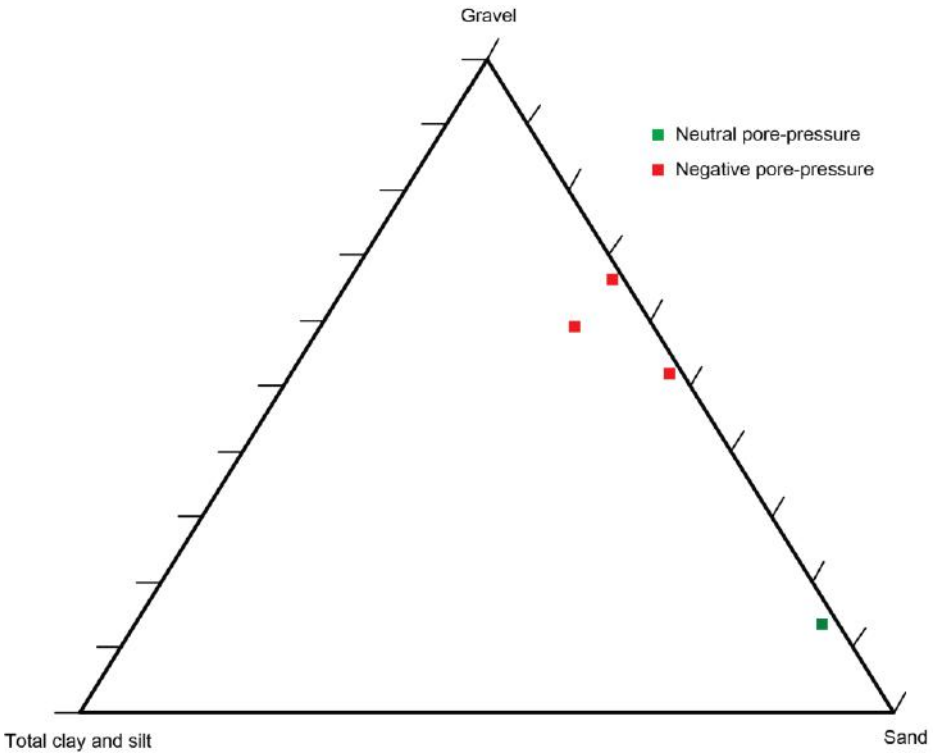

Figure 6.28. Grain-size compositions of debris-flow deposits that show negative and neutral pore-pressures in experimental debris flows of Major and Iverson (1999).

The slope to basin-floor transition can be characterised by a change in erosion from deep grooves and scours on the slope, to ploughing of the seafloor (Posamentier

and Martinsen, 2011). This transition appears where there is a maximum change in gradient marking the basin-floor margin, near the base-of-slope, or at local areas of seafloor roughness. At this point, stress vectors are directed into the substrate at a higher angle than locations on the slope or farther out on the basin floor (Posamentier and Martinsen, 2011). Sand and gravel can be entrained through almost explosive-like erosion in saturated underlying deposits (e.g., Iverson *et al.*, 2011), illustrated in Figure 6.29.

Based on this model, the coarse-grained fractions (such as sand and carbonate grains) observed at outcrop are likely to entrained through ploughing, shouldering aside and/or bulldozing of sandy SGF deposits as the debris flow travelled over the submarine fan, which ultimately is able to change the composition of the debris flow.

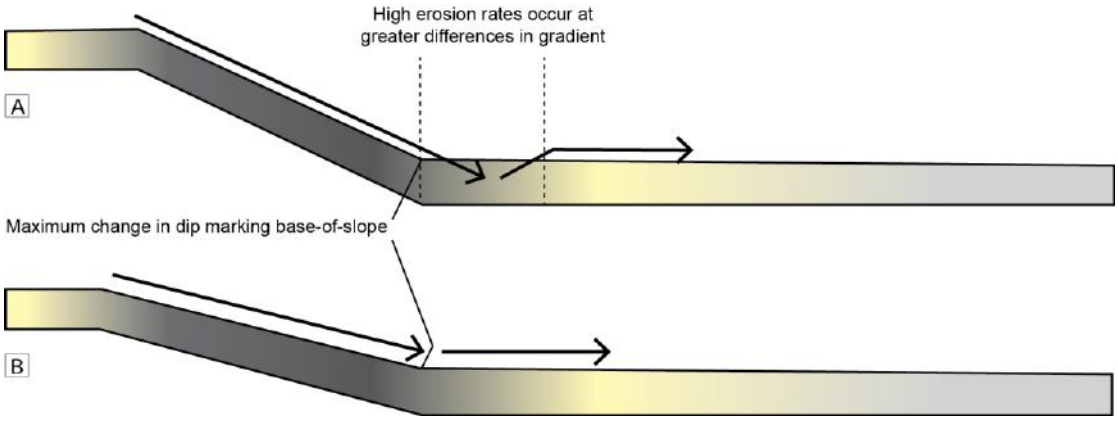

Figure 6.29. Schematic diagram showing flow stress vectors: (A) higher angle difference between slope and basin floor causes more erosion than; (B) lower angle differences between slope and basin floor. Yellow highlights sand-rich environments (near-shore shelf and submarine fan).

As discussed in Chapter 2, in a submarine setting, sediment instability causes mud-rich debris flows to be ignited from the shelf edge or slope. An important trait of debris flows involves their tendency to move down a slope as a discrete surge, or series of surges as a result of mass and momentum conservation operating in conjunction with solid-fluid stress partitioning and grain-size segregation (Davies, 1990; Iverson, 1997, Iverson, 2005). Through longitudinal sorting, debris flows typically exhibit a coarser-grained or denser 'head' at the front of the pulse and a finer-grained, less dense 'tail' immediately behind the head forming surges as the flow travelled down-dip. Experiments from Davies (1990) show this density contrast can occur over a matter of grain diametres. Debris flows could induce both cyclic and

monotonic shear in granular sediments due to the pulsing nature of the sediment flow causing repetitive cyclic pounding of the underlying sediment (acting similar to cyclic shear), and also shearing in one direction (monotonic shear), before arrest of the deposit (e.g., De Groot *et al.*, 2006).

Based on: (1) large-scale experiments of Major and Iverson (1999) showing negative basal pore pressure at the base of flows in sand and gravel-rich debris-flow deposits; (2) wet-bed entrainment of sand and gravel down-dip of debris flows (e.g., Iverson *et al.* (2010), and (3) where longitudinal sorting permits a dense, coherent, head immediately in front of a less dense tail, a model for plucking semi-lithified blocks of sandstone into the base of debris-flow deposits is presented in Figure 6.30. This model proposes that a 'plucking' mechanism is more likely to occur in dense, strongly coherent debris flows (e.g., Marr *et al.* 2001), which have a distinct contrast between the 'head' and 'tail' of any given flow (e.g., Davies, 1990).

As the initial 'head' of the debris flow travels over undrained sandy soils (i.e., sandy SGF deposits that are either saturated or partially saturated), at a stationary point on the seafloor it impacts, compresses and contracts the underlying granular sediment. It is envisaged that this instantaneous effect could be sufficient to induce excess pore pressure in the sandy sediments, removing the effective stress and potentially resulting in full or partial liquefaction of the substrate. The length of the head of the debris flow depends on the event magnitude and the volume of the coarse-fraction in the debris flow. The model, as shown in Figure 6.30, suggests an instantaneous contrast in mass at the transition point between the 'head' and the 'tail' of the flow. It is envisaged that at this point, the underlying sediment is decompressed and dilates, releasing the water in the pores and thus increasing the effective stress. Negative pore-pressure at this transitional zone of a dense and coherent debris flow, may be sufficient to form a suction mechanism, enabling blocks of sandstone to be plucked from a semi-lithified substrate into the base of the debris flow.

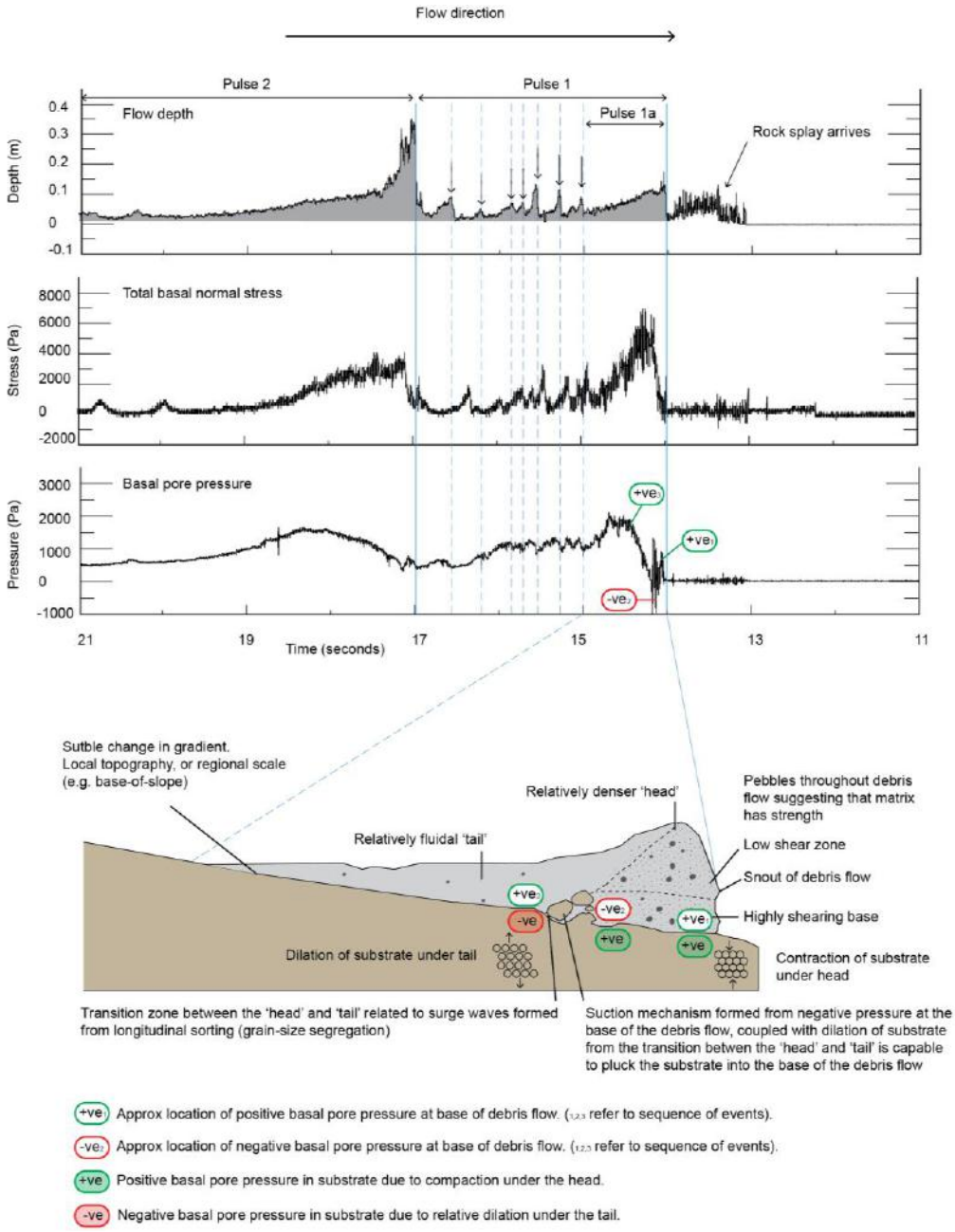

Figure 6.30. Model for the 'plucking' mechanism at the base of debris flows, based on surging debris flows and basal-pore pressure data from debris flow experiments (Major and Iverson, 1999). This experiment is based on experiment 083194 (51.8 wt% gravel, 46.6 wt% sand, 1.5 wt% silt and 0.1 wt% clay). Note that the time axis has been reversed for diagram (*cf*. Figure 6.27).

6.4.4.5.1 Loss of momentum from plucking mechanism

Type IIa deposits show partially disaggregated sandstone blocks in the initial stages of breaking up and fragmenting underlying sandstones *in situ*, suggesting the debris

flow was unable to fully lift the sands from their underlying stratigraphic position. Pierson (1980) showed that when the driving stress of a debris flow was unable to overcome the strength of the marginal rim, the debris flow stopped, effectively causing a 'damming' effect behind a retaining wall. Subaerial granular experiments from Mangeney *et al.* (2010) show that sediment entrainment can potentially accelerate or decelerate a flow depending on the nature of underlying erodible material, topography and dynamics of the flow. The study also showed that the kinetic energy of the flowing mass (e.g., debris flow) is exchanged to the static erodible substrate (e.g., sandstone turbidite), changing the potential energy of the substrate into kinetic energy. Experiments from Farin *et al.* (2013) show that continued flow momentum is achieved by adding energy to the system in a variety of ways, including increasing the slope angle, increasing the kinetic energy, enlarging the channel width to reduce friction against a channel margin or a higher initial driving force.

In the field, outcrops that preserve erosion *in situ* show that the flow lost momentum. Based on experimental data and outcrops documented in this study, it is suggested that the kinetic energy of the overriding debris flow transferred the potential energy of the substrate into kinetic energy (observed at outcrop by semi-lithified sandstone blocks plucked into the base of Type IIa MTDs). However, this transfer of energy must have been greater than the overall momentum, resulting in the cessation of flow. Where MTDs show basal erosion but do not show sandstone blocks in the process of disaggregation, may provide examples where the kinetic energy of the flow was greater than the amount of energy transferred to the static substrate and was therefore able to continue to flow down-dip, as discussed in Farin *et al.* (2013). Arrest of the cohesive flow occurred potentially only a short distance from the outcrop exposure and therefore it is likely the sandstone blocks are preserved out-of-outcrop in these examples.

6.4.5. Summary of erosive mechanisms documented at outcrop

Data presented in this chapter is summarised and compared to examples of mass-transport erosion from examples documented in literature (Table 6.1), as discussed in Chapter 2.

Type of erosion at base of MTD	Scale of erosion	MTD observed immediately above scour	Features of erosion observed at outcrop/in experimental studies	Process and references	Controls
***Plucking* of underlying substrate**	Moderate-scale erosion (2.5 m of erosion in Locality 23, Rio Ara), Ainsa Basin. Large-scale erosion (200 m blocks incorporated into MTD), Dykstra *et al.* (2011), Argentina	Type Ia MTD	Large semi-lithified angular sandstone rafts incorporated at or near the base of a deposit. Can form channel-like scours with 'U'-shaped geometry or show very-steep margins.	Negative pore pressure formed at the base, directly behind the head of a strongly coherent flow that has undergone longitudinal sorting (this study and Dyksra *et al.*, 2011)	**Flow dynamics:** Flow surges, composition of debris flow (sand *versus* mud), viscosity and coherency of flow **External dynamics:** Substrate saturation and composition, confinement of basin, slope gradient and topography
***Ploughing* into underlying substrate**	Small-scale erosion (0.5 m), (Locality 6, Banastón V Fan) Ainsa Basin.	Type III MTD	Ploughing beneath sediments on the seafloor. Lateral terracing at base of deposit forming 'U'-shaped channel-like scours	Shear stress exceeding the bed cohesive strength (this study, Baas *et al.*, 2013)	**Flow dynamics:** Velocity, viscosity and coherency of flow **External dynamics:** Substrate saturation, slope gradient and topography, confinement of basin
Channel-like *scouring* or *bulldozing*	Small scale erosion in the Ainsa Basin (Locality 62, Morillo II Fan) to seismic-scale scours (Moscardelli *et al.*, 2006; Ducassou *et al.*, 2012)	Type IIa, IIb and III MTDs	Channel-shaped scours with MTDs infilling incision surface	'Bull dozing' of sediment, shearing or explosive interaction with saturated sediments, hydraulic jumps and turbulence (this study, Major 1997; Gee *et al.*, 2005; Moscardelli *et al*., 2006; Iverson *et al.*, 2010; Alves and Cartwright, 2013, Alves, 2010, Alves *et al.*, 2013)	**Flow dynamics:** Velocity, magnitude of failure, viscosity and coherency of flow **External dynamics:** Substrate saturation and composition, slope gradient and topography, confinement of basin
Striating	Small scale erosion, affecting top 10's of centimetres of sediment (Localities 19, 40 and 7), Ainsa Basin. Can be seismically resolvable in large-scale striations (e.g., Moscardelli *et al*., 2006).	Type Ia, IIa and III MTDs	Top surfaces of sandstones showing soft sediment deformation	Basal drag and viscous basal shear at the base of dense laminar flows (this study, Davis, 1990, Alves and Cartwright, 2009, Alves, 2010, Alves *et al.*, 2013, Omosanya and Alves, 2013)	**Flow dynamics:** Objects within flow, depth of flow, viscosity and coherency of flow **External dynamics:** Substrate saturation and composition, bed roughness, topography
***Downward entrainment* into underlying substrate**	Small-scale to moderate-scale (Localities 6 and 52), Ainsa Basin. Not likely to be seismically resolvable.	Type IIa and III MTDs	Downward erosion and entrainment, or 'injection' of matrix and/or pebbles into underlying substrate	Strongly coherent, debris flow causing temporary loss of strength or liquefaction of the substrate (this study)	**Flow dynamics:** Density, viscosity and coherency and pounding of overriding flow **External dynamics:** Effective stress, liquefaction, substrate saturation and composition

Table 6.1. Summary of erosion resulting from MTD processes observed at outcrops in the Ainsa Basin, documenting likely scale of erosion and comparing with literature examples of mass-transport erosion in submarine environments.

6.4.6 Megascours formed at or near the base-of-slope

Outcrops from the Middle-Eocene Ainsa Basin, Spanish Pyrenees provide insights into the impact of erosive MTDs on sandy substrates in deep-marine environments. During these large-scale mass-transport events, passing flows are directed over the same position, continuously eroding the depression of the seafloor. This is likely to occur, as debris flows are observed to follow the course of channel-like geometries (e.g., Bernhardt *et al*., 2012). Based on MTDs showing basal erosion observed at outcrop, plucking ploughing, scouring, and liquefaction are all believed to play a fundamental role in the culmination of these large-scale submarine phenomena. Outcrops show erosive processes from local-scale and early stages of erosion and incorporation of material into MTDs, to larger-scale events that created mud-filled scours or channels, including megascours near or at the base-of-slope, believed to be formed by multiple individual erosive debris flows.

Large contorted sandstone rafts (up to 3 m) are located at the base of the Ainsa II, Morillo II and Guaso II megascours. Analogous features are discussed in Ogata *et al.*, (2012), where fluid-escape structures form centimetre to metre-sized vertical, lateral and oblique conduits through slide blocks present in large-scale MTDs. These blocks are commonly rooted in matrix-rich zones, such as the basal sliding horizon and internal shear zones of the flow (Figure 6.31).

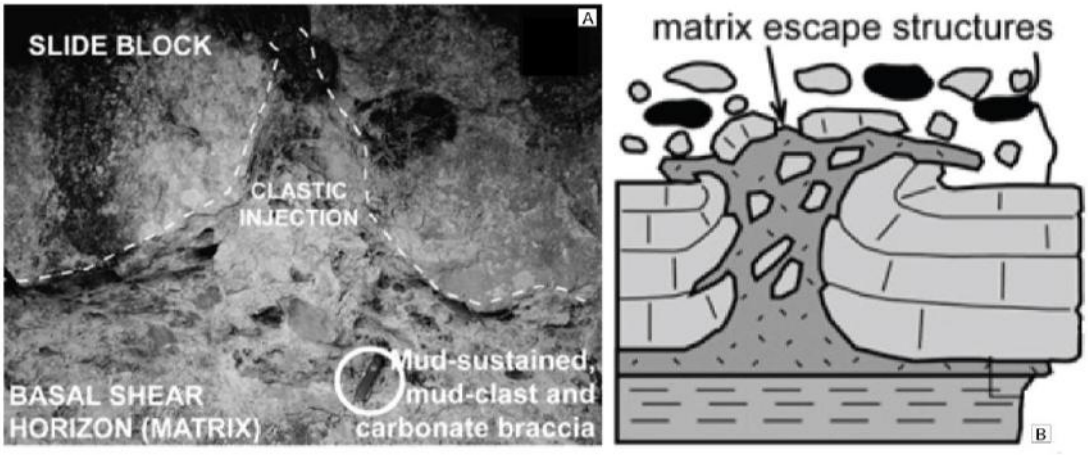

Figure 6.31. (A) Clastic injection into slide block resulting from a basal shear horizon (B) Model showing "mushroom-like", diapiric structures, representing forced expulsion of overpressure in the matrix. Modified from Ogata *et al.* (2012).

The contorted sandstone blocks observed at the base of the megascours in the Ainsa Basin may have deformed in similar way as described in Ogata *et al.,* (2012). Exceptionally sized flows are likely to have an intense basal shear interval and therefore any rafted blocks present at the base of the flow would result in the injection of liquefied, overpressured matrix into the slide blocks (Ogata *et al*, 2012). In the Ainsa Basin, the presence of these sandstone rafts at the base of the scours indicates the presence of an exceptional event(s) that formed the megascours.

The southern margin of the Ainsa II megascour shows a laterally-directed compression structure, where a low-angle thrust fault is present (Figure 6.20-C). An analogous feature is presented in Posamentier and Martinsen (2011), where a seismic-scale example, approximately the same scale as the Ainsa II scour, is identified (Figure 6.32).

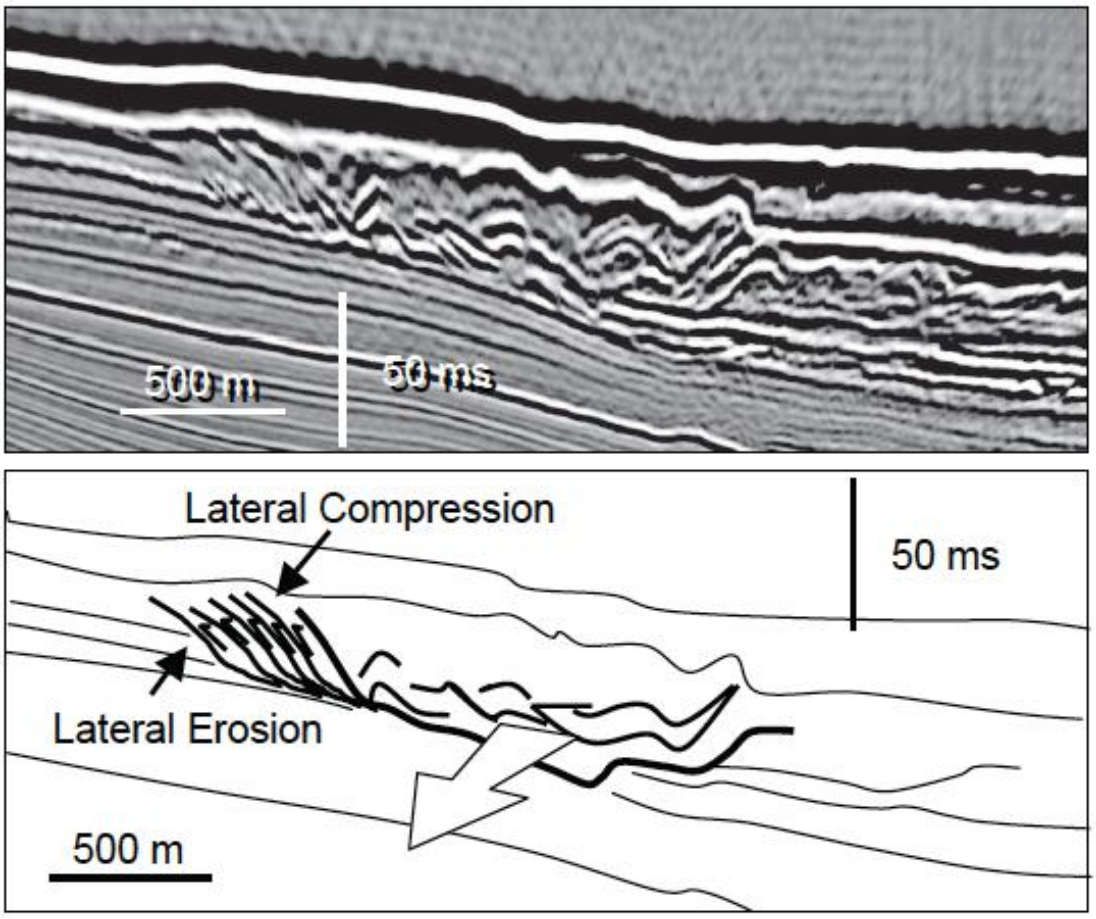

Figure 6.32. (A) Traverse seismic amplitude section (B) Interpreted section, illustrating lateral compression in the form of low-angle thrust faults on the lateral margin of an MTD. Flow is out of the image. Modified from Posamentier and Martinsen (2011).

In this seismic example, thrusts are observed to dip at ~ 15° and are characterised by listric curvature originating at the base and extending to the top of the deposit. Although these thrusts are commonly expressed near the upper surface of the deposit, orientated traverse to flow direction, in some instances successive flows can result in laterally-directed compression.

6.5 SUMMARY

Based on field observations and data collected in the Ainsa Basin, there is abundant evidence that MTDs, such as those associated with debris-flow processes, are amongst the most erosive SGFs that entered the basin to erode and sculpt the seafloor and baisn slopes. Erosive mechanisms and erosive features include: (1) pushing and shouldering aside (or bulldozing) of unconsolidated sediments (e.g., Major 1997 and this study); (2) explosive interaction with wet-bed sediments (e.g., Iverson *et al.*, 2010); (3) striations at the base of debris flows (e.g., Gee *et al.*, 2005; Alves and Cartwright, 2009, Alves, 2010, Alves *et al.*, 2013 and this study); (4) shear deformation at the base of slumps (this study), and finally; (5) In some cases, debris-flow deposits show erosion at the base and exhibit large angular sandstone boulders incorporated into the base of deposits, interpreted as plucked from the saturated sandy substrate (this study). Erosive mechanisms depend upon the rheological properties of the substrate, the debris-flow physical properties, and the seafloor gradient, including any changes in gradient over the flow run-out length. The amount of erosion associated at the base of an MTD is highly variable, varying from striated surfaces that potentially only relate to minor erosion of the seafloor, to large-scale scouring processes (e.g., Gee *et al.*, 2005; Moscardelli *et al.*, 2006, Alves and Cartwright, 2010 and this study).

CHAPTER 7

LABORATORY STUDY: MTD THIN-SECTION ANALYSIS FROM OUTCROPS, MIDDLE-EOCENE AINSA BASIN, SPANISH PYRENEES

7.1 INTRODUCTION

This study has identified Type IIa MTDs immediately above erosion surfaces in the deep-marine Middle-Eocene Ainsa Basin, interpreted from the erosion of debris flows into underlying sandy SGF deposits (Chapter 6 and Dakin *et al.*, 2013). In this chapter, both the data and interpretations of Dakin *et al*. (2013) are further investigated. Here, a quantitative and semi-quantitative approach has been used to measure the composition and grain-size variation between erosively-based and non erosively-based muddy Type IIa MTDs. The purpose of this additional study was to: (1) determine whether chaotic mudstones (Type IIa MTDs) have the same composition throughout the Ainsa Basin; (2) identify if Type IIa MTDs show vertical sorting, and; (3) document any compositional differences between sandy SGF deposits and Type IIa deposits. This was achieved by extracting whole rock samples of Type IIa MTDs in the field, making thin-sections and analysing each thin-section under a microscope to determine the grain-size compositional and trends of these deposits. Acquisition methods used in the pilot study and analytical study are outlined in Chapter 3 (methodology).

Firstly, data collected from the pilot study is presented and results are discussed, including the limitations of the initial sampling technique. Secondly, data from the full analytical study is presented, with discussions at the end of this chapter. Linking the processes to the deposits of debris flows provides a framework for presenting and interpreting the ancient deep-marine deposits conducted in this research.

7.2 PILOT STUDY RESULTS

7.2.1 Compositional data

Point-count data from twenty-two 'erosive' and nine 'non-erosive' MTDs (Type IIa chaotic mudstones), where single samples were taken from different deposits around the Ainsa Basin Point-count analysis was undertaken to identify the bulk composition of grains and the relative abundance of grains *versus* matrix found in Type IIa MTDs. Matrix was defined as silt- and mud-grade components $\leq$ 0.06 mm. Grain-size analysis was undertaken to determine variation in grain-sizes throughout all deposits sampled. Compositional results of the pilot study are shown in ternary diagrams (Figures 7.1-A and B).

The ternary diagram is plotted using the dominant components, identified as matrix, total quartz and 'other' (the sum total of all other components comprised of carbonate grains, lithic fragments [sedimentary and metamorphic], feldspar [P and K], nummulites, coral fragments, opaque minerals, mica and calcite). Individually, the 'other' components are minor, but together they form a significant part of the overall composition. Samples of erosive and non-erosive deposits show a linear relationship, related to a wide distribution in the siltstone/mudstone matrix content (in the bottom right apex). Sandy SGF deposits show a low siltstone/mudstone matrix and are enriched in the 'other' component.

A more robust dataset was required to provide further insights into the variation of composition and grain-size in erosive and non-erosive debris flow processes. Compositional analysis of samples DF-1, DF-2, DF-3 and DF-4 involved multiple samples taken per deposits, where up to 7 samples were taken from base-to-top in equal increments (Figure 7.1-B). These samples show an apparent grading trend, becoming increasingly matrix-rich towards the top of each deposit. This is graphically shown with sample DF-1, where a combined sedimentary log, photomicrographs and charts (Figure 7.2). This data was able to determine the variation in composition and grain-size through a vertical section, rather than comparing solitary samples from different deposits (i.e., Figure 7.1-A).

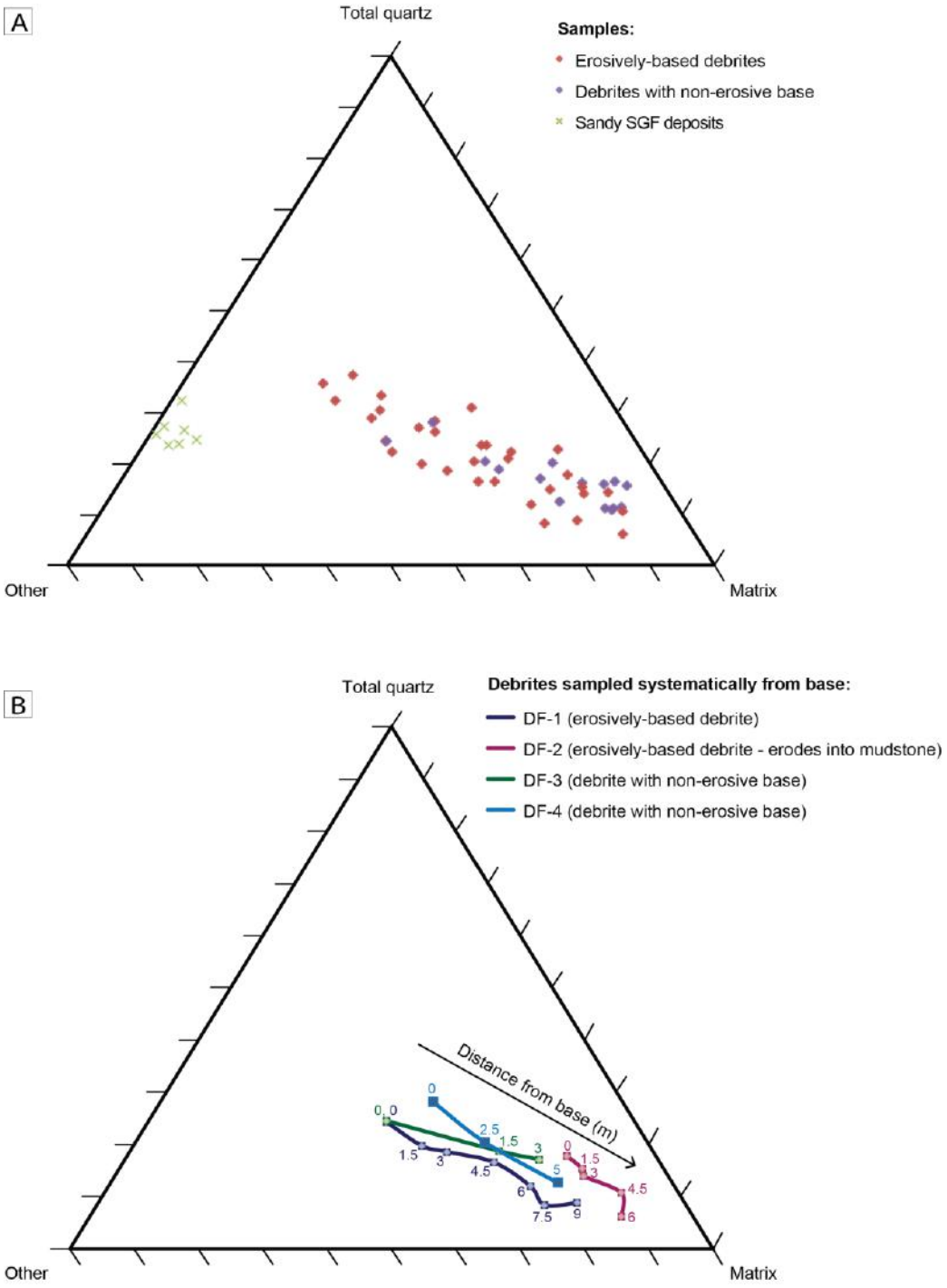

Figure 7.1. (A) Ternary diagram showing compositional data of all deposits sampled in pilot study. These include deposits that were only sampled once (B) MTD DF-1, 2 3 and 4 sampled at equal vertical increments from the base-to-top of each deposit. DF-1 = 7 samples; DF-2 = 5 samples; DF-3 = 3 samples, and; DF-4 = 3 samples. Numbers refer to metres sampled from base of the deposit. Grading implied by increase in matrix towards the top of deposits. Scale on ternary diagram shows 10 % increments.

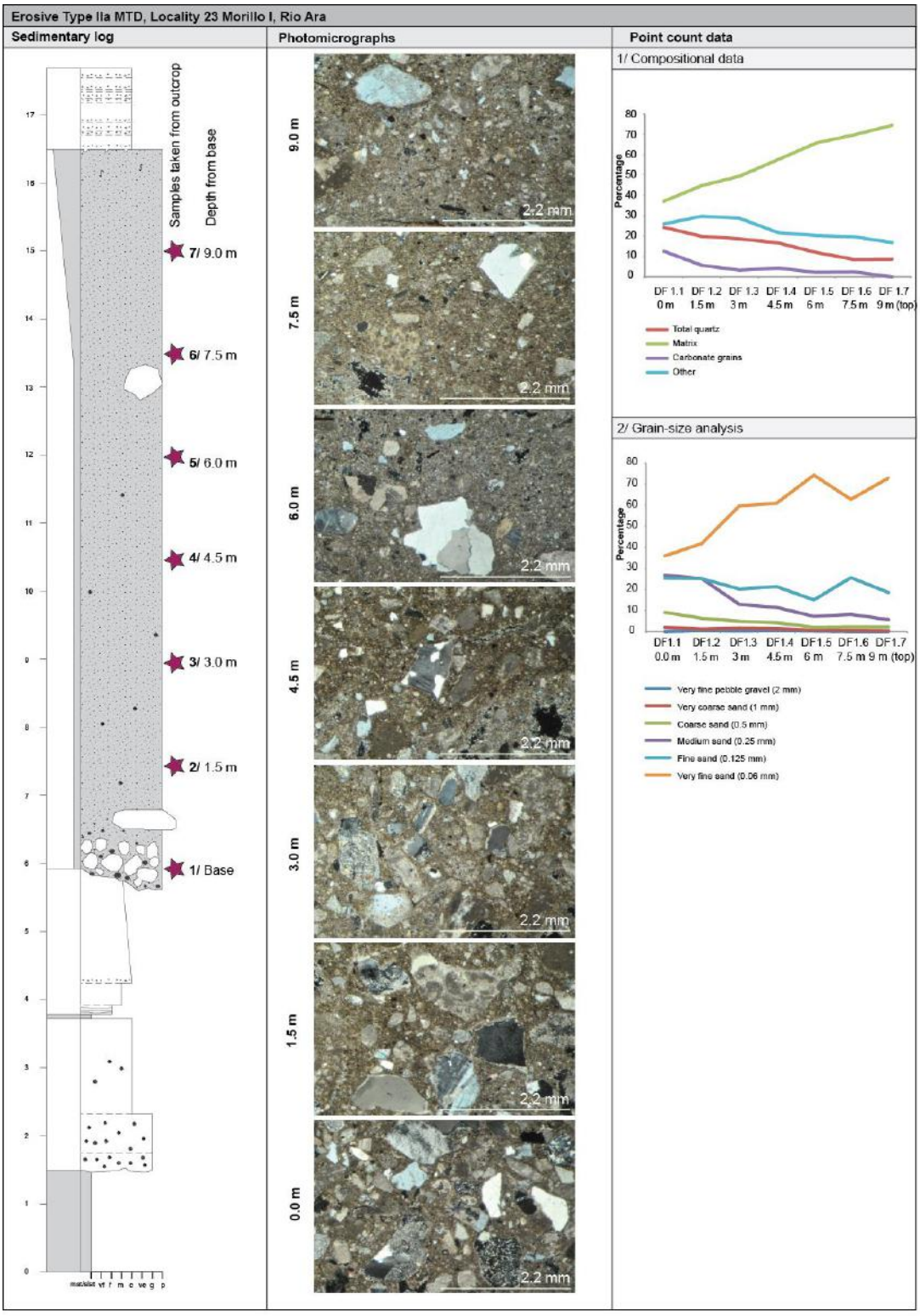

Figure 7.2. Sedimentary log, photomicrographs and graphs showing compositional and grain-size analysis from DF-1 (Rio Ara, Morillo I Fan Locality 23).

7.2.3 Grading observed from compositional and grain-size data

Results from the compositional data (left) and the grain-size profile (right) of samples DF-1, DF-2, DF-3 and DF-4 is shown in Figure 7.3.

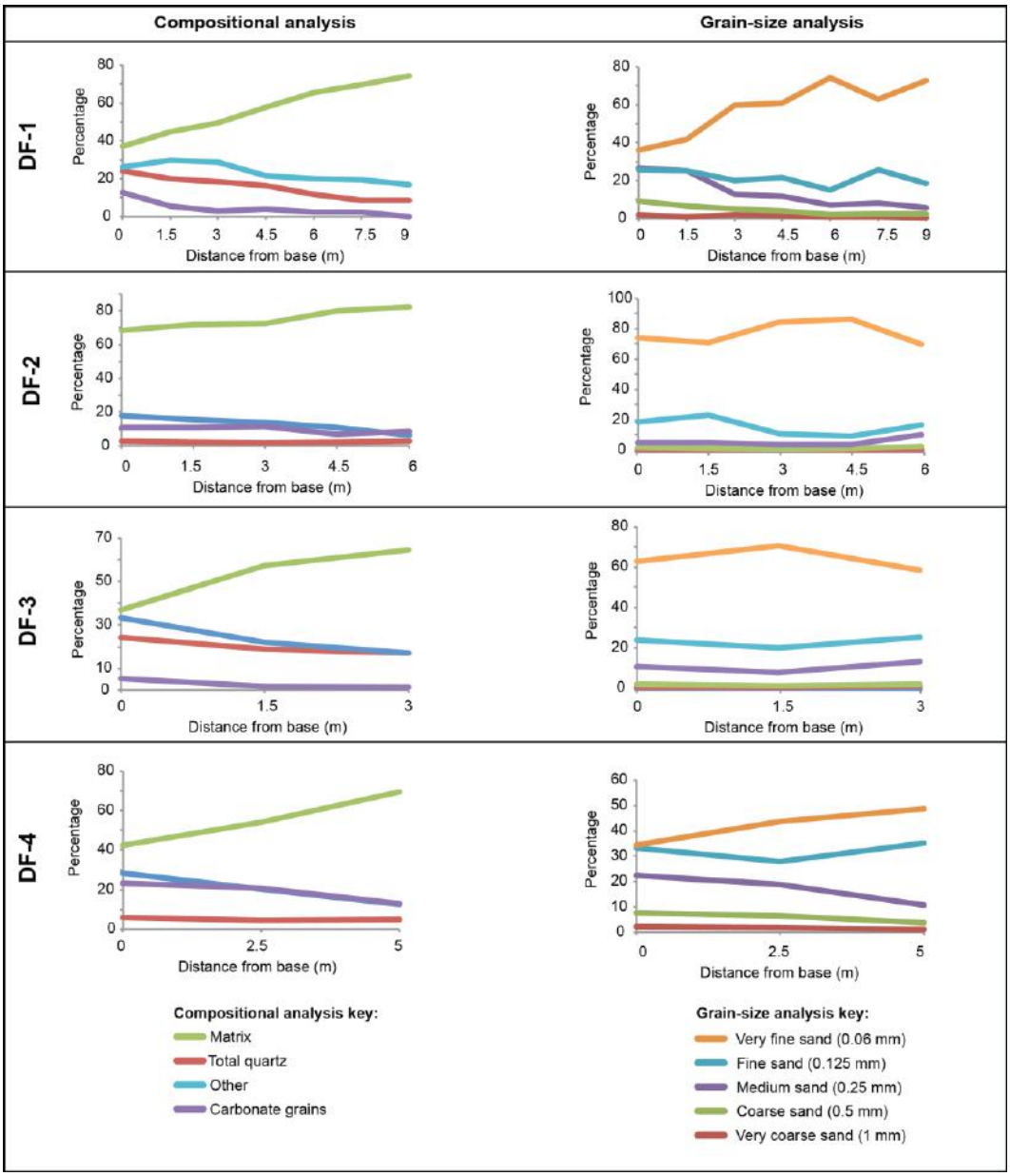

Figure 7.3. Data shows point-count analysis from 'erosive' (DF-1, DF-2 and DF-4) and 'non-erosive' (DF-3) Type IIa MTDs sampled at outcrop. Compositional analysis shows a 'normal' vertical grading profile in all samples with a vertical increase in the siltstone/mudstone matrix. Overall DF-1 and DF-4 show an overall increase the very-fine grained sand fraction (> 0.06 mm). DF-2 and DF-3 show variable grain-size profiles.

Compositional signatures of the four samples are observed as similar, each showing a vertical increase in siltstone/mudstone matrix and a vertical decrease in the grain components. The corresponding grain-size profiles for each sample are observed as variable. The very fine-grained fraction (< 0.06 mm) in samples DF-1 and DF-4 increases vertically, whereas the very fine-grained fraction remains relatively constant in samples DF-2 and DF-3.

7.3 ANALYTICAL STUDY RESULTS

A further 129 Type IIa samples were collected and prepared as thin sections from eighteen other MTDs in the Ainsa Basin. This culminated a sample population of twenty-two deposits (including samples DF-1 to 4), that provided a meaningful dataset to observe discrete vertical grain-size and compositional trends in each deposit, as identified in the pilot study. The sample catalogue is shown in Chapter 3 (methodology). Depending on exposure, weathering of outcrops and accessibility, four to seven samples were collected from base-to-top of each deposit at equal increments. MTD thickness varied between 1 – 10 m. Of the eighteen other deposits sampled for the full analytical study, nine were observed to have an erosive base (samples E-A, E-B, E-C, E-D, E-E, E-F, E-G, E-H, E-I), and nine did not show any visible signs of basal erosion (samples NE-B, NE-C, NE-D, NE-E, NE-F, NE-G, NE-H, NE-I and NE-J). The raw data gathered for this study is presented in Appendix F.

7.3.1 Grading observed from compositional and grain-size data

From the additional nine deposits showing erosion at the base and nine deposits showing non-erosive bases analysed, 3 groups are identified; Group 1, Type IIa MTDs showing basal erosion; Group 2, Type IIa MTDs not showing basal erosion, and; Group 3, anomalous data from Group 2 deposits. MTDs DF-1, DF-2 and DF-4 from the pilot study fit with Group 1 deposits, and sample DF-3 fits with Group 3, showing a larger population size was crucial for further investigation. Results are presented within the identified MTD groups.

7.3.1.1 Group 1: Type IIa MTDs showing basal erosion

The percentage analysis of compositional and grain-size profiles of erosively-based MTDs are shown in Figure 7.4. Compositional analyses shows grading, where the siltstone/mudstone matrix increases vertically and the abundance of quartz, carbonate and 'other' grains > 0.06 mm (i.e., the sum total of all other components composed of carbonate grains, lithic fragments [sedimentary and metamorphic], feldspar [P and K], nummulites, coral fragments, opaque minerals, mica and calcite) decrease vertically throughout the MTD profile. These trends suggest a fining-upward or normal grading, as there is a gradual vertical increase in siltstone/mudstone matrix content. However, it is likely that the graded signature is a local effect, caused by entraining grains from the eroded substrate.

Grain-size analyses shows that the very fine-grained sand fraction (> 0.06 mm) increases vertically and all other grain sizes (fine sand fraction > 0.125 mm to very coarse-grained sand > 1 mm) decrease vertically, providing further evidence of normal grading. All MTDs showed visible erosion into a sandy SGF deposit, apart from sample DF-2, which eroded into fine-grained siltstones/mudstones. However, through mapping this MTD is suggested to have also eroded into underlying sandstones. Although sample DF-2 has the same compositional trend as the others in Group 1, the grain-size trend is different, staying relatively constant vertically through the deposit, which may result from the fine-grained muddy substrate it eroded into.

It is important to understand whether 'normal grading' observed in these MTDs is a consequence of hydrodynamic sorting, or whether grading is caused by erosion of an immediately underlying coarse-grained deposit (e.g., a sandy SGF deposit), such that coarse grains are incorporated into the base of the MTD, giving the impression of normal grading. This is discussed further in Section 7.4.1.

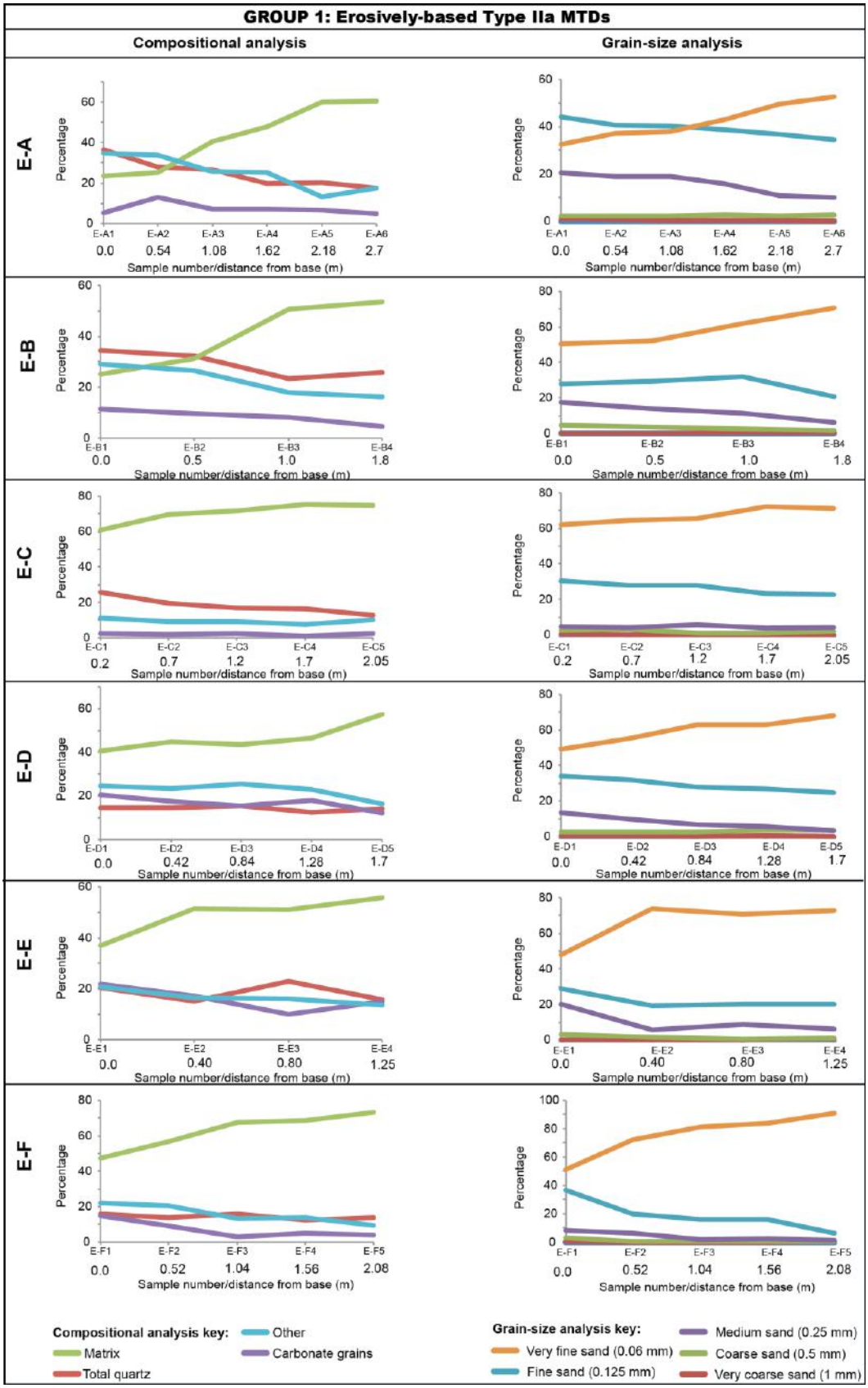
GROUP 1: Erosively-based Type IIa MTDs
Compositional analysis
Grain-size analysis
E-A
E-B
E-C
E-D
E-E
E-F
Percentage
Sample number/distance from base (m)
Compositional analysis key:
Matrix
Total quartz
Other
Carbonate grains
Grain-size analysis key:
Very fine sand (0.06 mm)
Fine sand (0.125 mm)
Medium sand (0.25 mm)
Coarse sand (0.5 mm)
Very coarse sand (1 mm)

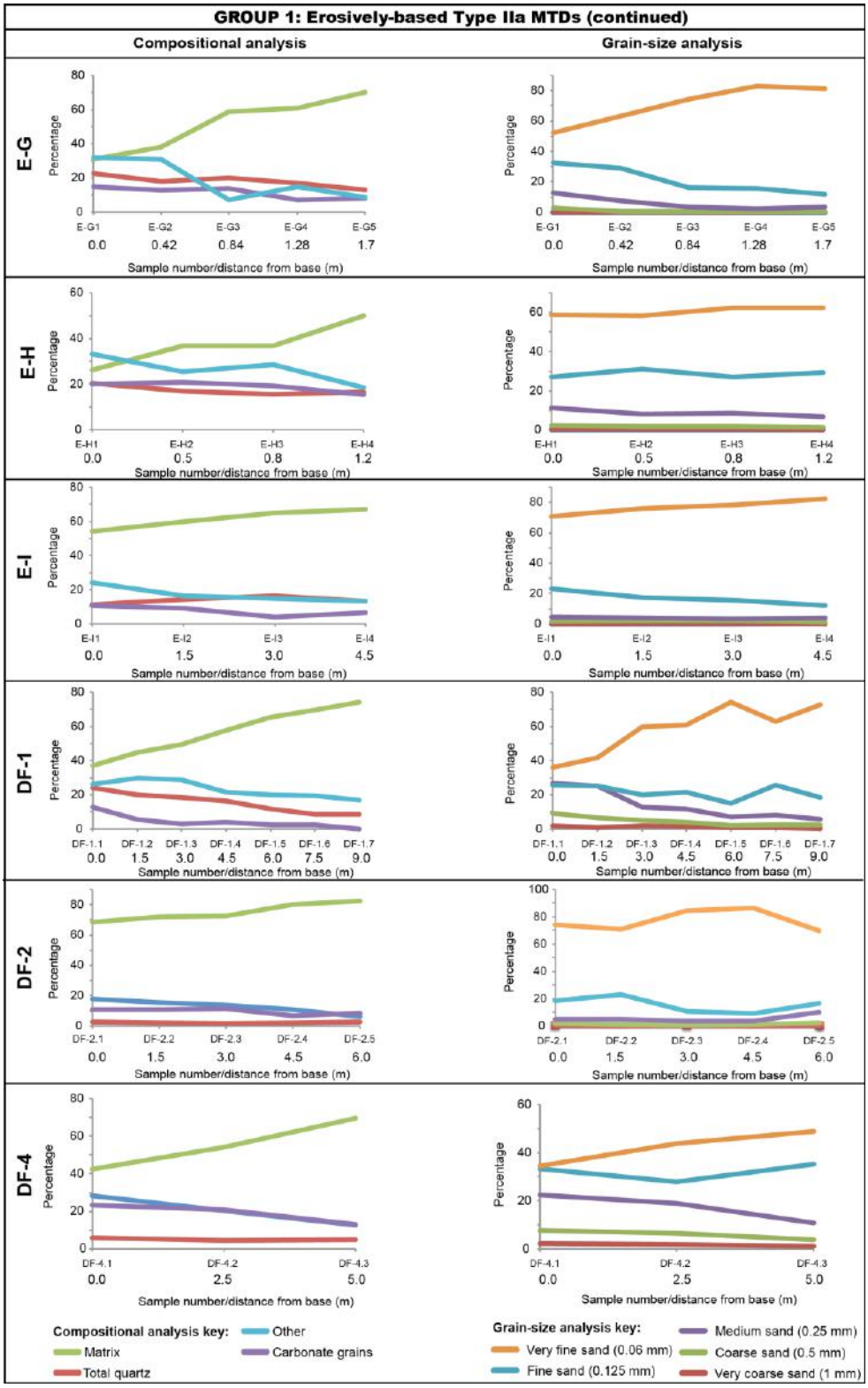

Figure 7.4. Group 1 Type IIa MTDs. Compositional and grain-size analysis show a normal vertical grading profile in the siltstone/mudstone matrix and very-fine grained sand fraction > 0.06 mm.

7.3.1.2 Group 2: Type IIa MTDs that do not show basal erosion

Group 2 Type IIa MTDs were sampled from deposits that appeared to have a non-erosional base. Group 2 deposits show different compositional and grain-size trends compared to Group 1 deposits, presented in Figure 7.5 (compositional and grain-size profiles are left and right, respectively).

Compositional analyses show that the siltstone/mudstone matrix decreases vertically and the abundance of quartz, carbonate and 'other' grains (> 0.06 mm) increase vertically in the deposit profile. These trends suggest overall inverse or reverse grading. Grain-size analyses shows that the very fine-grained sand fraction (> 0.06 mm) is more variable than the consistent increasing trend seen in Group 1 deposits (samples showing basal erosion). The very fine-grained sand fraction in Group 2 deposits remains relatively constant from the base-to-top. Fine (> 0.125 mm), to coarse-grained (> 1 mm) sand also remains constant. Of the 10 'non-erosive' samples, only 6 samples (NE-C, NE-D, NE-E, NE-F, NE-G and NE-H) show these trends.

The other samples, documented in the field as non-erosive samples (NE-B, NE-I, NE-J, DF-3), display 'normal' grading, analogous to a Group 1 (erosive) signature, and variable grain-size signatures, these are classified as Group 3 Type IIa MTDs.

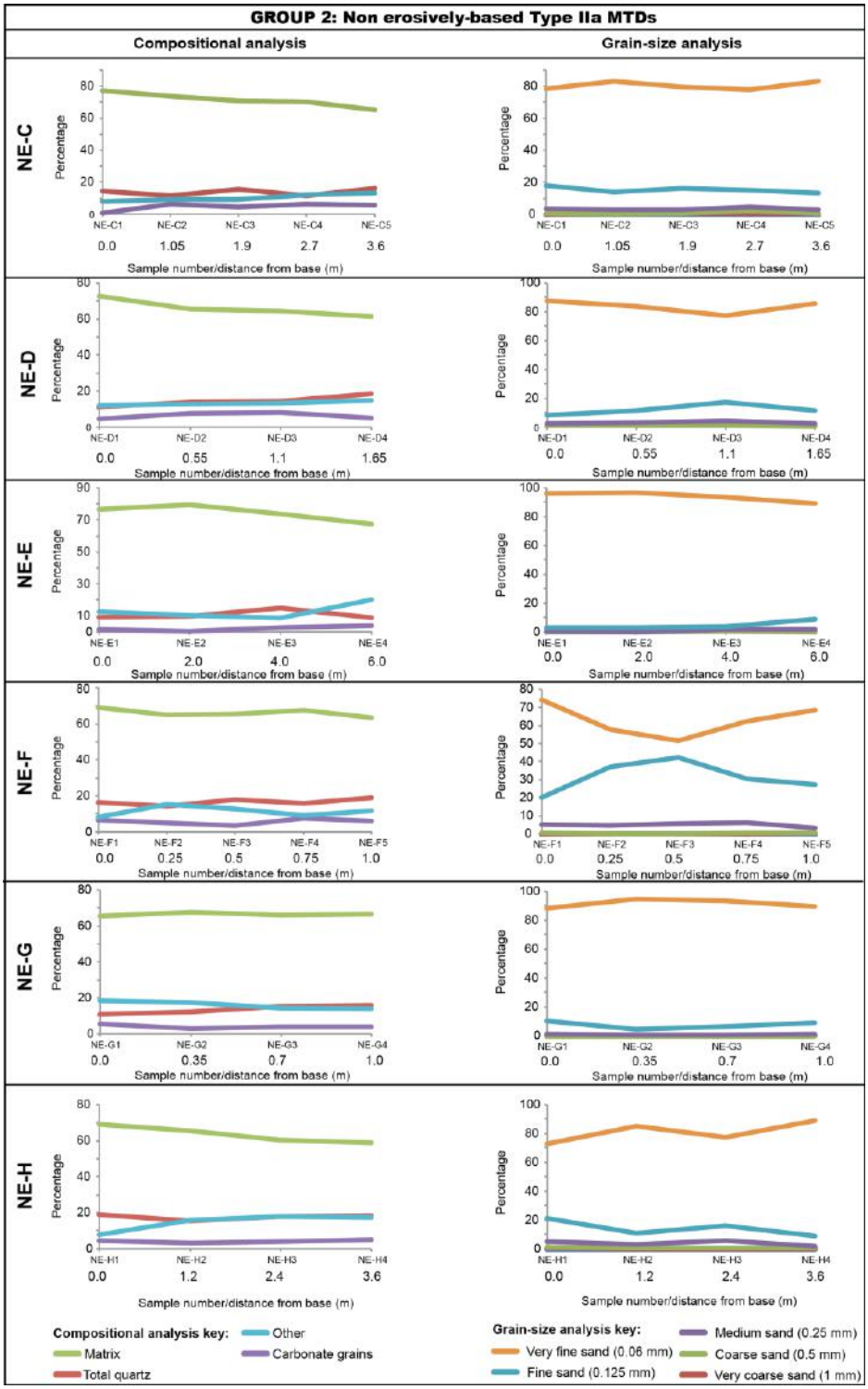

Figure 7.5. Group 2 Type IIa MTDs. Compositional analyses show a constant or reverse vertical grading profile in the siltstone/mudstone matrix and a relatively constant grain-size profile in the very-fine grained sand fraction (> 0.06 mm).

7.3.1.3 Group 3: Anomalous data from Group 2 deposits

Group 3 deposits were sampled from outcrops, similar to Group 2 Type IIa MTDs, which appeared to have a non-erosional base. Figure 7.6 shows the compositional and grain-size profiles of anomalous non-erosive deposits.

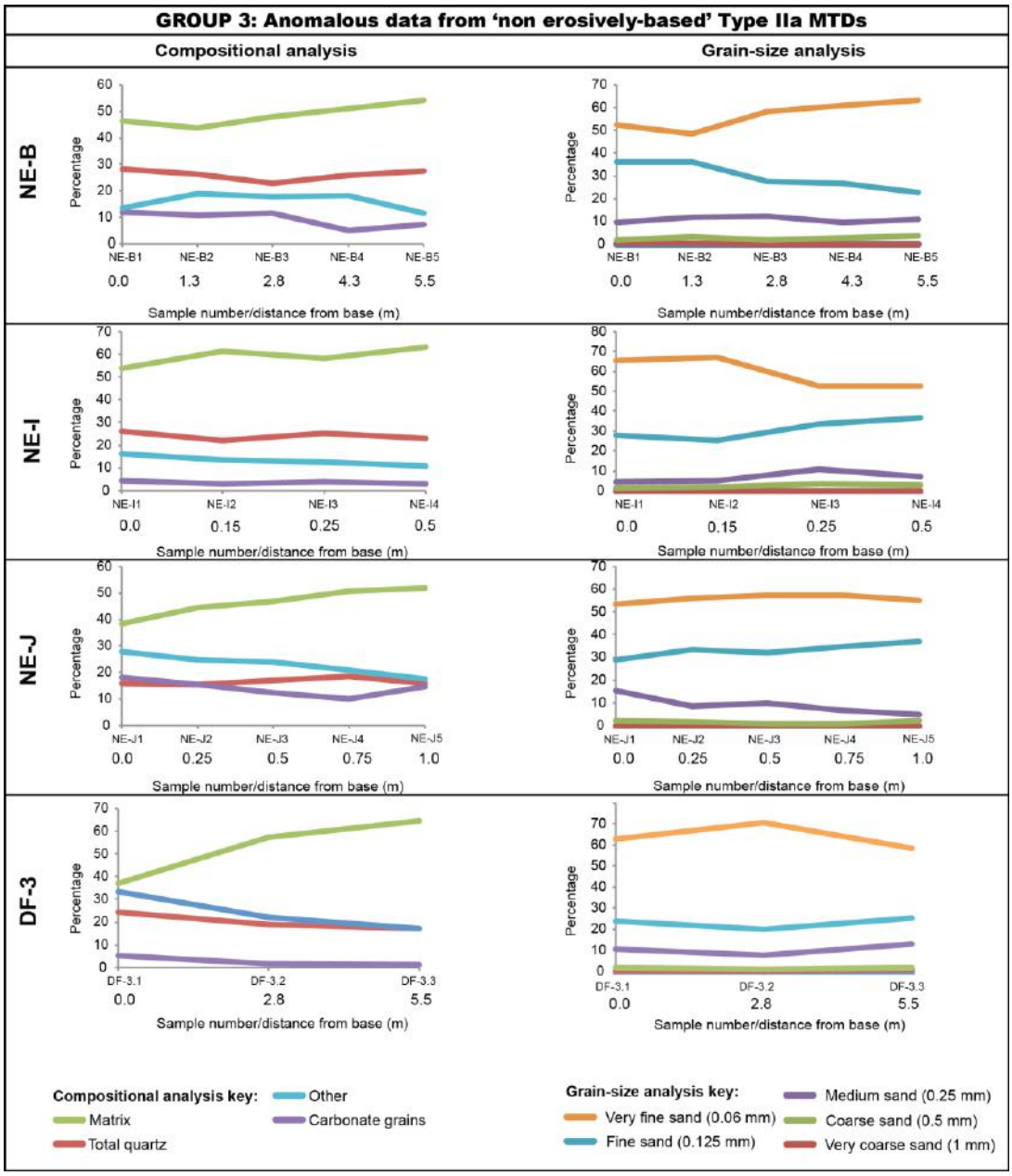

Figure 7.6. Group 3 Type IIa MTDs. Compositional analyses show a normal vertical grading profile in the siltstone/mudstone matrix and a variable grain-size profile in the very-fine grained sand fraction (> 0.06 mm).

Compositional analyses show that siltstone/mudstone matrix increases and the abundance of quartz, carbonate and 'other' grains (> 0.06 mm) decreases vertically, suggesting normal grading, as there is a vertical increase in siltstone/mudstone matrix content. This compositional signature is indicative of an erosive Type IIa deposit profile (Group 1), even though at outcrop, there was no evidence of erosion. Grain-size analyses of Group 3 deposits show the profile of very fine-grained sand (> 0.06 mm) as variable; it can increase (NE-B, DF-4), decrease (NE-I), or remain constant (NE-J, DF-3).

7.3.2 Thin-section images

Photomicrographs presented are grouped to show comparative fabrics at the base of Group 1, 2 and 3 deposits, and sandy SGF-deposits (Figure 7.7). Siltstone/mudstone matrix dominates the base of Group 2 deposits, whereas the base of Group 1 and 3 deposits are grain-rich. Individual thin sections show that all MTDs sampled are chaotic, showing poorly- to very poorly-sorted matrices (whether sampled at the base, middle, or top of each deposit). However, from base- to-top within Group 1 and 3 deposits, there is apparent grading between each thin section, as matrix increases vertically. The fabric at the base of Group 1 (erosive) samples can show an orientated fabric (from top left to bottom right) (Figure 7.7-A). Overall, carbonate grains are observed as well to very well-rounded and micritic. Das Gupta and Pickering (2008) discuss extrabasinal carbonate grains with Pithonellid tests grains originating from sediments, Late Cretaceous in age. Intrabasinal carbonate grains are documented as Eocene in age and include larger foraminifera, such as nummulites, alveolina and other shallow marine organisms such as miliolids and algal grains. Quartz and feldspars are observed as angular, sub-angular to rounded grains.

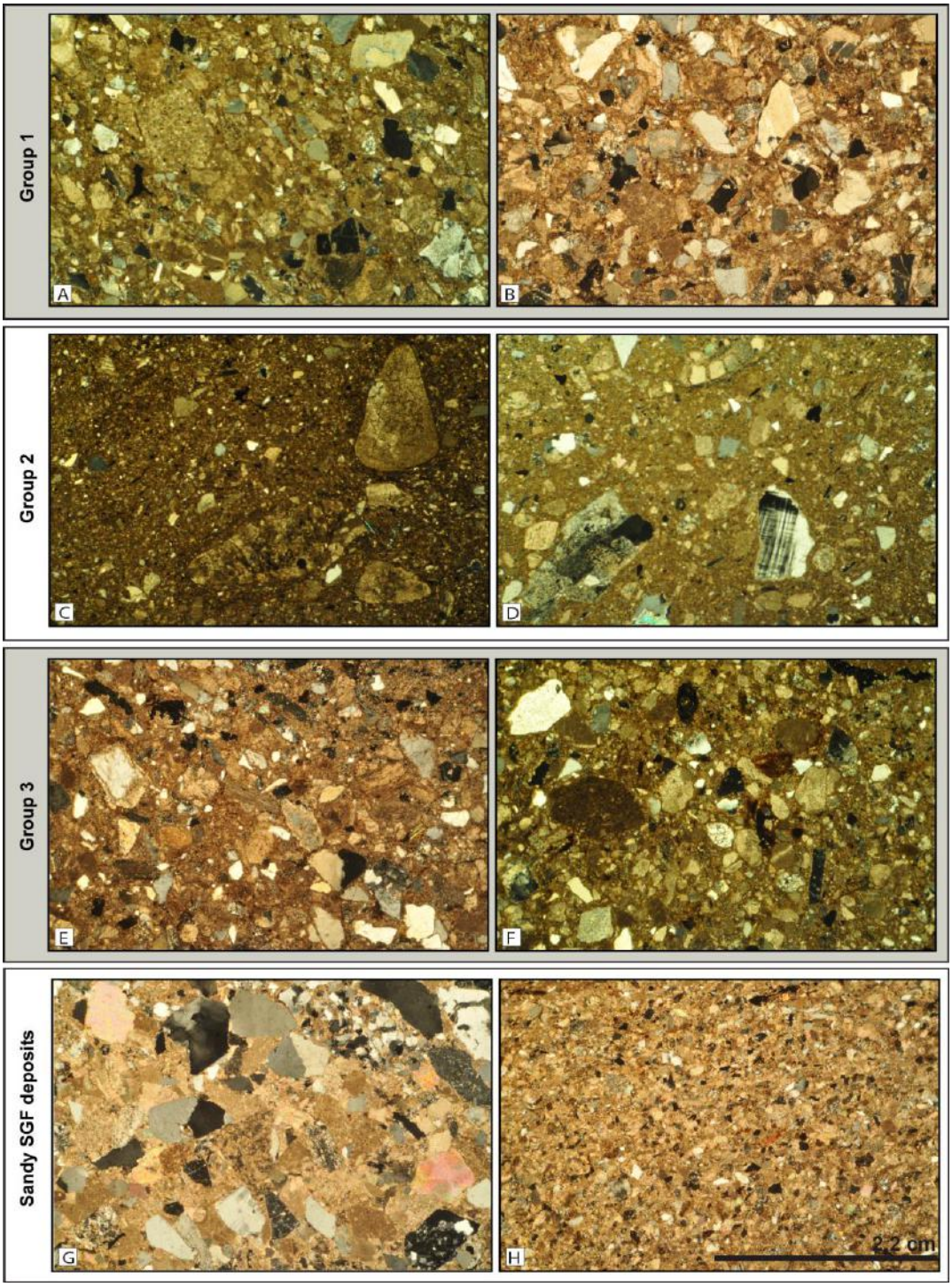

Figure 7.7. Group 1, Group 2 and Group 3 deposits photomicrographs.. (A) Sample E-A at 0.0 m (B) sample E-B at 0.0 m (C) sample NE-C at 0.0 m (D) sample NE-F at 0.0 m (E) sample NE-G at 0.0 m (F) sample NE-J at 0.0 m (G) sample Tu2, coarse-grained sandy SGF (H) sample Tu1, very-fine grained sandy SGF. All images are shown at the same scale (scale bar shown in bottom right corner, Figure H).

7.3.3 Grain-size analysis based on grouped data

Grain-size data is examined according to Groups 1, 2 and 3 to deduce further insight into identifying different debris flow processes in ancient marine settings.

7.3.3.1 Group 1: Erosively-based Type IIa MTDs deposits

Grain-size analyses from Group 1 MTDs are shown in Figure 7.8 (ranging from very coarse-grained (VCS) to very fine-grained (VFS), left to right, respectively, in each graph). Data in each graph is ordered according to depth from base (i.e., lower numbers [E-A1] were collected at the base of the deposit and higher numbers [E-A6] were collected at the top of the deposit).

Grain-size trends in Group 1 deposits generally fine vertically from the base of each deposit. A higher percentage of coarser grains are present at the base of deposits, and a higher percentage of the very fine-grained sand fraction is observed at the top of all deposits. Medium- to fine- sand grains (MS and FS, respectively) in the basal samples (at 0.0 m) of each deposit varies from 10 to 30 %. A wide distribution of grain-size fractions is observed from the base-to-top of each deposit (up to 35 % difference in the fine-grained sand fraction [FS], in sample E-F 1 to 5).

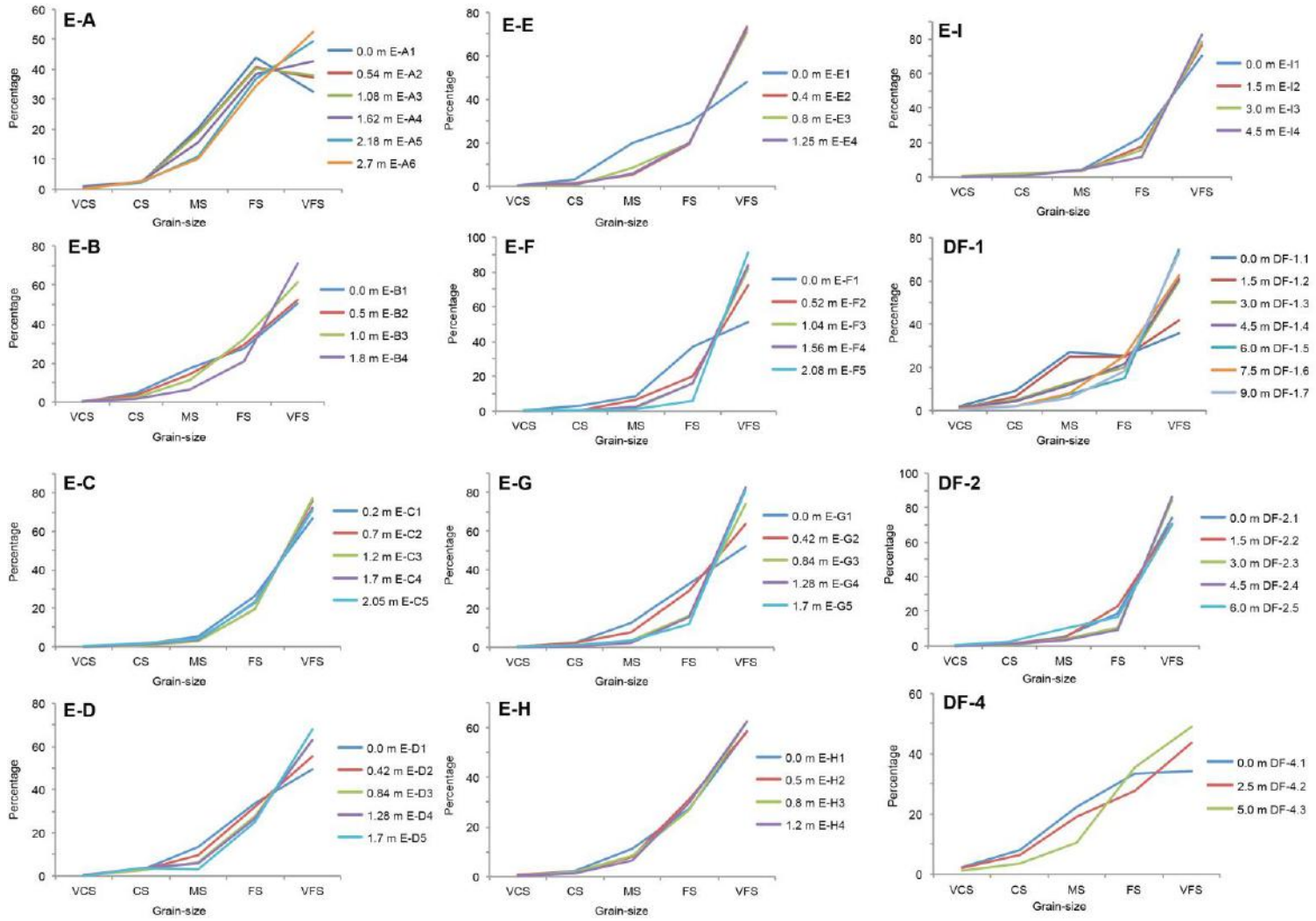

Figure 7.8. 'Normal' grading observed in Group 1 deposits. Key: VCS – very coarse-grained sand (> 1 mm); CS – coarse-grained sand; MS – medium-grained (> 0.5 mm) sand (> 0.25 mm); FS – fine-grained sand (> 0.125 mm), and VFS – very fine-grained sand (> 0.06 mm). Vertical distance from the base of each deposit increases with sample number; i.e., E-A1 is sampled at the base and E-A6 is sampled from the top.

7.3.3.2 Group 2: Non-erosively-based Type IIa MTDs deposits

Group 2 MTDs generally show a similar trend to each other, dominated by the very-fine grain fraction (> 0.06 mm), up to 90 % in sample NE-D for example (Figure 7.9).

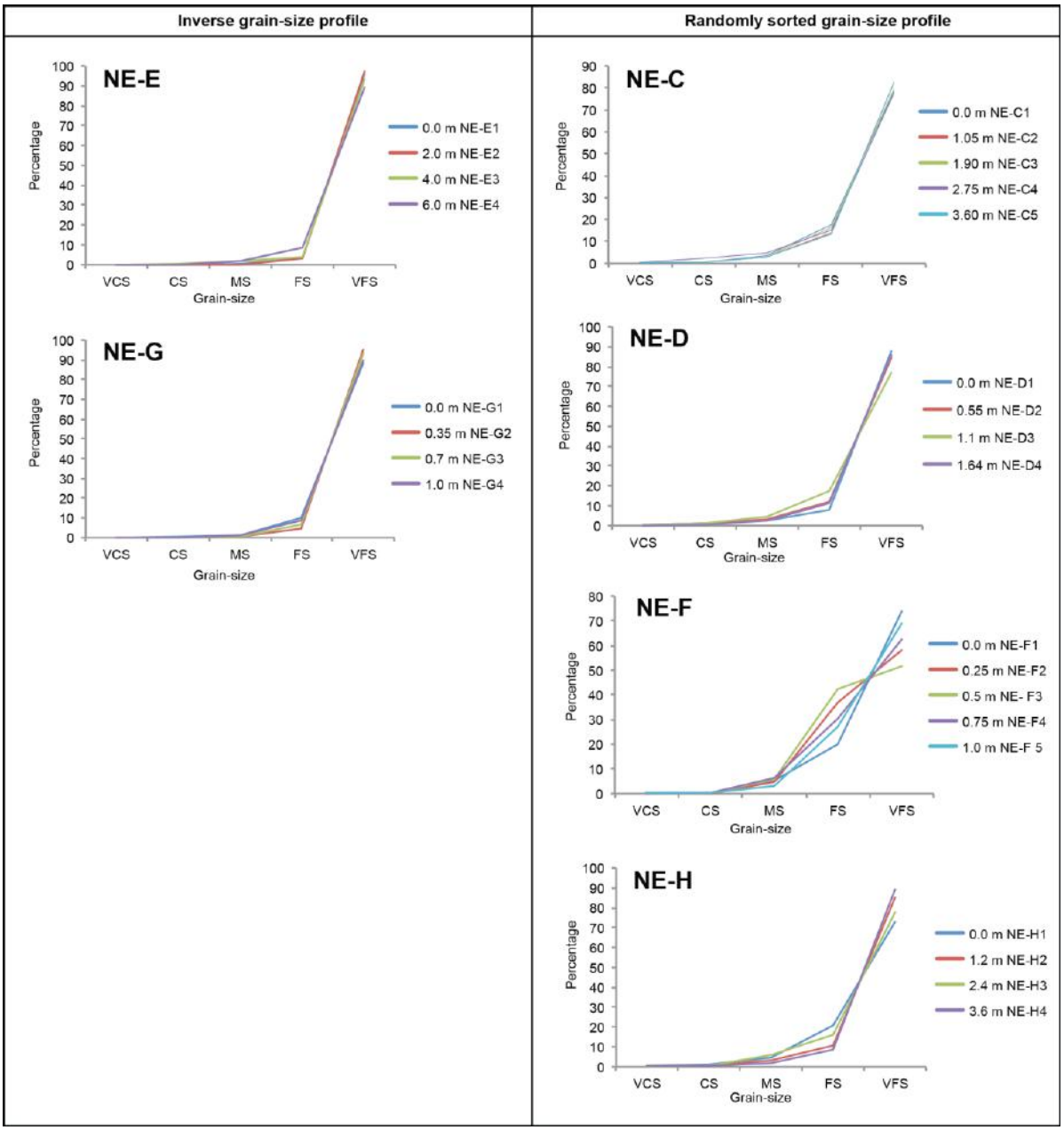

Figure 7.9. Grain-size data from Group 2 deposits. Key: VCS – very coarse-grained sand (> 1 mm); CS – coarse-grained sand; MS – medium-grained (> 0.5 mm) sand (> 0.25 mm); FS – fine-grained sand (> 0.125 mm), and VFS – very fine-grained sand (> 0.06 mm). Vertical distance from the base of each debris-flow deposit increases with sample number, i.e., NE-C1 is sampled at the base and NE-C5 is sampled from the top.

Deposits NE-E and NE-G both show that sequentially coarser grains are located nearer the top of each deposit, revealing an inverse-grading profile. Type IIa MTDs NE-C, NE-D, NE-F and NE-H (right in Figure 7.9) do not show this inverse-grading profile. In these deposits, grain-sizes are randomly sorted; best observed in NE-F, where the abundance of the medium-, fine- and very-fine grained sand fractions (MS, FS and VFS, respectively), show no discernable sequential order from base-to-top. There is a smaller distribution of grain-sizes from the base-to-top of these deposits (compared to Group 1), with the maximum spread of data (25 %) in the fine-grained size fraction [FS] in sample NE-F1 to 5. All other samples show < 10 % in grain-size variation between sample sets. Medium- to fine-sand grains (MS and FS, respectively) in the basal samples of each deposit vary from 10 to 20 %.

7.3.3.3 Group 3: Anomalous data from Group 2 deposits

Group 3 deposits (NE-B, NE-J, NE-I and DF-3) are observed to have variable grain-size trends (Figure 7.10). Group 3 deposits show variable grain-size profiles with no discernable grading trends, analogous to MTDs that did not show erosion at outcrop (Group 2).

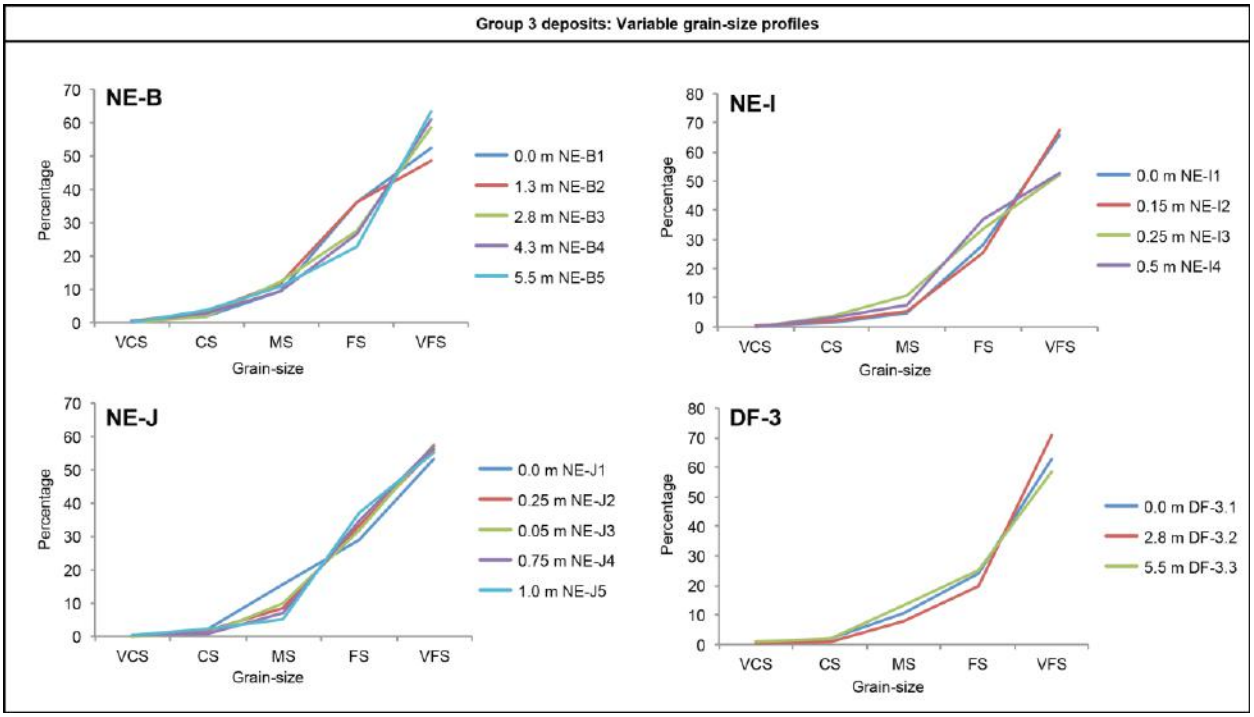

Figure 7.10. Grain-size data from anomalous data from 'non-erosive' debris flows showing no visible erosion; but display an 'erosional' compositional signature and a variable grain-size profile. Key: VCS – very coarse-grained sand (> 1 mm); CS – coarse-grained sand; MS – medium-grained (> 0.5 mm) sand (> 0.25 mm); FS – fine-grained sand (> 0.125 mm), and VFS – very fine-grained sand (> 0.06 mm). Vertical distance from the base of each debris-flow deposit increases with sample number; i.e., NE-B1 is sampled at the base and NE-B5 is sampled from the top.

7.3.3.4 Grain-size comparison between all Groups

Grain-size data is compared between Groups 1, 2 and 3 (Figure 7.11). Groups 1 and 3 are observed as coarser grained than non-erosive deposits (Figures 7.11-A [all data] and 7.12-B [averaged data]). Group 1 (erosive samples) are up to 35 % more enriched in coarser-grain size fractions (> 1 – 0.125 mm), coarse to fine-grained sand) compared to non-erosive samples (Group 2), which are up to 20 % enriched in the very-fine grained size fraction (> 0.06 mm). The coarser grain-size populations documented in Groups 1 and 3 is discussed in Section 7.4.1 and 7.4.3.

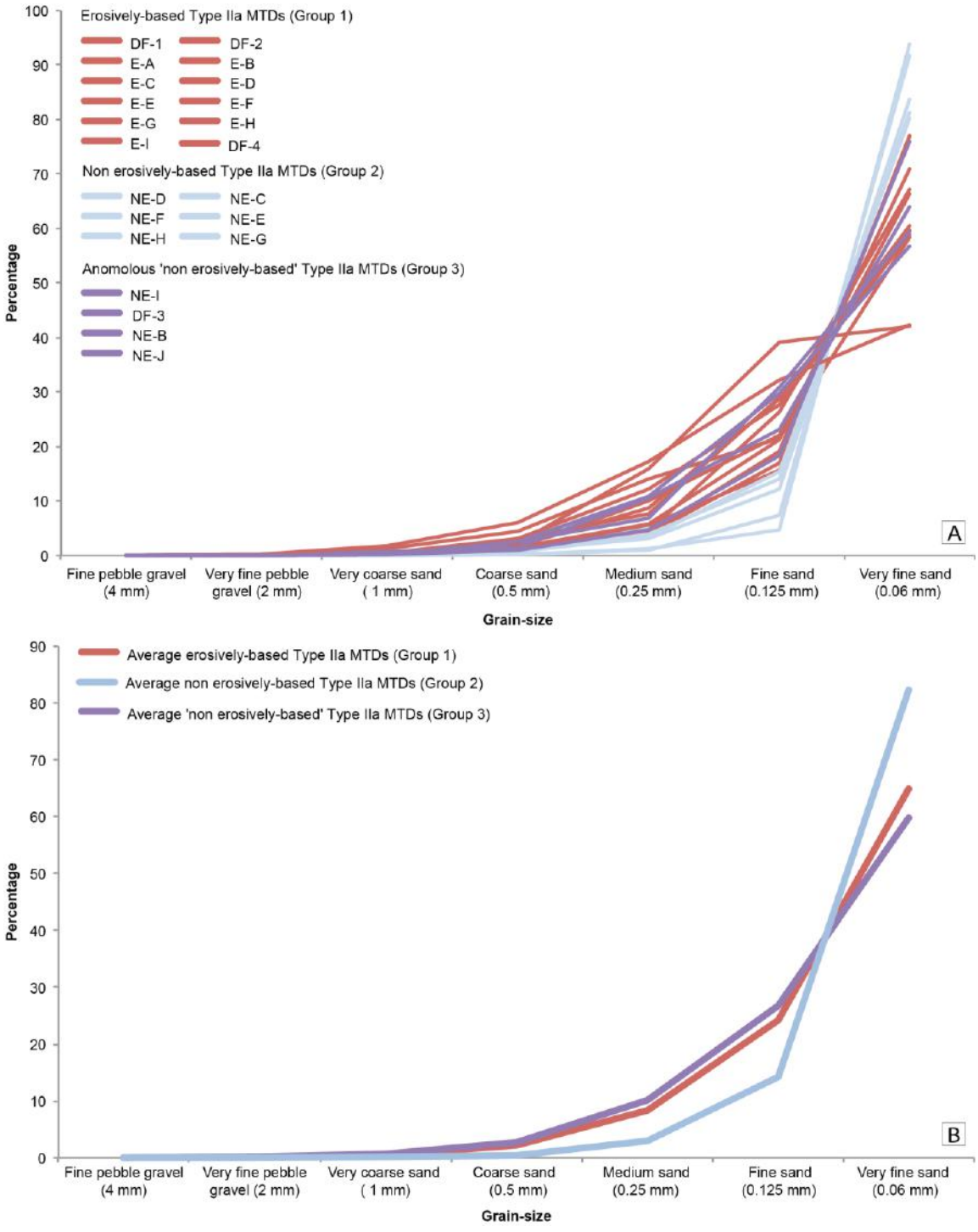

Figure 7.11. (A) Percentage grain-size analysis of debris-flow deposits (Groups 1, 2 and 3). (B) Average percentage of grouped data.

7.3.4 Overall grading and compositional analysis

To determine the distribution of the most frequently occurring components that comprise SGFs in the Ainsa Basin, a histogram showing the percentage of matrix and grain compositions of all SGFs (including sandy SGF deposits) analysed in this study are presented (Figure 7.12).

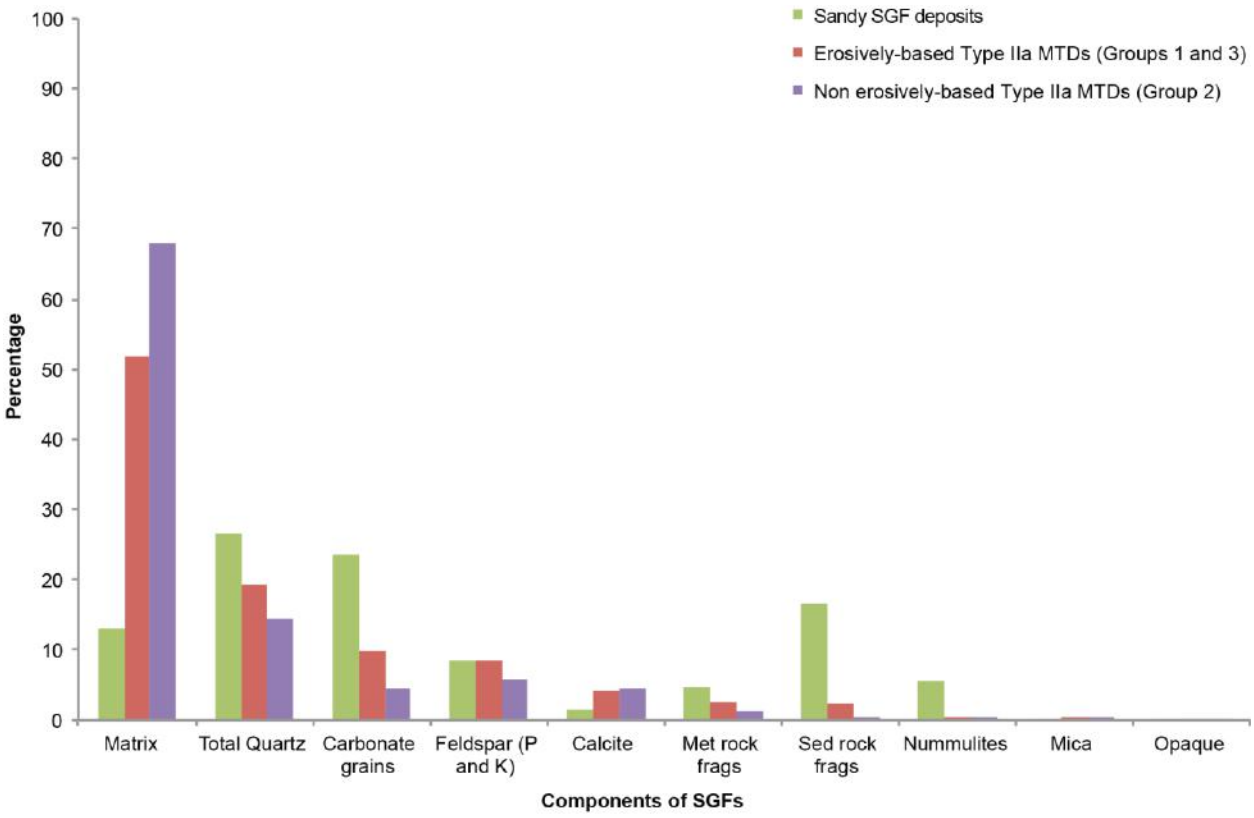

Figure 7.12. Average compositional data of SGFs analysed in the Ainsa Basin (18 sandstone sandy SGF deposits, 129 Type IIa MTDs). Total Quartz equals the sum of monocrystalline and polycrystalline quartz grains.

Siltstone/mudstone matrix is the dominant component of Type IIa deposits. Quartz and carbonate grains are the most abundant grain-type found in both debris-flow deposits and sandy SGF deposits. Determining the dominant grain composition of SGFs sampled in the Ainsa Basin allows the major components to be plotted on the ternary diagram for further analyses to evaluate how these variables change between Groups 1, 2 and 3 (Figure 7.13).

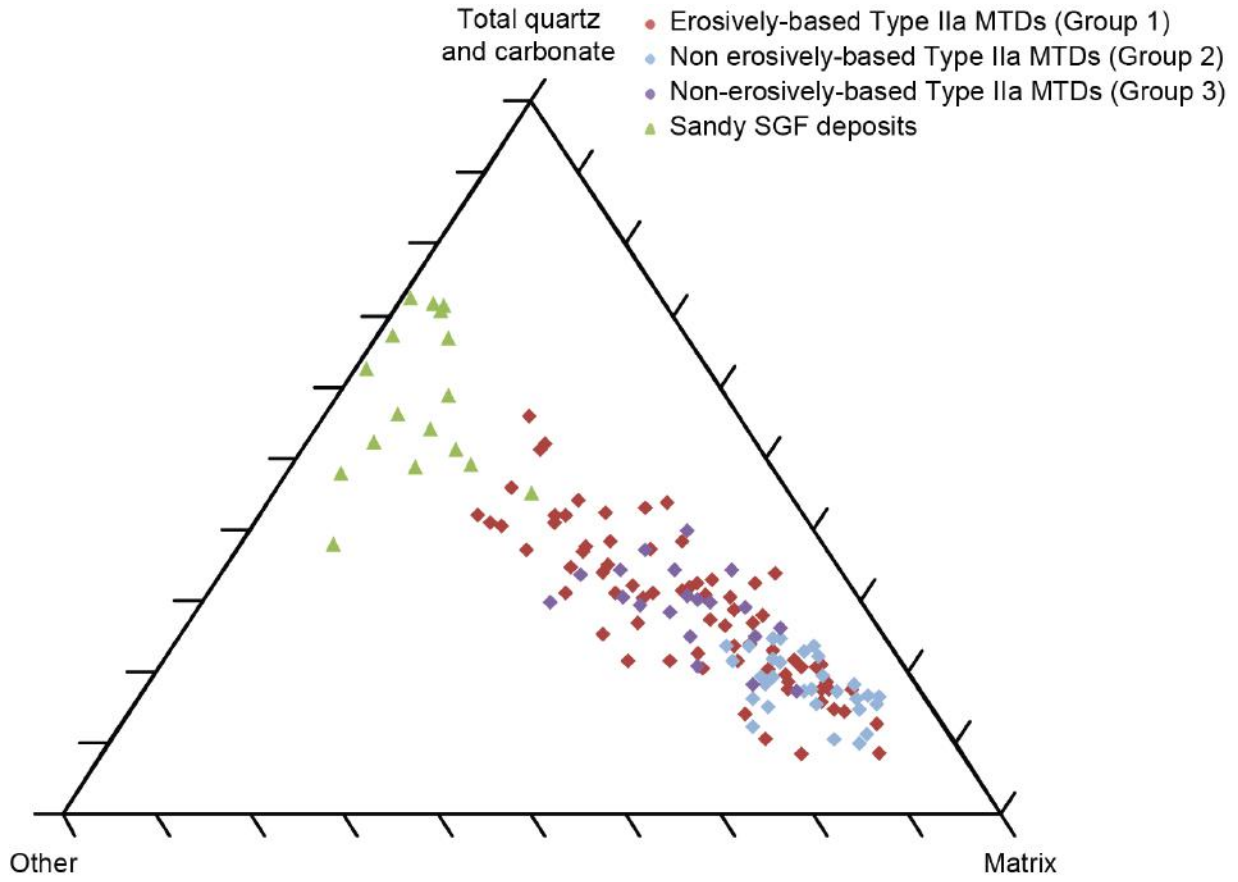

Figure 7.13 Ternary diagram showing the bulk compositional analysis of sandy SGF deposits and Type IIa Groups 1, 2 and 3. Sandy SGF-deposits show the least amount of matrix in the samples. Group 1 and 2 deposits show a linear relationship, controlled by the amount of matrix in the samples. Scale on ternary diagram shows 10 % increments.

The overall compositional variation between sandy SGF deposits and Type IIa MTDs is shown in Figure 7.13. There is a linear trend resulting from the decreasing (or increasing) amount of siltstone/mudstone matrix (%), which differentiates these SGFs. Sandy SGF deposits have very little matrix present (av. 13 %) compared to debris-flow deposits (av. 57 %). shows that Type IIa MTDs have variable grain-to-matrix ratios, covering a wide spectrum (20 – 80 % grains), compared to a relatively narrow range observed in sandy SGF deposits group (72 – 99 %). There is also a subtle grain-to-matrix segregation of debris-flow deposits between Groups 1, 2 and 3:

- Group 1 deposits showing basal erosion at outcrop, show the widest grain-to-matrix ratio, ranging between 17 to 78 % grains;
- Group 2 deposits cluster together, dominated by matrix ranging between 20 to 41 % grains, and;
- Group 3 deposits are intermediate, and populate between the two erosive and non-erosive end-members, ranging between 30 to 62 % grains (Groups 1 and 3, respectively).

7.3.5 Compositional analysis normalised without matrix

As siltstone/mudstone matrix is such a dominant component of Type IIa MTDs, the following data (including sandy SGF deposits) is normalised to negate the effect of matrix (Figure 7.14), which is ordered according to age of depositional system.

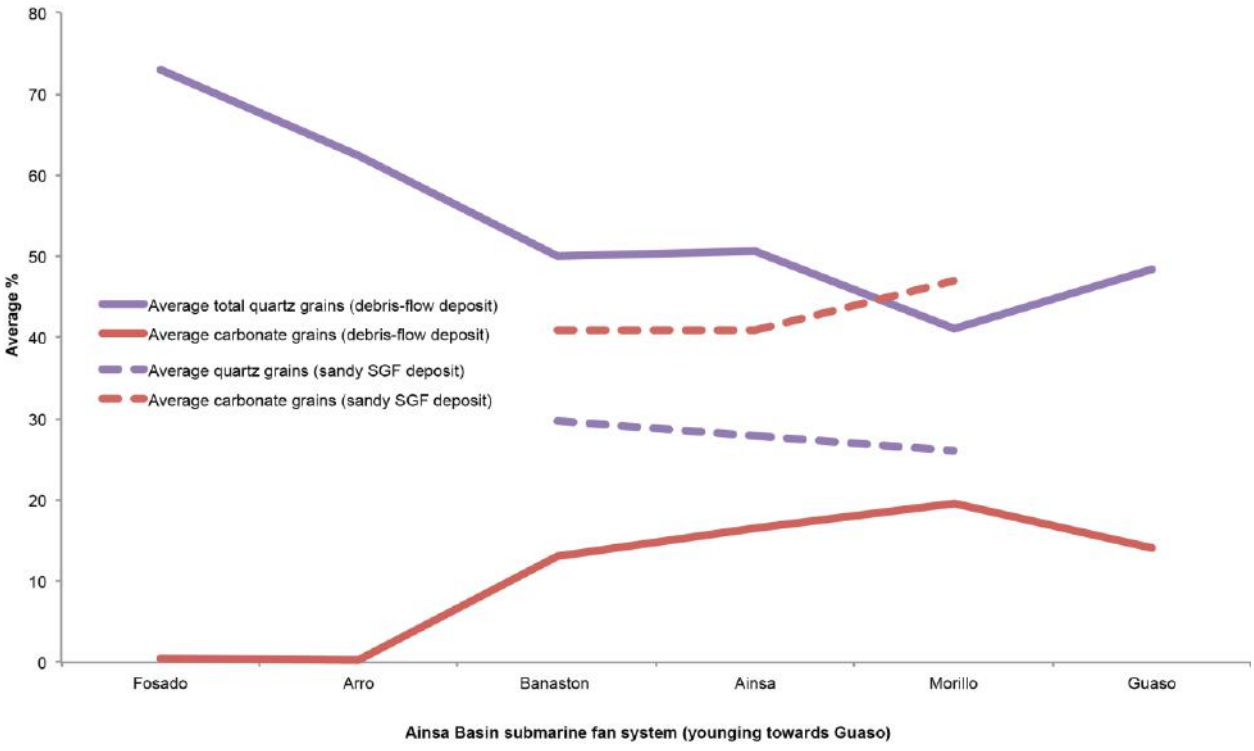

Figure 7.14. Graph showing difference in enrichment of quartz and carbonate grains between debris-flow deposits and sandy SGF deposits over time (Younging to the right towards Guaso).

A higher proportion of carbonate grains are found dominating the grain composition of sandy SGF deposits (av. 27.8 % quartz grains *versus* av. 42.91 % carbonate grains), and a higher proportion of quartz grains are found dominating debris-flow deposits (av. 54.26 quartz grains *versus* av. 10.33 % carbonate grains). Previous ternary diagrams (e.g., see Figure 7.13-B) do not show any discernable compositional differences between erosive and non-erosive debris-flow deposits, apart from some 'non-erosive' MTDs to be more matrix-rich. Bulk compositional data between Type IIa deposits and sandy SGF deposits is normalised without the presence of a siltstone/mudstone matrix to determine any differences specifically in grain abundance and composition (Figures 7.15-A, B and C). Sandy SGF deposits are enriched with carbonate grains compared to Group 2 deposits (non-erosive), plotting as separate data populations (Figure 7.15-A). Samples DF-3, NE-B and NE-I from Group 3 deposits have the same composition as Group 2 deposits, and sample NE-J, is analogous to a sandy SGF deposit compositional signature (Figure 7.16) separates Group 2 data to separate these trends.

Based on data presented in Figure 7.16, Group 1 deposits can be further divided into 3 sub-groups; (1) deposits that are enriched with carbonate grains and have the same composition as sandy SGF deposits (E-D, E-E, E-H); (2) deposits that only show enrichment of carbonate grains at the base, but vertically grade to a composition analogous to Group 2 deposits (E-F, E-G, E-I, DF-1), and (3) deposits that are not enriched in carbonate grains, and plot within Group 2, non-erosive samples (E-A, E-B, E-C, DF-2, DF-4).

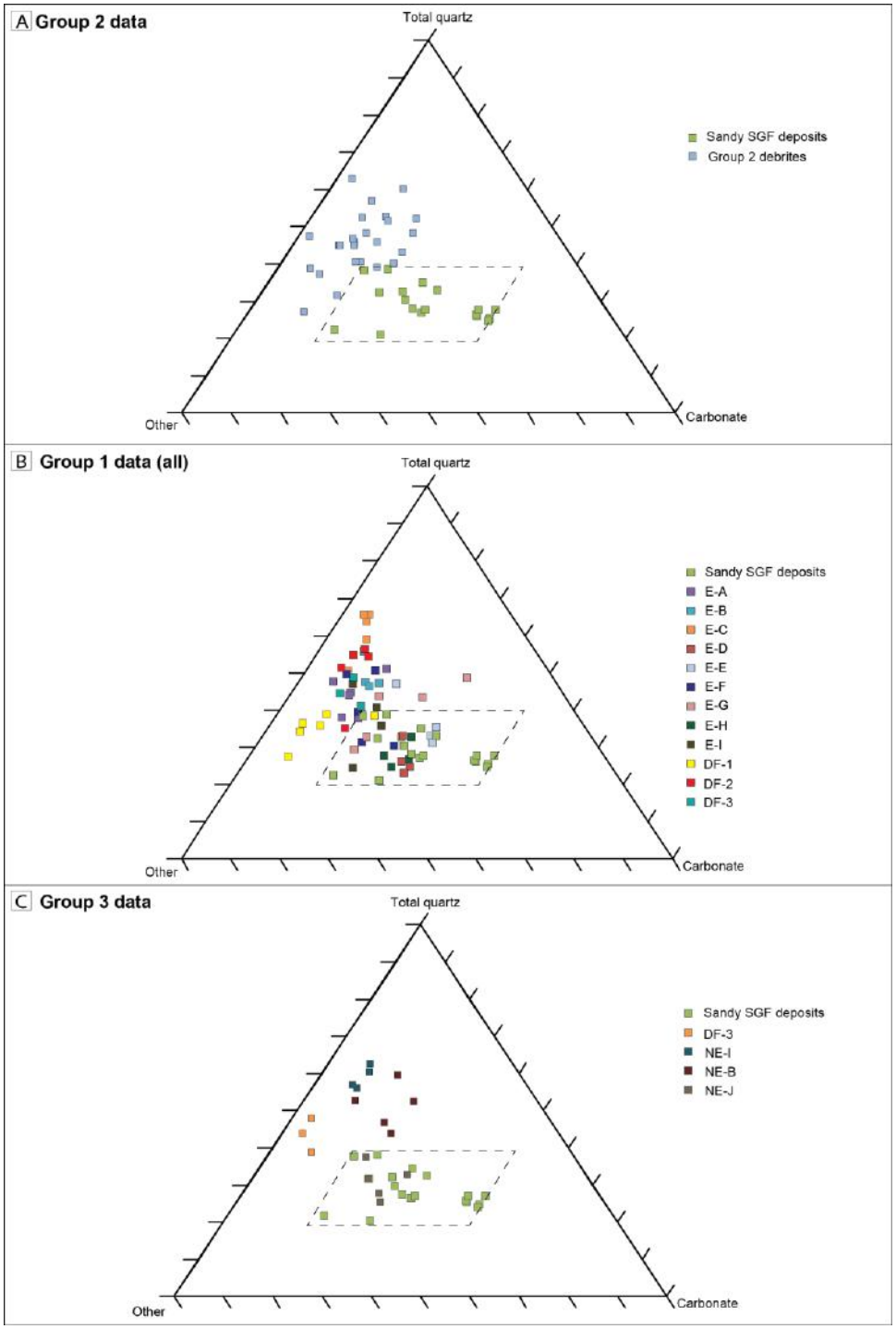

Figure 7.15. The bulk composition of ternary diagrams are normalised without siltstone/mudstone matrix. (A) Comparison of sandy SGF deposits and Group 2 deposits (non-erosive) (B) Comparison of sandy SGF deposits and Group 1 deposits (erosive) (C) Comparison of sandy SGF deposits and Group 3 deposits (erosion not preserved *in-situ*). Dashed polygon indicates where sandy SGF deposits plot. Scale on ternary diagram shows 10 % increments.

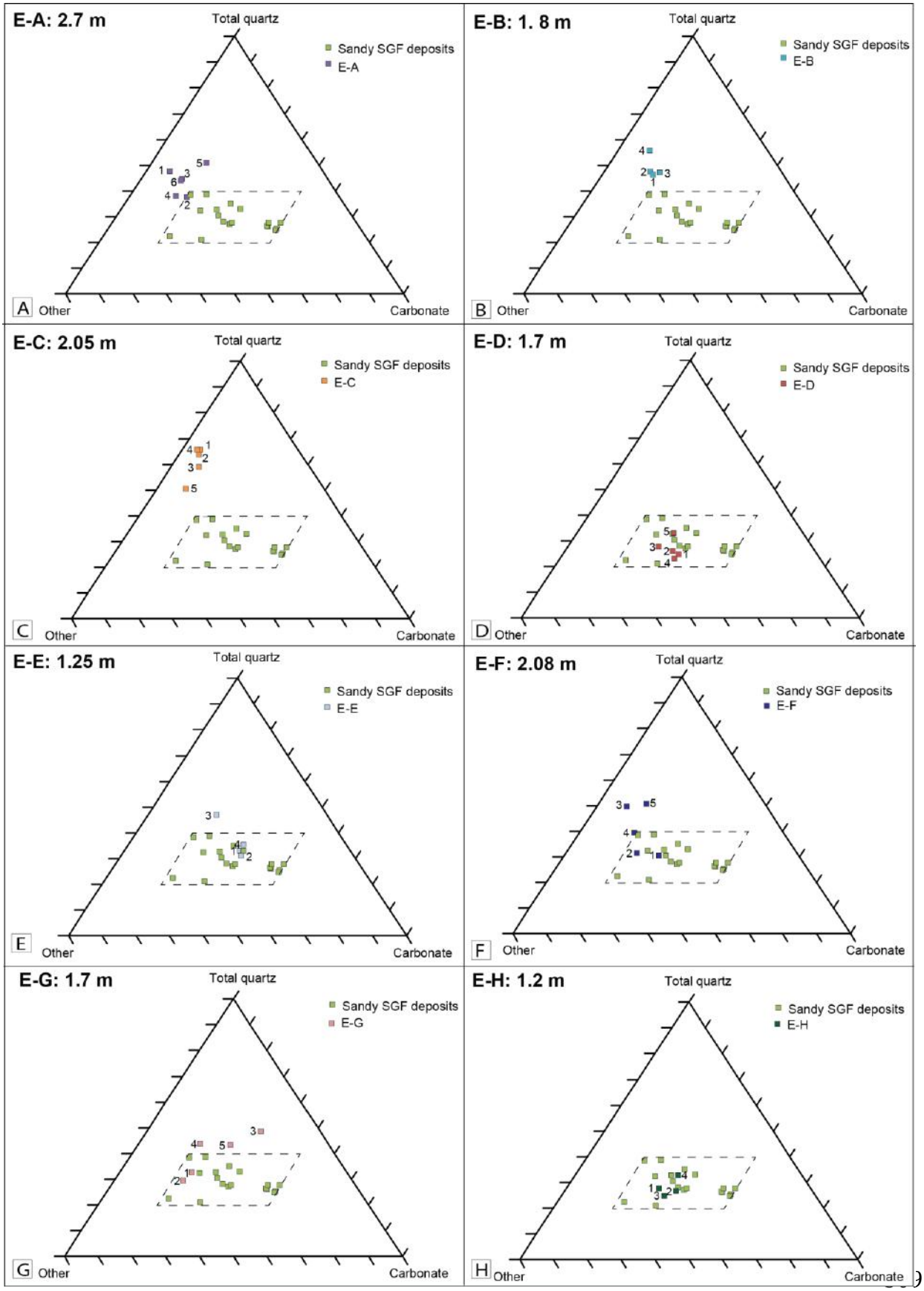
E-A: 2.7 m
Total quartz
Sandy SGF deposits
E-A
A Other
Carbonate
E-B: 1. 8 m
Total quartz
Sandy SGF deposits
E-B
B Other
Carbonate
E-C: 2.05 m
Total quartz
Sandy SGF deposits
E-C
C Other
Carbonate
E-D: 1.7 m
Total quartz
Sandy SGF deposits
E-D
D Other
Carbonate
E-E: 1.25 m
Total quartz
Sandy SGF deposits
E-E
E Other
Carbonate
E-F: 2.08 m
Total quartz
Sandy SGF deposits
E-F
F Other
Carbonate
E-G: 1.7 m
Total quartz
Sandy SGF deposits
E-G
G Other
Carbonate
E-H: 1.2 m
Total quartz
Sandy SGF deposits
E-H
H Other
Carbonate

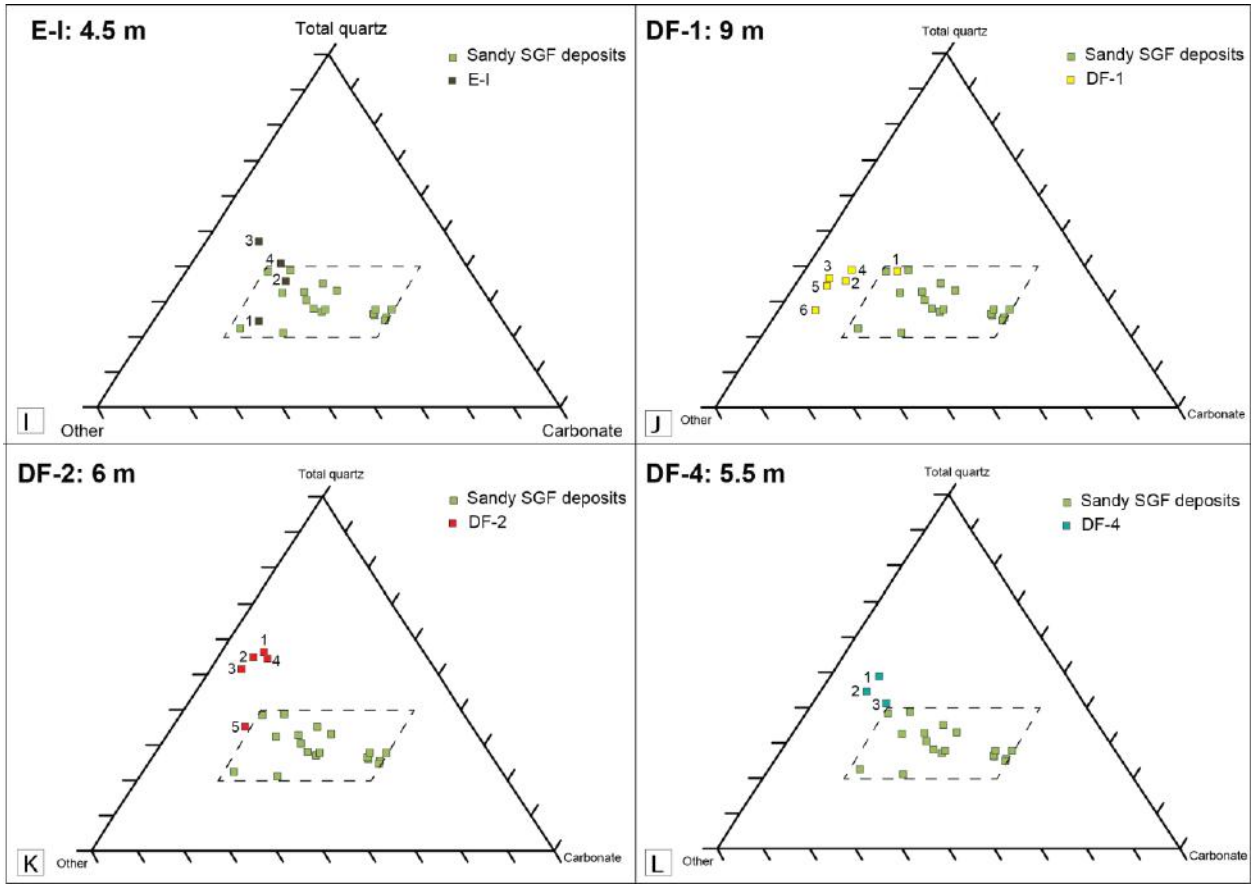

Figure 7.16. The bulk composition of ternary diagrams normalised without siltstone/mudstone matrix for Group 1 deposits. (A to L) Comparison of sandstone sandy SGF deposits and Group 1 MTDs. Thickness of deposit denoted next to deposit number. Numbers (1 to 9) adjacent to data points refer to sequential order sampled from base, i.e., 1 = base of deposit. Dashed polygon indicates where sandy SGF deposits plot. Scale on ternary diagrams shows 10 % increments.

7.4 DISCUSSION

Sampling Type IIa MTDs from the Ainsa Basin has provided insights to the various compositional and grain-size profiles of erosive and non-erosive MTDs, as observed at outcrop.

7.4.1 Group 1 MTDs

Chapter 6 summarises the mechanisms of erosion identified in the field (ploughing, plucking, scouring, striating and injecting into underlying sandy substrates). Group 1 deposits were sampled from MTDs that showed an irregular base or where erosion was preserved *in situ*, such as where semi-lithified sandstone blocks were plucked and incorporated into the base of Type IIa deposits, suggesting minimal, if any distance was travelled between erosion and freezing of the deposit (e.g., Rio Ara, Morillo I as a type-locality).

From thin-section analysis of 12 Type IIa deposits showing basal erosion, all deposits displayed 'normal' compositional grading trends, where the siltstone/mudstone matrix profile increased vertically (Figure 7.3). Group 1 MTDs also show vertically graded grain-size profiles, with coarser grains found nearer the base of the deposits (Figure 7.8). As these deposits dominantly show *in-situ* erosion or irregular basal contacts, it is plausible to suggest that grains from the underlying sandy SGF deposits were incorporated into the base of the Type IIa deposits. Basal erosion may preserve locally erosive processes. entraining and incorporating coarse-grains from underlying substrates into the base of the flow and thus preserve the effect of 'grading' upon deposition, not related to grading observed in fully turbulent flows (e.g., Bouma, 1964; Middleton and Hampton, 1973). A preferentially oriented fabric is observed at the erosive base of a Type IIa MTD, which could capture shear at the base of the deposit (Figure 7.7-A)

In some deposits, grains of the eroded sandy substrate are observed as incorporated into the base of the Type IIa deposits and, therefore, deposits appear to inherit the compositional 'memory' of erosion (e.g., Figure 7.16-D). Whereas other deposits do not show a similar compositional signature to sandy SGFs (e.g., Figure 7.16-C), which may relate to the type of sediment it has eroded, or could be related sediment source area, discussed in Section 7.4.5.

7.4.2 Group 2 MTDs

Group 2 MTDs were sampled from deposits that showed a planar, 'non-erosive' base. From thin-section analysis, of the 10 Type IIa deposits sampled, six deposits showed inverse to constant compositional grading trends, where the siltstone/mudstone matrix either decreased vertically, or

remains relatively constant throughout each deposit (Figure 7.5). These deposits also showed variable grain-size profiles (Figure 7.5). The remaining 4 MTDs showed vertical compositional trends analogous to Group 1 deposits and showed variable grain-size profiles, where grain-size trends were not observed (Figure 7.6). These deposits were classified as Group 3 MTDs, and showed there is greater complexity than only observing 'erosive' or 'non-erosive' MTDs at outcrop (i.e., Group 1 and 2 deposits).

Group 2 deposits in the deep-marine setting typically show < 10 % granular material and are dominated by a siltstone/mudstone matrix that showed an inverse or random grain-size grading trend, which may suggest that the matrix had cohesive strength, enabling coarser grains to be supported at the top of the flow. At the time of deposition, these flows were likely to be floating plugs of sediment inhibiting particle segregation throughout the flow. Type IIa MTDs that do not appear as erosive down-dip are interpreted from failure of the upper- to lower-slope, where finer-grained sediments are deposited from winnowing processes. These flows were likely to be cohesive and laminar, and may even suggest hydroplaning during transport (Mohrig *et al.*, 1998; 1999).

7.4.3 Group 3 MTDs

Group 3 deposits were derived as a sub-set of Group 2 deposits as these samples showed compositional grading trends analogous to Group 1 deposits (i.e., 'normal' grading trends, where the siltstone/mudstone matrix to grain percentage increases from vertically base-to-top of each deposit sampled). Group 3 deposits differ from Group 1, showing random vertical grain-size trends (Figure 7.6). MTD Groups 1 and 3 consistently show coarser grain-sizes compared to Group 2 deposits (Figure 7.11).

From these observations, it is suggested that Group 3 deposits record the deposition of flows that were previously erosive up-dip (sourcewards), which maintained momentum after erosion, therefore erosion is not preserved at outcrop, shown in the depositional model (Figure 7.17).

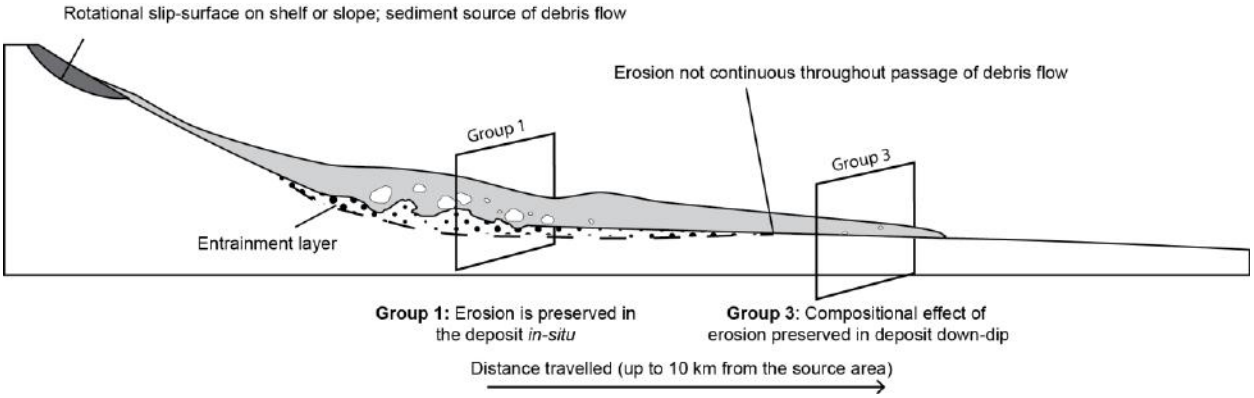

Figure 7.17. 2-D model showing possible variation between erosive Type IIa MTDs preserved up and down-dip (Groups 1 and 3, respectively).

The distance travelled between the point of erosion to deposition may have been sufficient to fully incorporate eroded grains into the flow preventing any locally formed graded grain-size profile to be preserved in these deposits. The volume of sediment eroded and incorporated into the base of the debris flow may also affect the grain-size profiles of these deposits. For example, the further a flow travelled away from the erosion site, the greater the potential to affect the typical 'erosive' grain-size signature, potentially via homogenisation, allowing grains to be more evenly distributed vertically throughout the deposit down-dip from the site of erosion.

7.4.4 Summary of MTDs observed in the Ainsa Basin

Groups 1, 2 and 3 MTDs are summarised in Table 7.1.

	Group identified from thin section study	Erosion observed at outcrop?	Erosion description recorded at outcrop?	Grain-size signature	Compositional signature	Implication
Type IIa MTDs	**Group 1**	Yes	Sandstone blocks incorporated into the base of Type IIa MTDs and irregular basal surface	'Normal grading'. Increase in very fine-grained sand ($\geq$ 0.06 mm) upwards	Increase in siltstone/mudstone matrix upwards	Debris flow arrested during erosive process and erosion is preserved *in situ* in the rock record. Likely to be ploughing/bull dozing/shouldering aside/striating the substrate
	Group 2	No	Not observed	Inverse grading. Decrease in fine-grained sand ($\geq$ 0.06 mm) upwards	Decrease in siltstone/mudstone matrix upwards	No erosion observed in outcrop and reverse grading suggests no erosion at sample station
	Group 3	No	Not observed. Likely to be ploughing/bull dozing/shouldering aside/striating the substrate	Variable grading: constant, increase or decrease of very fine-grained sand ($\geq$ 0.06 mm) upwards	Increase in siltstone/mudstone matrix upwards	Erosive debris flow. Although at sample station, it appears non-erosive. Erosion may have taken place up-dip from outcrop site. Although sorting is variable, based on the compositional profile, flows appear to inherit the 'memory' of erosion. Likely to be ploughing/bull dozing/shouldering aside/striating the substrate
Sandy SGF deposits	**Group 1**	Yes	Onlap. Mechanism of erosion is not recorded in outcrop	Normal to no grading	Fining-up to no grading	Although interpreted to be erosive, erosive base is not observed at outcrop.
	Group 2	No	N/A	Normal to no grading	Fining-up to no grading	Non-erosive flow regime.

Table 7.1. Type IIa Groups 1, 2 and 3, identified from compositional and grain-size signatures.

Table 7.1 separates sandy SGF deposits as Groups 1 and 2, as turbidity currents can be erosive, related to turbulence in the flow, or depositional (i.e., non-erosive) (Bouma, 1964). Whether erosional or depositional, sandy SGF deposits show analogous sedimentary characteristics, i.e., can show normal grading and fine up vertically (Mayall *et al.*, 2006).

7.4.5 Shelf morphology

Locally erosive processes may result in Group 1 and 3 MTDs being coarser-grained compared with Group 2 (non-erosive) deposits, however the effect of different source areas is explored here. Coarse-grained grain-size distributions in erosively-based deposits (Groups 1 and 3) could indicate the origin of environment of sediments trapped at successive environments on the shelf. Swift *et al.* (1987) propose a depositional model for an inner shelf transport system in the Kenilworth Member, Utah foreland basin USA, which occurred in response to nearshore storm processes. In this depositional model, Swift *et al.* (1987) envisage a fractional mill, where relatively coarser-grained sediment is found in the proximal surf zone environment and becomes progressively sorted as sediment moves down to the shoreface and shelf (Figure 7.18).

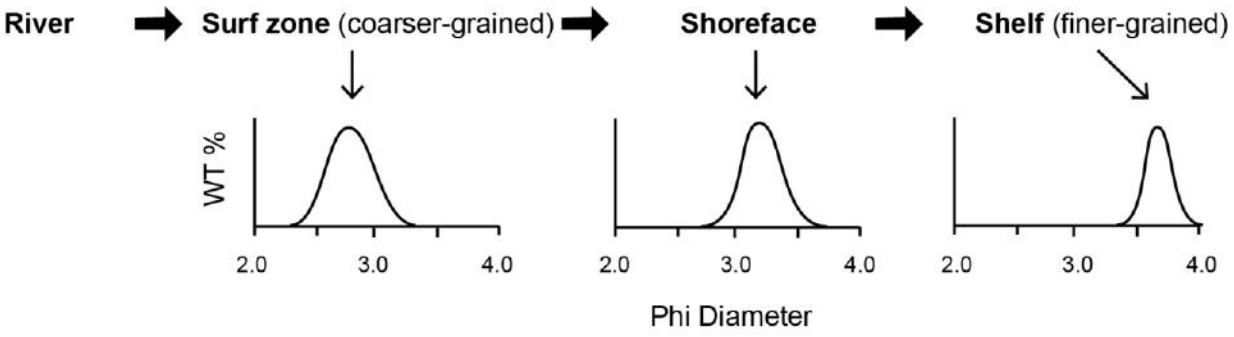

Figure 7.18. Depositional model based on the Kenilworth Member (Utah, USA). Arrows between environments indicate transport pathway. Size distributions indicated composition of sediment trapped at successive environments. Redrawn from Swift *et al.* (1987).

Based on nearshore processes identified by Swift *et al.* (1987), if debris flows in the Ainsa Basin were sourced from large-scale failure that was able to remobilise, not only upper slope and shelf environments but also nearshore and littoral environments, could suggest that

event magnitude could have a bearing on how erosive a debris flow is during its downslope movement.

Data analysis in this study shows that when data is normalised to negate the presence of matrix, a direct comparison of bulk grain composition can be made between Type IIa and sandy SGF deposits. Group 2 deposits are interpreted as non-erosive during sediment transport and contain between 1.98 to 23 % carbonate grains. These data plot as separate data populations compared to sandy SGF deposits, which show between 18 and 50 % carbonate grains (Figure 7.13). To account for these compositional differences between Type IIa deposits and sandy SGFs (e.g., turbidites), a shelf wide enough to segregate sediment is invoked during deposition of the deep-marine sediments of the Ainsa Basin (i.e., a shelf setting as identified in Labaume and Séguret, 1985). As shallow-marine processes sort littoral zone sediments (i.e., near-shore shallow-marine sediments), the outer shelf and slope may become dominated by relatively denser quartzose sediments through winnowing, reworking and re-deposition. In large-scale failure events, the shelf may have collapsed leading to the re-deposition of winnowed quartz-rich shelf or slope sediments into deeper-water submarine fan environments. A depositional model is presented in Figure 7.19.

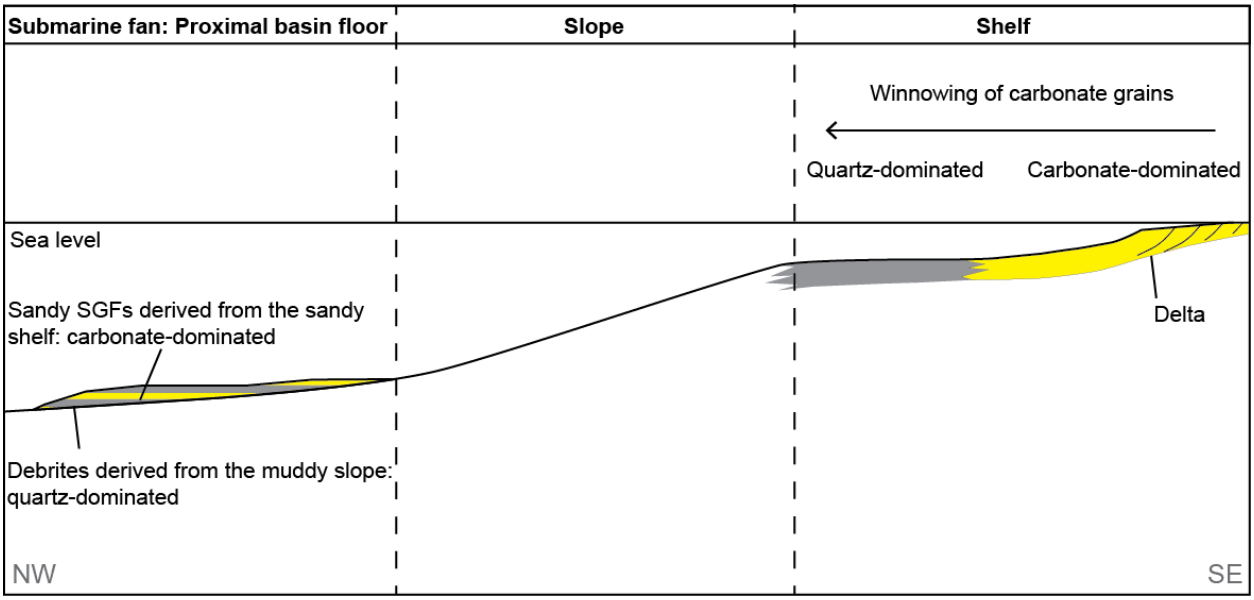

Figure 7.19. 2-D cross-section of the Ainsa Basin showing how the presence of a narrow shallow-marine shelf may potentially winnow less-dense carbonate grains from the mud-rich shelf/slope; the source of debris-flow deposits in the deep-marine fan environments of the Ainsa Basin.

All Group 2 (non-erosive samples) show different compositional grain populations from sandy SGFs, whereas Groups 1 and 3 show varying compositional trends. Within Group 1 (erosive samples), 3 from 12 sampled deposits (E-D, E-E and E-H) show that the entire deposit is enriched with carbonate grains, analogous to sandy SGF deposits, suggesting that some Type IIa MTDs are able to entrain the compositional signature of the underlying deposit (e.g., by becoming enriched with carbonate and 'other' grains when eroding a sandy SGF deposit). In other Group 1 deposits, only the base is enriched with carbonate grains (E-F, E-G, E-I and DF-1). Vertically from the base of these deposits, the compositional signature becomes the same as Group 2 (i.e., 'non-erosive') deposits. These deposits may suggest that as debris flows locally erode, they can entrain and pick up the compositional signature of the underlying substrate, however the enriched carbonate signature is only incorporated into the base of the flow before freezing. In the last of the Group 1 dataset, 5 of 12 sampled deposits (E-A, E-B, E-C, DF-2 and DF-4) do not show any enrichment with carbonate grains, and show the same compositional trends as 'non-erosive' Group 2 deposits. Group 3 deposits (interpreted to preserve the down-dip deposit from erosion that took place sourcewards), showed 3 of 4 samples not to be enriched in carbonate grains. There are 2 suggestions for the variation in these compositional trends:

(1) The compositional signature of these deposits may result from the composition of the eroded substrate not being enriched in carbonate grains, e.g., DF-2 which erodes a muddy substrate, or in samples E-A, E-B, E-C and DF-4, the sandy substrate may not always be enriched with carbonate grains.

(2) Some mass-flows located on the basin-floor could be sourced from a discrete source area away from the main fluvial input. The Castisent fluvial sandstone, which fed the Ainsa Basin, is typically a calcite cemented calc-lithic arenites with 20 – 32 % quartz, 5-8 % feldspars, 23 – 42 % non-carbonate rock fragments, and 10 – 30 %, (locally up to 64 %) of carbonate lithoclasts (Marzo *et al.*, 1988). The carbonate clasts are mainly derived from the Mesozoic of the Cotiella-Montsec Nappe exposed in the basin flanks (Marzo *et al.*, 1988), therefore, MTDs sourced near this sediment input may likely be enriched in carbonate grains. The marginal and flanking slopes, away from the main fluvial input of the Ainsa Basin, may be another source for MTDs (Figure 7.20).

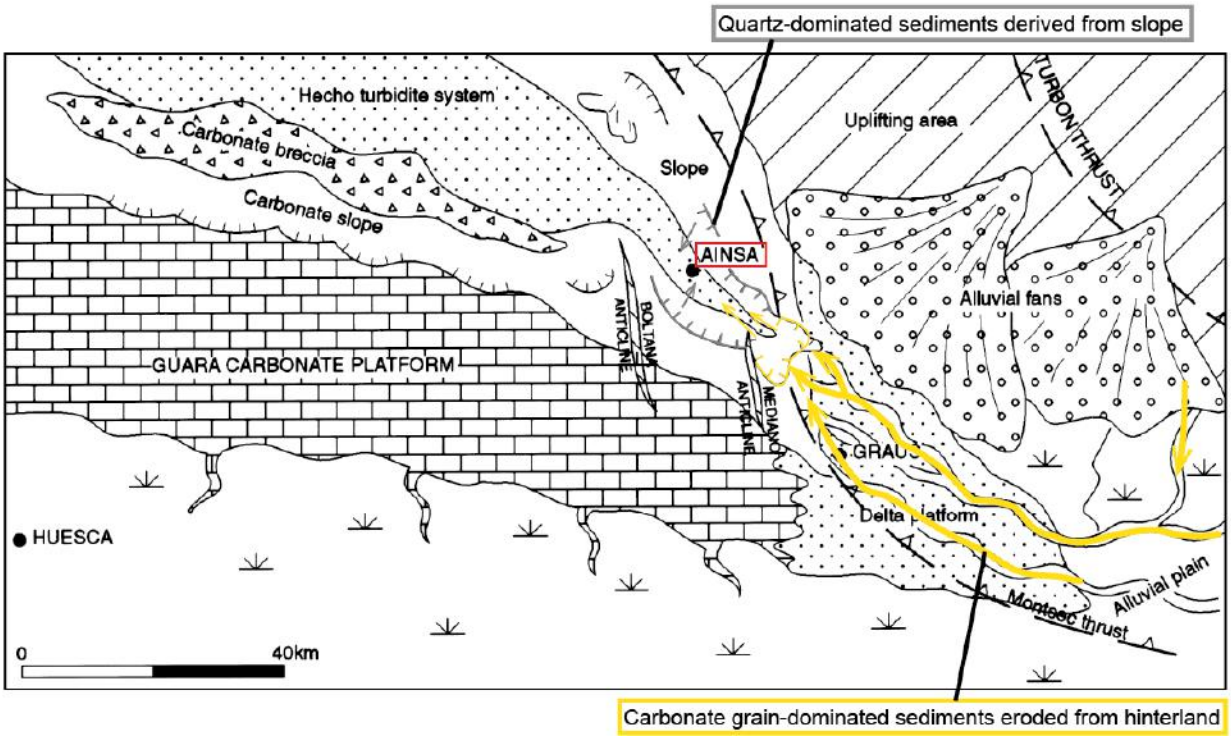

Figure 7.20. Map of the Ainsa Basin to demonstrate although a single sedimentary entry point is inferred, multiple sources for MTDs may result from failure of the surrounding slope of the Ainsa Basin. Modified from Dreyer *et al.*, (1999).

7.4.6 Flow processes

Erosively-based Type IIa MTDs may result from failure of the upper- to lower- slope and also potentially outer-shelf to littoral environments, with the erosive capability of the flow potentially related to the event magnitude. The coarser-grained elements in erosive samples are interpreted as resulting from failure of, or near to, higher energy littoral locations associated with coarser-grained environments (*sensu stricto* Swift *et al*., 1987). From the site of failure, these flows were likely to be travelling at a high velocity, able to erode the substrate. There is not enough information in the scope of this project to associate the numerical flow conditions required with such erosive processes. However it can be postulated that gradient of slope and event magnitude would dramatically affect the velocity, volume and basal shear rate of any flow, which may be related to these processes. This is supported by the abundance of erosive Type IIa MTDs in the

Banastón and Morillo systems, where higher slope gradients are inferred (Chapter 5, Figure 5.19). Type II deposits are likely to result from flow transformations and/or multi-granular flow, as described by Parsons *et al.* (2001) and Sohn *et al.* (2002).

7.5 SUMMARY

Outcrops show a limited 2-D view of what were almost certainly complex and variable 3-dimensional flows. Therefore, what is observed at any of the outcrop sample stations may not be representative in terms of both the sediment-transport and deposition processes, including their 'erosivity', not only up- and down-dip, but also laterally from the exposed section, i.e., proximal-to-distal, and axial-to-lateral in any flow. This study suggests that under appropriate conditions, debris flows can be erosive. As debris flows erode, they entrain material into the base of the flow and in some cases can pick-up the compositional signature of the substrate below. Results in this study suggest that more than one factor can determine the erosivity of debris flows, which is not easily determined from data collected in this study alone. Initially, the cause of grading observed in debrites that showed basal erosion was uncertain. In the field, debrites that preserved erosion *in situ* generally appeared 'sandier' than debris-flow deposits that did not show erosion, although grain fabric was not unanimous, as debrites with a planar base also showed fabrics with high grain-contents (these were incorporated into Group 3 MTDs, i.e., deposits frozen down-dip from the erosion site). Apparent grading is visually observed at outcrop by eye. The thin-section analysis in this study suggests that where grading occurs, it is likely that the MTD may have been erosive up-dip from the depositional site. This could provide a simple tool to identify MTDs either at outcrop, or in cored wells such as in the hydrocarbon industry. The coarser-grained fraction documented in this study measures grain-sizes between 0.06 and 1 mm. This study has not measured pebble to boulder-sized fractions, which may have had the destructive elements, able to plough and bulldoze the substrate effectively. Although, this style of erosion in granular material may be analogous to the experimental study of McCoy *et al.,* (2013), where force chains in subaerial granular material are found to be capable of eroding the substrate, previously discussed in Chapter 6. Although plausible, this study is does not document this style of erosion to occur in the Ainsa Basin.

In the Ainsa Basin, it is likely that a narrow shelf existed where wave-action (and possibly tidal processes) hydrodynamically sorted and winnowed sediment according to their density and, therefore, created a compositional archive between turbidity currents and cohesive debris flows. Sandy SGF deposits were likely sourced from a sandy, littoral, nearshore and shallow-marine environment that were compositionally distinct and dominated by carbonate grains. The non-erosive cohesive debris flows, however, were probably sourced from marginal muddy outer shelf and upper-slope environments dominated by relatively denser quartz grains. This setting may facilitate the identification of debrites that are enriched in carbonate grains, to suggest that flows were likely to have been erosive prior to deposition. However, the compositional analysis presented in this study, shows that not all debrites pick-up the character of an enriched sandy SGF signature, which may be related to the source area controlling composition of the sandy SGFs.

CHAPTER 8

MTDs AND MTCs IN THE UPPER JURASSIC BUZZARD FIELD, UK NORTH SEA

8.1 INTRODUCTION

The results and interpretations of work on the Upper Jurassic Buzzard Field, North Sea is presented in this chapter. This data is based mainly on research undertaken during a 3-month internship at CNOOC-Nexen (Uxbridge, UK).

Poor seismic imaging and resolution of the Buzzard Field is related to the presence of a thick Late Cretaceous chalk, limestone and marl succession, capping the Late Jurassic stratigraphy (Figure 8.1). The stratigraphic relationships within the Buzzard Formation are typically uncertain, and therefore the Buzzard Field would benefit from a better understanding of deposits that may affect sandy SGF sedimentation. A component of this research project is to evaluate MTDs and associated MTCs present in the subsurface from core and well-log data, and also to model the distribution and thickness variation of MTDs and MTCs within stratigraphy of the Buzzard Field. Fieldwork data presented from the Ainsa Basin, Spanish Pyrenees is also cross-referenced to determine similarities and differences of MTDs and MTCs between the two sedimentary basins. The outlines of the Buzzard and Ainsa basins are presented in Figure 1.19 (Chapter 1) to show the similarity in aerial extent between these basins.

8.1.1 Regional background

The North Sea has a complex, but well-constrained multiphase tectonic history (e.g., see summary in Underhill, 2003). This study focusses on the Upper Jurassic stratigraphy, therefore, a brief overview of the relevant geological history is provided for the purpose of this study.

Late Triassic continental deposits (locally termed the Smithbank Formation) are mainly inferred beneath the Buzzard Field. A sea-level rise in the Late Triassic led

to a marine incursion in the Early Jurassic. Coupled with a period of tectonic quiescence during this time, a marine transgression flooded the subsiding Permo-

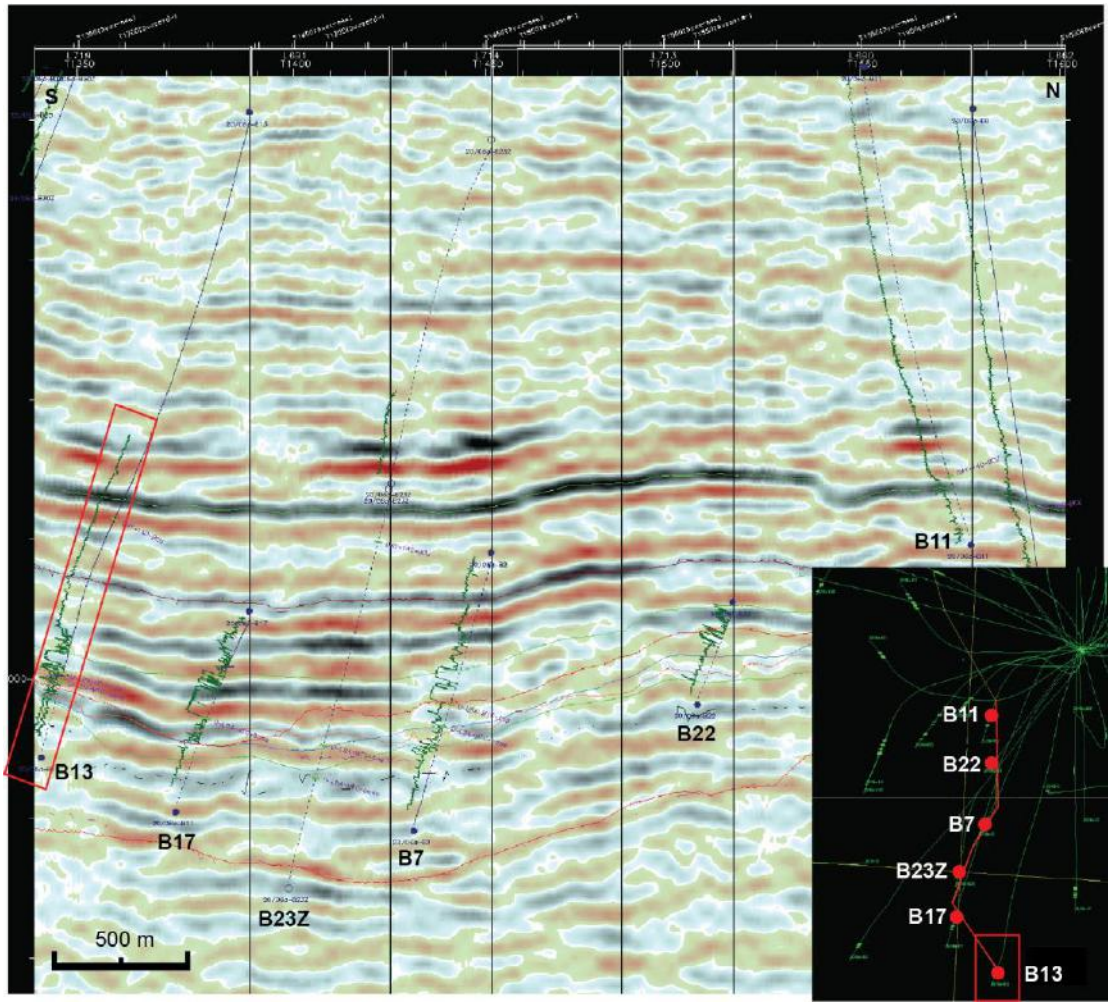

Figure 8.1. Seismic reflectivity data highlighting the limit of resolution. Image acquired using Seisworks. The B13 well is highlighted in the red boxes. Depth is in TWT. In general, peak-to-trough resolution of ~ 46 m (150 ft) is attainable.

Triassic post-rift basins and deposited marine sediments, recorded by the Blue Lias Formation (Underhill, 2003). Although this marine incursion extended to the Inner Moray Firth Basin, the Buzzard Field does not record Early Jurassic sedimentation. During the Mid-Jurassic, a major regional unconformity developed across much of the North Sea, termed the Mid Cimmerian Unconformity, which was a result of thermal doming, potentially associated with a mantle plume (Underhill and Partington, 1993). Deflation of the dome during the Mid- to Late Jurassic initiated the trilete rift arms and formed the Viking Graben, Central Graben and Moray Firth rifts systems, creating the main structural framework of the North Sea. The Upper Jurassic

rift system represents the most important period of basin development in the North Sea in terms of both trap formation and source rock deposition. Rifting occurred as multiple pulses formed extensional fault blocks resulting in the growth, propagation and linkage of normal faults (Underhill, 1993).

With continued rifting and relative sea level rise throughout the Late Jurassic, deep-marine deposits typically overlie shallow marine deposits. A continued overall marine transgression is observed throughout the Late Jurassic, depositing the Humber Group, which includes the open marine shelf deposits of the Heather Formation to more restricted marine, organic-rich shales of the Kimmeridgian Formation (Richards *et al.*, 1993). Palaeoenvironmental maps from Fraser *et al.* (2003) show the geographical area around Buzzard as emergent until the Late Oxfordian. At this time, a major transgression in the Moray Firth Basin resulted in a deepening of sea-level forming a deep-marine environment during the Kimmeridgian (Figure 8.2). However, biostratigraphy data obtained from the Heather Formation in the Buzzard Field suggest the area was fully marine at this time (in-house CNOOC-Nexen report).

Fraser *et al.* (2003) show the onset of coeval deep-water turbidite deposition along strike of the Outer Moray Firth. This led to the deposition of deep-water slope and submarine fan sandstone reservoirs including the Buzzard, Ettrick and Burns Members throughout the Kimmeridge Clay and Volgian Formation into the Early Cretaceous.

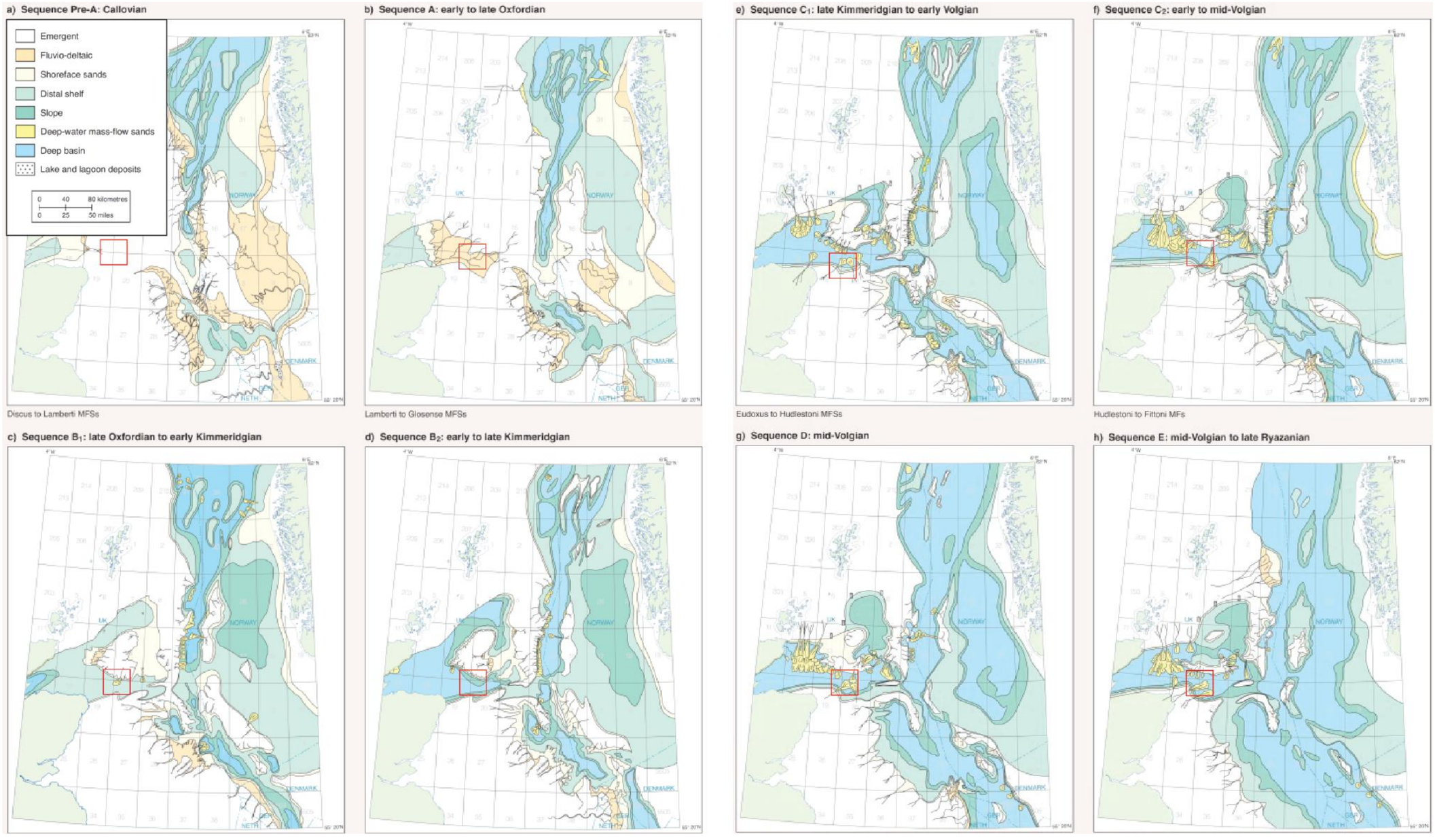

Figure 8.2. Palaeogeographic maps showing the development of depositional environments through the Upper Jurassic. Approximate location of Buzzard Field in red box. Modified from Fraser *et al.* (2003).

8.1.2 Buzzard Field structure and stratigraphy

A series of major west-to-east oriented faults define the Buzzard Basin, which form a sequence of half grabens resulting from Late Jurassic rifting. Reactivation of existing basement structures resulted in a maximum offset of 76.2 m (~ 250 ft). The major west-east faults define the basin into five areas including the Northern Terrace (NT), Northern Panel (NP), Central Panel (CP), Southern Panel (SP), and the Southern Terrace (ST) (Figure 8.3).

Throughout basin evolution, formation of half grabens created accommodation space and subsequently became the focus of depositing sandy SGFs to form the reservoir sandstones that currently produce hydrocarbons in the present day (Doré and Robbins, 2005). Stratigraphy pinches out, up-dip and to the west of the field forming a stratigraphic trap, which creates a wedge-shaped geometry that thickens down-dip to the east (Figure 8.4). The half-graben structure of Buzzard is shown in the seismic well-section (Figure 8.4-C).

The Upper Jurassic stratigraphy of the Buzzard Field is divided into units on the basis of regional lithological and biostratigraphic markers of the North Sea (Ray *et al*., 2010). Jurassic-aged sediments are divided into the Pentland, Sgiath, Heather and Kimmeridge Clay Formations, which young respectively. The Kimmeridge Clay Formation encompasses three major reservoir units named the Buzzard, Ettrick and Burns Sandstone Members, and acts as both the source rock to the petroleum system and the seal encompassing the sandstone reservoirs. The Ettrick and Burns Sandstone Members are interpreted to be younger and are deposited down-dip (further east and northeast, respectively) of the Buzzard Sandstone Member.

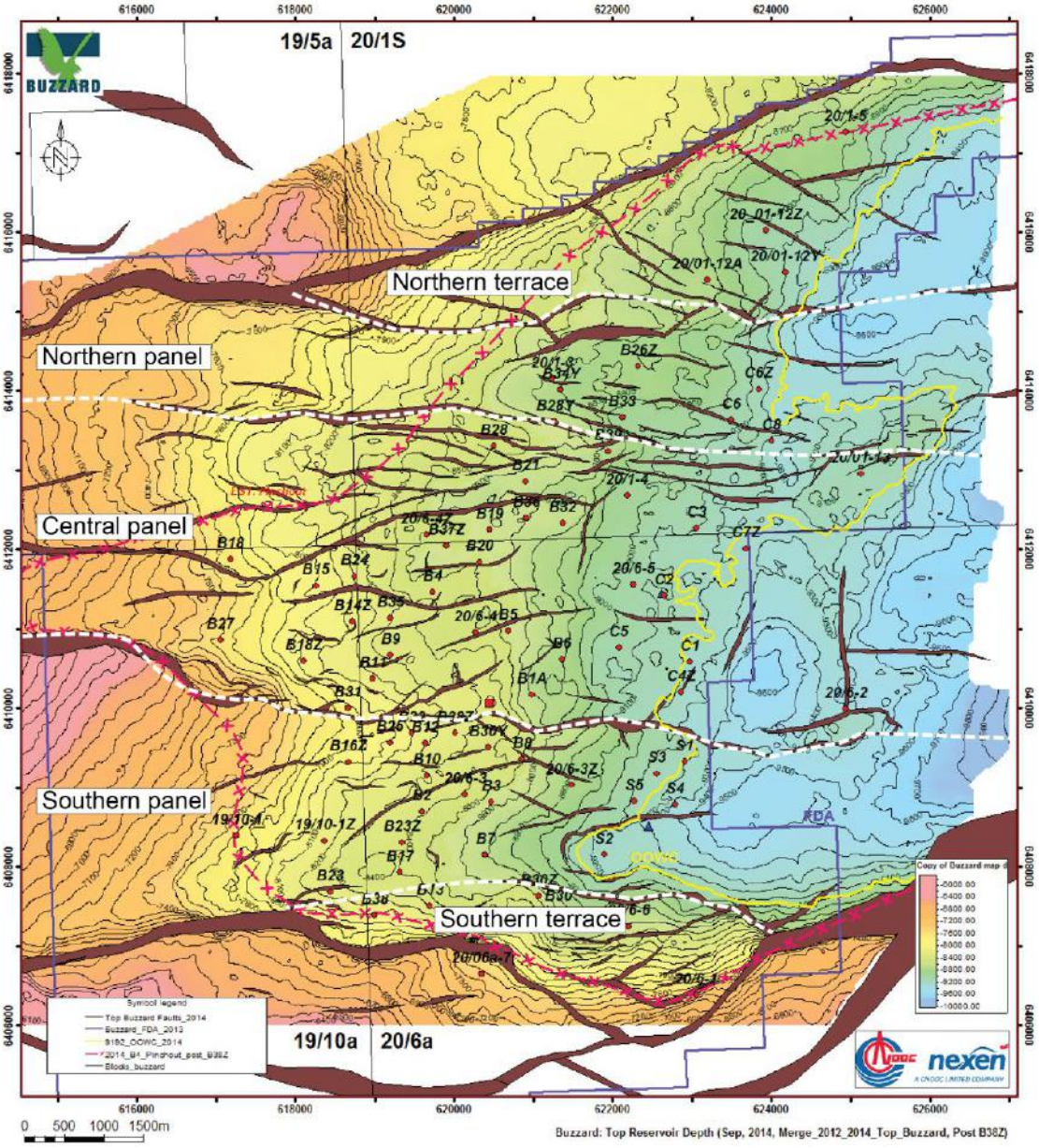

Figure 8.3. Depth map of Top Buzzard surface. The Buzzard Field is divided into five main depositional areas, separated by faults, believed to have formed topographic highs. CNOOC-Nexen in-house data.

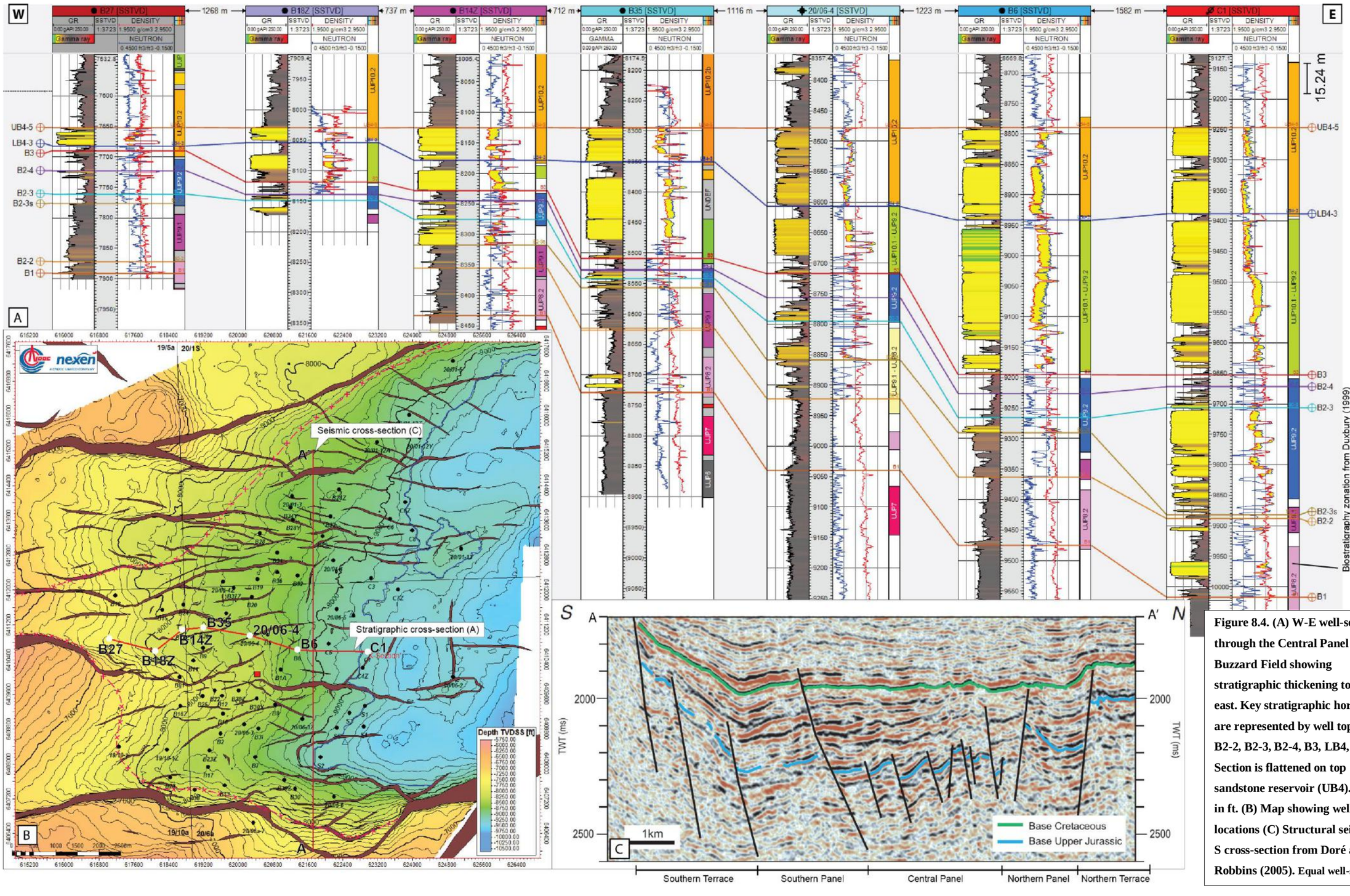

Figure 8.4. (A) W-E well-section through the Central Panel of the Buzzard Field showing stratigraphic thickening to the east. Key stratigraphic horizons are represented by well tops (B1, B2-2, B2-3, B2-4, B3, LB4, UB4). Section is flattened on top sandstone reservoir (UB4). Depth in ft. (B) Map showing well-section locations (C) Structural seismic N-S cross-section from Doré and Robbins (2005). Equal well-spacing.

A river or braid delta system is interpreted to have fed sediment in an eastwards direction into the Buzzard Graben. Sediment input into the deep-marine environment is interpreted as fed by a canyon system situated along a relatively high gradient bypass zone (Doré and Robbins, 2005). Sand provenance is interpreted as Permian and Triassic aged continental clastics eroded from the Grampian Spur hinterland to the west of the study area (Doré and Robbins, 2005) (Figure 1.19-B, Chapter 1). Reservoir sandstones of the Buzzard Field are mineralogically and texturally mature arenites with grain sizes that vary between very fine- to very coarse-sand, but with the fine- to medium-grained fraction predominating. The sand source is postulated to have been recycled in a shelf area to the east before forming sandy SGFs (Doré and Robbins, 2005, and in-house Nexen petrographic report). Sandstones were deposited from sandy SGFs in a structurally confined deep-water intra-slope to base-of-slope environment, and are interbedded with both *in situ* and remobilised mudstone units (interpreted as muddy MTDs and MTCs). The presence of widespread MTDs and MTCs suggests periodic instability of mudstones within the basin. These chaotic deposits are non-net reservoir, fine-grained clays and silts, sourced from margins prone to mass-wastage, such as the peripheral faulted north and southern margins (Ray *et al.*, 2010). A depositional model is shown in Figure 8.5.

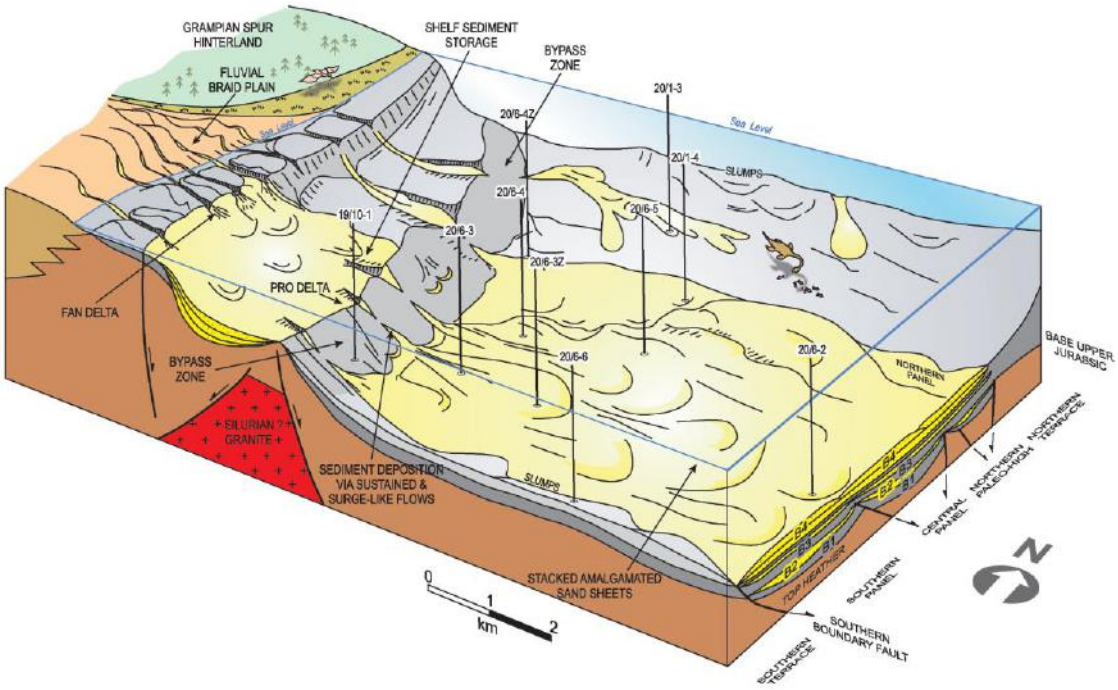

Figure 8.5. Buzzard Field depositional model. From Doré and Robbins (2005).

In mid-2003, the Buzzard Field Development Plan (FDP) divided the Buzzard Member in to five major units, first defined from well 20/06-3 (Ray *et al*., 2010). Three major sandstone units identified as the B2, LB4 and UB4 were deposited over ~ 5 Ma within a confined setting, related to the formation of east-west oriented basin-bounding faults (Figure 8.3). The oldest unit is defined as Buzzard 0 (B0), Buzzard 1 (B1), Buzzard 2 (B2), Buzzard 3 (B3), and Buzzard 4 (B4), which young upwards respectively (Figure 8.6).

- The B0 and B1 units represent a sequence of laterally extensive shales deposited directly upon the Heather Formation. Although the B0 interval is comprised of laminated mudstones, thin and uneconomic sandstone reservoirs do occasionally penetrate the B1 mud-dominated interval.

- The B2 unit contains lower sandstone reservoirs of the Buzzard Field. It comprises a laterally extensive heterolithic interval consisting of a series of interbedded shales and sandstones of variable reservoir quality. Based on lithology, the B2 unit is divided into 4 sub-units (B2-1 to B2-4), with the B2-2, B2-3 and B2-4 identified as reservoir units, estimated to contain ~ 5 – 10 % of overall Buzzard reserves. These lithostratigraphic units are identified in the C1 well (Figure 8.4). The base of the B2-3 sub-unit, interpreted to potentially contain channelised sandbodies, is defined by the presence of an MTC. Both the B2-3 reservoir and the MTC beneath the B2-3 reservoir have been mapped for the purpose of this this study (Figures 8.10 and 8.11, respectively).

- The B3 unit is shale-dominated, believed to be regionally extensive and dominantly comprises *in situ* mudstones acting as an impermeable barrier between the B2 and B4 sandstone reservoir intervals. This mudstone unit is interpreted from deposition from a sea-level highstand.

- B4 sandstones are interpreted as deposition from abrupt mass-failure of the marginal shallow-marine environment. Deposition of the B4 sandstones is likely to have occurred over a fairly short geological time period. Sandstone architecture is interpreted as compensationally stacked ‘lobe-like’ deposits with low-density turbidite silts and mudrocks draping the sands. The B4 unit comprises thick laterally extensive structureless sandstones, estimated to

contain up to 90 – 95 % of reserves in the Buzzard Field. The B4 sandstones are divided into two sub-units, named the LB4 and UB4 sandstones and are separated by the intra-B4 shale. The LB4 and UB4 sandstones typically further divided, primarily based on reservoir quality. For example, the LB4 unit contains a high permeability interval (> 20,000 mD permeability) and is captured as the LB4-2d sub-zone. The UB4 sandstone unit is also sub-divided as the UB4-4 and UB4-5 units. Two MTCs at the base of the UB4 unit are correlated and mapped for the purpose of this study, named the LB4 and UB4 MTCs, respectively (Figures 8.12 and 8.13).

The top of the Buzzard reservoir is marked by an abrupt change from thick, amalgamated sandstones into non-reservoir clays, identified as a widespread MTC. No gradual system abandonment is noted. This MTC has also been mapped for the purpose of this study (Figure 8.20).

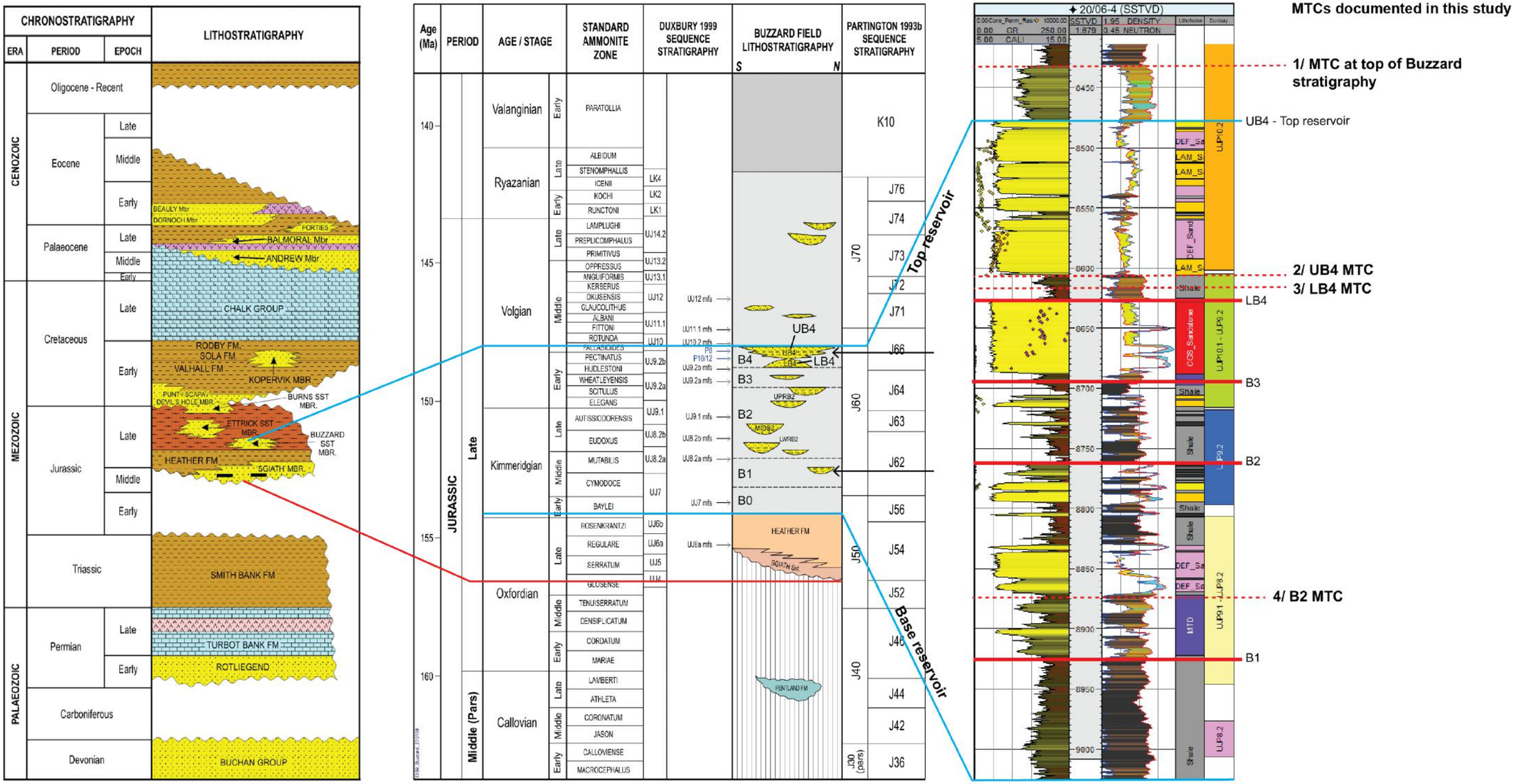

Figure 8.6. Stratigraphic model of Buzzard stratigraphy. The Palynological zones are shown as UJ9.2b-UJ10.1 (~147 Ma, Early Volgian) in the B4 unit, UJ9.2a-UJ9.2b (149 Ma, Early Volgian) in the B3 unit, UJ8.2a-UJ9.2a (152 Ma, Early Volgian) in the B2 unit, and UJ7-UJ8.2a (153 Ma, Mid Kimmeridgian) in the B1 unit. To the right shows the four MTCs documented in this study. Lithostratigraphic charts from Doré and Robbins (2005). CNOOC-Nexen in-house data.

8.2 MTDS AND MTCS IN THE BUZZARD FIELD

8.2.1 Core photographs

High-resolution core photographs were used to identify MTDs and MTCs from cored well intervals (Table 3.3, Chapter 3). Identifying individual MTDs within MTCs was undertaken with care, and although it is difficult to distinguish individual events in core, MTDs were identified by systematically noting the various facies changes, such as changes from Type Ia to Type IIa MTDs and/or vice versa, which are frequent facies attributes observed in the Guaso System, Ainsa Basin (discussed in Chapter 4). MTDs identified in core data from the Buzzard Field are comparable to those identified at outcrop in the Ainsa Basin (Figure 8.7).

Type Ia, Ib facies are typically identified as coherent, contorted laminated muddy sediments that show tilted and micro-faulted fractured mudstones along detachment surfaces. These facies generally show variations in dip-angles along basal shear surfaces and truncated units to suggest remobilisation. Plastic deformation is identified from the presence of coherent folds, whereas pervasive brittle microfaults that offset laminae identify brittle deformation (Figure 8.7-A). Low to moderate deformation of these sediments preserve the primary depositional structure and are interpreted as sediment slump/slide facies, analogous to Type Ia, Ib facies identified in the Ainsa Basin.

Type Ic facies are typically identified by pale-grey cemented rounded to sub-rounded carbonate blocks. These blocks show a very subtle parallel to sub-parallel bedding or lamination, up to 2 m, encased within structureless dark-grey mudstones. The carbonate blocks show calcite veining of random orientation throughout (veins fizz when in contact with dilute HCl) and terminate at the outer margins of the blocks. The origin of these blocks is currently unknown; they could be interpreted as intrabasinal concretions that were remobilised during failure of mudstones, or extrabasinal limestones that were remobilised during failure of mudstones. These MTD facies are unique to the B2 unit (Figure 8.7-B).

Figure 8.7-A. MTD facies in Buzzard core comparable to those identified at outcrop in the Ainsa Basin: Type Ia, b MTDs. Different dip angles are dashed in a white line suggesting mass movement within fine-grained mudstones. CNOOC-Nexen in-house data.

Figure 8.7-B. MTD facies in Buzzard core comparable to those identified at outcrop in the Ainsa Basin: Type Ic MTD. Carbonate blocks typically observed in homogenous to slumped fine-grained mudstones – base of carbonate block marked by white dashed line. CNOOC-Nexen in-house data.

Figure 8.7-C. MTD facies in Buzzard core comparable to those identified at outcrop in the Ainsa Basin: Type IIa MTD. Homogeneous mudstone (debrite) containing rounded carbonate blocks. A white dashed line defines the base of the debrite. CNOOC-Nexen in-house data.

Figure 8.7-D. MTD facies in Buzzard core comparable to those identified at outcrop in the Ainsa Basin: Type IId MTD 'starry night' facies. No grading is observed. Top and base of MTDs are marked by white dashed lines. CNOOC-Nexen in-house data.

Type IIa facies are typically identified by observing structureless, mudstones (Figure 8.7-C). Primary depositional structures are not observed in core suggesting abundant reworking. These facies are dominated by mudstones, containing < 20 % sand in the matrix, and can also show fragmented and disarticulated shelly fragments, including nummulites, belemnites and bivalves. Rarely, 'starry-night' facies (i.e., chaotic mudstone) are observed in Buzzard core data, however core photographs do not reveal any deposits with sand contents greater than 20 %. The fabric of the matrix is typically well-mixed to patchy, analogous to Type II deposits (Groups 1 and 3), as observed in the Ainsa Basin. Cobble, pebble and boulder-sized fractions, such as Type IIb and Type IIIa, b deposits documented in the Ainsa Basin, are not typically found in MTDs identified in core data of the Buzzard Field, however a rare example is shown in Figure 8.8.

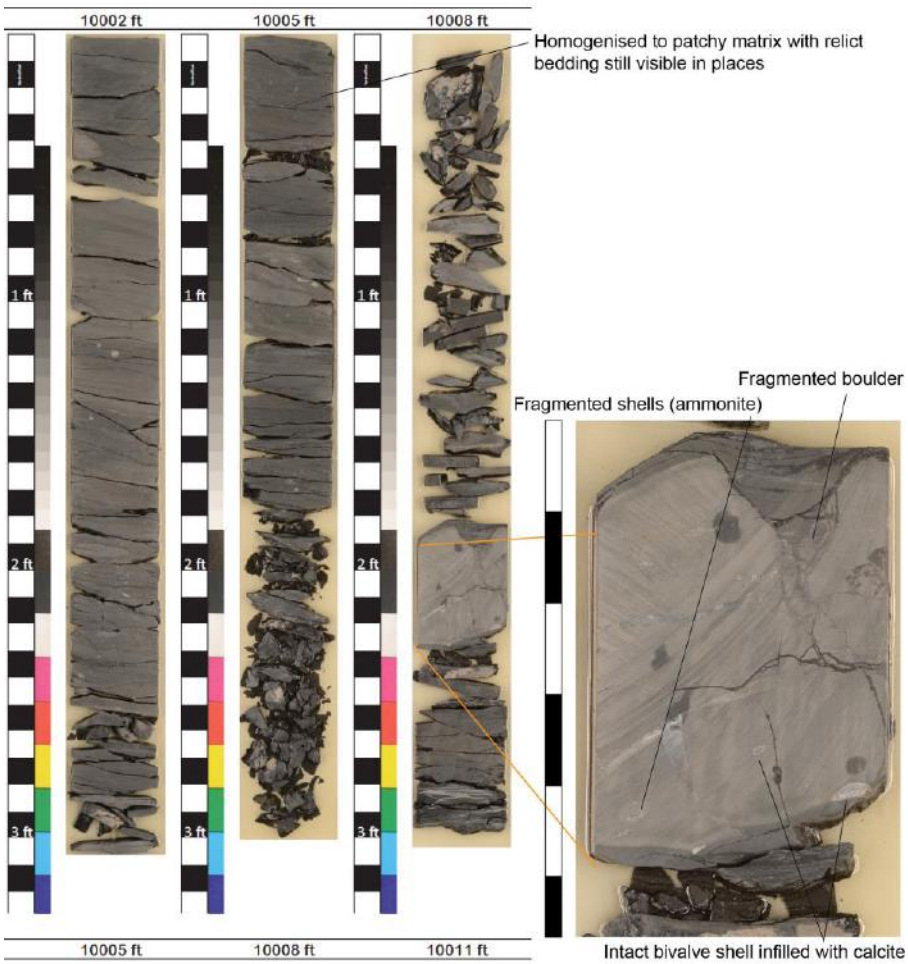

Figure 8.8. Boulder interpreted as incorporated within a MTC. Bivalve and ammonite fragments found within a boulder. CNOOC-Nexen in-house data.

A sub-rounded, fragmented fine-grained and pale-grey clast (~ 20 cm in height) appears to be within the process of disaggregation. These mud-rich deposits are likely to be sourced from unconsolidated mud-dominated environments such as a 'soupy' seafloor or slope deposits.

8.2.2 MTD frequency analysis

MTDs were identified from high-resolution photographs of cored wells in the B2, LB4 and UB4 units. To avoid overcomplicating depositional processes with associated deposits, MTDs are documented as either Type Ia MTDs, if they exhibited steep or irregular coherent laminations within mudstone facies, or as Type IIa MTDs if mudstones were chaotic or homogenised. This dataset is limited as MTD-type is highly dependent on which intervals were cored at each location. It is, however, the only data available to determine detailed bed-by-bed sedimentary-scale information of MTDs. MTD count analysis from core images are shown in Figure 8.9.

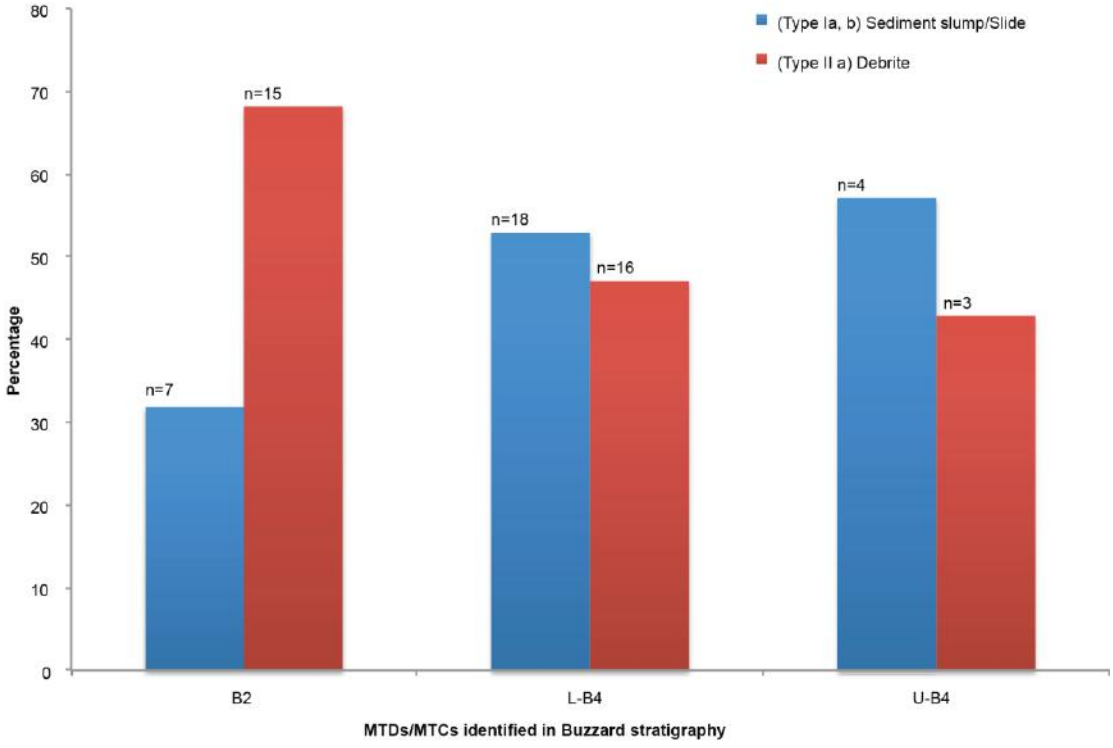

Figure 8.9. Graph shows percentage of MTD types identified from core data. n=x shows number of MTDs counted in core.

The B2 MTDs (documented immediately beneath the B2-3 sandstone reservoir unit) shows a higher percentage of Type IIa facies relative to Type Ia MTDs found in core (15 vs. 7, respectively). The younger LB4 and UB4 MTDs show similar abundances of Type IIa and Type Ia MTDs, however Type Ia MTDs are more abundant in both units.

8.2.3 MTD distribution

A broader data collection away from the cored wells required interpretation of wireline data. The presence and distribution of MTDs basin-wide, is then determined, as opposed to being constrained to the cored wells, which enables the bed-scale of MTD type to be interpreted in the subsurface. Although this type of data analysis loses sedimentary detail, 2-D models can be created to determine gross overall geometries of MTDs, not possible to do at outcrop due to a lack of down-dip exposure (for example, in the Ainsa Basin).

As presented in Chapter 5, MTD thickness is typically measured as very thin (< 1 m) to thin-bedded (1 to 2 m) and rarely MTDs are measured as very-thick (> 10 m). It is therefore likely that data captured at such a coarse resolution, as on wireline data, will be greater than a single event (i.e., an MTC). Sedimentological interpretation away from the cored sections can be problematic, particularly in deep-marine environments where bed thicknesses can change rapidly over short distances. To overcome this uncertainty, dip data and gamma ray logs were also used to help identify MTCs in the Buzzard Field.

Using Petrel 2013 (version 12), the tops and bases of MTCs and sandstone packages in the B2, LB4 and UB4 units were identified and correlated across Buzzard using well tops. Gamma ray and neutron-density curves were used to identify MTC and sandstone facies. Biostratigraphic data guided interpretations, which typically showed mixed aged zones to suggest remobilistion. To correlate the MTCs, all 65 wells were interpreted to ensure maximum control for gridding purposes. The intervals between the top and base of each unit were zoned, and using the make/edit surface function, were gridded using the convergent interpolation algorithm to

produce 2-D distribution maps in true vertical thickness (TVT) (Figures 8.10, 8.11 and 8.12).

8.2.3.1 B2 MTC distribution

The B2 MTC is deposited immediately below the B2-3 sandstone, located predominantly in the Central Panel (Figure 8.10). The B2 MTC shows a strong west to east orientation, forming a linear tongue-like shape ~ 5 km in length and up to 1.8 km in width. A west-to-east dip-line was taken through the centre of the MTC to capture the variation in stratigraphic thickness (Figure 8.10-A). The minimum and maximum thicknesses are measured from < 3 to 27.4 m (< 10 to ~ 90 ft), furthest west (B27) to furthest east (C4Z), respectively. The MTC thickness in wells B11, B9, 20/06-4 and C5 is observed to be approximately consistent (12 – 14 m [~ 40 to 45 ft]). The gamma log character of the MTC is variable, from ~ 80 to 200 API, however values predominately lie between 80 – 100 API to suggest a silty- to muddy character. The variable gamma character within this unit suggests a complex comprised of multiple events. The presence of potentially discontinuous sandstones within the MTC supports this interpretation (Figure 8.10).

8.2.3.2 B2-3 sandstone distribution

The B2-3 sandstone is deposited immediately above the B2 MTC (Figure 8.11). When correlating this sandstone unit, the B2-3 sands were packaged into sands of the same biostratigraphic age, which also show a similar gamma log character, i.e., have a blocky, low gamma ray response, typically showing greater than one event, bounded by thin shale units (identified by high gamma units). The distribution map shows that sandstone thickness varies from < 3 to 15 m (< 10 to ~ 50 ft) which generally thickens to the east, down-dip from the source area. The thickest sandstones were deposited in the B1A and C1 wells, suggests a ‘channel-like’ geometry down-dip from B18-Z to B1A, before showing a broader geometry from the east of the C5 well.

8.2.3.3 LB4 and UB4 MTC distribution

The LB4 and UB4 sandstones form the main reservoir units in the Buzzard Field are separated by the LB4 and UB4 MTCs (Figure 8.6). The LB4 and UB4 MTCs are typically separated by a sandstone unit up to ~ 7.5 m (25 ft) in thickness, observed in wells 19/10-1Z, B3i and S1, which appears non-continuous across the field (Figure 8.12-A). The LB4 MTC is logged up to 9 m (30 ft) in thickness. The 2-D plan geometry of this MTC is not well defined, but shows a broad west-to-east to a northwest distribution and appears across the entire field (Figure 8.12-B).

The UB4 MTC is interpreted to have a slightly lower, potentially siltier, gamma response compared to the LB4 MTC. The distribution map of the UB4 MTC shows a strong west-to-east orientation that is ~ 4 km in length, is approximately 1.3 km in width and is dominantly located in the Southern Panel (Figure 8.12-C). The UB4 MTC shows greatest thickness in the west, nearest to the base-of-slope in B23Z, logged up to 33.5 m (110 ft). However, a comparative MTC thickness is documented 3750 m to the east in S5 suggesting a fairly consistent thickness. The terminal margins of the MTC appear as relatively sharp, shown by the absence of this deposit in 20/06-3, up to 542 m from the main deposit.

8.2.3.4 B4 sandstone distribution

The UB4 sandstones (deposited immediately above the UB4 MTC, Figure 8.6) are the thickest and most laterally continuous sandstones across the Buzzard Field (Figure 8.13). Sandstone thickness varies between 3 and 45.7 m (< 10 to 150 ft), with thick sandstones suggesting highly amalgamated stacked sand successions. The sandstone distribution map may suggest a more northeast trend (palaeoflow towards the northeast Figure 8.13), compared to the B2 sandstones (palaeoflow towards the east, Figure 8.13).

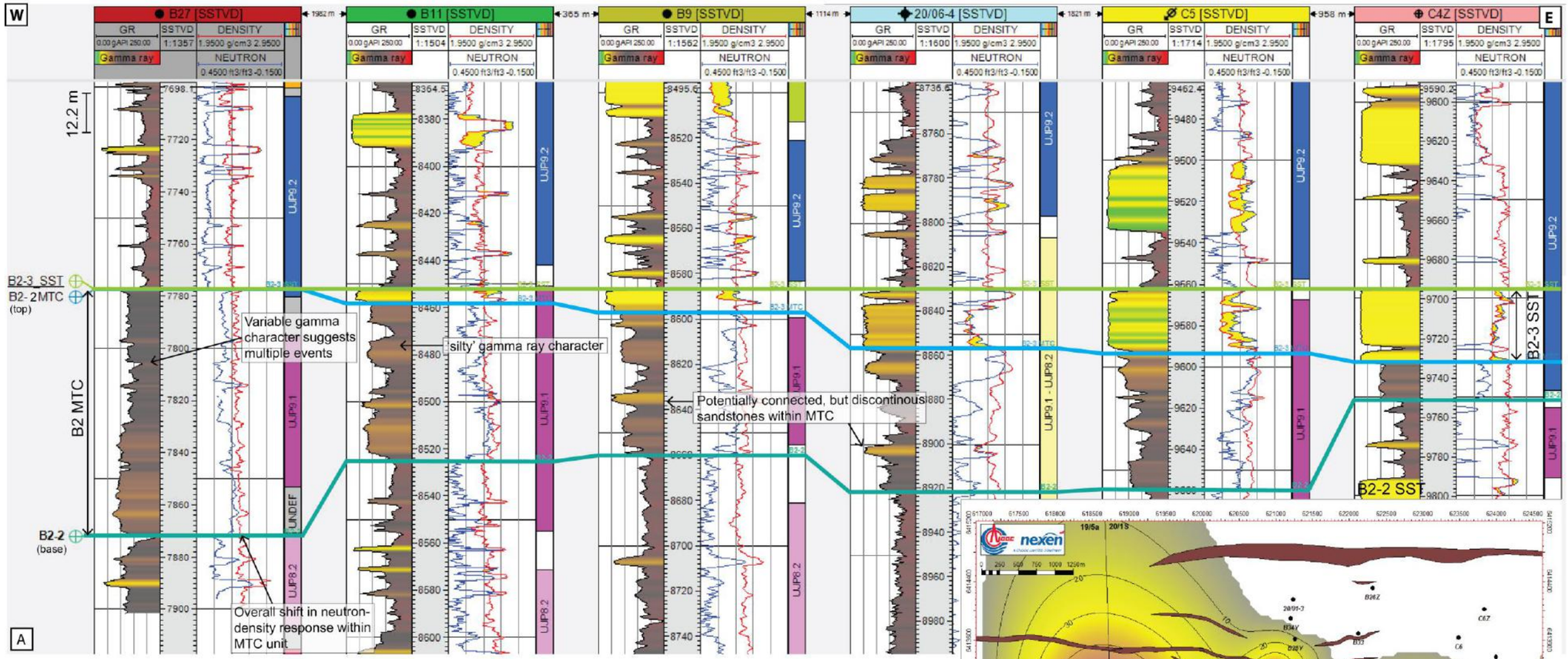

B2 MTD well-section and distribution map

Figure 8.10. (A) West to east well-section through the southern part of the Central Panel in the Buzzard Field. Well tops are flattened on B2-3 sandstone. Well-section location shown in Figure B (B) Thickness map of B2 MTC Unit shows true vertical thickness (TVT) in ft. CNOOC-Nexen in-house data. Equal well-spacing.

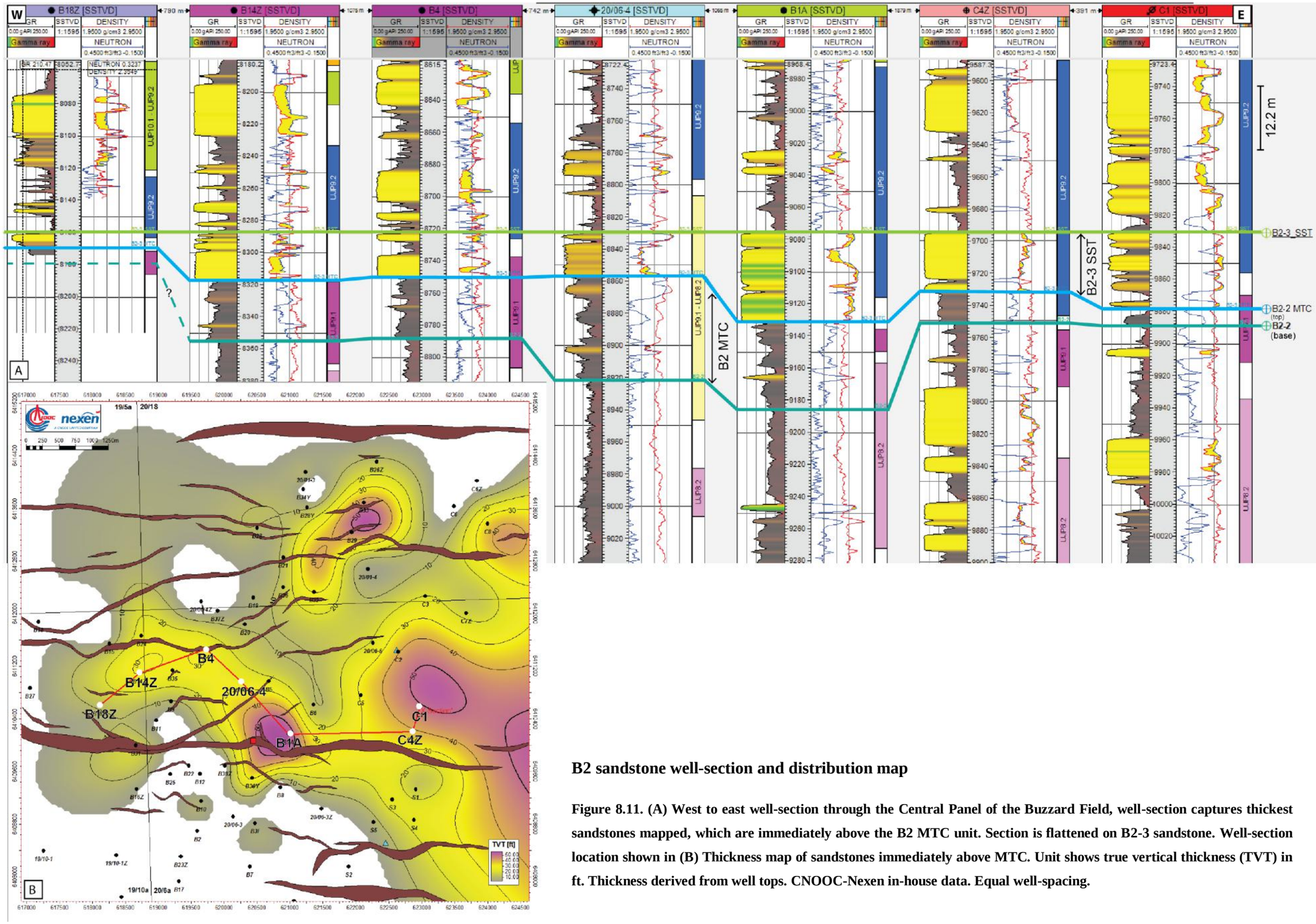

B2 sandstone well-section and distribution map

Figure 8.11. (A) West to east well-section through the Central Panel of the Buzzard Field, well-section captures thickest sandstones mapped, which are immediately above the B2 MTC unit. Section is flattened on B2-3 sandstone. Well-section location shown in (B) Thickness map of sandstones immediately above MTC. Unit shows true vertical thickness (TVT) in ft. Thickness derived from well tops. CNOOC-Nexen in-house data. Equal well-spacing.

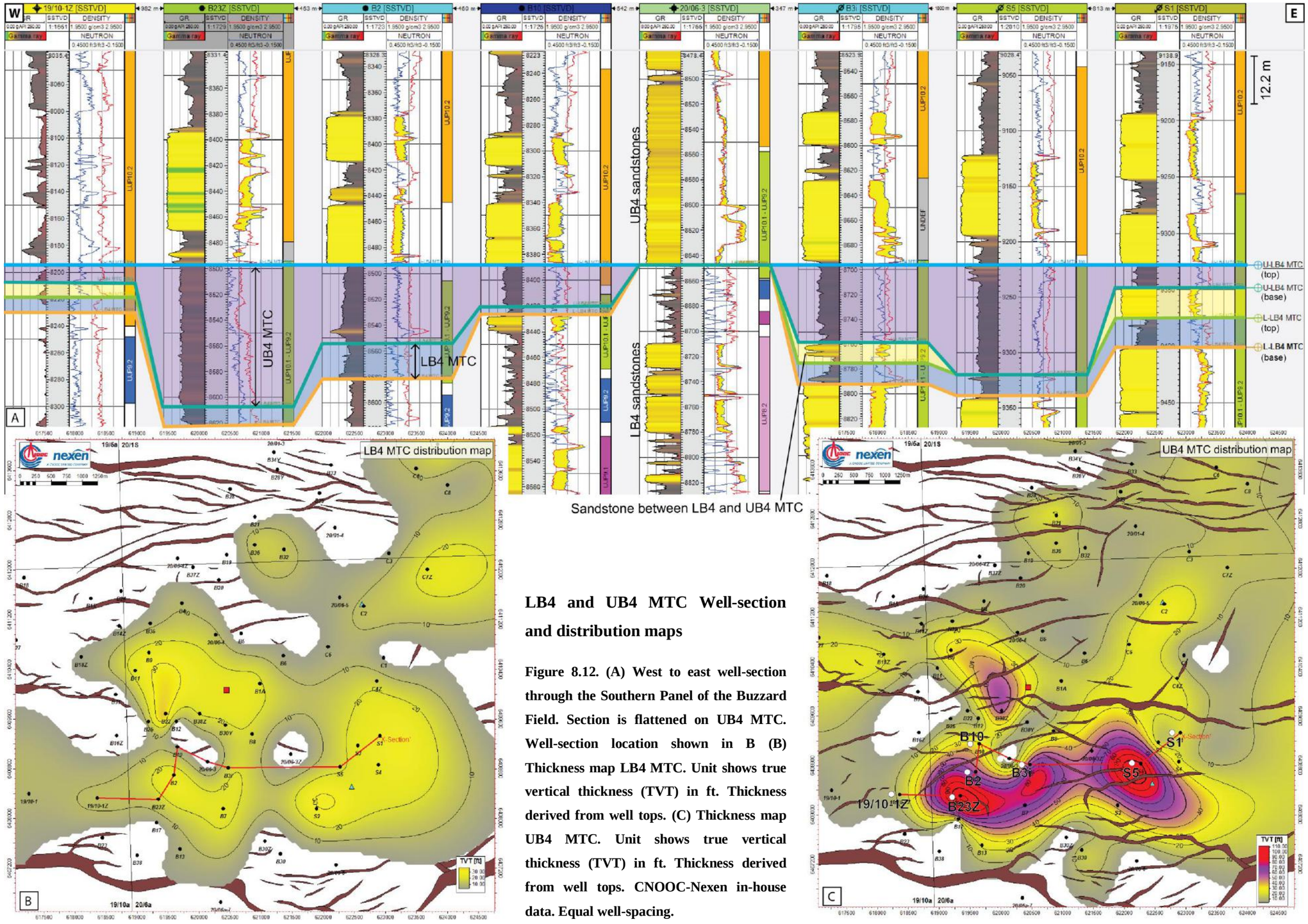

LB4 and UB4 MTC Well-section and distribution maps

Figure 8.12. (A) West to east well-section through the Southern Panel of the Buzzard Field. Section is flattened on UB4 MTC. Well-section location shown in B (B) Thickness map LB4 MTC. Unit shows true vertical thickness (TVT) in ft. Thickness derived from well tops. (C) Thickness map UB4 MTC. Unit shows true vertical thickness (TVT) in ft. Thickness derived from well tops. CNOOC-Nexen in-house data. Equal well-spacing.

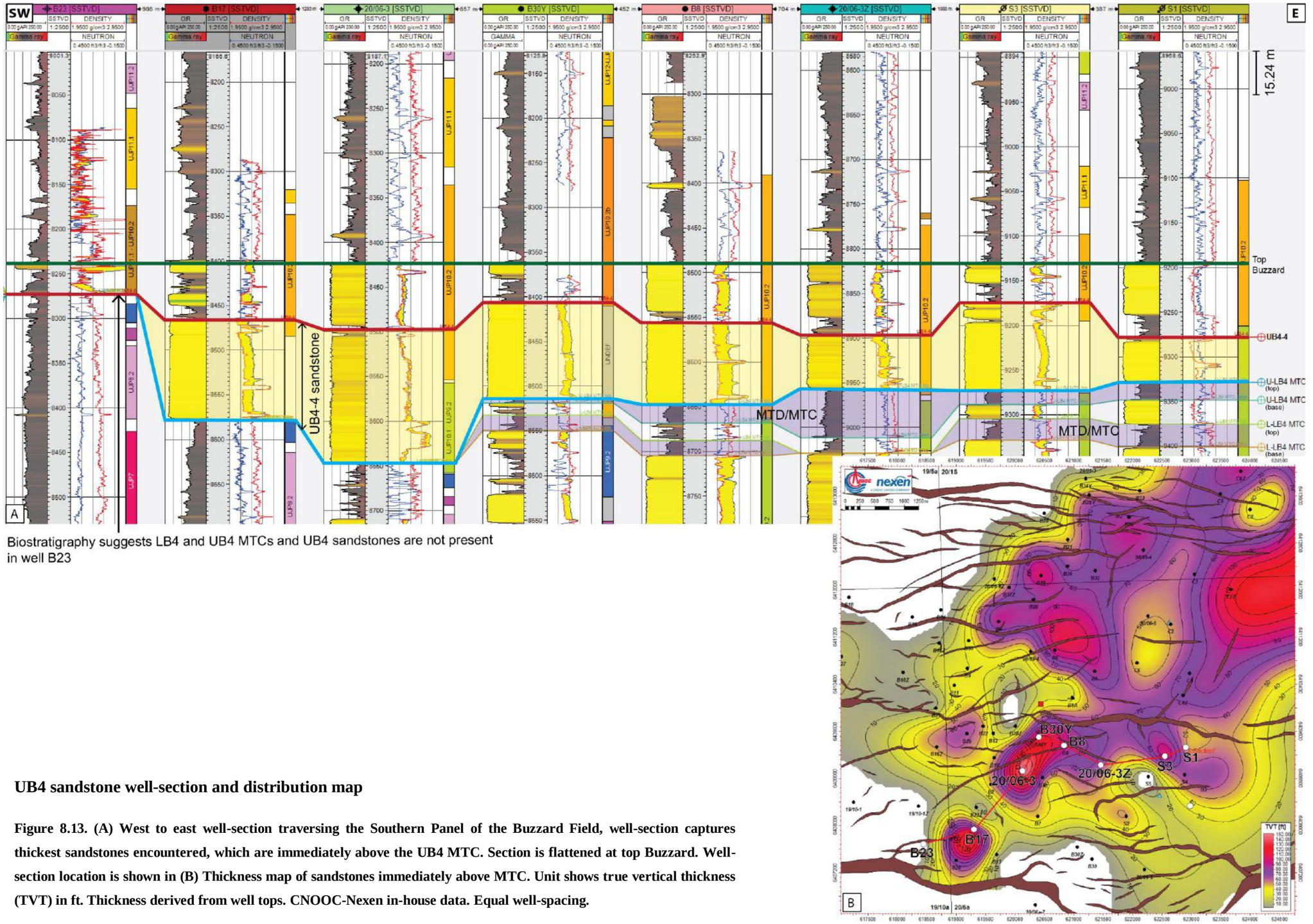

Biostratigraphy suggests LB4 and UB4 MTCs and UB4 sandstones are not present in well B23

UB4 sandstone well-section and distribution map

Figure 8.13. (A) West to east well-section traversing the Southern Panel of the Buzzard Field, well-section captures thickest sandstones encountered, which are immediately above the UB4 MTC. Section is flattened at top Buzzard. Well-section location is shown in (B) Thickness map of sandstones immediately above MTC. Unit shows true vertical thickness (TVT) in ft. Thickness derived from well tops. CNOOC-Nexen in-house data. Equal well-spacing.

8.2.4 Channelised sandstone geometry in MTC

The B4 Formation is comprised of two major sandstones units (LB4 and UB4 sandstones, Figure 8.6). The southern panel shows a complex interplay between the LB4 and UB4 MTCs and the overlying UB4 sandstone, mapped as northeast-trending deposits (Figures 8.12 and 8.13). A well-section of the southern panel shows the gross geometry of the B4 unit, where the LB4 sandstones are observed to erode into a lower MTC (Figure 8.14-A).

The lower MTC shows a varying gamma log character and contains non-continuous sandstones, and is therefore interpreted as multiple MTDs. The U-B4-4 sandstone is observed to potentially erode ~ 20 m (70 ft) into the MTC forming a channelised geometry (modelled in Figure 8.14-B and C). Similar isolated channelised sandstone bodies are observed to erode into MTDs in the Ainsa Basin, interpreted as erosion from large-scale sandy flows (*cf.* Elliott, 2000; Chapter 4, Figures 4.18 and 4.19).

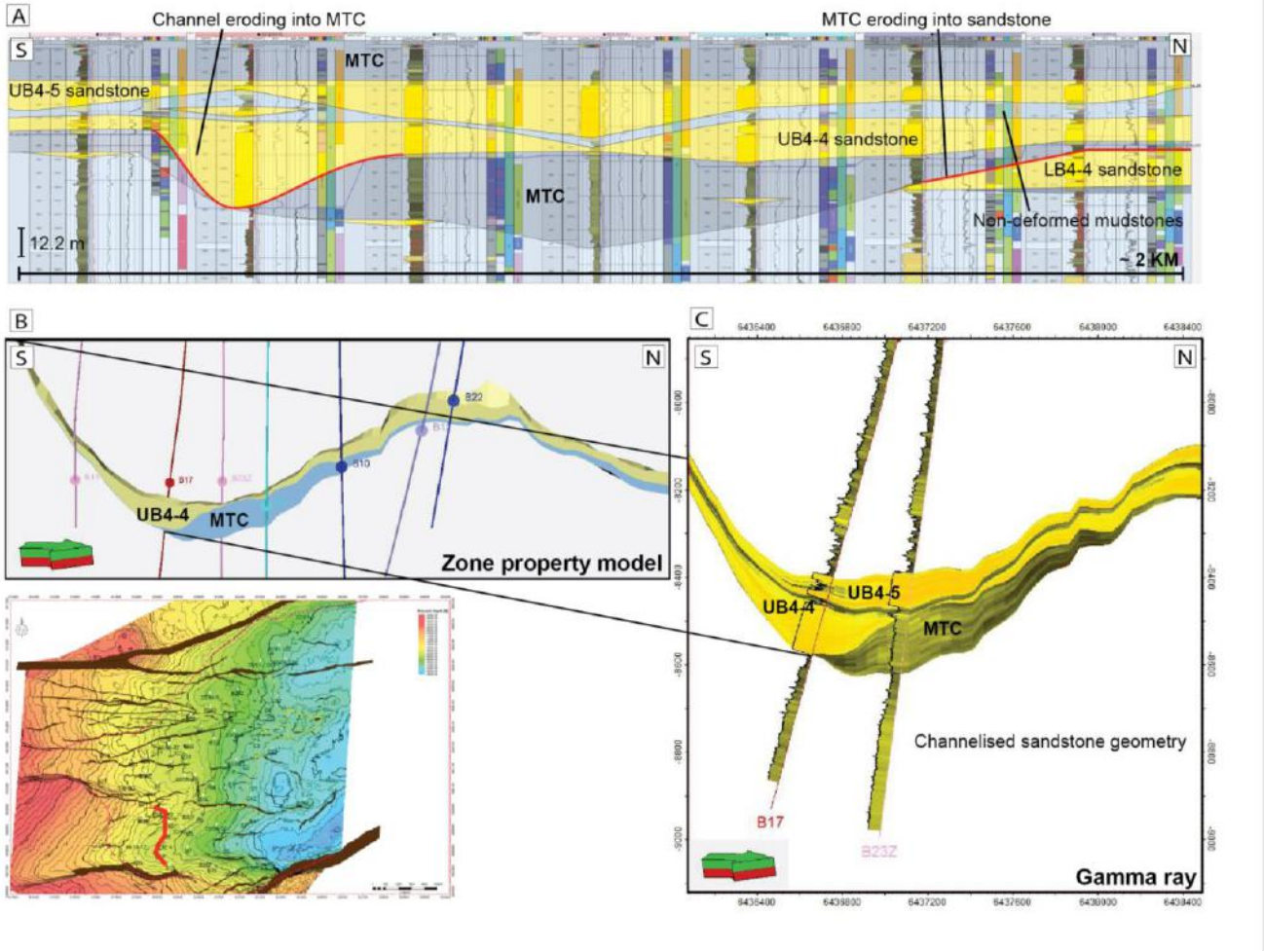

Figure 8.14. (A) Interpretation of MTC and sandstone geometry of the LB4 and UB4 reservoir intervals, southern panel. (B) CNOOC-Nexen in-house data.

8.2.5 Comparison of MTC thickness in proximal *versus* distal settings

To determine the average MTC thickness away from the base of slope, an arbitrary line was drawn to separate 'proximal' and 'distal' areas (Figure 8.15).

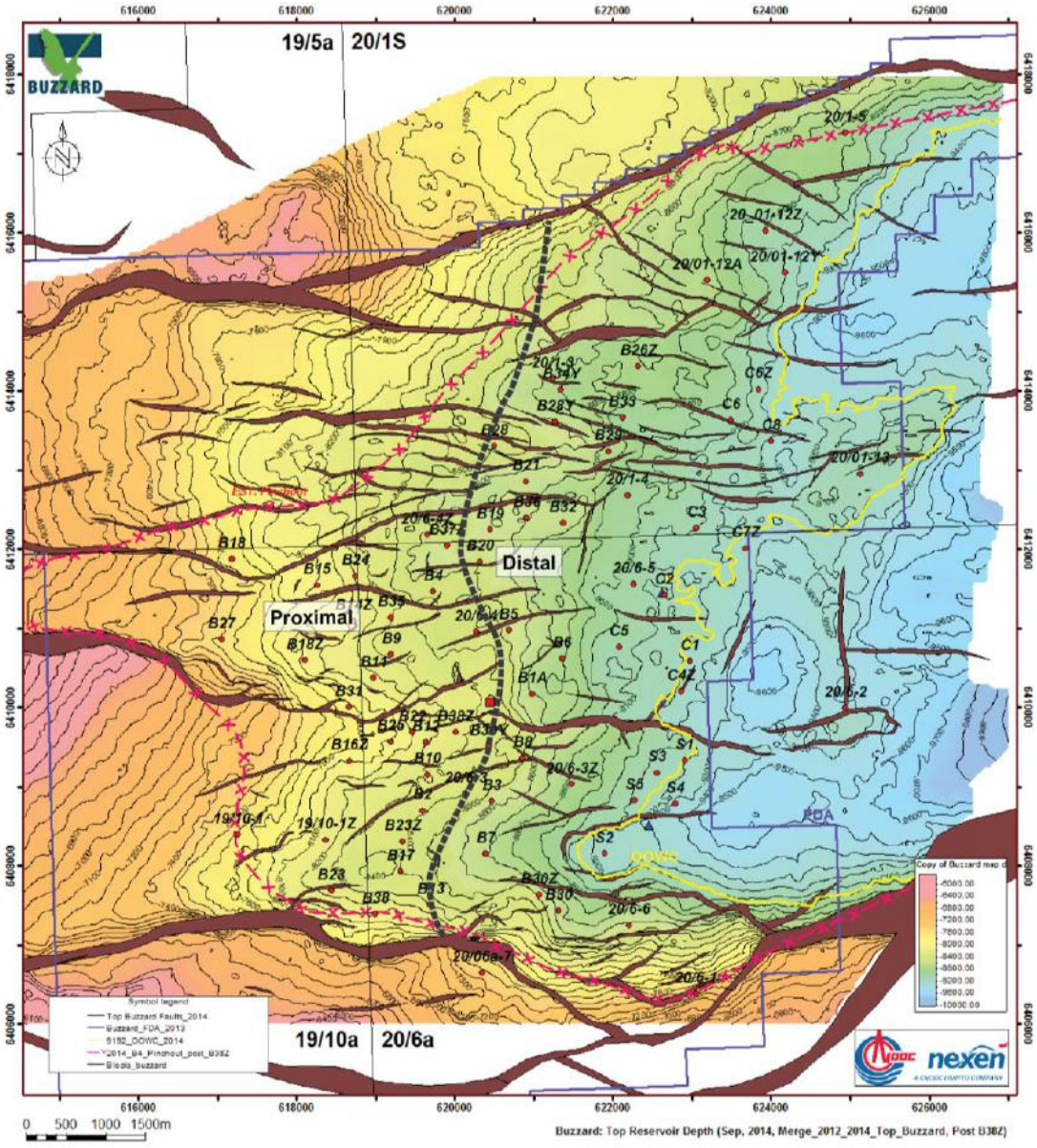

Figure 8.15. Map of Buzzard Field, approximately divided into 'proximal' and 'distal' settings. CNOOC-Nexen in-house data.

The average thickness of MTCs in proximal and distal settings in Buzzard and Ainsa are compared (Figure 8.16).

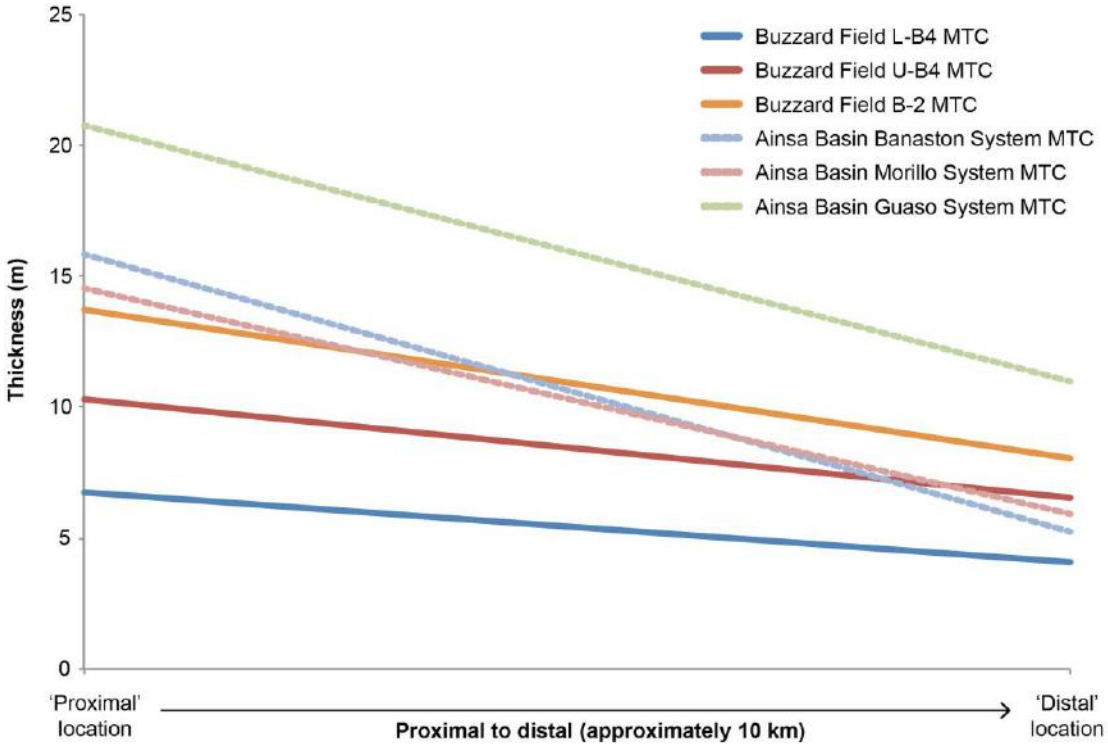

Figure 8.16. Graph shows average thickness of MTCs in the Buzzard and Ainsa basins. Buzzard MTCs were interpreted from well data. Top and base picks were interpreted and zone logs made in Petrel to determine TVT. Ainsa MTCs were logged from stacked MTD events in the field.

MTCs (multiple stacked events) found proximally and distally in both the Ainsa and Buzzard basins show an analogous trend; average MTC thickness decreases downdip. Proximal MTCs in the Ainsa Basin are thicker (21, 16 and 14.5 m in the Guaso, Banastón and Morillo systems, respectively), compared to MTCs located in proximal settings defined in the Buzzard Field (13, 10.5 and 7 m in B2, UB4 and LB4 MTCs, respectively). MTCs in both the Ainsa and Buzzard basins pinch-out between 5 to 14 m down-dip. This data suggests event magnitudes are comparable in basins of similar sizes. The gradient between the thickness of proximal and distal MTCs is greater in the Ainsa Basin compared to the Buzzard Field. Type Ia MTDs are observed as the dominant chaotic facies in the Ainsa Basin, measured as the thickest deposits in proximal locations. The change in gradient at the base-of-slope may have also been greater in the Ainsa Basin, causing flows to freeze closer to the base of slope.

8.2.6 Basal erosion in core data

Results from the thin-section study on Type IIa MTDs (Chapter 7) suggested grain-size and compositional grading were likely to occur in deposits that were erosive prior to deposition. In the Ainsa Basin, erosively-based Type IIa MTDs contained up to 50 % grains (Figure 6.2-A, Chapter 6). The next step is to see how these observations can be translated into the limited subsurface core data.

By analysing core photographs it is possible to see that Type IIa MTDs (containing greater than ~ 20 % sand grains) are typically infrequent within Buzzard core. In the Ainsa Basin, Type IIa MTDs were documented as having up to 50 % grains (Figure 6.2, Chapter 6). Sand-rich and 'graded' muddy deposits are not generally observed in Buzzard core, therefore MTDs that show basal erosion will not be easily answered within the scope of this project. However an example of potential features to look for are presented. In the Buzzard Field, Type IIa MTDs comprising a sand-rich matrix are observed as thin deposits (< 1 m), showing a patchy to well-mixed fabric up to 0.5 m maximum thickness (e.g., Figure 8.8-D). A very thin Type IIa deposit showing an irregular basal surface is immediately above a sandstone bed at ~ 2846 m (9339 ft) in the B1A well (Figure 8.17).

As documented from outcrops in the Ainsa Basin, Type IIa MTDs that show an irregular basal surface typically show interaction and erosion with the underlying sandy substrate. The Type IIa facies at the base of the MTC shows angular sandstone clasts (5.5 cm width) that appear to 'float' within the deposit. From the limited 2-D window from core data such as this, it is not possible to determine the potential erosive mechanism of this MTD, i.e., ploughing, plucking, shouldering aside, bull-dozing, as identified from outcrops in the Ainsa Basin. This particular example is also not sufficiently thick enough to sample from base-to-top, as carried out in the field.

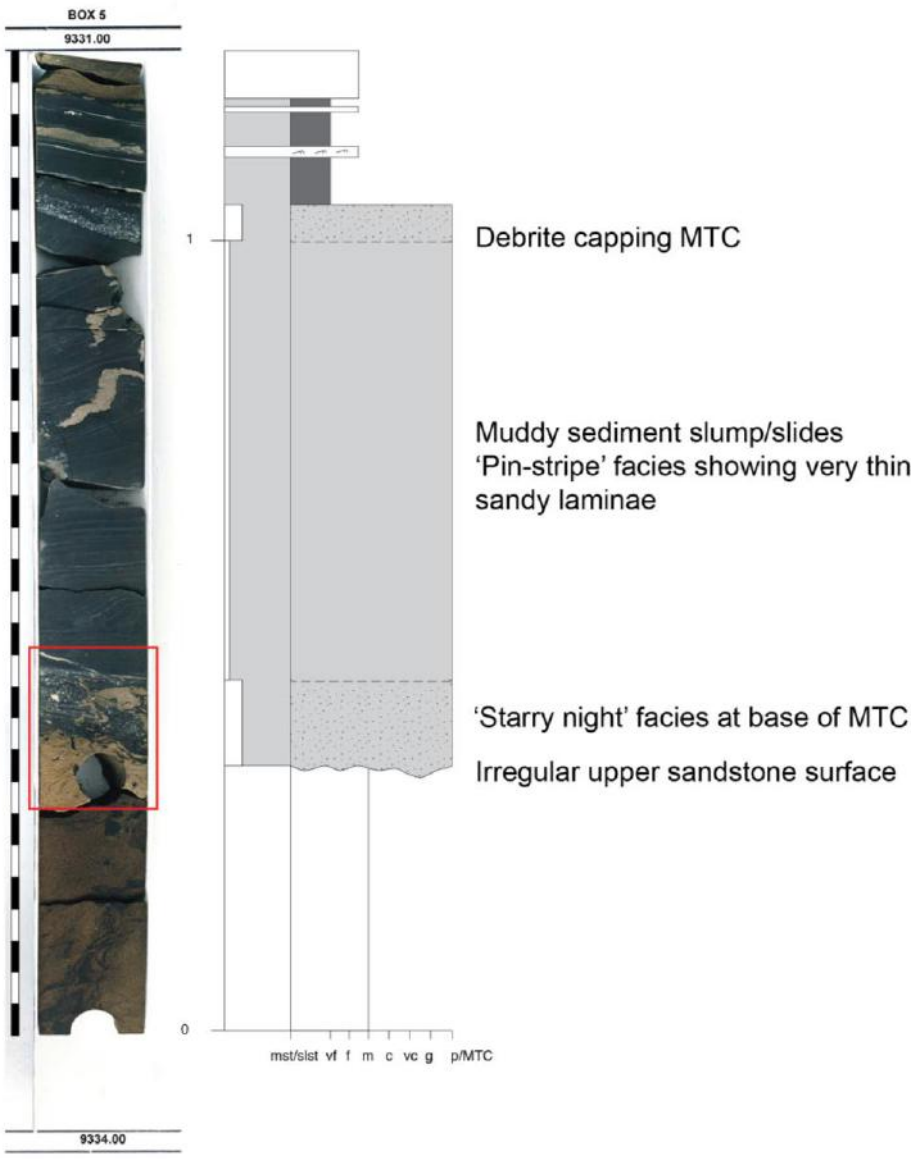

Figure 8.17. To the left, core data showing 'starry night' facies at base of MTC showing potential erosion into lower sandstone (black and white scale is divided into 3 inch segments). To the right, log interpretation of MTC (scale is in inches). CNOOC-Nexen in-house data.

8.2.7 Abrupt sandstone deposition

The UB4 unit forms the ultimate reservoir sandstones deposited in the Buzzard Field (Figure 8.6). Sandstones in this unit are coarse- to very coarse-grained and typically do show not show grading. The B28-Y well is the only well in the Buzzard Field that has cored top Buzzard stratigraphy and the antecedent overburden. Immediately above the UB4 sandstones, remobilised mudstones are present. A Type IIa MTD

immediately above the UB4 sandstone in B28-Y shows a well-mixed fine- to medium grained sand-rich matrix that has an irregular basal surface. Incorporation of sandy material into the matrix could suggest truncation of the upper sandstone (Figure 8.18).

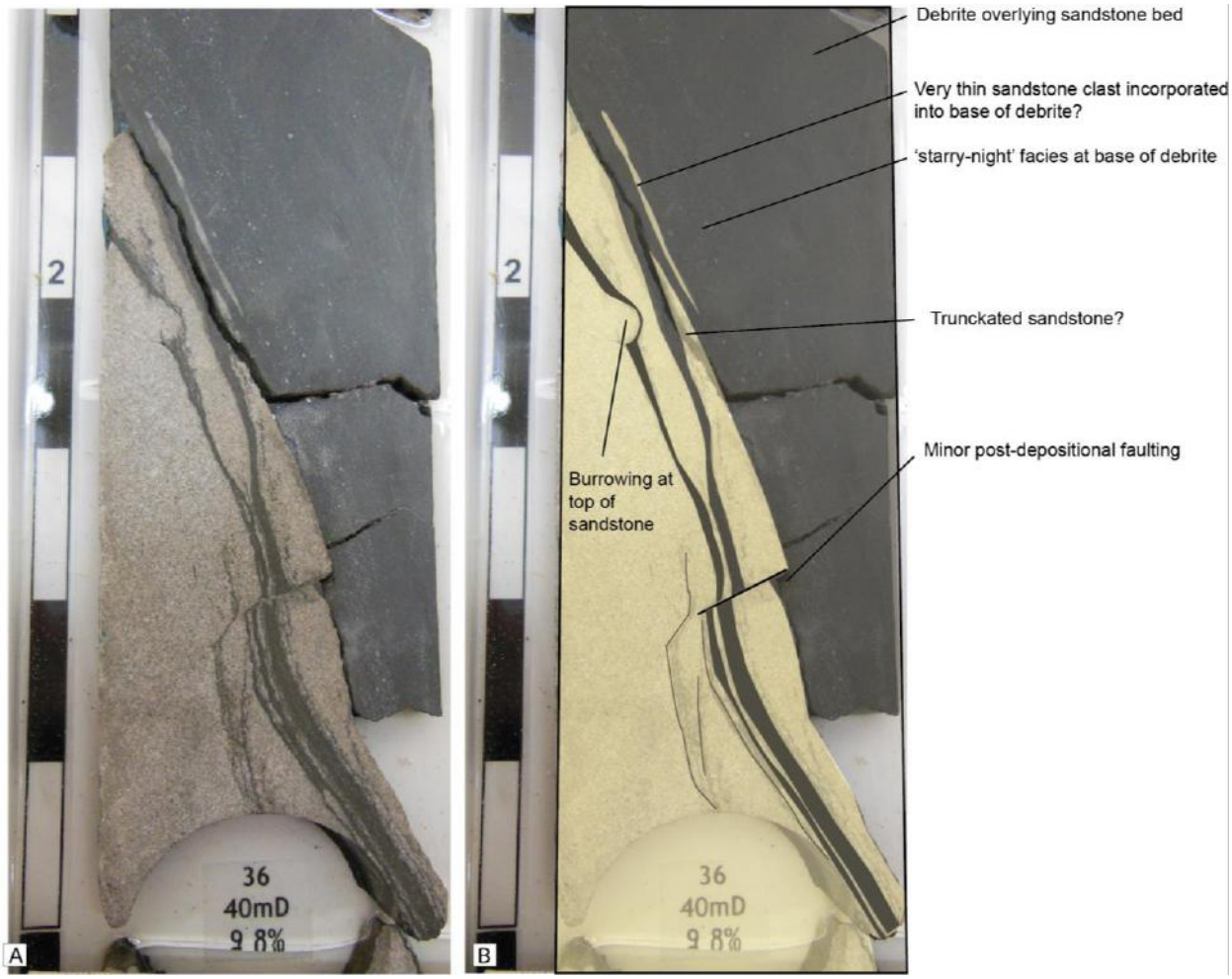

Figure 8.18. (A) Photo of top Buzzard sandstone immediately under ultimate debrite at the top of the Buzzard stratigraphy (B) Photo interpretation showing starry-night facies and truncated sandstone at the top of the sandstone. CNOOC-Nexen in-house data.

A full interpretation of the MTC immediately above the Buzzard B4 reservoir in the B-28Y well is shown in Figure 8.19.

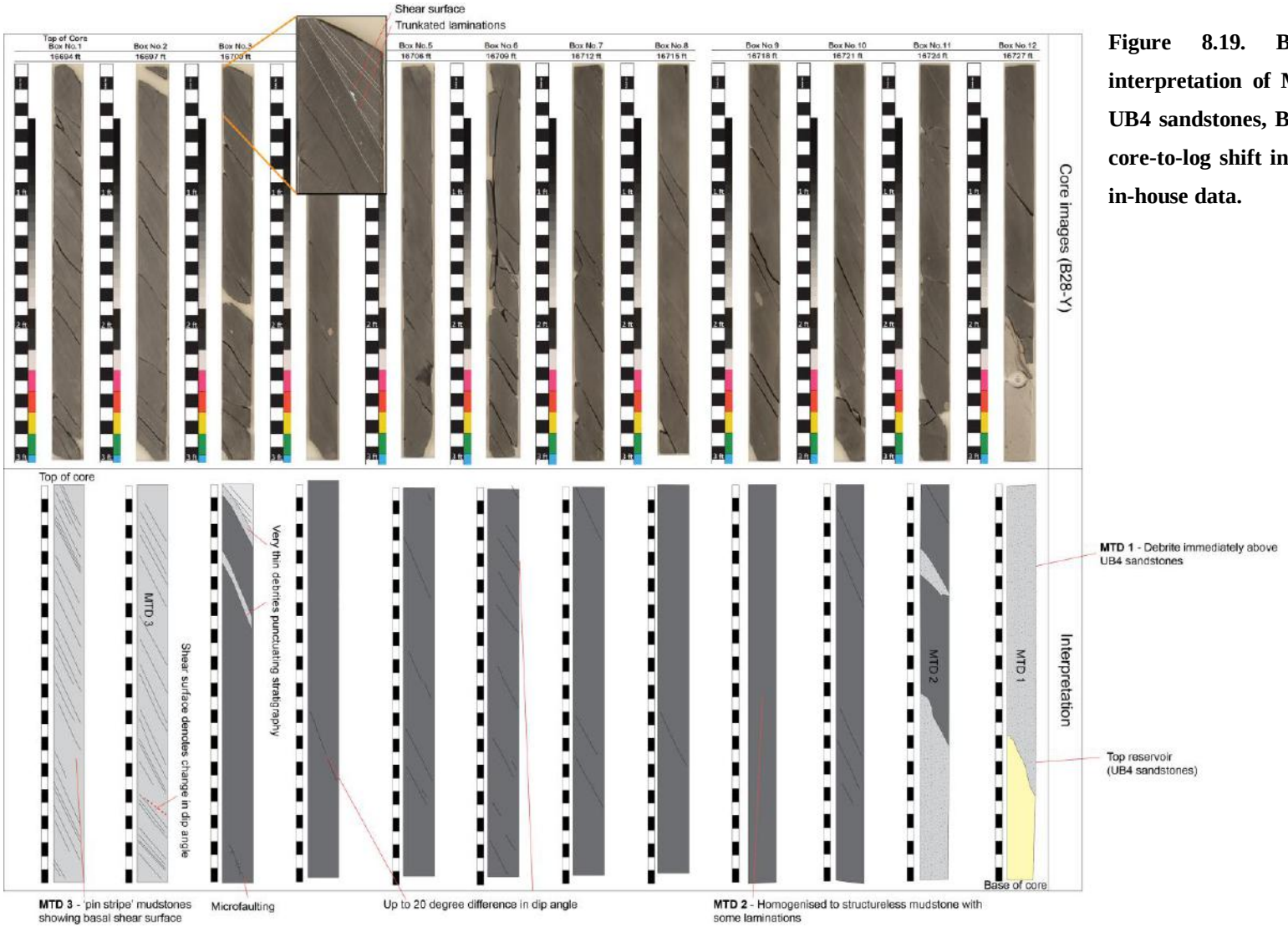

Figure 8.19. B28-Y core photos and interpretation of MTC immediately above the UB4 sandstones, Buzzard Field. 0.76 m (2.5 ft) core-to-log shift in B28-Y well. CNOOC-Nexen in-house data.

Immediately above the UB4 sandstones, a 1 m Type IIa MTD is present and is overlain by 11 m of fine-grained homogenised to laminated mudstones, before termination at the top of the core barrel (at 5088 m [16694 ft]). The laminated mudstones show up to 20˚ variation in dip. Occasional micro-faulting is observed within the laminated mudstones to suggest remobilisation, and is therefore interpreted as a Type Ia MTD. Two very thin Type IIa MTDs are observed between 5090.16 – 5090.46 m (16700 and 16701 ft).

A well-section of the UB4-5 sandstone and an interpretation of the MTC immediately above the sandy reservoir interval is shown in Figure 8.20. The well-section starts west of the field, heads east (wells C2 and C7Z) and traverses back west to show how this unit appears to thin down-dip. The MTC has been divided into three MTDs (1, 2 and 3), based on gamma and neutron-density log character. The B28-Y well is interpreted to show the thickest MTC, up to ~ 61 m (200 ft) in thickness.

The implication of the interpreted MTC above the UB4 sandstone interval could be significant with regards to the controlling factors that terminated sandstone deposition in the Buzzard Graben. In the Ainsa Basin, the Quarry (Locality 19, approximately 1 km south of Ainsa), exposes the Ainsa I System, comprised of sandstone channel facies (discussed in Chapter 4). Immediately above the Ainsa I sandstones, a 50 – 70 m thick MTC is present, comprised of Type Ia and IIa MTDs (Figure 8.21). The base of the MTC is easily accessible from the quarry, however, measuring and describing the entire thickness of this unit is not possible due to weathering and outcrop accessibility. The abrupt termination of the Ainsa I sandstone deposition that suggests other processes, other than channel abandonment, may have caused the termination of sandstone deposition at this location. One interpretation is related to instability of the slope, causing a period of mass-wasting within a tectonically active basin, as identified by Cronin *et al.* (1998).

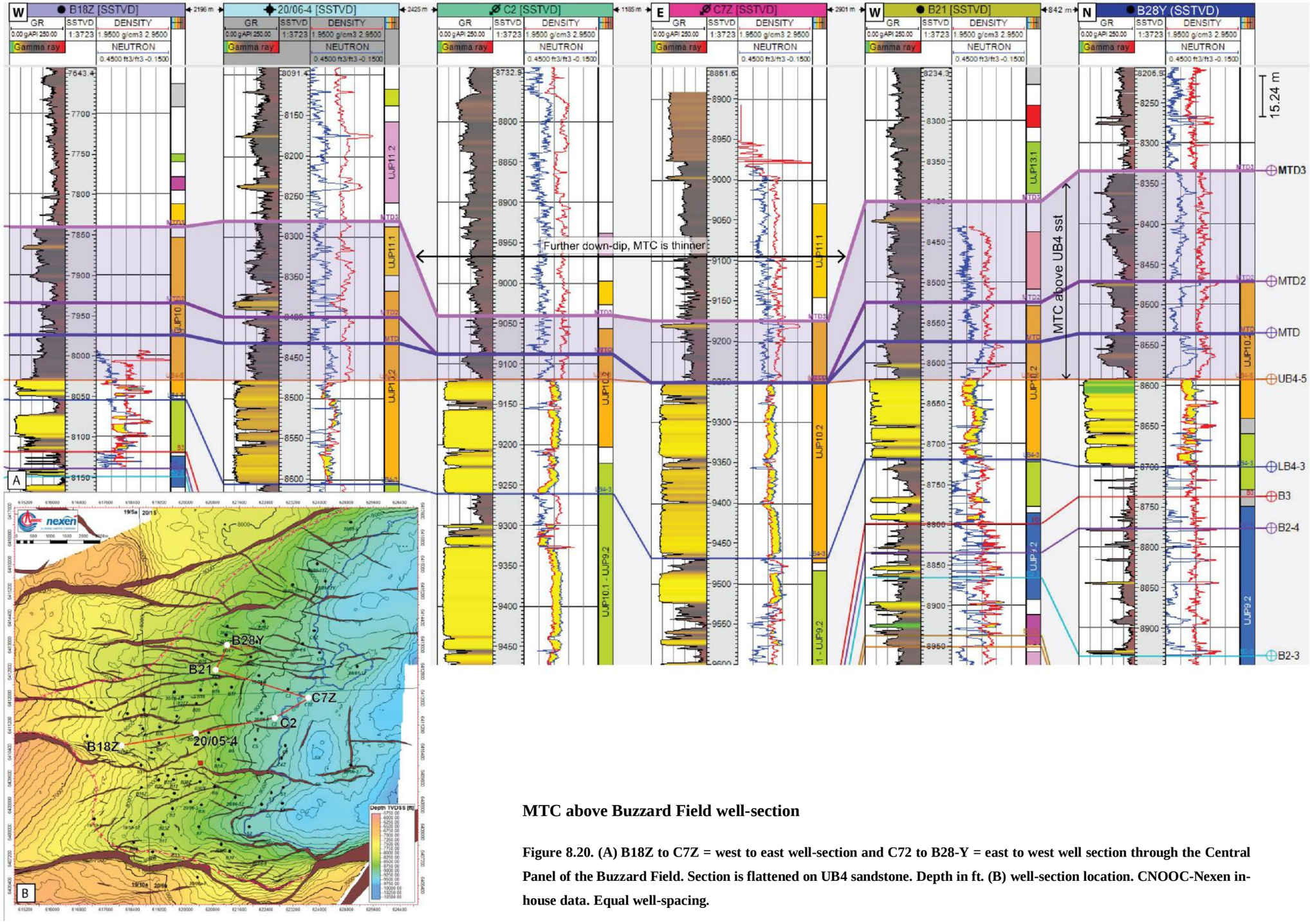

MTC above Buzzard Field well-section

Figure 8.20. (A) B18Z to C7Z = west to east well-section and C72 to B28-Y = east to west well section through the Central Panel of the Buzzard Field. Section is flattened on UB4 sandstone. Depth in ft. (B) well-section location. CNOOC-Nexen in-house data. Equal well-spacing.

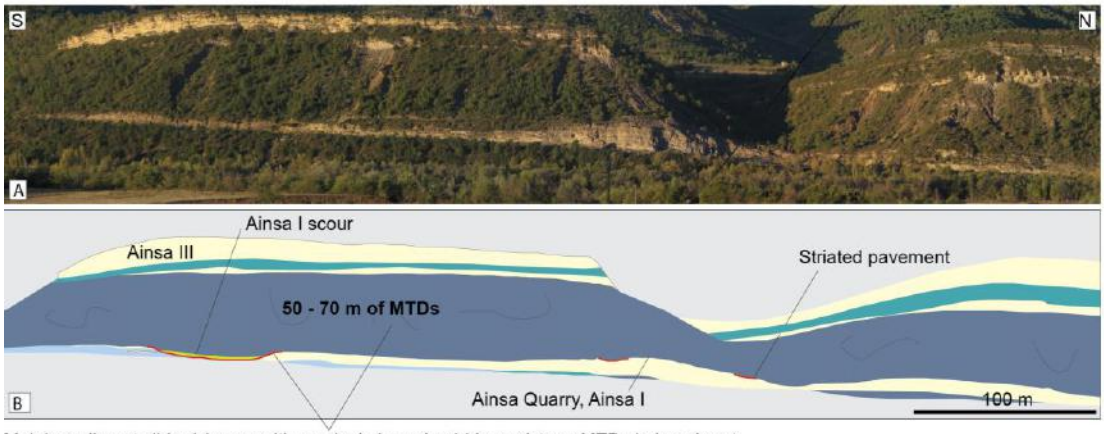

Figure 8.21. (A) Photo, and (B) photointerpretation of the Ainsa Quarry. View looking west from Usana-Banastón. Modified from Pickering *et al.* (2015).

At the top of the sandstone succession in the Ainsa Quarry, the top sandstone surface is striated, which is located immediately under a debrite at the base of the 50 – 70 m MTC (Figure 8.22). Pebbles are also found embedded into the sandstone, interpreted as a residual pebble that originated from the over-riding erosive debris flow (Dakin *et al.*, 2013).

Above the ~ 60 m MTC in the Ainsa Quarry is the channelised Ainsa III System. Cronin *et al.* (1998) suggested the bases of the sandy depositional systems (Ainsa I and III) are sequence boundaries, associated with relative sea level falls.

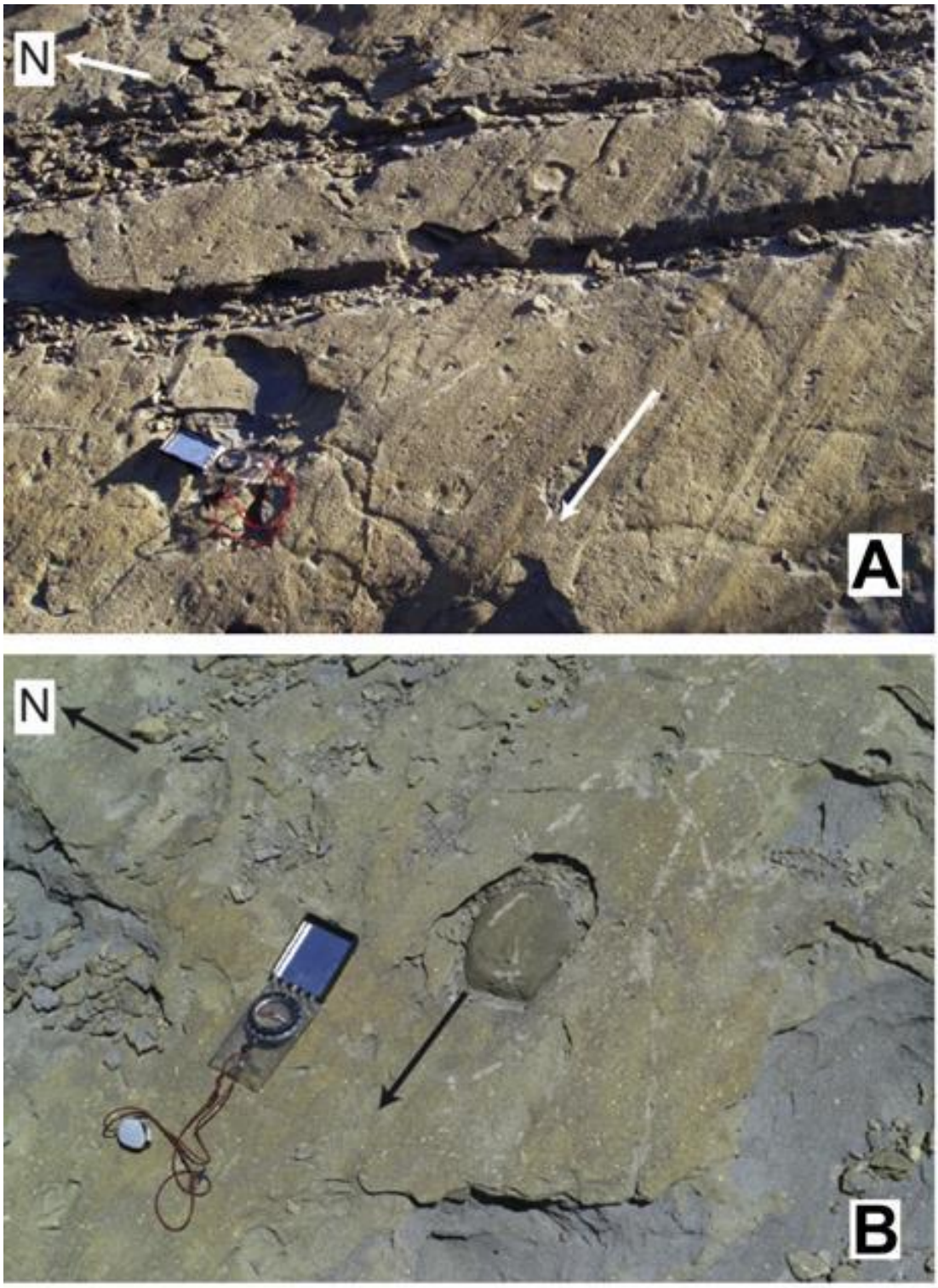

Figure 8.22. (A) Striations at the top sandstone surface in the Ainsa Quarry (B) embedded pebble on top sandstone surface. Modified from Dakin *et al*. (2013)

8.3 INTERPRETATION

During the three-month internship at CNOOC-Nexen, MTDs and MTCs in the Buzzard Field, UK North Sea were identified and evaluated using core and wireline data. The potential origin, geometry and effect that these deposits have on sandstone distribution and the presence of erosive MTDs are discussed. MTDs and associated MTCs in the Buzzard Field are also compared to those identified in the Ainsa Basin.

8.3.2 Comparison of MTD and frequency analysis

Core data from the Buzzard Field shows the reservoirs are comprised of very-fine sand- to gravel-grade sandstones. Pebble-, cobble- or boulder-grade fractions are not identified in any of the core images. In the Ainsa Basin, cobble and pebble- grade clasts deposited pebbly debrites, conglomerates and pebbly sandstones and account for up to 10 % of MTDs. During deposition of the Upper Hecho Group, the source area to Ainsa comprised alluvial fans, eroding sediment in the immature hinterland from the rising mountains of the Pyrenean Orogen and feeding sediment to the deep-marine fore-deep basin through canyon systems (Farrell, 1984; Puigdefábregas and Souquet, 1986; Gong *et al.,* 2008; Vissers and Meijer, 2012). The Buzzard Basin was fed by a mature fluvial system (Ray *et al.*, 2010), likely to result in an absence of cobble- and pebble-grade clasts (analogous to the Fosado, Los Molinos and Arro Systems, in the Ainsa Basin). Catastrophic failure of the shelf resulted in sands being remobilsed into deep-water from surge-like flows (Doré and Robbins, 2005; Ray *et al*., 2010).

Core images from the Buzzard Field show that Type IIa facies are typically identified in the older (B2) stratigraphy. The dominant mass-transport facies identified in core in the LB4 and UB4 MTCs are marginally dominated by Type Ia MTDs (Figure 8.9). Doré and Robbins (2005) and Ray *et al*. (2010) suggest the majority of MTDs and associated MTCs in the Buzzard Basin were derived from local palaeohighs. This is interpreted to have occurred as a result of the formation of rift grabens during extension in the Upper Jurassic, or from failure of the lower slope. An observation from the Ainsa Basin MTD study (Chapter 6) shows 41 % of MTDs found in proximal localities comprise Type Ia MTDs, interpreted as derived from

upper, mid and lower slope environments. The dominance of Type Ia deposits in the LB4 and UB4 MTCs may suggest proximity to the site of failure in the Buzzard Basin, such as from local fault movement from the west-east bounding faults through the basin (Figure 8.3). The dominance of Type IIa deposits documented in the B2 MTC (Figure 8.9) may suggest relative distal failure from the slope, at a time when the major west-east faults did not compartmentalise flow deposition in early stages of basin formation. MTDs and MTCs from both Ainsa and Buzzard show average thickness of deposits are thicker in proximal locations (i.e., at or near the base-of-slope), and more-layer cake stratigraphy down-dip in Buzzard (around the injector wells) supports the observation that MTDs and MTCs pinch-out distally.

8.3.3 MTC distribution

8.3.3.1 B2

The dominant lithofacies of the B2 MTC in cored intervals are documented as homogenous mudstones, interpreted as muddy Type IIa MTDs, although Type Ia MTDs are also present. The B2 distribution map shows an elongate tongue-like geometry, confined to the Central Panel. This suggests that at B2 times, the basin may have been at least partially confined, potentially by the presence of the basin-bounding faults observed (Figure 8.3). The B27 well is located furthest west of the field, in closest proximity to the base-of-slope and shows an MTC measured 30.48 m (> 100 ft) in thickness. The B2 MTC shows that the thickest deposits are found proximally, proportionate to the magnitude of MTCs measured in a proximal setting in the Ainsa Basin. Along with the 2-D distribution model, the dominance of debrites observed in core and correlations of the chaotic interval suggests that the B2 MTC was derived from the west, potentially from near the base of slope. Immediately above the B2 MTC, the geometry of the B2 sandstone unit appears more ‘channelised’. Beyond the termination of the ‘snout’ of the B2 MTC (at the C5 well), is where the B2 sandstones broaden in width. This observation suggests the MTC could be controlling sandstone deposition.

8.3.3.2 LB4

Stratigraphy of the Southern Panel is complicated, governed by the presence of semi-regional MTCs that occur almost entirely within this area. The LB4 MTC shows Type Ia and Type IIa (homogenous chaotic mudstones) that typically appear bedded in core. The overall MTC has a poorly defined geometry, but is mainly located in the Southern and Central panels. The poorly defined geometry of the LB4 MTC (Figure 8.12) could be related to periodic fault failure, depositing discontinuous deposits that are difficult to correlate between wells.

8.3.3.3 UB4

The sandstone event that separates the LB4 and UB4 MTCs could represent semi-regional events that in-filled residual topography from the LB4 MTC. The abundance of MTDs under the UB4 sandstone suggests that Late Kimmeridgian rifting made the area tectonically active and producing locally unstable zones vulnerable to mass-wasting. The overall geometry of the UB4 MTC shows a strong west-to-east elongate orientation, similar to the B2 MTC, however is predominantly located in the Southern Panel, suggesting confinement at the time of deposition. The UB4 MTC distribution map shows greatest thickness in the west, nearest to the base-of-slope in B23Z.

Literature studies discuss varying size and areal distribution of MTDs that deposit elongate to more equi-dimensional lobes (Diaz *et al.*, 2010). The plan-view geometries modelled in the large-scale B2 and UB4 MTCs suggest failure of the slope, not from fault instability, proposed by Doré and Robbins, (2005), and Ray *et al*. (2010). Although it is likely that the east-west basin-bounding faults remobilised smaller MTDs and other sediment in the basin, including sandstones.

8.3.4 Distal and proximal thickness variations

Without a significant basin-wide marker bed and lack of down-dip exposure, it is not possible to measure the down-dip thickness variation of one, or sequence of events. Therefore, the average thicknesses of MTCs across the Ainsa and Buzzard basins are

measured and separated into ‘proximal’ and ‘distal’ locations based on relative proximity to the slope. Grouping average MTC data from proximal and distal locations and comparing how overall thickness variations change down-dip is fairly crude, however both the Ainsa and Buzzard basins show decreasing thickness away from the base-of-slope. This trend tends to be consistent with high-resolution seismic data from larger basins, that although have a limited vertical resolution, shows excellent lateral resolution. Zhao *et al.* (2015) use 3-D seismic data to investigate the internal structure of MTDs in the South China Sea. Of 3 MTDs documented, one MTD is found to have a continuous geometry along the continental slope, and the others are documented to thin downslope (Figure 8.23-A). Gamboa *et al.* (2010) show that the average proportional thickness of MTDs offshore Brazil decrease from 70 – 80 ms TWT to 50 – 60 ms TWT. The authors suggest that decreasing values reflect an important sediment source northwest of the study area (Figure 8.23-B).

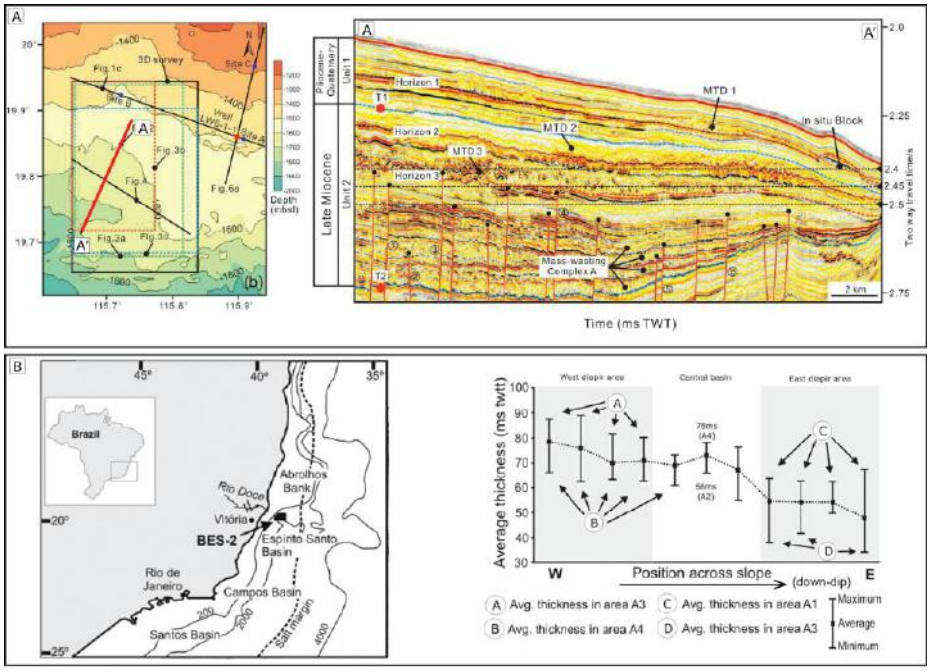

Figure 8.23. (A) Seismic profile down-dip from the continental slope showing MTCs thinning basinwards, Pearl River Mouth Basin, offshore South China Sea, Zhao *et al.* (2010) (B) Graphic representation of MTD thickness in the Abrolhos Unit, Espírito Santo Basin, SE Brazil. Plot shows average MTC thickness thins down-dip. Modified from Gamboa *et al.* (2010).

The average consistent ‘thinning’ of MTDs in Ainsa and Buzzard could suggest that MTDs are also sourced from a common area, such as the slope.

8.3.5 Abrupt sandstone deposition

Other factors, apart from system abandonment, could play a role in the termination of sandstone deposition. Thick MTCs are documented immediately above the Ainsa I Fan and the B4 sandstones in the Buzzard Field. Maximum MTC thicknesses are measured as similar in scale (~ 60 m). Above the ~ 60 m MTC in the Ainsa Quarry, sandstones of the Ainsa III Fan are deposited. However, in the Buzzard Field the B4 sandstone unit is the final sandy hydrocarbon-bearing Jurassic System in the Buzzard Graben.

The Ainsa Fans (I, II and III) are interpreted as erosive base-of-slope and proximal basin-floor channelised submarine fans (Pickering and Corregidor, 2005; Pickering and Bayliss, 2009). The Ainsa III Fan may have been able to recover the geographical location of the Ainsa I Fan due to basin confinement, and through continual bypass and deposition of energetic erosive turbidity currents. Unlike the Ainsa depositional systems, sandstones deposited in Buzzard are interpreted as largely non-turbulent surge-like high-concentration density currents resulting from failure of the shelf (i.e., Grampian Spur). The Buzzard Field is located at the base of slope within a known active tectonic area during the Upper Jurassic. A catastrophic event causing instability of the slope may have caused successive MTDs to deposit on top of the sandstones that effectively 'choked' the system. The MTC above the Buzzard sandstone reservoir may have produced sufficient topography to divert these largely non-erosive sandy SGFs away from the Buzzard area, to potentially deposit the hydrocarbon-bearing Ettrick sandstones further down-dip (to the east) in the basin. Progradation of the slope may have also permitted sands to be deposited further down-dip in the Ettrick System, away from the Buzzard Field.

8.3.6 Basal erosion

Basal MTD contacts are not seismically resolvable in the Buzzard Field, therefore core data and field analogues are important to determine if this relationship occurs in the Buzzard Field.

Chapter 6 of this study presents outcrops from the Ainsa Basin showing Type IIa MTDs with *in situ* basal erosion. These MTDs generally showed visual signs of vertical 'normal grading' in the field. Chapter 7 presented thin-section point-count data from 'non-erosive' MTDs that were likely to have been erosive up-dip from its depositional site. These MTDs showed a vertical decrease of sand grains within the matrix, becoming mud dominated at the top. Core data from the Buzzard Field rarely shows the presence of 'starry night' facies (i.e., sand-rich Type IIa MTDs). However where present, visually, Type IIa MTDs generally do not appear to show vertical grading. The matrix of homogenised muddy chaotic mudstones observed in core in the Buzzard Field is generally sand-poor, particularly MTDs in the B2 unit, identified in wells S2, B8, B22 and 20/06-6. Sand-rich Type IIa MTDs may not be present in the B2 MTDs as the B2 unit is stratigraphically above the B1 and B0 units, which characteristically have very few- to no sandstone beds, and therefore may not have had the opportunity to erode any sandy substrates.

Sandstone blocks are also not observed incorporated at the base of Type IIa MTDs in core. The absence of coarse-grained sandstone boulders that are generally observed in MTDs in the Ainsa Basin could suggest that Buzzard MTCs were not as erosive, although core data only captures 6" of an entire width of an MTD. Seismic resolution also does not permit blocks of sandstone 'plucked' or grooved into the base of MTDs at the scale of Buzzard (e.g., Jackson, 2013). The sandstone clast incorporated into the very-thin sand-rich Type IIa deposit (e.g., Figure 8.17) could have been incorporated either through erosion, or injected as a result of overpressure of the underlying saturated sandstone, potentially as a result of compaction, forcing liquefied sands through weaknesses in the overlying rock. However, it is not possible to resolve the process interpretation at this scale.

The sedimentological detail of the matrix between erosive Type IIa MTDs in Ainsa and Type IIa MTDs in Buzzard appear visually different. A distinct lack of grain-size and compositional 'grading' in Buzzard MTDs suggests erosion may not have occurred in this basin. However, the presence of 'starry night' facies may indicate that debris flows were capable of at least minor erosion of the seafloor.

8.4 SUMMARY

This project has identified variable MTD facies, including homogenised mudstones interpreted as muddy Type IIa MTDs, to more coherent remobilised units interpreted as Type Ia deposits. These MTDs are typically discrete and can be difficult to observe in core, however can be identified by measuring the subtle differences in angle and looking for basal shear and truncated surfaces for Type Ia MTDs, or homogenised mudstones in Type IIa MTDs.

Subtle differences of MTD facies between the Ainsa and Buzzard result from the differing source area characteristics. Sediments of the Ainsa Basin were fed from the newly emerging Pyrenean mountain belt and the Buzzard Basin was fed from an extensive mature braided fluvial system. MTDs in the Buzzard Basin were also likely to be shed from local faults as well as the lower slope, whereas MTDs in Ainsa were shed from the lower shelf to the upper, mid and lower slope.

The B2, LB4 and UB4 MTCs were mapped to document the presence and thickness variation of remobilised deposits directly beneath the B2 and UB4 sandstones. The B2 MTC shows a potential degree of control on the deposition of the overlying sandstones in the Central Panel. Beyond the 'snout' of the B2 MTC, a 2-D model of the overlying B2 sandstones show an immediate broadening in width to suggest less confinement. Stratigraphy of the Southern Panel is complicated, governed by the presence of the semi-regional LB4 and UB4 MTCs that occur almost entirely within this area. The elongate tongue-like plan geometries of the B2 and UB4 MTCs suggest failure of at least the lower slope. The top MTC above the B4 sandstone was correlated as to attempt to understand what caused the end of sandstone deposition in the Buzzard Graben. It is suggested that the MTC created sufficient topography to divert subsequent sandy SGFs further down-dip in the basin.

MTDs showing basal erosion in the Buzzard Field are not yet fully identified within the scope of this project. However, the absence of very-thick sand-rich Type IIa deposits that show grading, as observed in the Ainsa Basin, could initially suggest that erosive MTDs are yet to be identified. Failure magnitude of the lower-slope and localised faults in Buzzard may not have been sufficient for debris flows to erode the sandy substrate.

CHAPTER 9

SYNTHESIS

9.1 INTRODUCTION

Outcrop measurements and observations from the Middle-Eocene Ainsa Basin, Spanish Pyrenees have investigated the internal complexity of MTD facies and the temporal and spatial distribution of these chaotic deposits in a proximal basin-floor setting. This data reveals various scales and geometries of MTDs, from intrafan deposits that likely act as heterogeneities within sandy submarine fan deposits (e.g., baffles to the flow of hydrocarbons in reservoirs), to rare and large-scale catastrophic events, such as the formation of megascours, with processes that dramatically impact basin-floor stratigraphy. Seismic-scale MTDs and MTCs provide evidence of erosion at the base of these deposits (e.g., Gee *et al.*, 1999, 2001, 2005; Nygård *et al.*, 2002; Moscardelli *et al.*, 2006; Alves and Cartwright, 2009, 2010, Alves, 2010, Alves *et al.*, 2013, Omosanya and Alves, 2013a, b, Alves *et al.*, 2014, Alves, 2015), whereas outcrops documented in the Ainsa Basin can provide evidence of such erosive mechanisms (this research). Data from the Jurassic Buzzard Field, UK North Sea has provided additional insights into the subsurface stratigraphy of ancient deep-marine systems. The interpretation of core and well data, together with computer-based models of these deposits has aimed to improve the prediction of the subsurface distribution of MTCs in the field. Comparative literature studies show differences in scale and magnitude of chaotic deposits in the Ainsa Basin (this study) compared to larger events, such as failure of a passive margin (e.g., Jackson, 2013).

9.2 DATA SYNTHESIS

9.2.1 MTD classification scheme

Fieldwork undertaken in the Ainsa Basin (Chapters 4 – 6) and laboratory analysis of Type IIa MTDs (Chapter 7) has provided an improved understanding of the effects of basal erosion and how this might influence the grain-size and compositional character

of such chaotic deposits. Using this information, a classification scheme is developed (Table 9.1), which modifies the scheme of Pickering and Corregidor (2005).

Type Ia and IIa MTDs are recorded as the most commonly occurring facies, accounting for ~ 90 % of all MTDs (Table 5.4, Chapter 5). Thin-section analyses of Type IIa deposits in the Ainsa Basin suggest three discrete groups of these deposits, defined as Groups 1, 2 and 3 (Chapter 7). The proposed revised classification scheme incorporates these groups and takes into account any erosional features observed at the base of Type IIa MTDs. An additional type, Type IIIb deposits, are included to highlight the presence of isolated clast-supported conglomerate-filled scours or small channels deposited immediately above a thin sandstone element, a feature that has been used to infer deposition from genetically linked flows (e.g., Sohn, 1999, 2002). Another additional type, Type IV deposits, are also included to describe MTDs that contain mixed facies, interpreted as the deposition of transitional flows (e.g., Mutti *et al.,* 2006; Ogata *et al.,* 2010), or those formed by basal shear such as at the base of rafts (Figure 6.31, Chapter 6 *cf.* Ogata *et al.,* 2012).

9.2.2 Sedimentary characteristics

In the Ainsa Basin study area, outcrop observations and measurements capture small-scale heterogeneities not observed in seismic datasets. These include: (1) detailed facies relationships (Figures 4.1 to 4.9, Chapter 4); (2) small- to medium-scale architectural elements (Figure 4.11, Chapter 4); (3) local erosion processes and deposits (Table 6.1, Chapter 6); (4) topographic relationships (Figures 4.16 and 4.17, Chapter 4); (5) small isolated scours and/or sandstone channels within MTDs and MTCs (Figures 4.18, 4.19, 4.20, Chapter 4), and; (6) erosively-based MTDs into sandy substrates (Chapter 6). Outcrop observations from the Ainsa Basin have provided some evidence that the vector of turbulent SGFs may be interrupted by the presence of topography, leading to localised increased flow velocity and variable sediment transport directions. This is identified from variable flute marks at the base of SGF deposits immediately above mounded MTDs (Figures 4.16 and 4.17, Chapter 4). The architecture and geometry of isolated sandstone bodies in the Ainsa Basin (e.g., ‘winged’ sandstones identified in the Ross Formation, Ireland [Elliott, 2000]) have provided analogues to document how exceptionally large flows form erosive

basal geometries and deposit amalgamated channelised sandstones within MTDs, also potentially observed in the Buzzard Field (Figure 8.14, Chapter 8).

9.2.3 Sedimentary provenance

In the Ainsa Basin, the abundance of woody (including terrestrial plant spores) and disarticulated bioclastic material, such as nummulites, alveolinids, echinoid spines, solitary corals and gastropods in some Type IIa deposits, suggests that much of the sediments were sourced from terrestrial and shallow-marine environments, respectively. The paucity of these types of source indicators in Type Ia deposits suggests failure of more mud-dominated environments, such as the upper-, mid-, or lower-slope. Based on the pebble composition analysis of Type IIa, b and III MTDs in the field (Figure 4.28, Chapter 4) and the thin-section study presented in this research (Chapter 7), discrete drainage patterns to the Ainsa Basin may suggest 'tapping' of different source areas located on the shelf and/or slope. This study compliments researchers who reconstructed depositional models for the Ainsa Basin, including an understanding of the principal sedimentary entry point/s (e.g., Mutti, 1977, 1983; Das Gupta and Pickering, 2008; Caja *et al.*, 2010). Alluvial fan systems originating from the rising Pyrenees in the hinterland, such as the Sis palaeovalley comprising fluvial conglomerates (Vincent and Elliott, 1997), the northwest-directed fluvial channels of the Castisent Formation (Marzo *et al.*, 1988) and slope failure away from the main sediment routing system (Figure 7.20, Chapter 7), are interpreted as the principal depositional inputs into the basin. Temporal distribution results suggest a 'switch-on' of pebble-rich sediment derived from alluvial fan systems from the rising Pyrenees in the hinterland of the Ainsa Basin (Figure 5.18, Chapter 5). Understanding sediment provenance and the number of sedimentary inputs into a deep-marine basin enables a greater understanding of the heterogeneity and 'quality' of sands in various parts of a sedimentary basin. Similar petrological studies as those outlined in Chapters 4 (Figure 4.28) and 7 (Figures 7.2, 7.14 and 7.17) in cored intervals may aid qualitative interpretations in subsurface fields to determine source characteristics and identifying potential inputs into a basin. The implications of this type of analysis include an improved understanding of hydrocarbon reservoirs and the development of more predictive reservoir models (e.g., Piper et al., 2012).

Pickering and Corregidor (2005)		Dakin classification (this study)		Pickering (1986, 1989) classification	Thickness variation of individual MTDs	Dominant matrix composition	Matrix/clast supported	Sedimentary properties and structures	Basal erosion	Extraformational features	Occurrence	Long-distance transport mechanism	Type example	Photo
Type I	Ia	Type I	Ia	F1	m to 10's m	Mudstones/ heterolithic sediments	N/A	Preservation of internal laminations, Subtle dip variations to coherent folds	Yes	No extraformational features.	Failure of slope	Viscoplastic. Gravitational slide pulling large, coherent/semi-coherent blocks downslope along a shear plane.	Locality 19, Forcaz Stream, Ainsa II Fan	
	Ib		Ib	F1	dm to m	Mudstones/ sandstones heterolithic sediments	N/A	Folds and internal deformation	Yes	No extraformational features.	Failure of channel margin	Viscoplastic	Locality 6, Boltaña N-260, Banaston IV Fan	
	Ic		Ic	Not classified	Rafts up to 20 x 10 m	Carbonate	N/A	Imbricated rafted carbonates comprising up to 3 divisions (basal shear zone, lower brecciated zone and upper non-brecciated zone)	Yes	Carbonate platform collapse south of the Ainsa Basin, near Mediano Anticline.	Failure of carbonate platform	Viscoplastic to brittle. Gravity pulling large, coherent/semi-coherent blocks downslope along a shear plane.	Locality 27, Sieste River, Morillo II Fan	
Type II	N/A	Type II	**IIa-1** (Group 1)	A1.3	dm to 10's m	Chaotic mudstone matrix comprising up to 50 % grains	Matrix-supported	Normal compositional grading (vertical increase in mudstone/siltstone matrix)	Yes (erosion at outcrop). Bulldozing, striating, plucking,	Well-rounded pebbles, nummulites, corals and shell fragments. Pebble composition include igneous, sedimentary and metamorphic. Many pebbles are covered in borings produced by molluscs.	Failure of slope and shoreface	Cohesive flow. Erosive basal surface.	Locality 23, Rio Ara, Morillo I Fan	
	N/A		**IIa-2**(Group 2)	A1.3	dm to 10's m	Chaotic mudstone matrix comprising < 5 % to 20 % grains	Matrix-supported	Inverse grading	No	Well-rounded pebbles, nummulites. Pebble composition include igneous, sedimentary and metamorphic. Many pebbles are covered in borings produced by molluscs. Some shell fragments.	Failure of slope and shoreface	Cohesive, laminar flow. Can be hydroplaning.	Locality 30, Guaso II MTC	
	N/A		**IIa-3** (Group 3)	A1.3	dm to 10's m	Chaotic mudstone matrix comprising up to 50 % grains	Matrix-supported	Variable grading	Yes, but not observed at outcrop (erosion up-dip from outcrop exposure)	Well-rounded pebbles, nummulites, corals and shell fragments. Pebble composition include igneous, sedimentary and metamorphic. Many pebbles are covered in borings produced by molluscs.	Failure of slope and shoreface	Cohesive flow. Erosive basal surface.	Boltaña N-260, Banaston-V	
	N/A		**IIb**	A1.2, A1.3	dm to m	Variable chaotic matrix with grains up to 50 %	Clast-supported	Variable grading and poor to moderate imbrication	Yes	Well-rounded pebbles, nummulites. Pebble composition include igneous, sedimentary and metamorphic. Many pebbles are covered in borings produced by molluscs	Failure of slope and shoreface	Cohesive to concentrated density flows	Locality 6, Boltaña N-260, Banaston V Fan	
Type III	N/A	Type III	**IIIa**	A1.1, A2.1, A2.2, A2.3, A2.4, A2.5	dm to m	Sandstone	Matrix-supported	Can show both normal and inverse grading	Yes	Well-rounded pebbles, nummulites, corals and shell fragments. Pebble composition include igneous, sedimentary and metamorphic. Many pebbles are covered in borings produced by molluscs.	Failure of upper shoreface	Concentrated density flows	Locality 25, Coscajuela de Sobrarbe, Morillo II Fan	
	N/A		**IIIb**	A1.1, A2.1, A2.2, A2.3, A2.4, A2.5	dm to m	Sandstone	Clast-supported	Can show both normal and inverse grading	Yes	Well-rounded pebbles, nummulites, corals and shell fragments. Pebble composition include igneous, sedimentary and metamorphic. Many pebbles are covered in borings produced by molluscs	Failure of upper shoreface	Concentrated density flows	Locality 7, Boltaña River, Banastón V Fan	
N/A	N/A	Type IV	**Type IV**	N/A	m to dm	Mud-rich <5% sand	Matrix-supported	Combination of coherent sediment folds and internal deformation to chaotic mudstone	Unknown	Mud-dominated. Contorted to structureless muddy facies. Mudstone appears slumped to more 'debritic' in nature. When documented beneath Type Ic deposits, contains angular, brecciated limestone clasts	Failure of slope or muddy facies	Viscoplastic to cohesive	Banaston VI, Usana (lower slope canyon)	

Table 9.1. MTD classification scheme, modified from Pickering and Corregidor (2005). Based on outcrops of the proximal deep-marine Ainsa Basin, Spanish Pyrenees.

9.2.4 MTDs versus MTCs and co-genetic deposits

Approximately 32 % of mass-transport deposits recorded from outcrops in the Ainsa Basin are documented as MTCs, i.e., comprised of greater than one event. Where sandstone beds do not separate discrete MTDs within an MTC, facies attributes show subtle sedimentological differences between deposits and may identify individual events within an MTC. These facies attributes include vertical burrowing, grading, channelised deposits, basal erosion, topography, colour variations and pebble concentrations, as identified in Chapter 4. Truncated basal surfaces may indicate at least some consolidation of the lower deposit to suggest a break in time between deposition of MTDs. Vertical burrows at the top of MTDs could also suggest a passing of time between deposits. Furthermore, where discrete vertical units are not separated by sandstones, it could be argued that in some cases, stacked muddy MTDs record longitudinal facies changes between different parts of a single flow, *sensu stricto* hybrid event beds (HEBs), as described by Haughton *et al.* (2003, 2009). Analysis of the facies attribute table (Figure 4.11 and Table 4.1, Chapter 4) suggests that in some cases, there could be a relationship between the successive orders of events (i.e., Type Ia MTDs deposited above Type IIa MTDs). This could be related to the transport distance permitting longitudinal sorting of some flows that could potentially deposit genetically related event beds (e.g., Davies, 1990). However, further research from other ancient basins is needed to create statistically valid results.

9.2.5 Depositional environments and MTD and MTC thickness

Using maps and outcrop interpretations from literature studies (Mutti and Ricci Lucchi, 1972; Puigdefábregas and Souquet, 1986; Millington and Clark, 1995a, b; Pickering and Bayliss 2009, Sutcliffe and Pickering, 2009, Bayliss and Pickering, 2015a, 2015b, Pickering *et al*., 2015), stratigraphy of the Ainsa Basin was divided into the following depositional environments: slope; base-of-slope; intrafan; base of submarine fan, and; marginal to submarine fan. To quantitatively investigate the variability of MTD thickness and facies-type, both temporal (between fans) and spatial (i.e., proximal-to-distal), thickness measurements were collected from sedimentary logs recorded in the field. The data was used to generate histograms and scatter plots (Figures 5.13 to 5.21, Chapter 5). Spatially, the abundance of Type IIa

and Type Ic facies increases in relation to relative distance from the source area, whereas Type Ia, III and IV facies are found in greater abundance in proximal locations, such as on, or near the slope. Therefore, the number of internally chaotic facies (i.e., debrites) increases away from the sediment source (Figure 5.17, Chapter 5). Type Ic MTDs (carbonate rafts) are interpreted as deposited near to the base-of-slope, where a lower slope gradient likely resulted in a loss of momentum and an increase in basal shear (Figures 4.23 and 4.24, Chapter 4), as discussed by Farin *et al.*, (2013), Section 2.4.3.6, Chapter 2.

MTD thickness variations across the Ainsa Basin are likely to be related to the initial volume of SGFs and any ponded topography, although outcrop exposure does not permit these factors to be quantitatively measured. The Guaso System is interpreted as deposited from a relatively shallow slope gradient (Sutcliffe and Pickering, 2009), where as the Banastón and Morillo systems are interpreted to have had relatively steeper slope gradients, due to the propagation of the Mediano Anticline (Bayliss and Pickering, 2015a, b). This study shows that MTD facies and thicknesses appear to vary between these systems (Figure 5.18, Chapter 5) and could suggest the seafloor gradient was likely to be an important factor to the type of MTD facies deposited in the marine system. In this study, a greater number of less internally deformed deposits (i.e., Type Ia MTDs, sediment slump/slides) are documented in the Guaso System (Figure 5.17, Chapter 5). Type Ia MTDs are also measured as the thickest MTD facies in the Ainsa Basin (Table 5.4, Chapter 5). Nardin *et al.* (1989) proposed that steep slopes are not necessary for the propagation of slides, with the data in this study fitting to this model. However, in the Banastón and Morillo systems, a greater number of Type IIa MTDs (i.e., internally chaotic facies) are documented in comparison to Type Ia facies (Figure 5.18, Chapter 5). Slope failure from steeper gradients, as inferred in these systems, may permit down-slope transformation to produce more internally chaotic flows (i.e., debrites).

9.2.6 Scaling and geometry of MTDs and MTCs

Based on observations in the Ainsa Basin, at the highest seismic resolution, it is likely that MTDs in many hydrocarbon fields comprise more than one event. Documenting MTC dimensions (as opposed to smaller scale individual events) helped to provide

better constraints when scaling up to analogues, such as for the Buzzard Field. Average thicknesses of MTDs and MTCs measured in the Ainsa Basin were recorded as ~ 2 and ~ 12.5 m, respectively, with both values typically below the highest seismic resolution (Chopra *et al.*, 2006). This shows the value of outcrop observations and the likely heterogeneity of reservoir architecture not visible in seismic datasets of small- to moderately-sized basins. Volume, area and run-out information are not easily obtained accurately from outcrops due to the lack of down-dip exposure, however comparable measurements are presented from the Ainsa Basin and Buzzard Field where possible. Compiled MTC thickness *versus* width data from the Ainsa Basin, Buzzard Field and literature are shown in Figure 9.1.

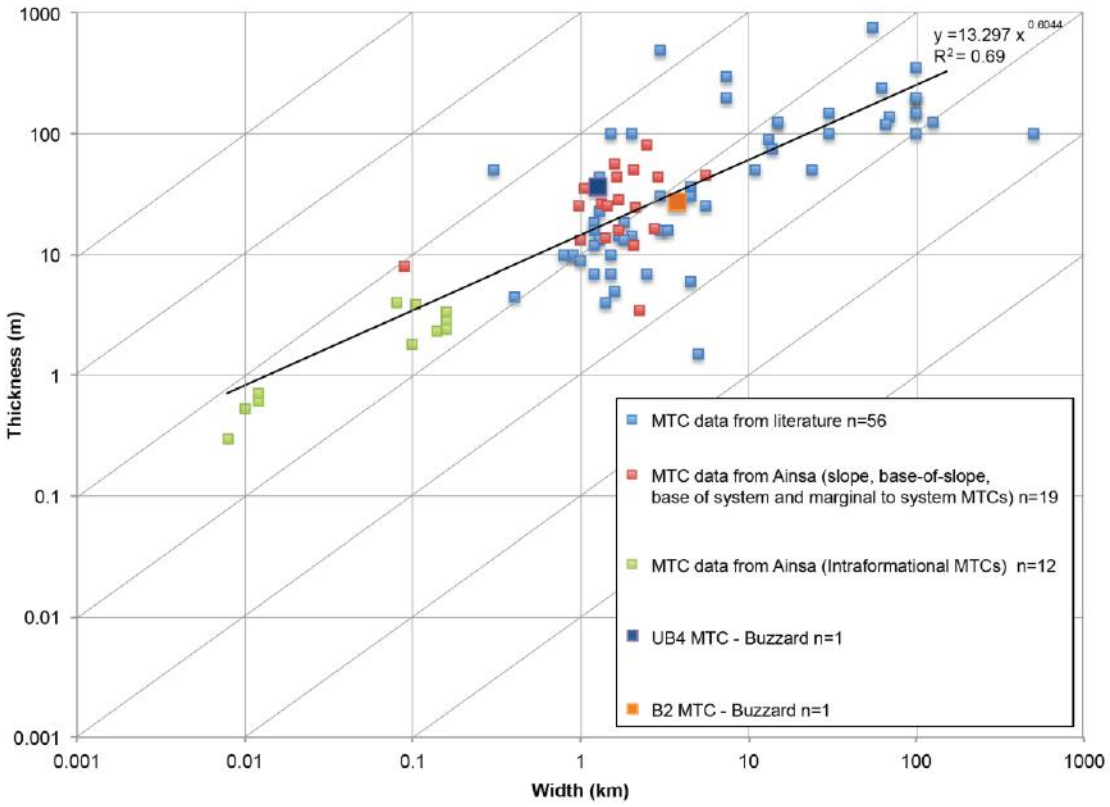

Figure 9.1. MTC aspect ratio (width *versus* thickness) data from the Ainsa Basin compared to dimensions of MTCs documented in literature. Data from the Ainsa Basin are only shown where accurate width and thickness data are available. Log-log scale.

The dataset in Figure 9.1 shows three populations. The green squares show intraformational MTCs in the Ainsa Basin are measured as deposits with the smallest dimensions (< 1 km width and < 10 m thickness). These deposits are not likely to be captured within seismic datasets due to resolution. The red squares represent MTCs measured on the slope, at the base of systems and those documented marginal to

systems. These deposits are almost two orders of magnitude larger than intraformational deposits (from 2.25 km width and 3.25 m thickness to 5.61 km width to ~ 45 m thickness). These deposits are comparable to some MTCs observed at seismic scale (e.g., MTDs measured in Bernhardt *et al.*, 2012). The B2 and UB4 MTCs of the Buzzard Field show dimensions analogous to these larger deposits. The light blue squares record dimensions collected from literature based on seismic data. Although this data population largely overlaps with deposits documented in the Ainsa Basin, part of the dataset spans nearly two orders of magnitude larger than those observed at outcrop and up to four dimensions larger than intraformational MTCs (i.e., 100 km width and 300 m thick deposits documented by Lawrence and Cartwright, 2009 in the mid-Norway margin, Møre Basin). When the 'intraformational' (intrafan) MTC measurements from the Ainsa Basin are included in the width and thickness dataset, the R^2 correlation increases from 0.51 to 0.69 (Figure 5.22-F, Chapter 5). This highlights how smaller-scaled deposits are missed when capturing data with a coarse resolution, such as from seismic studies.

Width *versus* run-out dimensions are compiled from literature and MTC distributions modelled from well correlations in the Buzzard Field (e.g., Figures 8.10 and 8.12, Chapter 8) (Figure 9.2). The dataset in Figure 9.2 show that the width and run-out of MTCs modelled in the Buzzard Field are comparable to MTD examples as documented in the Caspian Sea, 30 km in length deposited in ~ 1 km of water (Richardson *et al.*, 2011), West of Shetland, up to 400 km from the Wyville-Thompson Ridge to the Norwegian Basin (Wilson *et al.*, 2004), and the Austrian Molasse Basin, ~ 20 km in length (Bernhardt *et al.*, 2012). Other MTDs documented from the scientific literature are up to three orders of magnitude larger than those in Buzzard. These include the Amazon Fan (Maslin and Mikkelsen, 1997), offshore Brunei, Borneo (Gee *et al.*, 2007), the continental slope offshore Norway (Lawrence and Cartwright, 2009), the Santos Basin (Jackson, 2010), and the continental margin of Trinidad and Tobago, (Moscardelli *et al.*, 2006). Sedimentary basins of this size may have processes (such as magnitude of mass-failure of a continental margin) that are not observed in the Ainsa Basin and Buzzard Field. This is likely, as rafts up to 350 m in thickness and the geometry of scours up to 60 km in length (e.g., Alves and Cartwright, 2009, Jackson, 2011; Richardson *et al.*, 2011; Omosanya and Alves,

2013a, b) discussed in Chapters 4 and 5, are features not akin to those documented in this study.

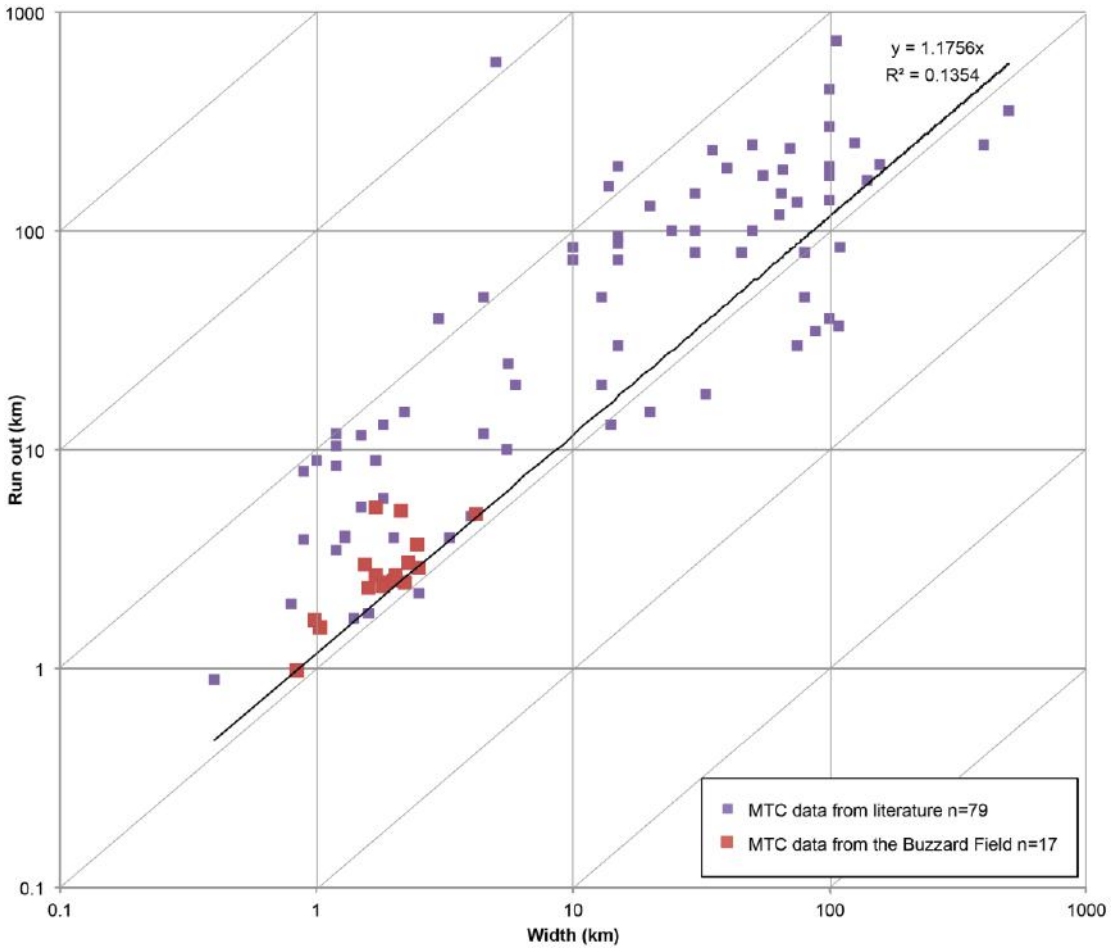

Figure 9.2. MTC aspect ratio (width *versus* run-out) data from the Buzzard Field compared to dimensions of MTCs documented in literature. Log-log scale.

The predication of sandstone presence when planning wells is a dominant impact that the presence of MTDs and MTCs have in terms of developing the Buzzard Field. The number of such deposits identified in outcrop and Buzzard core data suggests the presence of MTDs should be factored into reservoir models. MTC geometrical trends help to populate parameters required as an input for creating 2-D and 3-D models created in software such as Petrel. For example, a variogram is a plot of variability to describe the spatial variation of a property (i.e., dimension). This is based on the principle that closely spaced samples are likely to have a greater correlation than those located far from one another, and beyond a certain point, a minimum correlation is reached and the distance is no longer important. Variogram

analysis involves 3 directions orthogonal to each other (vertical, major and minor). The spatial correlation may be anisotropic and several variograms oriented in different directions may be required to describe the variation of a property. In determining the dimensions of MTDs and MTCs at outcrop, typical ranges such as the vertical (thickness), major (run-out) and minor (width) directions can be determined and used as inputs to constrain modelling parameters. Coring wells in the hydrocarbon industry is an expensive but invaluable tool that provides vital geological data in terms of lithology, sedimentology and also determining porosity and permeability. This study provides useful geological information that can be applied in hydrocarbon reservoirs, via documenting the dimensions of seismically resolvable MTCs (i.e., deposits greater than one event) and also measuring these deposits at outcrop, helps to constrain and predict the geometry of MTCs outside the borehole 'window'.

9.2.7 Analogues and basin configuration

Although the Ainsa and Buzzard basins are similar in size (Figure 1.19-C, Chapter 1), they were created under different tectonic regimes. The Ainsa Basin formed as a depocentre in response to compression from advancing thrust tectonics of the Pyrenean orogeny during the Eocene (Farrell, 1984; Puigdefábregas and Souquet, 1986; Gong *et al.,* 2008; Vissers and Meijer, 2012), comprising 19 predominately channelised sandy depositional systems deposited over ~ 10 Ma (Pickering and Bayliss, 2009). The Buzzard Basin formed in response to extension, related to rifting of the North Sea during the Late Jurassic, comprising three main sandy fan systems deposited over ~ 5 Ma (Doré and Robbins, 2005). The source areas are also different, reflected in the lack of cobble- and pebble-grade fractions in the Buzzard Basin. Configuration of Ainsa Basin is interpreted as an elongate shallow- to deep-marine basin with dominant point sources from the eastern part of the basin (Figure 1.13, Chapter 1). However, the presence of the Añisclo Anticline acted as a syndepositional growth structure, likely to affect the topography on the seafloor. Spatial analysis shows that Type Ia and IV MTDs typically characterise proximal depositional areas (such as on- and near the base-of-slope) and Type IIa deposits typically characterise distal environments (Figure 5.17, Chapter 5). Although the application of this type of

spatial analysis may aid palaeoenvironmental interpretations linked with MTDs and MTCs in ancient deep-marine systems, the geomorphological model applied to the Ainsa Basin could be too simplistic in the case of the Buzzard Field, where elongate basin-parallel faults segregate the basin into discrete depositional parts (Figure 8.3, Chapter 8). These faults are interpreted to deposit sediment and create locally steep seafloor gradients, subject to deposit MTDs as part of the basin fill (Doré and Robbins, 2005). However, despite these differences in tectonic setting and basin configuration, average MTC thickness is documented to pinch-out down-dip (from near to- and base-of-slope to basin floor) in both basins. This may suggest that in the Buzzard Field, the predominant input of MTDs may also have been from up-dip, towards the slope, particularly during deposition of the B2 MTC, where the present day basin-bounding faults do not appear to interrupt MTC thickness trends (Figure 8.10, Chapter 8). Despite these geometrical and tectonic differences between the Ainsa and Buzzard basins, useful comparisons can be made, particularly concerning sediment transport and deposition processes.

9.3 EROSIVE SGFs

Although the erosive potential of debris flows in subaerial settings is likely to differ from submarine settings, it was important to acknowledge the current understanding of how these destructive flows sculpt and change the surface morphology after single events (discussed in Chapter 2). Bedrock in steepland subaerial channels is generally composed of fully lithified ancient deposits, such as the Palaeozoic Oquirrh Quartzite Formation studied by Stock and Dietrich (2006), although the presence of loose material in a channel creates weak erodible layers that are prone to entrainment (Mangeney *et al.*, 2010). In subaerial settings, erosion can be a slow process. For example, McCoy *et al*. (2013) show that 34 – 64 mm of erosion was measured over 4 years. In recent years, there has been an increased appreciation that under some circumstances, debris flows can be both locally turbulent and erosive, with substantial excision of underlying stratigraphy (e.g., Dakin *et al.*, 2013 and references therein). Data collected in this study suggests that in many cases, Type IIa MTDs (likely deposited from highly-concentrated debris flow processes) are highly erosive. This study presents sub-seismic to highest-resolution seismic-scale outcrops showing the

potential erosivity of debris flows in a proximal submarine environment (i.e., at or near the base-of-slope). However, it is important to discuss other avenues of thought of sedimentary processes and associated deposits, as documented in literature. Here, the erosive styles and mechanisms of erosion via sandy SGFs (i.e., turbidity currents) are compared. The depositional styles of HEBs are also discussed.

9.3.1 Erosion from sandy SGFs (turbidity currents)

Bypassing processes, such as those associated with non-depositing turbidity currents, can either be erosive, where the flow has sufficient competence to entrain sediment, or bypassing, whereby the flow is able to keep its entire sediment load in suspension, yet not powerful enough to entrain any more sediment into the flow (Stevenson *et al.*, 2013, 2015). Evidence of erosion from sand-laden turbidity currents includes flute and sole marks at the base of sandy SGF deposits and larger-scale erosional events, e.g., channel incision and infill by turbidites (Figure 9.3).

The product of an erosive turbidity current observed at outcrop likely scoured, entrained and bypassed the depositional site to form scour surfaces that were subsequently backfilled with sand. This process forms sandstone-filled small-scale (low width: depth aspect ratio) channels within submarine fan systems. Erosive-depositional relationships of turbidites in the Ainsa Basin are a feature observed at outcrops worldwide (Ricci-Lucchi, 1975; Richards and Bowman, 1998; Elliott, 2000; Mayall *et al.*, 2006; Arbués *et al.*, 2007; Allen and Allen, 2009; Di Celma *et al.*, 2010; Van der Merwe *et al.*, 2010; Pickering *et al.*, 2015).

Baas *et al.* (2013) undertook flume tank experiments to show how turbidity currents are able to interact with cohesive soft muddy substrates without losing their shape, driven by bed shear stresses exceeding the bed cohesive strength. These flows appear to produce characteristic turbidites with internal mud layers, mixed cohesive to non-cohesive sediment layers, and flame and load structures. This type of interaction with the substrate, identified by Baas *et al.* (2013), is a feature observed as the ploughing mechanism at Locality 6, where a pebbly sandstone is observed to undercut thin- bedded sandstones and mudstones (Figure 6.10, Chapter 6). The contrary is not documented in this study (i.e., muddy MTDs ploughing into and under sandstones),

although other field outcrops and experimental data may prove similar processes in the future. Based on data collected within the Ainsa Basin, the mechanism of erosion between turbidity currents and debris flows must differ, as debrites identified in the field can preserve erosion *in situ* by incorporating semi-lithified sandstone blocks into the base of the deposit (Figure 6.3, Chapter 6). This erosive process is not recorded in 'classical' turbidites (*sensu stricto* Bouma, 1964).

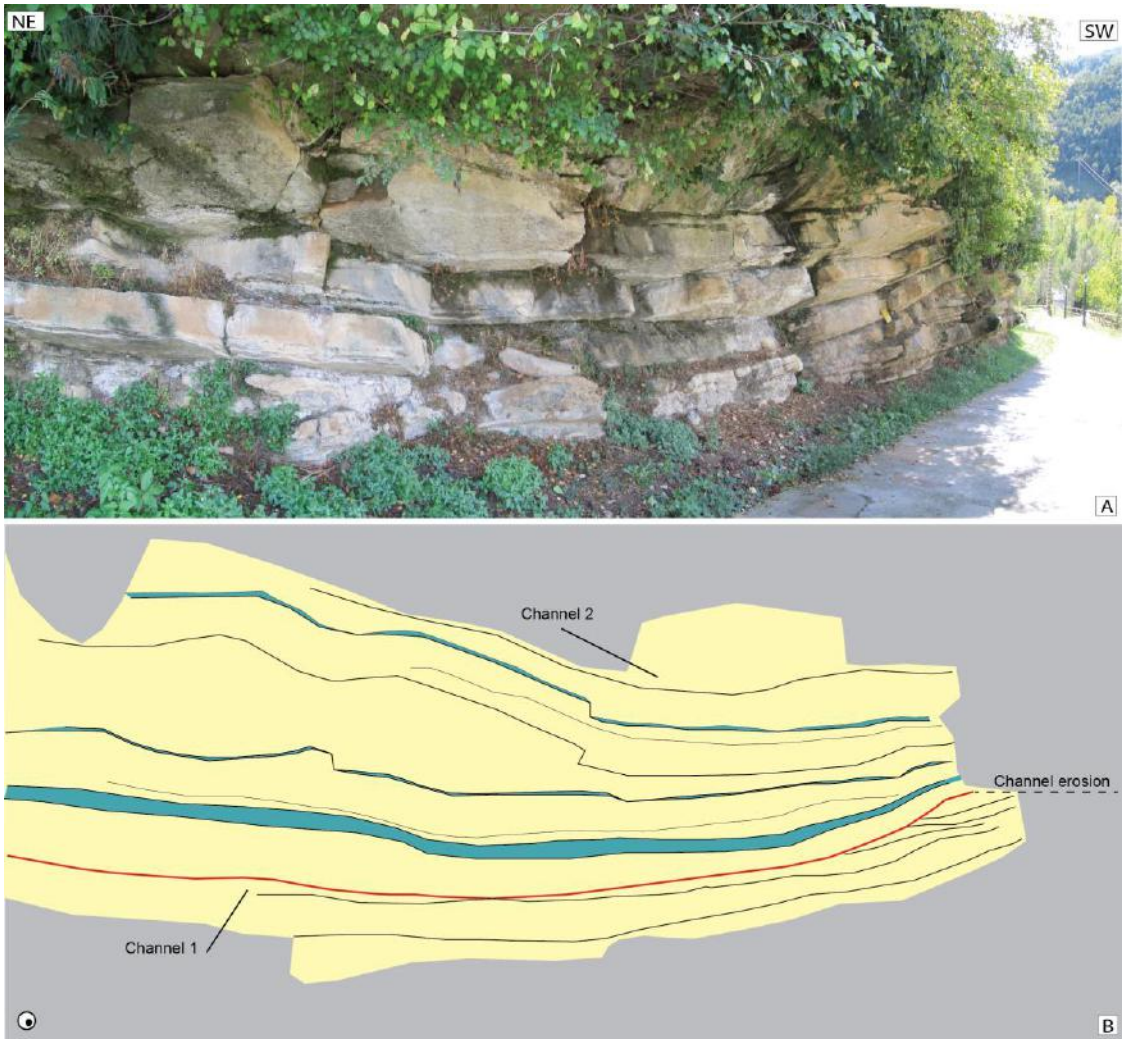

Figure 9.3. (A) Photograph and (B) interpretation of Ainsa III System showing channelised sandstones. Path connecting Boltaña old town to the N-260 (Locality 18). Yellow notebook used as scale (15 cm). Palaeoflow is approximately out of outcrop. Modified from Pickering *et al.* (2015).

9.3.2 Hybrid event beds

Hybrid event beds are defined as a type of SGF deposit that show characteristics intermediate between turbidites and debrites, 'linked' as part of the same event bed (Haughton *et al.* 2003; Talling *et al.*, 2004; Amy *et al.,* 2005; Haughton *et al.*, 2009; Fonnesu *et al.*, 2015), discussed in Chapter 2. Although HEB deposits characteristically have an irregular basal surface, they are generally sheet-like in geometry and typically have brecciated sandstones within the H3 division (Haughton *et al.,* 2009). As presented in this study (Chapter 6), at outcrop, the erosive basal surfaces of Type IIa MTDs are also observed as irregular, however are generally 'channel-like' or 'U' shaped perpendicular to palaeoflow (Figures 6.11 and 6.12, Chapter 6). From a few small-scale scours, the basal scour surface is observed as 'flute-like' in geometry, parallel to palaeoflow (Figures 6.15 and 6.16, Chapter 6). Type IIa MTDs showing basal erosion are able to support large, angular semi-consolidated sandstone rafts (from a few centimetres up to 2.8 m) incorporated into the base of the deposit (Figure 6.3, Chapter 6). The sandstone rafts are sub-angular to angular, suggesting sufficient time had passed to enable the substrate to consolidate prior to debris-flow erosion. This is compared to examples where linked debrites were deposited contemporaneously to the sands below, showing sandstones to appear brecciated, or injected (Figure 2.6, Chapter 2). In terms of grading, the H3 division is typically ungraded, shown in Figure 9.4 from Fonnesu *et al.* (2015). This example is compared to the thin-section analysis presented in Chapter 7, where Group 1 MTDs that preserve basal erosion *in situ* at outcrop show higher grain contents and appear 'graded', confirmed by the laboratory study undertaken in Chapter 7. These results showed coarse and fine-grained clastic material fining and decreasing in abundance vertically (Figure 7.4). It is likely the graded signature was a result of entraining loosely consolidated sands on the seafloor in a sandy submarine fan setting. Grading is not predictable in Type IIa deposits that may have been erosive up-dip (i.e., Group 3 deposits, Figure 7.6, Chapter 7).

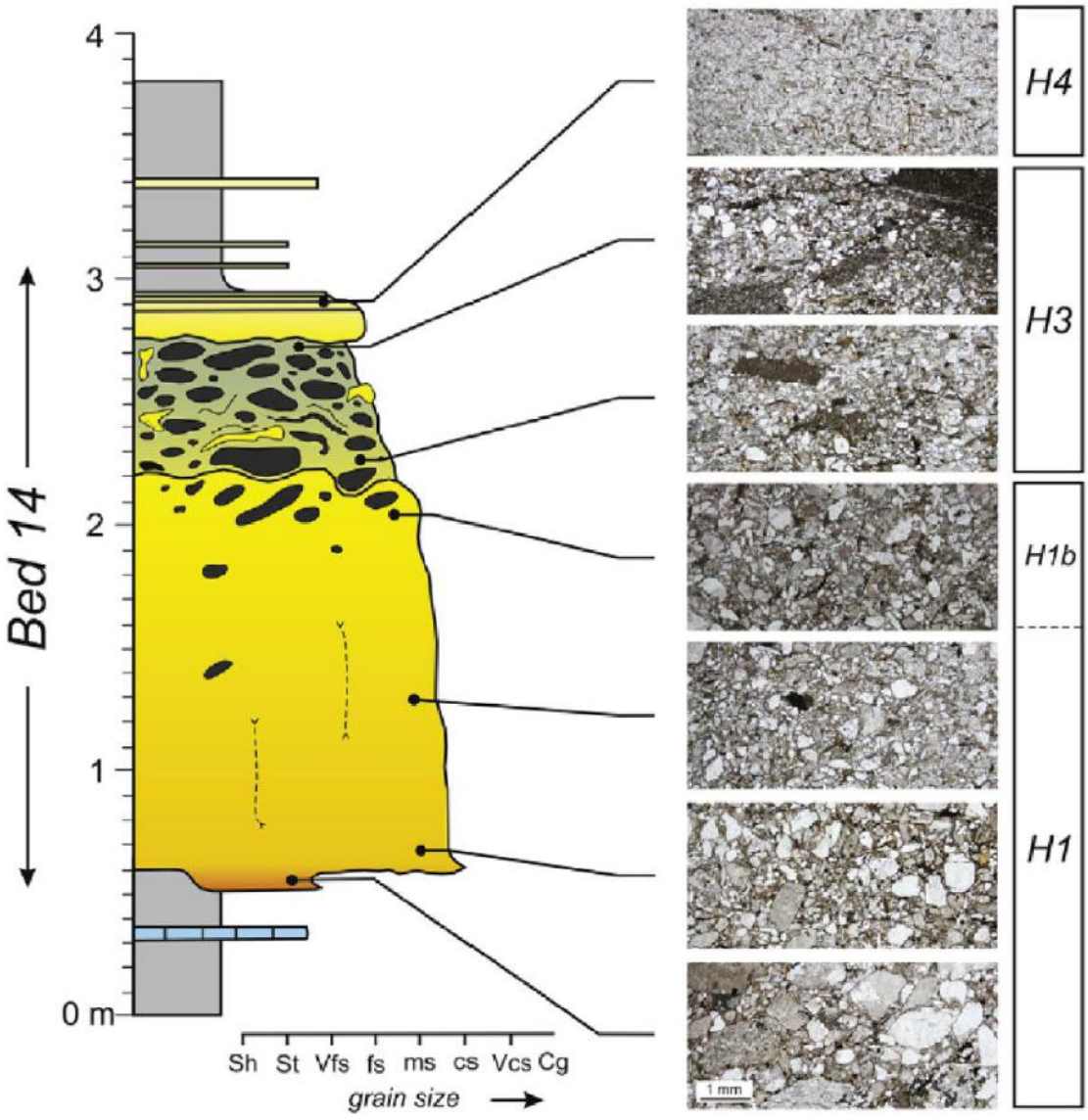

Figure 9.4. Bed profile and parallel light thin-section photographs of sandstone textures of a typical tripartite "event bed". Note ungraded structure in H3 interval from base to top. Figure from Fonnesu *et al.* (2015).

HEBs are typically recognised in lateral and distal settings such as fan-fringe environments due to longitudinal segregation of the flows (Haughton *et al.*, 2003, 2009). The longer the flow, the more differentiated the head and tail. The palaeogeography of the Ainsa Basin was located in a high-energy proximal base-of-slope environment, where numerous erosively-based MTDs are observed at outcrop. This suggests that the environment of deposition between HEBs and erosively-based MTDs are different (i.e., proximal *versus* distal).

9.3.3 Submarine debris-flow erosion

In some cases, subaerial erosion may be analogous to erosion in a submarine setting. For example, where decicentimetre-scale 'block plucking' is observed by Stock and Dietrich (2006), San Gabriel Mountains, Southern California (Figure 2.11, Chapter 2). However, in a submarine environment, wet-bed semi-lithified sediments may provide a substrate more susceptible to erosion when loaded, such as where sandstone blocks several metres in width are observed as 'plucked' from underlying sandstone beds (Figure 6.3, Chapter 6). In a submarine environment, if the sedimentation rate is low, then following accumulation, lithification or cementation can occur rapidly. However, if the sedimentation rate is high, then lithification is interrupted and continues again in a period of low sedimentation (Zankl, 1969). In an active submarine setting, it is likely that not enough time passed for complete lithification to occur between depositional events. The seabed was likely to be partially consolidated or partially- to fully-saturated with water, and the most recent deposits were likely to be 'soupy', as shown in DSDP data (Figure 2.20, Chapter 2).

This study has identified five erosive mechanisms of Type IIa MTDs, varying in scale of erosivity at outcrop, including plucking, ploughing, striating, scouring and injection processes. The model describing the 'plucking' mechanism described and outlined in Chapter 6 (Figure 6.30) is based on outcrop observations, with experimental data applied to test the idea of negative pressure created behind the head of a highly-concentrated flow.

A model is presented here to show how multiple events may result in deeper erosive scours on the seabed. As described in Chapter 2, as debris flows bypass a static position on the seafloor, the underlying saturated wet-bed sediments may become continuously weaker caused by pounding, cyclic and undrained loading, with cyclic loading attributed to multiple surges in a given flow. This effect may destabilise the structure of the underlying substrate by reorganising the grains and creating 'memory' of erosion (e.g., Mangeney *et al.*, 2010), where eventually, the substrate may become looser and more susceptible to erosion. Multiple events, from different surges of the same flow (e.g., Davies, 1990) or different flows related to one mass failure event (e.g., retrogressive failure), could potentially increase the chance of erosion (Figure 9.5). The transition from non-erodible to easily erodible substrates

could enhance the effect of erosion; e.g., muddy-slope material to submarine fans dominated by clastic grains (e.g., Mangeney *et al.*, 2010).

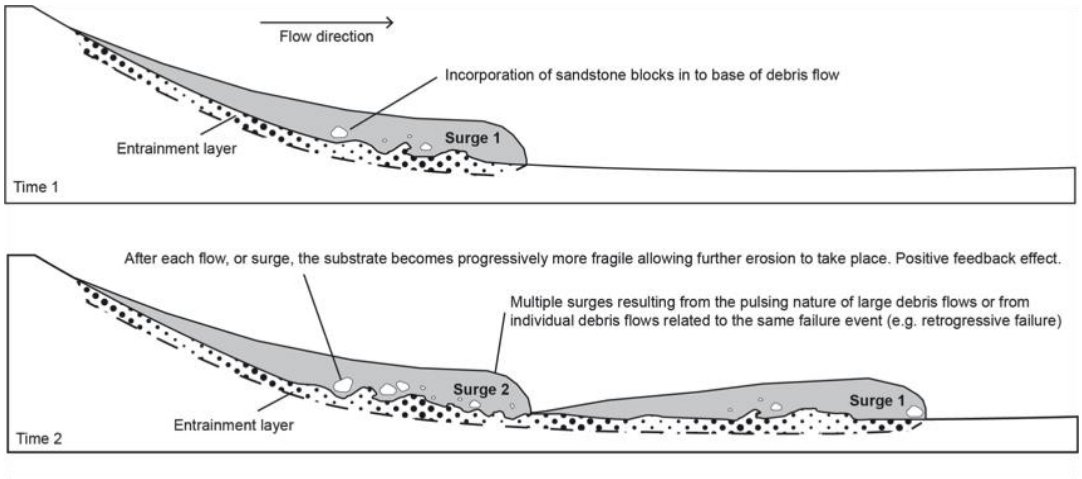

Figure 9.5. 2-D model showing progressive entrainment of the underlying substrate into the base of erosive debris flows.

9.3.3.1 Megascours

Megascours observed in the Ainsa Basin (Figures 6.20, 6.21 and 6.20, Chapter 6) may have formed solely through erosion and bypass of high velocity SGFs, such as turbidity currents, that were initiated from a seismically triggered large-scale collapse of the shelf or upper slope, resulting in substantial volumes of sediment to be remobilised and redeposited into deep-water. For example, megafluted surfaces (so-called 'ornamented surfaces') documented from the Ross Formation, County Clare, are interpreted to result from 'exceptionally-sized' or anomalous turbidity currents, with megaflutes up to 5 m deep that occur on discrete, mappable surfaces that are laterally traced into turbidite channels and mud-filled gullies, and can be lined with intraformational conglomerates (Elliott, 2000). However, megascour observations in the Ainsa Basin suggest other processes are involved, not solely erosion from bypassing turbidity currents. At outcrop, the bases of megascours are scalloped and pitted with pebble marks. The infill of these scours is typically back-filled with MTDs, MTCs and other heterolithic sediments.

Group 3 deposits identified from the thin-section study (Chapter 7) suggest that when the correct conditions are met, erosion of the seafloor takes place (though

either scouring, ploughing, bull-dozing and/or block plucking). Instead of freezing *in situ*, the flow had sufficient momentum to erode and bypass the seafloor, creating an open 'channel'. At this stage, a new equilibrium profile or grade of slope is established, providing a preferential pathway for other flows to bypass the same location (e.g., channelised debris flows in Bernhart *et al.*, 2012). Over time (such as the time taken of a large-scale shelf collapse event to subside), it is likely that the channel would be subject to repeated erosion, not only through debris-flow processes, but also erosion from turbidity currents. Repeated erosion may create a wider and deeper 'channel-like' geometry, analogous to sandstone-filled channels, which are formed from the continuous 'tapping' of a sand-rich source, e.g., near-shore sandy beach sediments. Dominantly mud-filled megascours may result from mass failure of a mud-rich source, such as failure of a mud-dominated shelf. This data complements the interpretation of Pickering and Corregidor (2005), where a shelf scenario of the Ainsa Basin is favoured.

Heterolithic infill of these scours (typically comprising MTDs and thin sands observed at outcrop. Figures 6.20, 6.21 and 6.22, Chapter 6) is interpreted because of continuous failure of the unstable shelf setting. Based on outcrop observations, measurements and information in the scientific literature, a model of the development of megascours in a submarine setting is proposed (Figure 9.6). Scours are likely to form in the vicinity of hydraulic jumps at a change in seafloor gradient, such as at the base-of-slope setting, or where there are changes in gradient on the basin-floor. The down-dip geometry of scours formed by bypassing erosive cohesive flows is likely to be dependent on the erosional process involved. Once a flow is ignited and travelling down-dip towards the base-of-slope, there is some evidence to suggest that local-flow conditions form flute-like geometries (Figures 6.15 and 6.16, Chapter 6). This could suggest that some scours (both small- and large-scale) are flute-like in geometry, and are therefore relatively isolated in plan view (Figure 9.6-B). Conversely, seismic data reveals the presence of other larger scours to be laterally extensive and longitudinal in plan geometry, documented up to 60 km in length (e.g., Moscardelli *et al.*, 2006). In seismic data, some MTDs reveal the presence of rafts up to 350 m in height, termed megaclasts (Jackson *et al.*, 2010). Remobilised blocks such as these are likely able to scour and striate the seafloor on their down-dip journey and could form such longitudinal scours, as observed in Moscardelli *et al.* (2006) and Omosanya and Alves

(2013). Another mechanism of the formation of these longitudinal geometries could be from multiple events able to bulldoze the substrate. Basins much larger than the Ainsa Basin are likely to form much larger-scaled scours, as documented from continental margin failure (Figures 1.5, 1.19 Chapter 1 and Figure 9.8, this chapter). The amount of failed sediment to occur in the relatively small Ainsa Basin, which formed in response to a propagating thrust sheet (Desegaulx *et al.*, 1990), is not deemed likely to form erosive scours from these types of processes.

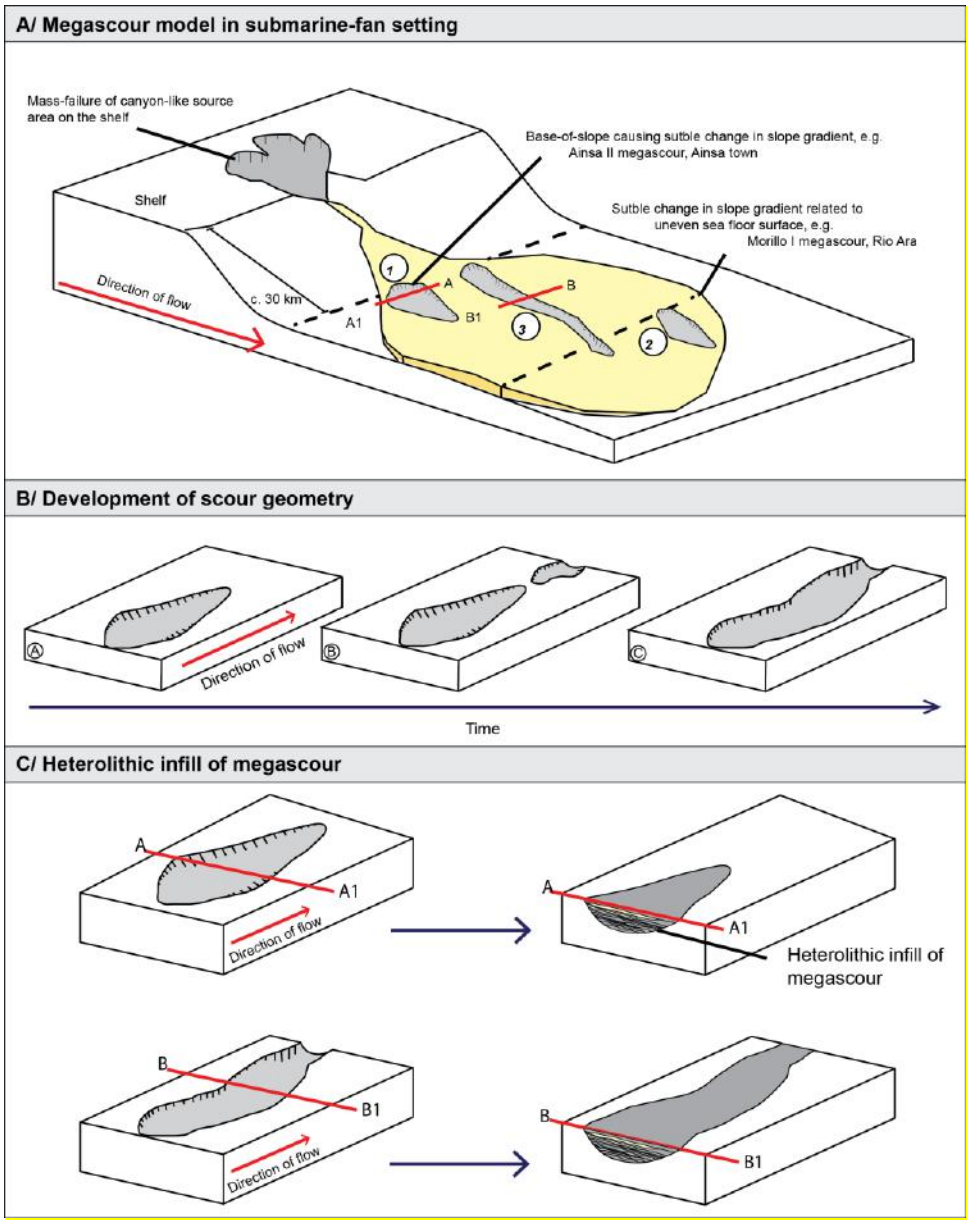

Figure 9.6. (A) Model of megascours in a submarine fan environment, based on the Ainsa Basin (B) Development of megascours. Scour development may be incremental i.e., phases A, B and then C, or scour may exist as A or C only. Moscardelli *et al*. (2006) show megascours up to 20 km in length. (C) Heterolithic infill of different geometries of megascours.

9.3.3.2 Identification of scours in seismic data

Bakke *et al.* (2009) created synthetic seismic models of the Ainsa II Fan sandstones, which included the Ainsa 'megascour' as interpreted in this study (but interpreted as a channel cut-and-fill by Bakke *et al.*, 2009) (Figure 9.7-A). Figure 9.7-B shows a 32 Hz synthetic seismogram based on an interpreted density distribution, which is a frequency typical in seismic data of deep-marine deposits in the North Sea (i.e., the Buzzard Field). This model highlights that such erosive features (dominantly filled by mud-rich sediments), can be poorly defined in seismic data and thus heterogeneities in sandstone distribution can occur in a scale such as the Buzzard Field.

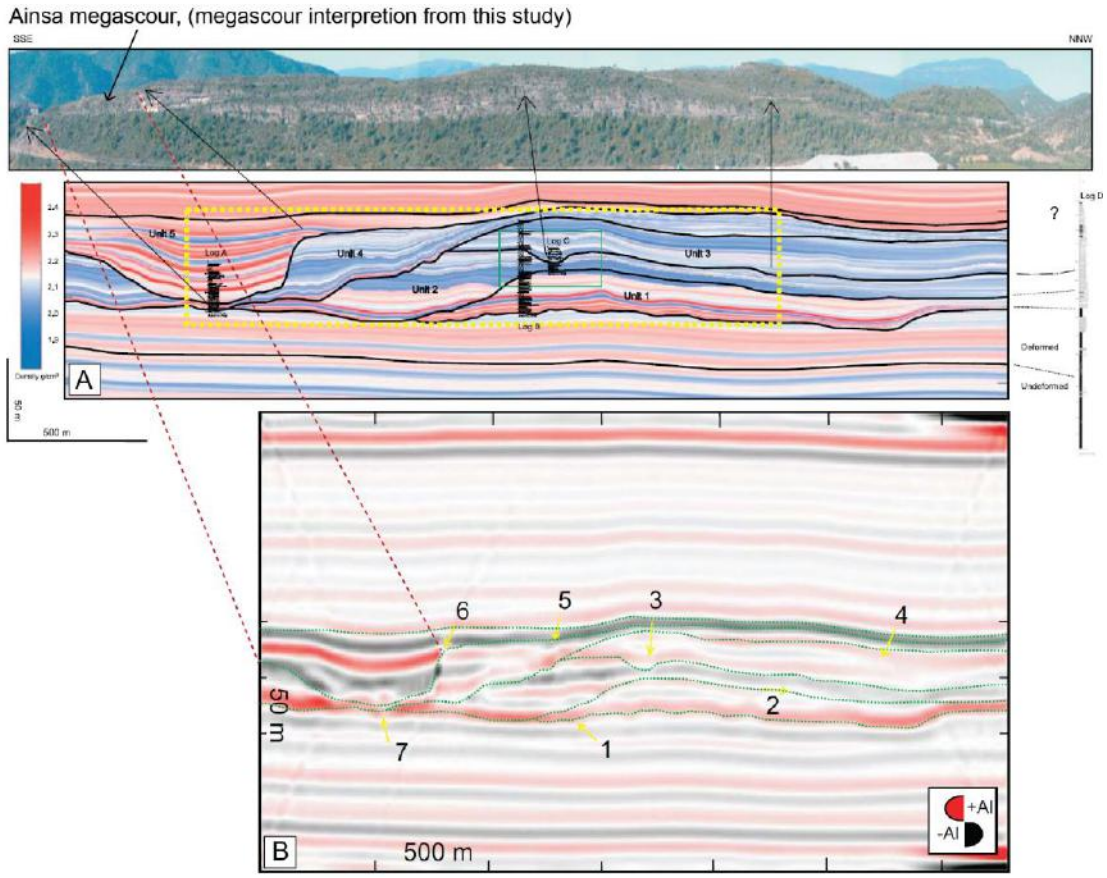

Figure 9.7. (A) Photo panel and density distribution map of the Ainsa II sandstones north of Ainsa. Blue reflects low density (sandstone) and red represents high-density (mudstone) (B) 32 Hz synthetic seismogram showing frequency compared to the North Sea. Figure modified from Bakke *et al.* (2009).

Based on observations in this study, it is suggested that the Ainsa Basin was a high-energy, proximal deep-marine basin. In the event of large-scale slope and shelf failure, multiple debris flow events were likely to be produced. As these large-scale

events travelled downslope and encountered a change in gradient, they were able to erode the sediment by scouring, striating and explosively interacting with wet-bed sediments that resulted in seismic-scale channel-like megascours. The down-dip correlative deposits of these larger-scaled events are not always documented at outcrop and therefore are likely to be recorded in the further down-dip Jaca Basin (Figures 6.18 Chapter 6). In other cases, smaller-scale events scoured the seafloor. However, in doing so, they lost momentum and energy and froze *in situ* preserving mechanisms such as plucking, ploughing, striating and injecting (Figures 6.3 to 6.18, Chapter 6).

9.4 OBSERVATIONS AND ALTERNATIVE INTERPRETATIONS FROM GLOBAL OUTCROPS

Scour features, such as those presented in this study, are not new to the scientific literature, however the erosive mechanisms behind such features are only starting to be unravelled. The seismic image in Figure 9.8 shows what has been interpreted as a channel-like scour showing near-vertical lateral margins and a relatively flat base against a horizontal high amplitude seismic reflector, published in Posamentier and Martinsen (2011).

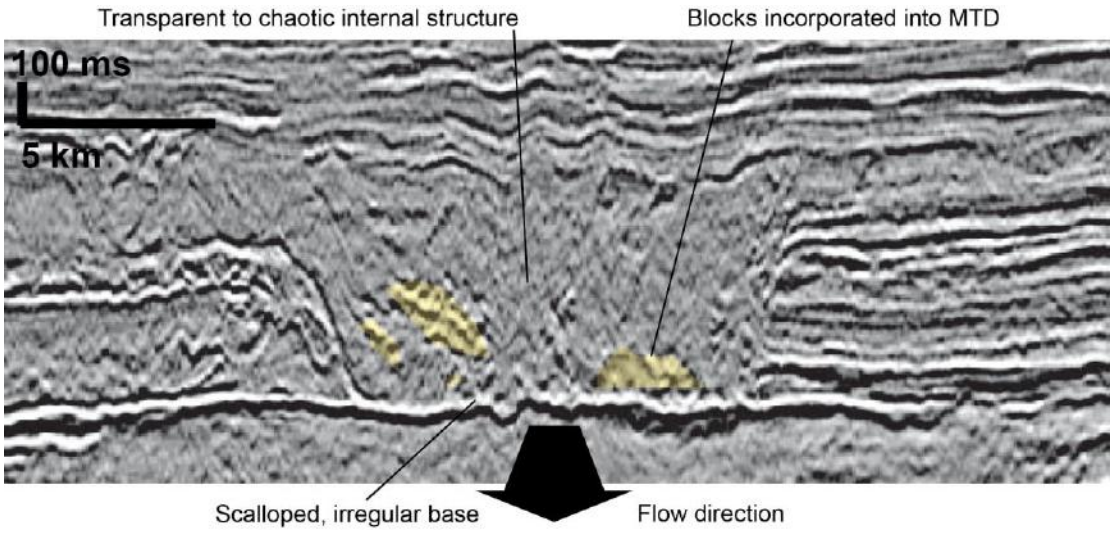

Figure 9.8. Near-vertical erosional lateral margins of MTC, showing scalloped basal surface and potential blocks incorporated into MTC, as observed at outcrops in the Ainsa Basin. Figure modified from Posamentier and Martinsen (2011).

The internal seismic character is transparent- to chaotic and contains some discordant truncated high amplitude reflectors. The infill of the scour is interpreted as an MTC. Using ancient analogues from the Ainsa Basin, debrites are observed to plough into the seafloor forming broad 'U-shaped' geometries, or some examples show nearly vertical margins, with sandstone blocks incorporated into the base of the deposit. Using field-based examples, it is possible to speculate that the chaotic seismic facies is a debrite showing steep basal erosion and the 'floating' discordant high amplitude reflectors are rafts incorporated into the flow from the base, or marginal of the scour surface.

Cossey (2011) presents ancient outcrop data from the Upper Paleocene Chicontepec Formation, Mexico. The sedimentary succession is composed of thin-bedded turbidites and MTDs (coherent and semi-coherent slumps and debrites), interpreted as a slope environment deposited in a deep-marine foreland basin, analogous to the Middle-Eocene Ainsa Basin, Spanish Pyrenees. Cossey (2011) describes a roadside outcrop showing a debrite, ~ 26 m thick, that appears to fill a "*void*" (or, in keeping with terminology presented in this thesis, a channel-like feature) with ~ 5 m of basal erosion (Figure 9.9).

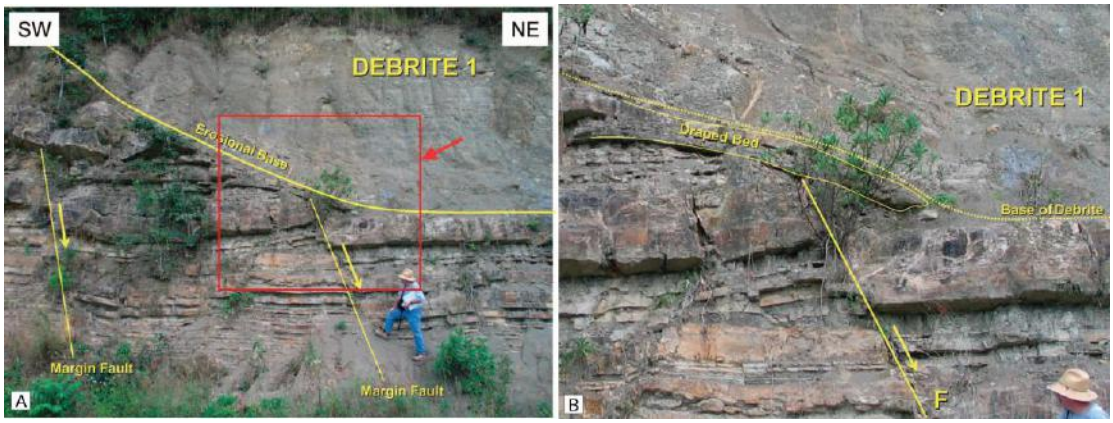

Figure 9.9. (A and B) Debrite forming a channel-like scour at outcrop. Upper Paleocene Chicontepec Formation, Mexico. Figure modified from Cossey (2011).

Two faults are observed at the basal erosional margin of the debrite. On top of margin fault (Figure 9.9), a thin, 'draped' sandstone bed is preserved in the pre-debrite strata. The significance of this bed has not been interpreted in the publication, stating only that the draped bed was at least partially consolidated when the erosional feature occurred. Immediately above the channel-like feature is the debrite. Cossey

(2011) states that "…*the actual debris flow, which filled the void, was most likely a non-erosional debris flow and would have filled the failure void sometime after the event… and since the debris flow was a laminar flow, and most likely non-erosional, the erosional void must have been created by another sedimentary process*", although does not speculate what process was involved. The publication also observes the same debrite exposed at another locality (down the road), where car-size pieces of ripped-up stratigraphy are incorporated into the chaotic deposit.

Based on debrites showing basal scour and erosion documented in the Ainsa Basin, it is proposed here that there are at least two episodes of erosion at this outcrop, as presented in the depositional model (Figure 9.10). Fault-1 does not penetrate the 'draped' bed and Fault-2 also does not appear to penetrate the sedimentary sequence to the right of the figure. This suggests that fault movements occurred early in the depositional sequence. The first episode of erosion must have occurred immediately after fault movement during Time 2, where the seafloor was 'smoothed'. Sandstones depositing the draped bed infilled topography created from the fault. During Time 4, ~ 1.5 – 2 m of medium bedded sandstones were deposited. The debrite was inferred to be the second episode of erosion, which appears to truncate all the sandstones above the draped bed, showing a channel-like geometry (shown in Time 5, Figure 9.12). As discussed above, the debrite infilling the scour is correlated down-dip from this outcrop and exposes car-sized sandstone rafts incorporated into the debrite. Based on evidence provided in the Ainsa Basin, it seems possible that these sandstone rafts were eroded from the stratigraphy and incorporated into the debrite flow and were subsequently deposited down-dip.

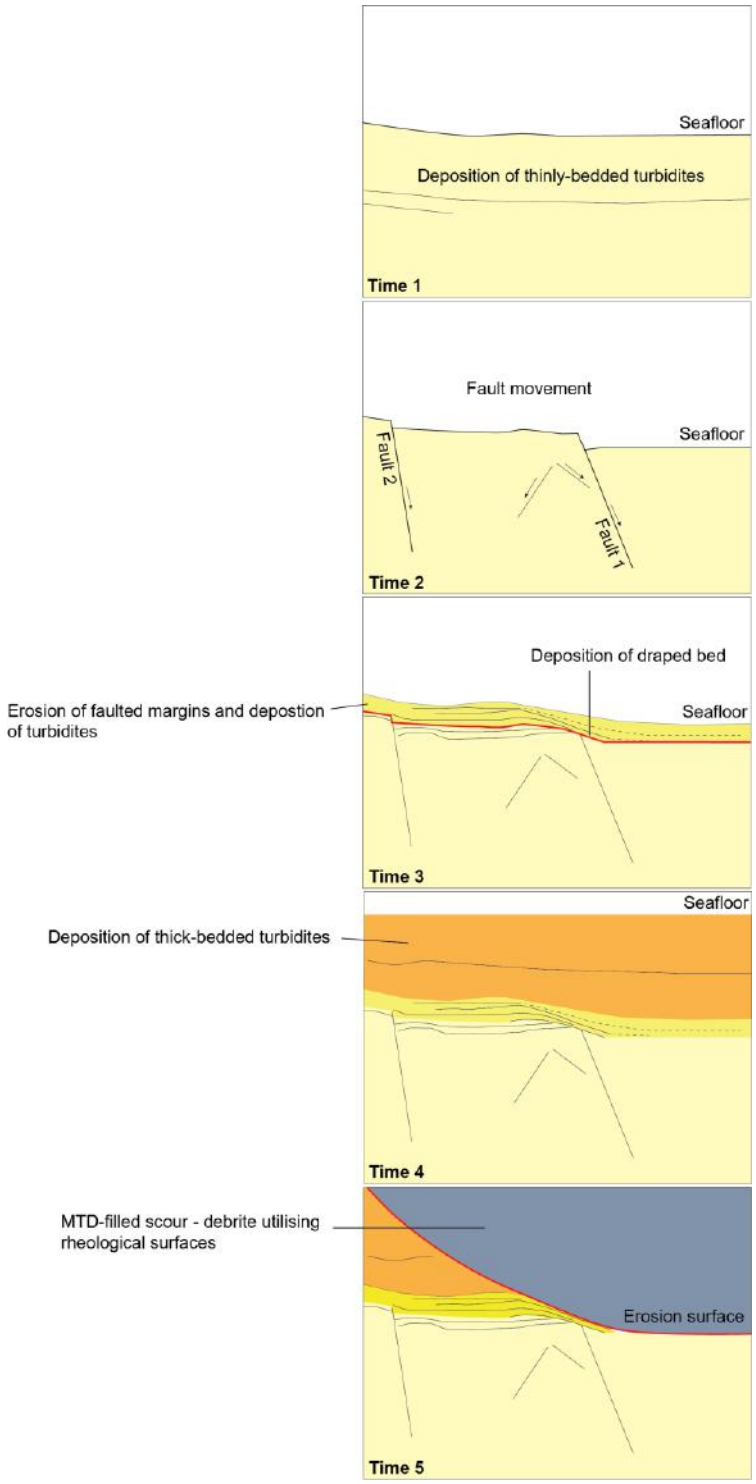

Figure 9.10. Based on outcrop studies showing erosive basal surfaces of MTDs in the Ainsa Basin, this figure shows a re-interpretion of the 'void' presented in the Upper Paleocene Chicontepec Formation, Mexico (Cossey, 2011). A five-step process is suggested: (Time 1) deposition of thinly-bedded sandy SGF deposits; (Time 2) fault movement; (Time 3) erosion from bypassing flows and deposition of thin sandy SGF deposits, forming the 'draped bed'; (Time 4) deposition of thick-bedded sandy SGF deposits; (Time 5) erosive debrite forming a channel-like feature at outcrop.

9.5 APPLICATION OF FINDINGS IN THIS STUDY

The results of this study should find wide applicability for the internal structure, erosive potential, geometry and stratigraphic positioning of proximal basin-floor scale MTDs and MTCs in other deep-water basins. Many of the MTDs and MTCs observed in the Ainsa Basin are below seismic resolution (i.e., < 25 m in thickness). Field observations and thin-section analysis identify basal erosive debris flow processes documented from Type IIa deposits. This study explores to see how such asperities can affect sandy submarine fan-systems, an important factor for the exploration of hydrocarbons. The Ainsa Basin appears to contain two end-members of erosive debris-flow deposits: (1) small-scale local erosion created from individual events, and: (2) large-scale mud-filled scour geometries (up to ~ 1 km width and ~ 70 m deep), interpreted as created from multiple events.

Although many studies of seismic data in submarine environments show examples of erosive scours formed from MTDs, they generally do not discuss the processes associated with erosion. Outcrop studies from scientific literature also highlight how the laminar nature of debris flows can discourage earth scientists to interpret submarine debris flows as erosive (e.g., Cossey *et al.*, 2011). Although the erosive mechanism(s) of MTDs (typically Type IIa MTDs) remain poorly understood, requiring further numerical and experimental work, particularly concerning the upscaling to large and complex flows (e.g., multiphase flows), field evidence provides an important tool to better document MTDs and their geometrical relationship with the substrate, including any erosional features. Such processes are not easily replicated in experiments. Based on findings from this study, a flow having either laminar, turbulent or even both flow regimes (e.g., concentrated density flow), does not appear to be the principle mechanisms to make a debris flow erosional. Whilst some flows may have sufficient energy to continue flowing after erosion, perhaps due to mass, acceleration and velocity in the flow, in other examples, frictional forces override the kinetic forces and the flow subsequently freezes *en masse*. This is one reason to suggest that debris flows may only erode locally, unless in exceptional large-scale events, or in multiple large-scale events. Understanding how and when MTDs erode is not easy to predict. However, documenting erosive features in the Ainsa Basin (at the slope, base-of-slope and within basin floor settings) suggests that MTDs are most erosive when they when they encounter changes in gradient, or when

flows are accelerating and/or travelling at their highest velocity, such as in a proximal submarine setting.

In hydrocarbon reservoirs, erosion of a sandy substrate (with 'net pay') is replaced by a muddy deposit, has clear implications on sandstone reservoir presence. Firstly, field evidence shows that local erosion from an individual erosive flow is localised, incising into the sandy substrate up to ~ 2.8 m (Rio Ara outcrop Figure 5.3, Chapter 5). Erosion from these field examples may cause heterogeneities of a sandy reservoir, however in the context of a large producing hydrocarbon fairway, i.e., a 70 m-thick sandstone reservoir such as the B4 reservoir, Buzzard Field, North Sea, these heterogeneities are not believed to be significant in terms of estimating reserves. It should be noted that this might depend on the frequency of erosive debris-flow events. Secondly, field evidence shows that the potential failure of a mud-rich source, i.e., a mud-dominated shelf, may cause a series of high magnitude debris flows that enable more erosion per event, as seen in subaerial field observations where higher volume flows cause more erosion (e.g., Breien *et al.*, 2008). These events are believed to be significant in terms of degrading a sandstone reservoir as they can erode up to a maximum 17.5 million m^3 of potential reservoir, seen in the Ainsa II sandy submarine fan megascour, Ainsa town, assuming a high net-to-gross and based on a 1 km wide, 35 m thick and 500 m long scour.

Methods similar to those used in this study could find wide application in the hydrocarbon industry. At outcrop, debris-flow deposits are typically 'graded'. In a subsurface setting, core samples collected from base-to-top of debrites could be made into thin-sections and analysed using point-counting methods to evaluate compositional and grain-size trends and, therefore, possible flow processes as determined in this study. Problems encountered in this method include incorrectly identifying individual MTDs within MTCs. The approach adopted in this study could potentially provide further evidence for the origin of mud-filled channels and, therefore, reduce uncertainties in reservoir heterogeneity currently faced in deep-marine hydrocarbon exploration.

9.6 CONCLUSIONS

In summary, the principal conclusions from this research are:

(1) Outcrop studies emphasise how typically muddy, impermeable non-reservoir MTDs and MTCs can affect reservoir-grade sandstones.

(2) The presentation of a classification scheme for MTDs provides a method for the description of MTDs and MTCs linked to their deep-water environmental setting (400-800 m water depth).

(3) MTDs and associated MTCs form a volumetrically significant component in many deep-water basins, including the Ainsa Basin. Facies associations and outcrop descriptions of MTDs and MTCs capture small-scale heterogeneities of potential submarine-fan reservoirs not captured in seismic datasets:

   a. The most cohesive MTDs (Type Ia sediment slumps/slides) form the greatest topographic relief, which are likely to form depocentres that pond or compartmentalise succeeding deposits. Roughness and topography can produce turbulence that could potentially further modify the topographic expressions of MTDs. In the Buzzard Field, the B2 and UB4 MTCs show complex topography making sandstone thickness difficult to predict.

   b. Different types of channel architecture associated with MTDs are observed at outcrop. Submarine channels are able to incise into MTDs and backfill with ungraded sand from one sandy SGF, or channels that laterally accrete along preferential flow pathways. Lateral accretion could be related to a topographic barrier to flow, formed from cohesive properties of the underlying MTD, or subsidence of the newly deposited MTD may cause a preferential lateral deposition of a depositing flow.

   c. Sandstone rafts within Type IIa MTDs typically show varying degrees of disaggregation. This suggests shear within and at the base of debris flows as they travelled down-dip, likely to result from differential shear stresses and a weakly turbulent flow.

d. Type IV, ‘transitional facies’ may record the depositional product of mass failure ignition processes, documenting the downslope evolution of mud-rich sediment slumps/slides to debris-flows, near to the source of failure.

(4) The abundance of woody material, disarticulated and unbroken bioclastic material (such as echinoid spines, solitary corals and gastropods) show redeposition from a shallow-marine and terrestrial sediment source area into deep-water. Petrographic and compositional observations from pebble analysis in chaotic mudstones and pebbly sandstones have provided an insight into sedimentary sources. Alluvial fans (such as the Sis palaeovalley) from the rising hinterland are candidate non-marine sources for the input of substantial amounts of pebble-grade material into the marine Ainsa Basin.

(5) Allocyclic and autocyclic processes can affect the type of slope and shelf-edge failure, which may result in spatial thickness variations. One example is failure of an unstable out-of-grade slope that may deposit a major basin-wide marker bed (i.e., the megaturbidtes in the Jaca Basin as documented by Labaume et al., 1987). With the evolution of the Ainsa Basin, tectonic controls likely resulted in changing seafloor and basin-margin gradients. Such changes are reflected in the nature of the MTDs documented from different sandy systems within the basin. At times of higher seafloor gradients, systems contain abundant coarser grain-sizes within the MTDs (i.e., conglomerates and pebbly sandstones), and a greater proportion of Type II MTDs (between 50 to 60 %). At times of lower overall seafloor gradients (e.g., during deposition of the Guaso System), the MTDs are dominated by Type Ia facies (sediment slides/slumps).

a. Depositional environments have been classified into: intraformational (intrafan); slope; base-of-slope; base- and marginal- to depositional systems, which enabled a broad overview of spatial and temporal information to document how thickness and facies change within a relatively small proximal deep-marine system. This included approximate distance travelled from the source area (proximal to distal settings) and stratigraphic locations identified in the field.

b. A higher percentage of Type II (debrite) facies compared to Type Ia, b (sediment slumps/slides) are documented in distal settings, beyond the base-of-slope, suggesting that as flows travel further down-dip they become more disaggregated.
c. The average thicknesses of MTDs decrease distally to suggest the dominant cohesive nature of these deposits result in a thinning down-dip. However, some of the thickest discrete events (> 10 m) are documented in distal settings, likely to be related to the significant large (and rarer) failure events that remobilise the largest volumes of sediment. These large-scale events were likely to have also deposited in the Jaca Basin, down-dip of the Ainsa Basin.

(6) Comparing aspect ratios (width to thickness) from outcrop scales to published literature studies shows an increased R^2 value (from 0.51 to 0.69, Figure 5.22, Chapter 5). This highlights how large numbers of MTCs are missed at seismic scales, which are typically located within sandy packages (i.e., intraformational MTDs). These MTCs are largely not accounted for in net to gross parameters, typically defined by petroleum geologists. This highlights how smaller-scale deposits can be missed when capturing data with a coarser resolution, such as from seismic datasets. Larger deposits, documented in all but intraformational MTCs, are comparable to MTCs documented in the Buzzard Field.

(7) In the absence of basin-bounding faults in the Ainsa Basin (such as the west-to-east trending faults that bound and compartmentalise the Buzzard Field into five distinct depocentres), the majority of MTDs and MTCs are interpreted as dominantly sourced from the slope. The thickest Buzzard MTCs documented in this study (B2 and UB4) are also interpreted as sourced from the slope. The B2 MTC shows a less-confined plan geometry compared the LB4 and UB4 MTCs to suggest minimal fault movement in the early stages of basin evolution. It is however likely smaller MTCs were sourced from destabilised fault margins during later deposition and fault movement.

(8) A key result of this research shows that erosion of deep-water sandstone reservoirs is a significant feature when describing MTDs and MTCs in seismic

data (if the vertical resolution permits this type of analysis). This study suggests that under appropriate conditions, MTDs, particularly debris flows can be extremely erosive. It is likely more than one factor determines the erosivity of debris flows, which is not easily determined from data collected in this study alone. Understanding the erosional and depositional processes of MTDs is still evolving to some degree and the flows that deposited debrites in this study appear to be some of the most erosive flows in the proximal Ainsa Basin. Five interpreted erosive mechanisms are documented at the base of MTDs, which include: plucking; scouring; ploughing; striating, and injecting into lower sandy SGF deposits. The amount of erosion able to occur from one event will likely reflect the magnitude and volume of failure, such as from a small basin-floor fan in an isolated body of water (such as a lake), up to continental margin failure. Rare and large tectonic triggers probably resulted in extremely large and catastrophic basin-margin failure events and the initiation of SGFs, including debris flows capable of large-scale erosion of the seafloor. Based on the presence of about 10 megaturbidites in the Jaca Basin and a comparable number of very thick MTDs in the Ainsa Basin, such events had a recurrence time in the order of 1 million years and, therefore, represent extreme high-magnitude seismicity.

(9) An investigation into the internal characteristics (e.g., grain-size distribution and fabric) of Type IIa MTDs has identified unique distinctions between MTDs that have eroded sandy substrates on the seafloor and documenting the smaller-scale (i.e., bed-scale) features. This has enabled further interpretation of larger-scale features, such as megascours. The thin-section study found that MTDs likely responsible to form megascour features belonged to a unique group of deposits, termed Group 3 deposits. These deposits are interpreted as the correlative down-dip deposits of flows that were erosive up-dip. Orientated fabric is observed in some rock samples at the base of a debrite to suggest shear at the base of some erosive debris flows. Failure to identify erosion in core data may lead to unexpected results during development drilling, for instance what appears to be a sand-filled channel-feature may be a mud-filled megascour, if created from retrogressive failure of a muddy slope.

(10) The thin-section study of debrites in the Ainsa Basin suggests that as debris flows erode, they entrain material into the base of the flow and in some cases can pick-up the compositional signature of the substrate below. From this, it is concluded that in the Ainsa Basin, a narrow shelf existed where wave-action (and, possibly, tidal processes) sorted and winnowed sediment according to density, therefore providing a compositional archive between turbidity currents and cohesive debris flows. Sandy SGF deposits were likely sourced from a sandy, littoral, nearshore and shallow-marine environments that were compositionally distinct and dominated by carbonate grains. The non-erosive cohesive flows, however, were probably sourced from muddy outer shelf and upper-slope environments dominated by relatively denser quartz grains. This setting may facilitate identification, as the compositional signatures of Type II facies are enriched in carbonate grains, to suggest flows were likely to have been erosive prior to deposition. The compositional analysis presented in this study shows that not all deposits epitomise the character of an enriched sandy SGF signature, which may be related to the source area, partly controlling composition of the sandy SGFs.

(11) In the Ainsa Basin, the Banastón and Morillo systems have a greater proportion of MTDs that show basal erosion compared to other systems in the basin. Data presented in Chapter 5 shows that the Banastón and Morillo systems comprise a higher abundance of Type IIa MTDs, supporting the idea that the Ainsa Basin was likely to have higher gradients during time of deposition (e.g., Bayliss and Pickering 2015a, 2015b). This may suggest that slope gradient is a primary control on the erosive ability of any debris flow in a submarine setting, an observation in subaerial settings from Breien *et al.* (2008) and Berger *et al.* (2010), where a change in gradient increased the amount of entrainment in a debris flow (Figure 2.13, Chapter 2).

(12) It is critically important to compare basins of both similar size and tectonic setting, as MTD processes appear to operate at different levels, such as those identified in seismic and literature studies (e.g., Barents Sea passive margin [Hjelstuen *et al.,* 2007], or the Ursa Basin, Gulf of Mexico [Sawyer *et al.,* 2009]). Seismic-scale sedimentary processes that occur on such continental-wide margin failure are not observed in the Ainsa Basin, or the Buzzard Field.

9.7 LIMITATIONS AND FUTURE RESEARCH RECOMMENDATIONS

Limitations of the study in the Ainsa Basin include the lack of down-dip exposure of single (correlateable) events, or the absence of major event marker beds. This has meant that field observations are mostly from 2-D cross-sections across strike of deposits. Investigations in this thesis have highlighted a number of aspects of MTDs and MTCs, which require further work to improve our understanding of debris-flow processes and their deposits. Further work should include:

(1) Documenting facies pairs (i.e., Figure 4.11, Chapter 4) and stacking patterns of MTCs from outcrops in other exposed ancient deep-marine basins would provide more data for statistically valid chi-tests on facies associations.

(2) A study of outcrops in the Tremp-Graus Basins could undertake a detailed provenance study to understand where MTDs are sourced, to also include regional mapping of pebble-rich lithostratigraphies of the Montañana Group and Sis palaeovalley conglomerate. This may lead to an improved understanding of the range of controls and transport mechanisms responsible for erosion at the base of MTDs.

(3) Comparative studies from several ancient submarine basins worldwide could provide further outcrop examples and variations of erosion via debris flow processes. The identification of other megascours in ancient deep-marine basin features would also further our understanding of this largely unknown topic.

(4) The thin-section study presented in this thesis is the first dataset of its type collected to specifically investigate the incorporation of sandy material into the matrix of cohesive debris-flow deposits. This has provided some indication of the likely erosive effects of debris flows moving over a sandy substrate in a proximal deep-marine environment. Erosive MTDs cutting into a predominantly muddy substrate will clearly not show an increased sand component and, therefore, a lack of sand cannot necessarily be used to infer little or no erosion. However, an observation in the Ainsa Basin is that many erosively based debrites contain coarser grain sizes in the matrix. Future research could evaluate this further by sampling the underlying eroded

sandstone substrate to document its unique composition and to compare the dominant grain compositions within the overlying debrite. This would enable to see if the unique composition of the underlying substrate is reflected in the composition of the erosively-based debris-flow deposits. Identifying 'graded' debrites that appear to document erosion, may benefit the hydrocarbon industry to determine whether MTDs present in a particular setting eroded during the down-dip translation of sediment. Methods, as presented in this study, could sample debrites from recovered core base to top of and made into thin sections. MTDs in the Buzzard Field are mainly comprised of slumps sourced from syndepositional faulting, or are composed of very muddy debrites, and therefore may not be applicable to cored intervals in the LB4 and UB4 MTDs. Problems encountered in this method include incorrectly identifying individual MTDs within MTCs in core.

(5) An understanding and quantification of the actual process involved that can generate large-scale erosive phenomena is required. Theoretical and experimental studies of erosion could be carried out using computer generated modelling or physical scaled models. Both approaches would be invaluable in re-creating primary erosive mechanisms in submarine systems.

(6) Experimental and numerical studies should further improve the understanding the 'plucking' mechanism at the base of debris flows, which could be developed from the laboratory experiments of researchers such as Major and Iverson (2009), aimed at investigating the formation of negative pressure immediately behind the head of granular flows.

(7) Additional studies of MTD and MTCs in other basins worldwide would provide a wider context for understanding the nature of such deposits. Analysis of other basins similar in scale to the Ainsa Basin would help to document if MTD trends are similar in all basins (e.g., the nature of down-dip pinch-out). Analysis of other deep-marine basins on various scales, such as the Karoo Basin, South Africa, or to undertake further study in the down-dip Jaca and Pamplona Basins. These types of data may show bigger scales of erosion comparable to those observed in seismic dataset.

(8) For any future Buzzard Field analogues, basins that have a similar size and tectonic setting may provide better constraints for predicting the nature and geometry of any MTDs and MTCs.

REFERENCES

ALLEN, P. A., ALLEN, J. R. (2009). Basin analysis: principles and applications, Wiley-Blackwell.

ALVES, T. M., CARTWRIGHT, J. A. (2009). Volume balance of a submarine landslide in the Espírito Santo Basin, offshore Brazil: quantifying seafloor erosion, sediment accumulation and depletion. Earth and Planetary Science Letters, 288, 572-580.

ALVES, T. M. (2010). 3D Seismic examples of differential compaction in mass-transport deposits and their effect on post-failure strata. Marine Geology, 271, 212-224.

ALVES, T. M. CARTWRIGHT, J. A. (2010). The effect of mass-transport deposits on the younger slope morphology, offshore Brazil. Marine and Petroleum Geology, 27, 2027-2036.

ALVES, T. M., LOURENÇO, S. D. (2010). Geomorphologic features related to gravitational collapse: Submarine landsliding to lateral spreading on a Late Miocene-Quaternary slope (SE Crete, eastern Mediterranean). Geomorphology, 123, 13-33.

ALVES, T. M., KURTEV, K., MOORE, G. F., STRASSER, M. (2014). Assessing the internal character, reservoir potential, and seal competence of mass-transport deposits using seismic texture: A geophysical and petrophysical approach. AAPG Bulletin, 98, 793-824.

ALVES., T. M. (2015). Submarine slide blocks and associated soft-sediment deformation in deep-water basins: A review. Marine and Petroleum Geology, 67, 262-285.

ANDRESON, A., BJERRUM, L. (1967). Slides in subaqueous slopes in loose sand and silt. In: Richards, A.F. (ed.), Marine geotechnique, 221–239. Urbana: University of Illinois Press.

AMY, L.A, TALLING, P.J, PEAKALL, J., WYNN, R. ARZOLA THYNNE, R. (2005) Bed geometry used to test recognition criteria of turbidites and (sandy) debrites. Sedimentary Geology., 179, 163–174.

AMY, L.A., TALLING, P.J. (2006). Anatomy of turbidites and linked debrites based on long distance (120 x 30 km) bed correlation, Marnoso Arenacea Formation, northern Apennines, Italy. Sedimentology, 53, 161–212.

ARBUÉS, P., MELLERE, D., FALIVENE, O., FERNÁNDEZ, O., MUÑOZ, J., MARZO, M., GIBERT, J. (2007). Architecture of the Ainsa-1 Quarry channel complex, Spain. Atlas of deep-water outcrops: AAPG Studies in Geology, 56, 330-332.

ARMITAGE, D.A., ROMANS, B.W., COVAULT, J.A., GRAHAM, S.A. (2009) The influence of mass-transport-deposit surface topography on the evolution of turbidite architecture; the Sierra Contreras, Tres Pasos Formation (Cretaceous), southern Chile: Journal of Sedimentary Research, v. 79/5, p. 287-301.

BAAS, J. H., DAVIES, A. G., MALARKEY, J. (2013). Bedform development in mixed sand-mud: The contrasting role of cohesive forces in flow and bed. Geomorphology, 182, 19-32.

BAGNOLD, R. A. (1954). Experiments on a Gravity-Free Dispersion of Large Solid Spheres in a Newtonian Fluid under Shear. Proceedings of the Royal Society of London. Series A. Mathematical and Physical Sciences, 225, 49-63.

BAGNOLD, R. A. (1962). Auto-Suspension of Transported Sediment; Turbidity Currents. Proceedings of the Royal Society of London. Series A, Mathematical and Physical Sciences, 265, 315-319.

BAKKE, K., GJELBERG, J., AGERLIN PETERSEN, S. (2008). Compound seismic modelling of the Ainsa II turbidite system, Spain: Application to deep-water channel systems offshore Angola. Marine and Petroleum Geology, 25, 1058-1073.

BARNOLAS, A., TEIXELL, A. (1994). Platform sedimentation and collapse in a carbonate-dominated margin of a foreland basin (Jaca basin, Eocene, southern Pyrenees). Geology, 22, 1107-1110.

BAYLISS, N., PICKERING, K. T. (2015a). Transition from deep-marine lower-slope erosional channels to proximal basin-floor stacked channel-levee-overbank deposits, and syn-sedimentary growth structures, Middle Eocene Banastón System, Ainsa Basin, Spanish Pyrenees. Earth-Science Reviews, 144, 23-46.

BAYLISS, N. J., PICKERING, K. T. (2015b) Deep-marine structurally confined channelised sandy fans: Middle Eocene Morillo System, Ainsa Basin, Spanish Pyrenees. Earth-Science Reviews, 144, 82-106.

BELLAICHE, G., COUTELLIER, V., DROZ, L. (1986). Seismic evidence of widespread mass transport deposits in the Rhone deep-sea fan: their role in the fan construction. Marine Geology, 71, 327-340.

BERNDT, C., COSTA, S., CANALS, M., CAMERLENGHI, A., DE MOL, B., SAUNDERS, M. (2012). Repeated slope failure linked to fluid migration: the Ana submarine landslide

complex, Eivissa Channel, Western Mediterranean Sea. Earth and Planetary Science Letters, 319, 65-74.

BERNHARDT, A., STRIGHT, L., LOWE, D. R. (2012). Channelized debris-flow deposits and their impact on turbidity currents: The Puchkirchen axial channel belt in the Austrian Molasse Basin. Sedimentology, 59, 2042-2070.

BERGER, C., MCARDELL, B. W., SCHLUNEGGER, F. (2011). Sediment transfer patterns at the Illgraben catchment, Switzerland: Implications for the time scales of debris flow activities. Geomorphology, 125, 421-432.

BOER, P. L., PRAGT, J. S., OOST, A. P. (1991). Vertically persistent sedimentary facies boundaries along growth anticlines and climate-controlled sedimentation in the thrust-sheet top South Pyrenean Tremp-Graus Foreland Basin. Basin Research, 3, 63-78.

BOUMA, A. (1964). Turbidites. Developments in sedimentology, 3, 247-256.

BREIEN, H., BLASIO, F., ELVERHØI, A., HØEG, K., (2008), Erosion and morphology of a debris flow caused by a glacial lake outburst flood, Western Norway: Landslides, v. 5, no. 3, p. 271-280.

BRUNET, M. F. (1986). The influence of the evolution of the Pyrenees on adjacent basins. Tectonophysics, 129, 343-354.

BRYN, P., BERG, K., FORSBERG, C. F., SOLHEIM, A., KVALSTAD, T. J. (2005). Explaining the Storegga Slide. Marine and Petroleum Geology, 22, 11-19.

BULL, S., CARTWRIGHT, J., HUUSE, M. (2009). A review of kinematic indicators from mass-transport complexes using 3D seismic data. Marine and Petroleum Geology, 26, 1132-1151.

CAJA, M., MARFIL, R., GARCIA, D., REMACHA, E., MORAD, S., MANSURBEG, H., AMOROSI, A., MARTÍNEZ-CALVO, C., LAHOZ-BELTRÁ, R. (2010). Provenance of siliciclastic and hybrid turbiditic arenites of the Eocene Hecho Group, Spanish Pyrenees: implications for the tectonic evolution of a foreland basin. Basin Research, 22, 157-180.

CALLOT, P., ODONNE, F., DEBROAS, E.-J., MAILLARD, A., DHONT, D., BASILE, C., HOAREAU, G. (2009). Three-dimensional architecture of submarine slide surfaces and associated soft-sediment deformation in the Lutetian Sobrarbe deltaic complex (Ainsa, Spanish Pyrenees). Sedimentology, 56, 1226-1249.

CAMPBELL, C. V. (1967). Lamina, laminaset, bed and bedset. Sedimentology, 8, 7-26.

CARTER, R. M. (1975). A discussion and classification of subaqueous mass-transport with particular application to grain-flow, slurry-flow, and fluxoturbidites. Earth-Science Reviews, 11, 145-177.

CARTER, L. (2001). A large submarine debris flow in the path of the Pacific deep western boundary current off New Zealand. Geo-Marine Letters, 21, 42-50.

CHOUKROUNE, P., ROURE, F., PINET, B. (1990). Main results of the ECORS Pyrenees profile. Tectonophysics, 173, 411-423.

CHOPRA, S., CASTAGNA, J., PORTNIAGUINE, O. (2006). Seismic resolution and thin-bed reflectivity inversion. CSEG recorder, 31, 19-25.

COLEMAN, J. M., PRIOR, D. B. (1988). Mass Wasting on Continental Margins. Annual Review of Earth and Planetary Sciences, 16, 101-119.

COSSEY, S. (2011). Mass Transport Deposits in the Upper Paleocene Chicontepec Formation, Mexico. SEPM (Society for Sedimentary Geology) Special Publication, 96, 269-277.

COSTA, J. (1984). Physical Geomorphology of Debris Flows. In: Costa, J. & Fleisher, P. J. (eds.) Developments and Applications of Geomorphology. Springer Berlin Heidelberg.

COUSSOT, P., MEUNIER, M. (1996). Recognition, classification and mechanical description of debris flows. Earth-Science Reviews, 40, 209-227.

CRONIN, B., OWEN, D., HARTLEY, A., KNELLER, B. (1998). Slumps, debris flows and sandy deep-water channel systems: implications for the application of sequence stratigraphy to deep water clastic sediments. Journal of the Geological Society, 155, 429-432.

DAKIN, N., PICKERING, K.T, MOHRIG, D., BAYLISS, N. (2013). Channel-like features created by erosive submarine debris flows: Field evidence from the Middle Eocene Ainsa Basin, Spanish Pyrenees. Marine and Petroleum Geology.

DALLA VALLE, G., GAMBERI, F., ROCCHINI, P., MINISINI, D., ERRERA, A., BAGLIONI, L., TRINCARDI, F. (2013). 3D seismic geomorphology of mass transport complexes in a foredeep basin: examples from the Pleistocene of the Central Adriatic Basin (Mediterranean Sea). Sedimentary Geology, 294, 127-141.

DASGUPTA, P. (2003). Sediment gravity flow--the conceptual problems. Earth-Science Reviews, 62, 265-281.

DAVIES, T. R. H. (1986). Large debris flows: A macro-viscous phenomenon. Acta Mechanica, 63, 161-178.

DAVIES, T. R. H. (1990). Debris-flow surges: experimental simulation. Journal of hydrology. New Zealand, 29, 18-46.

DE BLASIO, F. V., ELVERHØI, A., ISSLER, D., HARBITZ, C. B., BRYN, P., LIEN, R. (2004). Flow models of natural debris flows originating from overconsolidated clay materials. Marine Geology, 213, 439-455.

DE BLASIO, F. V., ELVERHØI, A. (2011a). Properties of mass-transport deposits as inferred from dynamic modeling of subaqueous mass wasting: a short review, SEPM Society for Sedimentology Geology.

DE BLASIO, F. V., ELVERHØI, A. (2011b). Properties of mass-transport deposits as inferred from dynamic modelling of subaqueous mass wasting: a short review. Mass Transport Deposits in Deepwater Settings: SEPM Special Publication, 96, 499 - 508.

DE GROOT, M., BOLTON, M., FORAY, P., MEIJERS, P., PALMER, A., SANDVEN, R., SAWICKI, A., TEH, T. (2006). Physics of liquefaction phenomena around marine structures. Journal of waterway, port, coastal, and ocean engineering, 132, 227-243.

DESEGAULX, P., ROURE, F., VILLEIN, A. (1990). Structural evolution of the Pyrenees: tectonic inheritance and flexural behaviour in the continental crust. Tectonophysics, 182, 211-225.

DI CELMA, C., CANTALAMESSA, G., DIDASKALOU, P. LORI, P. (2010). Sedimentology, architecture, and sequence stratigraphy of coarse-grained, submarine canyon fills from the Pleistocene (Gelasian-Calabrian) of the Peri-Adriatic basin, central Italy. Marine and Petroleum Geology, 27, 1340-1365.

DIAZ, J., WEIMER, P., BOUROULLEC, R., DORN, G. (2011) 3-D seismic stratigraphic interpretation of Quaternary Mass-transport Deposits in the Mensa and Thunder Horse intraslope basins, Mississippi Canyon, Northern Deep Gulf of Mexico, U.S.A. In: Shipp, R. C., Weimer, P., Posamentier, H. W. (Eds.). (2011). Mass-transport deposits in deepwater settings (No. 96). SEPM Society for Sedimentary Geology.

DUCASSOU, E., MIGEON, S., CAPOTONDI, L. MASCLE, J. (2012). Run-out distance and erosion of debris-flows in the Nile deep-sea fan system: Evidence from lithofacies and micropalaeontological analyses. Marine and Petroleum Geology.

DONDURUR, D., KÜÇÜK, H.M., ÇIFÇI, G. (2013). Quaternary mass wasting on the western Black Sea margin, offshore of Amasra. Global and Planetary Change, 103, 248-260.

DORÉ, G., ROBBINS, J. (2005). The Buzzard Field. Geological Society, London, Petroleum Geology Conference series, 6, 241-252.

DOTT, R. (1963). Dynamics of subaqueous gravity depositional processes. AAPG Bulletin, 47, 104-128.

DREYER, T., CORREGIDOR, J., ARBUÉS, P., PUIGDEFABREGAS, C. (1999). Architecture of the tectonically influenced Sobrarbe deltaic complex in the Ainsa Basin, northern Spain. Sedimentary Geology, 127, 127-169.

DUXBURY, S., KADOLSKY, D., JOHANSEN, S. (1999) Sequence Stratigraphic Subdivision of the Humber Group in the Outer Moray Firth Area (UKCS, North Sea). Geological Society, London Special Publication. 152.

DYKSTRA, M., KNELLER, B., MILANA, J. P. (2006). Deglacial and postglacial sedimentary architecture in a deeply incised paleovalley-paleofjord‚ÄîThe Pennsylvanian (late Carboniferous) Jejenes Formation, San Juan, Argentina. Geological Society of America Bulletin, 118, 913-937.

DYKSTRA, M., KNELLER, B. (2009). Lateral accretion in a deep-marine channel complex: implications for channelised flow processes in turbidity currents. Sedimentology, 56, 1411-1432.

DYKSTRA, M., GARYFALOU, K., KERTZNUS, V., KNELLER, B., MILANA, J., MOLINARO, M., SZUMAN, M. THOMPSON, P. (2011). Mass-transport deposits: Combining outcrop studies and seismic forward modeling to understand lithofacies distributions, deformation, and their seismic stratigraphic expression. Mass Transport Deposits in Deepwater Settings: SEPM Special Publication, 96, 293-310.

ELLIOTT, T. (2000). Depositional architecture of a sand-rich, channelized turbidite system: the Upper Carboniferous Ross Sandstone Formation, western Ireland. Deep-water Reservoirs of the World, 342-373.

ELVERHØI, A., BREIEN, H., DE BLASIO, F. V., HARBITZ, C. B., PAGLIARDI, M. (2010). Submarine landslides and the importance of the initial sediment composition for run-out length and final deposit. Ocean Dynamics, 60, 1027-1046.

EMBLEY, R. W. (1976). New evidence for occurrence of debris flow deposits in the deep sea. Geology, 4, 371-374.

EMBLEY, R. W. (1980). The role of mass transport in the distribution and character of deep-ocean sediments with special reference to the North Atlantic. Marine Geology, 38, 23-50.

ENOS, P. (1977). Flow regimes in debris flow. Sedimentology, 24, 133-142.

EVANS, D., HARRISON, Z., SHANNON, P., LABERG, J., NIELSEN, T., AYERS, S., HOLMES, R., HOULT, R., LINDBERG, B., HAFLIDASON, H. (2005). Palaeoslides and other mass failures of Pliocene to Pleistocene age along the Atlantic continental margin of NW Europe. Marine and Petroleum Geology, 22, 1131-1148.

FALIVENE, O., ARBUS, P., GARDINER, A., PICKUP, G., MUOZ, J. A., CABRERA, L. (2006). Best practice stochastic facies modeling from a channel-fill turbidite sandstone analog (the Quarry outcrop, Eocene Ainsa basin, northeast Spain). AAPG Bulletin, 90, 1003-1029.

FARIN, M., MANGENEY, A., ROCHE, O. (2013). Fundamental changes of granular flow dynamics, deposition and erosion processes at high slope angles: insights from laboratory experiments. Journal of Geophysical Research: Earth Surface.

FERNÁNDEZ, O., MUÑOZ, J. A., ARBUÉS, P., FALIVENE, O., MARZO, M. (2004). Three-dimensional reconstruction of geological surfaces: An example of growth strata and turbidite systems from the Ainsa basin (Pyrenees, Spain). AAPG Bulletin, 88, 1049-1068.

FARRELL, S. G. (1984). A dislocation model applied to slump structures, Ainsa Basin, South Central Pyrenees. Journal of Structural Geology, 6, 727-736.

FARRELL, S., WILLIAMS, G., ATKINSON, C. (1987). Constraints on the age of movement of the Montsech and Cotiella Thrusts, south central Pyrenees, Spain. Journal of the Geological Society, 144, 907-914.

FERNÁNDEZ, O., MUÑOZ, J. A., ARBUÉS, P., FALIVENE, O., MARZO, M. (2004). Three-dimensional reconstruction of geological surfaces: An example of growth strata and turbidite systems from the Ainsa basin (Pyrenees, Spain). AAPG Bulletin, 88, 1049-1068.

FERNÁNDEZ, O., MUÑOZ, J. A., ARBUÉS, P., FALIVENE, O. (2012). 3D structure and evolution of an oblique system of relaying folds: the Ainsa basin (Spanish Pyrenees). Journal of the Geological Society, 169, 545-559.

FISHER, R. V. (1983). Flow transformations in sediment gravity flows. Geology, 11, 273-274.

FLEMING, R. W., ELLEN, S. D., ALGUS, M. A. (1989). Transformation of dilative and contractive landslide debris into debris flows - an example from Marin County, California. Engineering Geology, 27(1), 201-223.

FONNESU, M., HAUGHTON, P., FELLETTI, F. MCCAFFREY, W. (2015). Short length-scale variability of hybrid event beds and its applied significance. Marine and Petroleum Geology.

FRASER, S.I., ROBINSON, A.M., JOHNSON, H.D., UNDERHILL, J.R., KADOLSKY, D.G.A., CONNELL, R., JOHANNESSEN, P., RAVNAS, R. (2003). Upper Jurassic. In: Evans, D., Graham, C., Armour, A., Bathurst, P. (Eds.), The Millennium Atlas: Petroleum Geology of the Central and Northern North Sea. The Geological Society of London, pp. 157–189.

FREDLUND, D. G., RAHARDJO, H. (1993). Soil mechanics for unsaturated soils, John Wiley & Sons.

FREY-MARTINEZ, J., CARTWRIGHT, J., JAMES, D. (2006). Frontally confined versus frontally emergent submarine landslides: A 3D seismic characterisation. Marine and Petroleum Geology, 23, 585-604.

GAMBERI, F. (2011). Subsurface sediment remobilization as an indicator of regional-scale defluidization within the upper Tortonian Marnoso-arenacea formation (Apenninic foredeep, northern Italy). Basin Research, 22, 562–577.

GAMBERI, F., ROVERE, M., MARANI, M. (2011). Mass-transport complex evolution in a tectonically active margin (Gioia Basin, Southeastern Tyrrhenian Sea). Marine Geology, 279, 98-110.

GAMBOA, D., ALVES, T. M, CARTWRIGHT, J., TERRINHA, P. (2010). MTD distribution on a 'passive' continental margin: The Espirito Santo Basin (SE Brazil) during the Palaeogene. Marine and Petroleum Geology, 27, 1311-1324.

GARDNER, J. V., PRIOR, D. B., FIELD, M. E. (1999). Humboldt slide - a large shear-dominated retrogressive slope failure. Marine Geology, 154, 323-338.

GARTNER, J., SANTI, P., CANNON, S. (2015). Predicting locations of post-fire debris-flow erosion in the San Gabriel Mountains of southern California. Natural Hazards, 77, 1305-1321.

GARZIGLIA, S., MIGEON, S., DUCASSOU, E., LONCKE, L., MASCLE, J. (2008). Mass-transport deposits on the Rosetta province (NW Nile deep-sea turbidite system, Egyptian margin): Characteristics, distribution, and potential causal processes. Marine Geology, 250, 180-198.

GEE, M.J., MASSON, D.G., WATTS, A.B., ALLEN. (1999). The Saharan debris flow: an insight into the mechanics of long runout submarine debris flows. Sedimentology, 46, 317-335.

GEE, M. J., MASSON, D. G., WATTS, A. B., MITCHELL, N. C. (2001). Passage of debris flows and turbidity currents through a topographic constriction: seafloor erosion and deflection of flow pathways. Sedimentology, 48, 1389-1409.

GEE, M.J., GAWTHORPE, R., FRIEDMANN, J. (2005). Giant striations at the base of a submarine landslide. Marine Geology, 214, 287-294.

GEE, M.J., UY, H., WARREN, J., MORLEY, C., LAMBIASE, J. (2007). The Brunei slide: a giant submarine landslide on the North West Borneo Margin revealed by 3D seismic data. Marine Geology, 246, 9-23.

GEORGE, D. L., IVERSON, R. M. (2011). A two-phase debris-flow model that includes coupled evolution of volume fractions, granular dilatancy, and pore-fluid pressure. Italian Journal of Engineering Geology and Environment. In press, DOI, 10, 2011-03.

GHIBAUDO, G. (1992). Subaqueous sediment gravity flow deposits: practical criteria for their field description and classification. Sedimentology, 39, 423–454.

GONG, Z., LANGEREIS, C. G., MULLENDER, T. A. T. (2008). The rotation of Iberia during the Aptian and the opening of the Bay of Biscay. Earth and Planetary Science Letters, 273, 80-93.

GUPTA, K.D., PICKERING, K.T. (2008). Petrography and temporal changes in petrofacies of deep-marine Ainsa-Jaca basin sandstone systems, Early and Middle Eocene, Spanish Pyrenees. Sedimentology, 55, 1083-1114.

HAFLIDASON, H., SEJRUP, H. P., NYGÅRD, A., MIENERT, J., BRYN, P., LIEN, R., FORSBERG, C. F., BERG, K. MASSON, D. (2004). The Storegga Slide: architecture, geometry and slide development. Marine Geology, 213, 201-234.

HAFLIDASON, H., LIEN, R., SEJRUP, H. P., FORSBERG, C. F., BRYN, P. (2005). The dating and morphometry of the Storegga Slide. Marine and Petroleum Geology, 22, 123-136.

HAMPTON, M.A., LEE, H.J., LOCAT, J. (1996). Submarine landslides. Rev. Geophysics., 34, 33-59.

HAUGHTON, P., BARKER, W. MCCAFFREY, W. (2003) 'Linked' debrites in sand-rich turbidite systems – origin and significance. Sedimentology, 50, 459–482.

HAUGHTON, P., DAVIS, C., MCCAFFREY, W., BARKER, S. (2009). Hybrid sediment gravity flow deposits - Classification, origin and significance. Marine and Petroleum Geology, 26, 1900-1918.

HE, Y., XIE, X., KNELLER, B. C., WANG, Z. LI, X. (2013). Architecture and controlling factors of canyon fills on the shelf margin in the Qiongdongnan Basin, northern South China Sea. Marine and Petroleum Geology, 41, 264-276.

HEEZEN, B. C., EWING, W. M. (1952). Turbidity currents and submarine slumps, and the 1929 Grand Banks, Newfoundland, earthquake. American Journal of Science, 250, 849-873.

HENDRY, H.E. (1972). Breccias deposited by mass flow in the Breccia Nappe of the French pre-Alps. Sedimentology, 8, 277–292.

HENRICH, R., HANEBUTH, T.J.J., KRASTEL, S., NEUBERT, N. WYNN, R.B. (2008). Architecture and sediment dynamics of the Mauritania Slide Complex. Marine and Petroleum Geology, 25, 17-33.

HISCOTT, R.N., PICKERING, K.T. BOUMA, A.H. HAND, B.M. KNELLER, B.C. POSTMA, G., SOH, W. (1997a). Basin-floor fans in the North Sea: sequence stratigraphic models vs. sedimentary facies: discussion. American Association of Petroleum Geologists Bulletin, 81, 662–665.

HJELSTUEN, B. O., ELDHOLM, O. FALEIDE, J. I. (2007). Recurrent Pleistocene mega-failures on the SW Barents Sea margin. Earth and Planetary Science Letters, 258, 605-618.

HSU, L., DIETRICH, W. E. SKLAR, L. S. (2008). Experimental study of bedrock erosion by granular flows. Journal of Geophysical Research: Earth Surface, 113, F02001.

HUGGEL, C., HAEBERLI, W., BIERI, D., RICHARDSON, S. (2004). An assessment procedure for glacial hazards in the Swiss Alps. Canadian Geotechnical Journal, 41, 1068-1083.

HUGHES CLARKE, J.E., SHOR, A.N., PIPER, D.J.W., MAYER, L.A. (1990). Large-scale current-induced erosion and deposition in the path of the 1929 Grand Banks turbidity current. Sedimentology, 37, 613–629.

HÜHNERBACK, V., MASSON, D.G. (2004). Landslides in the North Atlantic and its adjacent seas: an analysis of their morphology, setting and behaviour. Marine Geology, 213. 343-362.

HUNGR, O., MORGAN, G., KELLERHALS, R. (1984). Quantitative analysis of debris torrent hazards for design of remedial measures. Canadian Geotechnical Journal, 21, 663-677.

HUNGR, O. (2000). Analysis of debris flow surges using the theory of uniformly progressive flow. Earth Surface Processes and Landforms, 25, 483-495.

HUNGR, O., MCDOUGALL, S. BOVIS, M. (2005). Entrainment of material by debris flows. Debris-flow Hazards and Related Phenomena. Springer Berlin Heidelberg.

HUNGR, O. (2007). Dynamics of rapid landslides. Progress in Landslide Science. Springer.

HUTCHINSON, J., BHANDARI, R. (1971). Undrained loading, a fundamental mechanism of mudflows and other mass movements. Geotechnique, 21, 353-358.

HUYGHE, D., CASTELLTORT, S. B., MOUTHEREAU, F. D. R., SERRA-KIEL, J., FILLEAUDEAU, P.-Y., EMMANUEL, L., BERTHIER, B. Æ., RENARD, M. (2012). Large scale facies change in the middle Eocene South-Pyrenean foreland basin: The role of tectonics and prelude to Cenozoic ice-ages. Sedimentary Geology, 253,Äì254, 25-46.

INGRAM, R. L. (1954). Terminology for the thickness of stratification and parting units in sedimentary rocks. Geological Society of America Bulletin, 65(9), 937-938.

IVERSON, R. M. (1997). The physics of debris flows. Rev. Geophysics., 35, 245-296.

IVERSON, R. M., REID, M. E., LAHUSEN, R. G. (1997). Debris-flow mobilization from landslides Annual Review of Earth and Planetary Sciences, 25, 85-138.

IVERSON, R. M. (2005). Debris-flow mechanics. Debris-flow hazards and related phenomena. Springer.

IVERSON, R. M., REID, M. E., LOGAN, M., LAHUSEN, R. G., GODT, J. W., GRISWOLD, J. P. (2011). Positive feedback and momentum growth during debris-flow entrainment of wet bed sediment. Nature Geoscience, 4, 116-121.

JAKOB, M., HOLM, K., WEATHERLY, H., LIU, S., RIPLEY, N. (2013). Debris flood risk assessment for Mosquito Creek, British Columbia, Canada. Natural Hazards, 65, 1653-1681.

JACKSON, C. A-L., JOHNSON, H. D. (2009). Sustained turbidity currents and their interaction with debrite-related topography; Labuan Island, offshore NW Borneo, Malaysia. Sedimentary Geology, 219, 77-96.

JACKSON, C. A-L., ZAKARIA, A. A., JOHNSON, H. D., TONGKUL, F. CREVELLO, P. D. (2009). Sedimentology, stratigraphic occurrence and origin of linked debrites in the West Crocker Formation (Oligo-Miocene), Sabah, NW Borneo. Marine and Petroleum Geology, 26, 1957-1973.

JACKSON, C. A-L. (2011). Three-dimensional seismic analysis of megaclast deformation within a mass transport deposit; implications for debris flow kinematics. Geology, 39, 203-206.

JACKSON, C. A-L. (2012). The initiation of submarine slope failure and the emplacement of mass transport complexes in salt-related minibasins: A three-dimensional seismic-reflection case study from the Santos Basin, offshore Brazil. Geological Society of America Bulletin, 124, 746-761.

JOHNSON, A. M. (1970). Physical processes in geology: A method for interpretation of natural phenomena; intrusions in igneous rocks, fractures, and folds, flow of debris and ice, Freeman, Cooper.

KANE, I. A., KNELLER, B. C., DYKSTRA, M., KASSEM, A., MCCAFFREY, W. D. (2007). Anatomy of a submarine channel-levee: an example from Upper Cretaceous slope sediments, Rosario Formation, Baja California, Mexico. Marine and Petroleum Geology, 24, 540-563.

KING, P., ILG, B., ARNOT, M., BROWNE, G., STRACHAN, L., CRUNDWELL, M., HELLE, K. (2011). Outcrop and seismic examples of mass-transport deposits from a late Miocene deep-water succession, Taranaki Basin, New Zealand.

KNELLER, B.C (1995). Beyond the turbidite paradigm: physical models for deposition of turbidites and their implications for reservoir prediction. Special publication-Geological Society of London, 94, 31-31.

KNELLER, B.C., BRANNEY, M.J. (1995). Sustained high- density turbidity currents and the deposition of thick massive sands. Sedimentology, 42(4), 607-616.

KRASTEL, S., SCHMINCKE, H.U., JACOBS, C. L., RIHM, R., LE BAS, T.P., ALIBÉS, B. (2001). Submarine landslides around the Canary Islands. Journal of Geophysical Research: Solid Earth, 106, 3977-3997.

LABAUME, P., MUTTI, E., SÉGURET, M., ROSELL, J. (1983a). Mégaturbidites carbonatées du basin turbiditique de l'Eocene inférieur et moyen sud-pyrénéen. Bulletin de la Société Géologique de France, 7 (XXV-6), 927–941.

LABAUME, P., MUTTI, E., SÉGURET, M., ROSELL, J. (1983b). Mégaturbidites carbonates du basin turbiditique de l'Eocene inférieur et moyen sud-pyrénéen. Société Géologique de France, Bulletin, 25, 927–941.

LABAUME, P., SÉGURET, M., SEYVE, C. (1985). Evolution of a turbiditic foreland basin and analogy with an accretionary prism: Example of the Eocene South-Pyrenean basin. Tectonics, 4, 661–685.

LABAUME, P., MUTTI, E. SEGURET, M. (1987). Megaturbidites: A depositional model from the Eocene of the SW-Pyrenean Foreland basin, Spain. Geo-Marine Letters, 7, 91-101.

LABERG, J. S., VORREN, T. O. (1995). Late Weichselian submarine debris flow deposits on the Bear Island Trough Mouth Fan. Marine Geology, 127, 45-72.

LASTRAS, G., CANALS, M., URGELES, R., DE BATIST, M., CALAFAT, A., CASAMOR, J. (2004). Characterisation of the recent BIG'95 debris flow deposit on the Ebro margin, Western Mediterranean Sea, after a variety of seismic reflection data. Marine Geology, 213, 235-255.

LAWRENCE, G. W., CARTWRIGHT, J. A. (2009). The initiation of sliding on the mid Norway margin in the Møre Basin. Marine Geology, 259, 21-35.

LEEDER, M. R. (1999). Sedimentology and sedimentary basins: from turbulence to tectonics, Wiley-Blackwell.

LE FRIANT, A., HARFORD, C., DEPLUS, C., BOUDON, G., SPARKS, R., HERD, R., KOMOROWSKI, J. (2004). Geomorphological evolution of Montserrat (West Indies): importance of flank collapse and erosional processes. Journal of the Geological Society, 161, 147-160.

LEGROS, F. O. (2002). Can dispersive pressure cause inverse grading in grain flows? Journal of Sedimentary Research, 72, 166-170.

LE ROUX, J.P., NIELSEN, S. N., KEMNITZ, H., HENRIQUEZ, Å. (2008). A Pliocene mega-tsunami deposit and associated features in the Ranquil Formation, southern Chile. Sedimentary Geology, 203, 164-180.

LIPMAN, P.W., SISSON, T. W., UI, T., NAKA, J. (2000). In search of ancestral Kilauea volcano. Geology, 28, 1079-1082.

LEGROS, F.O. (2002). Can dispersive pressure cause inverse grading in grain flows? Journal of Sedimentary Research, 72, 166-170.

LOWE, D.R. (1976). Grain flow and grain flow deposits. Journal of Sedimentary Research, 46.

LOWE, D.R. (1979). Sediment gravity flows: their classification and some problems of application to natural flows and deposits.

LOWE, D.R. (1982). Sediment gravity flows: II Depositional models with special reference to the deposits of high-density turbidity currents. Journal of Sedimentary Research, 52.

LOWE, D.R., GUY, M. (2000). Slurry-flow deposits in the Britannia Formation (Lower Cretaceous), North Sea: a new perspective on the turbidity current and debris flow problem. Sedimentology, 47, 31-70.

LUCENTE, C. C. (2004). Topography and palaeogeographic evolution of a middle Miocene foredeep basin plain (Northern Apennines, Italy). Sedimentary Geology, 170, 107-134.

MAGALHAES, P.M., TINTERRI, R. (2011). Stratigraphy and depositional setting of slurry and contained (reflected) beds in theMarnoso-arenacea Formation (Langhian-Serravallian) Northern Apennines, Italy. Sedimentology, 57, 1685–1720

MAJOR, J. J. (1997). Depositional Processes in Large-Scale Debris-Flow Experiments. The Journal of Geology, 105, 345-366.

MAJOR, J. J. (1998). Pebble orientation on large, experimental debris-flow deposits. Sedimentary Geology, 117, 151-164.

MAJOR, J. J., IVERSON, R. M. (1999). Debris-flow deposition: Effects of pore-fluid pressure and friction concentrated at flow margins. Geological Society of America Bulletin, 111, 1424-1434.

MALGESINI, G., TALLING, P.J., HOGG, A.J., ARMITAGE, D., GOATER, A., FELLETTI, F. (2015). Quantitative analysis of submarine-flow deposit shape in the Marnoso-arenacea Formation: what is the signature of hindered settling from dense near-bed layers? Journal of Sedimentary Research, 85, 170–191.

MANGENEY, A., ROCHE, O., HUNGR, O., MANGOLD, N., FACCANONI, G., LUCAS, A. (2010). Erosion and mobility in granular collapse over sloping beds. Journal of Geophysical Research: Earth Surface, 115, F03040.

MARR, J. G., HARFF, P. A., SHANMUGAM, G., PARKER, G. (2001). Experiments on subaqueous sandy gravity flows: The role of clay and water content in flow dynamics and depositional structures. Geological Society of America Bulletin, 113, 1377-1386.

MARZO, M., NIJMAN, W., PUIGDEFÁBREGAS, C. (1988). Architecture of the Castissent fluvial sheet sandstones, Eocene, South Pyrenees, Spain. Sedimentology, 35, 719-738.

MASCLE, A., PUIGDEFÁBREGAS, C. (1998). Tectonics and sedimentation in foreland basins: results from the Integrated Basin Studies project. Geological Society, London, Special Publications, 134, 1-28.

MASLIN, M., MIKKELSEN, N. (1997). Amazon Fan Mass-transport deposits and underlying interglacial deposits: age estimates and fan dynamics

MASLIN, M., MIKKELSEN, N., VILELA, C., HAQ, B. (1998). Sea-level -and gas-hydrate-controlled catastrophic sediment failures of the Amazon Fan. Geology, 26, 1107-1110.

MASSON, D. G., HUGGETT, Q. J., BRUNSDEN, D. (1993). The surface texture of the Saharan Debris Flow deposit and some speculations on submarine debris flow processes. Sedimentology, 40, 583-598.

MATTAUER, M., HENRY, J. (1974). Pyrenees. Geological Society, London, Special Publications, 4, 3-21.

MATTHEWS, J. A., SHAKESBY, R. A., MCEWEN, L. J., BERRISFORD, M. S., OWEN, G., BEVAN, P. (1999). Alpine Debris-Flows in Leirdalen, Jotunheimen, Norway, with Particular Reference to Distal Fans, Intermediate-Type Deposits, and Flow Types. Arctic, Antarctic, and Alpine Research, 31, 421-435.

MAYALL, M., JONES, E., CASEY, M. (2006). Turbidite channel reservoirs - key elements in facies prediction and effective development. Marine and Petroleum Geology, 23, 821-841.

MCADOO, B., PRATSON, L., ORANGE, D. (2000). Submarine landslide geomorphology, US continental slope. Marine Geology, 169, 103-136.

MCGILVERY, T., COOK, D. L. (2003) The influence of local gradients on accommodation space and linked depositional elements across a stepped slope profile, offshore Brunei. Gulf Coast Section SEPM Foundation 23rd Annual Bob F. Perkins Research Conference Proceeding, 2003. SEPM, 23-55.

MCMURTRY, G., WATTS, P., FRYER, G., SMITH, J., IMAMURA, F. (2004). Giant landslides, mega-tsunamis, and paleo-sea level in the Hawaiian Islands. Marine Geology, 203, 219-233.

MCCOY, S. W., TUCKER, G. E., KEAN, J. W., COE, J. A. (2013). Field measurement of basal forces generated by erosive debris flows. Journal of Geophysical Research: Earth Surface Processes.

MECKEL, L.D.III. (2011). Reservoir characteristics and classification of sand-prone submarine mass-transport deposits. In: Shipp, R. C., Weimer, P., Posamentier, H. W. (Eds.). (2011). Mass-transport deposits in deepwater settings (No. 96). SEPM Society for Sedimentary Geology.

MICHAEL, N. A., WHITTAKER, A. C., CARTER, A., ALLEN, P. A. (2014). Volumetric budget and grain-size fractionation of a geological sediment routing system: Eocene Escanilla Formation, south-central Pyrenees. Geological Society of America Bulletin, 126, 585-599.

MIDDLETON, G. V., HAMPTON, M. A. (1973). Part I. Sediment gravity flows: mechanics of flow and deposition. 1-38.

MIDDLETON, A. P., FREESTONE, I. C., LEESE, M., (1985). Textural analysis of ceramic thin sections: evaluation of grain sampling procedures: Archaeometry, v. 27, no. 1, p. 64-74.

MIDDLETON, G. V. (1993). Sediment Deposition from Turbidity Currents. Annual Review of Earth and Planetary Sciences, 21, 89-114.

MILLINGTON, J.J, CLARK, J.D. (1995a). Submarine canyon and associated base-of-slope sheet system: the Eocene Charo-Arro system, south-central Pyrenees. In: Pickering, K.T., Hiscott, R.N., Kenyon, N.H., Ricci Lucchi, F. & Smith, R.D.A. (eds), Atlas of Deep-water Environments: Architectural Style in Turbidite Systems, 150–156. London: Chapman and Hall.

MILLINGTON, J.J., CLARK, J.D. (1995b). The Charo/Arro canyon-mouth sheet system, south-central Pyrenees, Spain; a structurally influenced zone of sediment dispersal. Journal of Sedimentary Research, 65, 443-454.

MILNE, J. (1897). Sub-Oceanic Changes. The Geographical Journal, 10, 129-146.

MINISINI, D., TRINCARDI, F., ASIOLI, A., CANU, M. FOGLINI, F. (2007). Morphologic variability of exposed mass-transport deposits on the eastern slope of Gela Basin (Sicily channel). Basin Research, 19, 217-240.

MINISINI, D., TRINCARDI, F. (2009). Frequent failure of the continental slope: the Gela Basin (Sicily Channel). Journal of Geophysical Research: Earth Surface (2003‚A2012), 114.

MINSHULL, T.A. (2012). Combinations of volcanic-flank and seafloor-sediment failure offshore Montserrat, and their implications for tsunami generation. Earth and Planetary Science Letters, 319, 228-240.

MOCHALES, T., CASAS, A. M., PUEYO, E. L., BARNOLAS, A. (2012). Rotational velocity for oblique structures (Boltaña anticline, southern Pyrenees). Journal of Structural Geology, 35, 2-16.

MOHRIG, D., ELLIS, C., PARKER, G., WHIPPLE, K. X., HONDZO, M. (1998). Hydroplaning of subaqueous debris flows. Geological Society of America Bulletin, 110, 387-394.

MOHRIG, D., ELVERHØI, A. PARKER, G. (1999). Experiments on the relative mobility of muddy subaqueous and subaerial debris flows, and their capacity to remobilize antecedent deposits. Marine Geology, 154, 117-129.

MOHRIG, D., MARR, J. G. (2003). Constraining the efficiency of turbidity current generation from submarine debris flows and slides using laboratory experiments. Marine and Petroleum Geology, 20, 883-899.

MOORE, J., CLAGUE, D., LUDWIG, K., MARK, R. (1990). Subsidence and volcanism of the Haleakala Ridge, Hawaii. Journal of Volcanology and Geothermal Research, 42, 273-284.

MOSCARDELLI, L., WOOD, L., MANN, P. (2006). Mass-transport complexes and associated processes in the offshore area of Trinidad and Venezuela. AAPG Bulletin, 90, 1059-1088.

MOSCARDELLI, L., WOOD, L. (2008). New classification system for mass transport complexes in offshore Trinidad. Basin Research, 20, 73-98.

MULDER, T., ALEXANDER, J. (2001). The physical character of subaqueous sedimentary density flows and their deposits. Sedimentology, 48, 269-299.

MUÑOZ, J. A. (1992). Evolution of a continental collision belt: ECORS-Pyrenees crustal balanced cross-section. Thrust tectonics. Springer.

MUÑOZ, J. A., MCCLAY, K., POBLET, J. (1994). Synchronous extension and contraction in frontal thrust sheets of the Spanish Pyrenees. Geology, 22, 921-924.

MUÑOZ, J. A., BEAMUD, E., FERNÁNDEZ, O., ARBUÉS, P., DINARÈS-TURELL, J., POBLET, J. (2013). The Ainsa Fold and thrust oblique zone of the central Pyrenees: Kinematics of a curved contractional system from paleomagnetic and structural data. Tectonics, 32, 1142-1175.

MUTTI, E., RICCI LUCCHI, F. (1972). Le torbiditi dell'Appennino settentrionale: introduzione all'analisi di facies. Memoirs Of The Geological Society, Italy, 11, 161-199. (1978 English translation by T.H. Nilsen, International Geology Review, 20, 125–166.)

MUTTI, E. (1977). Distinctive thin-bedded turbidite facies and related depositional environments in the Eocene Hecho Group (South-central Pyrenees, Spain).

MUTTI, E. (1983). The Hecho Eocene submarine fan system, south-central Pyrenees, Spain. Geo-Marine Letters, 3, 199-202.

NARDIN, T. R., HEIN, F., GORSLINE, D., EDWARDS, B. (1979). A review of mass movement processes, sediment and acoustic characteristics, and contrasts in slope and base-of-slope systems versus canyon-fan-basin floor systems. In: Geology of continental slopes, Doyle, L. J.

NARUSE, H., OTSUBO, M. (2011). Heterogeneity of internal structures in a mass-transport deposits, Upper Cretaceous to Paleocene Akkeshi Formation, Hokkaido Island, Northern Japan. Mass-Transport Deposits in Deepwater settings. SEPM Special publication No. 96. P 279-290.

NELSON, C. H., ESCUTIA, C., DAMUTH, J. E., TWICHELL, D. C. (2011). Interplay of mass-transport and turbidite-system deposits in different active tectonic and passive continental margin settings: external and local controlling factors. Mass-transport deposits in deep-water settings. SEPM Spec Publication, 96, 39-66.

NEUWERTH, R., SUTER, F., GUZMAN, C. A., GORIN, G. E. (2006). Soft-sediment deformation in a tectonically active area: The Plio-Pleistocene Zarzal Formation in the Cauca Valley (Western Colombia). Sedimentary Geology, 186, 67-88.

NICHOLS, G. J. (1987). The Structure and Stratigraphy of the Western External Sierras of the Pyrenees, Northern Spain. Geological Journal, 22, 245-259.

NIJMAN, W., NIO, S.D (1975). The Eocene Montanana delta (Tramp-Graus Basin, provinces of Lerida and Huesca, Southern Pyrenees, N.Spain). In: Sedimentary evolution of the Paleogene, South Pyrenean Basin. Eds Rosell, J., Puigdefábregas, C.

NIJMAN, W. (1998). Cyclicity and basin axis shift in a piggyback basin: towards modelling of the Eocene Tremp-Ager Basin, South Pyrenees, Spain. Special publication - Geological Society of London, 134, 135-162.

NYGÅRD, A., SEJRUP, H. P., HAFLIDASON, H., KING, E. L. (2002). Geometry and genesis of glaciogenic debris flows on the North Sea Fan: TOBI imagery and deep-tow boomer evidence. Marine Geology, 188, 15-33.

OGATA, K., MUTTI, E., PINI, G. A., TINTERRI, R. (2012). Mass transport-related stratal disruption within sedimentary melanges: Examples from the northern Apennines (Italy) and south-central Pyrenees (Spain). Tectonophysics, 568‚Äì569, 185-199.

OLAFIRANYE, K., JACKSON, C. A-L. HODGSON, D. M. (2013). The role of tectonics and mass-transport complex emplacement on upper slope stratigraphic evolution: A 3D seismic case study from offshore Angola. Marine and Petroleum Geology, 44, 196-216.

OMOSANYA, K. D. O. ALVES, T. M. (2013a). Ramps and flats of mass-transport deposits (MTDs) as markers of seafloor strain on the flanks of rising diapirs (Espírito Santo Basin, SE Brazil). Marine Geology, 340, 82-97.

OMOSANYA, K. O. ALVES, T. M. (2013b). A 3-dimensional seismic method to assess the provenance of Mass-Transport Deposits (MTDs) on salt-rich continental slopes (Espírito Santo Basin, SE Brazil). Marine and Petroleum Geology, 44, 223-239.

PAYROS, A., PUJALTE, V., ORUE-ETXEBARRIA, X. (1999). The South Pyrenean Eocene carbonate megabreccias revisited: new interpretation based on evidence from the Pamplona Basin. Sedimentary Geology, 125, 165-194.

PAYROS, A., ORUE-ETXEBARRIA, X., PUJALTE, V. (2006). Covarying sedimentary and biotic fluctuations in Lower, Middle Eocene Pyrenean deep-sea deposits: palaeoenvironmental implications. Palaeogeography, Palaeoclimatology, Palaeoecology, 234, 258-276.

PARSONS, J.D., WHIPPLE, K. X., SIMONI, A. (2001). Experimental study of the grain-flow, fluid-mud transition in debris flows. The Journal of Geology, 109, 427-447.

PARSONS, J.D., FRIEDRICHS, C.T., TRAYKOVSKI, P.A., MOHRIG, D., IMRAN, J., SYVITSKI, J.P.M., PARKER, G., PUIG, P., BUTTLES, J. L., GARCÍA, M.H. (2007). The Mechanics of Marine Sediment Gravity Flows, Blackwell Publishing Ltd.

PAYROS, A., TOSQUELLA, J., BERNAOLA, G., DINARTURELL, J., ORUE-ETXEBARRIA, X., PUJALTE, V. (2009). Filling the North European Early/Middle Eocene (Ypresian/Lutetian) boundary gap: Insights from the Pyrenean continental to deep-marine record. Palaeogeography, Palaeoclimatology, Palaeoecology, 280, 313-332.

PEAKALL, J., AMOS, K. J., KEEVIL, G. M., WILLIAM BRADBURY, P., GUPTA, S. (2007). Flow processes and sedimentation in submarine channel bends. Marine and Petroleum Geology, 24, 470-486.

PHILLIPS, E. (2006). Micromorphology of a debris flow deposit: evidence of basal shearing, hydrofracturing, liquefaction and rotational deformation during emplacement. Quaternary Science Reviews, 25, 720-738.

PIERSON, T. C. (1980). Erosion and deposition by debris flows at Mt Thomas, North Canterbury, New Zealand. Earth Surface Processes, 5, 227-247.

PICKERING, K.T, STOW, D.A.V., WATSON, M., HISCOTT, R. (1986). Deep-water facies, processes and models: a review and classification scheme for modern and ancient sediments. Earth-Science Reviews, 23, 75-174.

PICKERING, K.T., HISCOTT, R.N., HEIN, F.J. (1989). Deep-marine environments: clastic sedimentation and tectonics, Allen & Unwin Australia.

PICKERING, K., CLARK, J., SMITH, R., HISCOTT, R., LUCCHI, F. R., KENYON, N. (1995). Architectural element analysis of turbidite systems, and selected topical problems for sand-prone deep-water systems. Atlas of deep-water environments. Springer.

PICKERING, K.T., SOUTER, C., OBA, T., TAIRA, A., SCHAAF, M., PLATZMAN, E. (1999). Glacio-eustatic control on deep-marine clastic forearc sedimentation, Pliocene – mid-Pleistocene (c. 1180-600 ka) Kazusa Group, SE Japan. Journal of the Geological Society (London), 156, 125–136.

PICKERING, K.T., CORREGIDOR, J. (2000). 3D reservoir scale study of Eocene confined submarine fans, south central Spanish Pyrenees. Weimer, P., RM Slatt, J. Coleman, NC Rosen, H. Nelson, AH Bouma, MJ Styzen, and DT Lawrence, DT Deep Water Reservoirs of the World, 776-781.

PICKERING, K.T., CORREGIDOR, J. (2005). Mass-Transport Complexes (MTCs) and Tectonic Control on Basin-Floor Submarine Fans, Middle Eocene, South Spanish Pyrenees. Journal of Sedimentary Research, 75, 761-783.

PICKERING, K.T., BAYLISS, N. J. (2009). Deconvolving tectono-climatic signals in deep-marine siliciclastics, Eocene Ainsa basin, Spanish Pyrenees: Seesaw tectonics versus eustasy. Geology, 37, 203-206.

PICKERING, K.T., CANTALEJO, B. (2015). Deep-marine environments of the Middle Eocene Upper Hecho Group, Spanish Pyrenees: Introduction. Earth-Science Reviews, 144, 1-9.

PICKERING, K.T., CORREGIDOR, J., CLARK, J.D. (2015). Architecture and stacking patterns of lower-slope and proximal basin-floor channelised submarine fans, Middle Eocene Ainsa System, Spanish Pyrenees: An integrated outcrop‚Äìsubsurface study. Earth-Science Reviews, 144, 47-81.

PICKERING, K.T., HISCOTT, R. N. (2015). Deep Marine Systems: Processes, Deposits, Environments, Tectonics and Sedimentation, Wiley-Blackwell.

PIPER, D.J.W., PE-PIPER, G., TUBRETT, M., TRIANTAFYLLIDIS, S., STRATHDEE, G. (2012) Detrital zircon geochronology and polycyclic sediment sources, Cretaceous Scotian Basin, southeastern Canada: Canadian Journal of Earth Sciences, v. 49, p. 1540-1557.

POHL, F., MCCANN, T. (2014). Architecture and depositional development of the Eocene deep-marine Morillo and Coscojuela Formations, Aínsa Basin, Spain. Geological Journal, 49, 221-238.

POSAMENTIER, H.W., KOLLA, V. (2003). Seismic geomorphology and stratigraphy of depositional elements in deep-water settings. Journal of Sedimentary Research, 73, 367-388.

POSAMENTIER, H.W., WALKER, R.G. (2006) Deep-water turbidites and submarine fans: Special Publication Society for Sedimentary Geology, v. 84, p. 399-520.

POSAMENTIER, H.W, MARTINSEN, O. (2011). The character and genesis of submarine mass-transport deposits: insight from outcrop and 3D seismic data. Mass-transport deposits in deepwater settings. SEPM Special Publication, 96, 7-38.

POSTMA, G. (1986). Classification for sediment gravity-flow deposits based on flow conditions during sedimentation. Geology, 14, 291-294.

PRIOR, D. B., COLEMAN, J. M. (1979). Submarine landslides-geometry and nomenclature, Coastal Studies Institute, Center for Wetland Resources, Louisiana State Univ.

PRIOR, D. B., BORNHOLD, B. D., JOHNS, M. W. (1984). Depositional Characteristics of a Submarine Debris Flow. The Journal of Geology, 92, 707-727.

PUIGDEFÀBREGAS, C., SAMSO, J.M., SERRA-KIEL, J. and TOSQUELLA, J. (1985) Facies analysis and faunal assemblages of the Roda Sandstone Formation, Eocene of the southern Pyrenees. In: VI European Regional Meeting, Lerida, Spain. IAS abstracts and poster abstracts, pp. 639-642.

PUIGDEFÀBREGAS, C., SOUQUET, P. (1986). Tecto-sedimentary cycles and depositional sequences of the Mesozoic and Tertiary from the Pyrenees. Tectonophysics, 129, 173-203.

PUIGDEFÀBREGAS, C., MUÑOZ, J., VERGÉS, J. (1992). Thrusting and foreland basin evolution in the southern Pyrenees. Thrust tectonics, 247-254.

RASMUSSEN, T. L., THOMSEN, E., SLUBOWSKA, M. A., JESSEN, S., SOLHEIM, A., KOÇ, N. (2007). Paleoceanographic evolution of the SW Svalbard margin (76 N) since 20,000 14 C yr BP. Quaternary Research, 67, 100-114.

RAY, F.M., PINNOCK, S.J., KATAMISH, H., TURNBULL, J.B. (2010). The Buzzard Field: anatomy of the reservoir from appraisal to production. Geological Society, London, Petroleum Geology Conference series, 7, 369-386.

REMACHA, E., FERNÁNDEZ, L.P. (2003). High-resolution correlation patterns in the turbidite systems of the Hecho Group (South-Central Pyrenees, Spain). Marine and Petroleum Geology, 20, 711-726.

RICCI-LUCCHI, F. (1975). Depositional cycles in two turbidite formations of northern Apennines. Journal of Sedimentary Research, 45, 3-43.

RICHARDS, M., BOWMAN, M., READING, H. (1998). Submarine-fan systems I: characterization and stratigraphic prediction. Marine and Petroleum Geology, 15, 689-717.

RICHARDSON, S.E., DAVIES, R.J., ALLEN, M.B., GRANT, S.F. (2011). Structure and evolution of mass transport deposits in the South Caspian Basin, Azerbaijan. Basin Research, 23, 702-719.

SANTI, P.M., DEWOLFE, V.G., HIGGINS, J.D., CANNON, S.H., GARTNER, J.E. (2008). Sources of debris flow material in burned areas. Geomorphology, 96, 310-321.

SASSA, K., HUI WANG, G. (2005). Mechanism of landslide-triggered debris flows: Liquefaction phenomena due to the undrained loading of torrent deposits. Debris-flow hazards and related phenomena. Springer.

SAWYER, D.E., FLEMINGS, P.B., DUGAN, B., GERMAINE, J.T. (2009). Retrogressive failures recorded in mass transport deposits in the Ursa Basin, Northern Gulf of Mexico. Journal of Geophysical Research: Solid Earth (1978-2012), 114.

SAWYER, D.E., FLEMINGS, P.B., BUTTLES, J., MOHRIG, D. (2012). Mudflow transport behavior and deposit morphology: Role of shear stress to yield strength ratio in subaqueous experiments. Marine Geology, 307, 28-39.

SCHELLART, W. (2002). Alpine deformation at the western termination of the Axial Zone, Southern Pyrenees. Reconstruction of the Evolution of the Alpine-Himalayan Orogen: Journal of the Virtual Explorer, 7, 35-55.

SCHÜRCH, P., DENSMORE, A. L., ROSSER, N. J., MCARDELL, B. W. (2011). Dynamic controls on erosion and deposition on debris-flow fans. Geology, 39, 827-830.

SCOTCHMAN, J., BOWN, P., PICKERING, K., BOUDAGHER-FADEL, M., BAYLISS, N. ROBINSON, S. (2014). A new age model for the middle Eocene deep-marine Ainsa Basin, Spanish Pyrenees. Earth-Science Reviews, 144, 10-22.

SCOTCHMAN, J. I., PICKERING, K. T., SUTCLIFFE, C., DAKIN, N. ARMSTRONG, E. (2015). Milankovitch cyclicity within the middle Eocene deep-marine Guaso System, Ainsa Basin, Spanish Pyrenees. Earth-Science Reviews, 144, 107-121.

SHANMUGAM, G., MOIOLA, R. J. (1988). Submarine fans: Characteristics, models, classification, and reservoir potential. Earth-Science Reviews, 24, 383-428.

SHANMUGAM, G. (1996). High-Density Turbidity Currents: Are They Sandy Debris Flows?: PERSPECTIVES. Journal of Sedimentary Research, 66.

SHANMUGAM, G. (2002). Ten turbidite myths. Earth-Science Reviews, 58, 311-341.

SHANMUGAM, G. (2006). Deep-water processes and facies models: Implications for sandstone petroleum reservoirs, Elsevier Science.

SHERRIF, R.E. (1992). Vertical and lateral seismic resolution and attenuation: Part 7. Geophysical Methods. *In*: ME 10; Development Geology Reference Manual. 388-389.

SHIPP, C., WEIMER, P., POSAMENTIER, H. (2011) Mass-transport deposits in deep-water settings: An introduction. Mass-transport deposits in deep-water settings. SEPM Special Publication, 96, 3-6.

SHULTZ, A. W. (1984). Subaerial debris-flow deposition in the upper Paleozoic Cutler Formation, western Colorado. Journal of Sedimentary Research, 54.

SINGH, K. A. (2010). Geometry and nature of modern and ancient mass transport deposits worldwide.

SOHN, Y.K., RHEE, C.W., KIM, B.C. (1999). Debris flow and Hyperconcentrated flood-flow deposits in an alluvial fan, northwestern part of the Cretaceous Yongdong basin, Central Korea. The Journal of Geology, 107, 111-132.

SOHN, Y.K., CHOE, M., JO, H. (2002). Transition from debris flow to hyperconcentrated flow in a submarine channel (the Cretaceous Cerro Toro Formation, southern Chile). Terra Nova, 14, 405-415.

STEVENSON, C.J., TALLING, P.J., WYNN, R.B., MASSON, D.G., HUNT, J.E., FRENZ, M., AKHMETZHANHOV, A., CRONIN, B.T. (2013). The flows that left no trace: Very large-volume turbidity currents that bypassed sediment through submarine channels without eroding the sea floor. Marine and Petroleum Geology, 41, 186-205.

STEVENSON, C. J., JACKSON, C. A-L., HODGSON, D. M., HUBBARD, S. M., EGGENHUISEN, J. T. (2015). Deep-water sediment bypass. Journal of Sedimentary Research, 85, 1058-1081.

STOCK, J.D, DIETRICH, W.E. (2003). Valley incision by debris flows: Evidence of a topographic signature. Water Resources Research, 39, 1089.

STOCK, J. D., DIETRICH, W.E. (2006). Erosion of steepland valleys by debris flows. Geological Society of America Bulletin, 118, 1125-1148.

STOW, D.A.V., MAYALL, M. (2000). Deep-water sedimentary systems: New models for the 21st Century. Marine and Petroleum Geology, v. 17, p. 125-135.

SUMNER, E. J., TALLING, P. J., AMY, L. A. (2009). Deposits of flows transitional between turbidity current and debris flow. Geology, 37, 991-994.

SUMNER, E. J., PEAKALL, J., PARSONS, D. R., WYNN, R. B., DARBY, S. E., DORRELL, R. M., MCPHAIL, S. D., PERRETT, J., WEBB, A., WHITE, D. (2013). First direct measurements of hydraulic jumps in an active submarine density current. Geophysical Research Letters, 40, 2013GL057862.

SUTCLIFFE, C., PICKERING, K.T. (2009). End-signature of deep-marine basin-fill, as a structurally confined low-gradient clastic system: the Middle Eocene Guaso system, South-central Spanish Pyrenees. Sedimentology, 56, 1670-1689.

SCHWAB, W. C., LEE, H. J. & TWICHELL, D. C. (1993). Submarine landslides; selected studies in the US Exclusive Economic Zone. USGPO; US Geological Survey, Map Distribution.

SWIFT, D., HUDELSON, P., BRENNER, R., THOMPSON, P. (1987). Shelf construction in a foreland basin: storm beds, shelf sandbodies, and shelf-slope depositional sequences in the Upper Cretaceous Mesaverde Group, Book Cliffs, Utah. Sedimentology, 34, 423-457.

TAKAHASHI, T. (1981). Debris flow. Annual review of fluid mechanics, 13, 57-77.

TAKAHASHI, T. (2007). Debris flow: mechanics, prediction and countermeasures, Taylor & Francis.

TALLING, P.J, AMY, L., WYNN, R., PEAKALL, J., ROBINSON, M. (2004) Beds comprising debrite sandwiched with co-genetic turbidite: origin and widespread occurrence in distal depositional environments. Sedimentology, 51, 163–194.

TALLING, P.J, WYNN, R., MASSON, D., FRENZ, M., CRONIN, B., SCHIEBEL, R., AKHMETZHANOV, A., DALLMEIER-TIESSEN, S., BENETTI, S., WEAVER, P. (2007). Onset of submarine debris flow deposition far from original giant landslide. Nature, 450, 541-544.

TALLING, P.J., MASSON, D.G., SUMNER, E.J., MALGESINI, G. (2012). Subaqueous sediment density flows: Depositional processes and deposit types. Sedimentology, 59, 1937-2003.

TERRY, R. D., CHILLINGAR, G. V. (1989). Comparison chart for estimating percentage composition. AGI Data Sheets for Geology in the Field, Laboratory, and Office: American Geological Institute, Alexandria, Virginia, 23-21.

TONIOLO, H., HARFF, P., MARR, J., PAOLA, C., PARKER, G. (2003). Experiments on reworking by successive unconfined subaqueous and subaerial muddy debris flows. Journal of Hydraulic Engineering, 130, 38-48.

TRIPSANAS, E. K., PIPER, D. J. W., JENNER, K. A., BRYANT, W. R. (2008). Submarine mass-transport facies: new perspectives on flow processes from cores on the eastern North American margin. Sedimentology, 55, 97-136.

UENZELMANN-NEBEN, G., GOHL, K. (2012). Amundsen Sea sediment drifts: Archives of modifications in oceanographic and climatic conditions. Marine Geology, 299, 51-62.

UNDERHILL, J., PARTINGTON, M. (1993). Jurassic thermal doming and deflation in the North Sea: implications of the sequence stratigraphic evidence. Geological Society, London, Petroleum Geology Conference series. Geological Society of London, 337-345.

VANDINE, D. F., BOVIS, M. (2002). History and Goals of Canadian Debris Flow Research, A Review. Natural Hazards, 26, 67-80.

VAN DER MERWE, W.C., HODGSON, D.M., FLINT, S.S. (2009). Widespread syn-sedimentary deformation on a muddy deep-water basin-floor: the Vischkuil Formation (Permian), Karoo Basin, South Africa. Basin Research, 21, 389-406.

VAN DER MERWE, W.C., FLINT, S.S., HODGSON, D.M. (2010). Sequence stratigraphy of an argillaceous, deep-water basin-plain succession: Vischkuil Formation (Permian), Karoo Basin, South Africa. Marine and Petroleum Geology, 27, 321-333.

VAN DER MERWE, W.C., HODGSON, D.M., FLINT, S.S (2011). Origin and terminal architecture of a submarine slide: a case study from the Permian Vischkuil Formation, Karoo Basin, South Africa. Sedimentology, 58, 2012-2038.

VERGÉS, J., MILLÁN, H., ROCA, E., MUÑOZ, J. A., MARZO, M., CIRÉS, J., BEZEMER, T. D., ZOETEMEIJER, R., CLOETINGH, S. (1995). Eastern Pyrenees and related foreland basins: pre-, syn- and post-collisional crustal-scale cross-sections. Marine and Petroleum Geology, 12, 903-915.

VINCENT, S.J., ELLIOTT, T. (1997). Long-lived transfer-zone palaeovalleys in mountain belts: An example from the Tertiary of the Spanish Pyrenees. Journal of Sedimentary Research, 67.

VINCENT, S.J. (1999). The role of sediment supply in controlling alluvial architecture: an example from the Spanish Pyrenees. Journal of the Geological Society, 156, 749-759.

VINCENT, S.J. (2001). The Sis palaeovalley: a record of proximal fluvial sedimentation and drainage basin development in response to Pyrenean mountain building. Sedimentology, 48, 1235-1276.

VISSERS, R. L. M., MEIJER, P. T. (2012). Mesozoic rotation of Iberia: Subduction in the Pyrenees? Earth-Science Reviews, 110, 93-110.

VIZCAINO, A., GRÁCIA, E., PALLÁS, R., GARCIA-ORELLANO, J., ESCUTIO, C., CASAS, D., WILLMOTT, V., DIEZ, S., ASIOLI, A., DAÑOBEITIA, J. (2006). Sedimentology, physical properties and age of mass transport deposits associated with the Marques de Pombal Fault, Southwest Portuguese Margin. Norsk Geologisk Tidsskrift, 86, 177.

WALKER, R.G. (1970). Review of the geometry and facies organisation of turbidites and turbidite-bearing basins. In: Lajoie, J. (ed.), Flysch Sedimentology in North America, 219–251. Geological Association of Canada. Special Paper, 7. Toronto: Business & Economic Service.

WALKER, J. R., MASSINGILL, J. V. (1970). Slump features on the Mississippi Fan, northeastern Gulf of Mexico. Geological Society of America Bulletin,81(10), 3101-3108.

WALKER, R.G. (1975a). Generalized facies model for resedimented conglomerates of turbidite association. Geological Society of America Bulletin, 86, 737–748.

WALKER, R.G. (1975b). Upper Cretaceous resedimented conglomerates at Wheeler Gorge, California: description and field guide. Journal of Sedimentary Petrology, 45, 105–112.

WATT, S. F. L., TALLING, P. J., VARDY, M. E., HELLER, V., HÜHNERBACH, V., URLAUB, M., SARKAR, S., MASSON, D. G., HENSTOCK, T. J., MINSHULL, T. A. (2012). Combinations of volcanic-flank and seafloor-sediment failure offshore Montserrat, and their implications for tsunami generation. Earth and Planetary Science Letters, 319, 228-240.

WENTWORTH, C.K. (1922). A scale of grade and class terms for clastic sediments. The Journal of Geology, 377-392.

WILSON, C. K., LONG, D., BULAT, J. (2004). The morphology, setting and processes of the Afen Slide. Marine Geology, 213, 149-167.

WOODCOCK, N. H. (1979). Sizes of submarine slides and their significance. Journal of Structural Geology, 1, 137-142.

ZANKL, H. (1969). Structural and Textural Evidence of Early Lithification in Fine-Grained Carbonate Rocks. Sedimentology, 12, 241-256.

ZHAO, F., ALVES, T.M., LI, W., WU, S. (2015). Recurrent slope failure enhancing source rock burial depth and seal unit competence in the Pearl River Mouth Basin, offshore South China Sea. Tectonophysics 643, pp. 1-7. 10.1016/j.tecto.2014.12.006 file

ZICHENG, K. (1987). The mechanical analysis of the generation of debris flow Journal of Mountain Research, 4, 008.

APPENDIX A

Papers published from this research thesis

(1) Dakin, N., Pickering, K., Mohrig, D., Bayliss, N. (2013). Channel-like features created by erosive submarine debris flows: Field evidence from the Middle Eocene Ainsa Basin, Spanish Pyrenees. Marine and Petroleum Geology. 41, 62-71.

(2) Scotchman, J. I., Pickering, K. T., Sutcliffe, C., Dakin, N., Armstrong, E (2015). Milankovitch cyclicity within the middle Eocene deep-marine Guaso System, Ainsa Basin, Spanish Pyrenees. Earth-Science Reviews, 144, 107-121.